Arylbenzamide and Arylcarboxamide Derivatives as Modulators of Amyloid-Beta Aggregation

by

Yusheng Zhao

A thesis

presented to the University of Waterloo

in fulfillment of the

thesis requirement for the degree of

Doctor of Philosophy

in

Pharmacy

Waterloo, Ontario, Canada, 2024

© Yusheng Zhao 2024

Examining Committee Membership

The following served on the Examining Committee for this thesis. The decision of the Examining Committee is by majority vote.

External Examiner	NAME Kagan Kerman Title Professor
Supervisor(s)	NAME Praveen Rao Perampalli Nekkar Title Associate Professor
Internal Member	NAME Mónica Barra Title Associate Professor
Internal Member	NAME Emmanuel Ho Title Associate Professor
Internal-external Member	NAME John Mielke Title Associate Professor

Author's Declaration

I hereby declare that I am the sole author of this thesis. This is the true copy of the thesis, including any required final revisions, as accepted by my examiners.

I understand that my thesis may be made electronically available to the public.

Abstract

Alzheimer's disease (AD) is a complex neurodegenerative disease with increasing incidence and prevalence globally. The current AD therapies based on small molecules offer only symptomatic relief and are not curative therapies. The recently launched anti-amyloid monoclonal antibodies hold promise although these are new to the market and their long-term benefits and potential disease-modifying effects are unknown. The global increases in the aging population and increasing life span mandate the need to understand the mechanisms of AD and discover effective and safe therapies. Over the past several decades, few hypotheses have been proposed to explain the pathophysiology of AD, among which the amyloid beta (Aβ) cascade is now considered as one of the initiating factors that drives the progression and other pathological factors of AD. The aggregation of Aβ into oligomers and fibrils together with its downstream signaling pathway are neurotoxic. Thus, small molecule modulators that could reduce the overall toxic burden of Aβ aggregates are thought to be beneficial in treating AD.

In this thesis, a library of 72 small molecule derivatives were designed based on the chemical structure of chalcone and curcumin, two bioactive natural compounds that are able to modulate Aβ aggregation and reduce their neurotoxicity. The derivatives reported in this thesis encompass four different templates, namely, *N*-benzyl (**Chapter 2**), *N*-phenethyl (**Chapter 3**), *N*-benzyloxy (**Chapter 4**), and *N*-phenyl (**Chapter 5**) benzamide and carboxamides. These compounds were synthesized by coupling the amine substrates with either acid halides or carboxylic acids to obtain the target compounds in 72-93.6% yields. A number of biophysical and biochemical experiments were carried out to determine the ability of these small molecules to modulate the aggregation properties of Aβ42. The experiments carried out include i) thioflavin T based fluorescence aggregation kinetics experiments; ii) transmission electron microscopy studies; iii) 8-anilino-1-naphthalenesulfonic acid based fluorescence spectroscopy; iv) antioxidant assay by fluorescence spectroscopy; iv) cell viability studies in mouse hippocampal HT22 neuronal cells and Aβ42-induced neurotoxicity assay; v) fluorescence microscopy studies to assess the neurotoxicity using Proteostat® dye, and vi) computational modelling studies to determine the interactions of small molecules

with Aβ42 aggregates. From this library, 51 aggregation inhibitors were identified (inhibition of Aβ42 ranging from 7-53.1% at 25 μM). These derivatives were able to provide significant neuroprotection from Aβ42-induced cytotoxicity in mouse hippocampal HT22 cells (cell viability ranging from 80.8-96.8% versus 38.7% for Aβ42-treated control). Molecular docking studies indicate that these derivatives were able to interact with the hydrophobic domains of the Aβ42 oligomer and fibril through hydrophobic interactions. In a striking and unusual finding, 8 derivatives were identified as Aβ42 aggregation promotors with the ability to promote the aggregation by 1.2-5.1 folds. Two lead promotors **14b** (*N*-benzylbenzofuran-2-carboxamide) and **14c** (*N*-benzylbenzo[*b*]thiophene-2-carboxamide) were identified. These two compounds were able to rescue HT22 cells from Aβ42-induced cytotoxicity (cell viability 73.8% and 73.9% for **14b** and **14c** versus 19.7% for Aβ42-treated control). These two compounds have the ability to increase the surface hydrophobicity of Aβ42 aggregates and promote fibrillogenesis. Molecular docking studies suggested that Aβ42 aggregates might undergo conformational change upon binding and thus transit to much more stable and less toxic/nontoxic fibrils. Further structure-activity relationship study indicated that the hydroxy- and methoxy-disubstituted phenyl moiety was required to possess Aβ42 inhibition activity, where the presence of bicyclic aromatic rings such as benzofuran and benzothiophene, and 4-methoxyphenyl moiety is required for pro-aggregation activity. The results show that these benzamides and carboxamides possessing *N*-benzyl, *N*-phenethyl, *N*-benzyloxy, and *N*-phenyl templates hold promise in the design and development of novel small molecules as Aβ42 aggregation modulators. Remarkably **14b** (*N*-benzylbenzofuran-2-carboxamide) and **14c** (*N*-benzylbenzo[*b*]thiophene-2-carboxamide) were able to accelerate Aβ42 aggregation and remodel the aggregation pathway to form less toxic/nontoxic aggregates suggesting their application as novel chemical tools to understand the mechanisms of Aβ42 aggregation cascade.

Acknowledgements

I would like to express my deepest gratitude to my supervisor, Dr. Praveen Rao Perampalli Nekkar, whose unwavering support, mentorship, and academic guidance have been instrumental during the journey of my program. Dr. Nekkar's in-depth understanding and knowledge in the area of pharmaceutical sciences have been a constant source to inspire me to complete my research.

I would like to express my gratitude to my thesis committee members, Dr. Emmanuel Ho from the School of Pharmacy and Dr. Mónica Barra from the Department of Chemistry, for their valuable feedback and constructive suggestions which expanded the scope of my research project.

Special thanks to NSERC, Innovation Canada, the Government of Ontario, the Office of Research, University of Waterloo, Parkinson Society of Southwestern Ontario, and Mitacs Canada for their financial support which made the research happen.

Dedication

I dedicate this thesis to my parents Xin Zhao and Ying Liu, who unconditionally supported me with their enduring encouragement during my Ph.D. journey. I am also grateful to my lab members, office mates, colleagues, and many collaborators who accompanied me, inspired me, and expanded the scope of my knowledge. Last but not least, I would like to express my gratitude to my supervisor Dr. Praveen Rao Perampalli Nekkar for not only his academic guidance but also for providing support to overcome all aspects of the challenges during the research.

Table of Contents

Examining Committee Membership ii

Author's Declaration iii

Abstract iv

Acknowledgements vi

Dedication vii

List of Figures xiii

List of Tables xxiii

List of Abbreviations xxiv

List of Schemes xxvii

Chapter 1 Alzheimer's Disease (AD) 1

1.1 Introduction on AD 1

1.2 AD Pathophysiology 3

1.3 Current Treatment 6

1.4 Aβ Cascade Hypothesis 8

1.4.1 Hypothesis Overview 8

1.4.2 Production of Aβ 9

1.4.3 Aβ Structure and Function 18

1.4.4 Aβ Aggregation 20

1.4.5 Aβ Toxicity and AβO Hypothesis 26

1.4.6 Aβ Transportation, Clearance and Degradation 32

1.4.7 Drug Developing Strategies Targeting Aβ Cascade 34

1.5 AD Disease Continuum 37

1.6 Design of compound library 39

1.6.1 Curcumin 39

1.6.2 Chalcone 43

1.6.3 Pan assay interfering compounds 45
1.6.4 Compound library 49
Chapter 2 Design, Synthesis and Evaluation of *N*-Benzylbenzamide and *N*-Benzylcarboxamide Derivatives as Aβ Aggregation Modulators 53
2.1 Introduction 53
2.2 Hypothesis 54
2.3 Results and Discussion 55
2.3.1 Synthesis 55
2.3.2 Modulatory activity on amyloid-beta aggregation 62
2.3.3 Transmission electron microscopy 67
2.3.4 Neuroprotective effects against Aβ42-induced cytotoxicity 70
2.3.5 Molecular docking 72
2.4 Summary 75
2.5 Experimental 76
2.5.1 General 76
2.5.2 Chemistry 77
2.5.3 Aβ42 aggregation kinetic assay 78
2.5.4 Transmission electron microscopy 79
2.5.5 Cell viability assay 79
2.5.6 Molecular docking study 80
Chapter 3 Design, Synthesis and Evaluation of *N*-Phenethylbenzamide and *N*-Phenethylcarboxamide Derivatives as Aβ Aggregation Modulators 81
3.1 Introduction 81
3.2 Hypothesis 82
3.3 Results and Discussion 83
3.3.1 Synthesis 83
3.3.2 Modulatory activity on amyloid-beta aggregation 91

3.3.3 Transmission electron microscopy 95
3.3.4 Neuroprotective effects against Aβ42-induced cytotoxicity 97
3.3.5 Molecular docking 98
3.4 Summary 102
3.5 Experimental 103
3.5.1 General 103
3.5.2 Chemistry 103
3.5.3 Aβ42 aggregation kinetic assay 104
3.5.4 Transmission electron microscopy 105
3.5.5 Cell viability assay 106
3.5.6 Molecular docking study 107
Chapter 4 Design, Synthesis and Evaluation of *N*-Benzyloxybenzamide and *N*-Benzyloxycarboxamide Derivatives as Aβ Aggregation Modulators 108
4.1 Introduction 108
4.2 Hypothesis 109
4.3 Results and Discussion 110
4.3.1 Synthesis 110
4.3.2 Modulatory activity on amyloid-beta aggregation 117
4.3.3 Transmission electron microscopy 121
4.3.4 Neuroprotective effects against Aβ42-induced cytotoxicity 123
4.3.5 Molecular docking 124
4.4 Summary 127
4.5 Experimental 128
4.5.1 General 128
4.5.2 Chemistry 129
4.5.3 Aβ42 aggregation kinetic assay 130
4.5.4 Transmission electron microscopy 131

4.5.5 Cell viability assay 131

4.5.6 Molecular docking study 132

Chapter 5 Design, Synthesis and Evaluation of *N*-phenylbenzamide and *N*-phenylcarboxamide Derivatives as Aβ Aggregation Modulators 134

5.1 Introduction 134

5.2 Hypothesis 135

5.3 Results and Discussion 136

5.3.1 Synthesis 136

5.3.2 Modulatory activity on amyloid-beta aggregation 144

5.3.3 Transmission electron microscopy of lead AP 14b and 14c 152

5.3.4 8-Anilino-1-naphthalene sulfonicacid binding assay 154

5.3.5 Neuroprotective effects against Aβ42-induced cytotoxicity 156

5.3.6 Molecular docking 161

5.3.7 Synthesis and evaluation of *N*-(substitutedphenyl)benzofuran and benzo[*b*]thiophene-2-carboxamide derivatives (16a-d and 17a-d) as amyloid-beta aggregation modulators 166

5.4 Summary 183

5.5 Experimental 186

5.5.1 General 186

5.5.2 Chemistry 187

5.5.3 Aβ42 aggregation kinetic assay 188

5.5.4 Transmission electron microscopy 189

5.5.5 8-Anilino-1-naphthalenesulfonicacid binding assay 190

5.5.6 Cell viability assay 191

5.5.7 Live cell fluorescence imaging 191

5.5.8 2,2-Diphenyl-1-picrylhydrazyl (DPPH) scavenging assay 193

5.5.9 Molecular docking study 193

Chapter 6 Conclusion and Future Work 195

References.....202

Appendix A – Spectra for Chapter 2 248

Appendix B – Spectra for Chapter 3.....264

Appendix C – Spectra for Chapter 4.....280

Appendix D – Spectra for Chapter 5 295

List of Figures

Figure 1-1. AD facts. Global statistics are shown in the right; Canadian statistics are shown in the left. The world map was obtained from www.pixabay.com and free for use under Pixabay Content License. The figure was generated using PowerPoint. 2

Figure 1-2. Pathophysiology of AD overview. The neuron illustration was obtained from www.pixabay.com and free for use under Pixabay Content License. The figure was generated using PowerPoint. 4

Figure 1-3. FDA-approved small molecule drugs for AD. 7

Figure 1-4. Post-translational processing of APP. 12

Figure 1-5. Illustrative structure of APP and its major domains (colored in blue), proteolytic positions (colored in orange). Figure was created with PowerPoint and Chemdraw. 13

Figure 1-6. Amino acid sequence of Aβ40 and Aβ42 (above) and the structure of steric zipper KLVFFA (below). 19

Figure 1-7. Schematic illustration of Aβ aggregation pathway. 21

Figure 1-8. ThT probe used to study the aggregation of Aβ. 22

Figure 1-9. The characteristic sigmoidal curve of the ThT-monitored Aβ aggregation process. 24

Figure 1-10. Energy landscape of various Aβ species during the aggregation. 26

Figure 1-11. Mechanisms of Aβ toxicity. 28

Figure 1-12. Examples of AβO-binding receptors and downstream signaling pathways. 30

Figure 1-13. Summary of drug developing strategies that targeting Aβ hypothesis. 36

Figure 1-14. Chemical Structure of curcumin (left) and chalcone (right). The aromatic ring systems at the ends of the molecule are highlighted in yellow and pink, whereas the linker regions between the rings are highlighted in red. 40

Figure 1-15. General classification of PAINS. 47

Figure 1-16. Proposed scaffold to study Aβ aggregation (left) and genetic structures of compound series (right). 52

Figure 2-1. *N*-Benzylbenzamide and *N*-benzylcarboxamide derivatives (Series A). This series of compounds contains an amide bond linked to a sp^3 hybridized carbon linker. 54

Figure 2-2. Nucleophilic acyl substitution mechanism which includes three major steps: (1) addition of nucleophile to the electrophilic carbonyl carbon, (2) elimination of the leaving group, (3) loss of proton to form the product. 57

Figure 2-3. Reaction mechanism when using dehydrating agent EDC and activator HOBt for coupling phenylmethanamine (**1**) and corresponding carboxylic acid (**4a-c**) to obtain **5a-c**. 61

Figure 2-4. The Aβ42 aggregation kinetic curves for *N*-benzylbenzamide and carboxamide derivatives (**3a-m** and **5a-c**) in the ThT-based fluorescence assay. (A) Aggregation kinetic curves for derivatives **3a-d** and reference compounds resveratrol (RVT). (B) Aggregation kinetic curves for derivatives **3e-h**. (C) Aggregation kinetic curves for derivatives **3i-l**. (D) Aggregation kinetic curves derivatives for **3m**, **5a-c**. The test compounds (25 μM) were incubated with Aβ42 (10 μM) for 24 h at 37 ˚C, pH 7.4 and the ThT fluorescence was monitored (excitation = 440 nm, emission = 490 nm). Results were obtained based on triplicate readings from three independent experiments. 64

Figure 2-5. Percentage inhibition (PI) of *N*-benzylbenzamide and carboxamide derivatives (**3a-m** and **5a**), resveratrol (RVT) and chalcone (CHL) at 25 μM on Aβ42 (10 μM) aggregation. 67

Figure 2-6. The Aβ42 aggregation kinetic curve for chalcone (CHL) in the ThT-based fluorescence assay. CHL (25 μM) was incubated with Aβ42 (10 μM) for 24 h at 37 ˚C, pH 7.4 and the ThT fluorescence was monitored (excitation = 440 nm, emission = 490 nm). Results were obtained based on triplicate readings from three independent experiments. 67

Figure 2-7. TEM images of Aβ42 (10 μM) in the absence (Aβ42 control) and presence of *N*-benzylbenzamide **3a**, **3h-j**, and **3m** (25 μM). Scale: 200 μm. 69

Figure 2-8. TEM images of Aβ42 (10 μM) in the absence (Aβ42 control) and presence of chalcone (25 μM). Scale: 200 μm. 69

Figure 2-9. Neuroprotective effects of *N*-benzylbenzamide **3a**, **3h-j**, and **3m** (25 μM) on HT22 cells in the absence (A) and presence (B) of Aβ42 (5 μM) incubated over 48 h. Cell viability was determined by CCK-8 based colorimetric assay. The results shown are averages of quadruplicate readings based on three independent experiments. *$p < 0.01$ compared to Aβ42 treated group (One-way ANOVA followed by Bonferroni post hoc test). 71

Figure 2-10. Neuroprotective effects of chalcone (CHL) (25 μM) on HT22 cells in the absence and presence of Aβ42 (5 μM) incubated over 48 h. Cell viability was determined by CCK-8 based colorimetric assay. The results shown are averages of quadruplicate readings based on three independent experiments. *$p < 0.01$ compared to Aβ42 treated group (One-way ANOVA followed by Bonferroni post hoc test). 71

Figure 2-11. Molecular docking studies of **3a** with the Aβ42 fibril model (PDB ID: 5KK3). (A) Top docked pose of **3a**; (B) 2D interaction map of the top docking pose of **3a**. The hydrogen atoms are removed to enhance clarity. Protein is represented in line ribbon with blue indicating the N-terminus and red indicating the C-terminus. The small molecule is represented in the ball-and-stick model. Hydrophobic interaction is represented in pink dashed line and hydrogen bond interaction is represented in green dashed line. 73

Figure 2-12. Molecular docking studies of **3a** with Aβ42 fibril model (PDB ID: 5KK3). (A) Top docked pose of **3a**; (B) 2D interaction map of the top docking pose of **3a**. The hydrogen atoms are removed to enhance clarity. Protein is represented in line ribbon with blue indicating the N-terminus and red indicating the C-terminus. The small molecule is represented in the ball-and-stick model. Hydrophobic interaction is represented in pink dashed line and hydrogen bond interaction is represented in green dashed line. 74

Figure 2-13. Summary of *N*-benzylbenzamide and carboxamide derivatives. (A) 87% (14 out of 16) compounds were identified as aggregation inhibitor (AI) and 13% (2 out of 16) compounds were identified as weak aggregation modulator (WAM); (B) Key experimental data for lead compound **3a**.....76

Figure 3-1. *N*-Phenylethylbenzamide and *N*-phenylethylcarboxamide derivatives (Series B). This series of compounds contains an amide bond and a two carbon sp^3 hybridized linker region. 82

Figure 3-2. Nucleophilic acyl substitution mechanism which includes three major steps: (1) addition of nucleophile to the electrophilic carbonyl carbon. (2) elimination of the leaving group. (3) loss of proton. 85

Figure 3-3. Reaction mechanism when using the dehydrating agent EDC and activator HOBt for coupling 2-phenylethan-1-amine (**6**) and corresponding carboxylic acid (**4a-c**). 90

Figure 3-4. The Aβ42 aggregation kinetic curves for *N*-phenylethylbenzamide and carboxamide derivatives (**7a-m**, **8a-c**) in the ThT-based fluorescence assay. (A) Aggregation kinetic curves for derivatives **7a-d** and reference compound resveratrol (RVT). (B) Aggregation kinetic curves for derivatives **7e-h**. (C) Aggregation kinetic curves for derivatives **7i-l**. (D) Aggregation kinetic curves for derivatives **7m**, **8a-c**. The derivatives (25 μM) were incubated with Aβ42 (10 μM) for 24 h at 37 ˚C, pH 7.4 and the ThT fluorescence was monitored (excitation = 440 nm, emission = 490 nm). Results were obtained based on triplicate readings from three independent experiments.....93

Figure 3-5. Percentage inhibition (PI) of *N*-phenylethylbenzamide and carboxamide derivatives (**7a-m** and **8a-c**), resveratrol (RVT), and chalcone (CHL) at 25 μM on Aβ42 (10 μM) aggregation. 95

Figure 3-6. TEM images of Aβ42 (10 μM) in the absence (Aβ42 control) and presence of *N*-phenylethylbenzamide **7a**, **7b**, and **7j** (25 μM). Scale: 200 μm. 96

Figure 3-7. Neuroprotective effects of *N*-phenylethylbenzamide and carboxamide derivatives **7a**, **7b**, and **7j** (25 μM) on HT22 cells in the absence (A) and presence (B) of Aβ42 (5 μM) incubated over 48 h. Cell viability was determined by the CCK-8 based colorimetric assay. The results shown are averages of quadruplicate readings based on three independent experiments. *p < 0.01 compared to Aβ42 treated group (One-way ANOVA followed by Bonferroni post hoc test). 98

Figure 3-8. Molecular docking studies of **7a** with Aβ42 pentamer model (PDB ID: 5KK3). (A) Top docked pose of **7a**; (B) 2D interaction map of the top docking pose of **7a**. The hydrogen atoms are removed to enhance clarity. Protein is represented in line ribbon with blue indicating the N-terminus and red indicating the C-terminus. The small molecule is represented in the ball-and-stick model. Hydrophobic interaction is represented in pink dashed line and hydrogen bond interaction is represented in green dashed line. 100

Figure 3-9. Molecular docking studies of **7a** with Aβ42 fibril model (PDB ID: 5KK3). (A) Top docked pose of **7a**; (B) 2D interaction map of the top docking pose of **7a**. The hydrogen atoms are removed to enhance clarity. Protein is represented in line ribbon with blue indicating the N-terminus and red indicating the C-terminus. The small molecule is represented in the ball-and-stick model. Hydrophobic interaction is represented in pink dashed line and hydrogen bond interaction is represented in green dashed line. 101

Figure 3-10. Summary of *N*-phenethylbenzamide and carboxamide derivatives. (A) 87% (14 out of 16) compounds were identified as aggregation inhibitor (AI), and 13% (2 out of 16) compounds were identified as weak aggregation modulators (WAM); (B) Key experimental data for lead compound **7a**. 102

Figure 4-1. *N*-Benzyloxybenzamide and *N*-benzyloxycarboxamide derivatives (Series C). This series of compounds features an amide bond, a sp^3 hybridized carbon and an oxygen linker. 109

Figure 4-2. Nucleophilic acyl substitution mechanism which includes three major steps: (1) addition of nucleophile to the electrophilic carbonyl carbon, (2) elimination of the leaving group, (3) loss of proton. 112

Figure 4-3. Reaction mechanism for the synthesis of compounds **11a-c** using the dehydrating agent EDC and activator HOBt for coupling *O*-benzylhydroxylamine (**9**) and the corresponding carboxylic acids (**4a-c**). 116

Figure 4-4. The Aβ42 aggregation kinetic curves for *N*-benzyloxybenzamide and carboxamide derivatives (**10a-f**, **10h-j**, **10l-m** and **11a-c**) in the ThT-based fluorescence assay. (A) Aggregation kinetic curves for derivatives **10a-d** and reference compound resveratrol (RVT). (B) Aggregation kinetic curves for derivatives **10e-f** and **10h-i**. (C) Aggregation kinetic curves for derivatives **10j, 10l** and **10m**. (D) Aggregation kinetic curves for derivatives **11a-c**. The derivatives (25 μM) were incubated with Aβ42 (10

μM) for 24 h at 37 ˚C, pH 7.4 and the ThT fluorescence was monitored (excitation = 440 nm, emission = 490 nm). Results were obtained based on triplicate readings from three independent experiments. 119

Figure 4-5. Percentage inhibition rate (PI) of *N*-benzyloxybenzamide and carboxamide derivatives (**10a-f**, **10h-j**, **10l-m**, **11a-c**), resveratrol (RVT), and chalcone (CHL) at 25 μM on Aβ42 (10 μM) aggregation. 121

Figure 4-6. TEM images of Aβ42 (10 μM) in the absence (Aβ42 control) and presence of *N*-benzyloxybenzamide **10a**, **10h**, **10j**, and **11a** (25 μM). Scale: 200 μm. 122

Figure 4-7. Neuroprotective effects of *N*-benzyloxybenzamide **10a**, **10h**, **10j** and **11a** (25 μM) on HT22 cells in the absence (A) and presence (B) of Aβ42 (5 μM) incubated over 48 h. Cell viability was determined by CCK-8 based colorimetric assay. The results shown are averages of quadruplicate readings based on three independent experiments. *$p < 0.01$ compared to Aβ42 treated group (One-way ANOVA followed by Bonferroni post hoc test). 124

Figure 4-8. Molecular docking studies of **10a** with Aβ42 pentamer model (PDB ID: 5KK3). (A) Top docking pose of **10a**; (B) 2D interaction map of the top docking pose of **10a**. The hydrogen atoms are removed to enhance clarity. Protein is represented in line ribbon with blue indicating the N-terminus and red indicating the C-terminus. The small molecule is represented in the ball-and-stick model. Hydrophobic interaction is represented in pink dashed line. 125

Figure 4-9. Molecular docking studies of **10a** with Aβ42 fibril model (PDB ID: 5KK3). (A) Top docked pose of **10a**; (B) 2D interaction map of the top docking pose of **10a**. The hydrogen atoms are removed to enhance clarity. Protein is represented in line ribbon with blue indicating the N-terminus and red indicating the C-terminus. The small molecule is represented in the ball-and-stick model. Hydrophobic interaction is represented in pink dashed line and hydrogen bond interaction is represented in green dashed line. 127

Figure 4-10. Summary of *N*-benzyloxybenzamide and carboxamide derivatives. (A) 93% (13 out of 14) compounds were identified as aggregation inhibitors (AIs), and 7% (1 out of 14) compounds were identified as weak aggregation modulators (WAM); (B) key experimental data for lead compound **10a**. 128

Figure 5-1. *N*-Phenylbenzamide and *N*-phenylcarboxamide derivatives (Series D). This series of compounds is featured by an amide bond without any spacer in the linker region. 135

Figure 5-2. Nucleophilic acyl substitution mechanism which includes three major steps: (1) addition of nucleophile to the electrophilic carbonyl carbon. (2) elimination of the leaving group. (3) loss of proton. 138

Figure 5-3. Reaction mechanism to obtain **14a-c** using dehydrating agent EDC and activator HOBt for coupling aniline (**12**) and corresponding carboxylic acids (**4a-c**). 143

Figure 5-4. The Aβ42 aggregation kinetic curves for *N*-phenylbenzamide and carboxamide derivatives (**13a-m** and **14a-c**) in the ThT-based fluorescence assay. (A) Aggregation kinetic curves derivatives **13a-d** and reference compounds resveratrol (RVT). (B) Aggregation kinetic curves derivatives **13e-h**. (C) Aggregation kinetic curves derivatives **13i-l**. (D) Aggregation kinetic curves derivatives **13m**,and **14a-c**. The derivatives (25 μM) were incubated with Aβ42 (10 μM) for 24 h at 37 ˚C, pH 7.4 and the ThT fluorescence was monitored (excitation = 440 nm, emission = 490 nm). Results were obtained based on triplicate readings from three independent experiments.....146

Figure 5-5. Percentage inhibition (PI) of *N*-phenylbenzamide and carboxamide derivatives (**13a-m** and **14a-c**) at 25 μM on Aβ42 (10 μM) aggregation.....148

Figure 5-6. Spectrometric background reading of **14b**, **14c**, RVT. (A) ThT-based aggregation kinetics background interference reading. The results presented are the average of two independent experiments in triplicate measurements. (B) UV scanning of assay buffer (blank), **14b**, **14c** and RVT. .150

Figure 5-7. ThT-based 24 h aggregation kinetics of Aβ42 (10 μM) in the absence and presence of RVT, **14b** and **14c** at 1, 5, 10, and 25 μM respectively at 37 °C, pH 7.4. (A) Aggregation kinetic curves for **14b**; (B) aggregation kinetics curves for **14c**; (C) aggregation kinetic curves for resveratrol (RVT); (D) aggregation kinetic curves for chalcone (CHL). Aggregation kinetics were monitored by measuring ThT fluorescence (excitation = 440 nm, emission = 490 nm). Results are averages of three independent experiments in triplicate measurements.....151

Figure 5-8. Fold(s) of aggregation of lead compounds from *N*-phenylbenzamide and carboxamide derivatives (**14b** and **14c**), and chalcone (CHL) at 1, 5, 10, 25 μM on Aβ42 (10 μM) aggregation.....151

Figure 5-9. TEM images of Aβ42 (10 μM) alone and in the presence of **14b**, **14c**, resveratrol (RVT) and chalcone (CHL) at 1, 5, 10, and 25 μM respectively after 24 h incubation at 37 °C, pH 7.4. (A) TEM image of Aβ42 in the absence and presence of RVT, 7a and 7b at 1, 5, 10, and 25 μM respectively. (B) Quantification of TEM images of Aβ42 in the absence and presence of **14b**, **14c**, RVT, and CHL at 1, 5, 10, and 25 μM respectively. The images were analyzed by ImageJ and the percentage area covered by fibrils was measured. Image Scale: 100 nm. 153

Figure 5-10. ANS binding assay of **14b**, **14c**, and RVT with Aβ42 (10 μM) at 1, 5, 10, and 25 μM respectively after 24 h incubation at 37 °C, pH 7.4. The ANS fluorescence readings were taken at excitation 380 nm, emission 400 nm to 600 nm with 10 nm increments. Results are averages of three independent experiments in triplicate measurements. (A) ANS spectrum of **14b** in the presence of Aβ42; (B) ANS

spectrum of **14c** in the presence of Aβ42; (C) ANS spectrum of RVT in the presence of Aβ42; (D) Comparison of ANS fluorescence reading of **14b**, **14c**, and RVT (25 μM) at 490 nm in the presence of Aβ42. *p < 0.01 compared to Aβ42 control group, **p < 0.01 compared to Aβ42 control group (one-way ANOVA).....155

Figure 5-11. ANS binding assay of **14b**, **14c**, and RVT with Aβ42 (10 μM) at 1, 5, 10, and 25 μM respectively incubated at 37 °C, pH 7.4. The ANS fluorescence readings were taken at excitation 380 nm, emission 400 nm to 600 nm with 10 nm increments. Results are averages of three independent experiments in triplicate measurements. (A) ANS background readings in the absence of Aβ42; (B) ANS binding assay of Aβ42 at 0 h; (C) ANS binding assay of Aβ42 at 1 h; (D) ANS binding assay of Aβ42 at 8 h. 156

Figure 5-13. (A) Neuroprotective effects of **14b**, **14c**, and RVT at 25 μM on HT22 cells without Aβ42 after 48 h incubation. The cell viability was determined by cell counting kit-8 (CCK-8). The results are averages of three independent experiments with 5 replicates in each run. (B-E) Fluorescence cell imaging in the absence of Aβ42. Cell membranes were stained by Bio Tracker 490 and visualized with GFP filter; cell nuclei were stained by Hoechst 33342 and visualized with DAPI filter. (B) Untreated cell; (C) **14b** at 25 μM; (D) **14c** at 25 μM; (E) **RVT** at 25 μM. Image scale: 200 μm. 158

Figure 5-14. (A) Neuroprotective effects of **14b**, **14c**, and RVT at 25 μM on HT22 cells in the presence of Aβ42 (20 μM) after 48 h incubation. The cell viability was determined by cell counting kit-8 (CCK-8). The results are averages of three independent experiments with five replicates in each run. (B) Quantitative fluorescence cell imaging of ProteoStat® measured by relative mean pixel intensity (left y-axis, violin chart) in the absence and presence of **14b**, **14c**, and RVT (25 μM). The data is correlated with cell viability (right y-axis, line chart in red). The results presented are averages of three independent experiments from three randomized views. ns = not significant, *p < 0.01 compared to Aβ42 control group, **p < 0.01 compared to Aβ42 control group, ***p < 0.01 compared to Aβ42 control group, ****p < 0.01 compared to Aβ42 control group (one-way ANOVA followed by Bonferroni post hoc test). (C-F) Merged fluorescence images of HT22 cells in the presence of Aβ42 (20 μM). Cell membranes were stained by BioTracker 490 green, cell nucleus was stained blue with Hoechst 33342 and Aβ42 aggregates were stained by ProteoStat® dye. (C) Aβ42 treated cells; (D) Aβ42 + **14b** at 25 μM; (E) Aβ42 + **14c** at 25 μM; (F) Aβ42 + **RVT** at 25 μM; Image scale: 200 μm. 160

Figure 5-15. Molecular docking studies of **14b** and **14c** in Aβ42 pentamer model (PDB ID: 5KK3). (A) top docked pose of **14b**; (B) 2D interaction map of the top docking pose of **14b**; (C) top docked pose of **14c**; (D) 2D interaction map of the top docking pose of **14c**. The Aβ42 chains are color-coded with blue indicating N-terminal and red indicating C-terminal. The hydrogen atoms are removed to enhance clarity. 162

Figure 5-16. Molecular docking studies of **14b** and **14c** in the Aβ42 fibril model (PDB ID: 5KK3). The hydrogen atoms are removed to enhance clarity. (A) Top docked pose of **14b**; (B) 2D interaction map of the top docking pose of **14b**; (C) top docked pose of **14c**; (D) 2D interaction map of the top docking pose of **14c**. The Aβ42 chains are color coded with blue indicating N-terminal and red indicating C-terminal. The hydrogen atoms are removed to enhance clarity. 164

Figure 5-17. Proposed mechanism of **14b** and **14c** promoted Aβ42 fibrillogenesis. 165

Figure 5-18. *N*-(Substitutedphenyl)benzofuran and benzo[*b*]thiophene derivatives.....166

Figure 5-19. ThT-based 24 h aggregation kinetics of Aβ42 (10 μM) in the absence and presence of **16a-d** at 1, 5, 10, and 25 μM respectively at 37 °C, pH 7.4. (A) Aggregation kinetic curves for **16a**; (B) aggregation kinetics curves for **16b**; (C) aggregation kinetic curves for **16c**; (D) aggregation kinetic curves for **16d.** Aggregation kinetics were monitored by measuring ThT fluorescence (excitation = 440 nm, emission = 490 nm). Results are averages of three independent experiments in triplicate measurements.....170

Figure 5-20. ThT-based 24 h aggregation kinetics of Aβ42 (10 μM) in the absence and presence of **17a-d** at 1, 5, 10, and 25 μM respectively at 37 °C, pH 7.4. (A) Aggregation kinetic curves for **17a**; (B) aggregation kinetics curves for **17b**; (C) aggregation kinetic curves for **17c**; (D) aggregation kinetic curves for **17d.** Aggregation kinetics were monitored by measuring ThT fluorescence (excitation = 440 nm, emission = 490 nm). Results are averages of three independent experiments in triplicate measurements.....171

Figure 5-21. ThT-based aggregation kinetics spectrometric background reading of **16a-d**, **17a-d** and RVT. Readings were monitored by measuring ThT fluorescence (excitation = 440 nm, emission = 490 nm). The results presented are the average of one independent experiment in triplicate measurements.....173

Figure 5-22. TEM images. (A) Aβ42 (10 μM) alone. (B) Aβ42 (10 μM) in the presence of APs **16d** and **17d** at 25 μM. (C) Aβ42 (10 μM) in the presence of AIs **16a**, **16b**, **17a**, and **17b** at 25 μM. 174

Figure 5-23. ANS binding assay of **16d** and **17d** with Aβ42 (10 μM) at 1, 5, 10, and 25 μM respectively after 24 h incubation at 37 °C, pH 7.4. The ANS fluorescence readings were taken at 380 nm excitation, and 400 nm to 600 nm emission with 10 nm increments. Results are averages of three independent experiments in triplicate measurements. (A) ANS spectrum of **16d** in the presence of Aβ42; (B) ANS spectrum of **17d** in the presence of Aβ42. 175

Figure 5-24. ANS binding assay of AIs **16a**, **16b**, **17a**, and **17b** with Aβ42 (10 μM) at 1, 5, 10, and 25 μM respectively after 24 h incubation at 37 °C, pH 7.4. The ANS fluorescence readings were taken at 380 nm excitation, and 400 nm to 600 nm emission with 10 nm increments. Results are averages of three independent experiments in triplicate measurements. (A) ANS spectrum of **16a** in the presence of Aβ42;

(B) ANS spectrum of **16b** in the presence of Aβ42; (C) ANS spectrum of **17a** in the presence of Aβ42; (D) ANS spectrum of **17b** in the presence of Aβ42. 176

Figure 5-25. ANS spectrometric background reading of **16a-d**, **17a-d** and RVT. The ANS fluorescence readings were taken at 380 nm excitation, and 400 nm to 600 nm emission with 10 nm increments. Results are averages of one independent experiment in triplicate measurements. 177

Figure 5-26. Neuroprotective effects of **16a**, **16b**, **16d**, **17a**, **17b**, and **17d** at 25 μM on HT22 cells without Aβ42 after 48 h incubation. The cell viability was determined by cell counting kit-8 (CCK-8). The results are averages of three independent experiments (n = 5). 178

Figure 5-27. Antioxidant activity of substituted derivatives presented as percentage DPPH scavenging ability at 1 μM, 5 μM, 10 μM and 25 μM. (A) Antioxidant activity of AI **16a**, **b** and **17a**, **b**; (B) antioxidant activity of **16c**, **d** and **17c**, **d** (not active). Results are averages of three independent experiments in triplicate measurements. 179

Figure 5-28. Molecular docking studies of **16a** and **16d** in Aβ42 pentamer model (PDB ID: 5KK3). (A) Top docked pose of **16a**; (B) 2D interaction map of the top docking pose of **16a**; (C) top docked pose of **16d**; (D) 2D interaction map of the top docking pose of **16d**. The Aβ42 chains are color-coded with blue indicating N-terminal and red indicating C-terminal. The hydrogen atoms are removed to enhance clarity. The hydrophobic interactions between the small molecule ligand and protein receptor are shown in pink dashed line. 181

Figure 5-29. Molecular docking studies of **16a** and **16d** in the Aβ42 fibril model (PDB ID: 5KK3). The hydrogen atoms are removed to enhance clarity. (A) Top docked pose and zoom-in view of **16a**; (B) 2D interaction map of the top docking pose of **16a**; (C) top docked pose and zoom-in view of **16d**; (D) 2D interaction map of the top docking pose of **16d**. The Aβ42 chains are color-coded with blue indicating N-terminal and red indicating C-terminal. The hydrogen atoms are removed to enhance clarity. The intermolecular interactions are shown in dashed lines with green as hydrogen bond interactions, pink as hydrophobic interactions, and orange as electrostatic interactions. 183

Figure 5-30. Summary of *N*-phenylbenzamide and carboxamide derivatives. (A) 37% (6 out of 16) compounds were identified as aggregation inhibitor (AI), 37% (6 out of 16) compounds were identified as aggregation promotor (AP), and 25% (4 out of 16) compounds were identified as weak aggregation modulator (WAM); (B) key experimental data for lead compound **14b** and **14c**. 185

Figure 5-31. Summary of expanded SAR derivative library. Two derivatives with a 4-methoxylphenyl substituent were identified as APs and four derivatives with either a 4-hydroxy-3-methoxyphenyl or a 3-hydroxy-4-methoxyphenyl substituent were identified as AIs. 186

Figure 6-1. Proposed *N*-phenylalkylcarboxamides and *N*-phenylcycloalkylcarboxamide derivatives library with non-aromatic substituents. 198

Figure 6-2. Structure template of *N*-benzyl, *N*-phenethyl, *N*-benzyloxy, *N*-phenylbenzamide and carboxamide derivatives and lead derivatives. 199

List of Tables

Table 2-1. Percent inhibition (PI) of *N*-benzylbenzamide and carboxamide derivatives (**3a-m**, **5a-c**), resveratrol (RVT), and chalcone (CHL) at 25 μM on Aβ42 (10 μM) aggregation. 66

Table 3-1. Percent inhibition (PI) of *N*-phenylethylbenzamide and carboxamide derivatives (**7a-m**, **8a-c**), resveratrol (RVT) and chalcone (CHL) at 25 μM on Aβ42 (10 μM) aggregation. 95

Table 4-1. Percent inhibition (PI) of *N*-benzyloxybenzamide and carboxamide derivatives (**10a-m**, **11a-c**), resveratrol (RVT) and chalcone (CHL) at 25 μM on Aβ42 (10 μM) aggregation. 121

Table 5-1. Percent inhibition (PI) of *N*-phenylbenzamide and carboxamide derivatives (**13a-m** and **14a-c**), resveratrol (RVT), and chalcone (CHL) at 25 μM on Aβ42 (10 μM) aggregation. 148

Table 5-2. Relative mean pixel intensity of RFP channel (ProteoStat®). The results were taken from 3 random views of 3 independent studies. Quantification was carried out using the Image*J* software. 161

Table 5-3. Percent inhibition (PI) of **16a**, **16b**, **17a**, **17b** at 1 μM, 5 μM, 10 μM, and 25 μM on Aβ42 (10 μM) aggregation 172

Table 5-4. Fold(s) increase in Aβ42 (10 μM) fibrillogenesis of **16d** and **17d** at 1 μM, 5 μM, 10 μM, and 25 μM compared to Aβ42 control. 172

Table 6-1. Summary of arylbenzamide and arylcarboxamide derivatives as Aβ42 aggregation modulators. 200

Table 6-2. Summary of predicted physicochemical, pharmacokinetic, druglikeness, and medicinal chemistry properties of lead compounds calculated from Web Tool SwissADME. 201

List of Abbreviations

AD: Alzheimer’s disease

Aβ: amyloid beta

AβO: amyloid beta oligomer

ACh: acetylcholine

AChE: acetylcholinesterase

ADAM: a disintegrin and metalloproteinase

AI: aggregation inhibitor

AICD: amyloid precursor protein C-terminal domain

AM: aggregation modulator

AP: aggregation promotor

APLP: amyloid precursor protein-like protein

APP: amyloid precursor protein

BACE: beta-site amyloid precursor cleavage enzyme

BBB: blood-brain-barrier

BMEC: brain microvascular endothelial cell

CCK-8: cell counting kit 8

ChEI: cholinesterase inhibitor

ChI: cholinesterase

ClogP: calculated partition coefficient

CM: cell membrane

CR: congo red

CSF: cerebrospinal fluid

DCM: dichloromethane

ECE: endothelin-converting enzyme

EDC: 1-ethyl-3-(3-dimethylaminopropyl)carbodiimide

ER: endoplasmic reticulum

EtOAc: ethyl acetate

fAβ: fibrillary amyloid beta

FDA: Food and Drug Administration

FLR: fluorescence intensity

GDP: gross domestic product

GSK3β: glycogen synthase kinase

HFIP: 1,1,1,3,3,3-hexafluoroisopropanol

HOBt: hydroxytriazole

HTS: high throughput screening

IDE: insulin-degrading enzyme

ISF: interstitial fluid

LCMS: liquid chromatography and mass spectrometry

LRP: low-density lipoprotein receptor-related protein

MD: molecular dynamics

NFT: neurofibrillary tangles

NMDA: *N*-methyl-D-aspartate receptor

NMR: nuclear magnetic resonance

p75NTR: p75 neurotrophin receptor

PAINS: pan-assay interference compounds

PD: pharmacodynamics

PDB: protein data bank

PET: positron emission tomography

PI: percentage inhibition

PK: pharmacokinetics

PS: presenilin

RAGE: receptor for advanced glycation end products

RBF: round bottom flask

RFU: relative fluorescence unit

ROS: reactive oxygen species

RVT: resveratrol

SAR: structure-activity relationship

TEA: triethylamine

TEM: transmission electron microscopy

THF: tetrahydrofuran

ThS: thioflavin S

ThT: thioflavin T

TLC: thin layer chromatography

TNF: tumor necrosis factor

TREM2: triggering receptor expressed on myeloid cell

UPW: ultra-pure water

WAM: weak aggregation modulator

WHO: World Health Organization

List of Schemes

Scheme 2-1. Synthetic methodology to synthesize **3a-m** by coupling phenylmethanamine (**1**) and corresponding acid chlorides (**2a-m**). Reagents and conditions: (a) TEA, THF, room temperature/reflux 2-24 h. 56

Scheme 2-2. Synthetic methodology to synthesize **5a-c** by coupling phenylmethanamine (**1**) and corresponding carboxylic acid (**4a-c**). Reagents and conditions: (b) EDC•HCl, HOBt, TEA, THF, room temperature overnight. 56

Scheme 3-1. Synthetic scheme for **7a-m** by coupling 2-phenylethan-1-amine (**6**) and corresponding acid chlorides (**2a-m**). Reagents and conditions: (a) TEA, THF, room temperature/reflux 2-24 h. 84

Scheme 3-2. Synthetic scheme for **8a-c** by coupling 2-phenylethan-1-amine (**6**) and corresponding carboxylic acids (**4a-c**). Reagents and conditions: (b) EDC•HCl, HOBt, TEA, THF, room temperature overnight/reflux 4-12 h. 84

Scheme 4-1. Synthetic scheme for preparing **10a-m** by coupling *O*-benzylhydroxylamine (**9**) with the corresponding acid chlorides (**2a-m**). Reagents and conditions: (a) TEA, THF, room temperature/reflux 2-24 h. 111

Scheme 4-2. Synthetic scheme to prepare **11a-c** by coupling *O*-benzylhydroxylamine (**9**) with the corresponding carboxylic acid (**4a-c**). Reagents and conditions: (b) EDC•HCl, HOBt, TEA, THF, room temperature overnight or under reflux conditions for 4-12 h. 111

Scheme 5-1. Synthetic scheme to prepare **13a-m** by coupling aniline (**12**) with corresponding acid chlorides (**2a-m**). Reagents and conditions: (a) TEA, THF, room temperature/reflux 2-24 h. 137

Scheme 5-2. Synthetic scheme to prepare **14a-c** by coupling aniline (**12**) with corresponding carboxylic acids (**4a-c**). Reagents and conditions: (b) EDC•HCl, HOBt, TEA, THF, room temperature overnight or under reflux conditions for 24h. 137

Scheme 5-3. Synthetic scheme to prepare **16a-d** and **16a-d** by coupling aniline derivatives (**15a-d**) with corresponding carboxylic acids (**4b-c**). Reagents and conditions: EDC•HCl, HOBt, TEA, THF, room temperature overnight. 167

Chapter 1

Alzheimer's Disease (AD)

1.1 Introduction on AD

Alzheimer's disease (AD) is a progressive neurodegenerative disorder that considerably hampers the function of the central nervous system (CNS). AD mainly affects elder adults who are aged 65 or more. Despite that, in rare cases, early-onset AD might happen to people in their 40s.[1–4] AD is the main cause of dementia and is estimated to account for 60% to 80% of the cases.[5] The clinical manifestations of AD include memory loss, impaired judgement and decision-making abilities, behavior and mood changes, confusion with time and location, difficulty with language, and loss of executive abilities.[6–8] Due to the increase in the aging population, the prevalence and incidence of AD are predicted to rise dramatically in the coming years which makes AD a significant social and economic burden on the healthcare system worldwide. **Figure 1-1** shows AD dementia statistics worldwide and in Canada. With that being said, dementia, including AD, is a major category of non-communicable disease and ranks to be the 7th leading cause of death worldwide.[9] According to statistics from the World Health Organization (WHO), there are 46 million people living with dementia.[10] This number is rising rapidly with one new case of dementia developing every 3 seconds globally. In Canada, it is estimated that over half a million people are living with different types of dementia.[11] By 2031, this number is predicted to double to 937,000 and women are expected to share the major disease burden.[12] The prevalence is critically associated with age factors. Based on the data from Canadian Chronic Disease Surveillance System, the age-standard prevalence (patients with 65 years old and more) of diagnosed dementia is 7.1% with an incidence 14.3 new cases per 1,000 senior population.[13] On the other hand, AD is considered as one of the most expensive diseases given its chronic nature. The health impact of dementia is overwhelming, which often involves not only the patients,

but also their families, caregivers and health professionals. The economic cost of dementia per year is estimated to be 1084 billion CDN worldwide which represents 1.09% of global GDP.[14]



Figure 1-1. AD facts. Global statistics are shown in the right; Canadian statistics are shown in the left. The world map was obtained from www.pixabay.com and free for use under Pixabay Content License. The figure was generated using PowerPoint.

The story of AD can be dated back to 1906 when Dr. Alois Alzheimer presented his treatment and subsequent postmortem brain examination of his 51-year-old female patient Frau Auguste Deter.[15] The patient manifested severe memory loss and cognitive impairment along with other psychiatric symptoms, including hallucination, paranoid and aggressive behaviors. From the autopsy studies, he observed extensive brain atrophy and abnormal deposits, namely senile plaques and neurofibrillary tangles, around the neurons under the microscope which are unique to other neurological conditions.[16] It was not until 1910 that Kraepelin, for the first time, termed this novel neurological condition as Alzheimer's disease or AD.[17] In 1968, Blessed and coworkers suggested that the level of cortical burden of both senile plaques and neurofibrillary tangles is closely associated with the severity and progression of the disease.[18] This is the very first and important step towards the understanding of AD pathophysiology. In the following decades, efforts were made to identify, purify, and characterize the components of senile plaques and neurofibrillary tangles.[19] Surprisingly, in 1981, Whitehouse and coworkers found another potential disease mechanism of

AD which highlights the cholinergic deficiency hypothesis.[20] This is followed by a landmark discovery in 1984 that amyloid beta (Aβ) is the component of senile plaques.[21,22] Two years later, researchers around the world successively discovered that tau protein is the major component of neurofibrillary tangles.[23,24] So far, all three fundamental pathophysiological pathways of AD have been identified. From the late 20th century till now, with the help of structural biology and gene engineering, the understanding of Aβ and tau has been investigated at a molecular and even atomic level. Several gene mutations have been found associated with either familial AD or early-onset AD, such as amyloid precursor protein (APP), presenilin 1, and presenilin 2.[25–27] Moreover, in 1993, apolipoprotein ε4 was found to be an important gene risk factor underlying the most common type of sporadic AD, especially in women.[28,29] Biomarkers have also been developed to facilitate the early diagnosis of AD with better accuracy even before the manifestation of AD symptoms.[30–32] These advances have assisted in defining and developing disease stages and criteria for clinical therapy.[7,25,32]

1.2 AD Pathophysiology

The complexity of AD is fully illustrated by its multifaceted pathophysiological pathways. The understanding of AD is a retrospective approach where the disease mechanisms were proposed based on the observations from biopsy, biomarker, autopsy, imaging, epidemiological, and clinical studies with patients. At the early stage, sparse and unrelated biological pathways were proposed as disease mechanisms, such as the cholinergic deficiency, Aβ and tau cascades. However, the correlation and relationship between different biological pathways was not defined. In the past 20 years or so researchers have realized the importance of the interplay between different pathological pathways and their implications in AD pathophysiology. Rapid research developments in AD including novel biomarker detection and brain imaging technologies have provided great insight into the disease continuum and diagnosis. Herein, in this section, several major AD pathophysiological pathways are discussed (**Figure 1-2**).

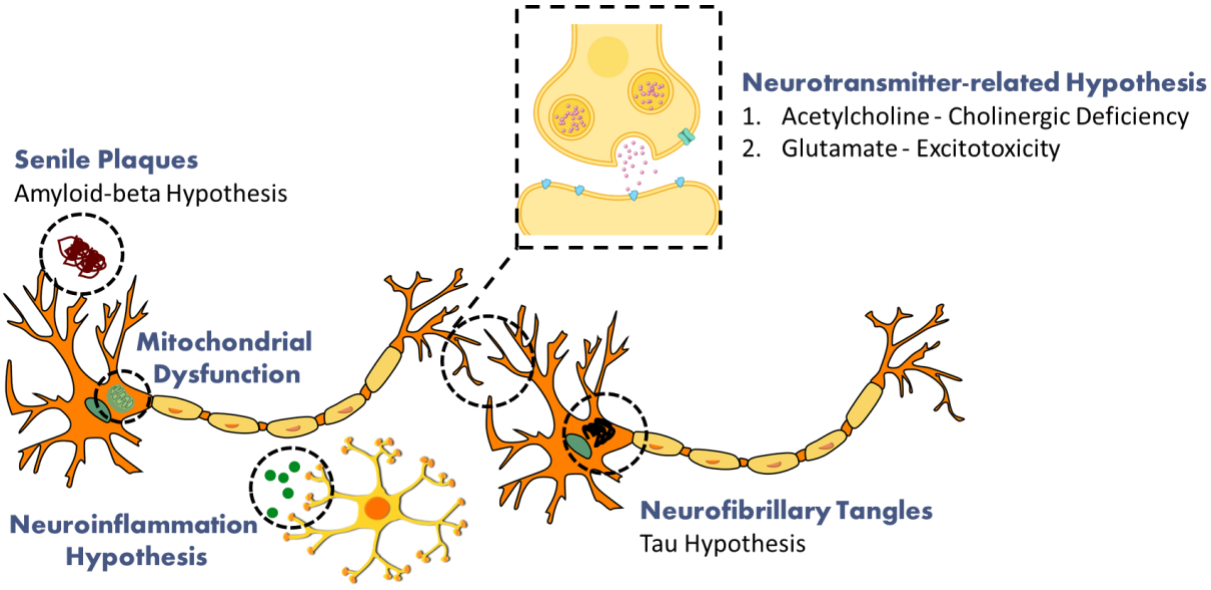


Figure 1-2. Pathophysiology of AD overview. The neuron illustration was obtained from www.pixabay.com and free for use under Pixabay Content License. The figure was generated using PowerPoint.

The cholinergic hypothesis was the very first pathological pathway that was addressed by treatment options for AD. It is the most widely accepted hypothesis of AD. The core idea of this hypothesis is that the loss of cholinergic neurons and the absence of sufficient neurotransmitter acetylcholine (ACh) in the neuronal and neuro-muscular regions lead to the development of AD.[33,34] The reduced activity level of ACh can be a result of either a decreased ACh synthesis or an increased enzymatic degradation by acetylcholinesterase (AChE, **Figure 1-2**).[35,36] Based on this, any intervention that can stimulate the level of available CNS ACh level or inhibit the enzymatic degradation of AChE would be beneficial.

Glutamate is another neurotransmitter in CNS with an excitatory nature that plays a key role in brain function, including learning process and memory storage. However, excessive glutamate in AD brain leads to excitotoxicity which ultimately cause the cell death (**Figure 1-2**).[37] *N*-methyl-*D*-aspartate receptor (NMDA) is one of the glutamate receptors found in neurons. The increased level of glutamate overstimulates the NMDA receptor which can contribute to neuronal damage and cognitive impairment.[38–

[40] The glutamate hypothesis has led to the discovery of AD treatment memantine (Namenda®) which is a non-competitive NMDA receptor antagonist.

Two other major hypothesis of AD pathophysiology are Aβ hypothesis and tau hypothesis (**Figure 1-2**). These are proposed based on the findings of senile plaques and neurofibrillary tangles of AD patient brain. The identification and purification of Aβ and tau proteins lead to an extensive understanding of these disease pathways. The details of Aβ hypothesis will be discussed in *Section 1.4*. In general, Aβ is a peptide that is produced by sequential enzymatic processing from its precursor protein APP. Once generated, Aβ is prone to undergo self-aggregation which forms neurotoxic senile plaques.[41] Tau protein, on the other hand, is a microtubule-associating protein. The hyperphosphorylation of tau makes it lose its ability to attach firmly to microtubules. Similarly, phosphorylated tau also undergoes aggregation that leads to the formation of toxic neurofibrillary tangles.[42–45] Recently, another hypothesis, namely dual cascade hypothesis, puts Aβ and tau hypothesis together which emphasizes on the interplay between these two proteins.[46–48] The cellular processes may simultaneously drive Aβ and tau pathology and Aβ might facilitate the formation of phosphorylated tau. In together, Aβ and tau aggregation leads to neurotoxicity, neurodegeneration and eventual development of AD.

Furthermore, the mitochondrial dysfunction hypothesis has also been proposed. Mitochondrial is of great significance to neurons, especially at the synapses where it can generate calcium gradient and ATP. This process is essential for eliciting membrane potential and enables the process of neurotransmission. The function of mitochondria is affected in AD with altered morphology, decreased numbers, increased reactive oxygen species (ROS), mitochondrial DNA mutation, and mitochondrial biogenesis.[49–54] The reduced mitochondrial activity and increase level of oxidative stress can lead to neuronal death.

In addition, there is the neuroinflammation hypothesis where AD is considered as a chronic inflammatory process. The accumulated Aβ and tau aggregates around the neurons can trigger the immune response of the CNS.[55,56] The activation of immune cells, especially glia cells, releases inflammatory cytokines that further dysregulate the biological activities of neurons.[57,58]

All these pathophysiological pathways of AD are not separated, instead they are interconnected closely to each other. No single pathological pathway on its own is sufficient enough to lead to the development of AD, rather in general several molecular mechanisms happen simultaneously or continuously to initiate the disease process. In the next section (*Section 1.3*), the current treatments of AD based on these hypotheses are introduced. This is followed by a detailed explanation and discussion on Aβ hypothesis (*Section 1.4*) which is the main focus of this thesis. Then, the overall macroscopic picture of AD pathophysiology is synthesized and discussed (*Section 1.5*).

1.3 Current Treatment

Unfortunately, there is no cure for AD so far. There are four small molecule drugs approved by the US Food and Drug Administration (FDA) that can be used as treatment of AD (**Figure 1-3**). These drugs merely provide symptomatic relief to the patients, especially cognitive decline, which are unable to alter the disease pathophysiology or halter disease progression. The goal of these treatments is not reversing or eliminating the disease progress, instead it helps to obtain a better management over the ongoing symptoms of dementia without severely influencing the life quality. Based on the modes of action, there are two classes of drugs: cholinesterase inhibitors (ChEIs) that target and inhibit the cholinesterase enzymes and the NMDA receptor antagonist that can reduce the excessive neuroexcitation. The very first discovered ChEI was tacrine (Cognex®). It can increase the CNS concentration of ACh by inhibiting its degrading enzyme AChE.[59,60] However, due to potential liver toxicity and severe side effects, it was withdrawn from the market after more than 60 years of usage in 2013.[61,62] Currently, three ChEI are being administered to treat symptoms of AD, including donepezil (Aricept®), rivastigmine (Exelon®), and galantamine (Razadyne®). Donepezil is approved to treat all stages of AD, while rivastigmine and galantamine are approved to treat mild-to-moderate AD. Patients' symptoms, such as cognitive decline, language impairment, memory loss, can be lessen or stabilized over a limited period of time when taking these medications.[63] It seems like the efficacy of these three medications toward symptom management are similar. However, the effects are generally

modest and the patients' response to the treatment is variable. There is a certain proportion of patients who received ChEI medications did not show any benefit.[64] As a result, the cost-effectiveness of these medications is generally considered low. The only approved NMDA receptor antagonist is memantine (Namenda®).[65] Research has shown that the use of memantine is recommended at a later, advanced stage of AD where the therapeutic effects can be maximized.[66] It is well tolerated in patient population with moderate-to-severe AD. The combination of donepezil and memantine, branded as Namzaric®, was also approved to treat moderate-to-severe symptoms of AD by simultaneously targeting two underlying pathologies. These medications, either targeting ACh or NMDA system, modulate the pathological changes that happened in the downstream of Aβ and tau cascade, which partially explains why they failed to reverse the disease.[67]

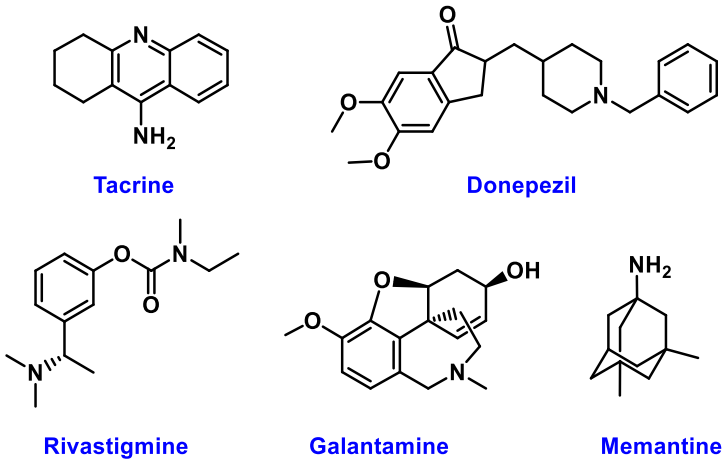


Figure 1-3. FDA-approved small molecule drugs for AD.

Intense AD research in the past decade has led to a better understanding of the disease mechanisms which is assisting in the discovery of the next generation of treatments.[68–70] These parameters include biomarkers, clinical trial redesigning, and neurological fluorescence imaging. These new elements help to diagnose AD dementia more accurately, to detect disease pathologies earlier, and to assess patients' response to treatment

more precisely. The inclusion of these parameters helps to identify novel AD treatments. In terms of immunotherapy approaches to treat AD, there are mainly two types of intervention: active immunization and passive immunization. The active immunization mainly involves administering the Aβ/tau or fragment of Aβ/tau to activate the human immune response. These vaccines include Aβ1-6 vaccine CAD106[71], tau vaccine AADvac1 (ADAMANT)[72], and Aβ synthetic peptide vaccine UB-311 (UBITh®)[73]. Whereas, the passive immunization involves administering antibodies that target Aβ and/or tau aggregates in the human body. Recently, two anti-amyloid immunotherapies were approved by FDA to treat MCI and mild dementia: aducanumab (Aduhelm®) and lecanemab (Leqembi®), respectively.[74,75] These two medications target the Aβ cascades, specifically by enhancing the clearance of Aβ aggregates. They are both anti-amyloid antibodies that are able to facilitate the removal of Aβ presented in the CNS by intravenous infusion. Phase II/III clinical trials of these two anti-Aβ antibodies were carried out with patients who have been diagnosed with MCI or mild dementia due to AD and have shown Aβ pathology indicated by biomarker screening or positron emission tomography (PET). The patients seem to benefit from the therapies by showing an enhancement in clinical measurements related to cognition and behavioral function.[76,77]

1.4 Aβ Cascade Hypothesis

1.4.1 Hypothesis Overview

As discussed in the previous section, the observation of senile plaques and neurofibrillary tangles from AD patients during the postmortem experiments led to the advent of the amyloid cascade hypothesis. Back in 1992 when the hypothesis was proposed, it was thought that the deposition of Aβ protein, the main component of senile plaques, was the causative agent of AD, and that the other downstream pathological events are the direct results of such protein deposition.[78,79] Even though the mechanisms and functions were not fully understood, the hypothesis was considered as a viable target for drug development. Built upon this hypothesis, numerous potential drug candidates started their journey in clinical trials decades ago. However,

the results backfired as the majority of the candidates failed to reach clinical endpoints at various stages of clinical trials due to safety issues, and lack of effectiveness.[48,80,81] Such demotivating real-world data inevitably triggered doubts around this hypothesis. With the help of new clinical and experimental technologies, the hypothesis has been further refined to explain the controversies found between research and real-world data. After more than 30 years of painstaking research, the contents of the hypothesis have been expanded largely, which currently includes the entire production and post-production handling pathways of Aβ. The accelerated approval of Aβ-specific antibodies, aducanumab and lacanemab, by US FDA has put the focus back on the amyloid cascade as viable molecular target in discovering novel disease-modifying agents to treat AD.

To start with, the Aβ cascade hypothesis mainly focuses on the imbalance between the formation and post-production processing (metabolism and clearance) of Aβ.[82] The deposition of various forms of Aβ aggregates is the direct outcome of the loss of such biological homeostasis. The accumulation of Aβ aggregates is often the very initial event that happens in the disease continuum. It leads to other downstream pathological changes as well as clinical manifestations which eventually leads to AD dementia.[83] In the following sections, the production, aggregation, and toxicity mechanism of Aβ will be explained in detail on a molecular level. In order to conceptualize the hypothesis from an overall biological perspective, the function of major products and secretases derived from Aβ production, either physiological or pathological, will be discussed as well.

1.4.2 Production of Aβ

1.4.2.1 Post-translational processing of APP

The term ‘Aβ species’ is used to describe a number of Aβ peptides varying from 38 to 43 amino acids in length. Among all these Aβ species, Aβ40 (consists of 40 amino acids) and Aβ42 (consists of 42 amino acids) are the two major species implicated in the pathophysiology of AD. These two Aβ species are derived

from the post-translational proteolytic processing of their mother protein, so-called amyloid precursor protein (APP) which is a larger transmembrane protein with an N-terminal ectodomain, a C-terminal intracellular domain and several hydrophobic transmembrane domains.[84] The post-translational proteolytic processing of APP is executed by α-, β-, and γ-secretases via two different pathways, amyloidogenic pathway and non-amyloidogenic pathway (**Figure 1-4**). It is the amyloidogenic pathway that generates Aβ species which then further elicits the aggregation process. For non-amyloidogenic pathway, the APP processing is completed through sequential cleaving of α-secretase and β-secretase.[85] Firstly, α-secretase cleaves APP between lysine 687 and leucine 770 (APP770 numbering) or lysine 16 and leucine 17 (Aβ40/42 numbering) near the cell membrane (CM) to yield a soluble N-terminal product sAPPα and a C-terminal fragment 83 (CTF83). Next, CTF83 is further cleaved by γ-secretase to release the APP intercellular C-terminal domain (AICD) and a small peptide p3 (3kD). The α-secretase cleaves the APP within the amino acids sequence of Aβ and thus no Aβ is produced from this processing pathway. Similarly, the amyloidogenic pathway involves the combination of two proteolytic enzymes as well, namely, β-secretase or β-site APP cleavage enzyme (BACE) and γ-secretase.[86] BACE cleaves APP further away from CM in the upstream of full Aβ sequence between methionine 671 and aspartic acid 672 (APP770 numbering system). This cleavage results in the release of the soluble large peptide sAPPβ and CTF99 which is further cleaved by γ-secretase to generate full-length Aβ peptide and AICD (**Figure 1-4**).

Under physiological conditions, the majority of APP is processed through non-amyloidogenic pathway. Still a certain percentage, although small proportion, of APP is proteolyzed via the amyloidogenic pathway which means that extremely low concentration of Aβ species (reported at picomolar level) is present at physiological conditions.[87] In contrast, under pathological conditions, there is a shift in the processing of APP from mainly non-amyloidogenic to mainly amyloidogenic pathway. The transition in the APP processing elevates the level of Aβ species in the CNS and thus leads to the aggregation and accumulation of various Aβ species.[88] However, the mechanism or trigger of such transition is not well defined at the molecular level. It is suggested that the trafficking of APP and its downstream products plays a role in this

transition. The APP is a transmembrane protein, it is not only localized at CM but also at other cellular locations. The maturity of APP involves the constitutive secretory pathway from endoplasmic reticulum (ER) to the CM, similar to the biosynthesis of most proteins. The majority of the APP is localized in the Golgi complex, while only a small portion of it is being trafficked to CM and internalized.[89] However, these membrane-bound APP can also be sorted into early endosomes, among which one fraction is recycled back to CM and the other fraction is trafficked to the lysosome/endosome system for degradation.[90] The precisely regulated trafficking pathway of APP provides many opportunities to co-residence with α-, β-, and γ-secretases. It is the co-residence of APP and its proteolytic enzymes that influences its preference to one of the two post-translation processing pathways. As α-secretase is primarily enriched at CM, the amyloidogenic pathway is obviously predominant on the cell surface under normal conditions. In pathological conditions, increasing levels of APP are being transported into different cell compartments, including trans-Golgi network and endosomes where β-secretase is mainly localized.[91] The co-residence of APP and β-secretase enables efficient β-cleavage of APP and thus a higher level of Aβ is being secreted. The slightly acidic pH environment in these cell compartments also facilitates the proteolytic activity of β-secretase. Research findings also suggest that the trigger of this transition might also be influenced by the elevated levels of BACE1 which is the main proteolytic enzyme that produces Aβ.

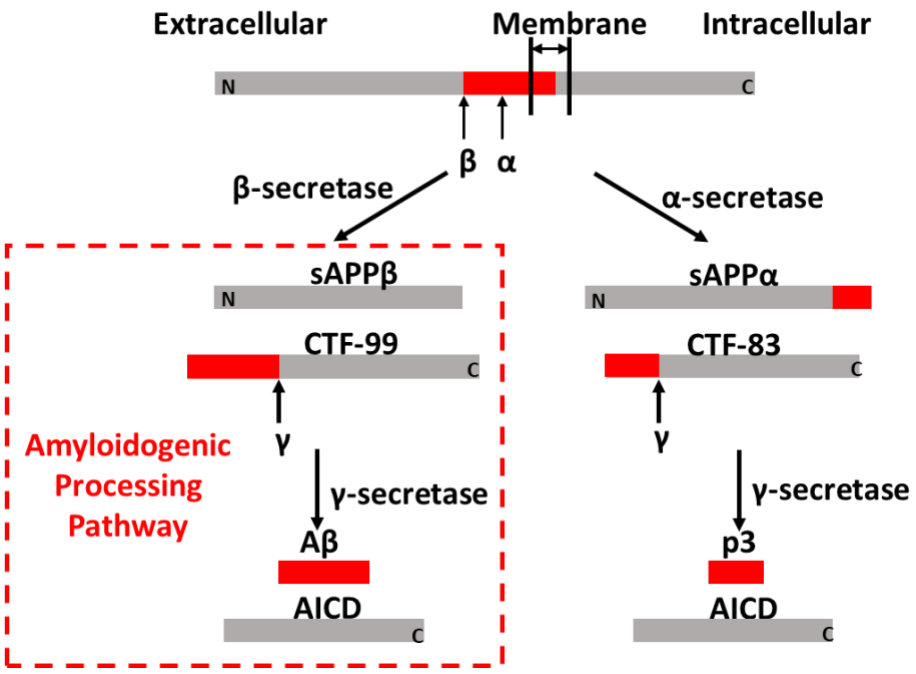


Figure 1-4. Post-translational processing of APP.

To summarize, Aβ species varying in length are produced by the post-translational proteolytic processing of APP by β-, and γ-secretases via amyloidogenic pathway at either physiological or pathological conditions. The transition of APP processing, from mainly non-amyloidogenic pathway to mainly amyloidogenic pathway presumably regulated by APP trafficking, results in the elevated production of Aβ species, especially Aβ40 and even more hydrophobic sequence Aβ42. Such shift disrupts the biological balance and homeostasis which initiates the downstream pathological changes in AD.

1.4.2.2 Amyloid precursor protein (APP)

Since the entire post-translational processing routes of APP has been introduced, it is important to understand the structural characteristics and function of each involving parties to understand the rationality of their existence in such delicate biological systems.

APP is a glycosylated integral membrane cell surface protein (**Figure 1-5**) whose encoding genes are located on chromosome 21.[92,93] Its unique gene sequence includes in total 18 exons. Due to gene splicing, three major isoforms of APP have been found to date, which are APP 695, APP 751, and APP 770 respectively. APP 695 is the most abundant isoform expressed in neurons which encoding cDNA lacks the gene sequence of exon 7 and exon 8.[94] It is generally believed that exon 7 encodes a Kunitz-protease inhibitor, which is a regulator of platelet aggregation and homeostasis.[95,96] On the other hand, exon 8 contains OX-2 homology sequence whose biological functions have not been deciphered clearly on a molecular level. The encoding cDNA of APP 751 or APP-like protein 1 (APLP1) lacks only exon 8, but not exon 7.[97,98] It is merely expressed in brains and has only been found in mammalian animals.[99] Whereas APP 770 or APLP2 are encoded by all 18 exons, which is ubiquitously expressed in human body.[85]

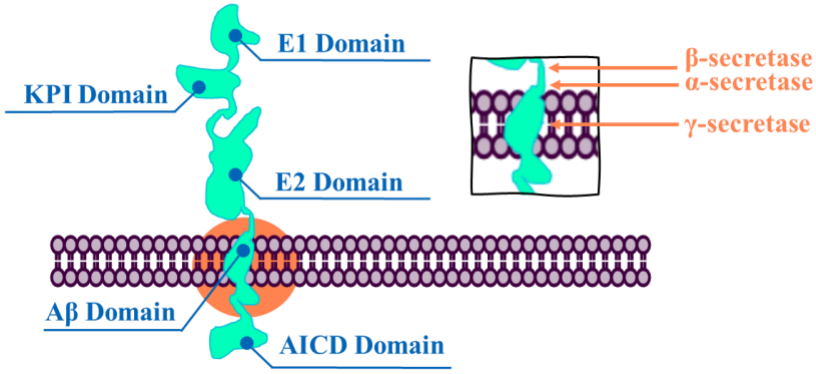


Figure 1-5. Illustrative structure of APP and its major domains (colored in blue), proteolytic positions (colored in orange). Figure was created with PowerPoint and Chemdraw.

In the context of this thesis, APP preferably refers to APP 695 due to its abundance in CNS. It has a larger extracellular region that can be further divided into E1 and E2 domains. These two domains are separated by a KPI domain, even though it is not expressed in APP 695. E1 domain is considered as the major active surface that is responsible for the interactions for APP/APLP dimerization.[100–102] However, the biological function of E2 is poorly defined. The transmembrane domain of APP which contains the Aβ

sequence is relatively conserved.[103] The remaining C-terminal domain is AICD which will be discussed later. The biological functions of full-length APP have been explored extensively. It is a cell surface receptor that can bind to several substrates, including Aβ, F-spondin, Nogo-66, netrin-1, BRI2.[104–108] The binding between APP and substrates is facilitated by the extracellular domain of APP. In addition, it also plays a role in cell adhesion as E1 and E2 domains can interact with extracellular matrix proteins and itself in a parallel or anti-parallel manner to form hetero-dimers (with APLPs) or homo-dimers (with APP itself).[109,110] It is suggested that APP is also involved in the regulation of neprilysin and transthyretin expression which is achieved by the direct binding of AICD to the gene promotors of neprilysin and transthyretin. These APP-mediated effects are, in parallel, modulated by BACE1 through which the AICD is being produced. Several mutations on genes encoding APP have been found which are closely related to early-onset AD or familial AD, including Swedish mutation K670N, M671L, and Osaka mutation.[3,111] These mutations, especially those within the sequence of Aβ, are capable of promoting the production and/or aggregation of Aβ.

1.4.2.3 α-Secretase and sAPP-α

Several A Disintegrin and Metalloproteinase (ADAM) possess α-secretase-like activities, among which three of those ADAMs are considered as α-secretase, including ADAM 9, ADAM 10, ADAM 17 respectively.[112] They are type I integral membrane zinc metalloproteases. These proteinases are mainly expressed on CM and anchored on the surface of neurons. Therefore, the non-amyloidogenic processing of APP predominately occurs on the CM. ADAM 10 is extensively expressed in CNS and responsible for constitutive α-cleavage activity.[113] Both ADAM 9 and ADAM 17 are more likely involved in the regulation of α-cleavage of APP rather than constitutive α-cleavage. The result of α-cleavage is the release of a large soluble peptide sequence sAPP-α. Generally, sAPP-α is considered neuroprotective. It plays an important role in neuronal plasticity and neuronal stem cell proliferation which is crucial to CNS development.[114] It can also promote neurite outgrowth, cell adhesion, and the synthesis of new synaptic.[115,116] Most

importantly, as the cleavage site of α-secretase is within the sequence of Aβ, the up-regulation of α-secretase may be beneficial in treating AD. α-Secretase mediated APP cleavage can be activated by several G protein-coupled receptors and receptor tyrosine kinases.[117,118] The activation of α-secretase can also happen when the cholesterol synthesis is blocked by statins. However, ADAMs are not APP specific and there are many others substates.[119] The strategy of promoting non-amyloidogenic pathway by activating α-secretase needs to be used under scrutiny.

1.4.2.4 β-Secretase/BACE and sAPP-β

BACE1 is a 501 amino-acids-long type I transmembrane aspartyl protease with its two active sites on the luminal side of the CM.[120,121] The first active site is called Asp 1 cleavage site which cleaves APP between Met596 and Asp597 to give CTF99. The other active site is called glutamate 11 cleavage site which cleaves APP between Tyr606 and Glu607 to give CTF89 from which a truncated type Aβ 11-40/42 is produced.[122] It is generally perceived that the activity of BACE1 is the rate-limiting process in the production of Aβ. The maturity of BACE1 includes glycosylation, phosphorylation, and cleavage of its precursor protein, pro-BACE1. Most of the BACE1 is found to be membrane-bound, but evidence shows that an acidic environment is required to exhibit its optimal catalytic activities. BACE1 is expressed in most body tissues and the highest level of activity are observed in neurons. Considering its correlation with Aβ generation, BACE1 has been suggested as one of the drug targets in treating AD.[123–125] Indeed, previous studies indicated that elevated levels of BACE1 found in AD patient's brain and the lack of Aβ generation has been accredited to BACE1 inhibition or knocked-out.[126] However, recently, some non-APP substrates of BACE1 have been identified, including the β2 subunit of voltage-gated sodium channel and P-selectin glycoprotein ligand 1.[127] The side effects of complete blockage of BACE1 in various AD models may be associated with this. BACE1 inhibitors that have been discontinued in randomized clinical trials due to futility or safety reasons include verubecestat[128], atabecestat[129], and umibecestat[130]. The major product of β-cleavage is the formation of sAPPβ and CTF99. The CTF99 fragment is an intermediate rather than end product, so the

function of this C-terminal fragment is not well understood. However, the function of sAPPβ is considered neurotoxic, in opposition to that of sAPPα. Compared to sAPPα, the sAPPβ lacks the Aβ1-16 domain near its N-terminus. It participates in mediating axonal pruning and neuronal cell death.[131] It is also a ligand of death receptor 6 or commonly referred tumor necrosis factor (TNF) receptor which is closely associated with cell apoptosis.

1.4.2.5 γ-Secretase and AICD

The γ-secretase is the enzyme that eventually proteolyzes CTF fragments to generate either Aβ or p3. It is a large proteinase complex which includes at least four major components: Presenilin (PS), Presenilin enhancer 2, Anterior pharynx-defective 1, and Nicastrin.[132] These four components are considered essential for the catalytic activity of γ-secretase. Two homologues of PS were found in human body, which are PS1 and PS2 respectively. Any mutations in these two gene sequences, especially PS1, are causative in most of the cases of familial AD. In terms of biological structure of γ-secretase, it is a multi-transmembrane protein where the active cleavage site lies within the transmembrane domain. The maturity of γ-secretase involves the cleavage between the 6th and 7th transmembrane domain at the cytoplasmic loop.[133] The cleavage generates an N-terminal and a C-terminal fragment. These two fragments interact with each other, together, making γ-cleavage happen. Only a small portion of the γ-secretase complex is located on the CM, while the rest mainly localize at ER, Golgi/TGN and endosome.[134] Therefore, Aβ can be produced in the endosome/lysosome system or on the CM where the mature γ-secretase can be found. Interestingly, γ-secretase can also mediate cleavage at different sites, namely, ξ-site (to generate Aβ46) and ε-site (to generate Aβ49).[135,136] Accordingly, various AICDs are generated varying in length (AICD 50, 53, 57, 59). Other substrates of γ-secretase are identified as well, including Notch, CD44, and cadherin.[137] Similar to the above-mentioned α- and β-secretase, the inhibition or complete blockage of γ-secretase as therapeutic approach to treat AD is risky due to potential side effects.[138]

The outcomes of γ-cleavage are p3/Aβ and AICD. p3 is a relatively small peptide which is rapidly degraded. It is believed to possess no important biological function. The function of Aβ will be discussed in detail in the next section. As for AICD, it also undergoes fast degradation so that the information on AICD is mostly deduced based on the exogenous system. From a biological structure perspective, few conserved regions are discovered, which are YTSI (653-656, APP695 numbering) motif near cell membrane, VTPEER (682-687, APP695 numbering) helix capping box, and YENPTY (682-687, APP695 numbering) respectively.[139,140] The biological functions of AICD closely depend on the interaction with its binding partners. These conserved motifs are considered as the major contributors to the interaction between AICD and other proteins. With that being said, many AICD-binding proteins have been identified, including kinesin light chain, APP tail 1, X11, Clathrin, mDab1.[141] It is also noted that the interaction of X11 and AICD has been suggested as a regulatory factor on the APP trafficking and metabolism which leads to a decreased level of Aβ production.[142] On the other hand, AICD contains some phosphorylation sites, including two threonine residue sites (Thr654, Thr668 based on APP695 numbering) and one serine residue site (Ser665 based on APP695 numbering).[85] The phosphorylation state of AICD plays a crucial role in the binding between AICD and its corresponding binding proteins, so the phosphorylation process is indirectly mediating its biological functions. Recently, the interplay between AICD and Aβ has been highlighted as it provides more insights into the pathological mechanism of AD. The AICD can be transported to the nucleus and acts as gene transcriptional regulator. For example, AICD up-regulates the expression of neprilysin, a secreted protease that cleaves Aβ, which leads to a lower Aβ level in the brain.[143] The AICD can also regulate the expression of transthyretin which is an extracellular protein capable of inhibiting Aβ aggregation and ameliorating its neurotoxicity.[144] The exact mechanism of how AICD works is still unclear. Whether the translocation of AICD to the nucleus is necessary for its biological function is poorly understood. But, for sure, AICD can influence Aβ levels in the brain potentially due to its binding to gene promotors or proteins. Some studies also suggest that AICD is neurotoxic which is also attributed to the binding with its interacting proteins.

1.4.3 Aβ Structure and Function

In this section the structure and function of the major isoforms of Aβ species, namely are Aβ40 and Aβ42, will be discussed (**Figure 1-6**). The Aβ40 consists of 40 amino acids and some regions within this sequence are found closely related to its aggregation propensity. Specifically, ^{16}KLVFFA^{21} fragment (**Figure 1-6**) functions as the center for the nucleation depended aggregation.[145] The hexapeptide ^{16}KLVFFA^{21} alone also acts as a steric zipper by undergoing spontaneous aggregation to form assemblies that resemble the core of Aβ structures. It can form well-ordered fibers exhibiting nearly all of the properties of its full-length parent peptide.[146] The ^{16}KLVFF^{21}A region contains mainly apolar amino acid residues which participate in the formation of fibril hydrophobic spine.[147,148] Another region of interest is the hydrophobic domain near the C-terminal end of the sequence, stretching from Isleu32 to the end Val40 for Aβ40.[149] Compared to Aβ40, there are two extra amino acids located at the C-terminal end of the peptide chain, namely Isleu41, and Ala42 which also participate in the formation of hydrophobic domain. It is suggested that the higher propensity of Aβ42 to form aggregates is due to the conformational change caused by the extra two amino acids.[150] These two amino acid sequences are generally regarded as the amyloidogenic core that facilitates the aggregation of Aβ. The shorter steric zipper domain may be the driving force for the initial aggregation phase, while the larger hydrophobic domain is essential in promoting the formation of higher-ordered aggregates, such as protofibrils and mature fibrils. In addition, the histidine residues (His6, His13, His14) found in Aβ sequence are known to coordinate with metal ions, such as copper and zinc ions.[151] The complex formed by Aβ and metal ions is capable of altering the electron-transfer chain in the cells and thus generates ROS implicated in the oxidative stress hypothesis of AD pathophysiology. Given the amino acid sequence characteristics of Aβ, both Aβ40 and Aβ42 are intrinsically unstructured peptides which do not adopt a certain fixed 3D conformation either in the solid state or in the solution phase.[152] The 3D structure of Aβ is often resolved by co-crystallization of Aβ and its ligand and then analyzed by nuclear magnetic resonance (NMR), molecular dynamics (MD), and X-ray diffraction.

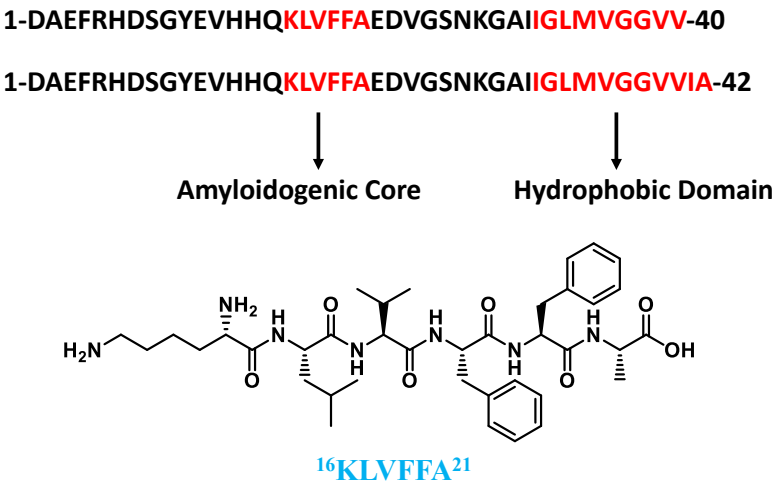


Figure 1-6. Amino acid sequence of Aβ40 and Aβ42 (above) and the structure of steric zipper KLVFFA (below).

The function of Aβ is controversial as the biological effects are strictly concentration dependent. It is an ancient molecule which has conserved amino acids in its sequence and has survived millions of years of evolution.[153] At picomolar physiological level, Aβ has many positive effects on the memory and the entire CNS.[154] It helps memory consolidation by regulating the synaptic function through the activation of nicotinic ACh receptors.[155] It also protects the homeostasis of CNS by blocking the leakage of BBB and suppression of neuronal tumor growth through the inhibition of the virus. In addition, at this low concentration, Aβ is also an antimicrobial peptide which is part of the innate immune system of CNS.[156] It can inhibit the growth of some most common clinically important pathogens, possibly by disturbing the membrane structures of microbes. However, with higher concentration of Aβ, it becomes neurotoxic and is believed to elicit the aggregation process. In the next section, the aggregation process and mechanism of Aβ will be described before discussing its toxicity mechanisms.

1.4.4 Aβ Aggregation

After Aβ is produced by cleaving its parent protein APP, it is in its monomer protein state which is featured by random-coil-like structure. Under certain circumstances, the native monomer undergoes conformational change from random coil to beta-sheet structure. This protein misfolding is one of the initiating factors involved in Aβ aggregation process (**Figure 1-7**). The trigger or reason of protein misfolding is still not well understood. However, some events have been found closely associated with protein misfolding including Aβ. Firstly, any mutations or errors happened during the protein transcription, production and post-translational modification processes will lead to the formation of sequence or modified protein conformation that is unable to fold normally.[157,158] Secondly, structural modification can be produced by environmental changes, such as pH, solvation effect, temperature, and concentration.[159] Generally, the misfolded state of Aβ40 monomer adopts a 'U' shape, while the misfolded Aβ42 monomer adopts an 'S' shape due to the extra amino acids at the C-terminus. The main contributors of Aβ aggregation at the initial stage are these misfolded Aβ40/42 monomers. The aggregation cascade is an extremely complex thermodynamic and kinetic process determined by its amino acid sequence, which ultimately generates more stable aggregates that are lower in overall energy.[160] Monomers start to interact with each other *via* the amyloidogenic cores to form dimers, trimers, tetramers, and oligomers mainly through hydrophobic interactions. Eventually, these small aggregates grow into protofibrils and mature fibrils with layers of paired Aβ40/42 (**Figure 1-7**). The X-ray diffraction pattern reveals a common structural feature of Aβ fibrils which is termed cross-β sheet/motif.[161] This is charactered by extended tightly paired β-sheets with individual β-strands arranged in the direction perpendicularly to the fibril main axis.[162] It is an unbranched structure with diameters ranging from 2 nm to 20 nm and length in several μm.[163] The spacing between strands of β-sheets is approximately 4.8 Å, whereas the spacing between two β-sheets is around 10 Å.[164]

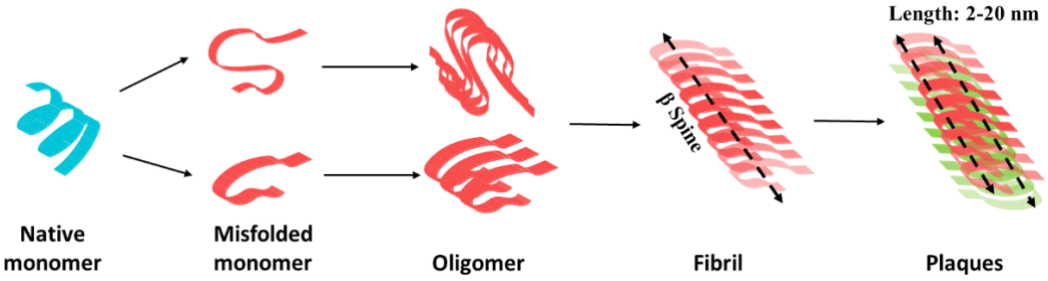


Figure 1-7. Schematic illustration of Aβ aggregation pathway.

Such structural features give rise of its tinctorial properties. Certain molecular probes can be used to monitor the protein state of Aβ during the aggregation. The probes are able to display changes in spectroscopic properties once binding to Aβ fibrils. Historically, Congo Red (CR) was the first Aβ molecular probe discovered. CR is long and flat in terms of its 3D conformation which can fit into the hydrophobic groove of Aβ fibrils.[165] Upon binding, the max absorption wavelength changes from 490 nm to 540 nm which can be monitored by a typical plate reader.[166] However, CR suffers from low sensitivity in the detection of Aβ fibrils. Also, CR interferes with aggregation kinetic by either promoting or inhibiting the aggregation.[167,168] Therefore, it is not recommended to monitor Aβ aggregation in situ. Later on, another class of fluorescent molecular probes were identified which includes thioflavin S (ThS) and thioflavin T (ThT).[169,170] The detection sensitivity is greatly improved with these types of molecular probes and they do not interfere with the aggregation process.[171] Gradually, ThT became the standard dye used to monitor Aβ aggregation. Due to the presence of a rotating single bond between two aromatic ring systems in the structure of ThS and ThT, they get locked upon binding to Aβ fibrils rich in β-sheets leading to fluorescence shifts. These changes can be monitored by fluorescence (FLR) spectroscopy (**Figure 1-8**).[169] Specifically, the unbound ThT shows characteristic FLR at 350 nm excitation and 450 nm emission. While the bounded ThT exhibits characteristic FLR at excitation 440 nm and emission 490 nm. These FLR changes can be monitored, recorded, and plotted as a function of time.

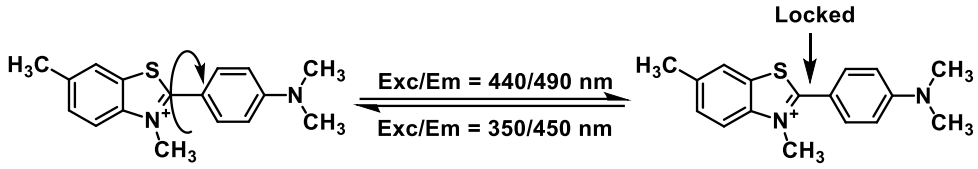


Figure 1-8. ThT probe used to study the aggregation of Aβ.

The aggregation kinetic curve monitored by ThT is in typical sigmoidal shape (**Figure 1-9**). The shape indicates that the aggregation kinetic is a nucleation-elongation mechanism. There are three consecutive stages identified. The first stage is the lag phase or nucleation phase as indicated by the initial low FLR. This stage mainly involves the formation of Aβ oligomers. Association and disassociation of monomers to and from the already-existed Aβ oligomers are both presenting in this stage. The rate of association and disassociation is approximately the same. Thus, the lag phase is considered as the rate-limiting process of the aggregation. Assembly of transient oligomers serves as seeding nuclei where additional monomeric Aβ units can latch to grow the fiber assembly. Simultaneously, due to the structural instability caused by transient weak interactions, monomers attached to the seeding nuclei can disassociate again off the oligomers. Such equilibrium slowly goes forward toward the formation of longer and bigger oligomer aggregates by continuous addition of Aβ monomers. Given the fact that Aβ42 is more prone to aggregation, the lag phase of Aβ42 is much shorter than that of Aβ40. Interestingly, the lag phase can also be shortened by adding pre-formed aggregates or fibrils into the solution, a process known as seeding.[172] The time period of lag phase is normally correlated with the exposure time of Aβ oligomers (AβOs) which is considered as the most toxic species found during aggregation. The shortening of the lag phase caused by Aβ-targeting drugs, to some extent, is considered beneficial as it indicates a shorter exposure time of toxic oligomers. The aggregation events in the nucleation phase can be explained by two mechanisms, primary nucleation and secondary nucleation respectively.[173] One type of primary nucleation involves the aggregation event in bulk solution of Aβ monomers. It is considered homogenous as it is the monomers that act as building blocks to form AβOs. The other type of primary nucleation is heterogeneous. It is the aggregation process

that occurs at the interface between two different surfaces. For example, the association of monomers on the surface of the experimental container, other proteins, air-water interface, and bilipid layers of CM.

Until a certain critical point has reached when there are enough oligomers presented in the solution, the second step of aggregation occurs. The second step is called elongation phase or growth phase where a drastic rise in FLR can be observed in the kinetic curve (**Figure 1-9**). Fibrillar structures, termed protofibrils, are rapidly formed by monomers, oligomers, and nuclei during this step. The result of elongation is the production of more stable protofibrils. Therefore, it is a faster and thermodynamically favorable process. It is the fibrillar structures that provide suitable binding pocket for ThT. As a result, more and more ThT gets bound to the newly formed protofibrils which display a significant increase in FLR. The slope of elongation phase calculated from the curve is a direct indicator of the aggregation rate. A higher slope equals a faster elongation process where the toxic AβOs are forming less toxic protofibrils quickly. Similarly, the shortening of elongation phase or higher slope is beneficial in terms of counteracting the toxic effects of toxic AβO.

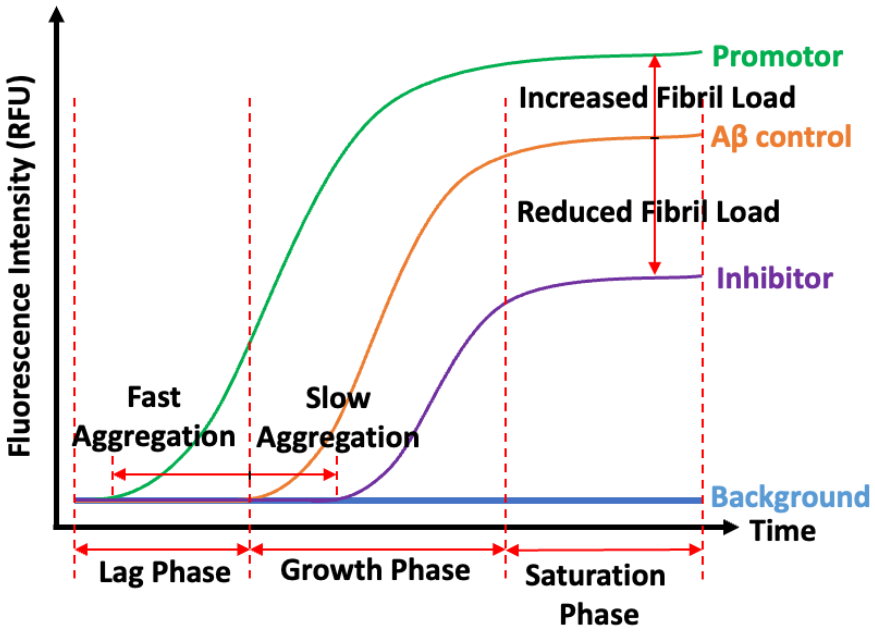


Figure 1-9. The characteristic sigmoidal curve of the ThT-monitored Aβ aggregation process.

The elongation step gets transitioned to the last step of aggregation. This phase is termed saturation phase, equilibrium phase or plateau phase where the kinetic curve reaches the highest FLR and stabilizes over time (**Figure 1-9**). The main process in this stage is the assembly of protofibrils into mature Aβ fibrils that are featured by the cross-β structure. The final FLR in this step is a direct indicator of the aggregation level. A higher FLR means more mature Aβ fibrils are formed, whereas a lower FLR means less Aβ fibrils are formed. Compounds or molecules that can lower the FLR of the saturation phase are regarded as aggregation inhibitors (AI) which have the potential drug candidates to treat AD. On the other hand, the aggregation promotors (AP) that induce a higher saturation FLR is not desirable compared to AI. However, research has shown that some of the APs are able to change the conformation of Aβ fibrils and make them less toxic or even not toxic.[174] Also, some APs are capable of reducing or bypassing the formation of toxic Aβ oligomers, even though a higher number of fibrils are formed at the end.[175,176] The overall effect is that the neurotoxicity and amyloid burden is reduced by APs. All these findings suggest that AβO plays a central role in neurotoxicity and disease progression.

It is always necessary to think of various protein states found in the aggregation from an energy point of view. Not only the aggregation process but also the formation of ligand-Aβ complex are all driven by and towards the global energy minimum. Currently, the energy model of Aβ aggregation is summarized as 'funnel' shape with the highest energy form as the corresponding unfolded protein state (**Figure 1-10**).[177] Any given amino acid sequence has its own folding and aggregation surface funnel. The unfolded protein state has the highest Gibbs free energy and highest conformational entropy due to its intrinsically unordered polypeptide sequence. The energy funnel profile is highly influenced by i) entropic contributions due to the interaction with the aqueous environment; ii) entropic contributions due to the changes in conformational freedom; iii) enthalpic contributions due to the interactions between the amino acid residues.[178] As for Aβ, the folding of native monomer is driven by the decrease in conformational entropy. On the other hand, the main driving force of lower-order aggregation is the hydrophobic collapse in aqueous environment.[179] The formation of hydrophobic interactions between the amyloidogenic core of Aβ, either intermolecular or intramolecular, decreases the Gibbs free energy. The resulting hydrophobic core or hydrophobic hollow is a result of the system trying to avoid the interactions between Aβ and the aqueous environment. For Aβ fibrils, the cross-β spine is maintained by mainly polar interactions consisting of hydrogen bond interactions and electrostatic interactions.[180] A clear understanding of energy landscape of Aβ aggregation can help with the design Aβ-targeting drugs. The energy function score is one of the essential and decisive factors when conducting molecular docking and molecular dynamics studies. Various conformations of each drug-Aβ complex will be generated based on certain algorithms during molecular docking. They are then ranked by the energy function score of the entire system. The complex with the lowest global energy is considered more stable and that specific drug candidate has a higher chance to be a potent Aβ aggregation modulator. Such computational modeling process can facilitate and direct rational drug research and development.

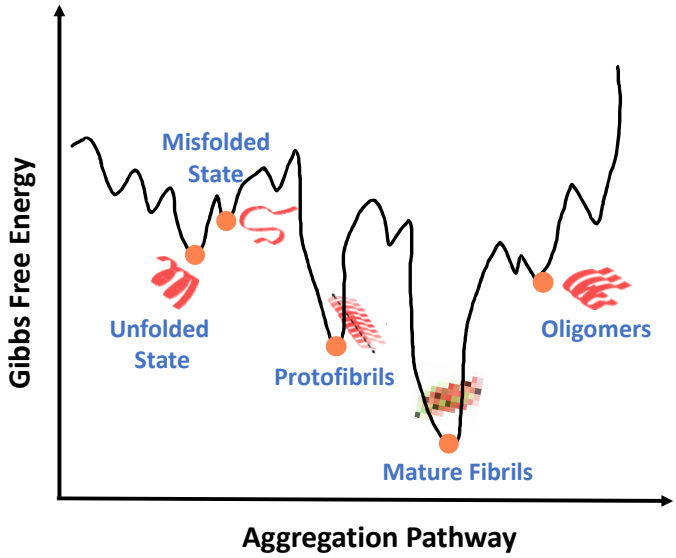


Figure 1-10. Energy landscape of various Aβ species during the aggregation.

1.4.5 Aβ Toxicity and AβO Hypothesis

The toxicity of Aβ has long been implicated in the pathophysiology of AD. Despite the fact that Aβ is an ensemble of various forms of aggregates, more or less every form shows some extent of neurotoxicity, including dimers, trimers, tetramers, pentamers, hexamers, oligomers, and fibrils. Lines of experimental evidence have shown that Aβ can lead to the downstream signaling pathway and other pathophysiological hallmarks of AD. It disrupts cell metabolism and homeostasis, impairs the function of mitochondria and electron transfer chain, destroys synaptic plasticity, and induces neuroinflammation. Generally, Aβ42 is considered more toxic than Aβ40 as it is more prone to undergo fast aggregation. Studies have demonstrated that an increased Aβ42/Aβ40 ratio is often an indicator of the disease severity which often correlates well with patients' clinical symptoms, especially in familial AD (FAD) cases. Herein, some of the widely accepted Aβ toxicity mechanisms are summarized (**Figure 1-11**):

i. The self-induced aggregation of Aβ on the CM of neurons can generate various toxic molecules, including aldehyde 4-hydroxy-2-nonenal, 2-propenal, and hydrogen peroxide.[181,182] These molecules can migrate to different compartments of neurons and lead to multiple neurotoxic

alterations to normal cellular activities. They are chemically reactive and capable of either oxidizing proteins or peroxide lipids presented in neurons. The oxidation of CM proteins is detrimental to membrane integrity[183] whereas the peroxidation can damage the function of glucose transporters, glutamate transporters, and ion channel ATPases.

ii. Aβ aggregation also promotes the release of inflammation-related signaling molecules, such as pro-inflammatory cytokines, eicosanoids, and chemokines.[184] The release of these signaling molecules can induce further harmful inflammation responses of CNS. The sustained high levels of Aβ can also activate the chronic response of innate immune system, mainly through the stimulation of microglia. In the long run, the activation of immunological toll-like receptors can cause extensive neuronal loss.

iii. The extracellular accumulation of Aβ aggregates can physically hinder the signaling transmission of neurons.[185] Neuron transmission is a process that happens at the synapse. The pre-synaptic terminal releases neurotransmitters to function as molecular messengers, which then can bind to post-synaptic cell membrane receptors to elicit further downstream signaling. The blockage of such communication mechanism at synaptic cleft caused by large Aβ aggregates can disrupt the signal transduction in CNS. The Aβ plaques are mainly deposited in hippocampus, amygdala, and entorhinal cortex of the brain. The disruption of signal transduction in these regions decreases the synaptic plasticity of neurons and thus influences memory formation and storage, learning process, and emotional behaviors.

iv. Aβ aggregates can bind to AMPA receptors and certain calcium channels, which leads to excessive calcium influx into the neurons.[186] Such increase of intracellular calcium concentration induces cell apoptosis and eventually cell death.

v. Ions entrapped by Aβ aggregates, especially iron, copper, and zinc, are electrochemically active which can produce ROS.[187] As discussed earlier, ROS can cause protein oxidation, lipid peroxidation and DNA damage. All these oxidative events build up together to cause oxidative stress to the neurons.

vi. Aβ can also hamper the mitochondrial function. It accumulates in the mitochondrial membrane and blocks the translocation of necessary supplies, including inner mitochondrial metabolites and proteins.[188] Such disruption of the electron-transportation chain leads to mitochondrial dysfunction. In turns, Aβ generation will be elevated which is a vicious cycle. Higher Aβ levels can also activate the mitochondrial fission protein Fis1 and Drp1 which further induce mitochondrial fragmentation.[189]

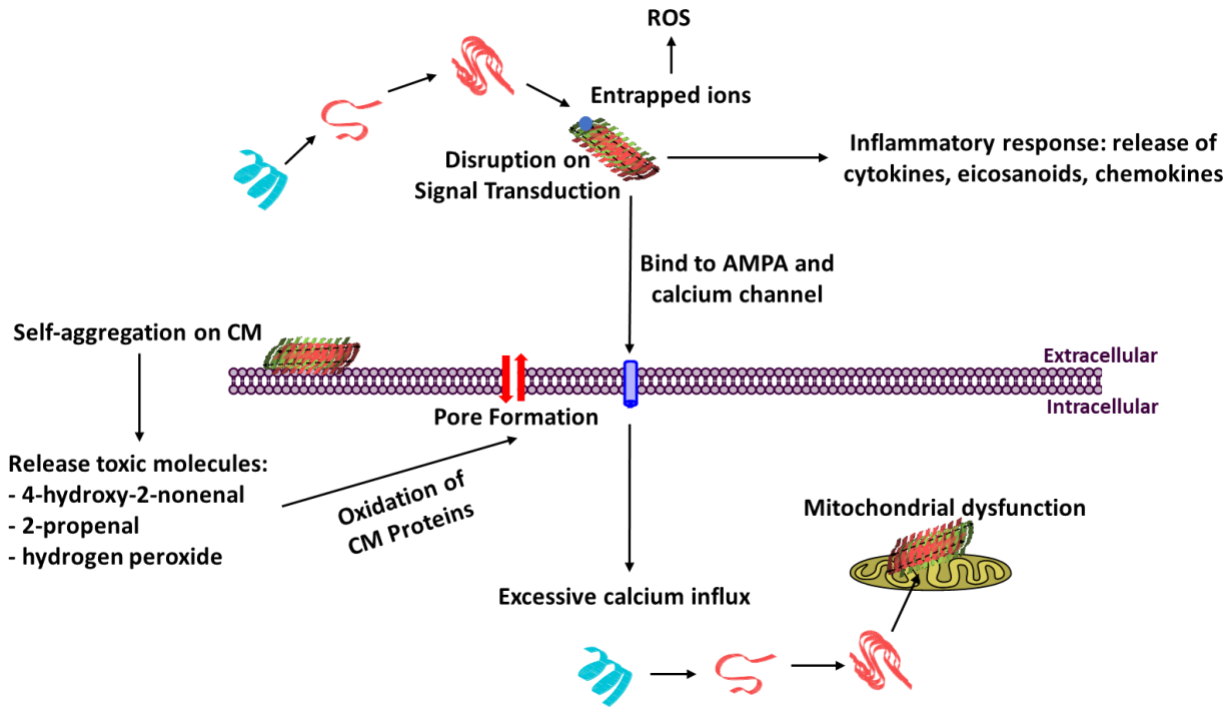


Figure 1-11. Mechanisms of Aβ toxicity.

Recently, studies have pointed out the significance of AβO as it is regarded as the most toxic species during the entire aggregation cascade. It is thought to confer disease-relevant toxic behaviors. In some cases of AD, Aβ plaques were not found in the patients' brain. Instead, AβOs were found extensively distributed among brain regions.[190] The CSF level of AβO has also been found to be elevated in AD patients. The intraneuronal AβO correlates well with cognitive dysfunction. The neurotoxicity of AβO might be due to

the fact that it is highly soluble in nature which can diffuse to various cell compartments freely. The toxicity of AβO, in general, manifests as the reduction in long-term potentiation and spine density, induction of tau pathology, impairment in axonal transport, loss or decrease expression of neurotrophic factors, and neuronal death. Based on all these observations, the AβO hypothesis of AD was proposed initially in 1998 and now it is an important component of the Aβ hypothesis.[191] There is no universal definition of AβO. These oligomeric Aβ aggregates are heterogeneous and transient, normally containing less than 100 subunits. The formation of oligomers is facilitated by hydrophobic collapse which eventually share the same β-sheet structures. However, none of these AβOs have a specific conformation or shape in 3D and they do not have cross-β structures as observed in mature Aβ fibrils. Therefore, they can be classified as soluble oligomeric Aβ species. There are two subpopulations of AβO: toxic subpopulation and non-toxic subpopulation.[153] The toxic subpopulation is also referred as type I AβO which has a higher molecular weight, normally above 50 kDa. This type of AβO is not related to fibrillar Aβ (fAβ) and has no immunological reaction with fAβ antibodies. In contrast, the non-toxic or type II AβO has a molecular weight less than 50 kDa which is thought to propagate into mature plaques. It is immune-reactive toward fAβ antibodies, but no toxicity has been found related to this subtype of AβO. The molecular mechanisms of AβO hypothesis are mainly two-fold: membrane-related toxicity and receptor-related toxicity.

i. AβO can deteriorate CM structures through its interactions with CM lipid, ganglioside GM1.[192] Then it can be directly inserted into the CM to create pores that hamper the integrity of CM. Downstream signaling pathway of these events include synaptic damage, calcium dyshomeostasis, oxidative stress/ER-stress, and cell death.

ii. AβO are pathogenic ligands of many CM receptors. The AβO/AβO-receptor interactions are proposed to generate and transduce neurotoxic signals, leading to cellular defects. Some of the AβO receptors are even able to internalize Aβ into neurons which then participate in intracellular Aβ aggregation. Some of the AβO receptors are discussed below (**Figure 1-12**).

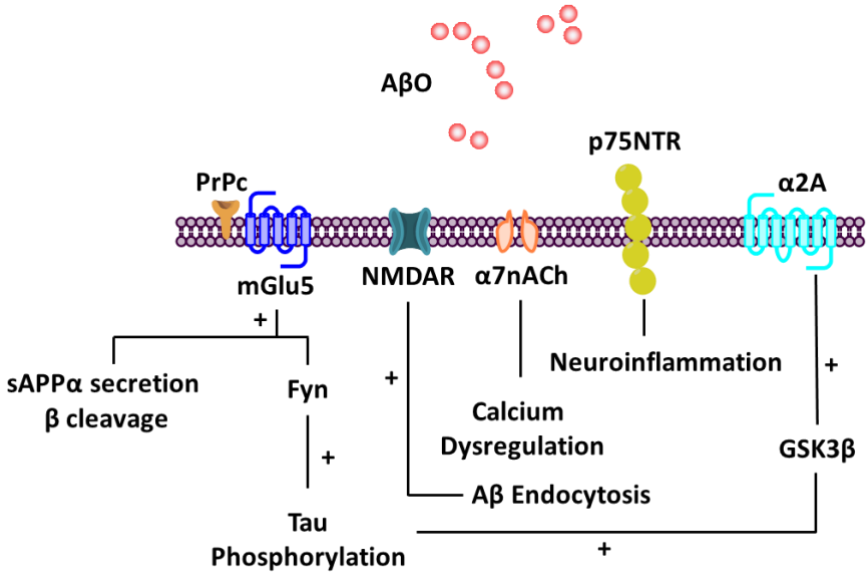


Figure 1-12. Examples of AβO-binding receptors and downstream signaling pathways.

Cellular prion protein PrPc is a glycosylphosphatidylinositol anchored membrane protein and AβO is one of its ligands.[193] Upon binding with AβO, it undergoes a conformational change to an infectious, pathological state. Such conformational change can activate metabotropic glutamate receptor mGlu5, which is a G-protein coupled receptor. The activation of mGlu5 can stimulate sAPPα secretion while inducing β-cleavage of APP and thus increase the production of Aβ. Besides, after the mGlu5 has been stimulated, proto-oncogene tyrosine protein kinase Fyn is further activated. Fyn leads to the phosphorylation of tau protein which triggers the hyper-phosphorylation of NR2B subunit of NMDA receptor.[194] The outcomes of this signal transduction are excessive calcium influx into neurons, tau hyper-phosphorylation, and synaptic dysfunction.[195]

NMDA receptor and α7nACh receptor are ion channels found on the CM. At post-synaptic level, AβO interacts with NMDA receptor to activate its signaling pathway which leads to calcium dysregulation, neuronal death, and synaptic dysfunction.[196] AβO is also a ligand of α7nACh receptor where the activation can induce the endocytosis of Aβ.[197] The Aβ-induced tau phosphorylation is also facilitated by the activation of α7nACh receptor mainly via ERK and JNK signaling pathways.[198]

p75 neurotrophin receptor (p75NTR) was initially found as a low-affinity nerve growth factor receptor and then various neurotrophins were found able to bound to it. Such neurotrophins include nerve growth factor, neurotrophin-3, neurotrophin-4, and brain-derived neurotrophic factor.[199] Recently, AβO has also been identified as a p75NTR ligand. AβO can bind to both monomer or trimer of p75NTR to activate its intracellular signaling pathway. It is shown to induce neuronal apoptosis in experiments. In addition, it can also activate caspase 3 and caspase 8 which will produce ROS and eventually leads to oxidative stress on neurons.[200] Interestingly, AβO can work synergically with cytokines, like TNFα and IL1β, to further strengthen the toxic effects of AβO-p75NTR route.[201]

AβO can also bind to the allosteric site of α2A receptor which changes the norepinephrine signaling and activates glycogen synthase kinase 3β (GSK3β) which then triggers the hyperphosphorylation of tau that is implicated in the pathophysiology of AD.[202]

Other AβO-binding receptors include: sodium potassium-ATPase α3 subunit, low density lipoprotein-related protein receptor (LRP), receptor for advanced glycation endproducts (RAGE), tyrosine kinase ephrin type A & type B receptor, leucocyte immunoglobulin receptor B2, triggering receptor expressed on myeloid cells (TREM2), toll-like receptor, AMPA receptor, frizzled receptor, adrenergic receptor, N-formyl peptide receptor, IgGFc receptor potential melastatin, insulin receptor, and Wnt receptor.[153]

To summarize, based on the observation of amyloid plaques found in AD patients' brain, scientists have uncovered the composition, physiological and pathological functions, aggregation properties, and toxicity of Aβ species. The Aβ aggregation process is not a single-direction process which ultimately transforms all Aβ monomers into structurally identical mature fibrils. Instead, it is a very intricate equilibrium with the entire balance going forward towards the global energy minimum.[203,204] The equilibrium nature of Aβ aggregation indicates that the Aβ species, at any given aggregation stage, are heterogeneous in their composition. The only difference is which type of Aβ species is taking the dominant proportion at the time. Therefore, to understand the toxicity of Aβ species, the best way is to put all the species into a scale of

toxicity with the AβOs being the most toxic species, followed by Aβ fibrils, protofibrils, and other lower-order structures. The goal of intervening in the Aβ aggregation process is not to reduce or eliminate a specific type of Aβ aggregates, but the reduction of overall amyloid burden/load and associated toxicity. With this being said, the drug designing strategies targeting the Aβ aggregation cascade will be introduced in a later section.

1.4.6 Aβ Transportation, Clearance and Degradation

Aβ monomer is a small peptide with a molecular weight around 4.5 kDa. As mentioned in previous sections, even though it is mainly generated by neurons in the CNS, it can be produced by many cells in the human body. It gets circulated in plasma, cerebrospinal fluid (CSF), and brain interstitial fluid (ISF). In ISF, the monomeric Aβ is stabilized by chemical chaperons, staying in a bounded state which is in equilibrium with free unbound Aβ. The Aβ concentration in ISF is strictly regulated by few biological processes: i) the rate of Aβ production from APP; ii) receptor-mediated Aβ influx into the brain from blood via blood-brain-barrier (BBB); iii) receptor-mediated Aβ efflux/clearance into the blood from brain via BBB; iv) enzymatic degradation of Aβ. These four processes are closely connected and rigorously regulated by different cellular signalling pathways. Together they maintain the balance of Aβ production and clearance at normal physiological level. In the case of AD, at least one out of the four processes are dysregulated and thus the Aβ level becomes higher and initiates the aggregation cascade.

The CNS resides in a conserved brain region that is partially insulated from other systems of the human body. It has its own circulation system and neuronal immune system which are also connected to the peripherals. However, in order to control the transportation of biological molecules in and out of the CNS, three barriers are formed between blood and brain which are the arachnoid barrier, the blood-ISF barrier, and most importantly BBB.[205] The BBB is the main physical barrier between the peripheral circulation and brain micro-circulation. It consists of brain microvascular endothelial cells (BMECs) wrapped by pericyte process and astrocyte end feet.[206] Tight junctions and adherence junction structures found in between

adjacent BMECs further constrain the transportation of biological molecules, including both nutritional supplies and brain waste.[207] Moreover, the apicobasal polarity and glycocalyx covering of the luminal surface of BMECs make the permeability of BBB highly selective.[208,209] There are few ways for biologically important molecules to cross the BBB. First, nutrients typically go through the BBB from blood to brain by transcellular route, even though the intercellular cleft between the BMECs are extremely small. Second, small lipophilic molecules with molecular weight less than 500 Da can cross the BBB freely by passive diffusion. The size, number of hydrogen bond donor and receptor, and concentration all play an important role in passive diffusion. Last but not least, most of the molecules need to cross BBB with the help of transporters or carriers located on the BBB, through either facilitated diffusion or active transportation. Indeed, the transportation of Aβ across BBB requires the participation of certain transporters, namely RAGE and LPR.

RAGE is a multiligand receptor that belongs to the immunoglobulin superfamily. It is expressed on the luminal surface of BMECs where its expression is determined by the level of its ligands. The transportation of Aβ in the direction from blood to brain is facilitated by RAGE.[210] It is the main Aβ influx transporter that binds to soluble monomeric Aβ and thus increases the level of Aβ in the brain. When pathological level of Aβ starts to accumulate in the brain, RAGE expression is up-regulated by the increasing concentration of Aβ.[211] The increasing expression of RAGE, in turns, uptakes more and more Aβ into the brain. This provides the potential for exacerbating cellular dysfunction due to the relationship between Aβ and RAGE.

Under normal physiological conditions, bulk flow of Aβ from brain to blood is the main clearance mechanism. It effluxes Aβ from ISF to CSF at a very slow rate. The resulting Aβ in CSF pool will be cleared together with CSF turnover which happens every 4-5 h.[212] However, in the cases of AD, the major Aβ clearance route is LRP-mediated efflux from brain to blood across the BBB.[213] LRP is a multifunctional scavenger and signaling receptor which belongs to the LDL receptor family. The physiological function of LRP is the transportation and metabolism of cholesterol associated lipoproteins.[214] It is being synthesized as a single polypeptide precursor which is then further cleaved into a heavy extracellular α chain and a light

transmembrane, and cytoplasmic β chain. These two chains coupled together to function as a transporter on the BBB. The affinity of LRP to Aβ40 is lower than that of Aβ42 which possesses a greater β-sheet content. It can also bind to a diverse array of ligands, such as ApoE and α-2-macrolgobulin.[215,216] Aβ interacts with ApoE containing lipoproteins which are ready to be cleared by LRP into the peripheral blood stream. It is found that the expression of LRP and its capacity to bind Aβ is reduced in AD which means that the clearance of Aβ is downregulated as a result.[217] In addition, the over-accumulation of copper ion in the brain also contributes to the decrease of LRP-mediated Aβ clearance.[156] In addition, LRP can also interact with APP and thus regulates APP regulation and processing.

The last player in maintaining the homeostasis of Aβ is enzymic degradation. Few Aβ-degrading proteases have been identified, including neprilysin, endothelin-converting enzyme (ECE), and insulin-degrading enzyme (IDE), and plasmin. Neprilysin is a membrane zinc metallo-endopeptidase.[218] It is the most efficient degrading enzyme of Aβ. The proteolytic degradation of Aβ by neprilysin can be inhibited by its potent and selective inhibitor thiorphan and the overexpression of neprilysin leads to the lack of Aβ accumulation in the brain.[219] ECE is a membrane-bound zinc metalloproteinase belonging to the same family of neprilysin, the so-called M3 family. The inhibition of ECE enzymic activity can be inhibited by ECE inhibitor phosphoramidon and the overexpression of ECE leads to a reduction of more than 90% of secreted Aβ.[220] IDE is a zinc metallo-endopeptidease that degrades Aβ and insulin.[221] The interplay between IDE and AICD is also correlated to its degradation activities. Lastly, plasmin is an important serine protease that dissolves fibrin blood clots. Some recent studies discovered that Aβ is also a degrading target of plasmin and it can degrade and reduce the neurotoxicity of both monomeric Aβ as well as fAβ.[222]

1.4.7 Drug Developing Strategies Targeting Aβ Cascade

The Aβ hypothesis of AD provides several drug targets to develop novel molecules and therapies (**Figure 1-13**). The upstream targets include: i) down-regulation of Aβ production by inhibiting APP proteolytic enzymes BACE and γ-secretase; ii) modulation of Aβ aggregation process. Structural biology and

molecular docking studies have assisted in the development of BACE and γ-secretase inhibitors. Rational drug design strategies can be used to design and screen either novel synthetic molecules or natural compounds to inhibit the activities of APP proteolytic enzymes. However, selectivity, off-target effects, and safety are the major concerns in developing enzyme inhibitors given the fact that these enzymes are also involved in other biological pathways.[223] In contrast, the modulation of Aβ aggregation is challenging due to the highly intricate aggregation mechanism. The drug target is not a single protein or enzyme with a well-defined structure or binding pocket. Instead, the aggregation modulators need to interact with a cohort of heterogeneous Aβ aggregates that vary in structure, toxicity, solubility, and composition with no well-defined binding pockets. Besides, the modulation of Aβ cascade is not simply just inhibiting or promoting the aggregation process. Aggregation inhibitors are thought to be beneficial as they can convert the more toxic fibrils into less toxic monomers or can prevent the aggregation process. The AβO is the most toxic form that is formed during the aggregation process. Therefore, no matter if a drug molecule is aggregation inhibitor or promotor, as long as the exposure time or formation of AβO can be reduced, it will be beneficial in reducing or preventing Aβ-mediated neurotoxicity. The objective of drug development targeting Aβ aggregation is to lessen the overall Aβ toxicity burden rather than simply inhibiting or stimulating the process itself per se.

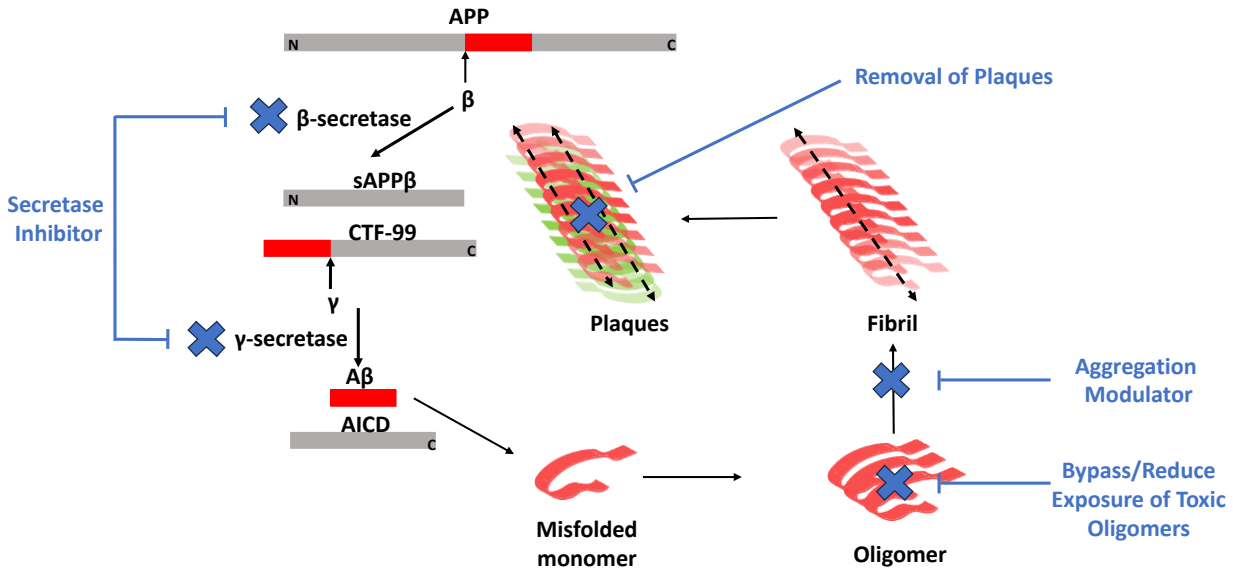


Figure 1-13. Summary of drug developing strategies that targeting Aβ hypothesis.

Some other downstream drug targets involved in Aβ hypothesis include: i) modulation of APP and its proteolytic product trafficking; ii) stimulation of Aβ degrading enzymes; and iii) upregulation of Aβ clearance from CNS.[224,225] The trafficking of APP and its proteolytic products, especially Aβ and AICD, play an important part in facilitating its neurotoxicity, clearance, and degradation. For example, stimulation of molecular pathways that regulate the transportation of Aβ into its degrading cell compartments is considered beneficial as it can increase the degradation of Aβ. Another drug development strategy would be to use molecules to downregulate molecular pathways that transport APP to the sublocation of the mature BACE.[226] By inhibiting the colocalization of APP and its proteolytic enzymes, the production of Aβ can be lowered. However, these strategies are theoretically correct and feasible but the detailed mechanisms of these trafficking routes and regulating factors are poorly defined. Without seeing the whole picture, doing so can lead to unwarranted off-target effects that may hamper the normal physiological signaling pathways. Some other direct strategies can be considered as well, such as upregulation of LPR activity, downregulation of RAGE activity, and stimulation of ECE and IDE. These strategies are making a direct influence on the Aβ clearance out of the brain or on the Aβ degradation, and as a result would alleviate the

available Aβ burden in CNS to initiate the aggregation cascade. Some immunotherapies can also achieve the same goal by administering the active anti-Aβ antibodies by injection. These antibodies are designed to selectively target the Aβ oligomers/fibrils and then speed up their removal by activating the innate immune system.[42]

Early drug development in the area of AD tends to put its focus on alleviating the symptoms of AD dementia, including cognitive decline and behavioral changes. With drugs controlling the symptoms being used for a few decades, the scientific community is beginning to realize that these types of drugs can not cure the disease as they are unable to alter the disease progression. There is an increasing demand for disease modifying drugs that target one or more factors of AD pathophysiology. A recent literature reported that there are 143 drugs in the AD drug development pipeline with more than 80% of those proposed to act as disease-modifying therapies. The list includes disease-modifying biologics and disease-modifying small molecules.[70] These potential medications target several biological pathways underlying AD, such as oxidative stress, gut-brain axis, Aβ hypothesis, synaptic plasticity, tau cascade, inflammation, and metabolism.

1.5 AD Disease Continuum

As implicated by its multifaceted pathophysiological pathways, AD is a complex neurodegenerative disorder and the exact cause is unknown. Historically, the clinical diagnostic standard and definition of AD went through revisions and modifications a few times. The initial definition was based on the systematic exclusion of other potential etiologies that may also cause the same symptoms. Later on, the definition primarily depended on the clinical manifestations of patients. AD is viewed in a series of progressive disease stages, defined by Braak staging, evaluated by the level of impairment present in the brain and the severity of clinical symptoms.[227] However, some recent findings make the traditional view of AD controversial. Patients with clear evidence of Aβ plaques and NFTs in the brain were not always exhibiting

AD symptoms. In the clinical trials, the severity of the disease, assessed by participants' symptoms, was not correlated well with the severity of Aβ burden.[228] All of these observations indicate that pathophysiological changes may begin a long time before clinical symptoms. Thus, AD is further classified into asymptomatic pre-clinical stage and clinical stage. These two stages are interconnected and happen in sequential order without a firm boundary. In the pre-clinical stage, patients are not showing any symptoms, instead evidence of pathological changes can be observed. The transition between the stages is described by brain and cognitive reserve. Brain reserve is the ability of the brain to withhold pathological changes without altering physiological functions. Cognitive reserve refers to the ability to engage alternate neuronal networks to function well in terms of cognition. When the brain and cognitive reserve cannot withstand the ongoing pathological changes, the transition from pre-clinical to clinical stage occurs. Therefore, it has been suggested that AD should be reconceptualized as a clinicopathophysiological condition.[229] It highlights the necessity of understanding disease progression from pathophysiological, biomarker, and clinical perspectives. AD is an assembly composed of multiple interconnected components where these components occur individually in parallel in their own trajectory, moving along a certain disease continuum. But the overall ultimate result is the progression and worsening of cognitive and functional abilities.

In this regard, the pathologies of AD can be synthesized. The core idea is that Aβ/AβO and tau/tau oligomer are the initiating factors that activate the downstream mechanisms.[230] The formation of Aβ/AβO and tau/tau oligomer is responsible for all the emerging pathological biomarkers of AD. The first step is termed initiating pathogenesis via AβO. Based on the AβO theory, AβO is soluble in nature and is able to diffuse across biological membranes. It is produced by cortical neurons which then spread to the entorhinal cortex, neocortex, and hippocampal regions of the brain as determined by the afferent and efferent projections of neurons. AβO at these regions can seed the aggregation for themselves forming Aβ fibrils which then initiate the Aβ cascade. On the other hand, it is thought that AβO can also cross-seed the aggregation of tau which then initiates the tau cascade.[231,232] The local production, transportation, and interplay between Aβ and tau spread the primary pathological factors throughout the brain regions that are

responsible for cognitive, behavioral, and functional activities. The next step of pathology is tau oligomer driven disease progression. At this stage, there is an extensive distribution of Aβ burden across the brain and gradually tau cascade becomes the leading event. The reason why tau burden is more closely related to the severity of symptoms is because tau is the major pathological factor that contributes to disease pathogenesis and disease continuum. The rapid development of tau cascade can breakthrough the threshold of brain reserve and cognitive reserve to worsen the AD symptoms over time. The last step of AD pathology is inflammation which contributes to disease progression and pathogenesis. It involves microglial activation, phagocytosis of Aβ, and release of inflammatory cytokines which can then initiate other pathological signaling pathways of AD. By conceptualizing AD as a disease continuum and summarizing pathological events, all the aspects of AD are then synthesized and organized as a whole.

1.6 Design of compound library

1.6.1 Curcumin

In the previous sections, the background, pathophysiology, and research and development strategies of AD were discussed. The objective of this thesis was to identify novel chemical probes to understand and study the aggregation mechanisms of Aβ as well as to develop potent small molecule Aβ aggregation modifiers that are able to alleviate the overall toxic burden induced by the Aβ aggregation process. A rational design approach was used to identify novel small molecules that can modulate the Aβ aggregation cascades. Small molecule compound libraries were investigated by structure-activity relationship (SAR) studies. The lead discovery has always been the initial and the most important part of drug discovery. The lead refers to chemical structure/template that exhibits potential biological activities towards the drug target which is the Aβ peptides in this case. From a medicinal chemistry point of view, various techniques and method can be used to identify the lead, including but not limited to serendipity, high throughput screening (HTS), virtual screening, *de novo* drug design, drug re-purposing of FDA-approved drug, and fragment-

based drug design etc. In this regard, several natural products are known to exhibit anti- Aβ activity. For example, extensive studies have demonstrated the Aβ inhibition properties of two of the natural products, namely, curcumin and chalcone (**Figure 1-14**). These two natural products and their derivatives have shown promising biological activities towards several factors involved in AD pathophysiology and are known to possess anti-oxidant, anti-inflammatory, anti-Aβ aggregation, and anti-tau aggregation activity. Next few sections will summarize the chemical, biological, and pharmaceutical nature of curcumin and chalcone.

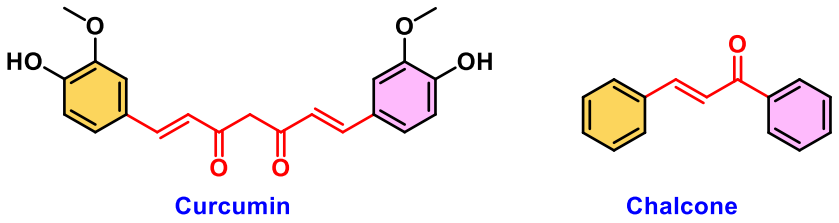


Figure 1-14. Chemical Structure of curcumin (left) and chalcone (right). The aromatic ring systems at the ends of the molecule are highlighted in yellow and pink, whereas the linker regions between the rings are highlighted in red.

Curcumin or more precisely turmeric is the powderobtained from the rhizome of the plant *Curcuma longa*. It is a yellow pigment that has been historically used as food preservatives, flavoring spices, and traditional herbal medicine in some Asian counties.[56] The constitutional ingredients of turmeric powder include volatile essential oils, fiber, minerals, protein, fat, carbohydrate, and most importantly curcuminoids.[233] Curcuminoids is the term used for the major phytoconstituents of turmeric powder. These curcuminoids are diarylheptanoids with a generic structure shown in **Figure 1-14**. The majority (70%) of curcuminoids is made up of the active constituent curcumin, (*E*, *E*)-1,7-bis(4-hydroxy-3-methoxyphenyl)-1,6-heptadiene-3,5-dione, and the other two main components are demethoxycurcumin and bisdemethoxycurcumin respectively.[234]

Previous studies have shown that curcumin can inhibit the aggregation of Aβ and reduce the level of toxic Aβ oligomers.[235] Its derivatives also have a broad biological activity spectrum, including anti-

inflammation, metal chelating, anti-oxidation, anti-microbial, enhance wound healing, neuroprotection, anti-angiogenic, and anti-cancer.[236–245] A plethora of research has been published during the past few decades revealing its potential application as drug candidate. An extensive curcumin resource database has been built by the scientific community to gather information regarding its biological activities. Curcumin and its derivatives, so far, have been discovered to have more than 120 different kinds of biological activities which makes it into a privileged structure in medicinal chemistry.[246,247] All of the evidence supports that curcumin and its derivatives can potentially become a drug candidate that targets the disease process of AD. However, there are few drawbacks of curcumin which makes it a challenging drug candidate.

First, curcumin is chemically unfavorable. The diketone moiety present can undergo keto-enol tautomerization in solution. NMR studies have suggested that it is the enol tautomer, not the diketone tautomer, as the major form.[248] The chemical nature of enol makes curcumin into a planar, intramolecularly hydrogen bonded structure which is not ideal to bind and fit specifically with disease target, normally a protein or enzyme.[249] It is practically insoluble in aqueous environment at neutral pH which proposes difficulty for pharmaceutical formulation. It degrades rapidly in aqueous environments via nucleophilic substitution or elimination to form vanillin, ferulic acid, and feruloyl methane.[250] Studies also suggest that curcumin can degrade in cell culture medium used by various in vivo assays and human blood. Curcumin is also photoreactive and undergoes photochemical degradation when exposed to sunlight.[250] Approximately 5% of curcumin is subjected to photodegradation during the sample preparation process if not protected from light. The photochemical degradation products of curcumin include ferulic aldehyde, vanillic acid, 4-hydroxy-3-methoxybenzaldehyde, and 3-(4-hydroxy-3-methoxyphenyl)acrylic acid.[251] Another degradation pathway of curcumin is facilitated by oxidation and the major product is bicyclopentadione.[252] It is necessary to note that the degradation products of curcumin under biological assay conditions and physiological conditions are generally different. Therefore, during the R&D stage, researchers should pay attention to the stability of curcumin and its derivatives before assessing their putative biological activity.

Second, curcumin has a poor pharmacokinetic and pharmacodynamic (PK/PD) profile. The bioavailability of curcumin is extremely low with less than 1% if administered orally.[253] However, it is suggested that curcumin has a poor membrane permeability with a ClogP value ranging from 2.3-3.2.[254] In the case of AD, the drug has to penetrate through BBB before reaching the disease target. The literature data on the distribution of curcumin is of high variability possibly due to its static and dynamic residual complexity.[255,256] The curcumin parent compound itself, regardless of its various metabolite/degradation products, does not distribute and concentrate at any specific organs based on studies conducted in rats.[247] In terms of metabolism, curcumin is extensively metabolized in the liver and intestine.[257] Phase I metabolism reduces double bonds in the linkage by alcohol dehydrogenase,[258] whereas Phase II metabolism is the conjugation with glucuronides and sulfates on the phenol group.[259,260] Considering all these facts, the concentrations where the desired biological effects were observed are so much higher than the actual blood drug concentration due to its poor PK/PD properties. Any efforts that try to maximize the biological effects by increasing the dosage of curcumin is fruitless as dose related toxicity and side effects might occur. The toxicity of curcumin is also a concern for its development. Curcumin and its biological degradation products are substrates for a variety of human enzymes which would lead to drug-linked toxicity. It can inhibit cytochrome P450 enzyme, UDP-glucuronosyltransferase, and glutathione-S-transferase to name a few.[261,262] This would facilitate drug-drug interactions and cause potential toxicity. Curcumin can also lead to toxicity in terms of generating ROS, induce DNA damage and alterations, iron chelating, and perturbate cell membrane.[263]

Third, the chemical structure of curcumin has been identified as one of the pan assay interfering compounds (PAINS) which may lead to false positive results in biological screening assays and its promiscuous biological activities.[264] The nature and mechanism of curcumin as PAINS will be discussed in detail in *Section 1.6.3*.

In summary, curcumin is the major component isolated from natural plant *curcumin longa* which shows a broad biological spectrum in both *in vitro* and *in vivo* assays. The chemical structure template of curcumin

is considered as a privileged structure in medicinal chemistry. Studies on curcumin and its derivatives reveal its potential role in the treatment of AD via various mechanisms of actions. However, the development of curcumin and its derivatives is complicated by chemical instability, poor PKPD profile, and PAINS nature. Several strategies have been made to overcome these above-mentioned drawbacks of curcumin, including its formulation as nanoparticles, liposomes, micelle, and phospholipid complex. Besides, piperine, a hepatic and intestinal glucuronidation inhibitor, has been used as an adjuvant of curcumin to increase its bioavailability and it is being studied in clinical trials. In addition, derivatives of curcumin have been rationally designed to keep its biological active template as well as remove the susceptible functional group.

1.6.2 Chalcone

Chalconoid or so-called chalcone (1, 3-diaryl-2-propen-1-one) is a major class of compounds isolated from natural sources. These compounds are important intermediates in the biosynthetic process of flavonoids.[265] It is an open-chain form of flavonoids which explains the reason why it can be processed by plants and microorganisms easily to produce flavonoids.[266] Numerous chalcone derivatives were isolated from natural sources with hydroxyl and methoxy groups as the most frequently seen substituents.[267] Currently, besides the natural isolated chalcones, many novel synthetic chalcone derivatives with biological activities have been developed. These chalcone derivatives have shown a broad biological activity spectrum, such as anti-cancer, anti-malarial, antimicrobial, anti-inflammatory, anti-protozoal, anti-oxidant, anti-diabetic, anti-tuberculosis, anti-virus, neuroprotective activities, and anti-Aβ aggregation activities.[268–277]

Chalcone is a styryl ketone that is flanked by two benzene rings at the ends. The carbon-carbon double bond can generate cis- and trans- conformations. The *trans*- conformation possesses lower steric hinderance compared with the *cis*- and thus is more thermodynamically stable. The chemical characteristics of chalcone gives it a relatively planar and flat conformation with two aromatic rings connected through the linker. The planar conjugated structure gives its fluorescent properties which has been utilized in imaging and target identification studies.[278]

In the context of AD, chalcone generic structure has been regarded as the privileged medicinal chemistry scaffold. Chalcone derivatives exhibit good activity toward various disease-related factors underlying AD. The most prevailing research strategy in this field pertains to the conception of hybrid molecules. By combining two or more fragments from different disease-modifying molecules, the hybrid compounds display a better biological activity. It is well acknowledged that many naturally inspired chalcone hybrid derivatives have anti-inflammatory, anti-Aβ aggregation, anti-oxidant, acetylcholinesterase inhibition, metal chelating and neuroprotective activities based on various *in vitro* and *in vivo* disease models of AD.[279–285]

Interestingly, evidence indicates that hybrid chalcone derivatives can intervene in the formation of Aβ fibrils. Koneni *et al* designed, and synthesized a series of novel hybrids incorporating benzofuran and chalcone fragments and screened their ability to decrease the Aβ aggregation in a transgenic mice model that expressed human Aβ peptide.[286] The SAR study revealed that the C_6-C_n-C_6 arrangement of carbon chain in chalcone is essential to the activity, particularly the fused benzofuran ring is the core moiety.[287]

In addition, chalcone derivatives have also been investigated for their ability to image Aβ aggregation. Due to their flexible chemical structure, chalcone derivatives demonstrate relative higher affinity with Aβ fibrils compared with classic reference compounds, such as Congo Red and ThT. Therefore, the isotope-labeled chalcone derivatives could serve as imaging probes in clinical settings to monitor the level and progression of Aβ aggregation. As an example, several studies have shown that radio-iodinated chalcone derivatives with various chemical scaffolds selectively bind to Aβ fibrils in both AD brain tissue and biodistribution studies in mice.[288–292] These chalcone derivatives have the potential to be used in clinical diagnosis of AD by positron emission tomography (PET), single-photon emission computed tomography technologies.

To conclude this section, the literature identified the generic chemical structure of chalcone as a favored scaffold in medicinal chemistry. Naturally modified and synthetic hybrid chalcone derivatives exhibited

multifaceted biological activity toward AD. Specifically, these derivatives showed high affinity toward Aβ, exhibited anti-Aβ aggregation properties and were able to reduce cytotoxicity induced by Aβ peptides.

1.6.3 Pan assay interfering compounds

In the workflow of drug discovery, after the disease target has been identified, confirmed, and validated, efforts will be made to screen and identify lead compounds with unique chemical structures from either a new synthetic library or a pre-assembled library containing hundreds or thousands of small molecule compounds. Various *in vitro* and *in vivo* biological assays are conducted to evaluate the modulatory activity of small molecules against different disease targets, exclusively disease-related proteins and enzymes. With the help of HTS, millions of entries of biological and chemical screening can be done rapidly with automated robotic arm and computerized system in parallel. This facilitates the efficient discovery of leads from a compound library. However, few observations were made when comparing the hits from different HTS campaigns: i) some compounds show up as frequent hits that exhibited promiscuous biological activities against numerous disease targets from different classes; ii) similar chemotype but not necessarily the identical compound kept appearing in different screening assays; iii) biological activity of some leads was not reproduceable in resynthesized or repurified samples; iv) early and promising SAR was dissipated for some leads, ending in flat or uninterpretable SAR; and v) when some of the early hits were verified by affinity assays, e.g. surface plasmon resonance, and orthogonal target assays, they turned out to be invalid and not amenable for further development.[293–296] The real drugs modulate the proteins either by inhibition or activation by fitting nicely into the binding pocket of the target enzymes. They interact specifically, efficiently, and selectively with desired proteins. Unlike real drugs, these frequent hitters are not discriminating drugs that satisfy those requirements and often they are merely the results of false positive readouts from the biological screening assays.[297] They may interact with disease target through non-drug-like mechanism with no specificity. These compounds are termed PAINS. These hits or PAINS are polluting the scientific soil and wasting valuable resources. The relationship between a true hit (true

positives) and PAINS (false positives and false hits) is summarized below. The active results (including true positives, false positives, and false hits) can arise from the ability of a compound to either modulate the target or modulate the readouts (**Figure 1-15**).[298] The former target modulators contain the true hit in the context of assays and targets. It can modulate the target by covalent or non-covalent binding to the pockets.[299,300] These true hits are often optimizable with medicinal chemistry methodologies toward an increasing specificity. Another situation of the target modulators is compounds that are inherently reactive in chemistry that interfere specifically with target or substrate. This type of target modulator can be considered as false hits or "bad actors" which seem to appear as true hits but it cannot be a drug candidate.[301] These false hits can give false positive readouts by indiscriminately binding to certain susceptible amino acids in biological molecules or the proteins (e.g. cysteine with appropriate pKa value) or simply can influence some other co-factors that the function of proteins heavily depend on (e.g. redox cycle, cytokines, metal ions). The latter type of actives, so-called readout modulators, includes false positives in the context of either the target or the assay. The readout modulators in the context of the target are those who are able to interact non-specifically with target leading to a false positive readouts regardless of the sequence, shape or conformation of the target. The other type of readout modulators includes compounds that interfere with assay setup or methodology. In this fashion, these compounds disguise as promising hits capable of modulating the activity of target, but instead, the results are artefacts.

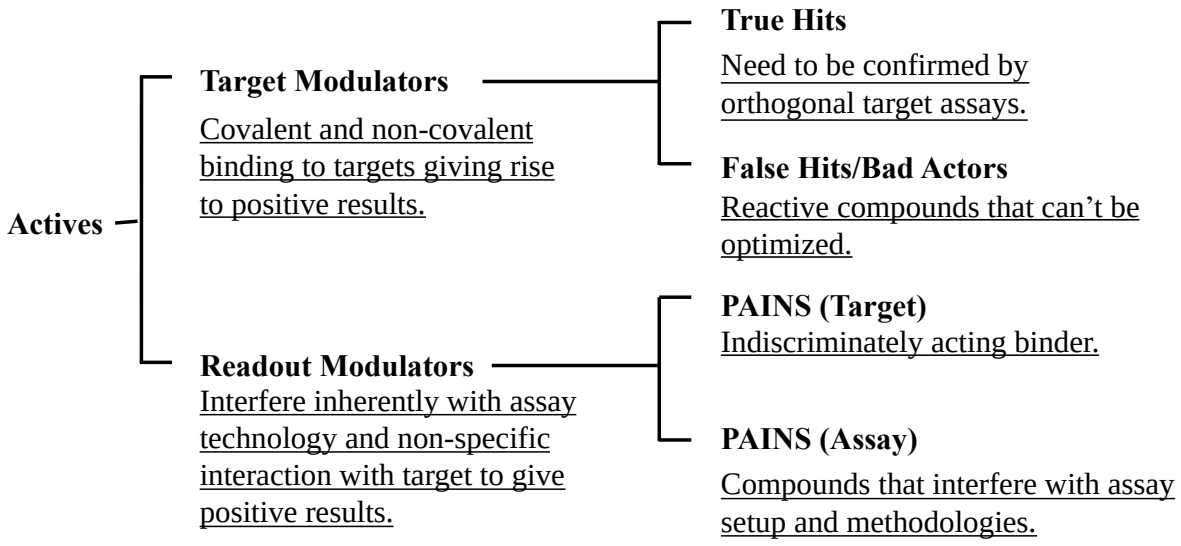


Figure 1-15. General classification of PAINS.

Originally, in 2010, Baell and Holloway established for the first time a PAINS structural filter that encompasses around 400 structural classes categorized into 16 easily recognizable groups.[302] This PAINS filter has been adopted by many drug predicting and discovery softwares (e.g. SwissADME tool) and has been mandated by many journals before the submission of a manuscript (American Chemistry Society and Journal of Medicinal Chemistry). Some other PAINS filters are ALARM NMR assay based filter, AstraZeneca-developed filter, Badapple filter, and promiscuity filter.[299,303–307] More or less these filters were built upon substructure search and categorization to assign a risk factor statistically to certain groups of compounds with similar substructure. For example, Badapple undertakes a hierarchical scaffold analysis and reports on the biological promiscuity score with a range 1 to 100 means no indication that the compound is PAINS, 100 to 200 indicates a moderate score with weak promiscuity, and a score above 300 points a strong suggestion of PAINS. Another delicate example is AstraZeneca's filter which compares the incidence of promiscuity of certain substructures to a control balanced library group (statistically 6.5% PAINS incidence rate). The more a substructure class deviates upward from this value, the more promiscuous it might be.

The identification of PAINS and its structural filters is mainly observational. Over the years researchers in the area of medicinal chemistry explored some potential mechanisms that underlie the non-drug like properties of PAINS. Herein, several mechanisms are briefly discussed.

i. Some PAINS are known as covalent modifiers which react with biological thiols mainly via Michael addition reactions. Normally, the covalent modifier possesses moieties that can function as Michael acceptor, such as an α, β-unsaturated system. Such structure is readily susceptible to nucleophilic attack from biological Michael donors such as solvent exposed cysteine within protein or enzyme.[308]
ii. Some PAINS can trap either toxic or reactive impurities, such as metals, during the synthesis. If such impurity is pivotal to the function or activity of the disease target, false positives may rise solely due to the presence of the impurity.[297]
iii. Some PAINS are able to produce ROS or interfere with the redox cycle of the target, such as hydrogen peroxide and nitric oxide, which in turn deactivate the disease target and masquerade the PAINS as protein inhibitors.[309]
iv. Some PAINS are fluorescently active and strongly colored whose absorption or emission wavelength overlaps with assay monitoring wavelength. In this case, these PAINS will give a false positive result even in the absence of proteins.[310]
v. Some PAINS are metal chelators, so they can sequester metal ions that is fundamental to protein function.[311]
vi. Reactive PAINS may interact with cytochrome enzymes and other essential proteins in human body irreversibly which leads to undesired drug-drug interaction and toxicity.[262,312]

With that being said, the previously mentioned bio-active natural products curcumin and chalcone have been proved to be PAINS. Almost all of the underlying PAINS-type behaviors are contributed by the presence of an α,β-unsaturated system in their structures. The β-unsaturated ketone has photochromic properties that interfere with typical measurements in biological assays.[310] The enol-ketone tautomerization enables the chelation of ions presumably through the formation of hydrogen bond and thus influences the

redox cycling and activity of target proteins.[313,314] They are also Michael acceptors that react readily with biological thiols to form a covalent bond with the target proteins.[315,316] They may also undergo self-aggregation or form micelles under certain experimental conditions at certain concentrations. All these factors flag curcumin and chalcone as PAINS. This doesn't mean that compounds containing PAINS substructure cannot become potential hits. A survey pointed out that a small proportion of FDA-approved drugs contain PAINS-recognized substructures and yet they are used as successful drugs.[298] Due to the structure of curcumin and chalone, the biological assays conducted should be examined to exclude assay interference and validated by complementary and affinity assays. The design of curcumin and chalone derivatives should make efforts on mimicking the basic generic structure template, in the meantime, avoiding the problematic PAINS moieties. This will help in retaining the biological activities without the risk of false positives.

1.6.4 Compound library

To summarize the information from *Section 1.6.1, Section 1.6.2, Section 1.6.3*, both curcumin and chalcone derivatives have the potential to treat AD, especially their ability to inhibit the aggregation and ameliorate the toxicity of Aβ peptides. However, the presence of α,β-unsaturated system within the chemical structures turns them into PAINS. Numerous studies on curcumin and chalcone derivatives have shown that these two represent privileged structures in medicinal chemistry and are able to modulate Aβ aggregation which was validated by both *in vitro* and *in vivo* animal studies. However, they are considered as PAINS which is a drawback for further development of these scaffolds. Based on the previous SAR studies, a model has been proposed which suggests the chemical structure requirements to design novel small molecule Aβ aggregation modulators. Generally, the binding interactions between small molecules and Aβ peptides are favored if the ligands have a C_6-C_n-C_6 carbon chain structure where C_6 refers to the existence of an aromatic ring and C_n refers to the linkage between two aromatic ring systems.[317] The conformation of the ligands tend to be flat and planar with substituted aromatic end groups. At least one

polar hydrogen bonding substitution is needed for optimal inhibition of Aβ aggregation. Both curcumin and chalcone fit in this model. The difference between these two molecules lies in their linker region (C_n). The length and flexibility (estimated by the number of sp^3 hybridized carbons) are important factors underlying their biological activities. It is believed that these parameters need to be within a reasonable range to facilitate the formation of optimal interactions. Nonetheless, no previous study has carried out a comprehensive study on modifying these templates.

In this regard, this thesis aims to propose a small molecule compound library that lacks the PAINS feature present in curcumin and chalcone by replacing the α,β-unsaturated system in the linker region to an amide bond and possibly rule out assay interference and false positives. The advantages of amide bonds are as follows:

i. The amide bond is a common functional group that can be found in many biologically active compounds, including peptides, proteins, chemical probes, FDA-approved drugs, and natural products. It rarely interferes with biological assays and possesses high druggability which is not considered a PAINS substructure.
ii. The resonance delocalization of an amide bond provides it with double bond characteristic which would restrict the conformation. It is also a bioisostere of α, β-unsaturated carbonyl system present in both curcumin and chalcone. Thus, the conformation, flexibility and possible biological activities of these compounds would be similar to that of parent compound curcumin and chalcone.
iii. Amide bond is part of mammalian proteins/enzymes and is not prone to Michael addition type of reactions in vivo which can largely reduce the possibility of future toxicity in the development.
iv. From a synthetic chemistry point of view, amide bond eliminates the formation, separation, and evaluation of stereoisomers, such as cis/trans or (*Z*)-/(*E*)-diastereomers which is possible with chalcones.

v. Various medicinal chemistry strategies can be used to further optimize the biological activity, stability, and selectivity of amide-containing leads, including cyclization and bioisostere replacement into hetero-aromatic rings, sulfamides, and carbamtes.

In this thesis, a series of compounds based on the C_6-C_n-C_6 template model was synthesized, modified and expanded by using amide-containing linkage with different lengths, structure, and flexibility (**Figure 1-16**). The first series of compounds (Chapter 2) embraces amide bond with one extra sp^3 hybridized carbon in the linker region (*N*-benzylbenzamide series). The second series of compounds (Chapter 3) consists of one more sp^3 hybridized carbon in the linker region to give *N*-phenethylbenzamide series. The third series of compounds (Chapter 4) is designed by replacing the carbon next to amide nitrogen into oxygen from the second series to give *N*-benzyloxybenzamide series. Whereas the fourth series of compounds (Chapter 5) are merely amide bond in the linker region to give *N*-phenylbenzamide series (**Figure 1-16**). The SAR was also modified to include a wide variety of 5- and 6-membered aromatic and aliphatic rings based on bioisosterism. These rings include pyridine, pyrrole, furan, thiophene, naphthalene, quinoline, indole, benzofuran, benzo[*b*]thiophene, piperidine, and pyrrolidine. For comparison and SAR studies, several known anti-Aβ aggregation pharmacophores were incorporated into the screening to enhance the biological activity of parent compounds. These pharmacophores are (3,4-dimethoxylphenyl), (3,4-difluorphenyl), 3-methoxyl-4-hydroxylphenyl, and 3-hydroxyl-4-methoxylphenyl moieties.

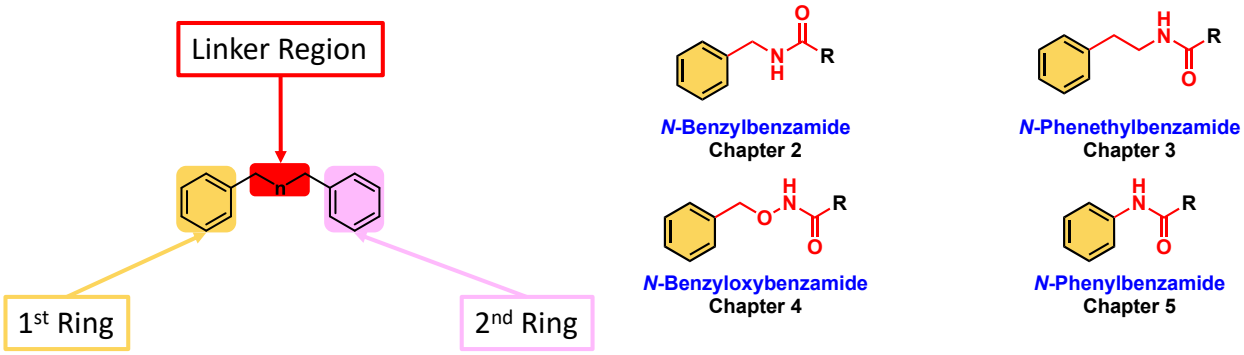


Figure 1-16. Proposed scaffold to study Aβ aggregation (left) and genetic structures of compound series (right).

Chapter 2

Design, Synthesis and Evaluation of *N*-Benzylbenzamide and *N*-Benzylcarboxamide Derivatives as Aβ Aggregation Modulators

Below is a list of publications, manuscripts submitted and in preparation along with author names based on this chapter:

Zhao, Y. Rao, P. P. N. *N*-Benzyl, *N*-phenethyl and *N*-benzyloxybenzamide derivatives inhibit amyloid-beta (Aβ42) aggregation and mitigate Aβ42-induced neurotoxicity. *Med. Chem. Res.* (Manuscript under revision)

2.1 Introduction

This chapter features the first series of compounds in the proposed library, where the three-carbon α,β-unsaturated system present in the chalcone template was replaced with an amide bioisostere along with an sp^3 hybridized carbon linker to obtain the *N*-benzylbenzamide template.[318,319] The structure-activity relationship (SAR) modifications for this library of 16 derivatives are shown in **Figure 2-1**. In this series of compounds, the *N*-benzyl moiety was kept constant while the other end of the molecule was modified by incorporating various aromatic rings such as benzene (**3a**), pyridine (**3b**, **3c**), pyrrole (**3h**), furan (**3i**), thiophene (**3j**). Furthermore, bicyclic aromatic rings were also included, such as naphthalene (**3l**), quinoline (**3m**), indole (**5a**), benzofuran (**5b**), and benzo[*b*]thiophene (**5c**). In addition, aliphatic rings were also incorporated including cyclohexane (**3f**), piperidine (**3g**), and pyrrolidine (**3k**). Besides, known pharmacophores 3,4-dimethoxylbenzene and 3, 4-difluorobenzene moieties were also incorporated in compounds **3d** and **3e**.[320] This chapter describes the synthesis, characterization, and evaluation of *N*-benzylbenzamide and *N*-benzylcarboxamide class of compounds via biophysical (thioflavin T based

fluorescence spectroscopy, transmission electron microscopy), biochemical (Aβ42-induced cytotoxicity in mouse hippocampal HT22 neuronal cell lines) and by computational modelling studies.

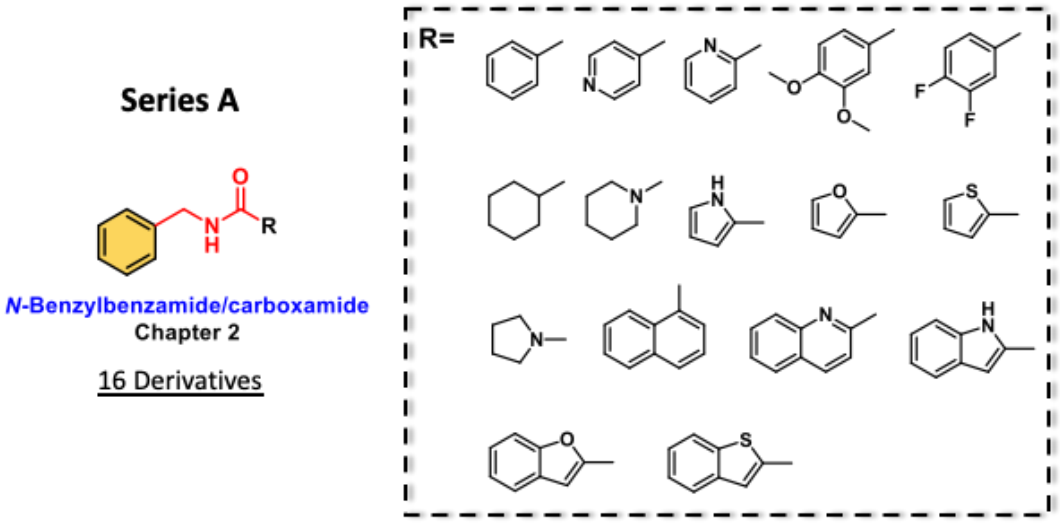


Figure 2-1. *N*-Benzylbenzamide and *N*-benzylcarboxamide derivatives (Series A). This series of compounds contains an amide bond linked to a sp^3 hybridized carbon linker.

2.2 Hypothesis

The three-carbon α,β-unsaturated system present in the chalcone moiety was replaced with a corresponding amide bioisostere along with a carbon spacer to obtain *N*-benzylbenzamide derivatives that lack the PAINS and thus provide novel small molecular templates possessing anti-Aβ42 aggregation properties. It is anticipated that these molecules can interact with the ^{16}KLVFFA^{21} region and the hydrophobic C-terminal regions of Aβ42 and thus prevent the formation of toxic Aβ42 aggregates with neuroprotective effects. Considering the hydrophobic nature of the amyloidogenic regions of Aβ42, it is predicted that compounds with aromatic rings are more efficient than those with aliphatic rings in inhibiting the aggregation process, possibly due to the higher chance of forming the hydrophobic interactions between the ligand and receptor. Furthermore, compounds with a bicyclic aromatic ring are predicted as the most potent aggregation inhibitors in the series given the same considerations. Substituted compounds with known pharmacophores (such as R = 3,4-dimethoxylbenzene and R = 3,4-difluorobenzene)[320] are expected

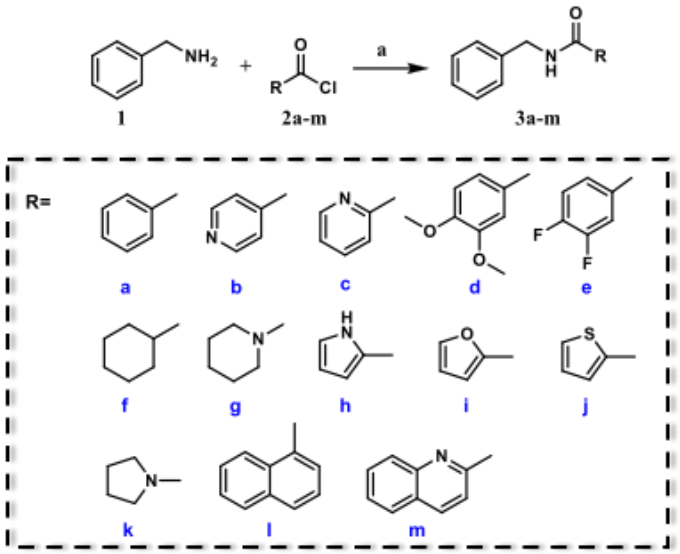
to demonstrate better inhibition on Aβ42 aggregation due to efficient van der Waals, hydrophobic and hydrogen bonding interactions with Aβ42. The SAR was investigated by incorporating monocyclic, bicyclic, aromatic, acyclic, 5- and 6-membered rings to study their effect on Aβ42 aggregation (**Figure 2-1**).

2.3 Results and Discussion

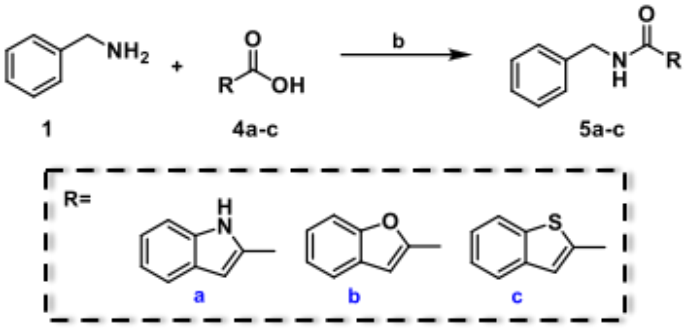
In this section, the synthesis, purification and characterization of the *N*-benzylbenzamide and *N*-benzylcarboxamide class of compounds (**3a-m** and **5a-c**) are discussed which is followed by biological activity screening, including anti-Aβ42 aggregation assay (thioflavin T, ThT, fluorescence spectroscopy), fibril morphology study by transmission electron microscopy, cell viability assay against Aβ42-induced cytotoxicity in mouse hippocampal HT22 neuronal cells. Representative compounds from this series were used in computational modelling studies to understand their interactions with Aβ42 using the solved 3D structures to understand the mechanisms of their anti-aggregation properties.

2.3.1 Synthesis

The retro-synthetic analysis of the compound library suggests that the starting building blocks should be coupled to form an amide bond found in the linker region of the template.[321] There are a variety of methods established to prepare benzamide and carboxamide derivatives. Given the fact that the proposed compounds in the library are small molecules, the formation of an amide bond was achieved either by coupling of acid halides with primary amines or by coupling of carboxylic acids with primary amines. The choice between using the acid halides or the corresponding carboxylic acids was made based on the commercial availability and cost of the starting materials. With that being said, compounds **3a-m** were synthesized by using a direct coupling method A (**Scheme 2-1**) where the corresponding acid chlorides (**2a-m**) were coupled with phenylmethanamine (**1**), whereas compounds **5a-c** were synthesized via method B where the phenylmethanamine (**1**) was coupled with the corresponding carboxylic acids **4a-c** (**Scheme 2-2**).



Scheme 2-1. Synthetic methodology to synthesize **3a-m** by coupling phenylmethanamine (**1**) and corresponding acid chlorides (**2a-m**). Reagents and conditions: (a) TEA, THF, room temperature/reflux 2-24 h.



Scheme 2-2. Synthetic methodology to synthesize **5a-c** by coupling phenylmethanamine (**1**) and corresponding carboxylic acid (**4a-c**). Reagents and conditions: (b) EDC•HCl, HOBt, TEA, THF, room temperature overnight.

In method A, phenylmethanamine (**1**) was coupled with corresponding acid halides. The reaction mechanism is described as follows[322] (**Figure 2-2**): First, nucleophile **1** attacks the electrophilic carbonyl carbon to form a tetrahedron intermediate by nucleophilic addition. Next, the chloride serves as a good leaving group. Then the hydrochloric acid is formed in the last step to give the desired products **3a-m**. Organic base triethylamine (TEA) was used to readily remove the hydrochloric acid in order to facilitate

the product formation. The overall yields of these reactions range from 72 to 93.6%. The analytical data (^{1}H NMR, MS and purity data obtained through LCMS) for **3a-m** are given below. Analytical spectral data for all the final compounds are given in **Appendix A**.

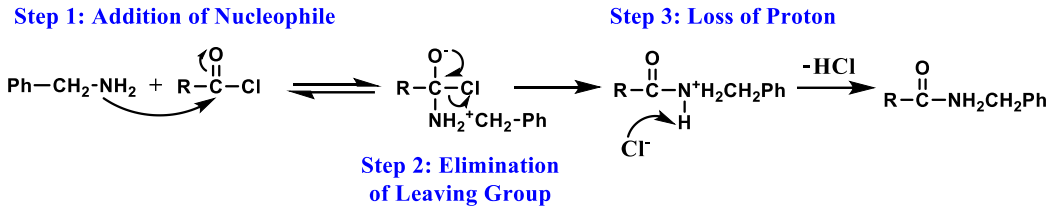


Figure 2-2. Nucleophilic acyl substitution mechanism which includes three major steps: (1) addition of nucleophile to the electrophilic carbonyl carbon, (2) elimination of the leaving group, (3) loss of proton to form the product.

2.3.1.1 *N*-Benzylbenzamide (**3a**)

The product was obtained as a white solid (Yield = 92.8%). ^{1}H NMR (300 MHz, DMSO-*d*6): δ 9.00 (t, *J* = 5.6 Hz, 1H), 7.90–7.81 (m, 2H), 7.53–7.39 (m, 3H), 7.29–7.10 (m, 5H), 4.45 (d, *J* = 6.0 Hz, 2H). mp: 105–108 °C. ESI-MS, m/z calcd for $C_{14}H_{14}NO$ $[M+H]^+$ 212.1, found 212.1. Purity: 100% (LCMS).

2.3.1.2 *N*-Benzylisonicotinamide (**3b**)

The product was obtained as a white solid (Yield = 72.0%). ^{1}H NMR (300 MHz, DMSO-d_6): δ 9.33 (t, *J* = 5.3 Hz, 1H), 8.79–8.67 (m, 2H), 7.85–7.75 (m, 2H), 7.34–7.27 (m, 5H), 4.51 (d, *J* = 6.0 Hz, 2H). mp: 95–98 °C. ESI-MS, m/z calcd for $C_{13}H_{13}N_2O$ $[M+H]^+$ 213.1, found 213.1. Purity: 99.0% (LCMS).

2.3.1.3 *N*-Benzylpicolinamide (**3c**)

The product was obtained as a white solid (Yield = 74.3%). ^{1}H NMR (300 MHz, DMSO-d_6): δ 9.32 (br s, 1H), 8.67–8.65 (m, 1H), 8.10–7.96 (m, 2H), 7.64–7.59 (m,1H), 7.35– 7.20 (m, 5H), 4.50 (d, *J* = 6.4 Hz, 2H). mp: 94–97 °C. ESI-MS, m/z calcd for $C_{13}H_{13}N_2O$ $[M+H]^+$ 213.1, found 213.1. Purity: 99.6% (LCMS).

2.3.1.4 *N*-Benzyl-3,4-dimethoxybenzamide (**3d**)

The product was obtained as a white solid (Yield = 86.4%). ^{1}H NMR (300 MHz, DMSO-d_6) δ 8.90 (t, *J* = 5.9 Hz, 1H), 7.57 – 7.51 (m, 1H), 7.51 – 7.47 (m, 1H), 7.38 – 7.18 (m, 5H), 7.03 (d, *J* = 8.4 Hz, 1H), 4.47 (d, *J* = 6.0 Hz, 2H), 3.81 (s, 3H), 3.80 (s, 3H). mp: 140-143 °C. ESI-MS, m/z calcd for $C_{16}H_{17}NO_3$ $[M+H]^+$ 272.1, found 272.1. Purity: 99.5% (LCMS).

2.3.1.5 *N*-Benzyl-3,4-difluorobenzamide (**3e**)

The product was obtained as a white solid (Yield = 81.9%). ^{1}H NMR (300 MHz, DMSO-d_6) δ 9.10 (t, *J* = 5.6 Hz, 1H), 7.97 – 7.84 (m, 1H), 7.80 – 7.70 (m, 1H), 7.59 – 7.45 (m, 1H), 7.35 – 7.26 (m, 4H), 7.25 – 7.17 (m, 1H), 4.44 (d, *J* = 5.9 Hz, 2H). mp: 94–97 °C. ESI-MS, m/z calcd for $C_{14}H_{11}F_2NO$ $[M+H]^+$ 248.1, found 248.1. Purity: 98.2% (LCMS).

2.3.1.6 *N*-Benzylcyclohexanecarboxamide (**3f**)

The product was obtained as a white solid (Yield = 79.8%). ^{1}H NMR (300 MHz, $CDCl_3$) δ 7.45 – 7.16 (m, 5H), 5.72 (s, 1H), 4.46 (d, *J* = 5.6 Hz, 2H), 2.13 (tt, *J* = 11.7, 3.4 Hz, 1H), 1.98 – 1.87 (m, 2H), 1.87 – 1.76 (m, 2H), 1.72 – 1.60 (m, 1H), 1.57 – 1.40 (m, 2H), 1.29 (q, *J* = 10.7, 8.8 Hz, 3H). mp: 117-120 °C. ESI-MS, m/z calcd for $C_{14}H_{19}NO$ $[M+H]^+$ 218.1, found 218.1. Purity: 100% (LCMS).

2.3.1.7 *N*-Benzylpiperidine-1-carboxamide (**3g**)

The product was obtained as a white solid (Yield = 82.6%). ^{1}H NMR (300 MHz, $CDCl_3$) δ 7.40 – 7.24 (m, 5H), 4.69 (s, 1H), 4.45 (d, *J* = 5.4 Hz, 2H), 3.36 (t, *J* = 5.1 Hz, 4H), 1.60 (d, *J* = 4.0 Hz, 6H). mp: 110-113 °C. ESI-MS, m/z calcd for $C_{13}H_{18}N_2O$ $[M+H]^+$ 219.1, found 219.1. Purity: 96.5% (LCMS).

2.3.1.8 *N*-Benzyl-1*H*-pyrrole-2-carboxamide (**3h**)

The product was obtained as a white solid (Yield = 79.6%). ^{1}H NMR (300 MHz, $CDCl_3$): δ 9.50 (br s, 1H), 7.51–7.12 (m, 5H), 6.92–6.90 (m, 1H), 6.53–6.51 (m, 1H), 6.23–6.20 (m, 1H), 6.13 (br s, 1H), 4.60 (d, *J* = 5.9 Hz, 2H). mp:122–125 °C. ESI-MS, m/z calcd for $C_{12}H_{13}N_2O$ $[M+H]^+$ 201.1, found 201.1. Purity: 96.1% (LCMS).

2.3.1.9 *N*-Benzylfuran-2-carboxamide (**3i**)

The product was obtained as a white solid (Yield = 93%). ^{1}H NMR (300 MHz, DMSO-d_6): δ 9.04 (t, *J* = 5.8 Hz, 1H), 7.84 (d, *J* = 3.7 Hz, 1H), 7.36–7.21 (m, 5H), 7.25 (d, *J* = 6.0 Hz, 1H), 6.62 (d, *J* = 5.0 Hz, 1H), 4.46 (d, *J* = 6.0 Hz, 2H). mp: 120–123 °C. ESI-MS, m/z calcd for $C_{12}H_{12}NO_2$ $[M+H]^+$ 202.1, found 202.1. Purity: 99.6% (LCMS).

2.3.1.10 *N*-Benzylthiophene-2-carboxamide (**3j**)

The product was obtained as a white solid (Yield = 78.7%). ^{1}H NMR (300 MHz, DMSO-d_6): δ 9.04 (t, *J* = 5.7 Hz, 1H), 7.88–7.81 (m, 1H), 7.39–7.19 (m, 5H), 7.15–7.05 (m, 2H), 4.45 (d, *J* = 6.2 Hz, 2H). mp: 115–118 °C. ESI-MS, m/z calcd for $C_{12}H_{12}NOS$ $[M+H]^+$ 218.1, found 218.1. Purity: 99.7% (LCMS).

2.3.1.11 *N*-Benzylpyrrolidine-1-carboxamide (**3k**)

The product was obtained as a white solid (Yield = 82.3%). ^{1}H NMR (300 MHz, $CDCl_3$) δ 7.41 – 7.24 (m, 5H), 4.47 (s, 2H), 3.37 (t, *J* = 6.6 Hz, 4H), 2.00 – 1.83 (m, 4H). mp: 127-130 °C. ESI-MS, m/z calcd for $C_{12}H_{16}N_2O$ $[M+H]^+$ 205.1, found 205.1. Purity: 97.2% (LCMS).

2.3.1.12 *N*-Benzyl-1-naphthamide (**3l**)

The product was obtained as a white solid (Yield = 87.6%). ^{1}H NMR (300 MHz, DMSO-d_6): δ 9.09 (t, *J* = 5.7 Hz, 1H), 8.22–8.19 (m, 1H), 8.06–7.95 (m, 2H), 7.66–7.53 (m, 4H), 7.38–7.26 (m, 5H), 4.55 (d, *J* = 6.2 Hz, 2H). mp: 127–130 °C. ESI-MS, m/z calcd for $C_{18}H_{16}NO$ $[M+H]^+$ 262.1, found 262.1. Purity: 98.3% (LCMS).

2.3.1.13 *N*-Benzylquinoline-2-carboxamide (**3m**)

The product was obtained as a white solid (Yield = 93.6%). ^{1}H NMR (300 MHz, DMSO-d_6): δ 9.47 (t, *J* = 6.2 Hz, 1H), 8.58 (d, *J* = 8.5 Hz, 1H), 8.20–8.04 (m, 3H), 7.88 (t, *J* = 7.6 Hz, 1H), 7.73 (t, *J* = 7.5 Hz, 1H), 7.40–7.22 (m, 5H), 4.58 (d, *J* = 6.2 Hz, 2H). mp: 128–131 °C. ESI-MS, m/z calcd for $C_{17}H_{15}N_2O$ $[M+H]^+$ 263.1, found 263.1. Purity: 99.5% (LCMS).

Method B was used to synthesize *N*-benzylcarboxamide derivatives (**5a-c**, **Scheme 2-2**). Compared to acid chlorides, carboxylic acids are less reactive for nucleophilic acyl substitution due to the electron-donating nature of the hydroxyl group. This can influence the reaction progress, yield and purity of the products. However, this limitation can be overcome by activating the carboxylic acid (**4a-c**) with the assistance of carbodiimide-dehydrating reagents, such as 1-ethyl-3-(3-dimethylaminopropyl)carbodiimide (EDC).[323,324] The detailed mechanism is illustrated in **Figure 2-3**. The carboxylic acids can be transformed

into an ester intermediate. In the presence of an activator, such as hydroxyltriazole (HOBt), the nucleophilic activator attacks the carbonyl carbon of the ester intermediate so that it can be transformed into an active ester (Path a).[325] The active ester contains a better leaving group compared to the original carboxylic acid so that it can react with phenylmethanamine (**1**) *via* nucleophilic acyl substitution as mentioned in the previous paragraph. However, in the absence or insufficient amount of the activator HOBt, the ester intermediate can undergo rapid self-rearrangement to form a urea by-product (Path b). The by-product as a result of using EDC as dehydrating reagent is a water-soluble urea which, therefore, can be washed away by aqueous extraction in the post-reaction workup. The overall yields of these reactions range from 75.2% to 90.6%. The analytical data (^{1}H NMR, MS and purity data obtained through LCMS) for **5a-c** are given below. Analytical spectral data for all the final compounds are given in **Appendix A**.

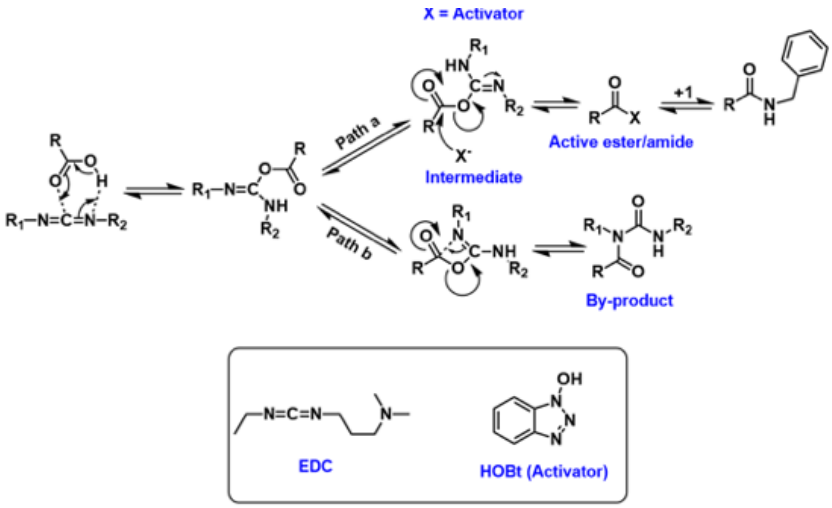


Figure 2-3. Reaction mechanism when using dehydrating agent EDC and activator HOBt for coupling phenylmethanamine (**1**) and corresponding carboxylic acid (**4a-c**) to obtain **5a-c**.

2.3.1.14 *N*-Benzyl-1*H*-indole-2-carboxamide (**5a**)

The product was obtained as a white solid (Yield = 90.6%). ^{1}H NMR (300 MHz, DMSO-d_6): δ 11.56 (s, 1H), 9.00 (t, *J* = 6.1 Hz, 1H), 7.57 (d, *J* = 8.0 Hz, 1H), 7.41 (d, *J* = 8.2 Hz, 1H), 7.38-7.27 (m, 4H), 7.17–

7.12 (m, 3H), 7.03–6.98 (m, 1H), 4.49 (d, *J* = 6.0 Hz, 2H). mp: 229–232. ESI-MS, m/z calcd for $C_{16}H_{15}N_2O$ $[M+H]^+$ 251.1, found 251.1.Purity: 95.4% (LCMS).

2.3.1.15 *N*-Benzylbenzofuran-2-carboxamide (**5b**)

The product was obtained as a white solid (Yield = 75.2%). ^{1}H NMR (300 MHz, DMSO-d_6) δ 9.29 (t, *J* = 5.9 Hz, 1H), 7.81 – 7.75 (m, 1H), 7.69 – 7.63 (m, 1H), 7.58 (s, 1H), 7.51 – 7.44 (m, 1H), 7.38 – 7.29 (m, 5H), 7.29 – 7.21 (m, 1H), 4.49 (d, *J* = 6.2 Hz, 2H). mp: 101-104 °C. ESI-MS, m/z calcd for $C_{16}H_{13}NO_2$ $[M+H]^+$ 252.1, found 252.1. Purity: 97.2% (LCMS).

2.3.1.16 *N*-Benzylbenzo[*b*]thiophene-2-carboxamide (**5c**)

The product was obtained as a white solid (Yield = 78.9%). ^{1}H NMR (300 MHz, $CDCl_3$ δ 7.41 – 7.24 (m, 5H), 4.47 (s, 2H), 3.37 (t, *J* = 6.6 Hz, 4H), 2.00 – 1.83 (m, 4H). mp: 146-149 °C. ESI-MS, m/z calcd for $C_{16}H_{13}NOS$ $[M+H]^+$ 268.1, found 268.1. Purity: 94.82% (LCMS).

2.3.2 Modulatory activity on amyloid-beta aggregation

The modulatory activity of *N*-benzylethylbenzamide and carboxamide derivatives **3a-m** and derivatives **5a-c** on Aβ42 aggregation was evaluated using the ThT aggregation kinetic assay.[326–329] It is the golden standard used in the field for rapid screening of small molecules to determine their Aβ42 aggregation modulation activity.[330–333] In this assay, ThT was used as the fluorescent dye which can selectively bind to the β-sheet structure of various forms of aggregated Aβ42. Upon binding, ThT gives a characteristic increase in the fluorescence reading (FLR) which is directly proportional to the amount of Aβ aggregates formed. By comparing the FLR of Aβ42 control and in the presence of various test compounds, the percentage inhibition (PI) can be calculated at the end of the assay. If the FLR is lower than that of the

control, it indicates that the compounds are inhibiting the Aβ42 aggregation. Similarly, if the FLR is higher than that of control, it indicates that the compounds are able to promote the Aβ42 aggregation. Compounds that are able to inhibit Aβ42 aggregation are termed aggregation inhibitors (AI) and compounds that are able to promote Aβ42 aggregation are termed aggregation promotors (AP), whereas compounds that weakly modulate the aggregation are termed weak aggregation modulators (WAM). Initially, all the test compounds were screened at 25 μM to determine their effect on Aβ42 aggregation. Compounds that show promising activity were further evaluated over a concentration range (1, 5, 10, 25 μM) to determine the aggregation kinetics. Resveratrol (RVT) which is a known inhibitor of Aβ42 aggregation was also included in the assay as the reference compound for comparison.

In **Figure 2-4**, the ThT aggregation kinetic curves of *N*-benzylbenzamide and carboxamide derivatives **3a-m** and **5a-c** were shown. In each panel, the blue curve at the bottom is the ThT background readings which suggests that ThT has no interference in the FLR in monitoring the aggregation of Aβ42. The red curve shows the Aβ42 aggregation curve in the absence of any testing compounds. In this curve, some characteristics of Aβ42 aggregation can be observed. It is a sigmoidal curve characterized by a very short lag phase (~ 30 min) which is followed by a rapid growth phase spanning the time course from around 0.5 h to 10 h. Then, the FLR tends to be stable with readings hovering around 8,000 RFUs, indicating the aggregation process has reached the equilibrium status or plateau. Such saturation phase was seen until the end of the assay at 24 h. Compared to the Aβ42 control curve, other curves, in the presence of different *N*-benzylbenzamide and carboxamide derivatives (**Figure 2-4**, A: **3a-d**, RVT, B: **3e-h**, C: **3i-l**, D: **3m**, **5a-c**), shared similar shapes without any major difference noticed. This observation suggests that none of these derivatives are able to alter the aggregation kinetics by either shortening or extending the lag/growth phase. However, lower FLR at the saturation phase than Aβ42 control for these curves was observed which indicates that some derivatives were capable of reducing the formation of Aβ42 fibrils. When co-incubating the reference compound RVT with Aβ42 (**Figure 2-4** A), a dramatic decrease in the FLR was noticed in

the saturation phase with FLR below 2,000 RFUs after 18 h. Such observation is not a surprise as RVT is a very potent Aβ AI.[334]

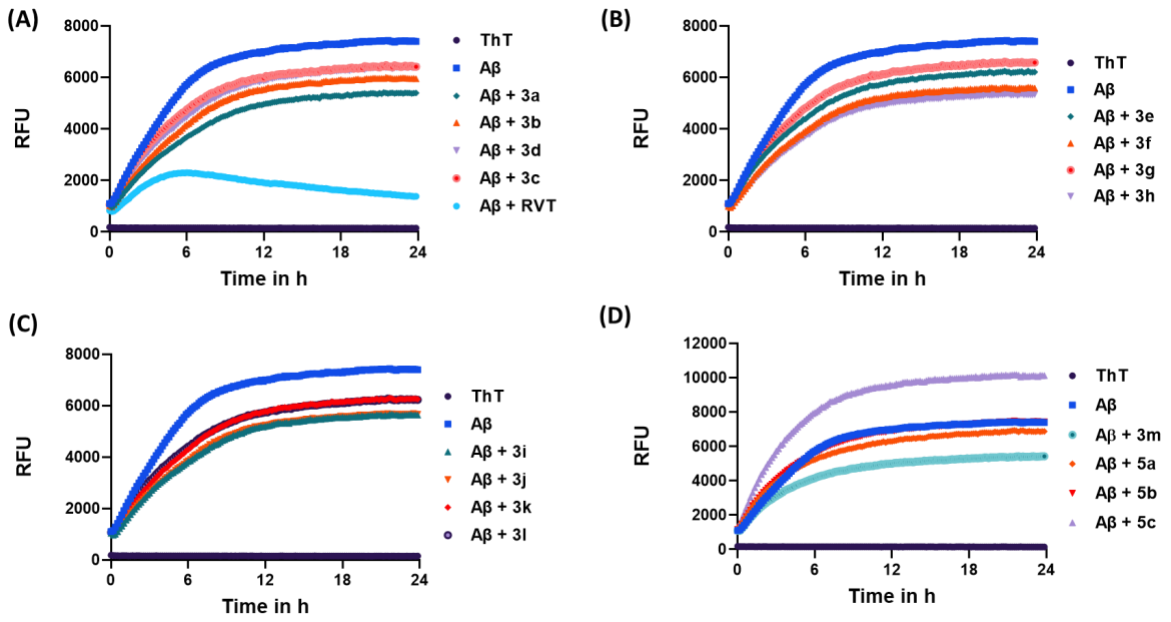


Figure 2-4. The Aβ42 aggregation kinetic curves for *N*-benzylbenzamide and carboxamide derivatives (**3a-m** and **5a-c**) in the ThT-based fluorescence assay. (A) Aggregation kinetic curves for derivatives **3a-d** and reference compounds resveratrol (RVT). (B) Aggregation kinetic curves for derivatives **3e-h**. (C) Aggregation kinetic curves for derivatives **3i-l**. (D) Aggregation kinetic curves derivatives for **3m**, **5a-c**. The test compounds (25 μM) were incubated with Aβ42 (10 μM) for 24 h at 37 ˚C, pH 7.4 and the ThT fluorescence was monitored (excitation = 440 nm, emission = 490 nm). Results were obtained based on triplicate readings from three independent experiments.

Most of the compound from this library (**3a-m**, **5a**, 14 out of 16 compounds) showed inhibitory activity toward Aβ42 aggregation at the 24 h time point, with PIs ranging from 7.0- 27.8 %. The results are listed in **Table 2.1**. A detailed bar plot of PI is shown in **Figure 2-5**. Compound **3a** (R = phenyl) which has a similar structure as the chalcone, except for the lack of the reactive three carbon α, β-unsaturated system, showed a PI of 27.1 ± 2.3 % which was identified as the best inhibitor of Aβ42 aggregation from this library. When the phenyl ring in **3a** was replaced with a more polar 2- or 4-pyridyl substituents in compounds **3b**

or **3c**, the PI decreased to 19.6 ± 5.2 % and 13.3 ± 6.7 % respectively. However, other bioisosteric replacements of the phenyl ring, with 5-member heterocycles such as **3h** (R = pyrrole), **3i** (R = furan), and **3j** (R = thiophene), were able to retain the inhibitory activity with PI ranging from 27.7± 1.03 %, 23.8 ± 7.6 %, and 23.4 ± 4.7 % respectively. Replacing the aromatic rings with aliphatic rings led to mixed results. For example, compound **3f** (R = cyclohexane) was able to retain the activity with PI at 24.5 ± 2.7 % which is very similar to the prototypic compound **3a**. However, the piperidine and pyrrolidine replacements failed to retain Aβ42 inhibitory effects with PI at 11.0 ± 4.0 % and 15.4 ± 0.7 % for **3g** and **3k** respectively. Furthermore, replacing the aromatic phenyl ring with planar bicyclic aromatic rings such as naphthalene (**3l**), led to a reduction in the PI to 15.8 ± 1.6 %, whereas the nitrogen-containing quinoline ring in compound **3m** was able to retain anti-aggregation activity with a PI of 26.7 ± 0.2 %. Interestingly, the presence of an indole ring in compound **5a,** led to a drastic reduction in its activity with a PI of 7.0 ± 2.6 % (**Table 2-1**). These findings suggest that Aβ42 inhibition activity is dependent on ligand conformation and hydrophilicity/hydrophobicity parameters (CLogP, **Table 2-1**).

Table 2-1. Percent inhibition (PI) of *N*-benzylbenzamide and carboxamide derivatives (**3a-m**, **5a-c**), resveratrol (RVT), and chalcone (CHL) at 25 μM on Aβ42 (10 μM) aggregation.

Cmpd	% Inhibition (PI)[a]	CLogP[b]	Cmpd	% Inhibition (PI)[a]	CLogP[b]
3a	27.10 ± 2.33	2.83	**3i**	23.80 ± 7.67	2.01
3b	19.58 ± 5.26	1.33	**3j**	23.45 ± 4.77	2.48
3c	13.30 ± 6.75	1.68	**3k**	15.41 ± 0.75	1.91
3d	13.46 ± 0.11	2.32	**3l**	15.79 ± 1.58	4.00
3e	16.04 ± 2.15	3.05	**3m**	26.75 ± 0.23	3.07
3f	24.56 ± 2.75	2.98	**5a**	7.07 ± 2.59	3.16
3g	11.08 ± 3.99	2.47	**5b**	NA[c]	3.39
3h	27.76 ± 1.03	1.78	**5c**	NA[c]	3.86
RVT	81.27 ± 5.59	2.83	**CHL**	-112.29 ± 7.13[d]	3.62

[a] Percent inhibition (PI) was calculated at the 24 h time point in the ThT aggregation kinetics assay. The results shown are average ± standard deviation of triplicate readings based on three independent experiments.
[b] CLogP values were calculated with ChemDraw.
[c] NA, not active indicating the compounds are WAM.
[d] Negative PI indicates the compounds can promote the aggregation.

Compound **5b** and **5c** containing a bicyclic benzofuran and benzo[*b*]thiophene were not active in modulating the Aβ42 aggregation which makes them WAMs (**Figure 2-5**). This needs further exploration. Interestingly, the chalcone (CHL) was able to promote Aβ42 aggregation significantly with PI at -112.29 ± 7.13 % (**Table 2-1**). As can be seen in its ThT aggregation kinetic curve (**Figure 2-6**), when Aβ42 was treated with CHL, it underwent rapid elongation with high RFU ~ 16,000 at the saturation phase. Compared to inhibitor control, none of the compounds in this library were as potent as RVT (81.3 ± 5.6% inhibition) in preventing Aβ42 aggregation. In general, these studies show that the *N*-benzylbenzamide derivatives are able to prevent Aβ42 aggregation. However, they exhibited weak-to-moderate activity in the ThT assay.

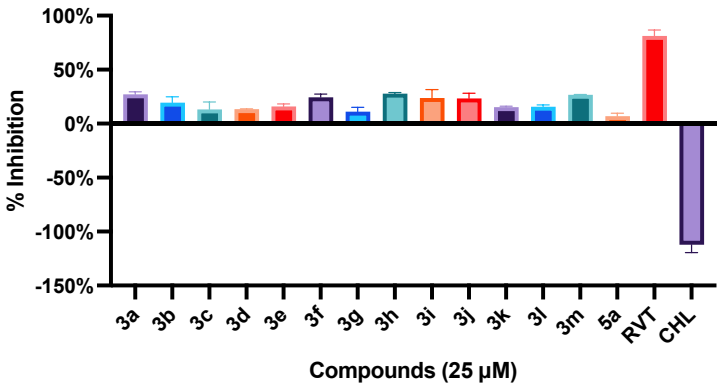


Figure 2-5. Percentage inhibition (PI) of *N*-benzylbenzamide and carboxamide derivatives (**3a-m** and **5a**), resveratrol (RVT) and chalcone (CHL) at 25 µM on Aβ42 (10 µM) aggregation.

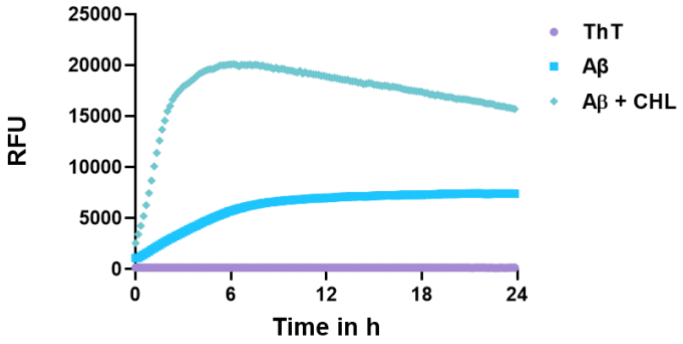


Figure 2-6. The Aβ42 aggregation kinetic curve for chalcone (CHL) in the ThT-based fluorescence assay. CHL (25 µM) was incubated with Aβ42 (10 µM) for 24 h at 37 ˚C, pH 7.4 and the ThT fluorescence was monitored (excitation = 440 nm, emission = 490 nm). Results were obtained based on triplicate readings from three independent experiments.

2.3.3 Transmission electron microscopy

In the next step, transmission electron microscopy (TEM) studies were conducted in order to study the morphology of Aβ42 aggregates in the absence and presence of various test compounds to evaluate their anti-aggregation properties. The effect of representative *N*-benzyl benzamide derivatives, **3a**, **3h-j**, and **3m** on Aβ42 morphology was investigated. The TEM is a qualitative technique and is often used in conjunction with ThT kinetic assays to provide further evidence of small molecules' modulatory activities on Aβ42

aggregation.[335,336] The samples taken for TEM studies were obtained from ThT aggregation kinetic assays at the end of the incubation period (24 h). The TEM images obtained in the presence of various lead compounds were compared to those of Aβ42 control.

As can be seen in **Figure 2-7**, the morphology of Aβ42 aggregates (10 μM) showed a combination of long, twisted, and unbranched mature fibrils. In the presence of *N*-benzylbenzamide derivatives (25 μM), there was a significant reduction in the formation of Aβ42 fibrils. These fibrils are characterized by the presence of sparse, thinner, and lower-ordered fibrils, despite some proto-fibrils and mature fibrils still observable in the images. The reduced Aβ42 fibril density seen in the images further validates that these lead compounds can inhibit the aggregation of Aβ42. Interestingly, the TEM image (**Figure 2-8**) for chalcone indicated its ability to promote aggregation as higher density and thicker fibrils were found. Such a conclusion aligned well with the results of ThT aggregation kinetic studies. Together, these studies quantitatively and qualitatively prove that the *N*-benzylbenzamide derivatives are capable of inhibiting the aggregation of Aβ42.

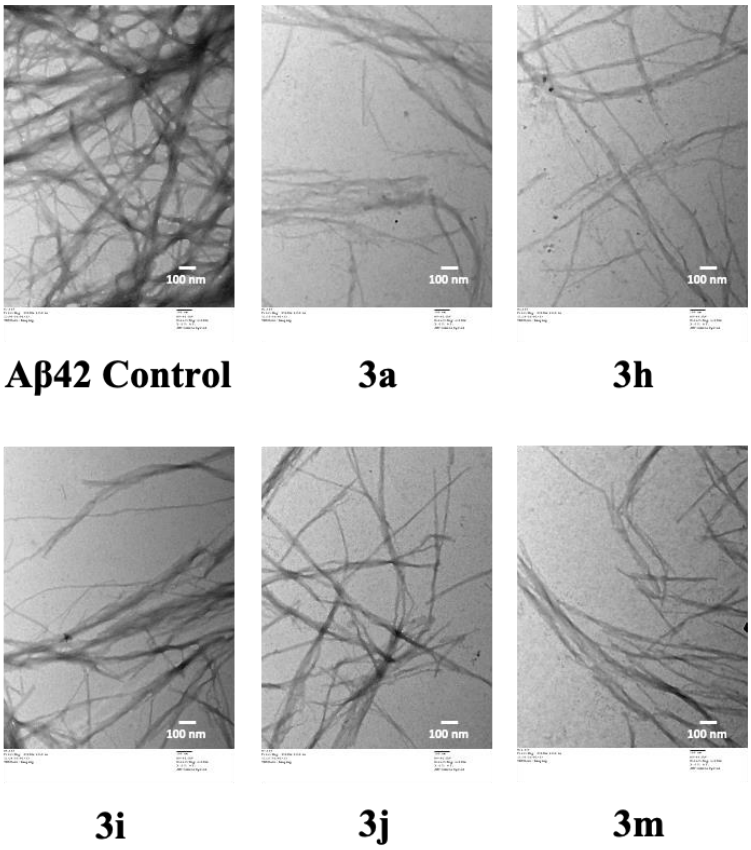


Figure 2-7. TEM images of Aβ42 (10 μM) in the absence (Aβ42 control) and presence of *N*-benzylbenzamide **3a**, **3h-j**, and **3m** (25 μM). Scale: 200 μm.

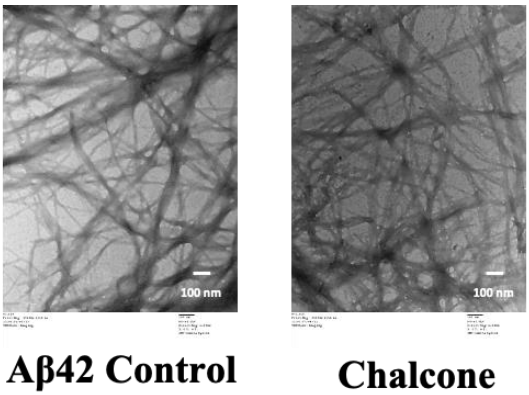


Figure 2-8. TEM images of Aβ42 (10 μM) in the absence (Aβ42 control) and presence of chalcone (25 μM). Scale: 200 μm.

2.3.4 Neuroprotective effects against Aβ42-induced cytotoxicity

Based on the anti-aggregation properties of *N*-benzylbenzamide derivatives observed in the ThT and TEM experiments, we investigated the effect of these compounds in preventing A42-induced cytotoxicity in mouse hippocampal HT22 neuronal cells. The ability of representative *N*-benzylbenzamide derivatives **3a**, **3h-j**, **3m** to prevent Aβ42-mediated cytotoxicity in mouse hippocampal HT22 neuronal cell lines was investigated. Initially, the cytotoxicity profile of compounds **3a**, **3h-j**, and **3m** alone to HT22 cells at 25 μM was determined. The cytotoxicity was evaluated based on cell viability using cell counting kit 8 (CCK-8) colorimetric assay.[337,338] As can be seen in **Figure 2-9** A, the results showed that, at 25 μM, these lead compounds are not toxic to the cells. The cell viability ranged from 104.0 to109.9 % compared to untreated cells. Next, HT22 cells were incubated with Aβ42 (5 μM) in the presence and absence of various lead compounds (25 μM) for 48 h to investigate their ability to rescue cells from Aβ42-mediated neurotoxicity (**Figure 2-9** B). After introducing Aβ42 into the cells, in the absence of testing compounds, there was a drastic decrease in the cell viability compared to untreated cells. Incubating the cells with 5 μM Aβ42 led to around 60% cell death. When Aβ42 treated cells were co-incubated with *N*-benzylbenzamide derivatives, the cell viability increased significantly. These compounds showed potent neuroprotective effects. For example, **3a** (R = benzene), **3h** (R = pyrrole), **3i** (R = furan), **3j** (R = thiophene), and **3m** (R = quinoline) exhibited excellent cell viability profiles (94.9 ± 5.9 %, 95. 8 ± 6.3 %, 85.0 ± 9.0 %, 96.0 ± 13.8 %, and 80.8 ± 10.3 % respectively) indicating that they were able to rescue HT22 cells from Aβ42-induced cytotoxicity. Chalcone was also included in the assay as a reference compound for comparison and the results are shown in **Figure 2-10**. In the absence of Aβ42, chalcone was not toxic to the HT22 cells at 25 μM with the cell viability around 103%. Then Aβ42-treated HT22 cells were co-incubated with chalcone and a slight increase in the cell viability was seen compared to Aβ42-treated control. The cell viability increased from 38.73% for Aβ42-treated cells to 58.24% when co-incubated with chalcone indicating that chalcone also provided neuroprotective effects against Aβ42-incuded cytotoxicity, although to a lesser extent than *N*-benzylbenzamide derivatives (**3a**, **3h-j**, and **3m**). These observations suggest that these *N*-

benzylbenzamide derivatives have the potential to convert toxic Aβ assemblies into nontoxic forms. Furthermore, the cell culture studies demonstrate their ability to prevent Aβ42-induced cytotoxicity which further supports their potential as novel templates to consider in the design of anti-Aβ molecules.

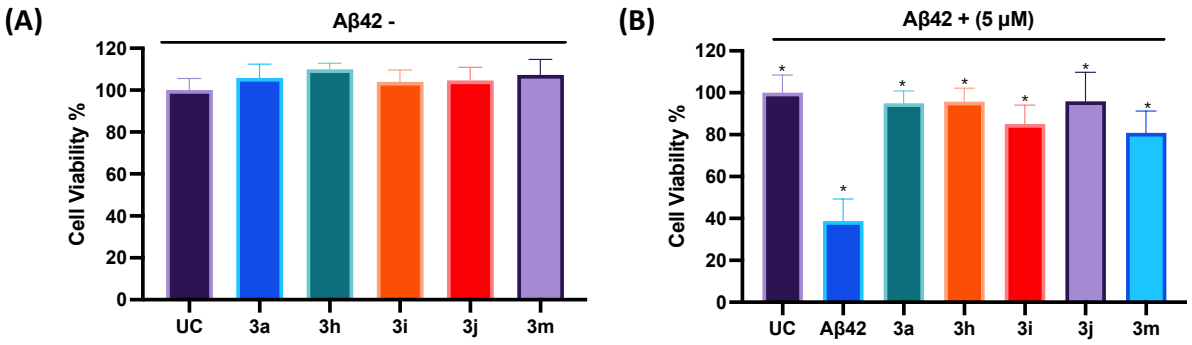


Figure 2-9. Neuroprotective effects of *N*-benzylbenzamide **3a**, **3h-j**, and **3m** (25 μM) on HT22 cells in the absence (A) and presence (B) of Aβ42 (5 μM) incubated over 48 h. Cell viability was determined by CCK-8 based colorimetric assay. The results shown are averages of quadruplicate readings based on three independent experiments. *p < 0.01 compared to Aβ42 treated group (One-way ANOVA followed by Bonferroni post hoc test).

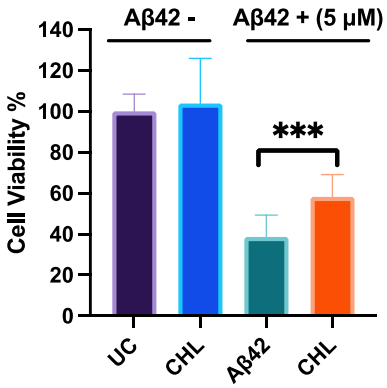


Figure 2-10. Neuroprotective effects of chalcone (CHL) (25 μM) on HT22 cells in the absence and presence of Aβ42 (5 μM) incubated over 48 h. Cell viability was determined by CCK-8 based colorimetric assay. The results shown are averages of quadruplicate readings based on three independent experiments. *p < 0.01 compared to Aβ42 treated group (One-way ANOVA followed by Bonferroni post hoc test).

2.3.5 Molecular docking

In order to better understand the mechanism of these AIs, molecular docking studies were conducted to investigate the interactions between a representative compound from the *N*-benzylbenzamide series and Aβ aggregates. For this purpose, the best *N*-benzylbenzamide derivative **3a** (~27% inhibition of Aβ42 aggregation in the ThT assay, nontoxic to HT22 cells - cell viability >95% and ~95% cell viability in Aβ42 treated cells) from this series was used in the docking studies. Compound **3a** was docked with both the Aβ42 oligomer and fibril model using the CDOCKER algorithm.[339]The oligomer and fibril models were prepared by using the 3D coordinates of the Aβ42 fibril structure (PDB id: 5KK3). This is an atomic resolution structure of monomorphic Aβ42 obtained through solid-state NMR.[340] The Aβ42 oligomer model was prepared from the Aβ42 fibril assembly.[341] Previous studies have shown that, in solution, Aβ42 is known to exist as either pentamer or hexamer aggregates, indicating these are the smallest forms of aggregates that can be detected in solution.[342] Therefore, a pentamer model was used as a representative example of the oligomer model in docking studies. In the sequence of Aβ42, two regions are responsible for its aggregation propensity and the hydrophobic nature of these regions is one of the initiating factors driving the aggregation process, namely, hydrophobic core ^{16}KLVFFA^{21}, and C-terminal hydrophobic tail ^{32}IGLMVGGVVIA^{42}.[343] Therefore, our docking method was designed to build a binding sphere (20 Å radius) that can accommodate the entire span of these two regions to facilitate the understanding of potential interactions in these important regions. The molecular docking was performed using the computational software Discovery Studio, Structure-Based-Design, v20.1.0.19295 (Biovia, USA).

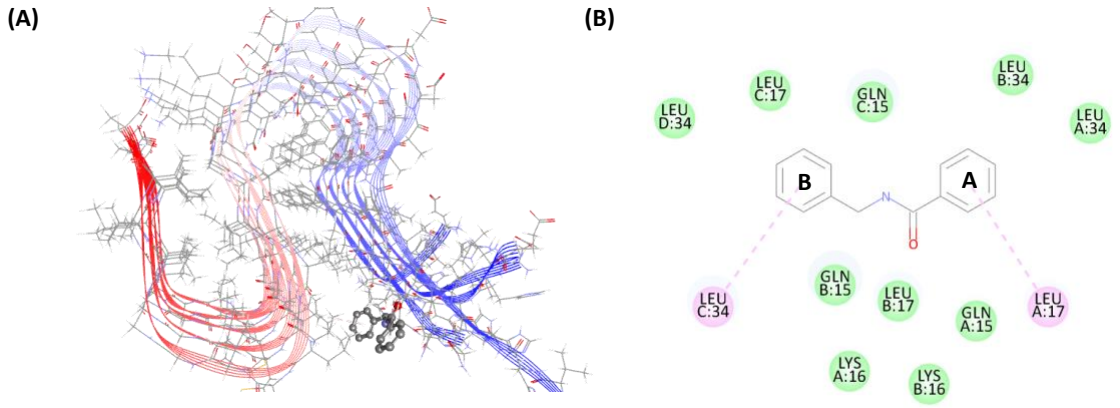


Figure 2-11. Molecular docking studies of **3a** with the Aβ42 fibril model (PDB ID: 5KK3). (A) Top docked pose of **3a**; (B) 2D interaction map of the top docking pose of **3a**. The hydrogen atoms are removed to enhance clarity. Protein is represented in line ribbon with blue indicating the N-terminus and red indicating the C-terminus. The small molecule is represented in the ball-and-stick model. Hydrophobic interaction is represented in pink dashed line and hydrogen bond interaction is represented in green dashed line.

The docking of **3a** and Aβ42 pentamer can be seen in **Figure 2-11**. The Aβ42 pentamer was shown in line ribbon representation color-coded from N- (blue) to C- (red) terminal and the small molecule was shown in ball and stick representation with carbon in grey, oxygen in red, and nitrogen in blue. Based on our docking method, 10 poses were generated, and they were ranked according to CDOCKER energy and CDOCKER interaction energy with the lowest energy (most stable) pose shown in the figure. This top binding pose (CDOCKER energy -18.83 kcal/mol and CDOCKER interaction energy -23.76 kcal/mol) of **3a** shows that it was oriented perpendicular to the long axis of the aggregates. Two hydrophobic interactions were observed interacting with both hydrophobic regions of Aβ42 pentamer. One of the hydrophobic interactions was found between the benzene ring (ring A) of **3a** and the alkyl group of A: Leu17 (distance ~ 5 Å). The other benzene ring (ring B) underwent hydrophobic interaction with the alkyl group of C: Leu34 (distance ~ 5 Å). These two hydrophobic interactions anchored the compound in the binding pocket which explains its ability to inhibit the aggregation process since it can interact with both hydrophobic regions of Aβ42. When **3a** was docked with the Aβ42 fibril model, the main interactions found were still hydrophobic interactions between the aromatic ring with Ala and Val residues within the hydrophobic core region as

shown in **Figure 2-12**. For the best docking pose, the CDOCKER energy was -17.92 kcal/mol and the CDOCKER interaction energy was -22.64 kcal/mol. The benzene ring (ring B) underwent hydrophobic interactions with the alkyl group of B: Ala21 (~ 5 Å), B: Val18 (2.64 Å), and C: Ala21 (~ 5 Å). Another major interaction was the hydrogen bond established between the carbonyl oxygen and the NH_3^+ of C: Lys16 with a distance of 2.32 Å, which further constrained the molecule in the hydrophobic core region of Aβ42. In summary, the molecular docking studies of **3a** in the Aβ42 pentamer and fibril models suggest that the hydrophobic interactions between the aromatic rings and the hydrophobic aggregation-prone regions play a significant role in determining its anti-aggregation activity observed in the experimental work.

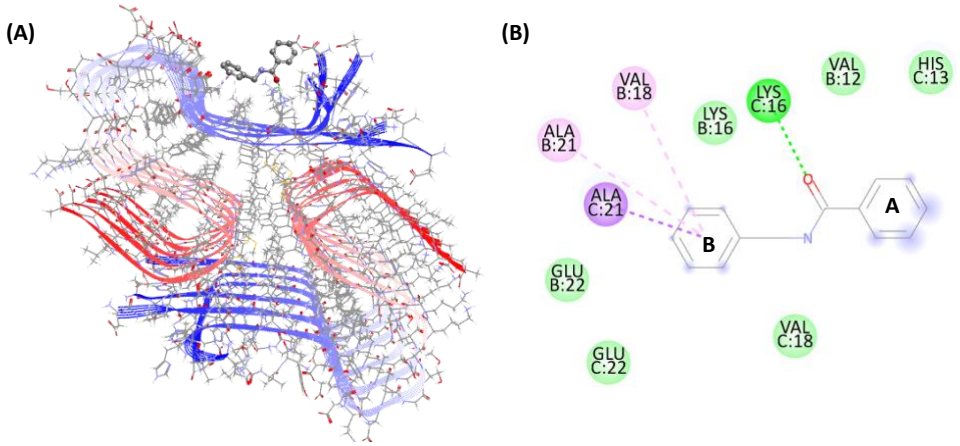


Figure 2-12. Molecular docking studies of **3a** with Aβ42 fibril model (PDB ID: 5KK3). (A) Top docked pose of **3a**; (B) 2D interaction map of the top docking pose of **3a**. The hydrogen atoms are removed to enhance clarity. Protein is represented in line ribbon with blue indicating the N-terminus and red indicating the C-terminus. The small molecule is represented in the ball-and-stick model. Hydrophobic interaction is represented in pink dashed line and hydrogen bond interaction is represented in green dashed line.

2.4 Summary

This chapter describes the design, synthesis, and evaluation of a library of 16 *N*-benzybenzamide and carboxamide derivatives **3a-m** and **5a-c** as Aβ42 aggregation modulators. These compounds were synthesized by coupling the benzylamine with either corresponding acid chlorides or carboxylic acids in good yields (72-93%). The structures of the compounds were characterized by ^{1}H NMR, MS and the purity was determined by HPLC or LCMS. These compounds exhibited weak-to-moderate inhibition on Aβ42 aggregation as confirmed by ThT-based aggregation kinetic assays. The TEM studies also demonstrated their anti-aggregation activity. Among them, **3a**, **3h**, **3i**, **3j**, and **3m** showed anti-Aβ42 activity with PI ranging from 23.4 to 27.8%. These compounds were not toxic to mouse hippocampal HT22 neuronal cells and were able to rescue HT22 cells from Aβ42-induced neurotoxicity (cell viability ~40% for Aβ42-treated control versus up to ~95% when co-incubated with lead AIs). Compound **3a** was identified as the best compound from this series (**Figure 2-13**) and its molecular docking studies in the Aβ42 oligomer and fibril models indicate that the aromatic rings underwent important non-polar and polar interactions in the aggregation-prone KLVFFA and the C-terminal regions in the Aβ42 pentamer and fibril models. Compared to chalcone which is an AP, the lead derivative **3a** does not contain a PAINS substurecture and was able to inhibit Aβ42 aggregation to provide neuroprotection.

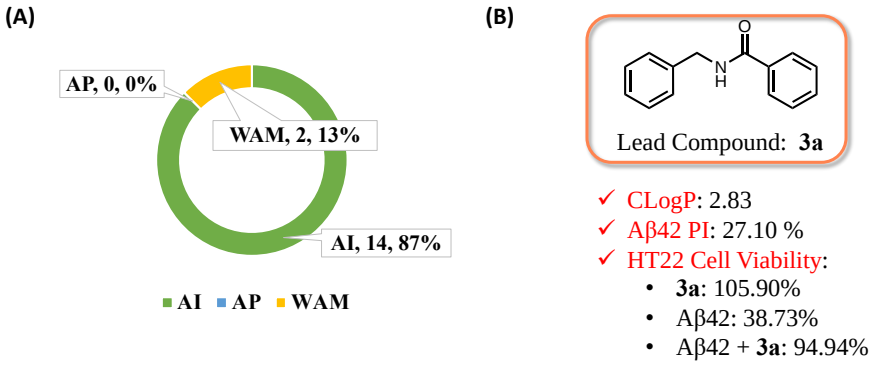


Figure 2-13. Summary of *N*-benzylbenzamide and carboxamide derivatives. (A) 87% (14 out of 16) compounds were identified as aggregation inhibitor (AI) and 13% (2 out of 16) compounds were identified as weak aggregation modulator (WAM); (B) Key experimental data for lead compound **3a**.

2.5 Experimental

2.5.1 General

All chemicals and reagents were purchased from various vendors (Sigma Aldrich Missouri USA, Alfa Aesar Massachusetts USA, Bio Basic Ontario Canada, AA Blocks California USA, Cayman Chemical Michigan USA, Thermo Fisher Massachusetts USA, and Corning New York USA), were >95% pure and used without further purification. The Aβ42 1,1,3,3,3-hexafluoroisopropanol (HFIP) >95% pure, was purchased from Anaspec California USA (Cat. No. AS-64129) or rPeptide Georgia USA (Cat. No. A-1163-1). The reactions were monitored by thin-layer chromatography (TLC) using the Merck silica gel 60, F254. Column chromatography was carried out using Merck silica gel 230-400 mesh. The spots were visualized with short or long wavelengths (254 nm or 365 nm). The melting points of compounds were determined using a digital melting point apparatus (REACH Devices, USA). The proton NMR (^{1}H NMR) spectra of compounds were obtained using a 300 MHz Bruker Avance spectrometer (Department of Chemistry, University of Waterloo). Either $CDCl_3$ or DMSO-d_6 were used as solvents. Coupling constants (*J* values) were recorded in Hertz (Hz). Abbreviations used to represent ^{1}H NMR signals were s – singlet, d – doublet, t – triplet, m – multiplet, br s – broad singlet. The mass and purity were confirmed on an Agilent 1260

Infinity liquid chromatography (LC) module equipped with a 6130 Quadrupole mass spectrometer (Agilent 6100 series LCMS). The column used on LCMS was a ZORBAX Eclipse AAA, 4.6 × 75 mm, 3.5 micron (Agilent Technologies, Canada) column. A mixture of water and acetonitrile 1:1 v/v with 0.1% formic acid (1.0 mL/min flow rate), was used as the solvent system to assess compound purity and mass. All final compounds were ≥ 95% pure as determined by LCMS analysis.

2.5.2 Chemistry

For the coupling of acid chlorides and primary amine, phenylmethanamine (**1**) (1 mmol) was added to a 50 mL round bottom flask (RBF) containing 15 mL anhydrous tetrahydrofuran (THF). To this mixture, 1.2 equivalents of TEA and 1.0 equivalent of corresponding acid chlorides with various R groups (**2a-m**) were added.[344] The reaction was kept at either room temperature or under reflux for 6-24h and monitored by thin layer chromatography (TLC). After the reaction was complete, the solvent THF was evaporated in vacuo and the resulting reaction mixture was dissolved in 15 mL ethyl acetate (EtOAc), and then washed with 15 mL brine solution (× 3). The organic layer was collected and dried over anhydrous $MgSO_4$ and filtered. The organic solvent was removed in vacuo and the residue/oil obtained was further purified by silica gel column chromatography using a combination of solvent systems (1:1 *n*-Hexanes:EtOAc or 5:2 *n*-Hexanes:EtOAc or 9:1 dichloromethane (DCM):Methanol (MeOH) or 4:1 DCM:*n*-Hexanes) to afford the final compounds **3a-m**.

As for the combination of carboxylic acid and primary amine, phenylmethanamine (**1**) (1 mmol), was added to a 50 mL round bottom flask containing 15 mL THF. Next, 1.0 equivalent carboxylic acid (**4a-c**), 1.2 equivalents EDC, 1.5 equivalents HOBt, and 2.2 equivalents TEA were added in sequence. The reaction mixture was kept at room temperature overnight or reflux conditions for 6 – 12 h. The solvent was evaporated in vacuo and the resulting reaction mixture was dissolved in 15 mL EtOAc and washed with 15 mL brine solution (× 3). The organic layer was collected, dried over anhydrous $MgSO_4$ and filtered. The

organic solvent was then removed in vacuo to obtain the residue/oil which was further purified by silica gel column chromatography using either 1:1 *n*-Hexanes:EtOAc or 5:2 *n*-Hexanes:EtOAc as mobile phase to afford compounds **5a-c**.

2.5.3 Aβ42 aggregation kinetic assay

The ability of *N*-benzylbenzamide and carboxamide derivatives **3a-m** and **5a-c** to inhibit the Aβ42 aggregation was evaluated using the thioflavin T (ThT) based fluorescence kinetic assay.[345] The 15 μM ThT solution was prepared in 50 mM glycine buffer using the ultra-pure water (UPW). The pH of the solution was adjusted to 7.4 with 50 mM sodium hydroxide solution. The aggregation assay was carried out using 215 mM sodium phosphate dibasic heptahydrate buffer prepared in UPW and the pH was adjusted to 7.4 by using 50 mM hydrochloric acid solution. The Aβ42•HFIP > 95% pure (Anaspec, USA) was treated with 1% ammonium hydroxide solution to afford 1 mg/mL stock solution. The stock solution was then vortexed and sonicated for 5 min before being diluted to a 25 μM working solution using the assay buffer. The stock solutions of the test compounds (**3a-m, 5a-c**, resveratrol RVT and chalcone) were prepared in assay buffer with DMSO as the solubilizing agent (final concentration per well was less than 2%). The 24 h aggregation kinetics assay was carried out using 384-well plates (Costar, black, clear-bottom), by adding 44 μL of ThT, 12 μL of assay buffer, 16 μL of Aβ42 solution (10 μM final well concentration), and 8 μL of test compound dilution (25 μM) into each well. The Aβ42 control wells contained ThT, Aβ42 solution and the assay buffer without any test compound. The plates were covered with a transparent plate cover and were incubated at 37 °C for 24 h with shaking at 300 cpm between readings for 30 s. The readings were taken every 10 min (bottom reading), with excitation wavelength of 440 nm and emission wavelength of 490 nm using the BioTek Synergy H1 microplate reader. Each sample was measured in triplicate readings and the results were obtained based on three independent experiments.

2.5.4 Transmission electron microscopy

The TEM assay was carried out by first running the Aβ42 aggregation assay by incubating 25 μM each of test compounds with 10 μM Aβ42 for 24 h at 37 °C.[327] The TEM grids were prepared by aliquoting 20 μL of each sample from the 384-well plate after the 24-hour incubation period. These samples were loaded onto 400-mesh formvar-coated copper grids (Electron Microscopy Sciences, Pennsylvania, USA). The grids were air-dried overnight before being washed with 40 μL UPW three times. After washing, 20 μL 2% phosphotungstic acid (PTA) solution was added to the grid and stayed for 1 min to stain the samples. Then the PTA solution was absorbed away with filter paper and then the grids were washed with 40 μL UPW three times. Then the grids were further air-dried overnight. The imaging studies were carried out using a Philips CM 10 TEM (Dept. of Biology, University of Waterloo) at 60 kV and the micrographs were obtained through a 14-megapixel AMT camera at 64,000X magnification. The samples used to prepare the grids were obtained by mixing the triplicate wells from ThT assay and image were taken at a randomized view for each grid.

2.5.5 Cell viability assay

The cell viability assay was carried out in the Aβ42-induced HT22 cell toxicity model.[346] The cytotoxicity and neuroprotective effects of benzamide/carboxamide derivatives **3a-m** and **5a-c** toward HT22 cells were carried out by using the UV-based cell metabolism assay kit (cell counting kit 8, CCK-8, TargetMol, Massachusetts, USA). The HT22 cells were cultured in DMEM/F12 1:1 with the addition of glutamate supplemented with 10% FBS and 1% penicillin and streptomycin at 37 °C in 5% CO_2. The cells were seeded at a density of 50,000 cells per mL. After 24 h, the cells were treated with various compounds at 25 μM prepared in phosphate buffer pH 7.4 and DMSO (less than 2%) and incubated for 48 h. After that, the CCK-8 reagent was added to each well, and incubated for another 2 h, before measuring the absorbance at 450 nm as per the manufacturer's protocol. The neuroprotective effects of test compounds toward Aβ42-induced

cytotoxicity were determined by treating the HT22 cells with 5 μM of Aβ42•HFIP (>95%, rPeptide, USA), and then incubating for 48 h. The cell viability assay was determined by adding the CCK-8 reagent and incubating for another 2 h to measure the absorbance at 450 nm. The cell viability was calculated as the average percent cell viability based on quadruplicate readings from three independent experiments. For statistical analysis, the results were analyzed by one-way ANOVA followed by Bonferroni post hoc analysis compared to Aβ control group. ns = not significant, *$p < 0.01$ compared to Aβ42 control group, **$p < 0.01$ compared to Aβ42 control group, ***$p < 0.01$ compared to Aβ42 control group, ****$p < 0.01$ compared to Aβ42 control group.

2.5.6 Molecular docking study

The binding interactions of **3a** with Aβ42 were investigated by carrying out molecular docking studies using the Discovery Studio software program v20.1.0.19295, Structure-Based-Design (BIOVIA Inc. San Diego, USA).[347] The Aβ42 pentamer model was prepared by extracting the coordinates from the solved 3D structure of the Aβ42 fibril (PDB id: 5KK3). [340] A binding sphere of 20 Å radius was selected and defined as the ligand binding site which covers the ^{16}KLVFFA^{21} and the C-terminal ^{32}IGLMVGGVVIA^{42} hydrophobic regions of the Aβ42 in the oligomer and fibril models. [343] Compound **3a** was built in 3D using the *Small Molecule* module in the software and was subjected to energy minimization protocol (1000 and 2000 steps of steepest descent followed by conjugate gradient method) using CHARMm force field. The CDOCKER algorithm was used to carry out the docking studies. The *Receptor-ligand Interactions* module in the software was used to perform CDOCKER simulations. The docking simulation included 2000 heating steps, a heating target temperature of 700 K and 5000 cooling steps and a cooling target temperature of 300 K. The top ligand binding modes of **3a** were analyzed by evaluating the CDOCKER energy and CDOCKER interaction energy (in kcal/mol). Further analysis was carried out by determining the polar and nonpolar contacts of **3a** in the Aβ42 oligomer and fibril models.

Chapter 3

Design, Synthesis and Evaluation of *N*-Phenethylbenzamide and *N*-Phenethylcarboxamide Derivatives as Aβ Aggregation Modulators

Below is a list of publications, manuscripts submitted and in preparation along with author names based on this chapter:

Zhao, Y. Rao, P. P. N. *N*-Benzyl, *N*-phenethyl and *N*-benzyloxybenzamide derivatives inhibit amyloid-beta (Aβ42) aggregation and mitigate Aβ42-induced neurotoxicity. *Med. Chem. Res.* (Manuscript under revision)

3.1 Introduction

This chapter features the second series of compounds in the proposed library, where the three-carbon α,β-unsaturated system present in the chalcone template was replaced with an amide bioisostere along with two sp^3 hybridized carbon linker to obtain *N*-phenethylbenzamide and *N*-phenethylcarboxamide derivatives.[318,319] The structure-activity relationship (SAR) modifications for this library of 16 derivatives are shown in **Figure 3-1**. In this series of compounds, the *N*-phenethyl moiety was kept constant while the other end of the molecule was modified by incorporating various aromatic rings such as benzene (**7a**), pyridine (**7b**, **7c**), pyrrole (**7h**), furan (**7i**), thiophene (**7j**). Furthermore, bicyclic aromatic rings were also included, such as naphthalene (**7l**), quinoline (**7m**), indole (**8a**), benzofuran (**8b**), and benzo[*b*]thiophene (**8c**). In addition, aliphatic rings were also incorporated including cyclohexane (**7f**), piperidine (**7g**), and pyrrolidine (**3k**). Besides, known pharmacophores where 3, 4-dimethoxylbenzene and 3, 4-difluorobenzene moieties were also incorporated in compounds **7d** and **7e**.[320] This chapter describes the synthesis, characterization, and evaluation of *N*-phenethylbenzamide and *N*-phenethylcarboxamide derivatives class of compounds *via* biophysical (thioflavin T based fluorescence spectroscopy, transmission electron

microscopy), biochemical (Aβ42-induced cytotoxicity in mouse hippocampal HT22 neuronal cell lines) and by computational modelling studies.

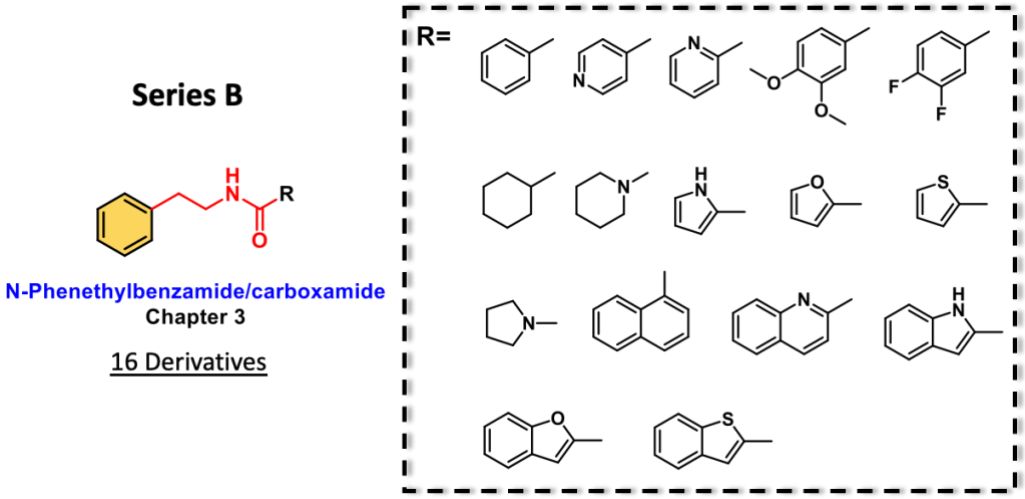


Figure 3-1. *N*-Phenylethylbenzamide and *N*-phenylethylcarboxamide derivatives (Series B). This series of compounds contains an amide bond and a two carbon sp^3 hybridized linker region.

3.2 Hypothesis

It is hypothesized that replacing the α,β-unsaturated system presented in either chalcone or curcumin with an amide bioisostere in the *N*-phenylethylbenzamide series will remove the presence of a reactive Michael acceptor and provide drug-like properties while retaining their Aβ42 aggregation modulation properties. The presence of the sp^3 hybridized two carbon linker (*N*-phenethyl) is expected to make the scaffold more flexible which would promote additional contacts in the KLVFFA and the C-terminal regions of Aβ42. Furthermore, given the hydrophobic nature of the amyloidogenic regions of Aβ, these compounds are expected to exhibit better binding compared to the *N*-benzylbenzamide series (Chapter 2). In this series of compounds, substituted compounds with known pharmacophores (such as R = 3, 4-dimethoxylbenzene and R = 3, 4-difluorobenzene)[320], is expected to demonstrate better inhibition of Aβ42-aggregation due to efficient van der Waals, hydrophobic and hydrogen bonding interactions with Aβ42 and also provide

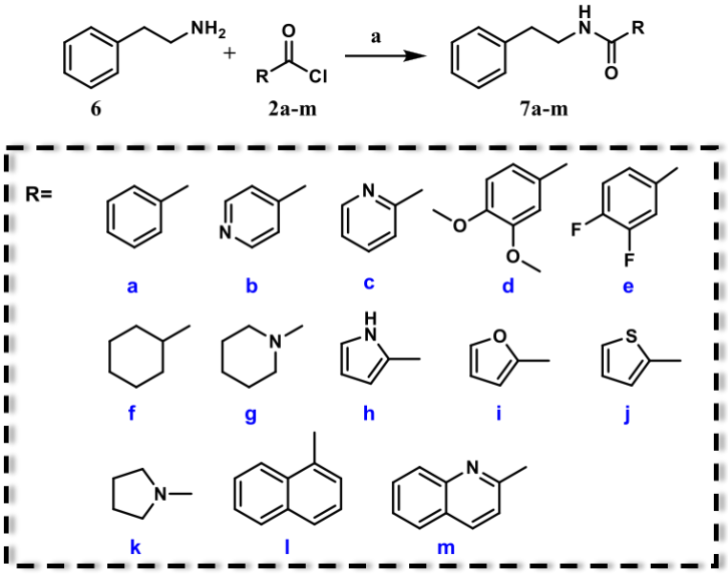
neuroprotection against Aβ42-induced cytotoxicity. The SAR was investigated by incorporating monocyclic, bicyclic, aromatic, acyclic, 5- and 6-membered rings to study their effect on Aβ42 aggregation (**Figure 3-1**). It is hypothesized that these SAR studies will provide novel insights on designing Aβ42 aggregation modulators.

3.3 Results and Discussion

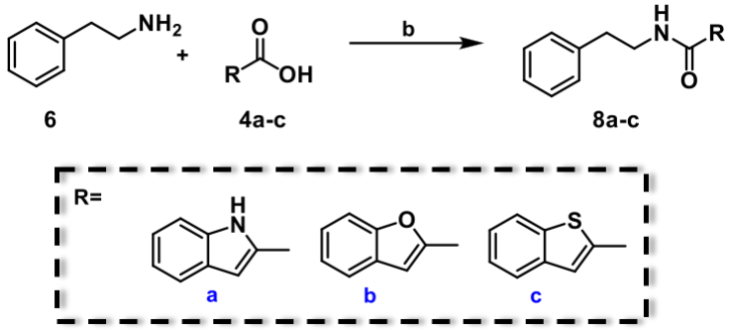
In this section, the synthesis, purification and characterization of the *N*-phenethylbenzamide and *N*-phenethylcarboxamide (**7a-m** and **8a-c**) library of the compounds are discussed which is followed by biological activity screening, including anti-Aβ42 aggregation assay (ThT-based spectroscopy), fibril morphology study (TEM experiment), compound cytotoxicity and neuroprotection in Aβ42-induced toxicity to mouse hippocampal HT22 neuronal cells and computational modeling studies in 3D structures of Aβ42 oligomer and fibril models..

3.3.1 Synthesis

The retro-synthetic analysis of the compound library suggests that the starting building blocks can be coupled to form the amide bond using suitable substrates to obtain the *N*-phenethylbenzamide and *N*-phenethylcarboxamide derivatives. This was achieved through either the direct coupling of acid halides (**2a-m**) with primary amines (2-phenylethan-1-amine **6**, Method A) or by coupling the carboxylic acids with primary amines (2-phenylethan-1-amine **6**, Method B). The preference for using the acid halides versus carboxylic acids coupling method was made based on the commercial availability and cost-effectiveness of the starting materials. With that being said, compounds **7a-m** were synthesized *via* Method A as shown in **Scheme 3-1**, whereas compounds **8a-c** were synthesized by method B as shown in **Scheme 3-2**.



Scheme 3-1. Synthetic scheme for **7a-m** by coupling 2-phenylethan-1-amine (**6**) and corresponding acid chlorides (**2a-m**). Reagents and conditions: (a) TEA, THF, room temperature/reflux 2-24 h.



Scheme 3-2. Synthetic scheme for **8a-c** by coupling 2-phenylethan-1-amine (**6**) and corresponding carboxylic acids (**4a-c**). Reagents and conditions: (b) EDC•HCl, HOBt, TEA, THF, room temperature overnight/reflux 4-12 h.

In Method A, 2-phenylethan-1-amine (**6**) was coupled with corresponding acid halides. Considering the leaving capability and reactivity, acid chlorides (**2a-m**) were used in the reactions. The reaction mechanism (**Figure 3-2**) is described as follows: First, the nucleophilic amine **6** attacks the electrophilic carbonyl carbon of the acid chloride to form a tetrahedron intermediate by nucleophilic addition; next, chloride serves as a good leaving group and then is eliminated from the tetrahedron intermediate; then hydrochloric acid is

also formed as the reaction by-product which can neutralize the base triethylamine (TEA) to facilitate product formation. [322] The overall yields of these reactions range from 72.8-87.9%. The analytical data for **7a-m** (^{1}H NMR, MS and purity data by LCMS) are given below. Analytical spectral data for all the final compounds are given in **Appendix B**.

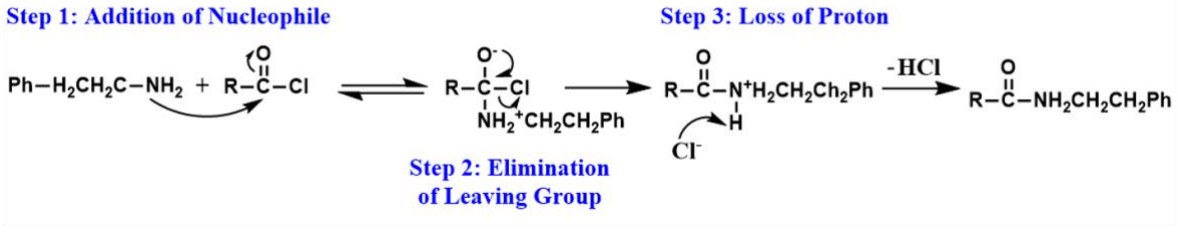


Figure 3-2. Nucleophilic acyl substitution mechanism which includes three major steps: (1) addition of nucleophile to the electrophilic carbonyl carbon. (2) elimination of the leaving group. (3) loss of proton.

3.3.1.1 *N*-Phenethylbenzamide (**7a**)

The product was obtained as a white solid (Yield = 79.8%). ^{1}H NMR (300 MHz, $CDCl_3$): δ 7.78–7.59 (m, 2H), 7.52–7.28 (m, 5H), 7.24 (m, *J* = 4.9, 4.4 Hz, 3H), 6.10 (s, 1H), 3.71 (q, *J* = 6.9 Hz, 2H), 2.93 (t, *J* = 6.9 Hz, 2H). mp: 122–125 °C. ESI-MS, m/z calcd for $C_{15}H_{16}NO$ $[M+H]^+$ 212.1, found 212.1. Purity: 99.9% (LCMS).

3.3.1.2 *N*-Phenethylisonicotinamide (**7b**)

The product was obtained as a white solid (Yield = 76.0%). ^{1}H NMR (300 MHz, $CDCl_3$): δ 8.71–8.68 (m, 2H), 7.50–7.48 (m, 2H), 7.36–7.20 (m, 5H), 6.15 (br s, 1H), 3.72 (q, *J* = 6.6 Hz, 2H), 2.93 (t, *J* = 6.8 Hz, 2H). mp: 129-132 °C. ESI-MS, m/z calcd for $C_{14}H_{15}N_2O$ $[M+H]^+$ 227.1, found 227.1. Purity: 98.7% (LCMS).

3.3.1.3 *N*-Phenethylpicolinamide (**7c**)

The product was obtained as a off white solid (Yield = 74.5%). ^{1}H NMR (300 MHz, $CDCl_3$): δ 8.53 (d, *J* = 4.5 Hz, 1H), 8.22 (d, *J* = 7.8 Hz, 1H), 8.16 (s, 1H), 7.85 (td, *J* = 7.7, 1.6 Hz, 1H), 7.44–7.23 (m, 6H), 3.72 (q, *J* = 7.0 Hz, 2H), 2.97 (t, *J* = 7.3 Hz, 2H). mp: 39-42 °C. ESI-MS, m/z calcd for $C_{14}H_{15}N_2O$ $[M+H]^+$ 227.1, found 227.1. Purity: 99.0% (LCMS).

3.3.1.4 *N*-Phenethyl-3,4-dimethoxybenzamide (**7d**)

The product was obtained as a white solid (Yield = 73.9%). ^{1}H NMR (300 MHz, $CDCl_3$) δ 7.42 – 7.22 (m, 5H), 7.22 – 7.12 (m, 1H), 6.89 – 6.81 (m, 1H), 6.07 (s, 1H), 3.93 (s, 3H), 3.94 (s, 3H), 3.73 (q, *J* = 6.7 Hz, 2H), 2.96 (t, *J* = 6.9 Hz, 2H). mp: 138-141 °C. ESI-MS, m/z calcd for $C_{17}H_{19}NO_3$ $[M+H]^+$ 286.1, found 286.1. Purity: 99.4% (LCMS).

3.3.1.5 *N*-Phenethyl-3,4-difluorobenzamide (**7e**)

The product was obtained as a white solid (Yield = 82.3%). ^{1}H NMR (300 MHz, $CDCl_3$) δ 7.64 – 7.51 (m, 1H), 7.47 – 7.13 (m, 6H), 6.04 (s, 1H), 3.73 (q, *J* = 6.6 Hz, 2H), 2.96 (t, *J* = 6.8 Hz, 2H). mp: 92-95 °C. ESI-MS, m/z calcd for $C_{15}H_{13}F_2NO$ $[M+H]^+$ 262.1, found 262.1. Purity: 99.2% (LCMS).

3.3.1.6 *N*-Phenethylcyclohexanecarboxamide (**7f**)

The product was obtained as a white solid (Yield = 87.9%). ^{1}H NMR (300 MHz, $CDCl_3$) δ δ 7.36 – 7.12 (m, 5H), 5.39 (s, 1H), 3.49 (q, *J* = 6.6 Hz, 2H), 2.79 (t, *J* = 6.9 Hz, 2H), 2.06 – 1.90 (m, 1H), 1.85 – 1.74 (m, 1H), 1.80 – 1.68 (m, 3H), 1.68 – 1.59 (m, 1H), 1.45 – 1.33 (m, 2H), 1.33 – 1.20 (m, 1H), 1.24 – 1.11

(m, 2H). mp: 116-119 °C. ESI-MS, m/z calcd for $C_{15}H_{21}NO$ $[M+H]^+$ 232.1, found 232.1. Purity: 96.1% (LCMS).

3.3.1.7 *N*-Phenethylpiperidine-1-carboxamide (**7g**)

The product was obtained as a white solid (Yield = 75.4%). ^{1}H NMR (300 MHz, $CDCl_3$) δ ^{1}H NMR (300 MHz, Chloroform-*d*) δ 7.39 – 7.18 (m, 5H), 4.43 (s, 1H), 3.51 (q, *J* = 6.6 Hz, 2H), 3.33 – 3.23 (m, 4H), 2.84 (t, *J* = 6.9 Hz, 2H), 1.66 – 1.46 (m, 6H). mp: 87-90 °C. ESI-MS, m/z calcd for $C_{14}H_{20}N_2O$ $[M+H]^+$ 233.1, found 233.1. Purity: 97.6% (LCMS).

3.3.1.8 *N*-Phenethyl-1*H*-pyrrole-2-carboxamide (**7h**)

The product was obtained as a white solid (Yield = 82.8%). ^{1}H NMR (300 MHz, $CDCl_3$): δ 9.38 (br s, 1H), 7.37–7.26 (m, 2H), 7.26–7.17 (m, 3H), 6.91–6.88 (m, 1H), 6.41–6.38 (m, 1H), 6.20–6.17 (m, 1H), 5.84 (br s, 1H), 3.66 (q, *J* = 6.7 Hz, 2H), 2.88 (t, *J* = 6.9 Hz, 2H). mp:134-137 °C. ESI-MS, m/z calcd for $C_{13}H_{15}N_2O$ $[M+H]^+$ 215.1, found 215.1. Purity: 98.6% (LCMS).

3.3.1.9 *N*-Phenethylfuran-2-carboxamide (**7i**)

The product was obtained as a white solid (Yield = 75.5%). ^{1}H NMR (300 MHz, $CDCl_3$): δ 7.38–7.20 (m, 5H), 7.08 (d, *J* = 3.5 Hz, 1H), 6.46–6.36 (m, 2H), 3.67 (q, *J* = 7.0 Hz, 2H), 2.90 (t, *J* = 7.0 Hz, 2H). mp: 115-118 °C. ESI-MS, m/z calcd for $C_{12}H_{12}NO_2$ $[M+H]^+$ 216.1, found 216.1. Purity: 99.7% (LCMS).

3.3.1.10 *N*-Phenethylthiophene-2-carboxamide (**7j**)

The product was obtained as a white solid (Yield = 73.2%). ^{1}H NMR (300 MHz, $CDCl_3$): δ 7.41–7.18 (m, 7H), 7.08–7.01 (m, 1H), 6.00 (br s, 1H), 3.67 (q, *J* = 7.0 Hz, 2H), 2.90 (t, *J* = 7.0 Hz, 2H). mp: 116–119 °C. ESI-MS, m/z calcd for $C_{13}H_{14}NOS$ $[M+H]^+$ 232.1, found 232.1. Purity: 99.8% (LCMS).

3.3.1.11 *N*-Phenethylpyrrolidine-1-carboxamide (**7k**)

The product was obtained as a white solid (Yield = 87.4%). ^{1}H NMR (300 MHz, $CDCl_3$) δ 7.35 – 7.14 (m, 5H), 4.16 (s, 1H), 3.48 (q, *J* = 6.9, 5.7 Hz, 2H), 3.27 – 3.21 (m, 3H), 2.81 (t, 2H), 1.93 – 1.77 (m, 4H), 1.68 (s, 1H). mp: 126-129 °C. ESI-MS, m/z calcd for $C_{13}H_{18}N_2O$ $[M+H]^+$ 219.1, found 219.1. Purity: 97.4% (LCMS).

3.3.1.12 *N*-Phenethyl-1-naphthamide (**7l**)

The product was obtained as a white solid (Yield = 72.8%). ^{1}H NMR (300 MHz, $CDCl_3$): δ 8.20–8.16 (m, 1H), 7.81–7.75 (m, 2H), 7.50–7.44 (m, 3H), 7.40–7.23 (m, 6H), 5.96 (br s, 1H), 3.82 (q, *J* = 6.6 Hz, 2H), 2.99 (t, *J* = 6.8 Hz, 2H). mp: 125–128 °C. ESI-MS, m/z calcd for $C_{19}H_{18}NO$ $[M+H]^+$ 276.1, found 276.1. Purity: 99.2% (LCMS).

3.3.1.13 *N*-Phenethylquinoline-2-carboxamide (**7m**)

The product was obtained as a white solid (Yield = 79.9%). ^{1}H NMR (300 MHz, $CDCl_3$): δ 8.36 (br s, 1H), 8.27 (s, 2H), 8.04 (d, *J* = 8.5 Hz, 1H), 7.86 (dd, *J* = 8.1, 1.5 Hz, 1H), 7.74 (ddd, *J* = 8.5, 6.9, 1.5 Hz, 1H), 7.60 (dd, *J* = 8.2, 6.8 Hz, 1H), 7.36–7.19 (m, 5H), 3.78 (q, *J* = 7.6

Hz, 2H), 2.99 (t, *J* = 7.3 Hz, 2H). mp: 81-84 °C. ESI-MS, m/z calcd for $C_{18}H_{17}N_2O$ $[M+H]^+$ 277.1, found 277.1. Purity: 99.56% (LCMS).

Method B was used to synthesize *N*-phenethylcarboxamide derivatives (**8a-c**, **Scheme 3-2**). Compared to acid chlorides, carboxylic acids are less reactive due to the electron-donating nature of the hydroxyl group. This can influence the reaction progress, yield and the purity of the products. However, this limitation can be overcome by activating the carboxylic acid (**4a-c**) with the assistance of carbodiimide-dehydrating reagents, such as 1-ethyl-3-(3-dimethylaminopropyl)carbodiimide (EDC). [323,324] The detailed reaction mechanism is shown in **Figure 3-3**. The carboxylic acids can be transformed into an ester intermediate. In the presence of an activator, such as hydroxyltriazole (HOBt), the nucleophilic activator attacks the carbonyl carbon of the ester intermediate so that an active ester is formed. [325] The active ester contains a better leaving group compared to the original carboxylic acid so that it can react with 2-phenylethan-1-amine (**6**) *via* nucleophilic acyl substitution as mentioned in the previous paragraph. The by-product urea formed as a result of using EDC as dehydrating reagent is water-soluble and therefore, can be washed away by aqueous extraction in the post-reaction workup. The overall yields of these reactions range from 80.9 to 87.5%. The analytical data (^{1}H NMR, MS and purity data by LCMS) for compounds **8a-c** are given below. Analytical spectral data for all the final compounds are given in **Appendix B**.

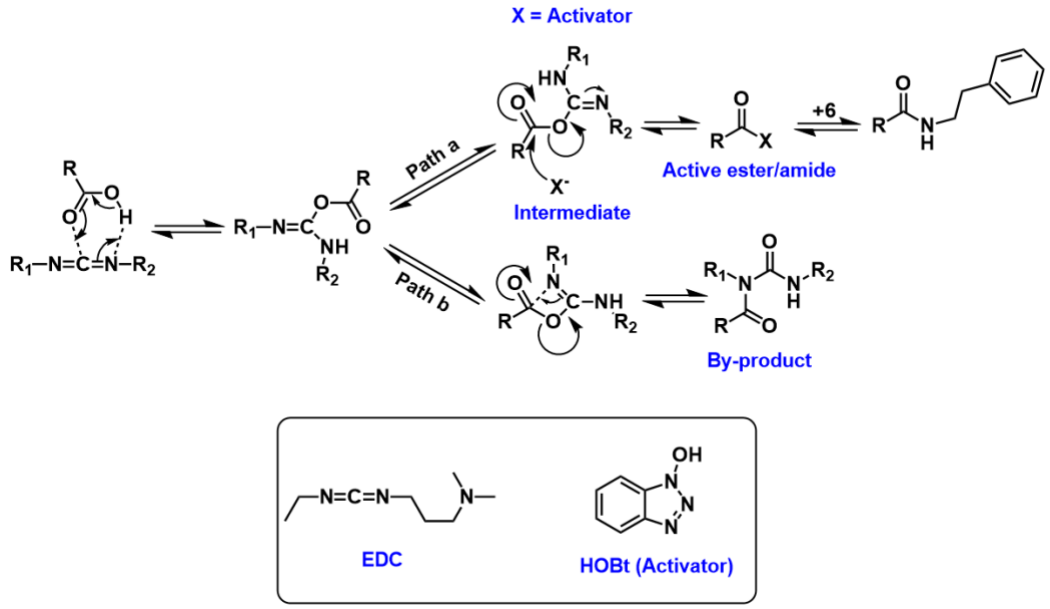


Figure 3-3. Reaction mechanism when using the dehydrating agent EDC and activator HOBt for coupling 2-phenylethan-1-amine (**6**) and corresponding carboxylic acid (**4a-c**).

3.3.1.14 *N*-Phenethyl-1*H*-indole-2-carboxamide (**8a**)

The product was obtained as a white solid (Yield = 87.5%). ^{1}H NMR (300 MHz, DMSO-d_6): δ 11.51 (br s, 1H), 8.57 (t, *J* = 5.6 Hz, 1H), 7.60 (d, *J* = 7.9 Hz, 1H), 7.43 (d, *J* = 8.2 Hz, 1H), 7.34–7.01 (m, 6H), 3.49–3.55 (m, 2H), 2.87 (t, *J* = 7.4 Hz, 2H). mp: 191-194. ESI-MS, m/z calcd for $C_{17}H_{17}N_2O$ $[M+H]^+$ 265.1, found 265.1.Purity: 97.6% (LCMS).

3.3.1.15 *N*-Phenethylbenzofuran-2-carboxamide (**8b**)

The product was obtained as a white solid (Yield = 86.1%). ^{1}H NMR (300 MHz, $CDCl_3$) δ 7.69 (d, *J* = 7.8 Hz, 1H), 7.52 – 7.23 (m, 9H), 6.71 (s, 1H), 3.78 (q, *J* = 6.8 Hz, 2H), 2.99 (t, *J* = 7.0 Hz, 2H). mp: 126-129 °C. ESI-MS, m/z calcd for $C_{17}H_{15}NO_2$ $[M+H]^+$ 266.1, found 266.1. Purity: 96.5% (LCMS).

3.3.1.16 *N*-Phenethylbenzo[*b*]thiophene-2-carboxamide (**8c**)

The product was obtained as a white solid (Yield = 80.9%). ^{1}H NMR (300 MHz, $CDCl_3$) δ 7.91 – 7.79 (m, 2H), 7.70 (s, 1H), 7.50 – 7.24 (m, 7H), 3.76 (t, *J* = 6.8 Hz, 2H), 2.98 (t, *J* = 6.9 Hz, 2H). mp: 126-129 °C. ESI-MS, m/z calcd for $C_{17}H_{15}NOS$ $[M+H]^+$ 282.1, found 282.1. Purity: 95.0% (LCMS).

3.3.2 Modulatory activity on amyloid-beta aggregation

The modulatory activity of *N*-phenethylbenzamide and carboxamide derivatives **7a-m** and **8a-c** on Aβ42 aggregation was evaluated by the ThT aggregation kinetic assay.[326–329] It is the golden standard used in the field for rapid screening of small molecules to determine their Aβ42 aggregation modulation activity.[330–333] In this assay, ThT was used as the fluorescent dye which can selectively bind to the β-sheet structure of various forms of aggregated Aβ42. Upon binding, ThT gives a characteristic increase in the fluorescence reading (FLR) which is directly proportional to the amount of Aβ aggregates formed. By comparing the FLR of Aβ42 control and in the presence of various test compounds, the percentage inhibition (PI) can be calculated at the end of the assay. If the FLR is lower than that of the control, it indicates that the compounds are inhibiting the Aβ42 aggregation. Similarly, if the FLR is higher than that of the control, it indicates that the compounds are able to promote the Aβ42 aggregation. Compounds that are able to inhibit Aβ42 aggregation are termed aggregation inhibitors (AI) and compounds that are able to promote Aβ42 aggregation are termed aggregation promotors (AP), whereas compounds that weakly modulate the aggregation are termed weak aggregation modulators (WAM). Initially, all the test compounds were screened at 25 μM to determine their effect on Aβ42 aggregation. Compounds that show promising activity were further evaluated at a concentration range (1, 5, 10, 25 μM) to determine the aggregation kinetics. Resveratrol (RVT) which is a known inhibitor of Aβ42 aggregation was also included in the assay as the reference compound for comparison.[334]

In **Figure 3-4**, the ThT aggregation kinetic curves of *N*-phenylethylbenzamide and carboxamide derivatives **7a-m** and **8a-c** were shown. In each panel, the blue curve at the bottom is the ThT background readings which suggests that ThT has no interference on the FLR in monitoring the aggregation of Aβ42. The red curve shows the Aβ42 aggregation in the absence of test compounds. In these curves, some characteristics of Aβ42 aggregation can be observed. It is a sigmoidal curve characterized by a very short lag phase (~ 30 min) which is followed by a rapid growth phase spanning the time course from around 0.5 h to 10 h. Then, the FLR tends to be stable with readings hovering around 8,000 RFU, indicating the aggregation process has reached the equilibrium status. Such saturation phase was maintained until the end of the assay at 24 h. Compared to the Aβ42 control, other curves, in the presence of different *N*-phenylethylbenzamide and carboxamide derivatives (**Figure 3-4**, A: **7a-d**, B: **7e-h**, C: **7i-l**, D: **7m**, **8a-c**), shared similar shapes without any major differences. This observation suggests these derivatives are not able to alter the aggregation kinetics by either shortening or extending the lag/growth phase. However, lower FLR at the saturation phase than Aβ42 control for these curves was observed at the 24 h time point which indicates that some derivatives were capable of reducing the formation of Aβ42 fibrils. When co-incubating the reference compound RVT with Aβ42 (**Figure 3-4** A), a dramatic decrease in the FLR was noticed in the saturation phase with FLR below 2,000 RFUs after 18 h. Such observation is not a surprise as RVT is a very potent Aβ AI.[334]

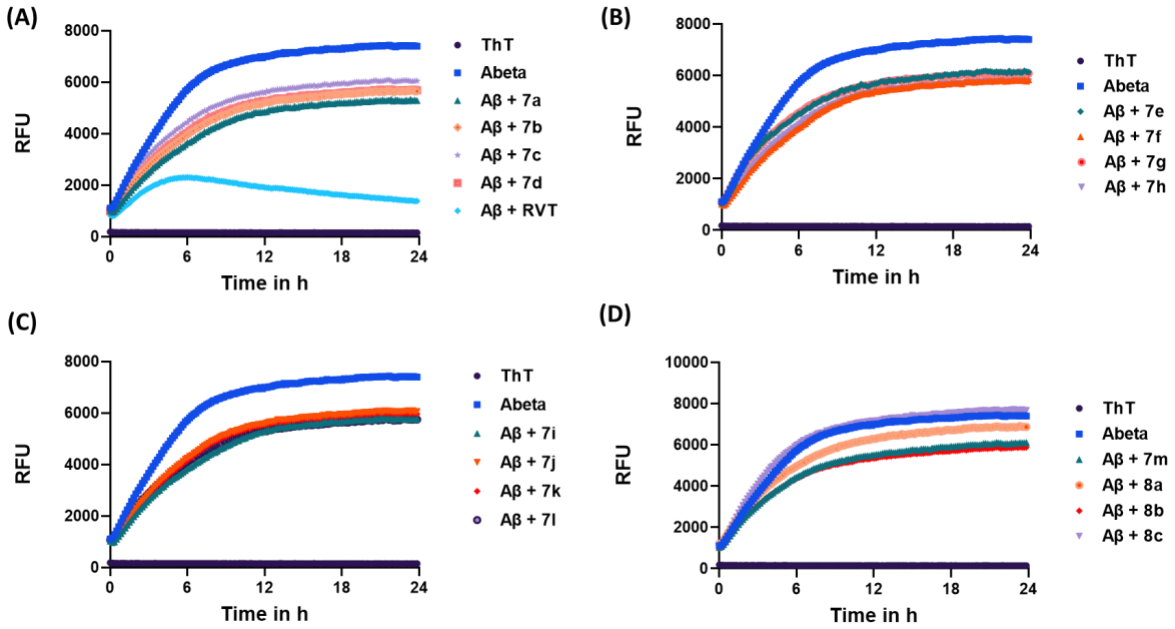


Figure 3-4. The Aβ42 aggregation kinetic curves for *N*-phenylethylbenzamide and carboxamide derivatives (**7a-m**, **8a-c**) in the ThT-based fluorescence assay. (A) Aggregation kinetic curves for derivatives **7a-d** and reference compound resveratrol (RVT). (B) Aggregation kinetic curves for derivatives **7e-h**. (C) Aggregation kinetic curves for derivatives **7i-l**. (D) Aggregation kinetic curves for derivatives **7m**, **8a-c**. The derivatives (25 μM) were incubated with Aβ42 (10 μM) for 24 h at 37 ˚C, pH 7.4 and the ThT fluorescence was monitored (excitation = 440 nm, emission = 490 nm). Results were obtained based on triplicate readings from three independent experiments.

Table 3-1 shows the anti-aggregation activity of test compounds as the percentage inhibition (PI) and **Figure 3-5** shows a bar plot of PI at the 24 h time point. A total of 14 out of 16 compounds from this series exhibited anti-Aβ42 activity in the ThT-based fluorescence assay with activity ranging from 17.0- 28.6 %. Compound **7a** (R = benzene) exhibited 28.6 ± 1.1% inhibition, whereas replacing the benzene ring with the more polar pyridine bioisostere in compounds **7b** (23.6 ± 5.9% inhibition of Aβ42 aggregation) and **7c** (18.2 ± 3.4% inhibition of Aβ42 aggregation) still showed anti-aggregation properties although these compounds were not as effective as **7a**. A similar SAR trend was observed for the *N*-benzylbenzamide series of compounds (**3a-c**, Chapter 2). Incorporation of the known anti-Aβ pharmacophores in **7d** and **7e** did not improve the activities as expected. The PI for **7d** (R = 3, 4-dimethoxylbenzene) and **7e** (R = 3, 4-

difluorobenzene) were 23.2 ± 3.4 % and 17.0 ± 2.8% respectively. Incorporating aromatic 5-member heterocyclic rings - showed slightly lower PI than the parent compound **7a**, with PI of 22.0 % ± 9.1 % for **7h** (R = pyrrole), 22.0 ± 7.1 % for **7i** (R = furan) and 18.1 ± 5.6 % inhibition for **7j** (R = thiophene). Furthermore, the aliphatic ring containing derivatives exhibited moderate inhibitory activities with PI of 21.1± 4.9 % for **7f** (R = cyclohexane), 17.8± 7.0 % for **7g** (R = piperidine) and 19.4 ± 3.9 % inhibition for **7k** (R = pyrrolidine). When the R groups were replaced by bicyclic aromatic rings, mixed results were seen regarding their aggregation inhibitory activities. For example, compounds **7l** (R = naphthalene) and **7m** (R= quinoline) were moderate AI (same as **3l** and **3m**) with PI of 22.3 ± 6.8 % and 17.3± 2.7 % respectively. Similarly, both **7a** and **8a** (R =indole) were WAM and showed PI around 7%, and both **7c** and **8c** with R group as benzo[*b*]thiophene were not active in modulating the aggregation process. However, the behaviors of derivatives with benzofuran as the R group showed different results. Derivative **7b** (R = benzofuran) is a weak AP with PI around 0.51%, in contrast, derivative **8b** turned out to be an AI with PI of 20.5 ± 9.5 %. Overall, in this series, adding an additional carbon spacer led to slight improvement in the anti-Aβ42 activity in most of the compounds including **7a**, **7b**, **7c**, **7d**, **7e**, **7g**, **7i**, **7j**, **7l**, and **8b** compared to the *N*-benzylbenzamide series (Chapter 2). These results demonstrate that *N*-phenylethylbenzamide and carboxamide scaffolds do exhibit anti-aggregation properties toward Aβ42 in the ThT-based fluorescence assay.

Table 3-1. Percent inhibition (PI) of *N*-phenylethylbenzamide and carboxamide derivatives (**7a-m**, **8a-c**), resveratrol (RVT) and chalcone (CHL) at 25 µM on Aβ42 (10 µM) aggregation.

Cmpd	% Inhibition[a]	CLogP[b]	Cmpd	% Inhibition[a]	CLogP[b]
7a	28.6 ± 1.1	2.96	**7i**	22.0 ± 7.1	2.13
7b	23.6 ± 5.9	1.46	**7j**	18.2 ± 5.68	2.60
7c	18.2 ± 3.4	1.81	**7k**	19.4 ± 3.9	2.16
7d	23.2 ± 3.4	2.45	**7l**	22.3 ± 6.8	4.13
7e	17.0 ± 2.8	3.17	**7m**	17.3 ± 2.6	3.20
7f	21.1 ± 4.9	3.05	**8a**	7.15 ± 4.56	3.29
7g	17.8 ± 7.0	2.72	**8b**	20.5 ± 9.5	3.52
7h	22.0 ± 9.1	1.90	**8c**	NA[c]	3.99
RVT	81.3 ± 5.6	2.83	**CHL**	-112.29 ± 7.13[d]	3.62

[a] Percent inhibition was calculated at the 24 h time point in the ThT aggregation kinetics assay. The results shown are average ± standard deviation of triplication readings based on three independent experiments.
[b] CLogP values were calculated with ChemDraw.
[c] NA, not active indicating the compounds are WAM.
[d] Negative PI indicates the compounds can promote the aggregation.

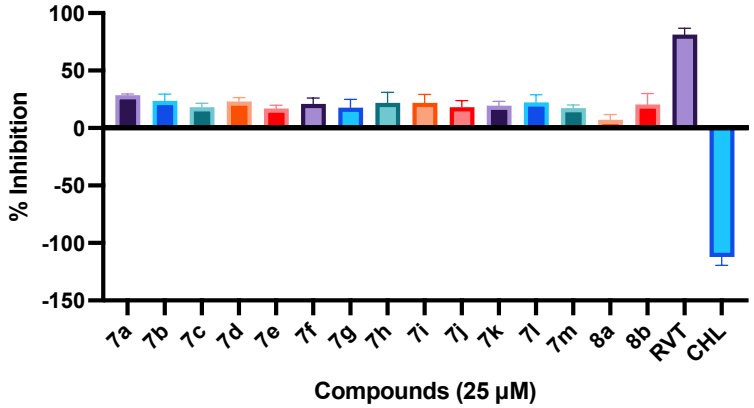


Figure 3-5. Percentage inhibition (PI) of *N*-phenylethylbenzamide and carboxamide derivatives (**7a-m** and **8a-c**), resveratrol (RVT), and chalcone (CHL) at 25 µM on Aβ42 (10 µM) aggregation.

3.3.3 Transmission electron microscopy

In the next step, transmission electron microscopy (TEM) studies were conducted in order to observe the morphology of Aβ42 aggregates in the absence and presence of various testing compounds. From this series,

representative compounds (**7a**, **7b**, and **7j**) were selected to study their effects on Aβ42 morphology. TEM experiments are often used in conjunction with ThT kinetic assays to provide further evidence to determine the anti-Aβ42 aggregation properties of novel molecules. The TEM sample grids were prepared by taking samples from the ThT aggregation kinetic assays at the end of the 24 h incubation period. The TEM images obtained in the presence of compounds **7a**, **7b**, and **7j** were compared to those Aβ42 control.

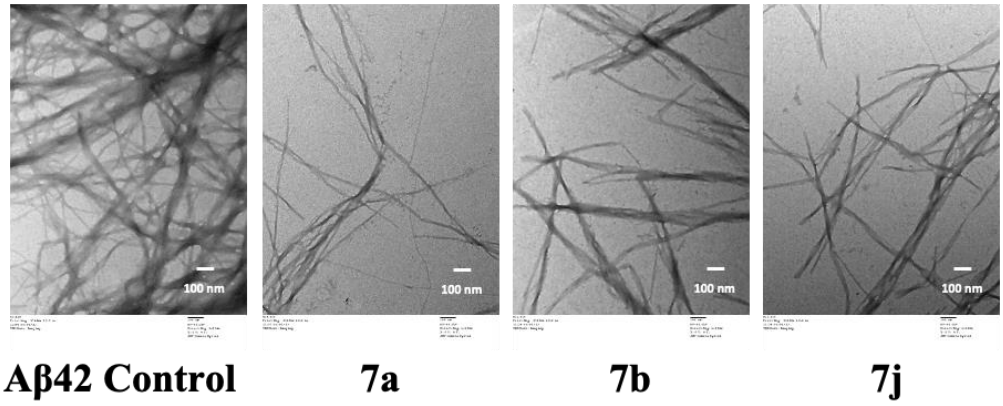


Figure 3-6. TEM images of Aβ42 (10 μM) in the absence (Aβ42 control) and presence of *N*-phenylethylbenzamide **7a**, **7b**, and **7j** (25 μM). Scale: 200 μm.

As can be seen in **Figure 3-6**, the morphology of Aβ42 showed a combination of long, twisted, and unbranched mature fibrils. In the presence of *N*-phenylethylbenzamide derivatives **7a**, **7b**, and **7j** at 25 μM, there was a significant reduction in the formation of Aβ42 fibrils. These fibrils were characterized by the existence of sparse, thinner, and lower-ordered fibrils. The reduced amyloid burden seen in the images, indicated by a reduction in the formation of dense Aβ42 fibrils compared to the control image, further validates that these compounds were able to inhibit the aggregation of Aβ42. These studies further demonstrate the anti-Aβ42 aggregation inhibition properties of *N*-phenylethylbenzamide derivatives.

3.3.4 Neuroprotective effects against Aβ42-induced cytotoxicity

The in vitro biophysical experiments based on the ThT aggregation kinetic studies and TEM investigations provide sufficient evidence to support that the *N*-phenylethylbenzamide and carboxamide derivatives can interact with Aβ42 aggregates and thus inhibit its aggregation process. In the next step of experiments, the ability of representative compounds **7a**, **7b** and **7j** to prevent Aβ42-mediated cytotoxicity in mouse hippocampal HT22 neuronal cell lines was investigated. Initially, the cytotoxicity profile of **7a**, **7b** and **7j** on HT22 cells at 25 µM were tested. The cytotoxicity was evaluated based on cell viability using the cell counting kit 8 (CCK-8) colorimetric assay. [337,338] As can be seen in **Figure 3-7**, the results showed that, at 25 µM, compounds **7a**, **7b** and **7j** were not toxic to the HT22 cells. The cell viability ranged from 103.6 to 109.9 % compared to untreated cells. Next, the HT22 cells were incubated with Aβ42 (5 µM) in the presence and absence of **7a**, **7b** and **7j** (25 µM) for 48 h to investigate their ability to rescue cells from Aβ42-mediated neurotoxicity. Treating the HT22 cells with Aβ42 led to a drastic decrease in cell viability. Incubating the cells with 5 µM Aβ42 resulted in significant cell death with ~60% cell death (**Figure 3-7**). Co-incubating the Aβ42 treated cells with either **7a**, **7b** or **7j** (25 µM) led to a significant increase in cell viability compared to Aβ42 treated cells (**Figure 3-7**). These compounds showed potent neuroprotective effects. For example, **7a** (R = benzene), **7b** (R = 4-pyridyl), and **7j** (R = thiophene) exhibited excellent cell viability profiles (96.8 ± 14.9 %, 94.8 ± 12.0 %, and 81.8 ± 8.9 % respectively), indicating that they were able to rescue HT22 cells from Aβ42-induced cytotoxicity. These observations suggest that these *N*-phenylethylbenzamide and carboxamide derivatives have the potential to convert toxic Aβ assemblies into nontoxic forms. Besides, the cell culture studies demonstrate their ability to prevent Aβ42-induced cytotoxicity which further supports their potential as novel templates to consider in the design of amyloid aggregation inhibitors.

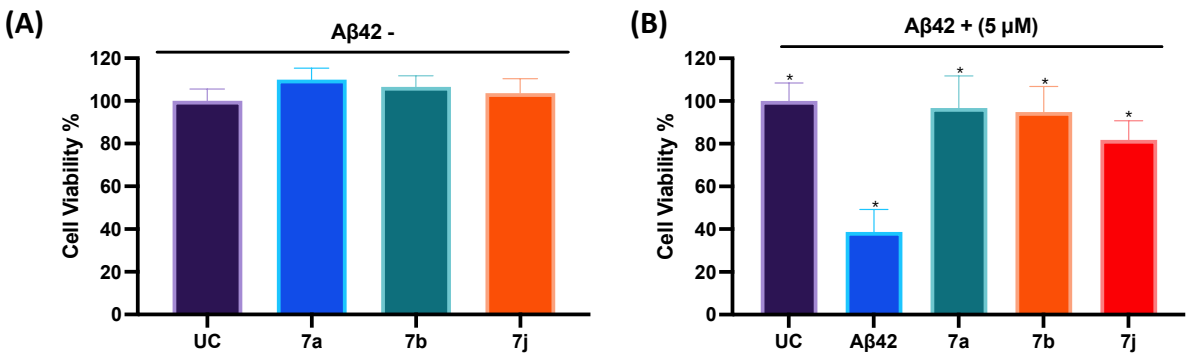


Figure 3-7. Neuroprotective effects of *N*-phenylethylbenzamide and carboxamide derivatives **7a**, **7b**, and **7j** (25 μM) on HT22 cells in the absence (A) and presence (B) of Aβ42 (5 μM) incubated over 48 h. Cell viability was determined by the CCK-8 based colorimetric assay. The results shown are averages of quadruplicate readings based on three independent experiments. *$p < 0.01$ compared to Aβ42 treated group (One-way ANOVA followed by Bonferroni post hoc test).

3.3.5 Molecular docking

In order to better understand the mechanism of these AIs, molecular docking studies were conducted to investigate the interactions between a representative compound from the *N*-phenethylbenzamide series and Aβ aggregates. For this purpose, the best *N*-benzylbenzamide derivative **7a** (~29% inhibition of Aβ42 aggregation in the ThT assay, nontoxic to HT22 cells - cell viability ~100% and ~96% cell viability in Aβ42 treated cells) from this series was used in the docking studies. Compound **7a** was docked with both the Aβ42 oligomer and fibril model using the CDOCKER algorithm.[339] The oligomer and fibril models were prepared by using the 3D coordinates of the Aβ42 fibril structure (PDB id: 5KK3). This is an atomic resolution structure of monomorphic Aβ42 obtained through solid-state NMR.[340] The Aβ42 oligomer model was prepared from the Aβ42 fibril assembly.[341] Previous studies have shown that, in solution, Aβ42 is known to exist as either pentamer or hexamer aggregates, indicating these are the smallest forms of aggregates that can be detected in solution.[342] Therefore, a pentamer model was used as a representative example of the oligomer model in docking studies. In the sequence of Aβ42, two regions are responsible for its aggregation propensity and the hydrophobic nature of these regions is one of the initiating factors driving the aggregation process, namely, hydrophobic core ^{16}KLVFFA^{21}, and C-terminal hydrophobic tail

^{32}IGLMVGGVVIA^{42}.^{343} Therefore, our docking method was designed to build a binding sphere (20 Å radius) that can accommodate the entire span of these two regions to facilitate the understanding of potential interactions in these important regions. The molecular docking was performed using the computational software Discovery Studio, Structure-Based-Design, v20.1.0.19295 (Biovia, USA).

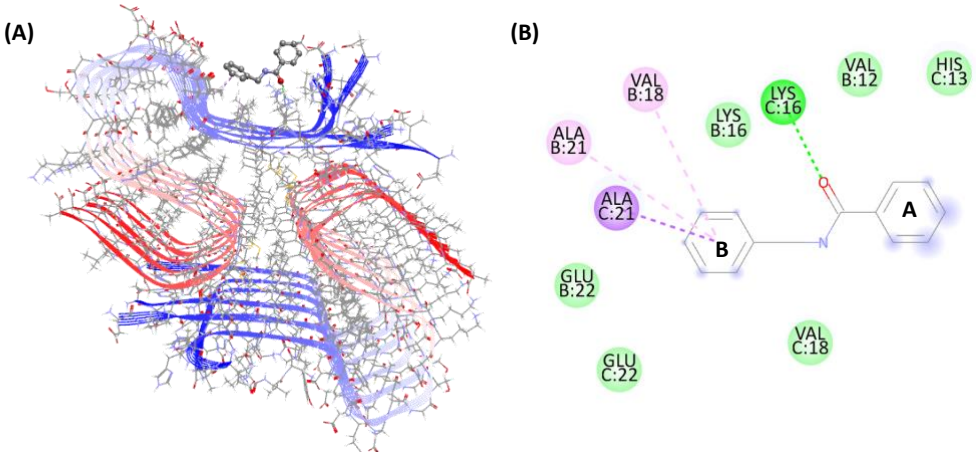


Figure 3-8. Molecular docking studies of **7a** with Aβ42 pentamer model (PDB ID: 5KK3). (A) Top docked pose of **7a**; (B) 2D interaction map of the top docking pose of **7a**. The hydrogen atoms are removed to enhance clarity. Protein is represented in line ribbon with blue indicating the N-terminus and red indicating the C-terminus. The small molecule is represented in the ball-and-stick model. Hydrophobic interaction is represented in pink dashed line and hydrogen bond interaction is represented in green dashed line.

The top binding mode of **7a** docked in the Aβ42 pentamer is shown in **Figure 3-8**. The Aβ42 pentamer was shown as line ribbon representation color-coded from N- (blue) to C- (red) terminal and the small molecule was shown in ball and stick representation with carbon in grey, oxygen in red, and nitrogen in blue. Based on our docking method, 10 poses of **7a** were generated, and they were ranked according to CDOCKER energy and CDOCKER interaction energy with the lowest energy (most stable) pose shown in **Figure 3-8**. In the top binding pose (CDOCKER energy = -21.78 kcal/mol and CDOCKER interaction energy = -26.50 kcal/mol), **7a** was oriented perpendicular to the long axis of the Aβ42 pentamer assembly. Three hydrophobic interactions were observed interacting with both hydrophobic regions of Aβ42 pentamer. One of the hydrophobic contacts was between the benzene ring (ring A) and alkyl group of C: Leu17 and C: Leu34 (distance ~ 5.5 Å and 5.0 Å respectively). The other benzene ring (ring B) underwent hydrophobic interaction with the alkyl group of A: Leu17 (distance ~ 4.9 Å). These hydrophobic interactions anchored the compounds in the binding pocket which explains its ability to inhibit the aggregation process since it can interact with both hydrophobic regions of Aβ42. Interestingly, **7a** also showed a similar binding pose

as compound **3a** (Section 2.5.6) and were both able to interact with three out of five strands in the oligomer model. Due to the presence of an additional carbon in the linker region, **7a** was able to form one more hydrophobic interaction. Docking **7a** in the Aβ42 fibril model shows that in the top binding pose (CDOCKER energy = -19.06 kcal/mol and CDOCKER interaction energy = -22.15 kcal/mol), the key interactions were still hydrophobic with interactions seen between the aromatic ring and Ala21 and Val18 as shown in **Figure 3-9**. The benzene ring (ring B) underwent hydrophobic interactions with the alkyl group of C: Ala21 (distance = 4.2 Å), C: Val18 (distance = 4.1 Å), and D: Ala21 (distance = 5.3 Å). Another major interaction was the hydrogen bond formed between the carbonyl oxygen of the amide group and the NH_3^+ of C: Lys16 (distance = 1.7 Å) which further constrained the **7a** in the hydrophobic core region of Aβ42. These docking studies of **7a** in both the pentamer and fibril models suggest that the extra carbon spacer in the linker region improved the overall stability of the ligand-receptor complex and thus can exhibit better binding to Aβ42. In summary, the molecular docking studies of **7a** in Aβ42 pentamer and fibril models suggest that the hydrophobic interactions between the aromatic rings and the hydrophobic aggregation-prone regions play a significant role in determining its anti-aggregation activity.

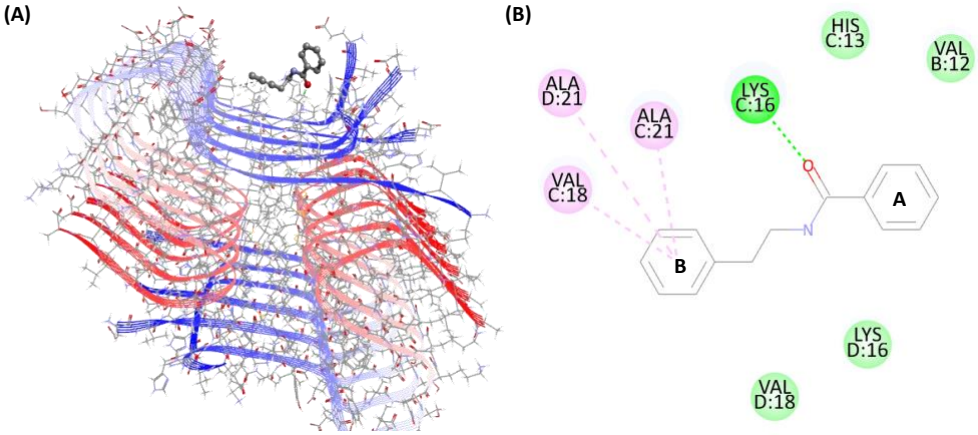


Figure 3-9. Molecular docking studies of **7a** with Aβ42 fibril model (PDB ID: 5KK3). (A) Top docked pose of **7a**; (B) 2D interaction map of the top docking pose of **7a**. The hydrogen atoms are removed to enhance clarity. Protein is represented in line ribbon with blue indicating the N-terminus and red indicating the C-terminus. The small molecule is represented in the ball-and-stick model. Hydrophobic interaction is represented in pink dashed line and hydrogen bond interaction is represented in green dashed line.

3.4 Summary

In this chapter, one more carbon spacer was added in the linker region to obtain *N*-phenethylbenzamide and carboxamide derivatives **7a-m** and **8a-c**. A total of 16 compounds were synthesized by coupling the 2-phenylethan-1-amine (**6**) with either corresponding acid chlorides or carboxylic acids to obtain the compound library in good yields (72-87.5%). The chemical structures were confirmed by ^{1}H NMR, MS and the purity was checked by LCMS. These compounds exhibited weak-to-moderate modulative activity on the aggregation of Aβ42 as confirmed by the ThT-based aggregation kinetic assay and TEM. Among them, **7a**, **7b**, and **7j** were identified as better inhibitors of Aβ42 aggregation (PI ranging from 18.2-28.6%). These lead compounds from this series were not toxic to HT22 cells and were able to rescue HT22 cells from Aβ42-induced neurotoxicity (cell viability ranging from 81-97% at 25 μM). Derivative **7a** was identified as the best compound (**Figure 3-10**). In the molecular docking studies, **7a** shows that the aromatic rings can undergo several important hydrophobic interactions with Aβ42 pentamer and fibril models at the aggregation-prone KLVFFA and C-terminal regions. The extra carbon spacer was able to form a more stable complex in the Aβ42 oligomer assembly compared to the *N*-benzylbenzamide derivative **3a**.

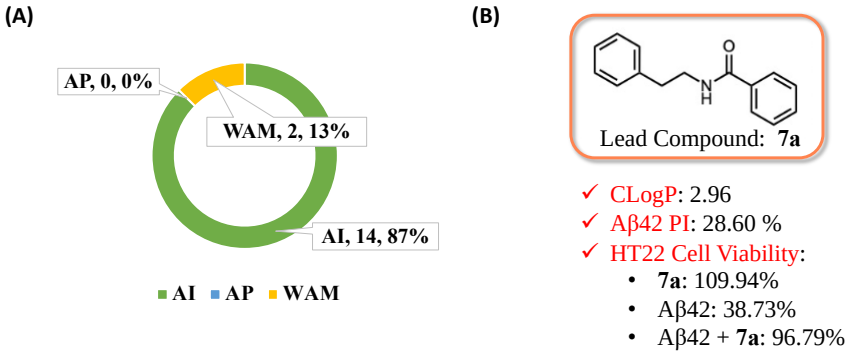


Figure 3-10. Summary of *N*-phenethylbenzamide and carboxamide derivatives. (A) 87% (14 out of 16) compounds were identified as aggregation inhibitor (AI), and 13% (2 out of 16) compounds were identified as weak aggregation modulators (WAM); (B) Key experimental data for lead compound **7a**.

3.5 Experimental

3.5.1 General

All chemicals and reagents were purchased from various vendors (Sigma Aldrich Missouri USA, Alfa Aesar Massachusetts USA, Bio Basic Ontario Canada, AA Blocks California USA, Cayman Chemical Michigan USA, Thermo Fisher Massachusetts USA, and Corning New York USA), were >95% pure and used without further purification. The Aβ42 1,1,3,3,3-hexafluoroisopropanol (HFIP) >95% pure, was purchased from Anaspec California USA (Cat. No. AS-64129) or rPeptide Georgia USA (Cat. No. A-1163-1). The reactions were monitored by thin-layer chromatography (TLC) using the Merck silica gel 60, F254. Column chromatography was carried out using Merck silica gel 230-400 mesh. The spots were visualized with short or long wavelengths (254 nm or 365 nm). The melting points of compounds were determined using a digital melting point apparatus (REACH Devices, USA). The proton NMR (^{1}H NMR) spectra of compounds were obtained using a 300 MHz Bruker Avance spectrometer (Department of Chemistry, University of Waterloo). Either $CDCl_3$ or DMSO-d_6 were used as the solvents. Coupling constants (*J* values) were recorded in Hertz (Hz). Abbreviations used to represent ^{1}H NMR signals were s – singlet, d – doublet, t – triplet, m – multiplet, br s – broad singlet. The mass and purity were confirmed on an Agilent 1260 Infinity liquid chromatography (LC) module equipped with a 6130 Quadrupole mass spectrometer (Agilent 6100 series LCMS). The column used on LCMS was a ZORBAX Eclipse AAA, 4.6 × 75 mm, 3.5 micron (Agilent Technologies, Canada) column. A mixture of water and acetonitrile 1:1 v/v with 0.1% formic acid (1.0 mL/min flow rate), was used as the solvent system to assess compound purity and mass. All final compounds were ≥ 95% pure as determined by LCMS analysis.

3.5.2 Chemistry

For the synthesis of **7a**-**m** the acid chlorides were coupled with 2-phenylethan-1-amine (**6**) (1 mmol) by taking them into a 50 mL round bottom flask (RBF) containing 15 mL of anhydrous tetrahydrofuran (THF).

To this mixture, 1.2 equivalents of TEA and 1.0 equivalent of corresponding acid chlorides with various R groups (**2a-m**) were added. The reaction mixture was kept at either room temperature or reflux for 2-24h and was monitored by thin layer chromatography (TLC). After the reaction was complete, the solvent THF was evaporated in vacuo and the resulting reaction mixture was dissolved in 15 mL ethyl acetate (EtOAc), and then washed with 15 mL brine solution (×3). The organic layer was collected and dried over anhydrous $MgSO_4$ and filtered. The organic solvent was removed in vacuo and the residue/oil obtained was further purified by silica gel column chromatography using a combination of solvent systems (1:1 *n*-Hexanes:EtOAc or 5:2 n-Hexanes:EtOAc or 9:1 dichloromethane (DCM): Methanol (MeOH) or 4:1 DCM:*n*-Hexanes) to afford the final compounds **7a-m**.

Compounds **8a-c** were synthesized by reacting 2-phenylethan-1-amine (**6**) (1 mmol) kept in an RBF with 15 mL THF, followed by the addition of 1.0 equivalent carboxylic acid (**4a-c**), 1.2 equivalents EDC, 1.5 equivalents HOBt, and 2.2 equivalents TEA added in sequence. The reaction was kept at room temperature overnight or under reflux conditions for 4–12 h. The solvent was evaporated in vacuo and the resulting reaction mixture was dissolved in 15 mL EtOAc and washed with 15 mL brine solution (×3). The organic layer was collected, dried over anhydrous $MgSO_4$ and filtered. The organic solvent was then removed in vacuo to obtain the residue/oil which was further purified by silica gel column chromatography using either 1:1 *n*-Hexanes:EtOAc or 5:2 *n*-Hexanes:EtOAc as mobile phase to afford compounds **8a-c**.

3.5.3 Aβ42 aggregation kinetic assay

The ability of benzamide and carboxamide derivatives **7a-m** and **8a-c** to inhibit the Aβ42 aggregation was evaluated using the thioflavin T (ThT) based fluorescence kinetic assay. The 15 μM ThT solution was prepared in 50 mM glycine buffer using ultra-pure water (UPW). The pH of the solution was adjusted to 7.4 with 50 mM sodium hydroxide solution. The aggregation assay was carried out using 215 mM sodium phosphate dibasic heptahydrate buffer prepared in UPW and the pH was adjusted to 7.4 by using 50 mM

hydrochloric acid solution. The Aβ42•HFIP > 95% pure was treated with 1% ammonium hydroxide solution to afford 1 mg/mL stock solution. The stock solution was then vortexed and sonicated for 5 min before diluted to a 25 μM working solution using the assay buffer. The stock solutions of the test compounds (**7a-m**, **8a-c** and resveratrol (RVT) were prepared in assay buffer with DMSO as the solubilizing agent (final concentration per well was less than 2%). The 24 h aggregation kinetics assay was carried out using 384-well plates (Costar, black, clear-bottom), by adding 44 μL of ThT, 12 μL of assay buffer, 16 μL of Aβ42 solution (10 μM final well concentration), and 8 μL of test compound dilution (25 μM) into each well. The Aβ42 control wells contained ThT, Aβ42 solution and the assay buffer without any test compound. The plates were covered with a transparent plate cover and were incubated at 37 °C for 24 h with shaking at 300 cpm between readings for 30 s. The readings were taken every 10 min (bottom reading), with excitation wavelength of 440 nm and emission wavelength of 490 nm using the BioTek Synergy H1 microplate reader. Each sample was measured in triplicate readings and the results were obtained based on three independent experiments.

3.5.4 Transmission electron microscopy

The TEM assay was carried out by first running the Aβ42 aggregation assay (as described in 3.5.3) by incubating test compounds at 25 μM with 10 μM Aβ42 for 24 h at 37 °C. The TEM grids were prepared by aliquoting 20 μL of each sample from the 384-well plate after the 24-hour incubation period. These samples were loaded onto 400-mesh formvar-coated copper grids (Electron Microscopy Sciences, Pennsylvania, USA). The grids were air-dried overnight before being washed with 40 μL UPW three times. After washing, 20 μL 2% phosphotungstic acid (PTA) solution was added to the grid and stayed for 1 min to stain the samples. Then the PTA solution was absorbed away with filter paper and then the grids were washed with 40 μL UPW three times. Then the grids were further air-dried overnight. The imaging studies were carried out using a Philips CM 10 TEM (Dept. of Biology, University of Waterloo) at 60 kV and the micrographs

were obtained through a 14-megapixel AMT camera at 64,000X magnification. The samples used to prepare the grids were obtained by mixing the triplicate wells from ThT assay and image were taken at a randomized view for each grid.

3.5.5 Cell viability assay

The cell viability assay was carried out in the Aβ42-induced HT22 cell toxicity model. The cytotoxicity and neuroprotective effects of benzamide/carboxamide derivatives **7a-m** and **8a-c** toward HT22 cells were carried out by using the UV-based cell metabolism assay kit (cell counting kit 8, CCK-8, TargetMol, Massachusetts, USA). The HT22 cells were cultured in DMEM/F12 1:1 with the addition of glutamate supplemented with 10% FBS and 1% penicillin and streptomycin at 37 °C in 5% CO_2. The cells were seeded at a density of 50,000 cells per mL. After 24 h, the cells were treated with various compounds at 25 μM prepared in phosphate buffer pH 7.4 and DMSO (less than 2%) and incubated for 48 h. After that, the CCK-8 reagent was added to each well, and incubated for another 2 h, before measuring the absorbance at 450 nm as per the manufacturer's protocol. The neuroprotective effects of test compounds toward Aβ42-induced cytotoxicity were determined by treating the HT22 cells with 5 μM of Aβ42•HFIP (>95%, rPeptide, Georgia, USA), and then incubating for 48 h. The cell viability assay was determined by adding the CCK-8 reagent and incubating for another 2 h to measure the absorbance at 450 nm. The cell viability was calculated as the average percent cell viability based on quadruplicate readings from three independent experiments. For statistical analysis, the results were subjected to one-way ANOVA followed by Bonferroni post hoc analysis compared to Aβ control group. ns = not significant, *$p < 0.01$ compared to Aβ42 control group, **$p < 0.01$ compared to Aβ42 control group, ***$p < 0.01$ compared to Aβ42 control group, ****$p < 0.01$ compared to Aβ42 control group.

3.5.6 Molecular docking study

The binding interactions of **7a** with Aβ42 were investigated by carrying out molecular docking studies on the Discovery Studio software program v20.1.0.19295, Structure-Based-Design (BIOVIA Inc. San Diego, USA). The Aβ42 pentamer and oligomer models were prepared by extracting the coordinates from the solved 3D structure of the Aβ42 fibril (PDB id: 5KK3). A binding sphere of 20 Å radius was selected and defined as the ligand binding site which covers the ^{16}KLVFFA^{21} and the C-terminal ^{32}IGLMVGGVVIA^{42} hydrophobic regions of the Aβ42. Compound **7a** was built in 3D using the Small Molecule module in the software and was subjected to energy minimization protocol (1000 and 2000 steps of steepest descent followed by conjugate gradient method) using CHARMm force field. The CDOCKER algorithm was used to carry out the docking studies. The Receptor-ligand Interactions module in the software was used to perform CDOCKER simulations. The docking simulation included 2000 heating steps, a heating target temperature of 700 K and 5000 cooling steps and a cooling target temperature of 300 K. The top ligand binding modes of selected lead compounds were analyzed by evaluating the CDOCKER energy and CDOCKER interaction energy (in kcal/mol). Further analysis was carried out by determining the polar and nonpolar contacts of **7a** in the Aβ42 pentamer and fibril assembly.

Chapter 4

Design, Synthesis and Evaluation of *N*-Benzyloxybenzamide and *N*-Benzyloxycarboxamide Derivatives as Aβ Aggregation Modulators

Below is a list of publications, manuscripts submitted and in preparation along with author names based on this chapter:

Zhao, Y. Rao, P. P. N. *N*-Benzyl, *N*-phenethyl and *N*-benzyloxybenzamide derivatives inhibit amyloid-beta (Aβ42) aggregation and mitigate Aβ42-induced neurotoxicity. *Med. Chem. Res.* (Manuscript under revision)

4.1 Introduction

This chapter features the third series of compounds, which contain an amide bond, an sp^3 hybridized carbon and an oxygen linker to obtain *N*-benzyloxybenzamide and *N*-benzyloxycarboxamide derivatives (**Figure 4-1**).[318,319] The benzyloxy group was kept constant and the amide end was varied by incorporating a number of aromatic rings and aliphatic substituents (**Figure 4-1**). For example, the aromatic benzene ring in **10a** was replaced with a pyridine bioisostere (**10b, 10c,** R = pyridine), various 5-membered aromatic rings were also incorporated in compounds **10h** (R = pyrrole), **10i** (R = furan) and **10j** (R = thiophene). The SAR was also studied by adding bicyclic aromatic rings such as **10l** (R = naphthalene), **10m** (R = quinoline), **11a** (R = indole), **11b** (R = benzofuran), and **11c** (R = benzo[*b*]thiophene). In addition, some of the aliphatic rings were also included, such as **10f** (R = cyclohexane), **10g** (R = piperidine), and **10k** (R = pyrrolidine). Besides, known Aβ binding pharmacophores **10d** (R = 3,4-dimethoxybenzene) and **10e** (R = 3,4-difluorobenzene) were also incorporated to investigate their effect on Aβ aggregation.[320] In this chapter, the synthesis, characterization, and biological evaluation of *N*-benzyloxybenzamide and *N*-benzyloxycarboxamide derivatives (**10a-m** and **11a-c**) toward Aβ aggregation will be discussed.

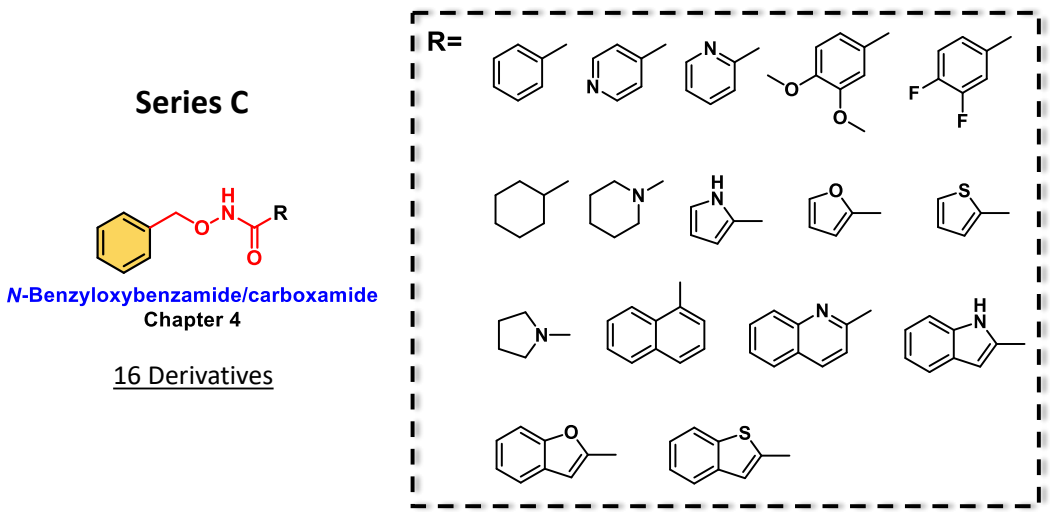


Figure 4-1. *N*-Benzyloxybenzamide and *N*-benzyloxycarboxamide derivatives (Series C). This series of compounds features an amide bond, a sp^3 hybridized carbon and an oxygen linker.

4.2 Hypothesis

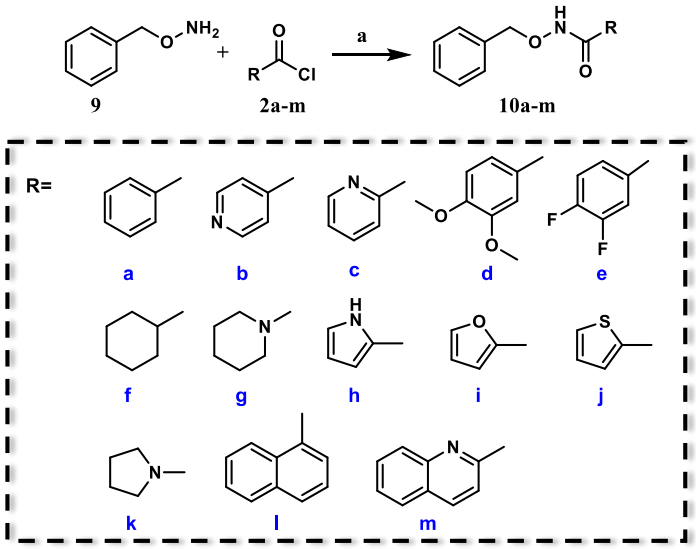
It is hypothesized that the *N*-benzyloxybenzamide and *N*-benzyloxycarboxamide derivatives **10a-m** and **11a-c** possessing the amide bioisostere along with a carbon and oxygen linker would exhibit Aβ42 aggregation inhibition properties and provide neuroprotective effects against Aβ42-induced cytotoxicity. Compared to the *N*-phenylethylbenzamide and carboxamide derivatives in Chapter 3, it is hypothesized that the presence of an oxygen linker in this series of compounds will enhance their anti-Aβ42 aggregation activity due to additional hydrogen bonding interactions with the KLVFFA region of Aβ42 aggregates (eg: Lys16 and Leu17). It is also hypothesized that variation of the electronic and steric features by incorporating various aromatic 5- and 6-membered rings and aliphatic substituents (**Figure 4-1**) will promote their interactions with the amyloidogenic regions of Aβ42 (KLVFFA and the C-terminal region) to enhance their inhibition properties toward Aβ42 aggregation. Furthermore, the addition of known Aβ binding pharmacophores (e.g., 3,4-dimethoxyphenyl and 3,4-difluorophenyl) would exhibit better inhibitory activity toward the Aβ42 aggregation.

4.3 Results and Discussion

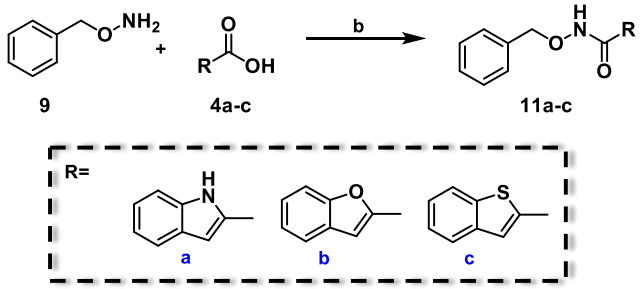
In this section, the synthesis, purification and characterization of compounds **10a**-**m** and **11a**-**c** are discussed which is followed by biological activity screening, including anti-Aβ42 aggregation assay based on the dye ThT fluorescence spectroscopy, fibril morphology study by TEM, cell viability assay against Aβ42-induced cytotoxicity in HT22 mouse hippocampal neuronal cells and computational modeling studies in the Aβ42 oligomer and fibril models.

4.3.1 Synthesis

The retro-synthetic analysis of the compound library suggests that the starting building blocks can be coupled to form the amide bond using suitable substrates to obtain the *N*-benzyloxybenzamide and *N*-benzyloxycarboxamide derivatives. This was achieved through either the direct coupling of acid halides (**2a**-**m**) with primary amines (*O*-benzylhydroxylamine **9**, Method A) or by coupling the carboxylic acids with primary amines (*O*-benzylhydroxylamine **9**, Method B). The preference for using the acid halides versus carboxylic acids coupling method was made based on the commercial availability and cost-effectiveness of the starting materials. With that being said, compounds **10a-m** were synthesized *via* Method A as shown in **Scheme 4-1**, whereas compounds **11a-c** were synthesized by method B as shown in **Scheme 4-2**.



Scheme 4-1. Synthetic scheme for preparing **10a-m** by coupling *O*-benzylhydroxylamine (**9**) with the corresponding acid chlorides (**2a-m**). Reagents and conditions: (a) TEA, THF, room temperature/reflux 2-24 h.



Scheme 4-2. Synthetic scheme to prepare **11a-c** by coupling *O*-benzylhydroxylamine (**9**) with the corresponding carboxylic acid (**4a-c**). Reagents and conditions: (b) EDC•HCl, HOBt, TEA, THF, room temperature overnight or under reflux conditions for 4-12 h.

In Method A, *O*-benzylhydroxylamine (**9**) was coupled with corresponding acid halides. Considering the leaving capability and reactivity, acid chlorides (**2a-m**) were used in the reactions. The reaction mechanism (**Figure 4-2**) is described as follows: first, the nucleophilic amine **9** attacks the electrophilic carbonyl carbon of the acid chloride to form a tetrahedron intermediate by nucleophilic addition; next, chloride serves as a good leaving group and then is eliminated from the tetrahedron intermediate; then hydrochloric acid is also formed as the reaction by-product which can neutralize the base triethylamine (TEA) to facilitate product

formation.[322] The overall yields of these reactions range from 72.1 to 93%. Interestingly, the coupling of acid halides and *O*-benzylhydroxylamine to obtain compounds **10g** (*N*-(benzyloxy)piperidine-1-carboxamide) and **10k** (*N*-(benzyloxy)pyrrolidine-1-carboxamide) led to poor yields and challenges in their purification due to their stability issues. Therefore, these two compounds were not pursued further. The analytical data for **10a-m** (^{1}H NMR, MS and purity data by LCMS) are given below. Analytical spectral data for all the final compounds are given in **Appendix C**.

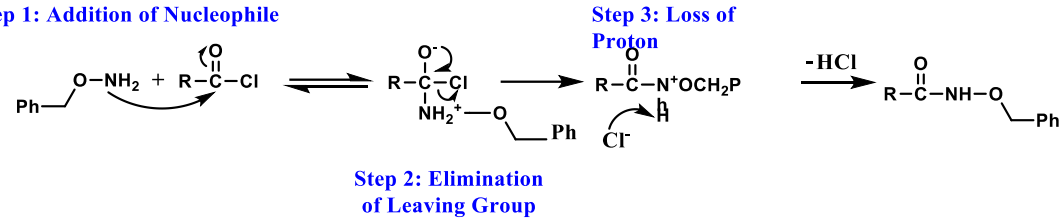


Figure 4-2. Nucleophilic acyl substitution mechanism which includes three major steps: (1) addition of nucleophile to the electrophilic carbonyl carbon, (2) elimination of the leaving group, (3) loss of proton.

4.3.1.1 *N*-(Benzyloxy)benzamide (**10a**)

The product was obtained as a white solid (Yield = 87.6%). ^{1}H NMR (300 MHz, DMSO) δ 11.76 (s, 1H), 7.75 (d, *J* = 7.6 Hz, 2H), 7.55 (t, *J* = 7.2 Hz, 1H), 7.51 – 7.32 (m, 7H), 4.93 (s, 2H). mp: 125-128 °C. ESI-MS, m/z calcd for $C_{14}H_{13}NO_2$ $[M+H]^+$ 228.1, found 228.1. Purity: 99.43% (LCMS).

4.3.1.2 *N*-(Benzyloxy)isonicotinamide (**10b**)

The product was obtained as a white solid (Yield = 86.1%). ^{1}H NMR (300 MHz, DMSO-d_6): δ 12.07 (br s, 1H), 8.72 (d, *J* = 4.9 Hz, 2H), 7.65 (d, *J* = 5.3 Hz, 2H), 7.43 (dd, *J* = 19.5, 6.8 Hz, 5H), 4.96 (s, 2H). mp: 117-120 °C. ESI-HRMS, m/z calcd for $C_{13}H_{14}N_2O_2$ $[M+H]^+$ 229.0977, found 229.0966. Purity: 99.4% (LCMS).

4.3.1.3 *N*-(Benzyloxy)picolinamide (**10c**)

The product was obtained as a yellowish oil (Yield = 77.0%). ^{1}H NMR (300 MHz, DMSO-d_6): 12.04 (s, 1H), 8.61 (d, J = 4.7 Hz, 1H), 8.00 (d, J = 4.0 Hz, 2H), 7.62–7.37 (m, 6H), 4.95 (s, 2H). mp: 104-107 °C. ESI-MS, m/z calcd for $C_{13}H_{13}N_2O_2$ $[M+H]^+$ 229.1, found 229.1. Purity: 99.7% (LCMS).

4.3.1.4 *N*-Benzyloxy-3,4-dimethoxybenzamide (**10d**)

The product was obtained as a white solid (Yield = 79.3%). ^{1}H NMR (300 MHz, $CDCl_3$) δ 8.45 (s, 1H), 7.48 – 7.28 (m, 6H), 7.13 (dd, J = 8.3, 2.0 Hz, 1H), 6.80 (d, J = 8.3 Hz, 1H), 5.01 (s, 2H), 3.89 (s, 3H), 3.88 (s, 3H). mp: 142-145 °C. ESI-MS, m/z calcd for $C_{16}H_{17}NO_4$ $[M+H]^+$ 288.1, found 288.1. Purity: 99.9% (LCMS).

4.3.1.5 *N*-Benzyloxy-3,4-difluorobenzamide (**10e**)

The product was obtained as a white solid (Yield = 77.4%). ^{1}H NMR (300 MHz, $CDCl_3$) δ δ 8.48 (s, 1H), 7.60 – 7.49 (m, 1H), 7.47 – 7.34 (m, 6H), 7.25 – 7.11 (m, 1H), 5.00 (s, 2H). mp: 124-127 °C. ESI-MS, m/z calcd for $C_{14}H_{11}F_2NO_2$ $[M+H]^+$ 264.1, found 264.1. Purity: 100.0% (LCMS).

4.3.1.6 *N*-(Benzyloxy)cyclohexanecarboxamide (**10f**)

The product was obtained as a white solid (Yield = 74.9%). ^{1}H NMR (300 MHz, $CDCl_3$) δ ^{1}H NMR (300 MHz, Chloroform-*d*) δ 7.42 – 7.30 (m, 5H), 4.88 (s, 2H), 1.98 – 1.60 (m, 6H), 1.56 – 1.36 (m, 2H), 1.30 – 1.09 (m, 3H). mp: 86-89 °C. ESI-MS, m/z calcd for $C_{14}H_{19}NO_2$ $[M+H]^+$ 234.1, found 234.1. Purity: 96.9% (LCMS).

4.3.1.7 *N*-Benzyloxy-1*H*-pyrrole-2-carboxamide (**10h**)

The product was obtained as a white solid (Yield = 81.6%). ^{1}H NMR (300 MHz, $CDCl_3$): δ 9.51(br s, 1H), 7.39–7.24 (m, 5H), 6.91 (td, *J* = 2.7, 1.3 Hz, 1H), 6.52 (dd, *J* = 3.8, 2.5 Hz, 1H), 6.21(dt, *J* = 3.7, 2.6 Hz, 1H), 6.13 (br s, 1H), 4.60 (d, *J* = 5.9 Hz, 2H). mp: 77-80 °C. ESI-MS, m/z calcd for $C_{12}H_{13}N_2O_2$ $[M+H]^+$ 217.1, found 217.1. Purity: 96.5% (LCMS).

4.3.1.8 *N*-(Benzyloxy)furan-2-carboxamide (**10i**)

The product was obtained as a white solid (Yield = 77.9%). ^{1}H NMR (300 MHz, DMSO-d_6): δ 11.74 (s, 1H), 7.86 (s, 1H), 7.46–7.36 (m, 5H), 7.10 (d, *J* = 4.3 Hz, 1H), 6.63 (s, 1H), 4.90 (s, 2H). mp: 82-85 °C. ESI-MS, m/z calcd for $C_{12}H_{12}NO_3$ $[M+H]^+$ 218.1, found 218.1. Purity: 99.9% (LCMS).

4.3.1.9 *N*-(Benzyloxy)thiophene-2-carboxamide (**10j**)

The product was obtained as a white solid (Yield = 92.9%). ^{1}H NMR (300 MHz, DMSO-d_6): δ 11.79 (s, 1H), 7.83–7.81 (m, 1H), 7.65–7.62 (m, 1H), 7.46–7.34 (m, 5H), 7.15 (d, *J* = 4.3 Hz, 1H), 4.92 (s, 2H). mp: 103-106 °C. ESI-MS, m/z calcd for $C_{12}H_{12}NO_2S$ $[M+H]^+$ 234.1, found 234.1. Purity: 98.7% (LCMS).

4.3.1.10 *N*-Benzyloxy-1-naphthamide (**10l**)

The product was obtained as a white solid (Yield = 72.1%). ^{1}H NMR (300 MHz, $CDCl_3$): δ 8.30–8.21 (m, 2H), 7.90 (d, *J* = 8.2 Hz, 1H), 7.87–7.79 (m, 1H), 7.58–7.32 (m, 8H), 5.13 (s, 2H). mp: 132-135 °C. ESI-MS, m/z calcd for $C_{18}H_{16}NO_2$ $[M+H]^+$ 278.1, found 278.1. Purity: 98.9% (LCMS).

4.3.1.11 *N*-(Benzyloxy)quinoline-2-carboxamide (**10m**)

The product was obtained as a light yellow solid (Yield = 80.1%). ^{1}H NMR (300 MHz, $CDCl_3$): δ 10.35 (s, 1H), 8.26 (dd, *J* = 8.5 1.5 Hz, 2H), 8.02 (d, *J* = 8.5 Hz, 1H), 7.9 (dd, *J* = 8.2, 1.4 Hz, 1H), 7.74 (dd, *J* = 8.5, 6.9 Hz, 1H), 7.61 (dd, *J* = 8.1, 6.8 Hz, 1H), 7.52–7.49 (m, 2H), 7.41–7.38 (m, 2H), 5.11 (s, 2H). mp: 162-165 °C. ESI-MS, m/z calcd for $C_{17}H_{18}N_2O_2$ $[M+H]^+$ 279.1, found 279.1. Purity: 99.7% (LCMS).

Method B was used to synthesize *N*-benzyloxycarboxamide derivatives (**11a-c**, **Scheme 4-2**). Compared to acid chlorides, carboxylic acids are less reactive due to the electron-donating nature of the hydroxyl group. This can influence the reaction progress, yield and purity of the products. However, this limitation can be overcome by activating the carboxylic acid (**4a-c**) with the assistance of carbodiimide-dehydrating reagents, such as 1-ethyl-3-(3-dimethylaminopropyl)carbodiimide (EDC). [323,324] The detailed reaction mechanism is shown in **Figure 4-3**. The carboxylic acids can be transformed into an ester intermediate. In the presence of an activator, such as hydroxyltriazole (HOBt), the nucleophilic activator attacks the carbonyl carbon of the ester intermediate so that an active ester is formed. [325] The active ester contains a better leaving group compared to the original carboxylic acid so that it can react with *O*-benzylhydroxylamine (**9**) *via* nucleophilic acyl substitution as mentioned in the previous paragraph. The by-product urea formed as a result of using EDC as dehydrating reagent is water-soluble and therefore, can be washed away by aqueous extraction in the post-reaction workup. The overall yields of these reactions range from 82.7 to 88.9%. Their analytical data (^{1}H NMR, MS and purity data by LCMS) are given below. Analytical spectral data for all the final compounds are given in **Appendix C**.

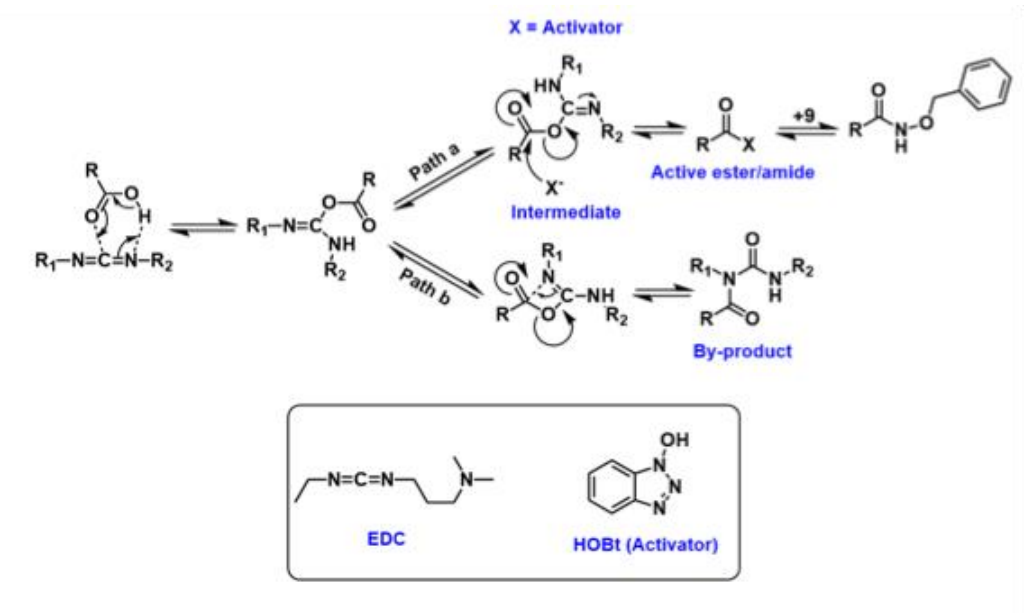


Figure 4-3. Reaction mechanism for the synthesis of compounds **11a-c** using the dehydrating agent EDC and activator HOBt for coupling *O*-benzylhydroxylamine (**9**) and the corresponding carboxylic acids (**4a-c**).

4.3.1.12 *N*-Benzyloxy-1*H*-indole-2-carboxamide (**11a**)

The product was obtained as a white solid (Yield = 82.7%). ^{1}H NMR (300 MHz, DMSO-d_6): δ 11.81 (s, 1H), 11.66 (s, 1H), 7.60 (d, *J* = 7.9 Hz, 1H), 7.42 (dq, *J* = 14.0, 7.0, 6.4 Hz, 6H), 7.20(t, *J* = 7.5 Hz, 1H), 7.09 – 6.96 (m, 2H), 4.96 (s, 2H). mp: 152-155 °C. ESI-MS, m/z calcd for $C_{16}H_{15}N_2O_2$ $[M+H]^+$ 267.1, found 267.1.Purity: 95.6% (LCMS).

4.3.1.13 *N*-(Benzyloxy)benzofuran-2-carboxamide (**11b**)

The product was obtained as a white solid (Yield = 88.9%). ^{1}H NMR (300 MHz, DMSO-d_6) δ 9.32 (t, *J* = 6.5 Hz, 1H), 8.66 (d, *J* = 4.7 Hz, 1H), 8.10 – 7.96 (m, 2H), 7.67 – 7.56 (m, 1H), 7.38 – 7.17 (m, 6H), 4.51 (d, *J* = 6.4 Hz, 2H). mp: 132-135 °C. ESI-MS, m/z calcd for $C_{16}H_{13}NO_3$ $[M+H]^+$ 268.1, found 268.1. Purity: 98.8% (LCMS).

4.3.1.14 *N*-(Benzyloxy)benzo[*b*]thiophene-2-carboxamide (**11c**)

The product was obtained as a white solid (Yield = 85.7%). ^{1}H NMR (300 MHz, DMSO-d_6) δ 8.03 (d, *J* = 7.8 Hz, 2H), 7.95 (d, *J* = 4.3 Hz, 3H), 7.54 – 7.31 (m, 5H), 4.96 (s, 2H). mp: 142-145 °C. ESI-MS, m/z calcd for $C_{16}H_{13}NO_2S$ $[M+H]^+$ 284.1, found 284.1. Purity: 93.3% (LCMS).

4.3.2 Modulatory activity on amyloid-beta aggregation

The modulatory activity of *N*-benzyloxybenzamide and carboxamide derivatives (**10a-m** and **11a-c**) on Aβ42 aggregation was evaluated using the ThT aggregation kinetic assay.[326–329] It is the golden standard used in the area for *in vitro* rapid screening of small molecules to determine their Aβ42 aggregation modulation activity.[330–333] In this assay, ThT was used as the fluorescent dye which can selectively bind to the β-sheet structure of various forms of aggregated Aβ42. Upon binding, it gives a characteristic increase in the fluorescence reading (FLR). Therefore, increases in FLR are correlated to the amount of Aβ aggregates formed. By comparing the FLR of Aβ42 control and in the presence of various test compounds, the percentage inhibition (PI) can be calculated at the end of the assay. If the FLR is lower than that of the control, it indicates that the compounds are inhibiting the Aβ42 aggregation. Similarly, if the FLR is higher than that of the control, it indicates that the compounds are able to promote the Aβ42 aggregation. Compounds that are able to inhibit the Aβ42 aggregation are termed aggregation inhibitors (AI) and compounds that are able to promote the Aβ42 aggregation are termed aggregation promotors (AP), whereas compounds that weakly modulate the aggregation are termed weak aggregation modulators (WAM). Initially, all the test compounds were screened at 25 μM to determine their effect on Aβ42 aggregation. Compounds that show promising activity were further evaluated over a concentration range (1, 5, 10, 25 μM) to determine the aggregation kinetics. Resveratrol (RVT) which is a known inhibitor of Aβ42 was also included in the assay as the reference compound for comparison. [334]

In **Figure 4-4**, the ThT aggregation kinetic curves of *N*-benzyloxybenzamide and carboxamide derivatives **10a-m** and **11a-c** are shown. In each panel, the blue curve at the bottom is the ThT background readings which suggests that ThT has no interference on the FLR in monitoring the aggregation of Aβ42. The red curve shows the Aβ42 aggregation in the absence of test compounds. In these curves, some characteristics of Aβ42 aggregation can be observed. It is a sigmoidal curve characterized by a very short lag phase (~ 30 min) which is followed by a rapid growth phase spanning the time course from around 0.5 h to 10 h. Then, the FLR tends to be stable with readings hovering around 8,000 RFU, indicating the aggregation process has reached the equilibrium status. Such saturation phase was maintained until the end of the assay at 24 h. Compared to the Aβ42 control, other curves, in the presence of different *N*-benzyloxybenzamide and carboxamide derivatives (**Figure 4-4**, A: **10a-d,** RVT, B: **10e-f, 10h-i**, C: **10j, 10l-m**, D: **11a-c**), shared similar shapes without any major differences. This observation suggests these derivatives are not able to alter the aggregation kinetics by either shortening or extending the lag/growth phase. However, lower FLR at the saturation phase than Aβ42 control for these curves was observed at the 24 h time point which indicates that some derivatives were capable of reducing the formation of Aβ42 fibrils. When co-incubating the reference compound RVT with Aβ42 (**Figure 4-4** A), a dramatic decrease in the FLR was noticed in the saturation phase with FLR below 2,000 RFUs after 18 h. Such observation is not a surprise as RVT is a very potent Aβ AI.[334]

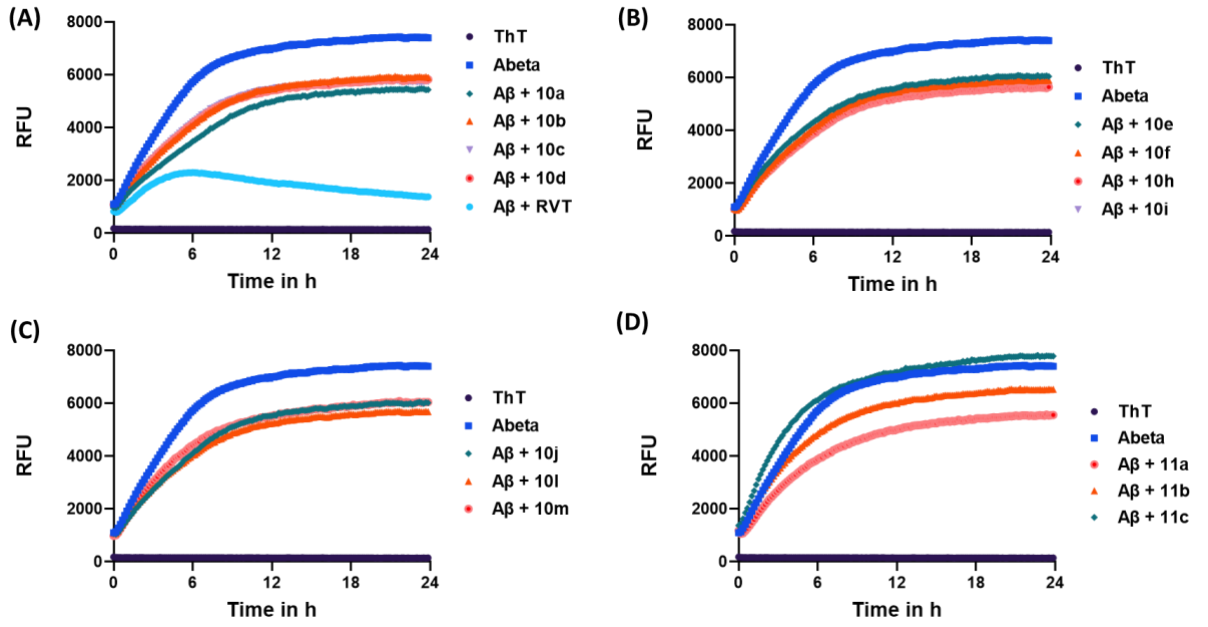


Figure 4-4. The Aβ42 aggregation kinetic curves for *N*-benzyloxybenzamide and carboxamide derivatives (**10a-f**, **10h-j**, **10l-m** and **11a-c**) in the ThT-based fluorescence assay. (A) Aggregation kinetic curves for derivatives **10a-d** and reference compound resveratrol (RVT). (B) Aggregation kinetic curves for derivatives **10e-f** and **10h-i**. (C) Aggregation kinetic curves for derivatives **10j, 10l** and **10m**. (D) Aggregation kinetic curves for derivatives **11a-c**. The derivatives (25 μM) were incubated with Aβ42 (10 μM) for 24 h at 37 ˚C, pH 7.4 and the ThT fluorescence was monitored (excitation = 440 nm, emission = 490 nm). Results were obtained based on triplicate readings from three independent experiments.

Table 4-1 shows the anti-aggregation activity of test compounds as the PI and **Figure 4-5** shows a bar plot of PI at 24 h time point. A total of 13 out of 14 compounds from this series exhibited anti-Aβ42 activity in the ThT-based fluorescence assay with activity ranging from 11.8 – 26.5 %. Compound, **10a** (R = benzene), showed the highest PI of 26.5 ± 7.3%. When replacing the benzene rings with the more polar pyridine bioisostere, the activity slightly dropped to 20.3 ± 0.7 % for **10b** and to 22.3 ± 1.5 % for **10c** (**Table 4-1**). The incorporation of the known anti-Aβ pharmacophores in **10d** and **10e** did not improve the activities as expected. The PI for **10d** (R = 3, 4-dimethoxybenzene) and **10e** (R = 3, 4-difluorobenzene) were 18.3 ± 4.8 % and 20.3 ± 1.8 %. Incorporating aromatic 5-member heterocyclic rings showed slightly lower PI than the parent compound **10a**, with PI of 23.8 ± 1.2 % for **10h** (R = pyrrole), 23.4 ± 6.3 % for **10i** (R = furan),

and 18.7 ± 6.8 % for **10j** (R = thiophene). The aliphatic ring containing derivative in this series **10f** (R = cyclohexane) exhibited 20.4 ± 1.8 % PI. A similar SAR trend was observed for both *N*-benzylbenzamide derivatives (**3a-j**, Chapter 2) and *N*-phenylethylbenzamide derivatives (**7a-j**, Chapter 3). When the R groups were replaced by bicyclic aromatic rings, mixed results were seen regarding their aggregation inhibitory activities. Compounds **10l** (R = naphthalene) and **10m** (R = quinoline) showed slightly lower PI than the parent compound **10a** with PI of 23.3 ± 1.0 % and 18.4 ± 2.6 %. However, compounds **11a** (R = indole) and **11b** (R=benzofuran) showed quite a different result than the indole/benzofuran-containing derivatives in the previous chapters (**4a-b** Chapter 2, **8a-b** Chapter 3). Unlike **4a-b** and **8a-b** which are WAMs, **11a** was able to inhibit the Aβ42 with PI of 24.9 ± 4.6 % which is similar to the parent compound **10a**, whereas **11b** showed a slightly lower PI of 11.9 ± 0.2 %. As for **11c** (R = benzo[*b*]thiophene), it was not active in modulating the aggregation of Aβ42. Overall, in this series, replacing one of the carbon linkers with oxygen, did not yield a significant increase in the activities, even though a similar PI was seen compared to the previous chapters. Four lead compounds (**10a**, **10h**, **10j**, and **11a**) were identified for further investigation. These results indicate that *N*-benzyloxybenzamide and carboxamide scaffolds also exhibit anti-aggregation properties toward Aβ42 in the ThT-based fluorescence assay.

Table 4-1. Percent inhibition (PI) of *N*-benzyloxybenzamide and carboxamide derivatives (**10a-m**, **11a-c**), resveratrol (RVT) and chalcone (CHL) at 25 μM on Aβ42 (10 μM) aggregation.

Cmpd	% Inhibition[a]	CLogP[b]	Cmpd	% Inhibition[a]	CLogP[b]
10a	26.5 ± 7.3	2.66	**10i**	23.4 ± 6.39	1.84
10b	20.3 ± 0.7	1.16	**10j**	18.7 ± 6.8	2.31
10c	22.3 ± 1.47	1.16	**10l**	23.3 ± 0.9	3.84
10d	21.3 ± 4.4	2.15	**10m**	18.3 ± 2.6	2.55
10e	18.3 ± 4.8	2.88	**11a**	24.9 ± 4.6	2.65
10f	20.3 ± 1.8	3.26	**11b**	11.8 ± 0.2	3.22
10h	23.7 ± 1.1	1.27	**11c**	NA[c]	3.69
RVT	81.3 ± 5.6	2.83	**CHL**	-112.29 ±7.13[d]	3.62

[a] Percent inhibition was calculated at the 24 h time point in the ThT aggregation kinetics assay. The results shown are average ± standard deviation of triplicate readings based on three independent experiments.
[b] CLogP values were calculated with ChemDraw.
[c] NA, not active indicating the compounds are WAM.
[d] Negative PI indicates the compounds can promote the aggregation.

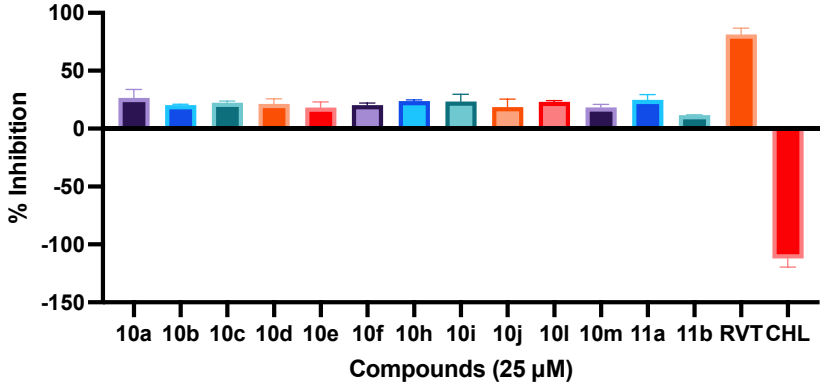


Figure 4-5. Percentage inhibition rate (PI) of *N*-benzyloxybenzamide and carboxamide derivatives (**10a-f**, **10h-j**, **10l-m**, **11a-c**), resveratrol (RVT), and chalcone (CHL) at 25 μM on Aβ42 (10 μM) aggregation.

4.3.3 Transmission electron microscopy

In the next step, transmission electron microscopy (TEM) studies were conducted in order to observe the morphology of Aβ42 aggregates in the absence and presence of representative compounds. From this series,

representative compounds (**10a**, **10h**, **10j** and **11a)** were selected to study their effects on Aβ42 morphology. TEM experiments are often used in conjunction with ThT kinetic assays to provide further evidence to determine the anti-Aβ42 aggregation properties of novel molecules. The TEM sample grids were prepared by taking samples from the ThT aggregation kinetic assays at the end of the 24 h incubation period. The TEM images obtained in the presence of compounds **10a**, **10h**, **10j** and **11a** were compared to those of Aβ42 control.

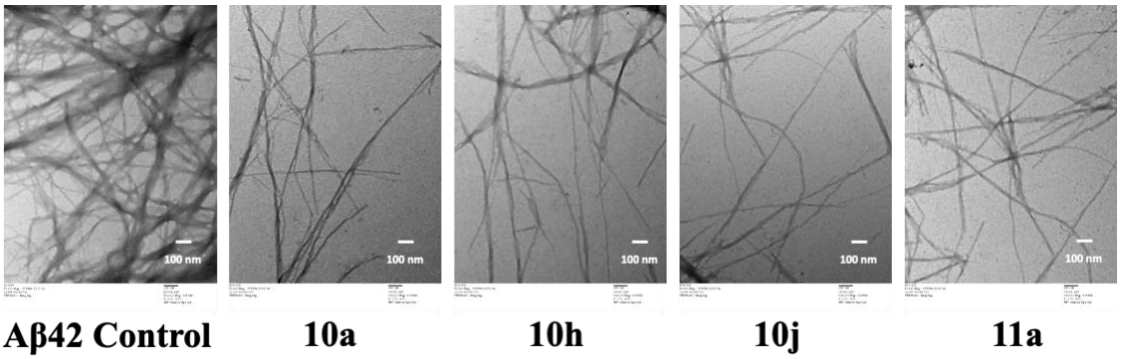


Figure 4-6. TEM images of Aβ42 (10 μM) in the absence (Aβ42 control) and presence of *N*-benzyloxybenzamide **10a**, **10h**, **10j**, and **11a** (25 μM). Scale: 200 μm.

As can be seen in **Figure 4-6**, the morphology of Aβ42 showed a combination of long, twisted, and unbranched mature fibrils. In the presence of *N*-benzyloxybenzamide derivatives **10a**, **10h**, **10j** and **11a** at 25 μM, there was a significant reduction in the formation of Aβ42 fibrils. These fibrils are characterized by the existence of sparse, thinner, and lower-ordered fibrils. The reduced amyloid burden seen in the image, indicated by a reduction in the formation of dense Aβ42 fibrils compared to the control image, further validates that these compounds were able to inhibit the aggregation of Aβ42. These studies further demonstrate the anti- Aβ42 aggregation inhibition properties of *N*-benzyloxybenzamide derivatives.

4.3.4 Neuroprotective effects against Aβ42-induced cytotoxicity

The ability of representative compounds from the *N*-benzyloxybenzamide and carboxamide series (**10a**, **10h**, **10j** and **11a**) were evaluated to study their effect in preventing Aβ42-mediated cytotoxicity in mouse hippocampal HT22 neuronal cell lines. Initially, the HT22 cells were treated with compound **10a**, **10h**, **10j** and **11a** only to determine if they were cytotoxic to HT22 cells. The cell viability was determined by using the cell counting kit 8 (CCK-8) colorimetric assay. These studies show that, at 25 μM, all the compounds (**10a**, **10h**, and **11a**) except **10j** were not toxic to cells (cell viability range 83-103.5 %, **Figure 4-7**). Compound **10j** (R = thiophene, ClogP 2.31) exhibited low cell viability (35 %) and was toxic to HT22 cells. Therefore, **10j** was excluded from the Aβ42-induced cytotoxicity assay. Next, HT22 cells were incubated with Aβ42 (5 μM) in the presence and absence of compounds **10a**, **10h**, and **11a** (25 μM) for 48 h to investigate their ability to rescue cells from Aβ42-mediated neurotoxicity. Treating the HT22 cells with Aβ42 led to a drastic decrease in cell viability compared to untreated cells. At 5 μM Aβ42, ~ 60 % cell death was observed. In the presence of test compounds, the cell viability increased significantly (**Figure 4-7**) indicating that these compounds were able to rescue the cells from neurotoxicity. For example, **10a** (R = benzene), **10h** (R = pyrrole), and **11a** (R = indole) exhibited excellent cell viability profiles (91.6 ± 8.3 %, 87.8 ± 9.7 %, and 82.9 ± 6.3 % respectively), indicating that their neuroprotective activity toward HT22 cells in the presence of Aβ42. These observations suggest that *N*-benzyloxybenzamide and carboxamide derivatives **10a**, **10h**, and **11a** have the potential to convert toxic Aβ assemblies into nontoxic forms. These cell culture studies demonstrate their ability to prevent Aβ42-induced cytotoxicity which further supports their potential as novel modulators of Aβ toxicity.

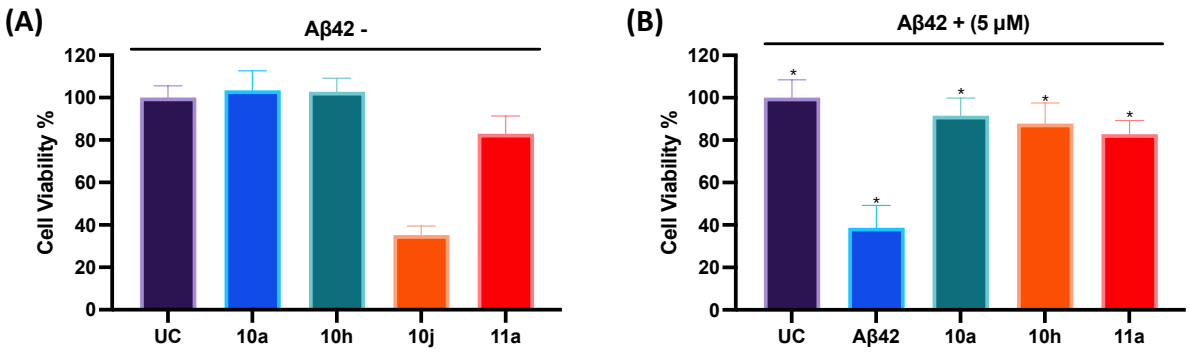


Figure 4-7. Neuroprotective effects of *N*-benzyloxybenzamide **10a**, **10h**, **10j** and **11a** (25 μM) on HT22 cells in the absence (A) and presence (B) of Aβ42 (5 μM) incubated over 48 h. Cell viability was determined by CCK-8 based colorimetric assay. The results shown are averages of quadruplicate readings based on three independent experiments. *p < 0.01 compared to Aβ42 treated group (One-way ANOVA followed by Bonferroni post hoc test).

4.3.5 Molecular docking

In order to better understand the mechanism of these AIs, molecular docking studies were conducted to investigate the interactions between a representative compound from the *N*-benzyloxybenzamide series and Aβ aggregates. For this purpose, the best *N*-benzylbenzamide derivative **10a** (~ 27 % inhibition of Aβ42 aggregation in the ThT assay, nontoxic to HT22 cells - cell viability ~ 100 % and ~ 92 % cell viability in Aβ42 treated cells) from this series was used in the docking studies. Compound **10a** was docked with both the Aβ42 oligomer and fibril model using the CDOCKER algorithm.[339] The oligomer and fibril models were prepared by using the 3D coordinates of the Aβ42 fibril structure (PDB id: 5KK3). This is an atomic resolution structure of monomorphic Aβ42 obtained through solid-state NMR.[340] The Aβ42 oligomer model was prepared from the Aβ42 fibril assembly.[341] Previous studies have shown that, in solution, Aβ42 is known to exist as either pentamer or hexamer aggregates, indicating that these are the smallest forms of aggregates that can be detected in solution.[342] Therefore, a pentamer model was used as a representative example of the oligomer model in docking studies. In the sequence of Aβ42, two regions are responsible for its aggregation propensity and the hydrophobic nature of these regions is one of the initiating factors driving the aggregation process, namely, hydrophobic core ^{16}KLVFFA^{21}, and C-terminal hydrophobic tail

^{32}IGLMVGGVVIA^{42}.^{343} Therefore, our docking method was designed to build a binding sphere (20 Å radius) that can accommodate the entire span of these two regions to facilitate the understanding of potential interactions in these important regions. The molecular docking was performed using the computational software Discovery Studio, Structure-Based-Design, v20.1.0.19295 (Biovia, USA).

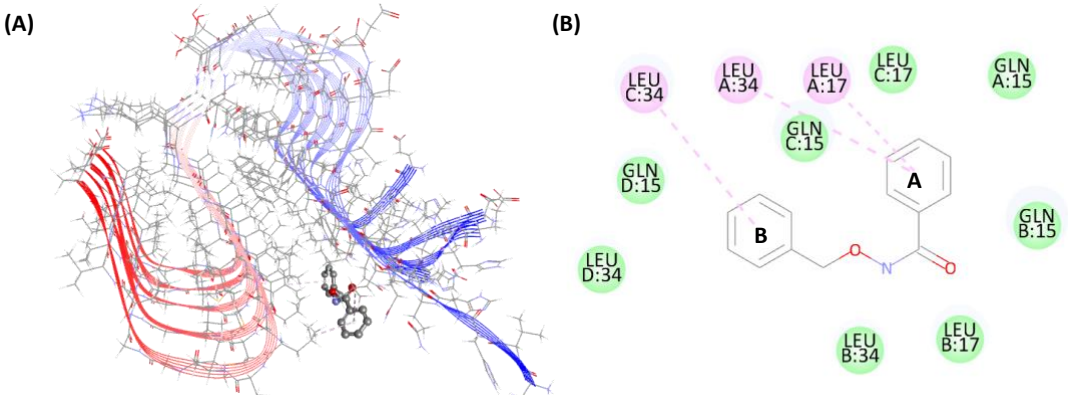


Figure 4-8. Molecular docking studies of **10a** with Aβ42 pentamer model (PDB ID: 5KK3). (A) Top docking pose of **10a**; (B) 2D interaction map of the top docking pose of **10a**. The hydrogen atoms are removed to enhance clarity. Protein is represented in line ribbon with blue indicating the N-terminus and red indicating the C-terminus. The small molecule is represented in the ball-and-stick model. Hydrophobic interaction is represented in pink dashed line.

The top binding mode of **10a** docked in the Aβ42 pentamer is shown in **Figure 4-8**. The Aβ42 pentamer was shown as line ribbon representation color-coded from N- (blue) to C- (red) terminal and the small molecule was shown in ball and stick representation with carbon in grey, oxygen in red, and nitrogen in blue. Based on our docking method, 10 poses of **10a** were generated, and they were ranked according to CDOCKER energy and CDOCKER interaction energy with the lowest energy (most stable) pose shown in **Figure 4-8**. In the top binding pose (CDOCKER energy = -17.42 kcal/mol and CDOCKER interaction energy = -23.17 kcal/mol), **10a** was oriented perpendicular to the long axis of the Aβ42 pentamer assembly. Three hydrophobic interactions were observed interacting

with both hydrophobic regions of Aβ42 pentamer. One of the hydrophobic contacts was between the benzene ring (ring A) and alkyl group of A: Leu17 and A: Leu34 (distance ~ 5.0 Å and 5.5 Å respectively). The other benzene ring (ring B) underwent hydrophobic interaction with the alkyl group of C: Leu34 (distance ~ 5.3 Å). These hydrophobic interactions anchored the compounds in the binding pocket which explains its ability to inhibit the aggregation process since it can interact with both hydrophobic regions of Aβ42. A similar trend was also found for the lead compounds **3a** and **7a** in the previous chapters. However, the oxygen spacer in the linker region did not yield any further interactions with the oligomer, possibly due to the constrained conformation of the molecule. Docking results of **10a** in the Aβ42 fibril model show that in the top binding pose (CDOCKER energy = -19.09 kcal/mol and CDOCKER interaction energy = -23.92 kcal/mol), the key interactions were still hydrophobic with interactions seen between the aromatic ring and Ala21 and Val18 as shown in **Figure 4-9**. The benzene ring (ring A) underwent hydrophobic interactions with the alkyl group of C: Ala21 (distance = 3.9 Å), C: Val18 (distance = 5.3 Å), and B: Val18 (distance = 5.2 Å). Another major interaction was the hydrogen bond formed between the carbonyl oxygen of the amide group and the NH_3^+ of C: Lys16 (distance = 2.5 Å) which further constrained the **10a** in the hydrophobic core region of Aβ42. Interestingly, the oxygen spacer in the linker region was also in contact with the NH_3^+ of C: Lys16 through hydrogen bond interaction (distance = 2.1 Å). This further suggests that the replacement of carbon with an oxygen spacer can enhance the compound binding to fibril and thus improve the overall stability of the ligand-receptor complex. In summary, the molecular docking studies of **10a** in Aβ42 pentamer and fibril models suggest that the hydrophobic interactions between the aromatic rings and the hydrophobic aggregation-prone regions play a significant role in determining its anti-aggregation activity.

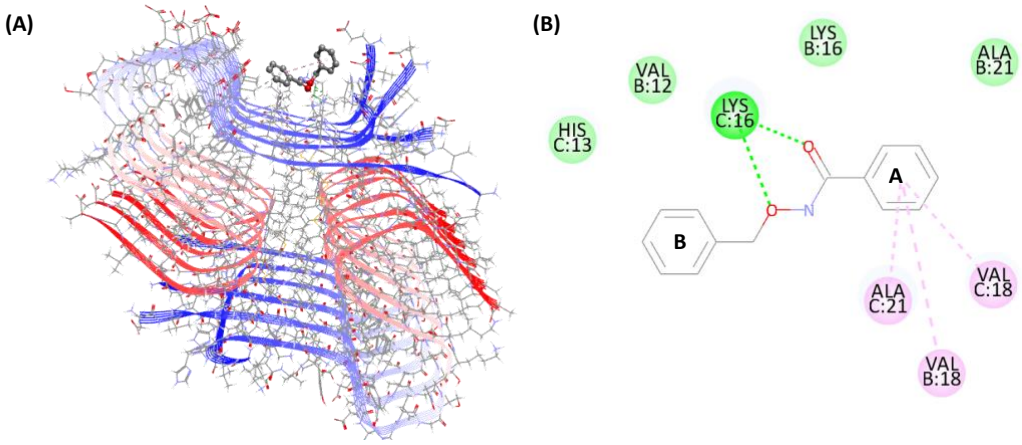


Figure 4-9. Molecular docking studies of **10a** with Aβ42 fibril model (PDB ID: 5KK3). (A) Top docked pose of **10a**; (B) 2D interaction map of the top docking pose of **10a**. The hydrogen atoms are removed to enhance clarity. Protein is represented in line ribbon with blue indicating the N-terminus and red indicating the C-terminus. The small molecule is represented in the ball-and-stick model. Hydrophobic interaction is represented in pink dashed line and hydrogen bond interaction is represented in green dashed line.

4.4 Summary

In this chapter, one of the carbon spacers in the linker region was replaced with an oxygen spacer to obtain *N*-benzyloxybenzamide and carboxamide derivatives **10a-m** and **11a-c**. A total of 14 compounds were synthesized by coupling the *O*-benzylhydroxylamine (**9**) with either corresponding acid chlorides or carboxylic acids to obtain the compound library in good yields (72.1-88.9%). The chemical structures were confirmed by ^{1}H NMR, MS and the purity was checked by LCMS. These compounds exhibited weak-to-moderate modulative activity on the aggregation of Aβ42 as confirmed by ThT-based aggregation kinetic assay and TEM. Among them, **10a**, **10h**, **10j**, and **11a** were identified as better inhibitors of Aβ42 aggregation (PI ranging from 18.7 to 26.5%). Except for **10j**, the lead compounds from this series were not toxic to HT22 cells and were able to rescue HT22 cells from Aβ42-induced neurotoxicity (cell viability ranging from 82.9-91.6% at 25 μM). Derivative **10a** was identified as the best compound (**Figure 4-10**). In the molecular docking studies, the aromatic ring of **10a** can undergo several important hydrophobic interactions with Aβ42 pentamer and fibril models at the aggregation-prone KLVFFA and C-terminal

regions. The oxygen spacer was able to interact with polar amino acid residues in the KLVFFA regions through hydrogen bond interactions in the fibril model.

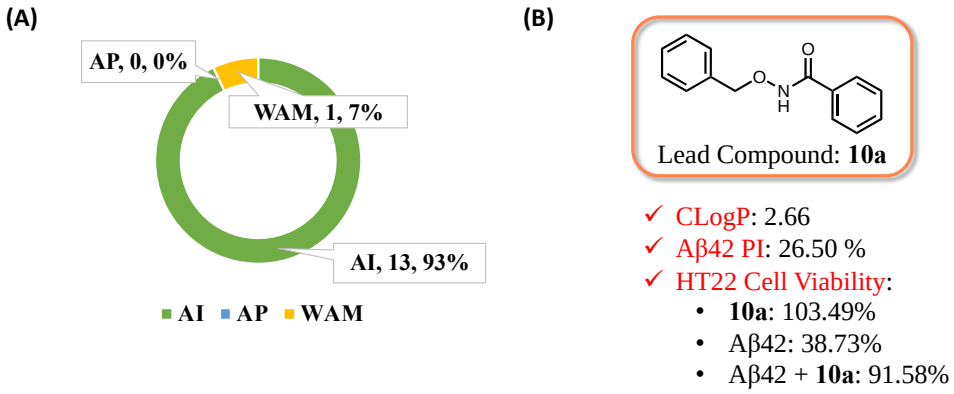


Figure 4-10. Summary of *N*-benzyloxybenzamide and carboxamide derivatives. (A) 93% (13 out of 14) compounds were identified as aggregation inhibitors (AIs), and 7% (1 out of 14) compounds were identified as weak aggregation modulators (WAM); (B) key experimental data for lead compound **10a**.

4.5 Experimental

4.5.1 General

All chemicals and reagents were purchased from various vendors (Sigma Aldrich Missouri USA, Alfa Aesar Massachusetts USA, Bio Basic Ontario Canada, AA Blocks California USA, Cayman Chemical Michigan USA, Thermo Fisher Massachusetts USA, and Corning New York USA), were >95% pure and used without further purification. The Aβ42 1,1,3,3,3-hexafluoroisopropanol (HFIP) >95% pure, was purchased from Anaspec California USA (Cat. No. AS-64129) or rPeptide Georgia USA (Cat. No. A-1163-1). The reactions were monitored by thin-layer chromatography (TLC) using the Merck silica gel 60, F254. Column chromatography was carried out using Merck silica gel 230-400 mesh. The spots were visualized with short or long wavelengths (254 nm or 365 nm). The melting points of compounds were determined using a digital melting point apparatus (REACH Devices, USA). The proton NMR (^{1}H NMR) spectra of

compounds were obtained using a 300 MHz Bruker Avance spectrometer (Department of Chemistry, University of Waterloo). Either $CDCl_3$ or DMSO-d_6 were used as solvents. Coupling constants (*J* values) were recorded in Hertz (Hz). Abbreviations used to represent ^{1}H NMR signals were s – singlet, d – doublet, t – triplet, m – multiplet, br s – broad singlet. The mass and purity were confirmed on the Agilent 1260 Infinity liquid chromatography (LC) module equipped with a 6130 Quadrupole mass spectrometer (Agilent 6100 series LCMS). The column used on LCMS was a ZORBAX Eclipse AAA, 4.6 × 75 mm, 3.5 micron (Agilent Technologies, Canada) column. A mixture of water and acetonitrile 1:1 v/v with 0.1% formic acid (1.0 mL/min flow rate), was used as the solvent system to assess compound purity and mass. All final compounds were ≥ 95% pure as determined by LCMS analysis.

4.5.2 Chemistry

For the synthesis of **10a-m** the acid chlorides were coupled with *O*-benzylhydroxylamine (**9**) (1 mmol) by taking them into a 50 mL round bottom flask (RBF) containing 15 mL of anhydrous tetrahydrofuran (THF). To this mixture, 1.2 equivalents of TEA and 1.0 equivalent of corresponding acid chlorides with various R groups (**2a-m**) were added. The reaction mixture was kept at either room temperature or reflux for 2-24h and was monitored by thin layer chromatography (TLC). After the reaction was complete, the solvent THF was evaporated in vacuo and the resulting reaction mixture was dissolved in 15 mL ethyl acetate (EtOAc), and then washed with 15 mL brine solution (×3). The organic layer was collected and dried over anhydrous $MgSO_4$ and filtered. The organic solvent was removed in vacuo and the residue/oil obtained was further purified by silica gel column chromatography using a combination of solvent systems (1:1 *n*-Hexanes:EtOAc or 5:2 n-Hexanes:EtOAc or 9:1 dichloromethane (DCM): Methanol (MeOH) or 4:1 DCM:*n*-Hexanes) to afford the final compounds **10a-m**.

Compounds **11a-c** were synthesized by reacting *O*-benzylhydroxylamine (**9**) (1 mmol) kept in an RBF with 15 mL THF, followed by the addition of 1.0 equivalent carboxylic acid (**4a-c**), 1.2 equivalents EDC,

1.5 equivalents HOBt, and 2.2 equivalents TEA added in sequence. The reaction was kept at room temperature overnight or under reflux conditions for 4–12 h. The solvent was evaporated in vacuo and the resulting reaction mixture was dissolved in 15 mL EtOAc and washed with 15 mL brine solution (×3). The organic layer was collected, dried over anhydrous $MgSO_4$ and filtered. The organic solvent was then removed in vacuo to obtain the residue/oil which was further purified by silica gel column chromatography using either 1:1 *n*-Hexanes:EtOAc or 5:2 *n*-Hexanes:EtOAc as mobile phase to afford compounds **11a-c**.

4.5.3 Aβ42 aggregation kinetic assay

The ability of benzamide and carboxamide derivatives **10a-m** and **11a-c** to inhibit the Aβ42 aggregation was evaluated using the thioflavin T (ThT) based fluorescence kinetic assay. A 15 μM ThT solution was prepared in 50 mM glycine buffer using ultra-pure-water (UPW). The pH of the solution was adjusted to 7.4 with 50 mM sodium hydroxide solution. The aggregation assay was carried out using 215 mM sodium phosphate dibasic heptahydrate buffer prepared in UPW and the pH was adjusted to 7.4 by using 50 mM hydrochloric acid solution. The Aβ42•HFIP > 95% pure (Anaspec, California, USA) was treated with 1% ammonium hydroxide solution to afford 1 mg/mL stock solution. The stock solution was then vortexed and sonicated for 5 min before being diluted to a 25 μM working solution using the assay buffer. The stock solutions of the test compounds (**10a-m**, **11a-c** and resveratrol (RVT) were prepared in assay buffer with DMSO as the solubilizing agent (final concentration per well was less than 2%). The 24 h aggregation kinetics assay was carried out using 384-well plates (Costar, black, clear-bottom), by adding 44 μL of ThT, 12 μL of assay buffer, 16 μL of Aβ42 solution (10 μM final well concentration), and 8 μL of test compound dilution (25 μM) into each well. The Aβ42 control wells contained ThT, Aβ42 solution and the assay buffer without any test compound. The plates were covered with a transparent plate cover and were incubated at 37 °C for 24 h with shaking at 300 cpm between readings for 30 s. The readings were taken every 10 min (bottom reading), with excitation wavelength of 440 nm and emission wavelength of 490 nm using the

BioTek Synergy H1 microplate reader. Each sample was measured in triplicate readings and the results were obtained based on three independent experiments.

4.5.4 Transmission electron microscopy

The TEM assay was carried out by first running the Aβ42 aggregation assay (as described in 4.5.3) by incubating test compounds at 25 μM with 10 μM Aβ42 for 24 h at 37 °C. The TEM grids were prepared by aliquoting 20 μL of each sample from the 384-well plate after the 24-hour incubation period. These samples were loaded onto 400-mesh formvar-coated copper grids (Electron Microscopy Sciences, Pennsylvania, USA). The grids were air-dried overnight before being washed with 40 μL UPW for three times. After washing, 20 μL 2% phosphotungstic acid (PTA) solution was added to the grid and stayed for 1 min to stain the samples. Then the PTA solution was absorbed away with filter paper and then the grids were washed with 40 μL UPW three times. Then the grids were further air-dried overnight. The imaging studies were carried out using a Philips CM 10 TEM (Dept. of Biology, University of Waterloo) at 60 kV and the micrographs were obtained through a 14-megapixel AMT camera at 64,000X magnification. The samples used to prepare the grids were obtained by mixing the triplicate wells from ThT assay and the images were taken at a randomized view for each grid.

4.5.5 Cell viability assay

The cell viability assay was carried out in the Aβ42-induced HT22 cell toxicity model. The cytotoxicity and neuroprotective effects of benzamide/carboxamide derivatives **10a-m** and **11a-c** toward HT22 cells were carried out by using the UV-based cell metabolism assay kit (cell counting kit 8, CCK-8, TargetMol, Massachusetts, USA). The HT22 cells were cultured in DMEM/F12 1:1 with the addition of glutamate supplemented with 10% FBS and 1% penicillin and streptomycin at 37 °C in 5% CO_2. The cells were seeded at a density of 50,000 cells per mL. After 24 h, the cells were treated with various compounds at 25 μM

prepared in phosphate buffer pH 7.4 and DMSO (less than 2%) and incubated for 48 h. After that, the CCK-8 reagent was added to each well, and incubated for another 2 h, before measuring the absorbance at 450 nm as per the manufacturer's protocol. The neuroprotective effects of test compounds toward Aβ42-induced cytotoxicity were determined by treating the HT22 cells with 5 μM of Aβ42•HFIP (>95%, rPeptide, Georgia, USA), and then incubating for 48 h. The cell viability assay was determined by adding the CCK-8 reagent and incubating for another 2 h to measure the absorbance at 450 nm. The cell viability was calculated as the average percent cell viability based on quadruplicate readings from three independent experiments. For statistical analysis, the results were subjected to one-way ANOVA followed by Bonferroni post hoc analysis compared to Aβ control group. ns = not significant, *$p < 0.01$ compared to Aβ42 control group, **$p < 0.01$ compared to Aβ42 control group, ***$p < 0.01$ compared to Aβ42 control group, ****$p < 0.01$ compared to Aβ42 control group.

4.5.6 Molecular docking study

The binding interactions of **10a** with Aβ42 were investigated by carrying out molecular docking studies on the Discovery Studio software program v20.1.0.19295, Structure-Based-Design (BIOVIA Inc. San Diego, USA). The Aβ42 pentamer and oligomer models were prepared by extracting the coordinates from the solved 3D structure of the Aβ42 fibril (PDB id: 5KK3). A binding sphere of 20 Å radius was selected and defined as the ligand binding site which covers the ^{16}KLVFFA^{21} and the C-terminal ^{32}IGLMVGGVVIA^{42} hydrophobic regions of the Aβ42. Compound **10a** was built in 3D using the Small Molecule module in the software and was subjected to energy minimization protocol (1000 and 2000 steps of steepest descent followed by conjugate gradient method) using CHARMm force field. The CDOCKER algorithm was used to carry out the docking studies. The Receptor-ligand Interactions module in the software was used to perform CDOCKER simulations. The docking simulation included 2000 heating steps, a heating target temperature of 700 K and 5000 cooling steps and a cooling target temperature of 300 K. The top ligand binding modes of selected lead compounds were analyzed by evaluating the CDOCKER

energy and CDOCKER interaction energy (in kcal/mol). Further analysis was carried out by determining the polar and nonpolar contacts of **10a** in the Aβ42 pentamer and fibril assembly.

Chapter 5

Design, Synthesis and Evaluation of *N*-phenylbenzamide and *N*-phenylcarboxamide Derivatives as Aβ Aggregation Modulators

Below is a list of publications, manuscripts submitted and in preparation along with author names based on this chapter:

Zhao, Y. Rao, P. P. N. (2023). Small molecules *N*-phenylbenzofuran-2-carboxamide and *N*-phenylbenzo[*b*]thiophene-2-carboxamide promote beta-amyloid (Aβ42) aggregation and mitigate neurotoxicity. *ACS Chem. Neurosci.*, *14* (23), 4185-4198.

Zhao, Y., Singh K., Karuturi C. R., Hefny, A., Shakeri, A., Beazley, M., Rao, P. P. N. *N*-(substitutedphenyl)benzofuran-2-carboxamide and *N*-(substitutedphenyl)benzo[*b*]thiophene-2-carboxamide derivatives modulate beta-amyloid (Aβ42) aggregation and mitigate neurotoxicity. *ChemMedChem* (Manuscript in preparation)

Zhao, Y., Shakeri, A., Karuturi C. R., Hefny, A., Wang, S., Rao, P. P. N. Medicinal chemistry of amyloid-beta (Aβ) aggregation promotors and Alzheimer's disease (AD). *Eur. J. Med. Chem* (Manuscript in preparation)

5.1 Introduction

This chapter features the fourth series of compounds in the proposed library, where the three-carbon α,β-unsaturated system present in the chalcone template was replaced with an amide bioisostere without any other spacer in the linker region to obtain *N*-phenylbenzamide template.[318,319] The structure-activity relationship (SAR) modifications for this library of 16 derivatives are shown in **Figure 5-1**. In this series of compounds, the *N*-phenyl moiety was kept constant while the other end of the molecule was modified by incorporating various aromatic rings such as benzene (**13a**), pyridine (**13b**, **13c**), pyrrole (**13h**), furan

(**13i**), thiophene (**13j**). Furthermore, bicyclic aromatic rings were also included, such as naphthalene (**13l**), quinoline (**13m**), indole (**14a**), benzofuran (**14b**), and benzo[*b*]thiophene (**14c**). In addition, aliphatic rings were also incorporated including cyclohexane (**13f**), piperidine (**13g**), and pyrrolidine (**13k**). Besides, known pharmacophores where 3,4-dimethoxylbenzene and 3, 4-difluorobenzene moieties were also incorporated in compounds **13d** and **13e**.[320] This chapter describes the synthesis, characterization, and evaluation of *N*-phenylbenzamide and *N*-phenylcarboxamide class of compounds via biophysical (thioflavin T based fluorescence spectroscopy, transmission electron microscopy), biochemical (Aβ42-induced cytotoxicity in mouse hippocampal HT22 neuronal cell lines) and by computational modelling studies.

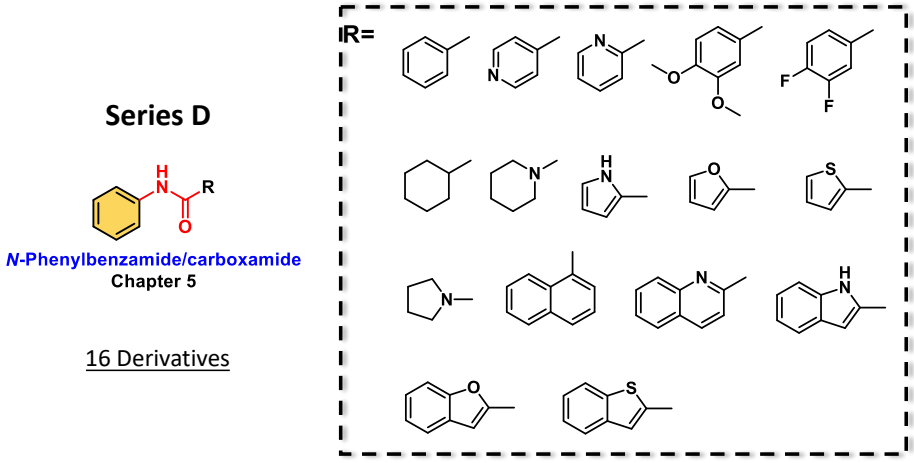


Figure 5-1. *N*-Phenylbenzamide and *N*-phenylcarboxamide derivatives (Series D). This series of compounds is featured by an amide bond without any spacer in the linker region.

5.2 Hypothesis

It is hypothesized that replacing the α,β-unsaturated system presented in either chalcone or curcumin with an amide bioisostere will remove the presence of a reactive Michael acceptor and provide drug-like properties while retaining their Aβ42 aggregation modulation properties. In the previous chapters, the SAR was explored by adding more degrees of freedom into the linker region. These modifications did not improve their Aβ42 modulation properties. Therefore, in this chapter, the extra carbon/oxygen linker atoms

were removed and instead, the phenyl ring was directly linked to various aromatic substituents to give a rigid conformation. These *N*-phenylbenzamide and carboxamide scaffolds are expected to be shorter in length and less flexible which would facilitate better fitting in the KLVFFA and the C-terminal regions of Aβ42. In this series of compounds, substituted compounds with known pharmacophores (such as R = 3,4-dimethoxylbenzene and R = 3,4-difluorobenzene)[320], are expected to demonstrate better inhibition of Aβ42-aggregation due to efficient van der Waals, hydrophobic and hydrogen bonding interactions with Aβ42 and also provide neuroprotection against Aβ42-induced cytotoxicity. The SAR was investigated by incorporating monocyclic, bicyclic, aromatic, acyclic, 5- and 6-membered rings to study their effect on Aβ42 aggregation (**Figure 5-1**). It is hypothesized these SAR studies will provide novel insights on designing Aβ42 aggregation modulators.

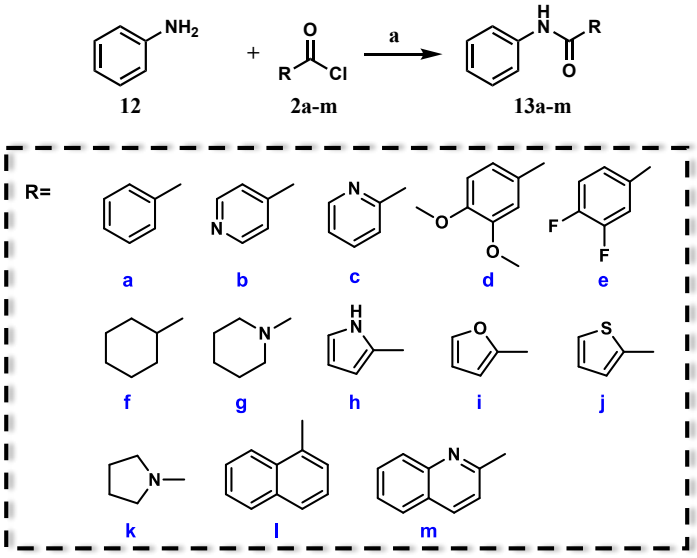
5.3 Results and Discussion

In this section, the synthesis, purification and characterization of the *N*-phenylbenzamide and *N*-carboxamide class of compounds (**13a-m** and **14a-c**) are discussed which is followed by biological activity screening, including anti-Aβ42 aggregation assay (thioflavin T, ThT, fluorescence spectroscopy), fibril morphology study by transmission electron microscopy, cell viability assay against Aβ42-induced cytotoxicity in mouse hippocampal HT22 neuronal cells. Representative compounds from this series were used in computational modelling studies to understand their interactions with Aβ42 using the solved 3D structures to understand the mechanisms of their anti-aggregation and aggregation modulating properties.

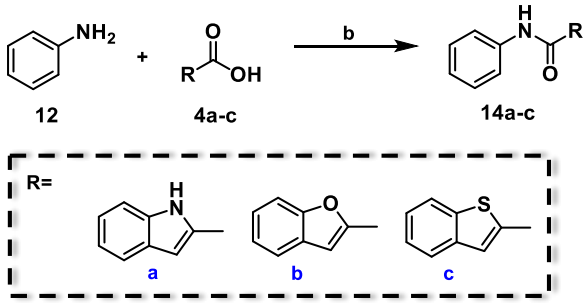
5.3.1 Synthesis

The retro-synthetic analysis of the compound library suggests that the starting building blocks can be coupled to form the amide bond using suitable substrates to obtain the *N*-phenylbenzamide and *N*-phenylcarboxamide derivatives. This was achieved through either the direct coupling of acid halides (**2a-**

m) with primary amines (aniline **12**, Method A) or by coupling the carboxylic acids with primary amines (aniline **12**, Method B). The preference for using the acid halides versus carboxylic acids coupling method was made based on the commercial availability and cost-effectiveness of the starting materials. With that being said, compounds **13a-m** were synthesized *via* Method A as shown in **Scheme 5-1**, whereas compounds **14a-c** were synthesized by method B as shown in **Scheme 5-2**.



Scheme 5-1. Synthetic scheme to prepare **13a-m** by coupling aniline (**12**) with corresponding acid chlorides (**2a-m**). Reagents and conditions: (a) TEA, THF, room temperature/reflux 2-24 h.



Scheme 5-2. Synthetic scheme to prepare **14a-c** by coupling aniline (**12**) with corresponding carboxylic acids (**4a-c**). Reagents and conditions: (b) EDC•HCl, HOBt, TEA, THF, room temperature overnight or under reflux conditions for 24h.

In Method A, aniline (**12**) was coupled with corresponding acid halides. Considering the leaving group capability and reactivity, acid chlorides (**2a-m**) were used in the reactions. The reaction mechanism (**Figure 5-2**) is described as follows: first, the nucleophilic amine **12** attacks the electrophilic carbonyl carbon of the acid chloride to form a tetrahedron intermediate by nucleophilic addition; next, chloride serves as a good leaving group and then is eliminated from the tetrahedron intermediate; then hydrochloric acid is also formed as the reaction by-product which can neutralize the base triethylamine (TEA) to facilitate product formation.[322] The overall yields of these reactions range from 82.3- 91.6 %. The analytical data for **13a-m** (^{1}H NMR, MS and purity data by LCMS) are given below. Analytical spectral data for all the final compounds are given in **Appendix D**.

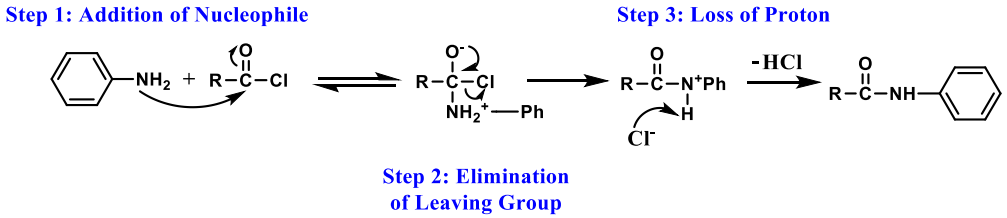


Figure 5-2. Nucleophilic acyl substitution mechanism which includes three major steps: (1) addition of nucleophile to the electrophilic carbonyl carbon. (2) elimination of the leaving group. (3) loss of proton.

5.3.1.1 *N*-Benzylbenzamide (**13a**)

The product was obtained as a white solid (Yield = 91.6%). ^{1}H NMR (300 MHz, DMSO-*d*6): δ 10.24 (s, 1H), 8.01 – 7.91 (m, 2H), 7.83 – 7.73 (m, 2H), 7.66 – 7.48 (m, 3H), 7.42 – 7.30 (m, 2H), 7.17 – 7.05 (m, 1H). mp: 167-170 °C. ESI-MS, m/z calcd for $C_{13}H_{11}NO$ $[M+H]^+$ 198.1, found 198.1. Purity: 99.73% (LCMS).

5.3.1.2 *N*-Benzylisonicotinamide (**13b**)

The product was obtained as a white solid (Yield = 90.8%). ^{1}H NMR (300 MHz, DMSO-d_6): δ 10.49 (s, 1H), 8.85 – 8.74 (m, 2H), 7.92 – 7.83 (m, 2H), 7.77 (d, *J* = 8.0 Hz, 2H), 7.45 – 7.31 (m, 2H), 7.20 – 7.10 (m, 1H). mp: 176-179 °C. ESI-MS, m/z calcd for $C_{12}H_{10}N_2O$ $[M+H]^+$ 199.1, found 199.1. Purity: 97.99% (LCMS).

5.3.1.3 *N*-Benzylpicolinamide (**13c**)

The product was obtained as a white solid (Yield = 86.4%). ^{1}H NMR (300 MHz, DMSO-d_6): δ 10.62 (s, 1H), 8.75 (d, *J* = 4.7 Hz, 1H), 8.22 – 8.02 (m, 2H), 7.91 (d, *J* = 8.1 Hz, 2H), 7.74 – 7.64 (m, 1H), 7.37 (t, *J* = 7.8 Hz, 2H), 7.13 (t, *J* = 7.4 Hz, 1H). mp: 83-86 °C. ESI-MS, m/z calcd for $C_{12}H_{10}N_2O$ $[M+H]^+$ 199.1, found 199.1. Purity: 96.88% (LCMS).

5.3.1.4 *N*-Benzyl-3,4-dimethoxybenzamide (**13d**)

The product was obtained as a white solid (Yield = 85.6%). ^{1}H NMR (300 MHz, DMSO-d_6) δ 10.06 (s, 1H), 7.80 – 7.71 (m, 2H), 7.63 (dd, *J* = 8.3, 2.1 Hz, 1H), 7.54 (d, *J* = 2.1 Hz, 1H), 7.41 – 7.30 (m, 2H), 7.15 – 7.04 (m, 2H), 3.85 (s, 3H), 3.84 (s, 3H). mp: 169-172 °C. ESI-MS, m/z calcd for $C_{15}H_{15}NO_3$ $[M+H]^+$ 258.1, found 258.1. Purity: 97.7% (LCMS).

5.3.1.5 *N*-Benzyl-3,4-difluorobenzamide (**13e**)

The product was obtained as a white solid (Yield = 89.3%). ^{1}H NMR (300 MHz, DMSO-d_6) δ 10.30 (s, 1H), 8.11 – 7.98 (m, 1H), 7.92 – 7.82 (m, 1H), 7.76 (d, *J* = 8.3 Hz, 2H), 7.63 (dd, *J* = 9.0 Hz, 1H), 7.37 (t, *J* = 7.8 Hz, 2H), 7.13 (t, *J* = 7.4 Hz, 1H). mp: 171-174 °C. ESI-MS, m/z calcd for $C_{13}H_9F_2NO$ $[M+H]^+$ 234.1, found 234.1. Purity: 99.43% (LCMS).

5.3.1.6 *N*-Benzylcyclohexanecarboxamide (**13f**)

The product was obtained as a white solid (Yield = 84.5%). ^{1}H NMR (300 MHz, $CDCl_3$) δ 7.51 (d, *J* = 7.9 Hz, 2H), 7.34 – 7.21 (m, 2H), 7.07 (t, *J* = 7.4 Hz, 1H), 2.21 (tt, *J* = 11.7, 3.5 Hz, 1H), 2.00 – 1.75 (m, 5H), 1.74 – 1.43 (m, 2H), 1.39 – 1.16 (m, 4H). mp: 147-150 °C. ESI-MS, m/z calcd for $C_{13}H_{17}NO$ $[M+H]^+$ 204.1, found 204.1. Purity: 99.81% (LCMS).

5.3.1.7 *N*-Benzylpiperidine-1-carboxamide (**13g**)

The product was obtained as a white solid (Yield = 88.7%). ^{1}H NMR (300 MHz, $CDCl_3$) δ 7.42 – 7.25 (m, 4H), 7.04 (t, *J* = 7.3 Hz, 1H), 6.35 (s, 1H), 3.52 – 3.43 (m, 4H), 3.20 – 3.16 (m, 1H), 1.71 – 1.52 (m, 3H), 1.28 (s, 2H). mp: 239-242 °C. ESI-MS, m/z calcd for $C_{12}H_{16}N_2O$ $[M+H]^+$ 205.1, found 205.1. Purity: 99.65% (LCMS).

5.3.1.8 *N*-Benzyl-1*H*-pyrrole-2-carboxamide (**13h**)

The product was obtained as a white solid (Yield = 82.3%). ^{1}H NMR (300 MHz, $CDCl_3$): δ 9.50 (br s, 1H), 7.51–7.12 (m, 5H), 6.92–6.90 (m, 1H), 6.53–6.51 (m, 1H), 6.23–6.20 (m, 1H), 6.13 (br s, 1H). mp: 152-155 °C. ESI-MS, m/z calcd for $C_{12}H_{13}N_2O$ $[M+H]^+$ 201.1, found 201.1. Purity: 98.26% (LCMS).

5.3.1.9 *N*-Benzylfuran-2-carboxamide (**13i**)

The product was obtained as a white solid (Yield = 90.6%). ^{1}H NMR (300 MHz, DMSO-d_6): δ 10.16 (s, 1H), 7.94 (s, 1H), 7.75 (d, *J* = 8.0 Hz, 2H), 7.40 – 7.29 (m, 3H), 7.10 (t, *J* = 7.3 Hz, 1H), 6.75 – 6.67 (m, 1H). mp: 126-129 °C. ESI-MS, m/z calcd for $C_{11}H_9NO_2$ $[M+H]^+$ 188.1, found 188.1. Purity: 99.74% (LCMS).

5.3.1.10 *N*-Benzylthiophene-2-carboxamide (**13j**)

The product was obtained as a white solid (Yield = 86.9%). ^{1}H NMR (300 MHz, DMSO-d_6): δ 10.21 (s, 1H), 8.03 (d, *J* = 3.7 Hz, 1H), 7.86 (d, *J* = 5.0 Hz, 1H), 7.72 (d, *J* = 8.3 Hz, 2H), 7.36 (t, *J* = 7.8 Hz, 2H), 7.23 (t, *J* = 4.4 Hz, 1H), 7.11 (t, *J* = 7.4 Hz, 1H). mp: 149-152 °C. ESI-MS, m/z calcd for $C_{11}H_9NOS$ $[M+H]^+$ 204.1, found 204.1. Purity: 99.56% (LCMS).

5.3.1.11 *N*-Benzylpyrrolidine-1-carboxamide (**13k**)

The product was obtained as a white solid (Yield = 88.1%). ^{1}H NMR (300 MHz, $CDCl_3$) δ 7.48 – 7.36 (m, 2H), 7.36 – 7.24 (m, 3H), 7.03 (t, *J* = 7.3 Hz, 1H), 6.21 (s, 1H), 3.53 – 3.43 (m, 4H), 2.04 – 1.91 (m, 4H). mp: 125-128 °C. ESI-MS, m/z calcd for $C_{11}H_{14}N_2O$ $[M+H]^+$ 191.1, found 191.2. Purity: 96.60% (LCMS).

5.3.1.12 *N*-Benzyl-1-naphthamide (**13l**)

The product was obtained as a white solid (Yield = 87.6%). ^{1}H NMR (300 MHz, DMSO-d_6): δ 10.56 (s, 1H), 8.23 – 8.14 (m, 1H), 8.09 (d, *J* = 8.2 Hz, 1H), 8.06 – 7.99 (m, 1H), 7.86 – 7.68 (m, 3H), 7.68 – 7.56 (m, 3H), 7.38 (t, *J* = 7.7 Hz, 2H), 7.13 (t, *J* = 7.4 Hz, 1H). mp: 164-167 °C. ESI-MS, m/z calcd for $C_{17}H_{13}NO$ $[M+H]^+$ 248.1, found 248.1. Purity: 98.87% (LCMS).

5.3.1.13 *N*-Benzylquinoline-2-carboxamide (**13m**)

The product was obtained as a white solid (Yield = 85.7%). ^{1}H NMR (300 MHz, DMSO-d_6): δ 10.74 (s, 1H), 8.65 (d, *J* = 8.6 Hz, 1H), 8.32 – 8.21 (m, 2H), 8.14 (d, *J* = 8.1 Hz, 1H), 8.00 – 7.88 (m, 3H), 7.77 (t, *J*

= 7.5 Hz, 1H), 7.42 (t, *J* = 7.7 Hz, 2H), 7.17 (t, *J* = 7.4 Hz, 1H). mp: 142-145 °C. ESI-MS, m/z calcd for $C_{16}H_{12}N_2O$ $[M+H]^+$ 249.1, found 249.1. Purity: 99.2% (LCMS).

Method B was used to synthesize *N*-phenethylcarboxamide derivatives (**14a-c**, **Scheme 5-2**). Compared to acid chlorides, carboxylic acids are less reactive due to the electron-donating nature of the hydroxyl group. This can influence the reaction progress, yield and purity of the products. However, this limitation can be overcome by activating the carboxylic acid (**4a-c**) with the assistance of carbodiimide-dehydrating reagents, such as 1-ethyl-3-(3-dimethylaminopropyl)carbodiimide (EDC). [323,324] The detailed reaction mechanism is shown in **Figure 5-3**. The carboxylic acids can be transformed into an ester intermediate. In the presence of an activator, such as hydroxyltriazole (HOBt), the nucleophilic activator attacks the carbonyl carbon of the ester intermediate so that an active ester is formed. [325] The active ester contains a better leaving group compared to the original carboxylic acid so that it can react with aniline (**12**) *via* nucleophilic acyl substitution as mentioned in the previous paragraph. The by-product urea formed as a result of using EDC as dehydrating reagent is water-soluble and therefore, can be washed away by aqueous extraction in the post-reaction workup. The overall yields of these reactions range from 82.7 to 88.9 %. The analytical data (^{1}H NMR, MS and purity data by LCMS) for compounds **14a-c** are given below. Analytical spectral data for all the final compounds are given in **Appendix D**.

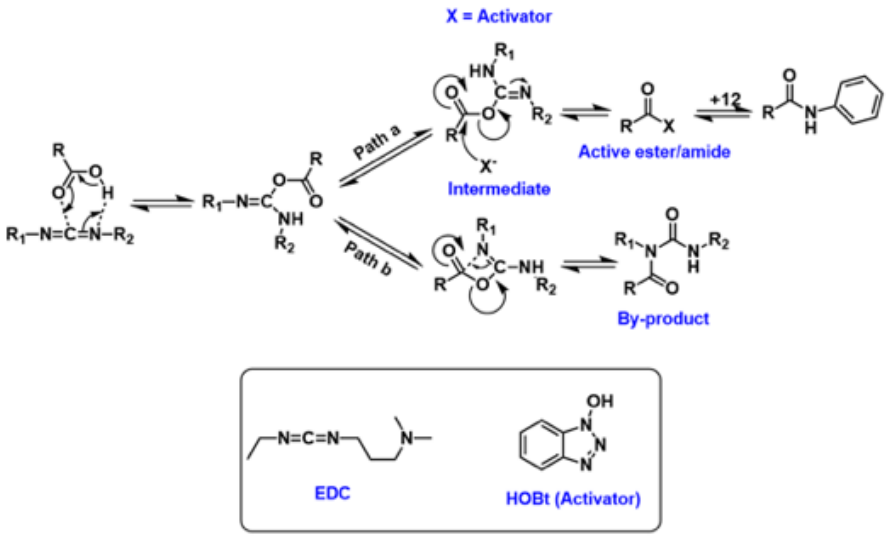


Figure 5-3. Reaction mechanism to obtain **14a-c** using dehydrating agent EDC and activator HOBt for coupling aniline (**12**) and corresponding carboxylic acids (**4a-c**).

5.3.1.14 *N*-Benzyl-1*H*-indole-2-carboxamide (**14a**)

The product was obtained as a white solid (Yield = 90.6%). ^{1}H NMR (300 MHz, DMSO-d_6): δ 11.74 (s, 1H), 10.20 (s, 1H), 7.82 (d, *J* = 8.0 Hz, 2H), 7.68 (d, *J* = 8.0 Hz, 1H), 7.51 – 7.32 (m, 4H), 7.23 (t, *J* = 7.6 Hz, 1H), 7.18 – 7.02 (m, 2H). mp: 197-200 °C. ESI-MS, m/z calcd for $C_{15}H_{12}N_2O$ $[M+H]^+$ 237.1, found 237.1.Purity: 98.17% (LCMS).

5.3.1.15 *N*-Benzylbenzofuran-2-carboxamide (**14b**)

The product was obtained as a white solid (Yield = 82.9%). ^{1}H NMR (300 MHz, DMSO-d_6) δ 10.52 (s, 1H), 7.92 – 7.70 (m, 5H), 7.52 (t, *J* = 7.8 Hz, 1H), 7.38 (t, *J* = 7.5 Hz, 2H), 7.14 (t, *J* = 7.3 Hz, 1H). mp: 160-163 °C. ESI-MS, m/z calcd for $C_{15}H_{11}NO_2$ $[M+H]^+$ 238.1, found 238.1. Purity: 96.37% (LCMS).

5.3.1.16 *N*-Benzylbenzo[*b*]thiophene-2-carboxamide (**14c**)

The product was obtained as a white solid (Yield = 88.3%). ^{1}H NMR (300 MHz, $CDCl_3$ δ 10.51 (s, 1H), 8.37 (s, 1H), 8.11 – 7.97 (m, 2H), 7.87 – 7.74 (m, 2H), 7.57 – 7.44 (m, 2H), 7.39 (t, *J* = 7.8 Hz, 2H), 7.14 (t, *J* = 7.4 Hz, 1H). mp: 190-193 °C. ESI-MS, m/z calcd for $C_{15}H_{11}NOS$ $[M+H]^+$ 254.1, found 254.1. Purity: 99.16% (LCMS).

5.3.2 Modulatory activity on amyloid-beta aggregation

5.3.2.1 Results overview

The modulatory activity of *N*-phenylbenzamide and carboxamide derivatives **13a-m** and **14a-c** on Aβ42 aggregation was evaluated using the ThT aggregation kinetic assay.[326–329] It is the golden standard used in the field for rapid screening of small molecules to determine their Aβ42 aggregation modulation activity.[330–333] In this assay, ThT was used as the fluorescent dye which can selectively bind to the β-sheet structure of various forms of aggregated Aβ42. Upon binding, ThT gives a characteristic increase in the fluorescence reading (FLR) which is directly proportional to the amount of Aβ aggregates formed. By comparing the FLR of the Aβ42 control and in the presence of various test compounds, the percentage inhibition (PI) can be calculated at the end of the assay. If the FLR is lower than that of the control, it indicates that the compounds are inhibiting the Aβ42 aggregation. Similarly, if the FLR is higher than that of control, it indicates that the compounds are able to promote the Aβ42 aggregation. Compounds that are able to inhibit Aβ42 aggregation are termed aggregation inhibitors (AI) and compounds that are able to promote Aβ42 aggregation are termed aggregation promotors (AP), whereas compounds that weakly modulate the aggregation are termed weak aggregation modulators (WAM). Initially, all the test compounds were screened at 25 μM to determine their effect on Aβ42 aggregation. Compounds that show promising activity were further evaluated over a concentration range (1, 5, 10, 25 μM) to determine the aggregation kinetics.

Resveratrol (RVT) which is a known inhibitor of Aβ42 aggregation was also included in the assay as the reference compound for comparison. [334]

In **Figure 5-4**, the ThT aggregation kinetic curves of *N*-phenylbenzamide and carboxamide derivatives **13a-m** and **14a-c** were shown. In each panel, the blue curve at the bottom is the ThT background readings which suggests that ThT has no interference on the FLR in monitoring the aggregation of Aβ42. The red curve shows the Aβ42 aggregation in the absence of test compounds. In these curves, some characteristics of Aβ42 aggregation can be observed. It is a sigmoidal curve characterized by a very short lag phase (~ 30 min) which is followed by a rapid growth phase spanning the time course from around 0.5 h to 10 h. Then, the FLR tends to be stable with readings hovering around 8,000 RFU, indicating the aggregation process has reached the equilibrium status. Such saturation phase was maintained until the end of the assay at 24 h. Compared to the Aβ42 control, other curves, in the presence of different *N*-phenylbenzamide and carboxamide derivatives (**Figure 5-4**, A: **13a-d**, **RVT**, B: **13e-h**, C: **13i-l**, D: **13m**, **14a-c**) shared similar shapes without any major differences. This observation suggests that these derivatives are not able to alter the aggregation kinetics by either shortening or extending the lag/growth phase. However, lower FLR at the saturation phase than Aβ42 control for these curves was observed at the 24 h time point which indicates that some derivatives were capable of reducing the formation of Aβ42 fibrils. When co-incubating the reference compound RVT with Aβ42 (**Figure 5-4** A), a dramatic decrease in the FLR was noticed in the saturation phase with FLR below 2,000 RFUs after 18 h. Such observation is not surprising as RVT is a very potent Aβ42 AI.[334] However, to our surprise, most of the test compounds in this series exhibited pro-aggregation activities (compound **13c, 13e, 13g, 13j, 13l, 13m** and **14a-c**, **Table 5-1**).

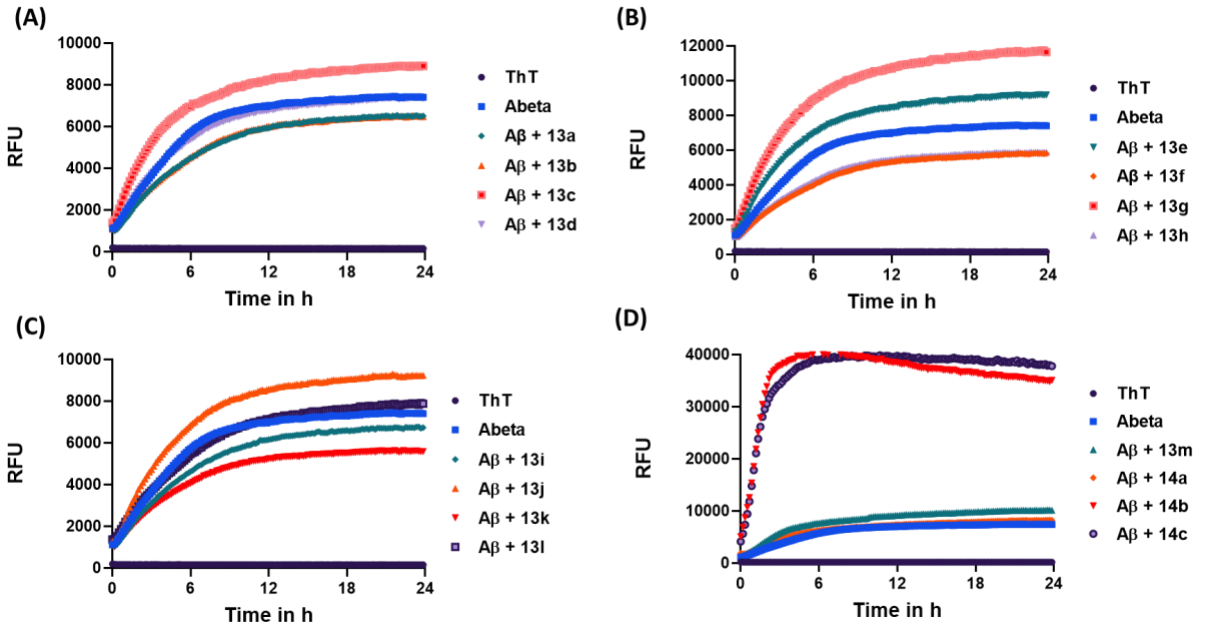


Figure 5-4. The Aβ42 aggregation kinetic curves for *N*-phenylbenzamide and carboxamide derivatives (**13a-m** and **14a-c**) in the ThT-based fluorescence assay. (A) Aggregation kinetic curves derivatives **13a-d** and reference compounds resveratrol (RVT). (B) Aggregation kinetic curves derivatives **13e-h**. (C) Aggregation kinetic curves derivatives **13i-l**. (D) Aggregation kinetic curves derivatives **13m**,and **14a-c**. The derivatives (25 μM) were incubated with Aβ42 (10 μM) for 24 h at 37 ˚C, pH 7.4 and the ThT fluorescence was monitored (excitation = 440 nm, emission = 490 nm). Results were obtained based on triplicate readings from three independent experiments.

Table 5-1 shows the anti-aggregation activity of test compounds as the percentage inhibition (PI) and **Figure 5-5** shows a bar plot of PI at the 24 h time point. A total of 6 out of 16 compounds from this series exhibited anti-Aβ42 activity in the ThT-based fluorescence assay with activity ranging from 9.0 - 24.7 %. Another 6 out of 16 compounds in this series exhibited pro-aggregation activities with promotion ranging from 20.2 – 412.2 %. Compound **13a** (R = benzene) exhibited 12.1± 5.2 % inhibition which is much lower than the compound containing same R group in the previous chapter (**3a**, Chapter 2, 27.1 % inhibition; **7a**, Chapter 3, 28.6 % inhibition; **10a**, Chapter 4, 26.5 % inhibition). Replacing the benzene ring with more polar pyridine bioisostere in compound **13b**, the anti-aggregation activity was maintained (12.5 ± 5.0 % inhibition). Interestingly, compound **13c** (R = pyridine) exhibited pro-aggregation activity instead of

inhibition (20.2 ± 8.15 % promotion). Incorporation of the known anti-Aβ pharmacophores in **13d** and **13e** did not improve the activities as expected. Compound **13d** (R = 3,4-dimethoxylbenzene) was not active in modulating the aggregation of Aβ42 and **13e** (R = 3,4-difluorobenzene) was an aggregation promotor (24.0 ± 6.47 % promotion). Incorporating aromatic 5-member heterocyclic rings showed mixed results. Compound **13h** (R = pyrrole) was able to exhibit moderate anti-aggregation activity with PI of 21.7 ± 2.6 %, whereas compound **13i** (R = furan) only exhibited PI of 20.8 ± 0.6 %. However, compound **13j** was an AP with the ability to promote the aggregation by 24.7 ± 1.5 %. Furthermore, the aliphatic ring containing derivatives showed moderate anti-aggregation activities, except for **13g** (R = piperidine) which is a WAM. For example, compound **13f** (R = cyclohexane) showed PI of 21.7 ± 2.6 % and compound **13k** (R = pyrrolidine) showed PI of 24.6 ± 5.3 %. When the R groups were replaced by bicyclic aromatic rings, mixed results were seen regarding their modulatory activities on the aggregation. For example, compounds **13l** (R = naphthalene) and **14a** (R = indole) were WAM, whereas **13m** (R= quinoline) showed pro-aggregation property with the ability to promote the aggregation by 36.8 ± 6.8 %. Interestingly, for compound **14b** (R = benzofuran) and **14c** (R = benzo[*b*]thiophene), these two derivatives exhibited remarkable ability to promote the Aβ42 aggregation. Compound **14b** was able to promote the aggregation by 3.76-fold and **14c** was able to promote the aggregation by 4.12-fold. Given their striking pro-aggregation properties, these two compounds were selected for further evaluation (Section 5.3.2.2).

Table 5-1. Percent inhibition (PI) of *N*-phenylbenzamide and carboxamide derivatives (**13a-m** and **14a-c**), resveratrol (RVT), and chalcone (CHL) at 25 µM on Aβ42 (10 µM) aggregation.

Cmpd	% Inhibition[a]	CLogP[b]	Cmpd	% Inhibition[a]	CLogP[b]
13a	12.14 ± 5.20	2.65	**13i**	9.03 ± 0.64	1.83
13b	12.56 ± 5.04	1.15	**13j**	-24.67 ± 1.51[d]	2.30
13c	-20.20 ± 8.15[d]	1.50	**13k**	24.57 ± 5.27	1.29
13d	NA[c]	2.14	**13l**	NA[c]	3.82
13e	-24.01 ± 6.47[d]	2.87	**13m**	-36.76 ± 6.81	2.89
13f	21.68 ± 2.59	3.19	**14a**	NA[c]	2.98
13g	NA[c]	1.85	**14b**	-376.36 ± 22.08[d]	3.21
13h	20.79 ± 0.59	1.60	**14c**	-412.18 ± 0.74[d]	3.68
RVT	81.3 ± 5.6	2.83	**CHL**	-112.29 ±7.13[d]	3.62

[a] Percent inhibition was calculated at the 24 h time point in the ThT aggregation kinetics assay. The results shown are average ± standard deviation of triplicate readings based on three independent experiments.
[b] CLogP values were calculated with ChemDraw.
[c] NA, not active indicating the compounds are WAM.
[d] Negative PI indicates the compounds can promote the aggregation.

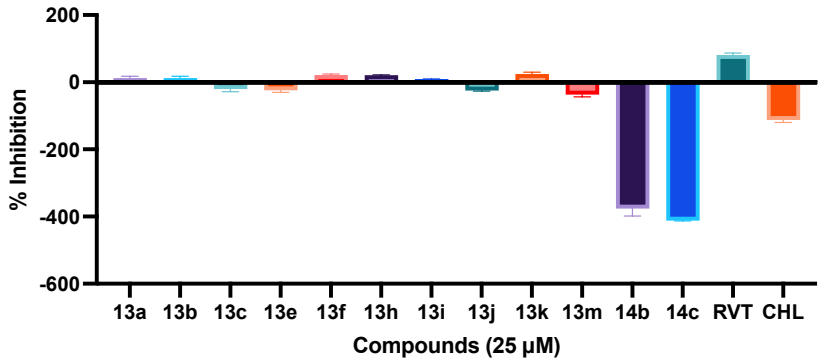


Figure 5-5. Percentage inhibition (PI) of *N*-phenylbenzamide and carboxamide derivatives (**13a-m** and **14a-c**) at 25 µM on Aβ42 (10 µM) aggregation.

5.3.2.2 Modulatory activity of AP **14b** and **14c** on amyloid-beta aggregation

In this sub-section, the pro-aggregation activity of **14b** and **14c** on Aβ42 was explored in more detail. Lead compounds, together with known AI resveratrol (RVT) were tested in ThT aggregation kinetic assays at four different concentrations 1 µM, 5 µM, 10 µM, and 25 µM respectively. To rule out interference in

the ThT assay due to competing fluorescence and or fluorescence quenching, we also ran control experiments to determine if **14b** and **14c** could potentially interfere in the ThT assay. These control experiments were carried out at 25 µM of **14b** and **14c** in the presence of ThT. The results from these control experiments clearly show that both **14ba** and **14c** show no interference in the ThT assay (**Figure 5-6**). Incubation of various concentrations of RVT (1, 5, 10 and 25 µM) with Aβ42, led to a concentration-dependent decline in the ThT RFU, indicating the inhibition of Aβ42 aggregation and fibrillogenesis (**Figure 5-7** C). At 1 µM, RVT exhibited ~15% inhibition of Aβ42 aggregation at 24 h time point which gradually increased to ~34%, 49% and 59% inhibition at 5, 10 and 25 µM respectively. At all the concentrations, RVT was able to reduce Aβ42 fibrillogenesis and fibril load. In contrast, in the presence of **14b**, there was a dramatic increase in the ThT RFU as shown in **Figure 5-7** A. Strikingly there was significant promotion in Aβ42 fibrillogenesis in the presence of 1, 5, 10 and 25 µM of **14b** with the maximum increase in RFU observed at 25 µM. For example, at 1 µM, **14b** was able to increase Aβ42 fibrillogenesis by 1.58-fold followed by a drastic promotion at 5 µM (2.65-fold), 10 µM (4.15-fold) and 25 µM (4.76-fold) respectively (**Figure 5-8**). Similarly, incubation of **14c** with Aβ42 also led to a drastic promotion in Aβ42 fibrillogenesis (**Figure 5-7** B). Compound **14c** promoted Aβ42 fibrillogenesis by a 2.98-fold increase at 1 µM, a 4.35-fold increase at 5 µM, a 4.55-fold increase at 10 µM, and a 5.12-fold increase at 25 µM respectively (**Figure 5-8**). Interestingly, chalcone can also promote the aggregation of Aβ42, however, its pro-aggregation capacity was less dramatic than that of derivatives **14b** and **14c** (**Figure 5-7** D). At lower concentrations (1 and 5 µM), chalcone exhibited limited modulative activity on the aggregation with folds of aggregation around 1-fold in aggregation (**Figure 5-8**). At higher concentrations, there was 1.4 and 2.1-fold in aggregation at 10 µM and 25 µM respectively (**Figure 5-8**). Our results demonstrate that both **14b** and **14c** were able to promote Aβ42 fibrillogenesis and significantly increase the Aβ42 fibril load during the 24 h incubation period (**Figure 5-7** D). This study demonstrates, for the first time, the unique properties of small molecules **14b** and **14c** in modulating Aβ42 aggregation kinetics.

Considering these unusual results, both **14b** and **14c** were further evaluated with additional experiments to better understand the molecular mechanisms of their pro-aggregation activity.

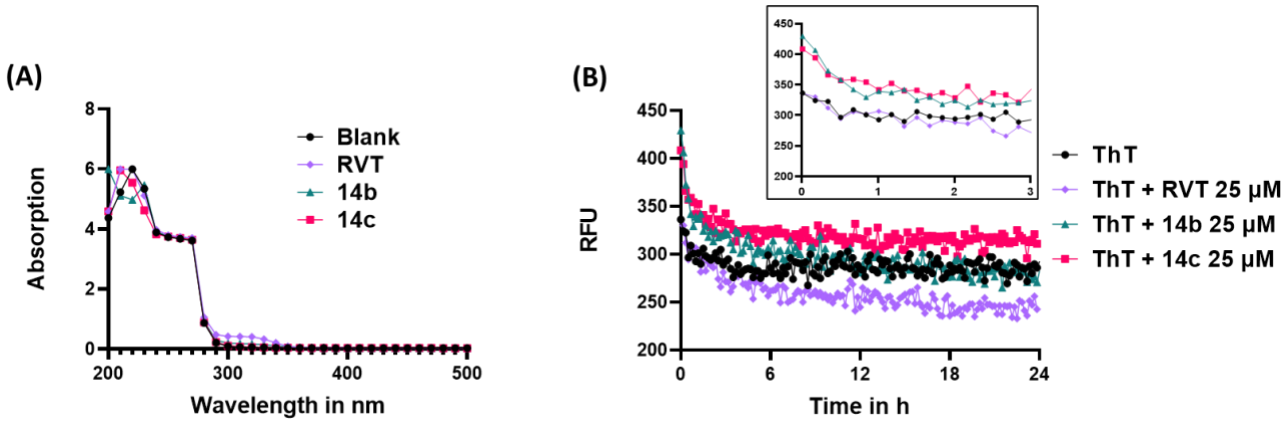


Figure 5-6. Spectrometric background reading of **14b**, **14c**, RVT. (A) ThT-based aggregation kinetics background interference reading. The results presented are the average of two independent experiments in triplicate measurements. (B) UV scanning of assay buffer (blank), **14b**, **14c** and RVT.

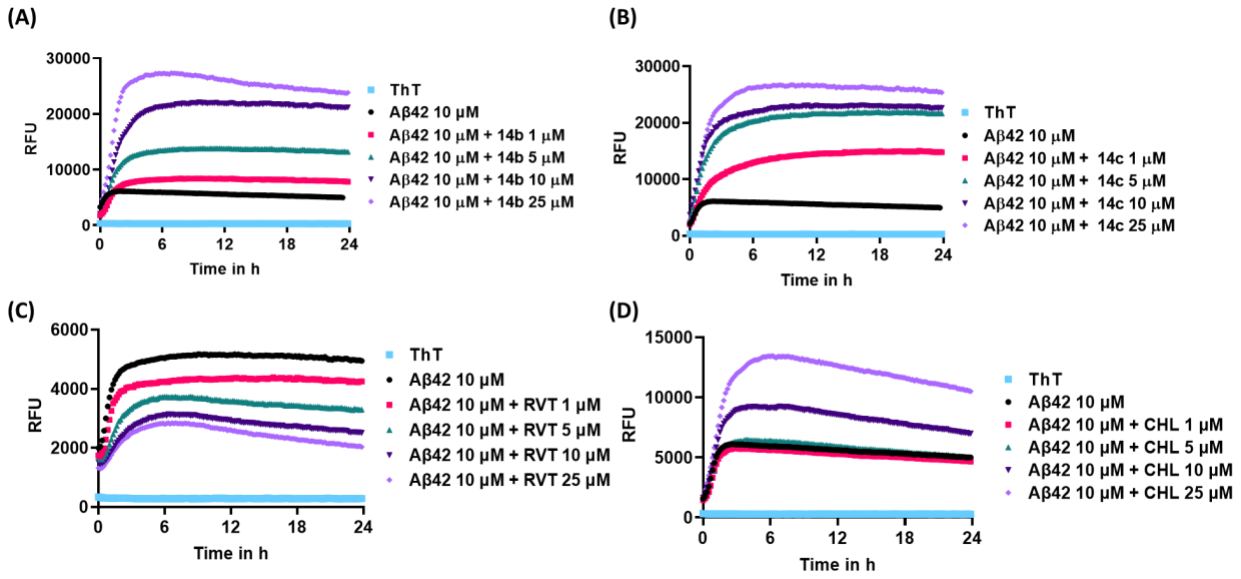


Figure 5-7. ThT-based 24 h aggregation kinetics of Aβ42 (10 μM) in the absence and presence of RVT, **14b** and **14c** at 1, 5, 10, and 25 μM respectively at 37 °C, pH 7.4. (A) Aggregation kinetic curves for **14b**; (B) aggregation kinetics curves for **14c**; (C) aggregation kinetic curves for resveratrol (RVT); (D) aggregation kinetic curves for chalcone (CHL). Aggregation kinetics were monitored by measuring ThT fluorescence (excitation = 440 nm, emission = 490 nm). Results are averages of three independent experiments in triplicate measurements.

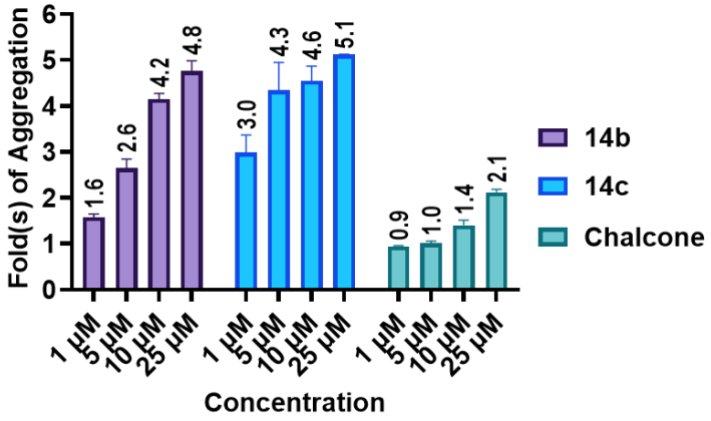


Figure 5-8. Fold(s) of aggregation of lead compounds from *N*-phenylbenzamide and carboxamide derivatives (**14b** and **14c**), and chalcone (CHL) at 1, 5, 10, 25 μM on Aβ42 (10 μM) aggregation.

5.3.3 Transmission electron microscopy of lead AP 14b and 14c

In order to confirm the promotion of Aβ42 fibrillogenesis by **14b** and **14c** observed in the ThT aggregation kinetics assay, transmission electron microscopy (TEM) experiments were carried out by incubating Aβ42 with different concentrations of RVT, **14b** and **14c**, and the fibril morphology was determined. The TEM images obtained after 24 h incubation with Aβ42 are shown in **Figure 5-9** A. In the absence of test compounds, Aβ42 alone underwent aggregation to form typical long, elongated and branched fibrils as can be seen from their morphology. Incubating the known inhibitor RVT at 1, 5, 10 and 25 μM led to a reduction in the formation of Aβ42 aggregates evidenced by a reduction in the density of long and branched Aβ42 fibrils in a concentration-dependent manner with the most drastic reduction seen at 25 μM. In contrast, in the presence of **14b**, the formation of dense fibrils increased proportionately with increasing in the concentration of **14b,** going from 1 μM to 25 μM, with a maximum increase in fibril density seen at 25 μM. Investigating the Aβ42 fibril morphology in the presence of **14c** also demonstrated a similar trend with significant increases in the formation of dense fibrils with increasing concentrations of **14c**. At 25 μM, **14c** was able to promote Aβ42 fibrillogenesis to a significant extent. Next, all of these TEM images were further processed using the Image*J* software to quantify the data as the percentage area covered by the fibrils (**Figure 5-9 B**). In the absence of test compounds, the area covered by Aβ42 fibrils was ~28%. With an increasing concentration of known inhibitor, RVT, co-incubated with Aβ42, the percentage area reduced in concentration-dependently with the percentage reduced from 30% (Aβ42 control) to ~26%, 24%, 21%, 17% at 1, 5, 10, 25 μM respectively. For **14b**, the percentage area increased to ~35%, 40%, 47%, 48% at 1, 5, 10, 25 μM. A similar trend was also observed for **14c**, with a slightly higher percentage area calculated (percentage area ~38%, 46%, 52%, 56% at 1, 5, 10, 25 μM) compared to **14b** at each concentration which is aligned well with ThT aggregation kinetic assay results. In contrast, the chalcone compound exhibited weaker ability to promote the Aβ42 aggregation at all the tested concentrations and the quantitative TEM analysis showed a percentage area of around 28%. These TEM studies further provide evidence of the ability of **14b** and **14c** to promote Aβ42 fibrillogenesis.

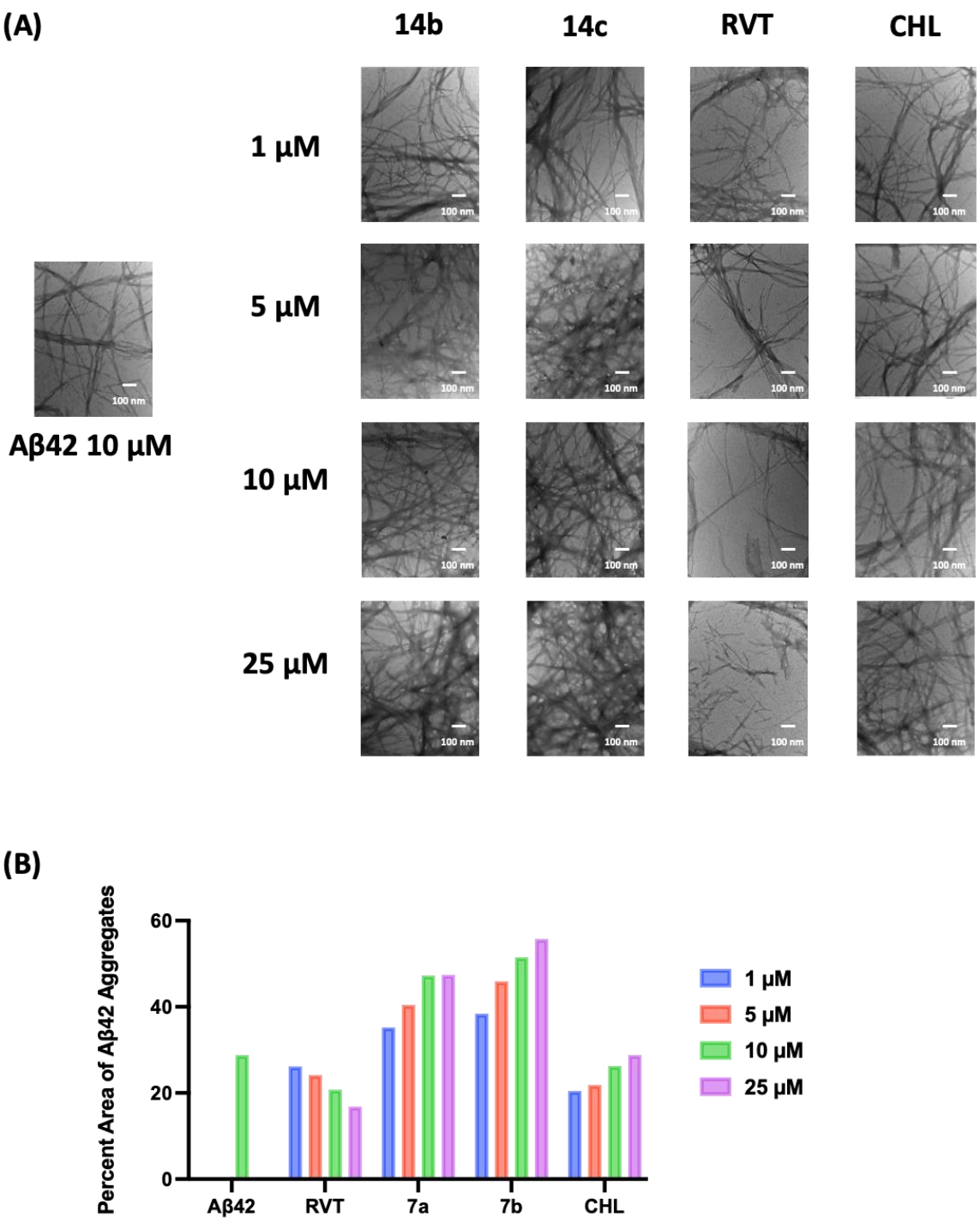


Figure 5-9. TEM images of Aβ42 (10 µM) alone and in the presence of **14b**, **14c**, resveratrol (RVT) and chalcone (CHL) at 1, 5, 10, and 25 µM respectively after 24 h incubation at 37 °C, pH 7.4. (A) TEM image of Aβ42 in the absence and presence of RVT, 7a and 7b at 1, 5, 10, and 25 µM respectively. (B) Quantification of TEM images of Aβ42 in the absence and presence of **14b**, **14c**, RVT, and CHL at 1, 5, 10, and 25 µM respectively. The images were analyzed by ImageJ and the percentage area covered by fibrils was measured. Image Scale: 100 nm.

5.3.4 8-Anilino-1-naphthalene sulfonicacid binding assay

Due to the striking promotion in Aβ42 fibrillogenesis observed in the ThT aggregation kinetics studies, we investigated the effect of **14b** and **14c** on 8-anilino-1-naphthalenesulfonic acid (ANS) fluorescence, to probe the ability of these compounds to expose the hydrophobic regions of Aβ42 aggregates. This helps to understand the mechanisms of the promotion of fibrillogenesis in the presence of **14b** and **14c**. In phosphate buffer solution, ANS exhibited an emission maximum at around 520 nm along with weak fluorescence intensity (RFU ~ 0.17, **Figure 5-10**). In the presence of Aβ42 fibrils, there was a clear blue shift with the emission maximum moving to 490 nm and a ~2-fold jump in the RFU (**Figure 5-10**), demonstrating the formation of Aβ42 aggregates with exposed ANS binding sites. In the presence of known inhibitor RVT, the RFU decreased in a concentration-dependent manner across the concentration range tested (1, 5, 10 and 25 μM), with the lowest reading observed 25 μM (**Figure 5-10** C). There was no change in the emission maximum (490 nm) which suggests that RVT was able to reduce Aβ42 fibrillogenesis as seen in the ThT assay. In contrast, in the presence of either **14b** or **14c**, the fluorescent intensity of ANS showed a significant concentration-dependent increase compared to Aβ42 control. The fluorescent intensity of ANS was increased by 1.4-fold (RFU = 0.51,) in the presence of **14b** (25 μM, **Figure 5-10** A) compared to Aβ42 control, whereas the fluorescent intensity of ANS was increased by 1.3-fold (RFU = 0.46) in the presence of **14c** (25 μM, **Figure 5-10** B). There was no change in the emission maximum (490 nm). This clearly shows that both compounds **14b** and **14c** are able to bind and modulate the conformation of Aβ42 aggregates thereby exposing additional ANS binding hydrophobic surface. Similarly, in order to rule out fluorescence interference arising from compounds, we conducted control experiments with 25 μM **14b** and **14c** in the presence of ANS. The results indicate that none of the compounds showed interference in the ANS assay (**Figure 5-11** A). Inspired by these results, we were curious to see what other information the ANS binding assay could tell at an early stage of the aggregation process. Therefore, the assay was conducted at time points 0 h, 1 h, and 8 h during the aggregation with the hope of investigating the hydrophobic feature of Aβ monomer, oligomer, and early immature fibrils. Interestingly, we did not observe

significant differences in the ANS FLR between groups at these time points (**Figure 5-11** B-D), indicating that **14b** and **14c** might interact with higher order fibrils, such as protofibrils and fibrils, and thus expose their hydrophobic surface to form much more stable and less toxic/nontoxic fibrils.

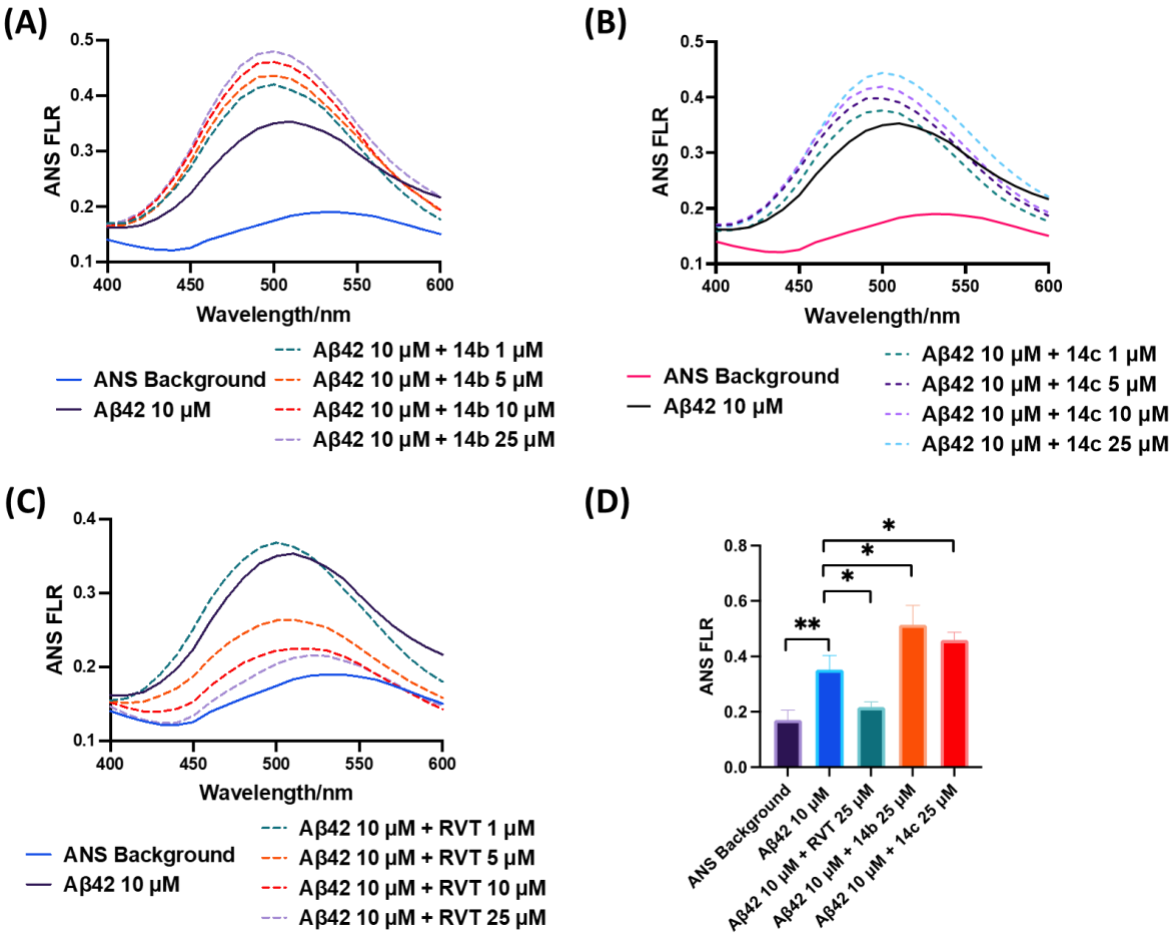


Figure 5-10. ANS binding assay of **14b**, **14c**, and RVT with Aβ42 (10 μM) at 1, 5, 10, and 25 μM respectively after 24 h incubation at 37 °C, pH 7.4. The ANS fluorescence readings were taken at excitation 380 nm, emission 400 nm to 600 nm with 10 nm increments. Results are averages of three independent experiments in triplicate measurements. (A) ANS spectrum of **14b** in the presence of Aβ42; (B) ANS spectrum of **14c** in the presence of Aβ42; (C) ANS spectrum of RVT in the presence of Aβ42; (D) Comparison of ANS fluorescence reading of **14b**, **14c**, and RVT (25 μM) at 490 nm in the presence of Aβ42. *p < 0.01 compared to Aβ42 control group, **p < 0.01 compared to Aβ42 control group (one-way ANOVA).

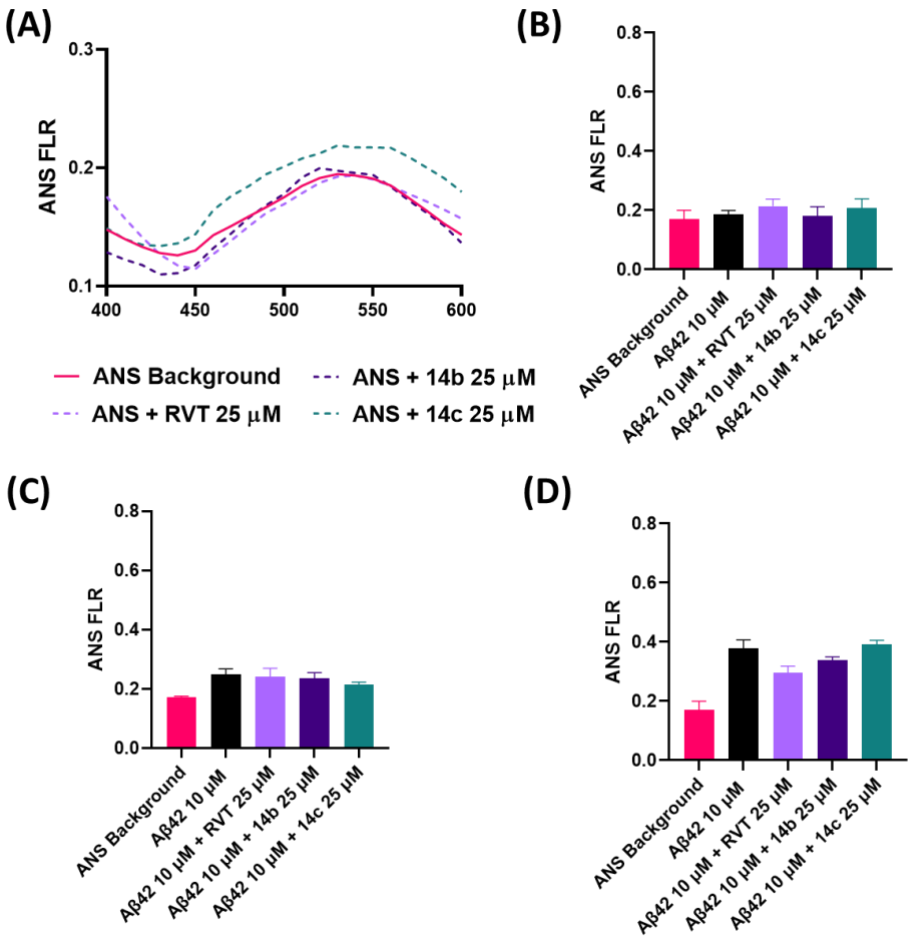


Figure 5-11. ANS binding assay of **14b**, **14c**, and RVT with Aβ42 (10 µM) at 1, 5, 10, and 25 µM respectively incubated at 37 °C, pH 7.4. The ANS fluorescence readings were taken at excitation 380 nm, emission 400 nm to 600 nm with 10 nm increments. Results are averages of three independent experiments in triplicate measurements. (A) ANS background readings in the absence of Aβ42; (B) ANS binding assay of Aβ42 at 0 h; (C) ANS binding assay of Aβ42 at 1 h; (D) ANS binding assay of Aβ42 at 8 h.

5.3.5 Neuroprotective effects against Aβ42-induced cytotoxicity

The discovery of Aβ42 pro-aggregation activity of **14b** and **14c** in the ThT fluorescence assay and TEM studies led us to investigate the effects of these two compounds in Aβ42-induced cytotoxicity in mouse hippocampal HT22 neuronal cells. The known Aβ aggregation inhibitor RVT was used as a reference agent for comparison. Initially, the effect of **14b**, **14c** and RVT (25 µM each) alone, toward HT22 cells was evaluated. None of the compounds showed any toxicity and they were able to maintain excellent cell

viability after 48 h of incubation (**Figure 5-12** A). Next, treating the cells with Aβ42 (20 μM) for 48 h, led to significant cell death (~20% cell viability, **Figure 5-13** A). In contrast, incubating the Aβ42 treated HT22 cells with either **14b** or **14c** (25 μM each), led to a dramatic increase in cell viability. Both **14b** and **14c** were able to rescue HT22 hippocampal cells from Aβ42-induced cytotoxicity (**Figure 5-13** A). Both **14b** and **14c** exhibited ~74% cell viability in the presence of Aβ42, a ~2.96–fold increase in cell viability compared with Aβ42 treated group (~20% cell viability). The reference compound, Aβ42 aggregation inhibitor RVT, was also able to rescue HT22 hippocampal cells from Aβ42-induced cytotoxicity (~30% cell viability, **Figure 5-13** A). However, it was not effective as **14b** and **14c**. These results suggest that both **14b** and **14c** are able to modulate the conformation of Aβ42 and promote the formation of nontoxic aggregates in the cellular environment further demonstrating their ability to modify the toxic Aβ42 aggregates into less toxic/nontoxic forms.

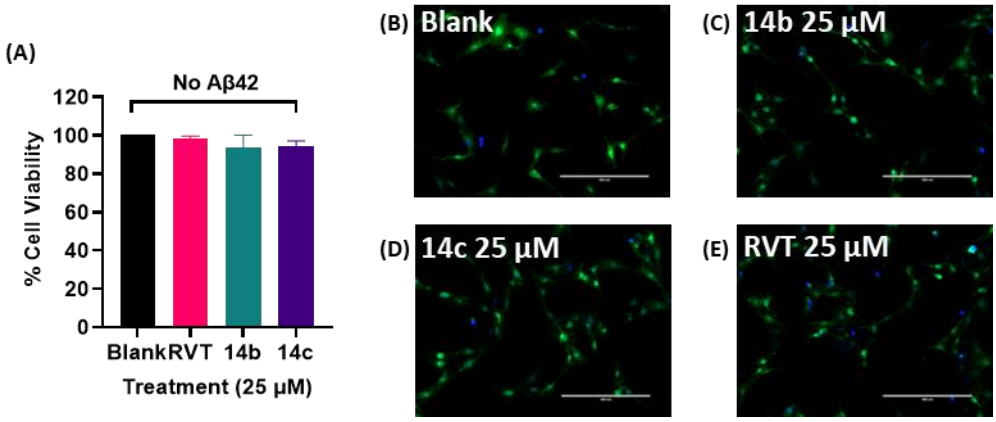


Figure 5-12. (A) Neuroprotective effects of **14b**, **14c**, and RVT at 25 μM on HT22 cells without Aβ42 after 48 h incubation. The cell viability was determined by cell counting kit-8 (CCK-8). The results are averages of three independent experiments with 5 replicates in each run. (B-E) Fluorescence cell imaging in the absence of Aβ42. Cell membranes were stained by Bio Tracker 490 and visualized with GFP filter; cell nuclei were stained by Hoechst 33342 and visualized with DAPI filter. (B) Untreated cell; (C) **14b** at 25 μM; (D) **14c** at 25 μM; (E) **RVT** at 25 μM. Image scale: 200 μm.

Live cell imaging studies were also carried out to determine the effect of **14b** and **14c** in HT22 cells incubated with Aβ42. The cell membrane was stained with BioTracker 490 dye, the nucleus was stained with Hoechst 33342 dye and Aβ42 aggregates were visualized using the ProteoStat® dye. Treating HT22 cells with **14b** or **14c** or RVT (25 μM) alone did not affect their viability or morphology as the green fluorescence of star-shaped cells and dendritic outgrowths were clearly visible (**Figure 5-12** B-E). The nucleus of neuronal cells was also observed (blue stain). These imaging studies demonstrate that the HT22 cells were in a healthy state when treated with **14b** or **14c** or RVT after 48 h incubation. Fluorescence images of HT22 cells treated with Aβ42 (20 μM) alone for a period of 48 h demonstrated significant cytotoxicity as the green fluorescence was barely visible, which indicates the loss of membrane integrity and cell death (**Figure 5-13** C). In addition, Aβ42 aggregates stained by ProteoStat® were visible. Strikingly, in the presence of either **14b** or **14c** (25 μM each), merged fluorescence images clearly show the presence of healthy neuronal cells treated with Aβ42 as indicated by the observation of green fluorescence signals demonstrating cell membrane integrity and the presence of star-shaped cells (**Figure 5-13** D, E).

Furthermore, fluorescence imaging studies also showed that **14b** and **14c** were also able to promote the formation of Aβ42 aggregates as seen with increases in the amount of ProteoStat® positive stains compared to cells treated with Aβ42 alone. This further demonstrates the ability of compounds **14b** and **14c** to promote Aβ42 fibrillogenesis and the formation of nontoxic aggregates. Fluorescence imaging studies also show that RVT was able to offer weaker neuroprotection to HT22 cells treated with Aβ42 compared to **14b** and **14c** (**Figure 5-13** E). These imaging studies further demonstrate the neuroprotective effects of compounds **14b** and **14c** in reducing Aβ42-induced cytotoxicity. In the next step, we quantified the fluorescence intensity data obtained (**Figure 5-13** C-F), using the ImageJ software and correlated this data with cell viability profile for HT22 cells treated with Aβ42, **14b**, **14c** and RVT. The results are summarized in **Figure 5-13** B and **Table 5.2**. The cells were treated with test compounds in the presence and absence of Aβ42 for 48 h before imaging. The amount of Aβ42 aggregates formed in HT22 cells after 48 h incubation period was quantified by measuring the pixel intensity of ProteoStat® stains. The amount of aggregates formed is directly proportional to ProteoStat® fluorescence intensity and was reported as relative mean intensity (RMI). Greater the RMI, greater is the formation of Aβ42 aggregates. The RMI for Aβ42 treated control group was 11.83 ± 2.68 and this correlates with a significant loss of cell viability (~20% cell viability). The pro-aggregation activity of **14b** and **14c** was indicated by 2.2- and 1.9-fold increases in the RMI values (RMI = 26.4 ± 1.7 and 22.9 ± 2.6) and these correlate with an increase in cell viability (~70% cell viability). In contrast, the known aggregation inhibitor RVT was able to reduce RMI value (RMI = 7.6 ± 1.1) compared to Aβ42-treated control group and this correlates with its ability to inhibit Aβ42 aggregation and reduce cytotoxicity (~30% cell viability). These biophysical, cell culture and fluorescence imaging experiments demonstrate the pro-aggregation and neuroprotective properties of compounds **14b** and **14c**.

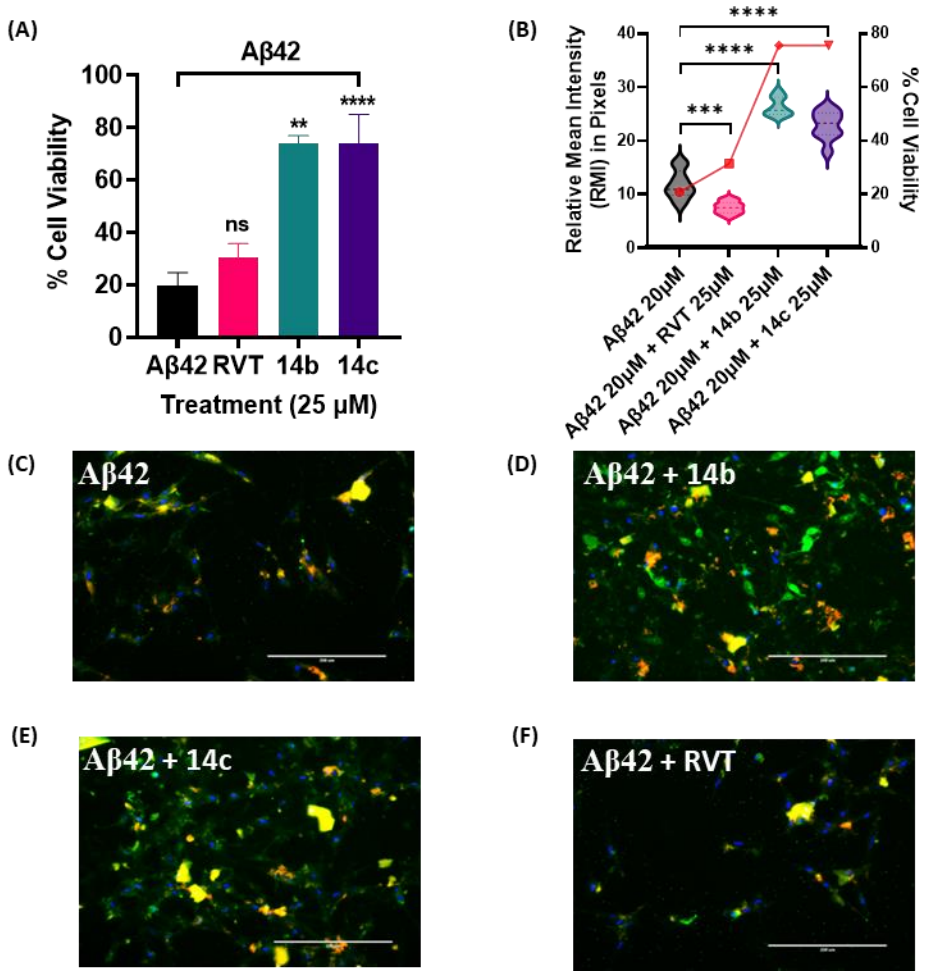


Figure 5-13. (A) Neuroprotective effects of **14b**, **14c**, and RVT at 25 μM on HT22 cells in the presence of Aβ42 (20 μM) after 48 h incubation. The cell viability was determined by cell counting kit-8 (CCK-8). The results are averages of three independent experiments with five replicates in each run. (B) Quantitative fluorescence cell imaging of ProteoStat® measured by relative mean pixel intensity (left y-axis, violin chart) in the absence and presence of **14b**, **14c**, and RVT (25 μM). The data is correlated with cell viability (right y-axis, line chart in red). The results presented are averages of three independent experiments from three randomized views. ns = not significant, *$p < 0.01$ compared to Aβ42 control group, **$p < 0.01$ compared to Aβ42 control group, ***$p < 0.01$ compared to Aβ42 control group, ****$p < 0.01$ compared to Aβ42 control group (one-way ANOVA followed by Bonferroni post hoc test). (C-F) Merged fluorescence images of HT22 cells in the presence of Aβ42 (20 μM). Cell membranes were stained by BioTracker 490 green, cell nucleus was stained blue with Hoechst 33342 and Aβ42 aggregates were stained by ProteoStat® dye. (C) Aβ42 treated cells; (D) Aβ42 + **14b** at 25 μM; (E) Aβ42 + **14c** at 25 μM; (F) Aβ42 + **RVT** at 25 μM; Image scale: 200 μm.

Table 5-2. Relative mean pixel intensity of RFP channel (ProteoStat®). The results were taken from 3 random views of 3 independent studies. Quantification was carried out using the Image*J* software.

	Aβ	**Aβ + 14b**	**Aβ + 14c**	**Aβ + RVT**
	8.17	24.56	20.93	9.28
	9.26	25.16	17.99	6.68
	10.45	29.27	21.66	8.11
	10.71	24.76	24.18	8.10
	10.96	25.25	26.15	6.52
	12.13	25.70	21.47	7.20
	13.20	28.17	23.29	5.89
	15.61	28.15	24.70	7.50
	16.00	26.55	25.77	8.90
AVE	**11.83**	**26.40**	**22.90**	**7.58**
STD	**2.68**	**1.73**	**2.63**	**1.13**

5.3.6 Molecular docking

In order to understand the pro-aggregation properties of **14b** and **14c**, their binding interactions with Aβ42 oligomer and fibril models were investigated by conducting molecular docking studies. The pentamer and fibril models for docking studies were derived from the solved structure of Aβ42 (PDB ID: 5KK3). This study used solid-state NMR to obtain the structure of monomorphic Aβ42 fibrils. This was one of the first report, that showed that the Aβ42 fibrils have S-shape/geometry and are a very relevant structure to model and study the interactions of novel molecules with Aβ42 aggregates. The pentamer model was prepared using the Aβ42 fibril assembly. The molecular docking studies carried out using the CDOCKER algorithm shows that both **14b** and **14c** bind to Aβ42 pentamer in a similar fashion (**Figure 5-14**). The top binding pose of **14b** (CDOCKER energy –20.53 kcal/mol, CDOCKER interaction energy –28.26 kcal/mol) and **14c** (CDOCKER energy –15.42 kcal/mol, CDOCKER interaction energy –25.77 kcal/mol) were further analyzed to study their interactions with Aβ42. Interestingly, both **14b** and **14c** bind to Aβ42 pentamer in the hydrophobic area consisting of Leu17 at N-terminus and Leu34 at C-terminus. Both compounds were oriented perpendicular to the pentamer axis and were primarily interacting with amino acids residues that

covers three out of the five strands. These interactions were mostly via hydrophobic and van der Waals contacts. As shown in **Figure 5-15** A-B, the benzofuran ring of **14b** underwent pi-alkyl interactions with chain C: Leu34 (distance ~ 5.0 Å), C: Leu17 (distance ~ 5.0 Å), and benzene ring with chain A: Leu17 (distance ~ 5.0 Å). For **14c**, the benzo[*b*]thiophene ring underwent pi-alkyl interactions with the chain B: Leu17 (distance = 4.6 Å, distance ~ 5.0 Å), chain A: Leu17 (distance < 5.0 Å), and chain B: Leu34 (distance ~ 5.0 Å) (Figure 7B). The benzene ring of **14c** also underwent similar pi-alkyl interactions with chain C: Leu34 (distance ~ 5.0 Å) (**Figure 5-15** C-D).

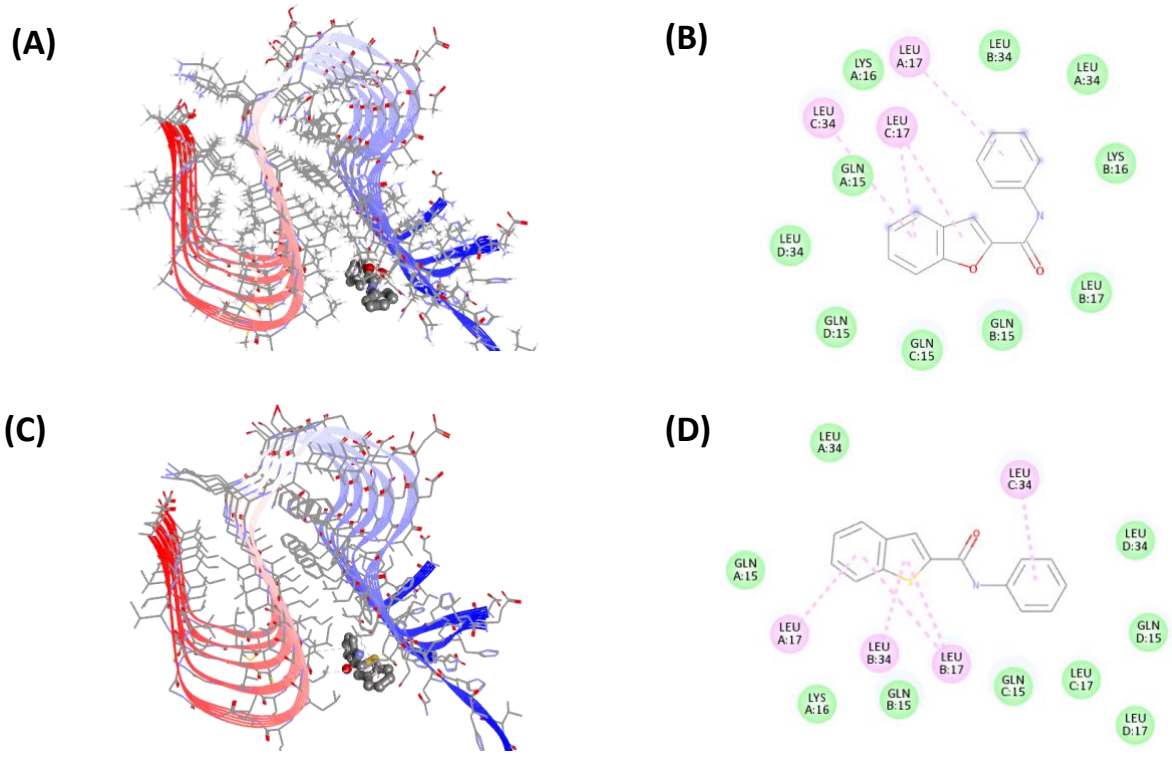


Figure 5-14. Molecular docking studies of **14b** and **14c** in Aβ42 pentamer model (PDB ID: 5KK3). (A) top docked pose of **14b**; (B) 2D interaction map of the top docking pose of **14b**; (C) top docked pose of **14c**; (D) 2D interaction map of the top docking pose of **14c**. The Aβ42 chains are color-coded with blue indicating N-terminal and red indicating C-terminal. The hydrogen atoms are removed to enhance clarity.

Similarly, the binding interactions of **14b** and **14c** with the Aβ42 fibril model were investigated using the CDOCKER algorithm. Interestingly, the most striking difference between the Aβ42 fibril and the Aβ42 pentamer model is the presence of a cross-β spine in the Aβ42 fibril. It is formed between the adjacent

hydrophobic regions along the long axis of two fibrils. These two fibril chains are aligned symmetrically and form the in-registry cross-β spine (**Figure 5-15**). This provides molecular basis for the fibril to grow both in length and thickness. Two hydrophobic domains within the amino acids sequence of Aβ42 were identified, ^{16}KLVFFA^{21} and ^{32}IGLMVGGVVIA^{42} respectively. These regions are involved in initiating the aggregation process.[19, 59] The conformations of these hydrophobic surfaces are complementary which promotes their interaction and aggregation. The cross-β spine structure of Aβ42 fibrils constrains small molecules to move in between fibril chains due to the tight packing. In the Aβ42 fibril assembly, the top ranked binding pose of **14b** (CDOCKER energy –14.66 kcal/mol, CDOCKER interaction energy –21.61 kcal/mol) and that of **14c** (CDOCKER energy –9.77 kcal/mol, CDOCKER interaction energy –20.15 kcal/mol) were mainly interacting in the ^{16}KLVFFA^{21} region (**Figure 5-15** A, C). For **14b**, the benzofuran ring underwent pi-alkyl interactions with chain C: Ala21 (distance < 5.0 Å), and C: Val18 (distance < 5.0 Å) (**Figure 5-15** B). Interestingly, stronger electrostatic and hydrogen bonding interactions were also observed which was not seen in the Aβ42 pentamer model. The benzene ring of **14b** interacted with NH_3^+ of D: Lys16 (distance < 5.0 Å) via a stabilizing pi-cation electrostatic interaction, whereas the oxygen atom of the amide bond underwent a hydrogen bonding interaction with the nitrogen atom of chain C: Lys16 (distance < 2.0 Å). The binding mode of **14c** to Aβ42 fibrils was more or less the same with **14b** slightly further away from the fibril center (**Figure 5-15** C-D). Compound **14b** was anchored by the pi-alkyl type hydrophobic interactions between the benzene ring and chain C: Ala21 (distance < 5.0 Å), and chain C: Val18 (distance < 5.0 Å). This was facilitated by the hydrogen bonding interaction between the oxygen atom of the amide bond and the nitrogen of C: Lys16 (distance < 2.0 Å). The benzo[*b*]thiophene ring of **14c** was in contact with chain B: Val12 (distance < 5.0 Å) via pi-alkyl interactions (Figure 8D). These computational studies suggest that **14b** and **14c** can bind and interact with both Aβ42 oligomers and fibrils. Furthermore, experimental evidence from the ANS assay (**Figure 5-11**) shows that upon **14b** and **14c** binding, the hydrophobic surface of Aβ42 (e.g., KLVFFA and C-terminal regions) does get exposed to the solvent which promotes their rapid self-assembly and fibrillogenesis.

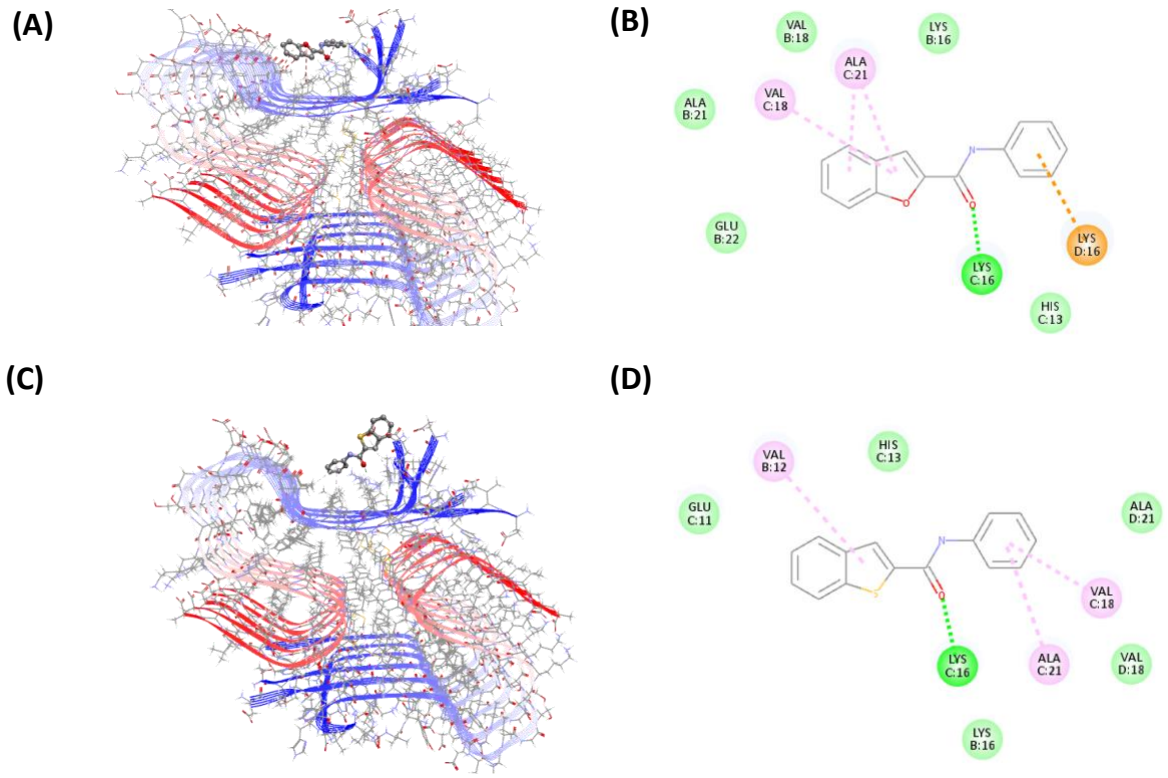


Figure 5-15. Molecular docking studies of **14b** and **14c** in the Aβ42 fibril model (PDB ID: 5KK3). The hydrogen atoms are removed to enhance clarity. (A) Top docked pose of **14b**; (B) 2D interaction map of the top docking pose of **14b**; (C) top docked pose of **14c**; (D) 2D interaction map of the top docking pose of **14c**. The Aβ42 chains are color coded with blue indicating N-terminal and red indicating C-terminal. The hydrogen atoms are removed to enhance clarity.

Previous studies on Aβ42 aggregation have shown that the ^{16}KLVFFAE^{22} and the C-terminal ^{29}GAIIGLMVGGVVIA^{42} regions exhibit faster aggregation propensities.[60] Both compounds **14b** and **14c** contain planar aromatic bicyclic ring systems (either a benzofuran or a benzothiophene ring) along with a phenyl ring. Molecular docking studies show that the aromatic bicyclic and the phenyl rings present in these two compounds can undergo π-alkyl interactions with nonpolar amino acids including Leu17, Val18, Al21 and Leu34. These amino acids are part of the aggregation-prone regions of Aβ42. This suggests that the binding of **14b** and **14c** can increase the surface hydrophobicity of Aβ42 aggregates to favor the association of hydrophobic regions of Aβ42 leading to an acceleration of fibrillogenesis. Furthermore, Bieschke and

coworkers, suggested that small molecules that are able to bind in the hydrophobic regions of Aβ42 can promote the conversion of oligomers into fibril by increasing the surface hydrophobicity.[33] These previous literature evidence suggest that small molecules **14b** and **14c** have the potential to increase the surface hydrophobicity of Aβ42 aggregates due to the presence of planar aromatic rings, and are able to remodel the Aβ42 aggregation and fibrillogensis pathway to form less toxic or nontoxic β-sheet assemblies as shown in **Figure 5-16**. This also suggests that these compounds have the potential to act as chemical chaperones that can modulate the Aβ42 aggregation and misfolding pathways.[33, 61] Our findings warrant further structure-activity relationship studies to determine the structural requirements to design and develop novel Aβ42 aggregation modulators.

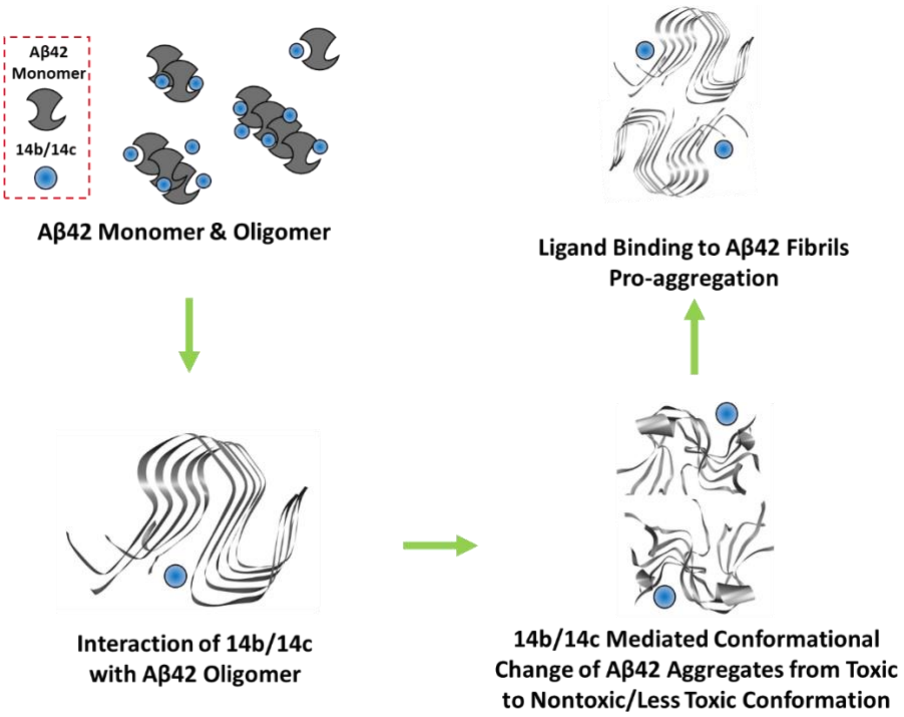


Figure 5-16. Proposed mechanism of **14b** and **14c** promoted Aβ42 fibrillogenesis.

5.3.7 Synthesis and evaluation of *N*-(substitutedphenyl)benzofuran and benzo[*b*]thiophene-2-carboxamide derivatives (16a-d and 17a-d) as amyloid-beta aggregation modulators

5.3.7.1 Synthesis

Based on the surprising results obtained for compounds **14b** (*N*-benzylbenzofuran-2-carboxamide) and **14c** (*N*-benzylbenzo[*b*]thiophene-2-carboxamide), where they were able to promote Aβ42 fibrillogenesis and demonstrated neuroprotective effects against Aβ42-induced toxicity, we wanted to expand the SAR of this class of compounds to understand the pro- and anti-aggregation mechanisms by incorporating additional substituents on the *N*-phenyl ring (e.g., anisole, 2-methoxyphenol, 1,2-dimethoxybenzene) and synthesized 8 additional compounds **16a-d** and **17a-d** (**Figure 5-17**) by coupling the respective acids with the aniline derivatives as per the previously described method (section 5.3.1, **Scheme 5-3**). The overall yields of these reactions range from 72.3-89.2%. Their analytical data (^{1}H NMR, MS and LCMS purity) are given below. Analytical spectral data for all the final compounds are given in **Appendix D**.

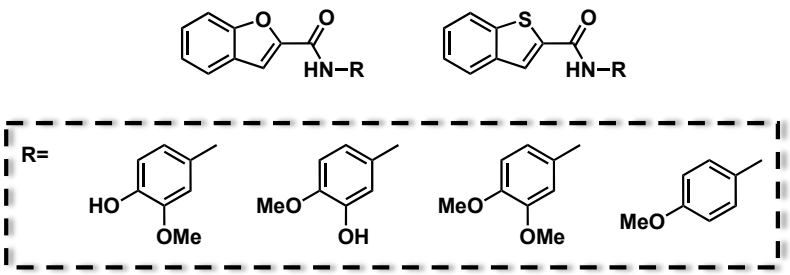
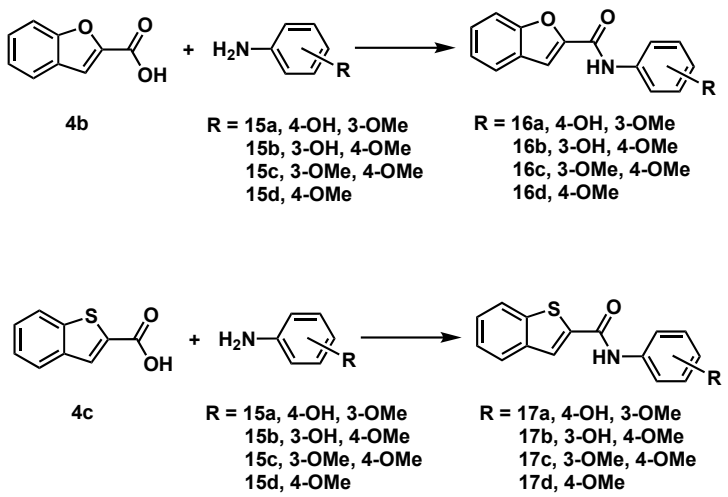


Figure 5-17. *N*-(Substitutedphenyl)benzofuran and benzo[*b*]thiophene derivatives.



Scheme 5-3. Synthetic scheme to prepare **16a-d** and **16a-d** by coupling aniline derivatives (**15a-d**) with corresponding carboxylic acids (**4b-c**). Reagents and conditions: EDC•HCl, HOBt, TEA, THF, room temperature overnight.

5.3.7.1.1 *N*-(4-hydroxy-3-methoxyphenyl)benzofuran-2-carboxamide (**16a**)

The product was obtained as a yellow solid (Yield = 86.5%). ^{1}H NMR (300 MHz, $CDCl_3$) δ 8.25 (s, 1H), 7.73 – 7.66 (m, 2H), 7.58 – 7.52 (m, 2H), 7.44 (ddd, *J* = 8.5, 7.2, 1.4 Hz, 1H), 7.31 (ddd, *J* = 8.0, 7.2, 1.1 Hz, 1H), 6.91 – 6.87 (m, 2H), 5.51 (s, 1H), 3.94 (s, 3H). ^{13}C NMR (75 MHz, DMSO) δ 156.62, 154.84, 149.60, 147.65, 143.69, 130.78, 127.69, 127.43, 124.26, 123.29, 115.57, 113.69, 112.34, 110.53, 106.49, 56.01. mp: 185-188 °C. ESI-MS, m/z calcd for $C_{16}H_{13}NO_4$ $[M+H]^+$ 284.1, found 284.0. Purity: 95.39% (LCMS).

5.3.7.1.2 *N*-(3-hydroxy-4-methoxyphenyl)benzofuran-2-carboxamide (**16b**)

The product was obtained as a yellow solid (Yield = 80.9%). ^{1}H NMR (300 MHz, DMSO) δ 10.25 (s, 1H), 9.08 (s, 1H), 7.81 – 7.74 (m, 1H), 7.70 – 7.64 (m, 2H), 7.50 – 7.42 (m, 1H), 7.36 – 7.28 (m, 2H), 7.14 (dd, *J* = 8.7, 2.5 Hz, 1H), 6.86 (d, *J* = 8.7 Hz, 1H), 3.72 (s, 3H). mp: 125-38 °C. ESI-MS, m/z calcd for $C_{16}H_{13}NO_4$ $[M+H]^+$ 284.1, found 284.0. Purity: 94.29% (LCMS).

5.3.7.1.3 *N*-(3,4-dimethoxyphenyl)benzofuran-2-carboxamide (**16c**)

The product was obtained as a yellow solid (Yield = 79.8%). ^{1}H NMR (300 MHz, $CDCl_3$) δ 8.26 (s, 1H), 7.70 (d, *J* = 7.7 Hz, 1H), 7.59 – 7.52 (m, 3H), 7.50 – 7.39 (m, 1H), 7.35 – 7.27 (m, 1H), 7.07 (dd, *J* = 8.6, 2.5 Hz, 1H), 6.92 – 6.82 (m, 1H), 3.93 (s, 3H), 3.88 (s, 3H). mp: 129-132 °C. ESI-MS, m/z calcd for $C_{17}H_{15}NO_4$ $[M+H]^+$ 298.1, found 298.0. Purity: 95.89% (LCMS).

5.3.7.1.4 *N*-(4-methoxyphenyl)benzofuran-2-carboxamide (**16d**)

The product was obtained as a yellow solid (Yield = 82.4%). ^{1}H NMR (300 MHz, DMSO) δ 10.40 (s, 1H), 7.83 – 7.75 (m, 1H), 7.73 – 7.62 (m, 4H), 7.47 (ddd, *J* = 8.6, 7.2, 1.3 Hz, 1H), 7.37 – 7.29 (m, 1H), 6.95 – 6.88 (m, 2H), 3.72 (s, 3H). mp: 156-159°C. ESI-MS, m/z calcd for $C_{16}H_{13}NO_3$ $[M+H]^+$ 268.1, found 268.0. Purity: 98.72% (LCMS).

5.3.7.1.5 *N*-(4-hydroxy-3-methoxyphenyl)benzo[*b*]thiophene-2-carboxamide (**17a**)

The product was obtained as a yellow solid (Yield = 72.3%). ^{1}H NMR (300 MHz, $CDCl_3$) δ 7.89 – 7.82 (m, 2H), 7.73 (s, 1H), 7.62 (d, *J* = 2.4 Hz, 1H), 7.49 – 7.36 (m, 2H), 6.88 (d, *J* = 8.5 Hz, 1H), 6.79 (dd, *J* = 8.5, 2.4 Hz, 1H), 5.52 (s, 1H), 3.92 (s, 3H). ^{13}C NMR (75 MHz, DMSO) δ 160.21, 147.68, 143.60, 140.96, 140.83, 139.67, 131.04, 126.81, 125.75, 125.63, 125.48, 123.31, 115.62, 113.49, 106.27, 55.99. mp: 182-185 °C. ESI-MS, m/z calcd for $C_{16}H_{13}NO_3S$ $[M+H]^+$ 300.1, found 300.0. Purity: 97.92% (LCMS).

5.3.7.1.6 *N*-(3-hydroxy-4-methoxyphenyl)benzo[*b*]thiophene-2-carboxamide (**17b**)

The product was obtained as a yellow solid (Yield = 72.7%). ^{1}H NMR (300 MHz, DMSO) δ 10.25 (s, 1H), 9.09 (s, 1H), 8.29 – 8.26 (m, 1H), 8.06 – 7.89 (m, 2H), 7.49 – 7.38 (m, 2H), 7.28 (d, *J* = 2.5 Hz, 1H), 7.11 (dd, *J* = 8.7, 2.5 Hz, 1H), 6.87 (d, *J* = 8.8 Hz, 1H), 3.72 (s, 3H). ^{13}C NMR (75 MHz, DMSO) δ 160.27, 146.84, 144.84, 140.93, 140.84, 139.66, 132.54, 126.81, 125.78, 125.77, 125.47, 123.29, 112.81, 111.64,

109.24, 56.31. mp: 170-173 °C. ESI-MS, m/z calcd for $C_{16}H_{13}NO_3S$ $[M+H]^+$ 300.1, found 299.9. Purity: 96.93% (LCMS).

5.3.7.1.7 *N*-(3,4-dimethoxyphenyl)benzo[*b*]thiophene-2-carboxamide (**17c**)

The product was obtained as a yellow solid (Yield = 75.5%). ^{1}H NMR (300 MHz, $CDCl_3$) δ 7.91 – 7.81 (m, 3H), 7.76 (s, 1H), 7.48 (s, 1H), 7.46 – 7.37 (m, 2H), 7.01 – 6.94 (m, 1H), 6.87 – 6.80 (m, 1H), 3.90 (s, 3H), 3.87 (s, 3H). mp: 181-184 °C. ESI-MS, m/z calcd for $C_{17}H_{15}NO_3S$ $[M+H]^+$ 313.1, found 314.0. Purity: 95.89% (LCMS).

5.3.7.1.8 *N*-(4-methoxyphenyl)benzo[*b*]thiophene-2-carboxamide (**17d**)

The product was obtained as a yellow solid (Yield = 89.2%). ^{1}H NMR (300 MHz, $CDCl_3$) δ 7.91 – 7.83 (m, 3H), 7.68 (s, 1H), 7.55 (s, 1H), 7.52 (s, 1H), 7.48 – 7.37 (m, 2H), 6.94 – 6.91 (m, 1H), 6.90 – 6.87 (m, 1H), 3.81 (s, 3H). mp: 185-188 °C. ESI-MS, m/z calcd for $C_{16}H_{13}NO_2S$ $[M+H]^+$ 283.1, found 284.0. Purity: 97.85% (LCMS).

5.3.7.2 Effect of compounds 16a-d and 17a-d on Aβ42 aggregation

The *N*-(substitutedphenyl)benzofuran and benzo[*b*]thiophene-2-carboxamide derivatives **16a-d** and **17a-d** were tested at 1 µM, 5 µM, 10 µM and 25 µM in the ThT-based aggregation kinetic study to determine their Aβ42 modulating properties. The presence of either a 4-hydroxy-3-methoxyphenyl or a 3-hydroxy-4-methoxyphenyl substituent (compounds **16a** and **16b** respectively) led to inhibition of Aβ42 aggregation as indicated by the decline in the RFU. They also exhibited a concentration-dependent inhibition of Aβ42 aggregation (**Figure 5-18** A, B). At 1 µM, **16a** was able to reduce the fibril load by ~26%, whereas a 47% PI was seen at 10 µM. However, when the Aβ42 was treated with higher concentrations of **16a**, the PI

seemed to reach saturation with ~54% inhibition at 10 µM and ~53% at 25 µM (**Table 5-3**). The corresponding regioisomer **16b**, showed a similar trend with PI ~21%, 41%, 51%, and 51% inhibition seen at 1 µM, 5 µM, 10 µM and 25 µM. At all concentrations, these two derivatives were able to reduce the formation of Aβ42 fibrils (**Table 5-3**). However, for di-methoxyphenyl substituted derivative **16c**, no significant change was seen in the ThT RFU compared to control (**Figure 5-18** C), indicating that it is a WAM in regulating the Aβ42 aggregation process. In contrast, compound **16d** (4-methoxyphenyl) was promoting Aβ42 aggregation similar to compound **14b**. At higher concentrations of **16d**, ThT RFU was increasing indicating its concentration-dependent pro-aggregation activity (**Figure 5-18** D). Specifically, at 1 µM and 5 µM, it was able to promote the aggregation by 1.74- and 1.92- folds, whereas, at 10 µM and 25 µM, 1.98- and 2.70- folds increases in Aβ42 aggregation was seen (**Table 5-4**).

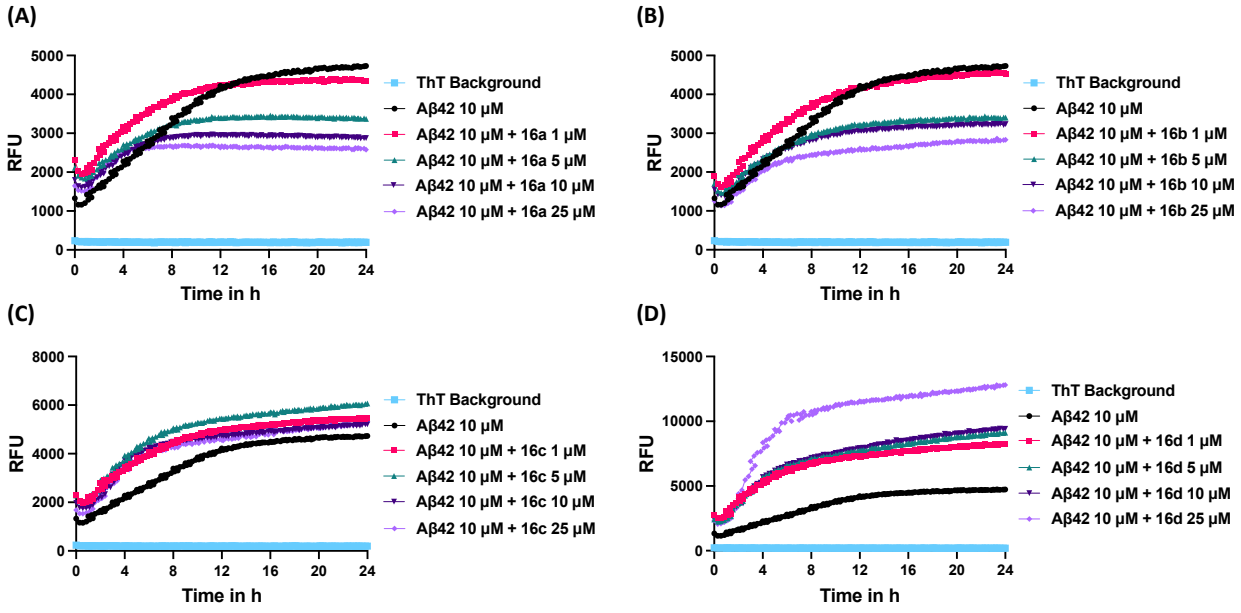


Figure 5-18. ThT-based 24 h aggregation kinetics of Aβ42 (10 µM) in the absence and presence of **16a-d** at 1, 5, 10, and 25 µM respectively at 37 °C, pH 7.4. (A) Aggregation kinetic curves for **16a**; (B) aggregation kinetics curves for **16b**; (C) aggregation kinetic curves for **16c**; (D) aggregation kinetic curves for **16d.** Aggregation kinetics were monitored by measuring ThT fluorescence (excitation = 440 nm, emission = 490 nm). Results are averages of three independent experiments in triplicate measurements.

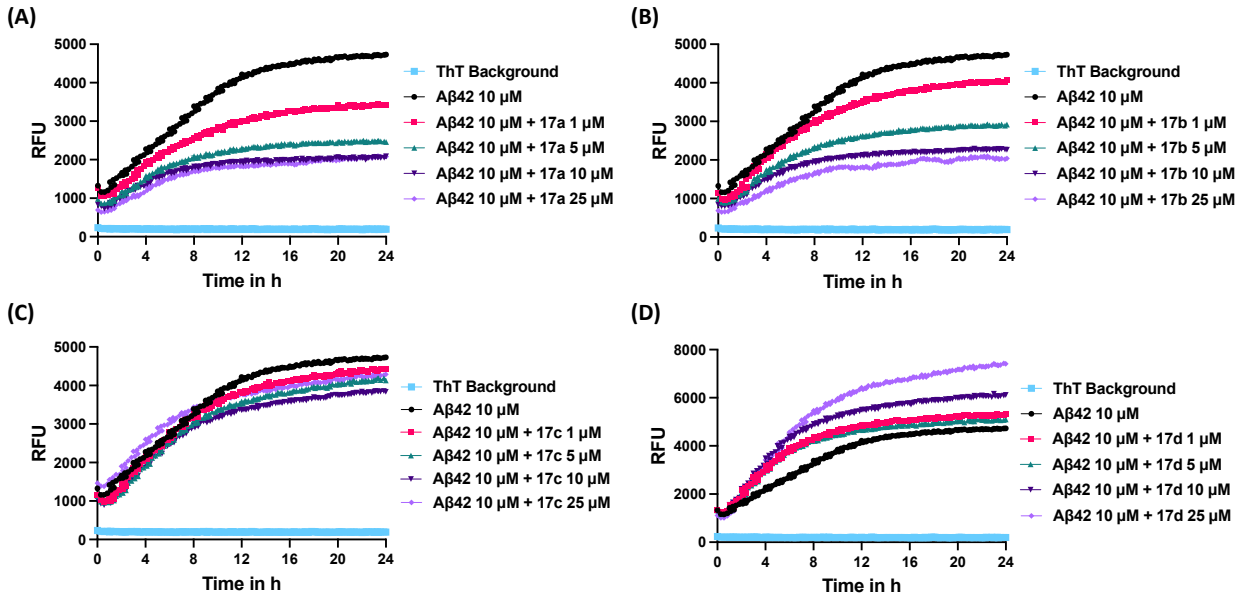


Figure 5-19. ThT-based 24 h aggregation kinetics of Aβ42 (10 μM) in the absence and presence of **17a-d** at 1, 5, 10, and 25 μM respectively at 37 °C, pH 7.4. (A) Aggregation kinetic curves for **17a**; (B) aggregation kinetics curves for **17b**; (C) aggregation kinetic curves for **17c**; (D) aggregation kinetic curves for **17d.** Aggregation kinetics were monitored by measuring ThT fluorescence (excitation = 440 nm, emission = 490 nm). Results are averages of three independent experiments in triplicate measurements.

A similar trend was seen for derivatives with *N*-phenylbenzo[*b*]thiophene-2-carboxamide template (**Figure 5-19**). The 4-methoxy substituted derivative **17d** exhibited concentration-dependent promotion of Aβ42 aggregation (**Figure 5-19** D). At 1 μM and 5 μM, it was able to promote fibrillogenesis by approximately 1.1-fold. The numbers were increased to 1.29- and 1.57-fold when Aβ42 was treated with 10 μM and 25 μM **17d** (**Table 5-4**). The 2-methoxyphenol substituted isomer compounds **17a** and **17b**, were able to inhibit Aβ42 fibrillogenesis of (**Figure 5-19** A, B). At the highest tested concentration (25 μM), a PI of ~40% and ~39% were seen for **17a** and **17b** (**Table 5-3**). In addition, the 3,4-dimethoxyphenyl substituted compound **17c** was not active in modulating the aggregation process at all the tested concentrations (**Figure 5-19** C).

Table 5-3. Percent inhibition (PI) of **16a**, **16b**, **17a**, **17b** at 1 μM, 5 μM, 10 μM, and 25 μM on Aβ42 (10 μM) aggregation

	16a	**16b**	**17a**	**17b**
1 μM	25.7 ± 3.9	20.7 ± 14.0	14.5 ± 12.5	5.8 ± 2.3
5 μM	47.1 ± 2.5	41.7± 8.6	32.5 ± 6.3	25.69 ± 8.0
10 μM	54.8 ± 3.1	51.8 ± 6.7	41.4 ± 6.2	33.3 ± 5.2
25 μM	53.1 ± 5.7	51.3 ± 10.8	40.9 ± 8.4	39.7 ± 1.3

Table 5-4. Fold(s) increase in Aβ42 (10 μM) fibrillogenesis of **16d** and **17d** at 1 μM, 5 μM, 10 μM, and 25 μM compared to Aβ42 control.

	16d	17d
1 μM	1.7 ± 0.0	1.1 ± 0.0
5 μM	1.9 ± 0.1	1.1 ± 0.0
10 μM	2.0 ± 0.0	1.3 ± 0.0
25 μM	2.7 ± 0.2	1.5 ± 0.0

Control experiments also demonstrate that compounds **16a-d** and **17a-d** do not interfere in the ThT assay. Incubating the test compounds with ThT and buffer alone at 25 μM gave rise to low FLR similar to ThT background (**Figure 5-20**).

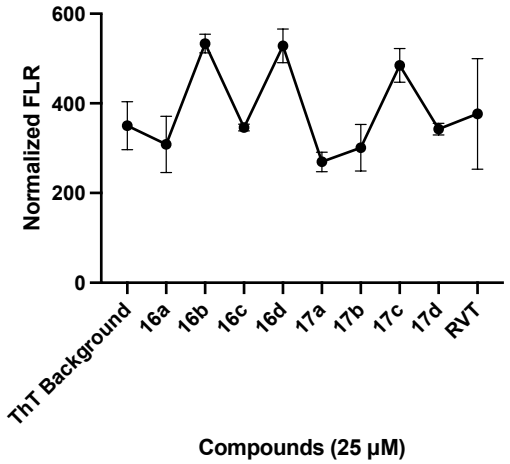


Figure 5-20. ThT-based aggregation kinetics spectrometric background reading of **16a-d**, **17a-d** and RVT. Readings were monitored by measuring ThT fluorescence (excitation = 440 nm, emission = 490 nm). The results presented are the average of one independent experiment in triplicate measurements.

5.3.7.3 TEM study of **16a-d**, **17a-d**

Similarly, TEM studies were conducted with APs **16d**, **17d** and AIs **16a**, **16b**, **17a**, **17b** to study the morphology of Aβ aggregates. In the absence of test compounds, Aβ42 exhibited typical densely packed bundles of mature fibrils after incubation for 24 h at 37 ˚C (**Figure 5-21 A**). When APs **16d** and **17d** were co-incubated with Aβ42 under the same conditions, more elongated, thread-like fibrils were observed in the images (**Figure 5-21 B**). These fibrils were much denser and thicker than the Aβ42 control indicating that these two derivatives can promote aggregation. However, when Aβ42 was co-incubated with AIs (**16a**, **16b**, **17a**, and **17b**), a lesser amount of Aβ42 aggregates were formed as can be seen in **Figure 5-21 C**, even though the morphology of the aggregates was still the same. All these results further validate the results obtained from the ThT-based aggregation kinetic study.

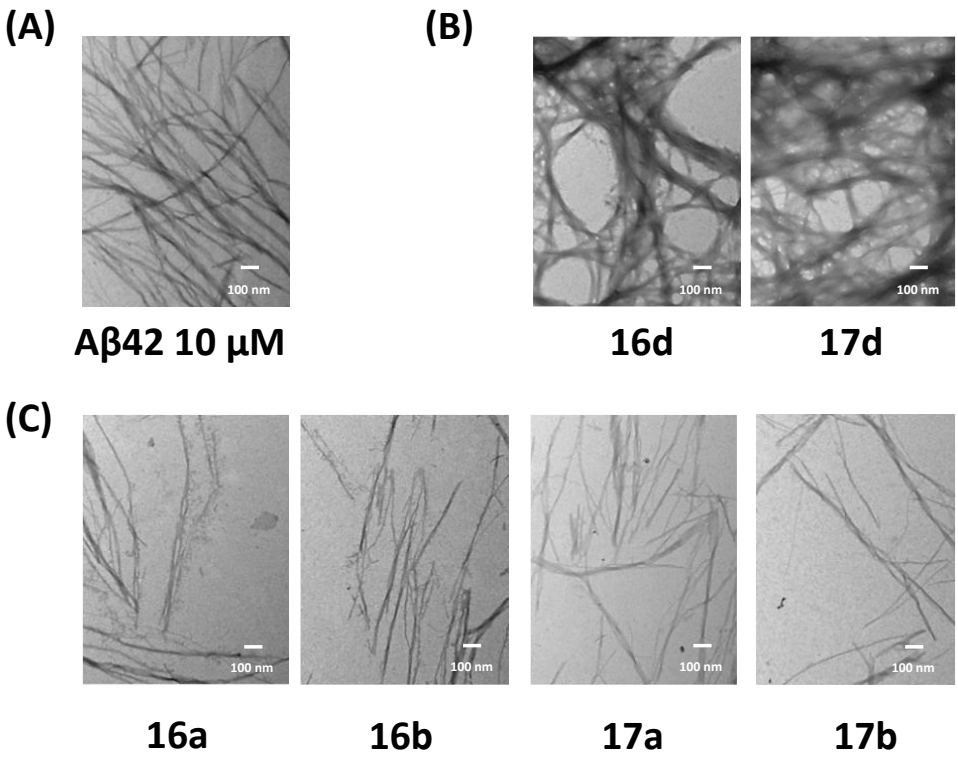


Figure 5-21. TEM images. (A) Aβ42 (10 μM) alone. (B) Aβ42 (10 μM) in the presence of APs **16d** and **17d** at 25 μM. (C) Aβ42 (10 μM) in the presence of AIs **16a**, **16b**, **17a**, and **17b** at 25 μM.

5.3.7.4 ANS binding assay of APs **16d**, **17d** and AIs **16a**, **16b**, **17a**, **17b**

In order to better understand the Aβ42 aggregation modulation mechanisms of these compounds, ANS dye binding assay was carried out to determine if these compounds are able to expose hydrophobic regions of Aβ42 aggregates and thereby promote their fibrillogenesis. As described in detail in Section 5.3.4, ANS in the absence of Aβ42 showed minimal interference on the FLR at 520 nm. However, in the presence of Aβ42 aggregates, ANS can bind to their hydrophobic regions and thus give rise to an increase in FLR with maximum absorption observed at 490 nm instead (RFU = 0.28). With AP **16d** and **17d**, similar effects on ANS binding were seen as their parent promotor compounds **14b** and **14c**. The FLR at 490 nm was further increased in a concentration-dependent manner (**Figure 5-22**). At the highest tested concentration (25 μM), the RFU was increased to ~0.45 and 0.40 respectively for **16d** and **17d**.

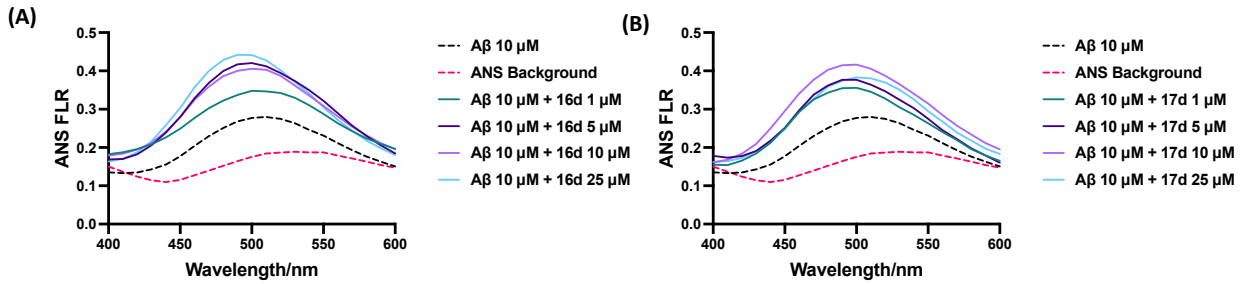


Figure 5-22. ANS binding assay of **16d** and **17d** with Aβ42 (10 μM) at 1, 5, 10, and 25 μM respectively after 24 h incubation at 37 °C, pH 7.4. The ANS fluorescence readings were taken at 380 nm excitation, and 400 nm to 600 nm emission with 10 nm increments. Results are averages of three independent experiments in triplicate measurements. (A) ANS spectrum of **16d** in the presence of Aβ42; (B) ANS spectrum of **17d** in the presence of Aβ42.

Next, we were curious to see the ANS results of the substituted AIs **16a-b** and **17a-b** (**Figure 5-23**). At 1 μM, these substituted derivatives exhibited the highest FLR with RFU ~0.35, 0.42, 0.40, and 0.40 at 490 nm for **16a**, **16b**, **17a**, and **17b** respectively. Interestingly, with higher concentrations, the RFUs were reduced in a concentration-dependent manner with the lowest RFU seen at 25 μM which is close to that of the Aβ42 control.

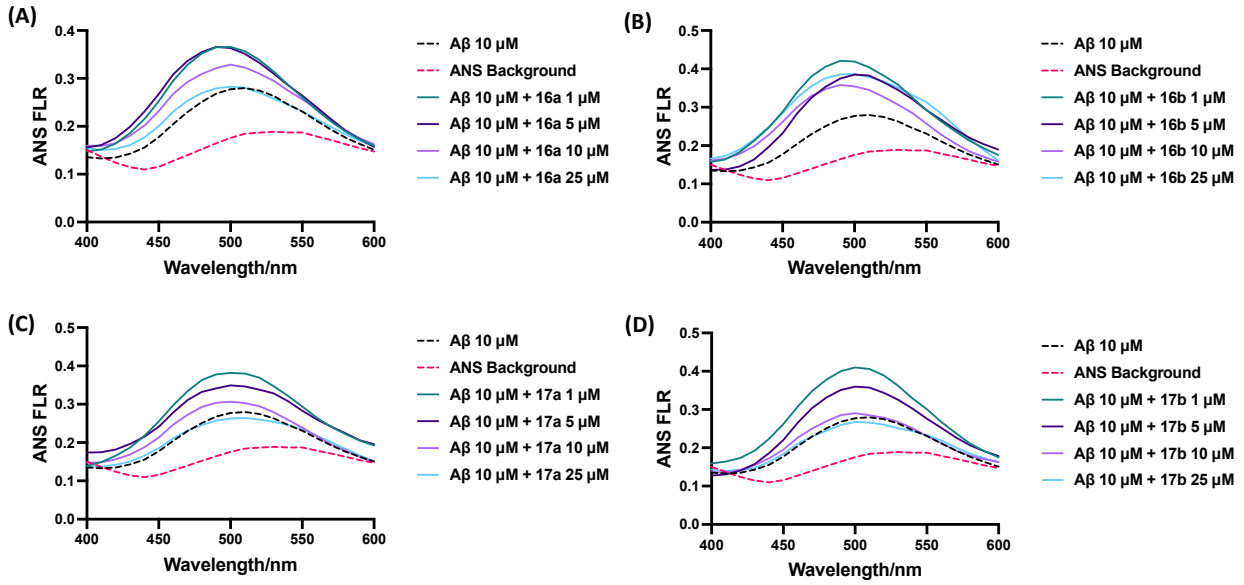


Figure 5-23. ANS binding assay of AIs **16a**, **16b**, **17a**, and **17b** with Aβ42 (10 μM) at 1, 5, 10, and 25 μM respectively after 24 h incubation at 37 °C, pH 7.4. The ANS fluorescence readings were taken at 380 nm excitation, and 400 nm to 600 nm emission with 10 nm increments. Results are averages of three independent experiments in triplicate measurements. (A) ANS spectrum of **16a** in the presence of Aβ42; (B) ANS spectrum of **16b** in the presence of Aβ42; (C) ANS spectrum of **17a** in the presence of Aβ42; (D) ANS spectrum of **17b** in the presence of Aβ42.

We also conducted experiments to determine whether the test compounds have any interference in the assay readouts. These derivatives were tested at 25 μM in the presence of ANS. As shown in **Figure 5-24**, there is no interference from the testing compounds themselves as the ANS FLR (RFU ~ 0.10) was around the same compared to the ANS control which is much lower than Aβ control (RFU ~ 0.30).

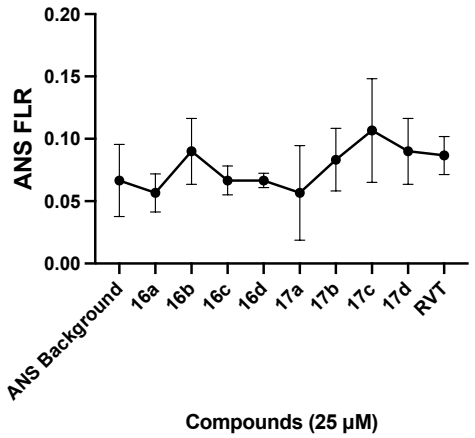


Figure 5-24. ANS spectrometric background reading of **16a-d**, **17a-d** and RVT. The ANS fluorescence readings were taken at 380 nm excitation, and 400 nm to 600 nm emission with 10 nm increments. Results are averages of one independent experiment in triplicate measurements.

The results obtained from the ANS fluorescence studies for these derivatives indicate that i) these compounds are able to change the conformation of Aβ42 aggregates on binding and ii) direct inhibition of Aβ42 aggregates by compound binding leads to a reduction in Aβ42 fibril load at higher compound concentrations. Nevertheless, it is clear that these compounds are able to modulate the conformation of Aβ42 aggregates which can lead to either promotion or inhibition of Aβ42 aggregation.

5.3.7.5 Neuroprotective effects against Aβ42-induced cytotoxicity of **16a-d**,**17a-d**

In order to investigate the effects of these derivatives, including AIs and APs, on Aβ42-induced neurotoxicity, these compounds were further tested in mouse hippocampal HT22 cell lines. Initially, the compounds were tested at 25 μM in the absence of Aβ42 to check whether these compounds themselves showed any toxicity to the cells. As indicated in the results (**Figure 5-25**), compared to untreated cells, when HT22 cells were co-incubated with AIs (**16a**, **16b**, **17a**, **17b**) and APs (**16d**, **17d**), the cell viability remained the same hovering around 100% which clearly showed that these derivatives were not toxic to the HT22 cells.

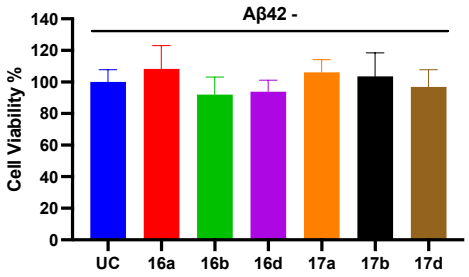


Figure 5-25. Neuroprotective effects of **16a**, **16b**, **16d**, **17a**, **17b**, and **17d** at 25 μM on HT22 cells without Aβ42 after 48 h incubation. The cell viability was determined by cell counting kit-8 (CCK-8). The results are averages of three independent experiments (n = 5).

5.3.7.6 Antioxidant activity of **16a-d**, **17a-d**

Oxidative stress has long been considered as one of the main pathophysiological pathways of AD which is initiated by the formation and accumulation of excessive amounts of reactive oxygen species (ROS). The aggregation of Aβ fibrils can activate the innate immunological response of CNS, resulting in the release of certain types of ROS. Besides, during the aggregation, some metal ions can be entrapped into the aggregates and thus unregulated ion influx can also facilitate the release of ROS species. Taken together, compounds that are able to capture and neutralize these excessive ROS species and related cytotoxicity would be beneficial in treating AD. Compounds **16a**, **b** and **17a**, **b** contain the antioxidant pharmacophore 2-methoxyphenol. Therefore, we evaluated their ability to scavenge the free radical 2,2-diphenyl-1-picrylhydrazyl (DPPH) which is a stable free radical that readily accepts electrons or hydrogen atoms and this change can be measured by the colorimetric assay. We also evaluated other compounds in this series (**16c**, **d** and **17c**, **d**). The results are shown in **Figure 5-26**. AIs **16a**, **b** and **17a**, **b** showed concentration-dependent antioxidant activity. It is not surprising given the fact that these derivatives contain phenolic groups in their structure. These four compounds exhibited similar magnitude of activities at 25 μM with 52.3%, 56.3%, 50.6%, and 45.6% DPPH scavenging for **16a**, **16b**, **17a**, and **17b** respectively. However, the 3,4-dimethoxyphenyl and 4-methoxyphenyl-containing compounds (**16c**, **d** and **17c**, **d**) were not able to effectively scavenge DPPH at all tested concentrations (**Figure 5-26** B). The results indicate that the

derivatives **16a**, **b** and **17a**, **b** can not only reduce the formation of Aβ fibrils but also exert antioxidant activity, which makes them a dual-acting agent with potential application for treating AD.

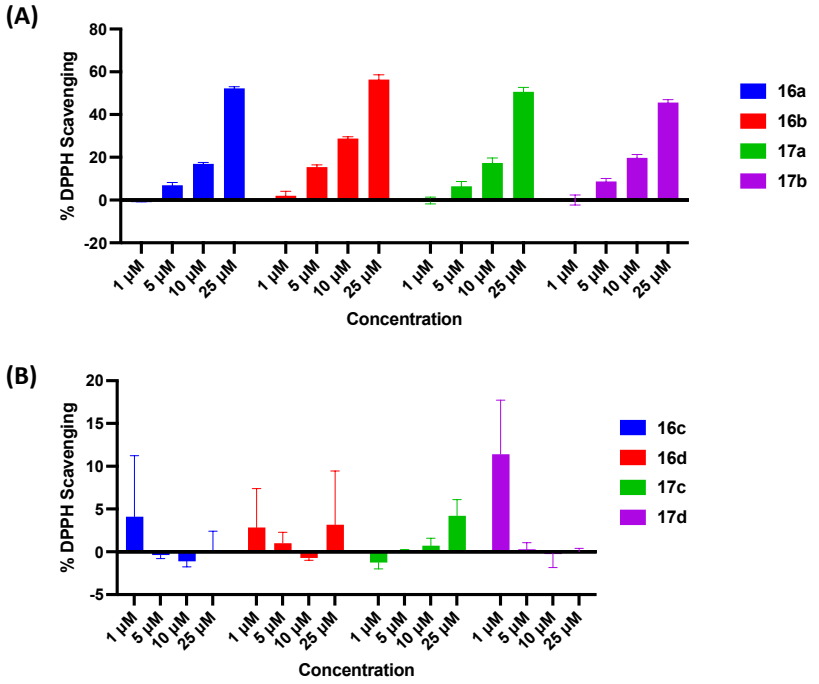


Figure 5-26. Antioxidant activity of substituted derivatives presented as percentage DPPH scavenging ability at 1 µM, 5 µM, 10 µM and 25 µM. (A) Antioxidant activity of AI **16a**, **b** and **17a**, **b**; (B) antioxidant activity of **16c**, **d** and **17c**, **d** (not active). Results are averages of three independent experiments in triplicate measurements.

5.3.7.7 Molecular docking results of lead compounds **16a** and **16d**

Molecular docking studies were also carried out to understand the binding interactions of compounds in this series with Aβ42 aggregates. Compound **16a** was selected as a representative inhibitor and **16d** was selected as a representative promotor of Aβ42 aggregation. The Aβ42 oligomer and fibrils models were used as described in the previous section (Section 5.3.6). In the oligomer docking, both compounds **16a** and **16d** primarily interacted through hydrophobic contacts and exhibited similar binding modes (**Figure 5-27**). Specifically, for **16a**, the aromatic benzofuran ring underwent hydrophobic interactions with the

alkyl group of C: Leu17 (5.1 Å) and C: Leu34 (5.0 Å from the benzene ring and 5.1 Å from furan ring), whereas the benzene ring interacted with the alkyl group of A: Leu17 (4.7 Å). In addition, the methoxy group underwent alkyl-alkyl hydrophobic interaction with A: Leu34 as well with a distance of 3.9 Å. Similarly, in the top binding pose of **16d**, the aromatic benzofuran ring underwent hydrophobic interactions with the alkyl group of C: Leu34 (5.0 Å) and C: Leu17 (5.1 Å from the benzene ring and 5.0 Å from furan ring), whereas the benzene ring interacted with the alkyl group of A: Leu17 (4.5 Å). The methoxy group at the 4th position underwent alkyl-alkyl hydrophobic interaction with A: Leu17 (4.1 Å). The overall docking poses of these two compounds in Aβ42 pentamer model showed similar results which suggest that these compounds can bind to Aβ42 pentamers.

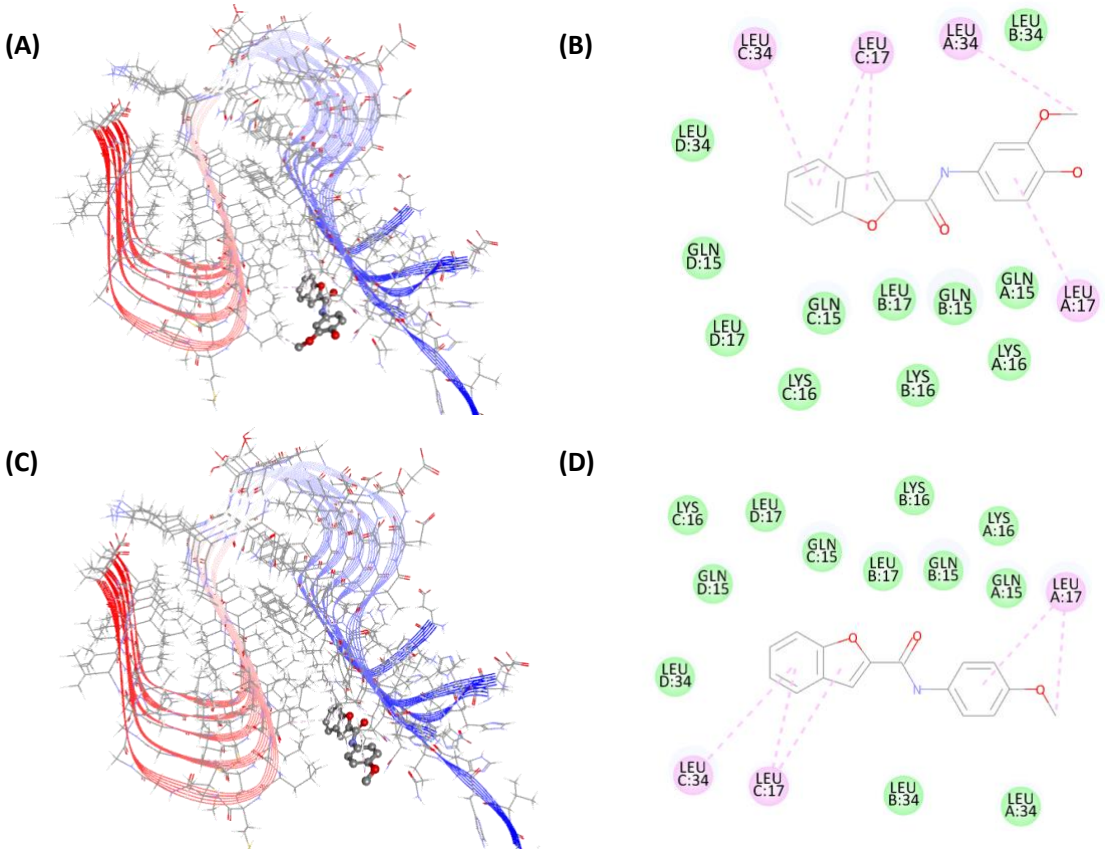


Figure 5-27. Molecular docking studies of **16a** and **16d** in Aβ42 pentamer model (PDB ID: 5KK3). (A) Top docked pose of **16a**; (B) 2D interaction map of the top docking pose of **16a**; (C) top docked pose of **16d**; (D) 2D interaction map of the top docking pose of **16d**. The Aβ42 chains are color-coded with blue indicating N-terminal and red indicating C-terminal. The hydrogen atoms are removed to enhance clarity. The hydrophobic interactions between the small molecule ligand and protein receptor are shown in pink dashed line.

In the next step, these two compounds were docked to the Aβ42 fibril model. For compound **16a**, few hydrogen bond interactions were found. The best binding pose of **16a** was oriented along the long axis of the fibril with the benzene ring perpendicular to the plane of the peptide backbone in the hydrophobic steric zipper region of Aβ42 (**Figure 5-28**). The CDOCKER energy for this binding pose was -17.70 kcal/mol and the CDOCKER interaction energy was -27.69 kcal/mol. The hydroxyl substituent on the benzene ring was able to interact with the NH_3^+ of B: Lys16 (1.90 Å). The carbonyl oxygen and the oxygen on the

benzofuran ring also underwent hydrogen bond interactions with the NH_3^+ group of C: Lys16 (distance = 1.88 Å and 2.25 Å respectively). These strong hydrogen bond interactions anchored the compound in the hydrophobic pocket of the fibril and this binding was further supported by few hydrophobic interactions formed between the 4-methoxy substituent and C: Ala21 (4.3 Å) and B: Val21 (3.8 Å). For the AP **16d**, the top binding pose was oriented along the long axis of the fibril as well, but the conformation was different (CDOCKER energy = -15.40 kcal/mol and the CDOCKER interaction energy = -25.33 kcal/mol, **Figure 5-28**). The benzofuran ring and benzene ring were oriented in parallel to the peptide backbone in the steric zipper region of the Aβ42 thus enabling pi-cation electrostatic interactions with the NH_3^+ group of Lys residue. The benzofuran ring underwent pi-cation electrostatic interactions with D: Lys16 (distance = 3.6 Å from the benzene ring and 4.4 Å from the furan ring respectively) and the benzene ring underwent electrostatic interaction with C: Lys (4.72 Å). Besides, hydrogen bond interaction was also found between the carbonyl oxygen and C: Lys 16 (1.7 Å). The compound was located in a hydrophobic region and the benzene ring was in hydrophobic contact with C: Val18 (5.5 Å) and C: Ala21 (5.4 Å). Another set of hydrophobic interactions was seen between the 4-methoxy substituent and B: Val18 (3.9 Å) and B: Ala21 (3.8 Å). This orientation of **16d** and the pi-cation interaction of the benzofuran with the Lys16 might play a role in facilitating its pro-aggregation activity. In contrast, for the inhibitor compound **16a**, due to its different conformation in the steric zipper region, the phenolic OH is able to form hydrogen bond with B: Lys16, the oxygen atom of benzofuran and the amide carbonyl also formed hydrogen bonds with C: Lys16 and these interactions might explain its ability to inhibit Aβ42 aggregation.

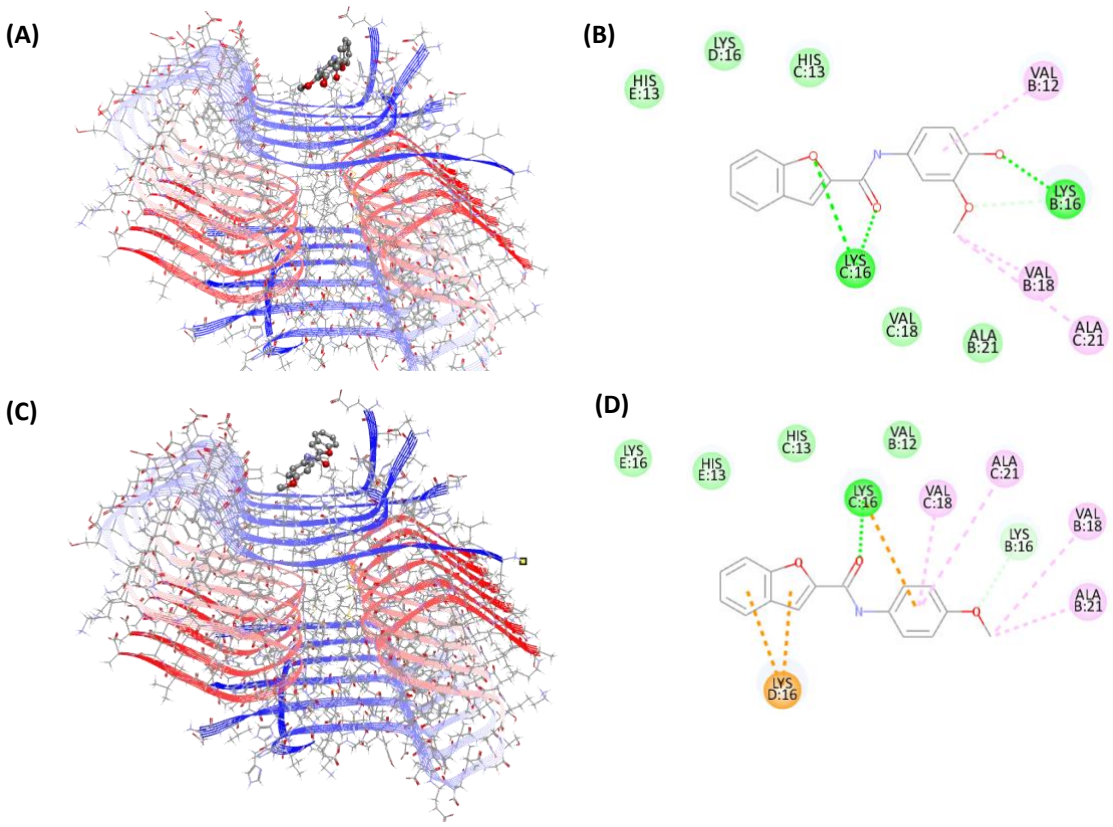


Figure 5-28. Molecular docking studies of **16a** and **16d** in the Aβ42 fibril model (PDB ID: 5KK3). The hydrogen atoms are removed to enhance clarity. (A) Top docked pose and zoom-in view of **16a**; (B) 2D interaction map of the top docking pose of **16a**; (C) top docked pose and zoom-in view of **16d**; (D) 2D interaction map of the top docking pose of **16d**. The Aβ42 chains are color-coded with blue indicating N-terminal and red indicating C-terminal. The hydrogen atoms are removed to enhance clarity. The intermolecular interactions are shown in dashed lines with green as hydrogen bond interactions, pink as hydrophobic interactions, and orange as electrostatic interactions.

5.4 Summary

In this chapter, the three-carbon α,β-unsaturated system present in the chalcone template was replaced with an amide bioisostere without any other spacer in the linker region to obtain *N*-phenylbenzamide derivatives **13a-m** and **14a-c**. Initially, a total of 16 compounds were synthesized by coupling the aniline (**12**) with either corresponding acid chlorides or carboxylic acids to obtain the compound library in good yields (72.3-89.2%). The chemical structures were confirmed by ^{1}H NMR, MS and the purity was checked

by LCMS. The modulatory activities of these derivatives on Aβ42 aggregation were determined by the ThT-based aggregation kinetic assay and TEM studies (**Figure 5-29**). Among them, 6 derivatives (**13a**, **13b**, **13f**, **13h**, **13i**, **13k**) were identified as AIs with PI ranging from 9.0% to 24.57%. Even though the inhibitory effects on Aβ42 aggregation were much lower than those reported in the previous chapters, interestingly, another 6 derivatives (**13c**, **13e**, **13j**, **13m**, **14b**, **14c**) were identified as APs with **14b** and **14c** demonstrating remarkable ability in promotion of Aβ42 fibrillogenesis. Compound **14b** and **14c** demonstrated concentration dependently promoted the aggregation of Aβ42 with 4.76 and 5.12 folds of aggregation observed at the highest testing concentration (25 μM). These two compounds were not toxic to HT22 cells and were able to rescue HT22 cells from Aβ42-induced neurotoxicity (cell viability 73.78% and 73.91% at 25 μM versus 19.7% for Aβ42 control) and this was also confirmed by live cell imaging studies (**Figure 5-29**). ANS binding assay indicated that these two APs were able to increase the surface hydrophobicity of Aβ42 aggregates in a concentration-dependent manner. In molecular docking studies, the aromatic rings of **14b** and **14c** were able to undergo several hydrophobic interactions with Aβ42 pentamer and fibril models at the aggregation-prone KLVFFA and C-terminal regions. Based on these results, we proposed that the binding of **14b** and **14c** can increase the exposure of hydrophobic regions of Aβ42 aggregates to favor the association of these hydrophobic regions leading to the acceleration of fibrillogenesis.

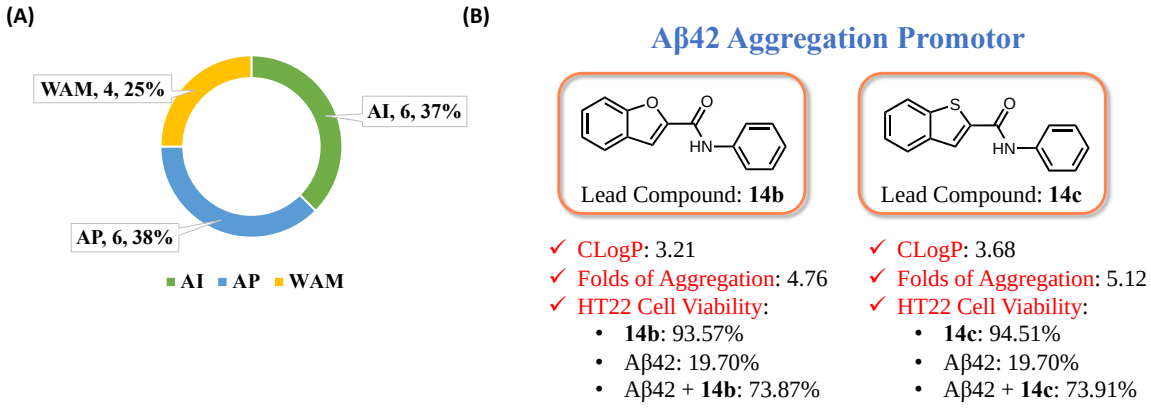


Figure 5-29. Summary of *N*-phenylbenzamide and carboxamide derivatives. (A) 37% (6 out of 16) compounds were identified as aggregation inhibitor (AI), 37% (6 out of 16) compounds were identified as aggregation promotor (AP), and 25% (4 out of 16) compounds were identified as weak aggregation modulator (WAM); (B) key experimental data for lead compound **14b** and **14c**.

We then further expanded the SAR of these classes of compounds by incorporating additional substituents on the *N*-phenyl ring. A total of 8 compounds were synthesized by coupling the substituted aniline with corresponding carboxylic acids to obtain the compound library in good yields (72.3-89.2 %). The chemical structures were confirmed by ^{1}H NMR, MS and the purity was checked by LCMS. The modulatory activities of these derivatives on Aβ42 aggregation were determined by ThT-based aggregation kinetic assay and TEM studies (**Figure 5-30**). Derivatives with either 4-hydroxy-3-methoxyphenyl or 3-hydroxy-4-methoxyphenyl substituents (**16a-b** and **17a-b**) were able to inhibit the aggregation of Aβ42 in a concentration-dependent manner (PI ranging from 39.7-53.1%). In contrast, the 4-methoxyphenyl substituent-containing derivatives (**16d** and **17d**) were able to concentration-dependently promote the aggregation of Aβ42 similair to their parent compounds (**14b** and **14c**) with 2.7- and 1.5-folds in aggregation respectively. These derivatives were not toxic the HT22 cells at 25 μM. The ANS binding assay showed that both AIs and APs were able to increase the hydrophobicity of Aβ42 aggregates indicating that upon binding, these derivatives are able to change the conformation of the aggregates. Molecular docking studies showed that the main interactions established between AIs, APs and Aβ42 pentamer and fibril models were hydrophobic interactions. However, AIs with hydroxyl moiety were able to undergo

extra hydrogen bond interactions with the hydrophobic KLVFFA region and this might explain its inhibitory effects on the aggregation.

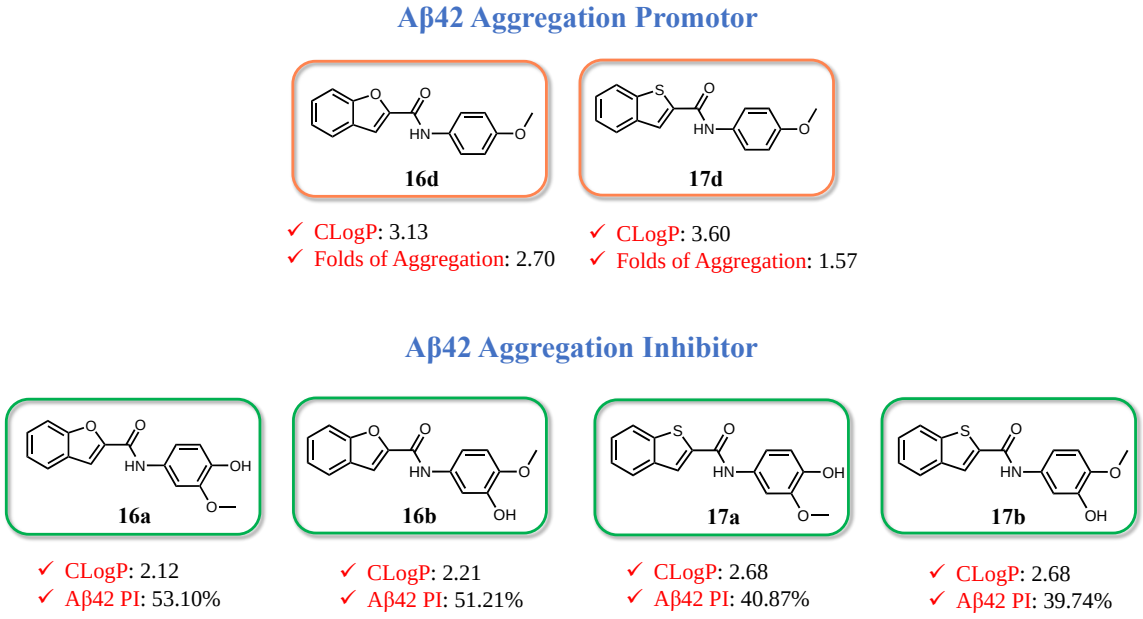


Figure 5-30. Summary of expanded SAR derivative library. Two derivatives with a 4-methoxylphenyl substituent were identified as APs and four derivatives with either a 4-hydroxy-3-methoxyphenyl or a 3-hydroxy-4-methoxyphenyl substituent were identified as AIs.

5.5 Experimental

5.5.1 General

All chemicals and reagents were purchased from various vendors (Sigma Aldrich Missouri USA, Alfa Aesar Massachusetts USA, Bio Basic Ontario Canada, AA Blocks California USA, Cayman Chemical Michigan USA, Thermo Fisher Massachusetts USA, and Corning New York USA), were >95% pure and used without further purification. The Aβ42 1,1,3,3,3-hexafluoroisopropanol (HFIP) >95% pure, was purchased from Anaspec California USA (Cat. No. AS-64129) or rPeptide Georgia USA (Cat. No. A-1163-1). The reactions were monitored by thin-layer chromatography (TLC) using the Merck silica gel 60, F254.

Column chromatography was carried out using Merck silica gel 230-400 mesh. The spots were visualized with short or long wavelengths (254 nm or 365 nm). The melting points of compounds were determined using a digital melting point apparatus (REACH Devices, USA). The proton NMR (^{1}H NMR) and carbon NMR (^{13}C NMR) spectra of compounds were obtained using a 300 MHz Bruker Avance spectrometer (Department of Chemistry, University of Waterloo). Either $CDCl_3$ or DMSO-d_6 were used as solvents. Coupling constants (*J* values) were recorded in Hertz (Hz). Abbreviations used to represent ^{1}H NMR signals were s – singlet, d – doublet, t – triplet, m – multiplet, br s – broad singlet. The mass and purity were confirmed on the Agilent 1260 Infinity liquid chromatography (LC) module equipped with a 6130 Quadrupole mass spectrometer (Agilent 6100 series LCMS). The column used on LCMS was a ZORBAX Eclipse AAA, 4.6 × 75 mm, 3.5 micron (Agilent Technologies, Canada) column. A mixture of water and acetonitrile 1:1 v/v with 0.1% formic acid (1.0 mL/min flow rate), was used as the solvent system to assess compound purity and mass. All final compounds were ≥ 95% pure as determined by LCMS analysis.

5.5.2 Chemistry

For the synthesis of **13a-m** the acid chlorides were coupled with aniline (**12**) (1 mmol) by taking them into a 50 mL round bottom flask (RBF) containing 15 mL of anhydrous tetrahydrofuran (THF). To this mixture, 1.2 equivalents of TEA and 1.0 equivalent of corresponding acid chlorides with various R groups (**2a-m**) were added. The reaction mixture was kept at either room temperature or reflux for 2-24h and was monitored by thin layer chromatography (TLC). After the reaction was complete, the solvent THF was evaporated in vacuo and the resulting reaction mixture was dissolved in 15 mL ethyl acetate (EtOAc), and then washed with 15 mL brine solution (×3). The organic layer was collected and dried over anhydrous $MgSO_4$ and filtered. The organic solvent was removed in vacuo and the residue/oil obtained was further purified by silica gel column chromatography using a combination of solvent systems (1:1 *n*-Hexanes:EtOAc or 5:2 n-Hexanes:EtOAc or 9:1 dichloromethane (DCM): Methanol (MeOH) or 4:1 DCM:*n*-Hexanes) to afford the final compounds **13a-m**.

Compounds **14a-c** were synthesized by reacting aniline (**12**) (1 mmol) kept in an RBF with 15 mL THF, followed by the addition of 1.0 equivalent carboxylic acid (**4a-c**), 1.2 equivalents EDC, 1.5 equivalents HOBt, and 2.2 equivalents TEA added in sequence. The reaction was kept at room temperature overnight or under reflux conditions for 24h. The solvent was evaporated in vacuo and the resulting reaction mixture was dissolved in 15 mL EtOAc and washed with 15 mL brine solution (×3). The organic layer was collected, dried over anhydrous $MgSO_4$ and filtered. The organic solvent was then removed in vacuo to obtain the residue/oil which was further purified by silica gel column chromatography using either 1:1 *n*-Hexanes:EtOAc or 5:2 *n*-Hexanes:EtOAc as mobile phase to afford compounds **14a-c**.

Compounds **16a-d** and **17a-d** were synthesized by reacting aniline derivatives (**15a-d**) (1 mmol) kept in an RBF with 15 mL THF, followed by the addition of 1.0 equivalent carboxylic acid (**4b-c**), 1.2 equivalents EDC, 1.5 equivalents HOBt, and 2.2 equivalents TEA added in sequence. The reaction was kept under reflux conditions for 4–12 h. The solvent was evaporated in vacuo and the resulting reaction mixture was dissolved in 15 mL EtOAc and washed with 15 mL brine solution (×3). The organic layer was collected, dried over anhydrous $MgSO_4$ and filtered. The organic solvent was then removed in vacuo to obtain the residue/oil which was further purified by silica gel column chromatography using either 1:1 *n*-Hexanes:EtOAc or 5:2 *n*-Hexanes:EtOAc as mobile phase to afford compounds **16a-d** and **17a-d**.

5.5.3 Aβ42 aggregation kinetic assay

The ability of benzamide and carboxamide derivatives **13a-m**, **14a-c**, **16a-d**, and **17a-d** to inhibit the Aβ42 aggregation was evaluated using the thioflavin T (ThT) based fluorescence kinetic assay. A 15 μM ThT solution was prepared in 50 mM glycine buffer using ultra-pure-water (UPW). The pH of the solution was adjusted to 7.4 with 50 mM sodium hydroxide solution. The aggregation assay was carried out using 215 mM sodium phosphate dibasic heptahydrate buffer prepared in UPW and the pH was adjusted to 7.4 by using 50 mM hydrochloric acid solution. The Aβ42•HFIP > 95% pure (Anaspec, California, USA) was

treated with 1% ammonium hydroxide solution to afford 1 mg/mL stock solution. The stock solution was then vortexed and sonicated for 5 min before being diluted to a 25 μM working solution using the assay buffer. The stock solutions of the test compounds (**10a-f**, **10h-j**, **10l-m**, **11a-c** and resveratrol (RVT)) were prepared in assay buffer with DMSO as the solubilizing agent (final concentration per well was less than 2%). The 24 h aggregation kinetics assay was carried out using 384-well plates (Costar, black, clear-bottom), by adding 44 μL of ThT, 12 μL of assay buffer, 16 μL of Aβ42 solution (10 μM final well concentration), and 8 μL of test compound dilution (25 μM) into each well. The Aβ42 control wells contained ThT, Aβ42 solution and the assay buffer without any test compound. The plates were covered with a transparent plate cover and were incubated at 37 °C for 24 h with shaking at 300 cpm between readings for 30 s. The readings were taken every 10 min (bottom reading), at an excitation wavelength of 440 nm and emission wavelength of 490 nm using the BioTek Synergy H1 microplate reader. Each sample was measured in triplicate readings and the results were obtained based on three independent experiments.

5.5.4 Transmission electron microscopy

The TEM assay was carried out by first running the Aβ42 aggregation assay (as described in 5.5.3) by incubating test compounds at 25 μM with 10 μM Aβ42 for 24 h at 37 °C. The TEM grids were prepared by aliquoting 20 μL of each sample from the 384-well plate after the 24-hour incubation period. These samples were loaded onto 400-mesh formvar-coated copper grids (Electron Microscopy Sciences, Pennsylvania, USA). The grids were air-dried overnight before being washed with 40 μL UPW for three times. After washing, 20 μL 2% phosphotungstic acid (PTA) solution was added to the grid and stayed for 1 min to stain the samples. Then the PTA solution was absorbed away with filter paper and then the grids were washed with 40 μL UPW three times. Then the grids were further air-dried overnight. The imaging studies were carried out using a Philips CM 10 TEM (Dept. of Biology, University of Waterloo) at 60 kV and the micrographs were obtained through a 14-megapixel AMT camera at 64,000X magnification. The samples

used to prepare the grids were obtained by mixing the triplicate wells from ThT assay and the images were taken at a randomized view for each grid.

5.5.5 8-Anilino-1-naphthalenesulfonicacid binding assay

ANS binding studies were carried out to explore the potential mechanism regarding the pro-aggregation activity of **14b-c**, **16a-d**, and **17a-d** on Aβ42. The Aβ42•HFIP stock solution (1 mg/mL) was prepared as described in the ThT assay protocol by dissolving in ammonium hydroxide (1% v/v), followed by dilution with phosphate buffer (215 mM, pH 7.4) to obtain 25 μM stock solution and sonication for 5 min. Stock solutions of RVT, **14b-c**, **16a-d**, and **17a-d** were prepared in DMSO and were further diluted with phosphate buffer (215 mM, pH 7.4) to prepare various concentrations (1–25 μM). The final concentration of Aβ42 in each well was 10 μM. Aβ42 binding studies were carried out in 384-well plates (Costar, black, clear-bottom), by adding 56 μL of phosphate buffer, 16 μL of Aβ42 and 8 μL of testing compounds at different concentrations (1, 5, 10 or 25 μM) into each well. The control wells contained Aβ42 solution and the assay buffer without any test compounds. The plates were covered with a plate cover and were incubated at 37 °C for 24 h with shaking and the ANS was added into the well plate at 0 h, 1 h, 8 h, and 24 h time points. ANS was dissolved in UPW and further diluted down to 100 μM. At the end of the 24 h incubation period, 4 μL of the ANS solution prepared was added to each well. Then the plate was incubated at 37 °C with shaking (700 cpm) for 10 min before taking readings. The fluorescence readings (RFUs) of ANS were collected using the Thermo Scientific Varioskan LUX multimode plate reader at 380 nm excitation and 400 nm to 600 nm emission with 10 nm increments. The results were presented as average fluorescence readings RFUs (± standard deviation, SD) based on triplicate measurements from three independent experiments.

5.5.6 Cell viability assay

The neuroprotective effect of the lead compounds on cell death induced by Aβ42 was evaluated *in vivo* using mouse hippocampal HT22 cell line. The cells were cultured in Dulbecco's modified eagle media (DMEM) and Ham's F12 (1:1) with the addition of glutamate (2.5 mM) supplemented with 10% fetal bovine serum (FBS), and 1% penicillin & streptomycin at 37 °C, in 5% CO_2 until 70–80% confluence. Then the cells were seeded at a density of 50,000 cells/1 mL to 96 well plates. The plate was incubated for 24 h before adding treatment in. Compounds and RVT were prepared through serial dilution with phosphate buffered saline (PBS) and DMSO to 25 μM. The final DMSO concentration was 0.05% v/v or lower. The PBS solution was used as blank vehicle for untreated cells. The Aβ42 HFIP (>95% pure), was solubilized in DMSO to obtain a 5,000 μM solution and then the solution was diluted with DMEM to obtain a 200 μM stock which was kept at 4 °C for 24 h. The HT22 cells were then co-incubated with lead compounds or RVT (25 μM each) in the presence or absence of Aβ42 (20 μM each) for another 48 h. At the end of the incubation period, the cell viability was determined using the cell counting kit (CCK-8). The absorbance readings were taken at 450 nm 2 h after adding the CCK-8 reagent. The percent viability of cells was calculated based on the following equation: cell viability = reading for treatment group / reading for untreated group × 100%. The results were obtained based on three independent experiments (n = 5 or 6 as indicated in the figure legend). For statistical analysis, the results were analyzed by one-way ANOVA followed by Bonferroni post hoc analysis compared to Aβ control group. ns = not significant, *$p < 0.01$ compared to Aβ42 control group, **$p < 0.01$ compared to Aβ42 control group, ***$p < 0.01$ compared to Aβ42 control group, ****$p < 0.01$ compared to Aβ42 control group.

5.5.7 Live cell fluorescence imaging

Qualitative and quantitative analyses of fluorescence cell imaging were conducted with mouse hippocampal HT22 cell lines. The cells were cultured in Dulbecco's modified eagle media (DMEM) and Ham's F12 (1:1) with the addition of glutamate (2.5 mM) supplemented with 10% fetal bovine serum (FBS),

and 1% penicillin and streptomycin at 37 °C, in 5% CO_2 until 70% - 80% confluence. Then the cells were seeded at a density of 10,000 cells/1 mL to 96 well plates. 24 h after seeding, treatments including lead compounds (25 μM), reference compounds (25 μM), and Aβ42 (20 μM) were added into cells. Then the cells were further incubated for another 48 h before fluorescence imaging. At the end of the incubation period, treatments were removed, and cells were washed with PBS three times. The ProteoStat® working solution was prepared according to the manufacturer's instructions and used as dye to stain Aβ42 aggregates that contain a rich beta-sheet structure. Hoechst 33342 was used to track the location of cell nucleus and was prepared by serial dilution with PBS to 50 μg/mL. BioTraker 490 green was used to stain the cell membrane and prepared according to the manufacturer's instruction. The counter-staining solution containing 0.5 μL ProteoStat®, 0.5 μL Hoechst 33342, and 0.5 μL BioTracker 490 green was added to cells containing 100 μL DMEM (phenol red free). The cells with counter-staining solution were incubated at 37 °C in the dark environment for 20 min with gentle shaking around 300 cpm. Then the cells were washed three times with PBS with incubation between washes for 5 min under the same conditions. At the end, the cells were cultured in DMEM (phenol red free) for fluorescence imaging. The EVOS® FL Auto imaging system equipped with different light filters was used for imaging. ProteoStat® staining was visualized with a RFP light filter; Hoechst 33342 was visualized with a DAPI light filter, BioTracker 490 green was visualized with a GFP light filter. For qualitative analysis, images from different color channels were merged in ImageJ with adjustment on brightness and contrast for the best visualization. For quantitative analysis, the light intensity was fixed at certain level while taking images. All the following adjustment and analysis were conducted in ImageJ. First, the RFP channel images were converted into 8-bit monochrome images. Then the threshold was determined automatically with the Huang algorithm with the resulting binary images used as masks to measure the gray value intensity of pixels in the original image. The results were presented as average pixel intensity (± standard deviation, SD) based on triplicate measurements from three independent experiments. For statistical analysis, the results were subjected to one-way ANOVA followed by Bonferroni post hoc analysis compared to Aβ control group. ns = not significant, *$p < 0.01$

compared to Aβ42 control group, **p < 0.01 compared to Aβ42 control group, ***p < 0.01 compared to Aβ42 control group, ****p < 0.01 compared to Aβ42 control group.

5.5.8 2,2-Diphenyl-1-picrylhydrazyl (DPPH) scavenging assay

The antioxidant activities of selected lead compounds were evaluated by the DPPH scavenging assay. The stable free radicals of DPPH can be reduced in the presence of antioxidant in the sample. The DPPH reagent was prepared by dissolving DPPH in methanol to obtain 0.09 mM stock solution. Trolox was used as a positive antioxidant control in the assay. The test and reference compounds were prepared by serial dilution with methanol to obtain 1, 5, 10, 25 µM stock solutions. The assay was conducted in transparent 96-well plate and protected from the light exposure. The compound background control was taken by adding 100 µL methanol and 25 µM compound solution at various testing concentrations. Whereas, for DPPH control group, 100 µL DPPH stock solution and 25 µL methanol were added into the wells. For compound screening, similarly, 100 µL DPPH stock solution with 25 µL compound dilution at various concentrations were added. The well plate was covered with aluminum foil and kept shaking under room temperature at 700 cpm for 60 min. After incubation, the readings were taken at 517 nm. The percentage DPPH scavenging activity was calculated by the following formular: % DPPH scavenging activity = (reading of DPPH control – reading of compound screening)/reading of DPPH control × 100%. Each sample was measured in triplicate readings and the results were obtained based on three independent experiments.

5.5.9 Molecular docking study

The binding interactions of lead compounds with Aβ42 were investigated by carrying out molecular docking studies on the Discovery Studio software program v20.1.0.19295, Structure-Based-Design (BIOVIA Inc. San Diego, USA). The Aβ42 pentamer and oligomer models were prepared by extracting the coordinates from the solved 3D structure of Aβ42 fibril (PDB id: 5KK3). A binding sphere of 20 Å radius

was selected and defined as the ligand binding site which covers the ^{16}KLVFFA^{21} and the C-terminal ^{32}IGLMVGGVVIA^{42} hydrophobic regions of the Aβ42. Lead derivatives were built in 3D using the Small Molecule module in the software and were subjected to energy minimization protocol (1000 and 2000 steps of steepest descent followed by conjugate gradient method) using CHARMm force field. The CDOCKER algorithm was used to carry out the docking studies. The Receptor-ligand Interactions module in the software was used to perform CDOCKER simulations. The docking simulation included 2000 heating steps, a heating target temperature of 700 K and 5000 cooling steps and a cooling target temperature of 300 K. The top ligand binding modes of selected lead compounds were analyzed by evaluating the CDOCKER energy and CDOCKER interaction energy (in kcal/mol). Further analysis was carried out by determining the polar and nonpolar contacts of lead derivatives in the Aβ42 pentamer and fibril assembly.

Chapter 6

Conclusion and Future Work

AD is a complex neurodegenerative disease with increasing incidence and prevalence globally. Currently, there are no effective therapy for AD. The recent launch of anti-Aβ monoclonal antibodies hold promise as novel class of disease-modifying agents. Over the past several decades, few hypotheses have been proposed to explain the pathophysiology of AD, among which the Aβ cascade is now considered as one of the initiating factors that drives the progression and other pathological factors of AD. The aggregation of Aβ into oligomers and fibrils together with its downstream signaling pathway are neurotoxic. Thus, small molecule modulators that could reduce the overall toxic burden of Aβ aggregates are thought beneficial to treat AD.

In this thesis, a library of 72 derivatives were designed based on the chemical structure of chalcone and curcumin, two bioactive natural compounds that are able to reduce Aβ aggregation and toxicity. These derivatives encompass four different templates, namely, *N*-benzyl (Chapter 2, **3a-m** and **4a-c**), *N*-phenethyl (Chapter 3, **7a-m** and **8a-c**), *N*-benzyloxy (Chapter 4, **10a-m** and **11a-c**), and *N*-phenyl (Chapter 5, **14a-m**, **15a-c**, **16a-d**, and **17a-d**) benzamide and carboxamides. The results are summarized in **Error! Not a valid bookmark self-reference.** and **Figure 6-2**. These compounds were synthesized by coupling corresponding acid chlorides or carboxylic acids with primary amines with moderate to high yields ranging from 72 to 93.6%. Then these derivatives were screened for their modulating activity on Aβ42 aggregation by ThT-based aggregation kinetic assay and TEM studies. Three different types of aggregation modulators were identified which are WAM, AI, and AP. Specifically, 13 derivatives were identified as WAM which has little impact on the Aβ42 aggregation, whereas 51 derivatives were identified as AI with PI ranging from 7-53.1%. These observations were confirmed by studying the morphology of Aβ42 aggregates. The lead AIs from each Chapter were selected to further explore their neuroprotective effects against Aβ42 in HT22 cells. These AIs were able to rescue cells from Aβ42-induced neurotoxicity with cell viability ranging from

80.8 to 96.8% versus 38.73% for Aβ42-treated control. Molecular docking studies indicate that these derivatives were able to interact with the hydrophobic domains of Aβ42 oligomer and fibril through hydrophobic interactions.

In addition, another 8 derivatives were identified as AP with folds of aggregation ranging from 1.2 to 5.1. Two lead derivatives **14b** (*N*-benzylbenzofuran-2-carboxamide) and **14c** (*N*-benzylbenzo[*b*]thiophene-2-carboxamide) were selected for further investigation given their striking pro-aggregation activity. The results indicate that these two derivatives can promote the aggregation of Aβ42 in a concentration-dependent manner (4.76-fold and 5.12-fold of aggregation at 25 μM) which was confirmed by investigating the morphology of Aβ42 aggregates by TEM studies. Upon binding, they can interact with Aβ42 and thus facilitate the exposure of hydrophobic surfaces in a concentration-dependent manner. When they were tested in HT22 cells against Aβ42-induced neurotoxicity, a significant increase in the cell viability was seen (73.8% and 73.9% cell viability of **14b** and **14c**) compared to Aβ42-treated control (19.7% cell viability) and their pro-aggregation activity was reproducible in the cell environment as evident from the fluorescence live cell imaging studies with ProteoStat® dye. Molecular docking studies indicate that these APs likely interact with higher order Aβ42 species and facilitate the conformational change to a much more stable and non-toxic/less-toxic fibrils. In the next step, to further expand the SAR of this class of compounds and to understand the pro- and anti-aggregation mechanism, another 8 derivatives with substituted *N*-phenyl rings with the same template as **14b** and **14c** were synthesized and evaluated. The findings are summarized here: (i) 4-methoxyphenyl containing derivatives were able to promote the aggregation by 1.57-2.70 folds, and increase the hydrophobic exposure of Aβ42 species in a concentration-dependent manner; (ii) 3-hydroxy-4-methoxyphenyl and 4-hydroxy-3-methoxyphenyl containing derivatives were AIs with PI ranging from 39.7. to 53.1% at 25 μM; (iii) these AIs were able to increase the hydrophobic exposure of Aβ42 species; (iv) molecular docking studies suggest that the hydrophobic and hydrogen bonding interaction between the substituents and Aβ42 fibril might explain the mechanism of their inhibitory activity.

The key physicochemical properties of the lead compounds in this thesis are listed in **Table 6-2**. These benzamide and carboxamide derivatives exhibit drug-like properties and do not possess any structural alerts unlike curcumin and chalcone templates which are considered as PAINS in medicinal chemistry research. The CLogP values of these derivatives range from 1.15-4.13 which is suitable for brain penetration. The results show that these benzamides and carboxamides possessing *N*-benzyl, *N*-phenethyl, *N*-benzyloxy, and *N*-phenyl templates hold promise in the design and development of novel small molecules as Aβ42 aggregation modulators.

There are certain limitations in this work, especially when evaluating the biological efficacies of the synthesized derivatives in targeting the Aβ. Even though, the cLogP values has been used to estimate the BBB penetration ability of the lead compounds (**Table 6-1**, **Table 6-2**), experimental assays are required to better determine the BBB permeability, including parallel artificial membrane permeability assay and BBB co-cell culture model. These studies will further assist in structure optimization by SAR studies. In addition, the cell culture model (mouse hippocampal neuronal cells) used in the thesis can only provide a general idea of lead compounds' ability to provide neuroprotection against Aβ -induced cytotoxicity. The cell death assay used (CCK8) measures mitochondrial activity and is not able to detect damage to cell membrane. Therefore, measurement of apoptotic biomarker proteins in these assays would provide a better understanding on the mechanisms of neuroprotection. . Given the fact that the neurotoxicity induced by Aβ is a long term effects, our treatment methods (eg: 48 h incubation with Aβ) may not fully replicate the actual biological changes introduced by Aβ aggregates. Last not but least, in this thesis, we found that not only the AIs but also the APs can mitigate the neurotoxicity of Aβ in HT22 cells. However, the detailed mechanism of such protection is not fully understood at molecular level. This also suggests that AP's **14b** and **14c** might have multiple modes of action in preventing Aβ-induced cytotoxicity. All these warrant further research which can be addressed in the future as below.

Future research directions to consider includes: (i) further optimization of the structure of AIs (*N*-phenylbenzamide and carboxamide series, Chapter 4), by expanding the chemical diversity to explore the

SAR; (ii) explore the neuroprotective mechanisms of APs by using immunochemical methodologies (dot blot assay, western blot assay, ELISA etc.), to understand the effects of lead compounds on the sub-population of Aβ aggregates (oligomers, toxic epitope fibrils); and (iii) use molecular dynamics simulation studies to better understand the interactions of lead APs and AIs with various forms of Aβ42 aggregates. In Chapter 4, the effect of aromatic substituents on Aβ42 aggregation was investigated which gave rise to few compound that were able to promote Aβ42 fibrillogenesis. The SAR for this series of compounds can be expanded by designing a series of compounds containing nonaromatic substituents such as the *N*-phenylalkylcarboxamides and *N*-phenylcycloalkylcarboxamide series (**Figure 6-1**). These future studies will assist in understanding the structural features required to design and develop novel Aβ42 aggregation modulators including promoters and inhibitors. These small molecules will be useful as chemical/pharmacological tools to study the mechanisms of Aβ42 aggregation, misfolding and self-assembly.

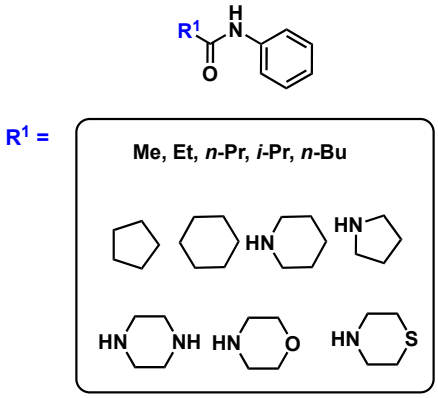


Figure 6-1. Proposed *N*-phenylalkylcarboxamides and *N*-phenylcycloalkylcarboxamide derivatives library with non-aromatic substituents.

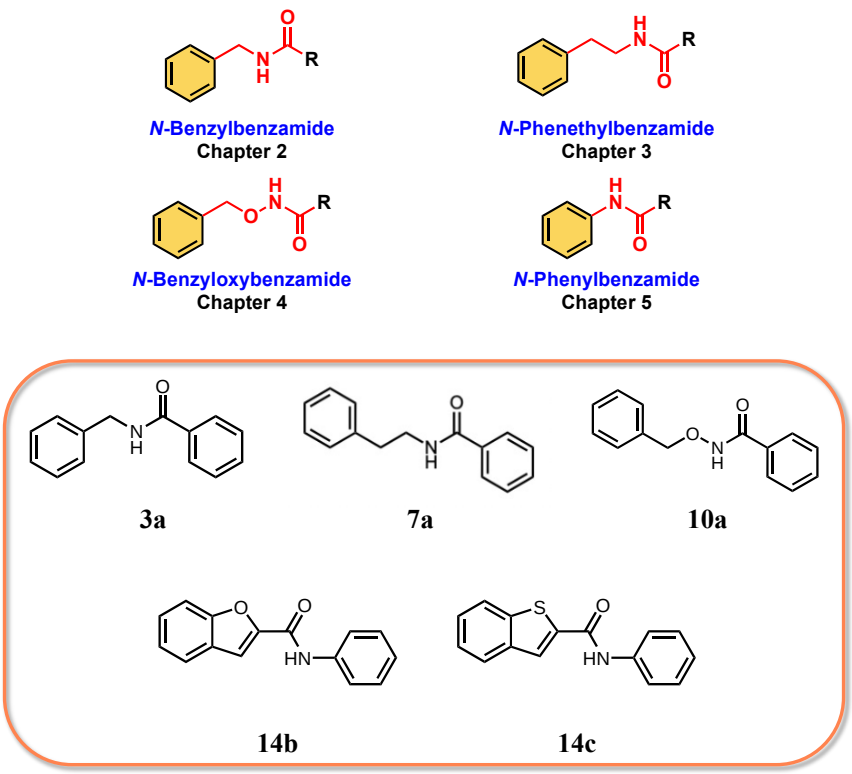
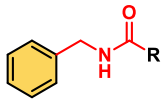


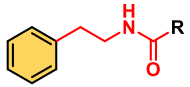
Figure 6-2. Structure template of *N*-benzyl, *N*-phenethyl, *N*-benzyloxy, *N*-phenylbenzamide and carboxamide derivatives and lead derivatives.

Table 6-1. Summary of arylbenzamide and arylcarboxamide derivatives as Aβ42 aggregation modulators.

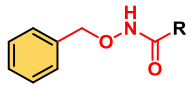
Structure Template	Yield%	# of Aggregation Inhibitor	Percentage Inhibition	# of Aggregation Promotor	Folds of Aggregation	Neuro-protection	CLogP	Molecular Weight (g/mol)
N-Benzylbenzamide and carboxamide (Chapter 2)	72-93.6	14	7.0-27.8%	-	-	Aβ42: 38.73% **3a**: 94.9% **3h**: 95. 8%, **3i**: 85.0%, **3j**: 96.0% **3m**: 80.8%	1.33-4.00	200.24-271.32
N-Phenethylbenzamide and carboxamide (Chapter 3)	72.8-87.9	14	17-28.6%	-	-	Aβ42: 38.73% **7a**: 96.8% **7b**: 94.8% **7j**: 81.8%	1.46-4.13	214.27-285.34
N-Benzyloxybenzamide and carboxamide (Chapter 4)	72.1-93	13	11.8-26.5%	-	-	Aβ42: 38.73% **10a**: 91.6% **10h**: 87.8% **11a**: 82.9%	1.16-3.84	216.24-287.32
N-Phenylbenzamide and carboxamide (Chapter 5)	72.3-91.6	10	9-53.1%	8	1.2-5.12	Aβ42: 19.70% **14b**: 73.87% **14c**: 73.91%	1.15-3.82	257.29-262.31



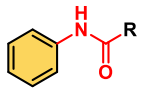
3



7



10



14

Table 6-2. Summary of predicted physicochemical, pharmacokinetic, druglikeness, and medicinal chemistry properties of lead compounds calculated from Web Tool SwissADME.

		3a	7a	10a	14b	14c	Chalcone	Resveratrol
Physicochemical Property	**Molecular Weight (g/mol)**	211.26	225.29	227.26	237.25	253.32	208.26	228.24
	Rotatable Bonds	4	5	5	3	3	3	2
	H-bond Acceptors	1	1	2	2	1	1	3
	H-bond Donors	1	1	1	1	1	0	3
	TPSA ($Å^2$) [a]	29.1	29.1	38.33	42.24	57.34	17.07	60.69
	BBB Permeability[b]	Yes	Yes	Yes	Yes	Yes	Yes	Yes
	P-gp Substrate[c]	No	No	No	No	No	No	No
	CLogP[d]	2.83	2.96	2.66	3.21	3.68	3.62	2.83
Druglikeness	**Lipinski**	Yes	Yes	Yes	Yes	Yes	Yes	Yes
	Ghose	Yes	Yes	Yes	Yes	Yes	Yes	Yes
	Veber	Yes	Yes	Yes	Yes	Yes	Yes	Yes
	Egan	Yes	Yes	Yes	Yes	Yes	Yes	Yes
Alert	**PAINS**[e]	0 alert	0 alert	0 alert	0 alert	0 alert	1 alert	0 alert

[a] TPSA: topological polar surface area; [b] BBB: blood-brain barrier; [c] P-gp: p-glycoprotein; [d] CLogP: calculated partition coefficient; [e] PAINS: pan-assay interfering structure.

References

(1) Mendez, M. F. Early-Onset Alzheimer Disease. *Neurol Clin* **2017**, *35* (2), 263–281. https://doi.org/10.1016/j.ncl.2017.01.005.

(2) Ayodele, T.; Rogaeva, E.; Kurup, J. T.; Beecham, G.; Reitz, C. Early-Onset Alzheimer's Disease: What Is Missing in Research? *Curr Neurol Neurosci Rep* **2021**, *21* (2). https://doi.org/10.1007/s11910-020-01090-y.

(3) Wu, L.; Rosa-Neto, P.; Hsiung, G. Y. R.; Sadovnick, A. D.; Masellis, M.; Black, S. E.; Jia, J.; Gauthier, S. Early-Onset Familial Alzheimer's Disease (EOFAD). *Canadian Journal of Neurological Sciences* **2012**, *39* (4), 436–445. https://doi.org/10.1017/S0317167100013949.

(4) Tellechea, P.; Pujol, N.; Esteve-Belloch, P.; Echeveste, B.; García-Eulate, M. R.; Arbizu, J.; Riverol, M. Early- and Late-Onset Alzheimer Disease: Are They the Same Entity? *Neurologia* **2018**, *33* (4), 244–253. https://doi.org/10.1016/j.nrl.2015.08.002.

(5) Barker, W.; Luis, C.; Kashuba, A; Luis, M; Harwood, DG; Loewenstein, D; Waters, C; Jimison, P; Shepherd, E; Sevush, S; Graff-Radford, N; Newland, D; Todd, M; Gold, M; Heilman, K; Doty, L; Goodman, I; Robinson, B; Pearl, G; Dickson, D; Duara, R. Relative Frequencies of Alzheimer Disease, Lewy Body, Vascular and Frontotemporal Dementia, and Hippocampal Sclerosis in the State of Florida Brain Bank. *Alzheimer Dis Assoc Disord* **2002,** *16* (4), 203-212. https://doi.org/10.1097/00002093-200210000-00001.

(6) Lyketsos, C. G.; Carrillo, M. C.; Ryan, J. M.; Khachaturian, A. S.; Trzepacz, P.; Amatniek, J.; Cedarbaum, J.; Brashear, R.; Miller, D. S. Neuropsychiatric Symptoms in Alzheimer's Disease. *Alzheimer's and Dementia* **2011**, *7* (5), 532–539. https://doi.org/10.1016/j.jalz.2011.05.2410.

(7) Atri, A. The Alzheimer's Disease Clinical Spectrum: Diagnosis and Management. *Medical Clinics of North America* **2019**, *103* (2), 263–293. https://doi.org/10.1016/j.mcna.2018.10.009.

(8) Porsteinsson, A. P.; Isaacson, R. S.; Knox, S.; Sabbagh, M. N.; Rubino, I. Diagnosis of Early Alzheimer's Disease: Clinical Practice in 2021. *Journal of Prevention of Alzheimer's Disease* **2021**, *8* (3), 371–386. https://doi.org/10.14283/jpad.2021.23.

(9) Alzheimer's Disease Fact Sheet. *National Institute on Aging*. https://www.nia.nih.gov/health/alzheimers-disease-fact-sheet (accessed 2023-04-07).

(10) World Alzheimer Report 2018. The State of the Art of Dementia Research: New Frontiers. *Alzheimer's Disease International.* **2018**. https://www.alzint.org/u/WorldAlzheimerReport2018.pdf (accessed 2023-04-07).

(11) Dementia numbers in Canada. *Alzheimer Society of Canada*. https://alzheimer.ca/en/about-dementia/what-dementia/dementia-numbers-canada (accessed 2023-04-07).

(12) Chambers, L. W.; Bancej, C.; McDowell, I. Prevalence and Monetary Costs of Dementia in Canada: Population Health Expert Panel. *The Alzheimer Society of Canada* **2016**, 1–70. https://doi.org/10.1017/CBO9781107415324.004.

(13) Dementia in Canada, including Alzheimer's disease. *Government of Canada*.https://www.canada.ca/en/public-health/services/publications/diseases-conditions/dementia-highlights-canadian-chronic-disease-surveillance.html (accessed 2023-04-07)

(14) Dementia statistics. *Alzheimer's Disease International*. https://www.alzint.org/about/dementia-facts-figures/dementia-statistics/#:~:text=There%20are%20over%2055%20million,will%20be%20in%20developing%20countris (accessed 2023-04-07)

(15) Reichman, W. E.; Rose, N. S. History and Experience: The Direction of Alzheimer's Disease. *Menopause* **2012**, *19* (7), 724–734. https://doi.org/10.1097/gme.0b013e31825a28f2.

(16) Strassnig, M.; Ganguli, M. About a Peculiar Disease of the Cerebral Cortex: Alzheimer's Original Case Revisited. *Psychiatry (Edgmont)* **2005**, *2* (9), 30.

(17) Ahmed, T. F.; Ahmed, A.; Imtiaz, F. History in Perspective: How Alzheimer's Disease Came to Be Where It Is? *Brain Res* **2021**, *1758* (February), 147342. https://doi.org/10.1016/j.brainres.2021.147342.

(18) Blessed, G.; Tomlinson, B. The Association between Quantitative Measures of Dementia and of Senile Change in the Cerebral Grey Matter of Elderly Subjects. *Br J Psychiatry* **1968**, *114* (512), 797–811. https://doi.org/bjp.114.512.797.

(19) Ramirez-Bermudez, J. Alzheimer's Disease: Critical Notes on the History of a Medical Concept. *Arch Med Res* **2012**, *43* (8), 595–599. https://doi.org/10.1016/j.arcmed.2012.11.008.

(20) Whitehouse, P. J.; Price, D. L.; Clark, A. W.; Coyle, J. T.; DeLong, M. R. Alzheimer Disease: Evidence for Selective Loss of Cholinergic Neurons in the Nucleus Basalis. *Ann Neurol* **1981**, *10* (2), 122–126. https://doi.org/10.1002/ANA.410100203.

(21) Glenner, G.; Wong, C. Alzheimer's Disease and Down's Syndrome: Sharing of a Unique Cerebrovascular Amyloid Fibril Protein. *Biochem Biophys Res Commun* **1984**, *122*(3), 1131-1135. https://doi.org/0006-291x(84)91209-9.

(22) Glenner, G. G.; Wong, C. W. Alzheimer's Disease: Initial Report of the Purification and Characterization of a Novel Cerebrovascular Amyloid Protein. *Biochem Biophys Res Commun* **1984**, *120* (3), 885–890. https://doi.org/10.1016/S0006-291X(84)80190-4.

(23) Grundke-Iqbal, I.; Iqbal, K.; Tung, Y. C.; Quinlan, M.; Wisniewski, H. M.; Binder, L. I. Abnormal Phosphorylation of the Microtubule-Associated Protein Tau (Tau) in Alzheimer Cytoskeletal Pathology. *Proc Natl Acad Sci U S A* **1986**, *83* (13), 4913–4917. https://doi.org/10.1073/PNAS.83.13.4913.

(24) Kosik, K. S.; Joachim, C. L.; Selkoe, D. J. Microtubule-Associated Protein Tau (τ) Is a Major Antigenic Component of Paired Helical Filaments in Alzheimer Disease. *Proc Natl Acad Sci U S A* **1986**, *83* (11), 4044–4048. https://doi.org/10.1073/PNAS.83.11.4044.

(25) Bondi, M. W.; Edmonds, E. C.; Salmon, D. P. Alzheimer's Disease: Past, Present, and Future. *Journal of the International Neuropsychological Society* **2017**, *23* (9-10 Special Issue), 818–831. https://doi.org/10.1017/S135561771700100X.

(26) Nikolac Perkovic, M.; Pivac, N. Genetic Markers of Alzheimer's Disease. *Adv Exp Med Biol* **2019**, *1192*, 27–52. https://doi.org/10.1007/978-981-32-9721-0_3.

(27) Reitz, C. Genetic Diagnosis and Prognosis of Alzheimer's Disease: Challenges and Opportunities. *Expert Rev Mol Diagn* **2015**, *15* (3), 339–348. https://doi.org/10.1586/14737159.2015.1002469.

(28) Strittmatter, W. J.; Saunders, A. M.; Schmechel, D.; Pericak-Vance, M.; Enghild, J.; Salvesen, G. S.; Roses, A. D. Apolipoprotein E: High-Avidity Binding to β-Amyloid and Increased Frequency of Type 4 Allele in Late-Onset Familial Alzheimer Disease. *Proc Natl Acad Sci U S A* **1993**, *90* (5), 1977–1981. https://doi.org/10.1073/PNAS.90.5.1977.

(29) Serrano-Pozo, A.; Das, S.; Hyman, B. T. APOE and Alzheimer's Disease: Advances in Genetics, Pathophysiology, and Therapeutic Approaches. *Lancet Neurol* **2021**, *20* (1), 68–80. https://doi.org/10.1016/S1474-4422(20)30412-9.

(30) Tan, C. C.; Yu, J. T.; Tan, L. Biomarkers for Preclinical Alzheimer's Disease. *Journal of Alzheimer's Disease* **2014**, *42* (4), 1051–1069. https://doi.org/10.3233/JAD-140843.

(31) Graff-Radford, J.; Yong, K. X. X.; Apostolova, L. G.; Bouwman, F. H.; Carrillo, M.; Dickerson, B. C.; Rabinovici, G. D.; Schott, J. M.; Jones, D. T.; Murray, M. E. New Insights into Atypical Alzheimer's Disease in the Era of Biomarkers. *Lancet Neurol* **2021**, *20* (3), 222–234. https://doi.org/10.1016/S1474-4422(20)30440-3.

(32) Khan, S.; Barve, K. H.; Kumar, M. S. Recent Advancements in Pathogenesis, Diagnostics and Treatment of Alzheimer's Disease. *Curr Neuropharmacol* **2020**, *18* (11), 1106–1125. https://doi.org/10.2174/1570159x18666200528142429.

(33) Chen, Z. R.; Huang, J. B.; Yang, S. L.; Hong, F. F. Role of Cholinergic Signaling in Alzheimer's Disease. *Molecules* **2022**, *27* (6). https://doi.org/10.3390/molecules27061816.

(34) Hampel, H.; Mesulam, M. M.; Cuello, A. C.; Farlow, M. R.; Giacobini, E.; Grossberg, G. T.; Khachaturian, A. S.; Vergallo, A.; Cavedo, E.; Snyder, P. J.; Khachaturian, Z. S. The Cholinergic System in the Pathophysiology and Treatment of Alzheimer's Disease. *Brain* **2018**, *141* (7), 1917–1933. https://doi.org/10.1093/brain/awy132.

(35) Dubois, B.; Feldman, H. H.; Jacova, C.; Cummings, J. L.; DeKosky, S. T.; Barberger-Gateau, P.; Delacourte, A.; Frisoni, G.; Fox, N. C.; Galasko, D.; Gauthier, S.; Hampel, H.; Jicha, G. A.; Meguro, K.; O'Brien, J.; Pasquier, F.; Robert, P.; Rossor, M.; Salloway, S.; Sarazin, M.; de Souza, L. C.; Stern, Y.; Visser, P. J.; Scheltens, P. Revising the Definition of Alzheimer's Disease: A New Lexicon. *The Lancet Neurology*. Lancet Neurol November 2010, pp 1118–1127. https://doi.org/10.1016/S1474-4422(10)70223-4.

(36) Francis, P. T.; Palmer, A. M.; Snape, M.; Wilcock, G. K. The Cholinergic Hypothesis of Alzheimer's Disease: A Review of Progress. *J Neurol Neurosurg Psychiatry* **1999**, *66* (2), 137–147. https://doi.org/10.1136/jnnp.66.2.137.

(37) Wang, R.; Reddy, P. H. Role of Glutamate and NMDA Receptors in Alzheimer's Disease. *Journal of Alzheimer's Disease* **2017**, *57* (4), 1041–1048. https://doi.org/10.3233/JAD-160763.

(38) Andersen, J. V.; Markussen, K. H.; Jakobsen, E.; Schousboe, A.; Waagepetersen, H. S.; Rosenberg, P. A.; Aldana, B. I. Glutamate Metabolism and Recycling at the Excitatory Synapse in Health and Neurodegeneration. *Neuropharmacology* **2021**, *196*. https://doi.org/10.1016/j.neuropharm.2021.108719.

(39) Song, J.; Yang, X.; Zhang, M.; Wang, C.; Chen, L. Glutamate Metabolism in Mitochondria Is Closely Related to Alzheimer's Disease. *Journal of Alzheimer's Disease* **2021**, *84* (2), 557–578. https://doi.org/10.3233/JAD-210595.

(40) Czapski, G. A.; Strosznajder, J. B. Glutamate and GABA in Microglia-Neuron Cross-Talk in Alzheimer's Disease. *Int J Mol Sci* **2021**, *22* (21). https://doi.org/10.3390/ijms222111677.

(41) Imbimbo, B. P.; Lombard, J.; Pomara, N. Pathophysiology of Alzheimer's Disease. *Neuroimaging Clin N Am* **2005**, *15* (4), 727–753. https://doi.org/10.1016/j.nic.2005.09.009.

(42) Kumar, A.; Singh, A.; Ekavali. A Review on Alzheimer's Disease Pathophysiology and Its Management: An Update. *Pharmacological Reports* **2015**, *67* (2), 195–203. https://doi.org/10.1016/j.pharep.2014.09.004.

(43) Abeysinghe, A. A. D. T.; Deshapriya, R. D. U. S.; Udawatte, C. Alzheimer's Disease; a Review of the Pathophysiological Basis and Therapeutic Interventions. *Life Sci* **2020**, *256* (June), 117996. https://doi.org/10.1016/j.lfs.2020.117996.

(44) Šerý, O.; Povová, J.; Míšek, I.; Pešák, L.; Janout, V. Molecular Mechanisms of Neuropathological Changes in Alzheimer's Disease: A Review. *Folia Neuropathol* **2013**, *51* (1), 1–9. https://doi.org/10.5114/fn.2013.34190.

(45) Weller, J.; Budson, A. Current Understanding of Alzheimer's Disease Diagnosis and Treatment. *F1000Res* **2018**, *7* (0), 1–9. https://doi.org/10.12688/f1000research.14506.1.

(46) Gallardo, G.; Holtzman, D. M. Amyloid-β and Tau at the Crossroads of Alzheimer's Disease. *Adv Exp Med Biol* **2019**, *1184*, 187–203. https://doi.org/10.1007/978-981-32-9358-8_16.

(47) Arnsten, A. F. T.; Datta, D.; Del Tredici, K.; Braak, H. Hypothesis: Tau Pathology Is an Initiating Factor in Sporadic Alzheimer's Disease. *Alzheimer's and Dementia* **2021**, *17* (1), 115–124. https://doi.org/10.1002/alz.12192.

(48) Kametani, F.; Hasegawa, M. Reconsideration of Amyloid Hypothesis and Tau Hypothesis in Alzheimer's Disease. *Frontiers in Neuroscience*. Frontiers Media S.A. January 30, 2018. https://doi.org/10.3389/fnins.2018.00025.

(49) Srivastava, S.; Ahmad, R.; Khare, S. K. Alzheimer's Disease and Its Treatment by Different Approaches: A Review. *Eur J Med Chem* **2021**, *216*, 113320. https://doi.org/10.1016/j.ejmech.2021.113320.

(50) Sukhorukov, V. S.; Mudzhiri, N. M.; Voronkova, A. S.; Baranich, T. I.; Glinkina, V. V.; Illarioshkin, S. N. Mitochondrial Disorders in Alzheimer's Disease. *Biochemistry (Moscow)* **2021**, *86* (6), 667–679. https://doi.org/10.1134/S0006297921060055.

(51) Swerdlow, R. H. Mitochondria and Mitochondrial Cascades in Alzheimer's Disease. *Journal of Alzheimer's Disease* **2018**, *62* (3), 1403–1416. https://doi.org/10.3233/JAD-170585.

(52) Perez Ortiz, J. M.; Swerdlow, R. H. Mitochondrial Dysfunction in Alzheimer's Disease: Role in Pathogenesis and Novel Therapeutic Opportunities. *Br J Pharmacol* **2019**, *176* (18), 3489–3507. https://doi.org/10.1111/bph.14585.

(53) Wang, X.; Wang, W.; Li, L.; Perry, G.; Lee, H. gon; Zhu, X. Oxidative Stress and Mitochondrial Dysfunction in Alzheimer's Disease. *Biochim Biophys Acta Mol Basis Dis* **2014**, *1842* (8), 1240–1247. https://doi.org/10.1016/j.bbadis.2013.10.015.

(54) Gowda, P.; Reddy, P. H.; Kumar, S. Deregulated Mitochondrial MicroRNAs in Alzheimer's Disease: Focus on Synapse and Mitochondria. *Ageing Res Rev* **2022**, *73*. https://doi.org/10.1016/j.arr.2021.101529.

(55) Carson, M. J.; Doose, J. M.; Melchior, B.; Schmid, C. D.; Ploix, C. C. CNS Immune Privilege: Hiding in Plain Sight. *Immunol Rev* **2006**, *213* (1), 48–65. https://doi.org/10.1111/J.1600-065X.2006.00441.X.

(56) Morales, I.; Guzmán-Martínez, L.; Cerda-Troncoso, C.; Farías, G. A.; Maccioni, R. B. Neuroinflammation in the Pathogenesis of Alzheimer's Disease. A Rational Framework for the Search of Novel Therapeutic Approaches. *Front Cell Neurosci* **2014**, *8* (1 APR). https://doi.org/10.3389/FNCEL.2014.00112/FULL.

(57) Zhang, F.; Jiang, L. Neuroinflammation in Alzheimer's Disease. *Neuropsychiatr Dis Treat* **2014**, *11*, 243–256. https://doi.org/10.2147/NDT.S75546.

(58) Bronzuoli, M.; Iacomino, A.; Steardo, L.; Scuderi, C. Targeting Neuroinflammation in Alzheimer's Disease. *J Inflamm Res.* **2016**, *9*, 199–208. https://doi.org/10.2147/JIR.S86958.

(59) Manning F.C. Tacrine Therapy for the Dementia of Alzheimer's Disease. *Am Fam Physician.* **1994**, *50* (4), 819-826.

(60) Davis, K. L.; Thal, L. J.; Gamzu, E. R.; Davis, C. S.; Woolson, R. F.; Gracon, S. I.; Drachman, D. A.; Schneider, L. S.; Whitehouse, P. J.; Hoover, T. M.; Morris, J. C.; Kawas, C. H.; Knopman, D. S.; Earl, N. L.; Kumar, V.; Doody, R. S. A Double-Blind, Placebo-Controlled Multicenter Study of Tacrine for Alzheimer's Disease. *New England Journal of Medicine* **1992**, *327* (18), 1253–1259. https://doi.org/10.1056/NEJM199210293271801.

(61) Qizilbash, N.; Birks, J.; Arrieta, J.L.; Lewington, S.; Szeto, S. WITHDRAWN: Tacrine for Alzheimer's Disease. *Cochrane Database Syst Rev.* **2007**, *Jul 18* (3), CD000202. https://doi.org/10.1002/14651858.CD000202.

(62) Eagger, S.A.; Levy, R.; Sahakian, B.J. Tacrine in Alzheimer's Disease. *Lancet.* **1991,** *337* (8748), 989-992. https://doi.org/10.1016/0140-6736(91)92656-m.

(63) Briggs, R.; Kennelly, S. P.; O'Neill, D. Drug Treatments in Alzheimer's Disease. *Clinical Medicine, Journal of the Royal College of Physicians of London* **2016**, *16* (3), 247–253. https://doi.org/10.7861/clinmedicine.16-3-247.

(64) Herrmann, N.; Chau, S.; Kircanski, I.; Lanctot, K. Current and Emerging Drug Treatment Options for Alzheimer's Disease: A Systematic Review. *Springer* **2011**, *71* (15), 2031–2065. https://doi.org/10.2165/11595870-000000000-00000.

(65) McShane, R.; Westby, M.; Roberts, E.; Minakaran, N.; Schneider, L.; Farrimond, L.; Maayan, N.; Ware, J; Debarros, J. Memantine for Dementia. *Cochrane Database Syst Rev*. **2019**, *20* (3), CD003154. https://doi.org/10.1002/14651858.CD003154.pub6.

(66) Robinson, D. M.; Keating, G. M. Memantine: A Review of Its Use in Alzheimer's Disease. *Drugs* **2006**, *66* (11), 1515–1534. https://doi.org/10.2165/00003495-200666110-00015.

(67) Schelterns, P.; Scheltens, P.; Feldman, H. Treatment of Alzheimer's Disease: Current Status and New Perspectives. *Lancet Neurol.* **2003**, *2* (9), 539-547. https://doi.org/10.1016/s1474-4422(03)00502-7.

(68) Cummings, J.; Lee, G.; Ritter, A.; Sabbagh, M.; Zhong, K. Alzheimer's Disease Drug Development Pipeline: 2020. *Alzheimer's and Dementia: Translational Research and Clinical Interventions* **2020**, *6* (1), 1–29. https://doi.org/10.1002/trc2.12050.

(69) Cummings, J.; Lee, G.; Zhong, K.; Fonseca, J.; Taghva, K. Alzheimer's Disease Drug Development Pipeline: 2021. *Alzheimer's and Dementia: Translational Research and Clinical Interventions* **2021**, *7* (1), 1–24. https://doi.org/10.1002/trc2.12179.

(70) Cummings, J.; Lee, G.; Nahed, P.; Kambar, M. E. Z. N.; Zhong, K.; Fonseca, J.; Taghva, K. Alzheimer's Disease Drug Development Pipeline: 2022. *Alzheimer's and Dementia: Translational Research and Clinical Interventions* **2022**, *8* (1). https://doi.org/10.1002/trc2.12295.

(71) Vandenberghe, R.; Riviere, M. E.; Caputo, A.; Sovago, J.; Maguire, R. P.; Farlow, M.; Marotta, G.; Sanchez-Valle, R.; Scheltens, P.; Ryan, J. M.; Graf, A. Active Aβ Immunotherapy CAD106 in Alzheimer's Disease: A Phase 2b Study. *Alzheimer's & Dementia : Translational Research & Clinical Interventions* **2017**, *3* (1), 10. https://doi.org/10.1016/J.TRCI.2016.12.003.

(72) Novak, P.; Kovacech, B.; Katina, S.; Schmidt, R.; Scheltens, P.; Kontsekova, E.; Ropele, S.; Fialova, L.; Kramberger, M.; Paulenka-Ivanovova, N.; Smisek, M.; Hanes, J.; Stevens, E.; Kovac, A.; Sutovsky, S.; Parrak, V.; Koson, P.; Prcina, M.; Galba, J.; Cente, M.; Hromadka, T.; Filipcik, P.;

Piestansky, J.; Samcova, M.; Prenn-Gologranc, C.; Sivak, R.; Froelich, L.; Fresser, M.; Rakusa, M.; Harrison, J.; Hort, J.; Otto, M.; Tosun, D.; Ondrus, M.; Winblad, B.; Novak, M.; Zilka, N. ADAMANT: A Placebo-Controlled Randomized Phase 2 Study of AADvac1, an Active Immunotherapy against Pathological Tau in Alzheimer's Disease. *Nat Aging* **2021**, *1* (6), 521–534. https://doi.org/10.1038/S43587-021-00070-2.

(73) Wang, C. Y.; Wang, P. N.; Chiu, M. J.; Finstad, C. L.; Lin, F.; Lynn, S.; Tai, Y. H.; De Fang, X.; Zhao, K.; Hung, C. H.; Tseng, Y.; Peng, W. J.; Wang, J.; Yu, C. C.; Kuo, B. S.; Frohna, P. A. UB-311, a Novel UBITh® Amyloid β Peptide Vaccine for Mild Alzheimer's Disease. *Alzheimers Dement (N Y)* **2017**, *3* (2), 262–272. https://doi.org/10.1016/J.TRCI.2017.03.005.

(74) Dyck, C.; Swanson, C.; Aisen, P.; Bateman R.; Chen, C.; Gee, M.; Kanekiyo, M.; Li, D.; Reyderman, L.; Cohen, S.; Froelich, L.; Katayama, S.; Sabbagh, M.; Vellas, B.; Watson, D.; Dhadda, S.; Irizarry, M.; Kramaer, L.; Iwatsubo, T. Lecanemab in Early Alzheimer's Disease. *N Engl J Med* **2023**, *388* (1), 142–143. https://doi.org/10.1056/NEJMOA2212948.

(75) Sevigny, J.; Chiao, P.; Bussière, T.; Weinreb, P. H.; Williams, L.; Maier, M.; Dunstan, R.; Salloway, S.; Chen, T.; Ling, Y.; O'Gorman, J.; Qian, F.; Arastu, M.; Li, M.; Chollate, S.; Brennan, M. S.; Quintero-Monzon, O.; Scannevin, R. H.; Arnold, H. M.; Engber, T.; Rhodes, K.; Ferrero, J.; Hang, Y.; Mikulskis, A.; Grimm, J.; Hock, C.; Nitsch, R. M.; Sandrock, A. The Antibody Aducanumab Reduces Aβ Plaques in Alzheimer's Disease. *Nature* **2016**, *537* (7618), 50–56. https://doi.org/10.1038/nature19323.

(76) Budd Haeberlein, S.; Aisen, P. S.; Barkhof, F.; Chalkias, S.; Chen, T.; Cohen, S.; Dent, G.; Hansson, O.; Harrison, K.; von Hehn, C.; Iwatsubo, T.; Mallinckrodt, C.; Mummery, C. J.; Muralidharan, K. K.; Nestorov, I.; Nisenbaum, L.; Rajagovindan, R.; Skordos, L.; Tian, Y.; van Dyck, C. H.; Vellas, B.; Wu, S.; Zhu, Y.; Sandrock, A. Two Randomized Phase 3 Studies of Aducanumab in Early Alzheimer's Disease. *Journal of Prevention of Alzheimer's Disease* **2022**, *9* (2), 197–210. https://doi.org/10.14283/jpad.2022.30.

(77) Swanson, C. J.; Zhang, Y.; Dhadda, S.; Wang, J.; Kaplow, J.; Lai, R. Y. K.; Lannfelt, L.; Bradley, H.; Rabe, M.; Koyama, A.; Reyderman, L.; Berry, D. A.; Berry, S.; Gordon, R.; Kramer, L. D.; Cummings, J. L. A Randomized, Double-Blind, Phase 2b Proof-of-Concept Clinical Trial in Early Alzheimer's Disease with Lecanemab, an Anti-Aβ Protofibril Antibody. *Alzheimers Res Ther* **2021**, *13* (1). https://doi.org/10.1186/s13195-021-00813-8.

(78) Hardy, J.; Allsop, D. Amyloid Deposition as the Central Event in the Aetiology of Alzheimer's Disease. *Trends Pharmacol Sci* **1991**, *12* (C), 383–388. https://doi.org/10.1016/0165-6147(91)90609-V.

(79) John, H.; Gerald, H. Alzheimer's Disease: The Amyloid Cascade Hypothesis. *Science* **1992**, *256* (5054), 184–185. https://doi.org/science.1566067.

(80) Doig, A. J.; Del Castillo-Frias, M. P.; Berthoumieu, O.; Tarus, B.; Nasica-Labouze, J.; Sterpone, F.; Nguyen, P. H.; Hooper, N. M.; Faller, P.; Derreumaux, P. Why Is Research on Amyloid-β Failing to Give New Drugs for Alzheimer's Disease? *ACS Chem Neurosci* **2017**, *8* (7), 1435–1437. https://doi.org/10.1021/acschemneuro.7b00188.

(81) Selkoe, D. J.; Hardy, J. The Amyloid Hypothesis of Alzheimer's Disease at 25 Years. *EMBO Mol Med* **2016**, *8* (6), 595–608. https://doi.org/10.15252/emmm.201606210.

(82) Vijayan, D.; Chandra, R. Amyloid Beta Hypothesis in Alzheimer's Disease: Major Culprits and Recent Therapeutic Strategies. *Curr Drug Targets* **2019**, *21* (2), 148–166. https://doi.org/10.2174/1389450120666190806153206.

(83) Gallardo, G.; Holtzman, D. M. Amyloid-β and Tau at the Crossroads of Alzheimer's Disease. *Adv Exp Med Biol* **2019**, *1184*, 187–203. https://doi.org/10.1007/978-981-32-9358-8_16.

(84) Ling, Y.; Morgan, K.; Kalsheker, N. Amyloid Precursor Protein (APP) and the Biology of Proteolytic Processing: Relevance to Alzheimer's Disease. *International Journal of Biochemistry and Cell Biology* **2003**, *35* (11), 1505–1535. https://doi.org/10.1016/S1357-2725(03)00133-X.

(85) Zhang, H.; Ma, Q.; Zhang, Y. W.; Xu, H. Proteolytic Processing of Alzheimer's β-Amyloid Precursor Protein. *J Neurochem* **2012**, *120* (SUPPL. 1), 9–21. https://doi.org/10.1111/j.1471-4159.2011.07519.x.

(86) O'Brien, R. J.; Wong, P. C. Amyloid Precursor Protein Processing and Alzheimer's Disease. *Annu Rev Neurosci* **2011**, *34*, 185–204. https://doi.org/10.1146/annurev-neuro-061010-113613.

(87) De Strooper, B.; Annaert, W. Proteolytic Processing and Cell Biological Functions of the Amyloid Precursor Protein. *J Cell Sci* **2000**, *113* (11), 1857–1870. https://doi.org/10.1242/jcs.113.11.1857.

(88) Nunan, J.; Small, D. H. Proteolytic Processing of the Amyloid-β Protein Precursor of Alzheimer's Disease. *Essays Biochem* **2002**, *38*, 37–49. https://doi.org/10.1042/bse0380037.

(89) Tan, J. Z. A.; Gleeson, P. A. The Role of Membrane Trafficking in the Processing of Amyloid Precursor Protein and Production of Amyloid Peptides in Alzheimer's Disease. *Biochim Biophys Acta Biomembr* **2019**, *1861* (4), 697–712. https://doi.org/10.1016/j.bbamem.2018.11.013.

(90) Mañucat-Tan, N. B.; Saadipour, K.; Wang, Y. J.; Bobrovskaya, L.; Zhou, X. F. Cellular Trafficking of Amyloid Precursor Protein in Amyloidogenesis Physiological and Pathological Significance. *Mol Neurobiol* **2019**, *56* (2), 812–830. https://doi.org/10.1007/s12035-018-1106-9.

(91) Agostinho, P.; Pliássova, A.; Oliveira, C. R.; Cunha, R. A. Localization and Trafficking of Amyloid-β Protein Precursor and Secretases: Impact on Alzheimer's Disease. *Journal of Alzheimer's Disease* **2015**, *45* (2), 329–347. https://doi.org/10.3233/JAD-142730.

(92) Kang, J.; Lemaire, H. G.; Unterbeck, A.; Salbaum, J. M.; Masters, C. L.; Grzeschik, K. H.; Multhaup, G.; Beyreuther, K.; Müller-Hill, B. The Precursor of Alzheimer's Disease Amyloid A4 Protein Resembles a Cell-Surface Receptor. *Nature* **1987**, *325* (6106), 733–736. https://doi.org/10.1038/325733a0.

(93) Cappai, R. Making Sense of the Amyloid Precursor Protein: Its Tail Tells an Interesting Tale. *J Neurochem* **2014**, *130* (3), 325–327. https://doi.org/10.1111/jnc.12707.

(94) Sandbrink, R.; Masters, C. Beta A4-Amyloid Protein Precursor MRNA Isoforms without Exon 15 Are Ubiquitously Expressed in Rat Tissues Including Brain, but Not in Neurons. *J bIol Chem*. **1994**, *269* (2), 1510-1517.

(95) Kang, J.; Müller-Hill, B. Differential Splicing of Alzheimer's Disease Amyloid A4 Precursor RNA in Rat Tissues: PreA4695 MRNA Is Predominantly Produced in Rat and Human Brain. *Biochem Biophys Res Commun* **1990**, *166* (3), 1192–1200. https://doi.org/10.1016/0006-291X(90)90992-V.

(96) Silva, H. De; Jen, A.; Wickenden, C.; Jen, L.; Wikinson, S.; Patel, A. Cell-Specific Expression of β-Amyloid Precursor Protein Isoform MRNAs and Proteins in Neurons and Astrocytes. *Brain Res Mol Brian Res* **1997**, *47* (1-2), 147-156. https://doi.org/10.1016/s0169-328x97)00045-4.

(97) Wasco, W.; Gurubhagavatula, S.; Paradis, M. D.; Romano, D. M.; Sisodia, S. S.; Hyman, B. T.; Neve, R. L.; Tanzi, R. E. Isolation and Characterization of APLP2 Encoding a Homologue of the Alzheimer's Associated Amyloid Beta Protein Precursor. *Nat Genet* **1993**, *5* (1), 95–100. https://doi.org/10.1038/NG0993-95.

(98) Wasco, W.; Bupp, K.; Magendantz, M.; Gusella, J. F.; Tanzi, R. E.; Solomon, F. Identification of a Mouse Brain CDNA That Encodes a Protein Related to the Alzheimer Disease-Associated Amyloid Beta Protein Precursor. *Proc Natl Acad Sci U S A* **1992**, *89* (22), 10758–10762. https://doi.org/10.1073/PNAS.89.22.10758.

(99) Coulson, E. J.; Paliga, K.; Beyreuther, K.; Masters, C. L. What the Evolution of the Amyloid Protein Precursor Supergene Family Tells Us about Its Function. *Neurochem Int* **2000**, *36* (3), 175–184. https://doi.org/10.1016/S0197-0186(99)00125-4.

(100) Burrinha, T.; Cláudia, G. A. Aging Impact on Amyloid Precursor Protein Neuronal Trafficking. *Curr Opin Neurobiol* **2022**, *73*. https://doi.org/10.1016/j.conb.2022.102524.

(101) Delport, A.; Hewer, R. The Amyloid Precursor Protein: A Converging Point in Alzheimer's Disease. *Mol Neurobiol* **2022**, *59* (7), 4501–4516. https://doi.org/10.1007/s12035-022-02863-x.

(102) Strope, T. A.; Wilkins, H. M. Amyloid Precursor Protein and Mitochondria. *Curr Opin Neurobiol* **2023**, *78*. https://doi.org/10.1016/j.conb.2022.102651.

(103) Wilkins, H. M.; Swerdlow, R. H. Amyloid Precursor Protein Processing and Bioenergetics. *Brain Res Bull* **2017**, *133*, 71–79. https://doi.org/10.1016/j.brainresbull.2016.08.009.

(104) Zheng, H.; Koo, E. H. Biology and Pathophysiology of the Amyloid Precursor Protein. *Mol Neurodegener* **2011**, *6* (1). https://doi.org/10.1186/1750-1326-6-27.

(105) Shah, S.; Lee, S. F.; Tabuchi, K.; Hao, Y. H.; Yu, C.; LaPlant, Q.; Ball, H.; Dann, C. E.; Südhof, T.; Yu, G. Nicastrin Functions as a γ-Secretase-Substrate Receptor. *Cell* **2005**, *122* (3), 435–447. https://doi.org/10.1016/j.cell.2005.05.022.

(106) Xu, Y.; Kim, H.; Joo, Y.; Choi, Y.; Chang K-A.; Park, C.; Shin, K-Y.; Kim, S.; Cheon, Y-H.; Baik, T-K.; Kim, J-H.; Suh, Y-H. Intracellular Domains of Amyloid Precursor-like Protein 2 Interact with CP2 Transcription Factor in the Nucleus and Induce Glycogen Synthase Kinase-3β. *Cell Death Differ*. **2007**, *14* (1), 79-91. https://doi.org/10.1038/sj.cdd.4401928.

(107) Lorenzo, A.; Yuan, M.; Zhang, Z.; Paganetti, P.; Sturchler-Pierrat, C.; Staufenbiel, M.; Mautino, J.; Vigo, F.; Sommer, B.; Yankner, B. Amyloid β Interacts with the Amyloid Precursor Protein: A Potential Toxic Mechanism in Alzheimer's Disease. *Nat Neurosci.* **2000**, *3* (5), 460-464. https://doi.org/10.1038/74833.

(108) Lu, D. C.; Shaked, G. M.; Masliah, E.; Bredesen, D. E.; Koo, E. H. Amyloid β Protein Toxicity Mediated by the Formation of Amyloid-β Protein Precursor Complexes. *Ann Neurol* **2003**, *54* (6), 781–789. https://doi.org/10.1002/ANA.10761.

(109) Dahms, S. O.; Hoefgen, S.; Roeser, D.; Schlott, B.; Gührs, K. H.; Than, M. E. Structure and Biochemical Analysis of the Heparin-Induced E1 Dimer of the Amyloid Precursor Protein. *Proc Natl Acad Sci U S A* **2010**, *107* (12), 5381–5386. https://doi.org/10.1073/PNAS.0911326107.

(110) Soba, P.; Eggert, S.; Wagner, K.; Zentgraf, H.; Siehl, K.; Kreger, S.; Löwer, A.; Langer, A.; Merdes, G.; Paro, R.; Masters, C. L.; Müller, U.; Kins, S.; Beyreuther, K. Homo- and Heterodimerization of APP Family Members Promotes Intercellular Adhesion. *EMBO Journal* **2005**, *24* (20), 3624–3634. https://doi.org/10.1038/SJ.EMBOJ.7600824.

(111) Cacace, R.; Sleegers, K.; Van Broeckhoven, C. Molecular Genetics of Early-Onset Alzheimer's Disease Revisited. *Alzheimer's and Dementia* **2016**, *12* (6), 733–748. https://doi.org/10.1016/j.jalz.2016.01.012.

(112) Lammich, S.; Kojro, E.; Postina, R.; Gilbert, S.; Pfeiffer, R.; Jasionowski, M.; Haass, C.; Fahrenholz, F. Constitutive and Regulated α-Secretase Cleavage of Alzheimer's Amyloid Precursor Protein by a Disintegrin Metalloprotease. *Proc Natl Acad Sci U S A* **1999**, *96* (7), 3922–3927. https://doi.org/10.1073/PNAS.96.7.3922.

(113) Howard, L.; Lu, X.; Mitchell, S.; Griffiths, S.; Glynn, P. Molecular Cloning of MADM: A Catalytically Active Mammalian Disintegrin-Metalloprotease Expressed in Various Cell Types. *portlandpress.com* **1996**, *317*, 45–50.

(114) Taylor, C.; Ireland, D.; Ballagh, I.; Bourne, K.; Marechal, N.; Turner, P.; Bilkey, D.; Tate, W.; Abraham, W. Endogenous Secreted Amyloid Precursor Protein-α Regulates Hippocampal NMDA Receptor Function, Long-Term Potentiation and Spatial Memory. *Neurobiol Dis*. **2008**, *31* (2), 250-260. https://doi.org/10.1016/j.nbd.2008.04.011.

(115) Siemes, C.; Quast, T.; Kummer, C.; Wehner, S.; Kirfel, G.; Müller, U.; Herzog, V. Keratinocytes from APP/APLP2-Deficient Mice Are Impaired in Proliferation, Adhesion and Migration in Vitro. *Elsevier* **2006**. https://doi.org/10.1016/j.yexcr.2006.02.025.

(116) Hooper, N. M.; Turner, A. J. The Search for α-Secretase and Its Potential as a Therapeutic Approach to Alzheimer's Disease. *Curr Med Chem* **2012**, *9* (11), 1107–1119. https://doi.org/10.2174/0929867023370121.

(117) Postina, R. Activation of α-Secretase Cleavage. *J Neurochem* **2012**, *120* (SUPPL. 1), 46–54. https://doi.org/10.1111/j.1471-4159.2011.07459.x.

(118) Vincent, B.; Govitrapong, P. Activation of the α-Secretase Processing of AβPP as a Therapeutic Approach in Alzheimer's Disease. *J Alzheimers Dis* **2011**, *24 Suppl 2* (SUPPL. 2), 75–94. https://doi.org/10.3233/JAD-2011-110218.

(119) Altmeppen, H. C.; Prox, J.; Puig, B.; Kluth, M. A.; Bernreuther, C.; Thurm, D.; Jorissen, E.; Petrowitz, B.; Bartsch, U.; De Strooper, B.; Saftig, P.; Glatzel, M. Lack of A-Disintegrin-and-Metalloproteinase ADAM10 Leads to Intracellular Accumulation and Loss of Shedding of the Cellular Prion Protein in Vivo. *Mol Neurodegener* **2011**, *6* (1). https://doi.org/10.1186/1750-1326-6-36.

(120) Vassar, R.; Bennett, B.; Babu-Khan, S.;Kahn, S.; Mendiaz, E.; Denis, P.; Teplow, D.; Ross, S.; Amarante, P. Loeloff, R.; Luo, Y.; Fisher, S.; Fuller, J.; Edenson S.; Lile, J.; Jarosinski, M.; Biere, A.; Curran, E.; Burgess, T.; Louis, J.; Collins, F.; Treanor, J.; Rogers, G.; Citron, M. β-Secretase Cleavage of Alzheimer's Amyloid Precursor Protein by the Transmembrane Aspartic Protease BACE. *Science*. **1999**, *286* (5440), 735–741. https://doi.org/10.1126/science.286.5440.735.

(121) Hussain, I.; Powell, D.; Howlett, D.; Chapman, G.; Gilmour, L.; Murdock, P.; Tew, D.; Meek, T.; Chapman, C.; Schneider, K.; Ratcliffe, S.; Tattersall, D.; Testa, T.; Southan, C.; Ryna D.; Simmons, D.; Walsh, F.; Dingwall, C.; Christie, G. ASP1 (BACE2) Cleaves the Amyloid Precursor Protein at the β-Secretase Site. *Mol Cell Neurosci.* **2000**, *16* (5), 609-619. https://doi.org/10.1006/mcne.2000.0884.

(122) Mohamed, T.; Shakeri, A.; Rao, P. P. N. Amyloid Cascade in Alzheimer's Disease: Recent Advances in Medicinal Chemistry. *Eur J Med Chem*. **2016**, *113*, 258–272. https://doi.org/10.1016/j.ejmech.2016.02.049.

(123) Bazzari, F. H.; Bazzari, A. H. BACE1 Inhibitors for Alzheimer's Disease: The Past, Present and Any Future? *Molecules* **2022**, *27* (24). https://doi.org/10.3390/molecules27248823.

(124) Taylor, H. A.; Przemylska, L.; Clavane, E. M.; Meakin, P. J. BACE1: More than Just a β-Secretase. *Obesity Reviews* **2022**, *23* (7). https://doi.org/10.1111/obr.13430.

(125) Hampel, H.; Vassar, R.; De Strooper, B.; Hardy, J.; Willem, M.; Singh, N.; Zhou, J.; Yan, R.; Vanmechelen, E.; De Vos, A.; Nisticò, R.; Corbo, M.; Imbimbo, B. Pietro; Streffer, J.; Voytyuk, I.; Timmers, M.; Tahami Monfared, A. A.; Irizarry, M.; Albala, B.; Koyama, A.; Watanabe, N.; Kimura, T.; Yarenis, L.; Lista, S.; Kramer, L.; Vergallo, A. The β-Secretase BACE1 in Alzheimer's Disease. *Biol Psychiatry* **2021**, *89* (8), 745–756. https://doi.org/10.1016/j.biopsych.2020.02.001.

(126) Patel, S.; Bansoad, A. V.; Singh, R.; Khatik, G. L. BACE1: A Key Regulator in Alzheimer's Disease Progression and Current Development of Its Inhibitors. *Curr Neuropharmacol* **2021**, *20* (6), 1174–1193. https://doi.org/10.2174/1570159x19666211201094031.

(127) Zhang, Y. W.; Thompson, R.; Zhang, H.; Xu, H. APP Processing in Alzheimer's Disease. *Mol Brain* **2011**, *4* (1), 1–13. https://doi.org/10.1186/1756-6606-4-3.

(128) Egan, M. F.; Kost, J.; Tariot, P. N.; Aisen, P. S.; Cummings, J. L.; Vellas, B.; Sur, C.; Mukai, Y.; Voss, T.; Furtek, C.; Mahoney, E.; Harper Mozley, L.; Vandenberghe, R.; Mo, Y.; Michelson, D. Randomized Trial of Verubecestat for Mild-to-Moderate Alzheimer's Disease. *N Engl J Med* **2018**, *378* (18), 1691–1703. https://doi.org/10.1056/NEJMOA1706441.

(129) Henley, D.; Raghavan, N.; Sperling, R.; Aisen, P.; Raman, R.; Romano, G. Preliminary Results of a Trial of Atabecestat in Preclinical Alzheimer's Disease. *N Engl J Med* **2019**, *380* (15), 1483–1485. https://doi.org/10.1056/NEJMC1813435.

(130) Neumann, U.; Ufer, M.; Jacobson, L. H.; Rouzade-Dominguez, M.; Huledal, G.; Kolly, C.; Lüönd, R. M.; Machauer, R.; Veenstra, S. J.; Hurth, K.; Rueeger, H.; Tintelnot-Blomley, M.; Staufenbiel, M.; Shimshek, D. R.; Perrot, L.; Frieauff, W.; Dubost, V.; Schiller, H.; Vogg, B.; Beltz, K.;

Avrameas, A.; Kretz, S.; Pezous, N.; Rondeau, J.; Beckmann, N.; Hartmann, A.; Vormfelde, S.; David, O. J.; Galli, B.; Ramos, R.; Graf, A.; Lopez Lopez, C. The BACE-1 Inhibitor CNP520 for Prevention Trials in Alzheimer's Disease. *EMBO Mol Med* **2018**, *10* (11). https://doi.org/10.15252/EMMM.201809316.

(131) Nikolaev, A.; McLaughlin, T.; O'Leary, D.; Tessier-Lavigne, M. APP Binds DR6 to Trigger Axon Pruning and Neuron Death via Distinct Caspases. *Nature*. **2009,** *457* (7232), 981-989. https://doi.org/10.1038/nature07767.

(132) Mal, S.; Malik, U.; Pal, D.; Mishra, A. Insight γ-Secretase: Structure, Function, and Role in Alzheimer's Disease. *Curr Drug Targets* **2021**, *22* (12), 1376–1403. https://doi.org/10.2174/1389450121999201230203709.

(133) Yang, G.; Zhou, R.; Guo, X.; Yan, C.; Lei, J.; Shi, Y. Structural Basis of γ-Secretase Inhibition and Modulation by Small Molecule Drugs. *Cell* **2021**, *184* (2), 521-533.e14. https://doi.org/10.1016/j.cell.2020.11.049.

(134) Zhang, X.; Song, W. The Role of APP and BACE1 Trafficking in APP Processing and Amyloid-β Generation. *Alzheimers Res Ther* **2013**, *5* (5), 1–8. https://doi.org/10.1186/alzrt211.

(135) Zhao, G.; Mao, G.; Tan, J.; Dong, Y.; Cui, M.; Kim, S. Identification of a New Presenilin-Dependent ζ-Cleavage Site within the Transmembrane Domain of Amyloid Precursor Protein. *J Biol Chem.* **2004**, *279* (49), 50647-50650. https://doi.org/10.1074/jbc.C400473200.

(136) Weidemann, A.; Eggert, S.; Reinhard, F. B. M.; Vogel, M.; Paliga, K.; Baier, G.; Masters, C. L.; Beyreuther, K.; Evin, G. A Novel ε-Cleavage within the Transmembrane Domain of the Alzheimer Amyloid Precursor Protein Demonstrates Homology with Notch Processing. *Biochemistry* **2002**, *41* (8), 2825–2835. https://doi.org/10.1021/BI015794O.

(137) Hitzenberger, M.; Götz, A.; Menig, S.; Brunschweiger, B.; Zacharias, M.; Scharnagl, C. The Dynamics of γ-Secretase and Its Substrates. *Semin Cell Dev Biol* **2020**, *105*, 86–101. https://doi.org/10.1016/j.semcdb.2020.04.008.

(138) Xia, W. γ-Secretase and Its Modulators: Twenty Years and Beyond. *Neurosci Lett* **2019**, *701*, 162–169. https://doi.org/10.1016/j.neulet.2019.02.011.

(139) Inomata, H.; Nakamura, Y.; Hayakawa, A.;Takata, H.; Suzuki, T.; Miyazawa, K.; Kitamura, N. A Scaffold Protein JIP-1b Enhances Amyloid Precursor Protein Phosphorylation by JNK and Its Association with Kinesin Light Chain 1. *J Biol Chem.* **2003**, *278* (25), 22946-22955. https://doi.org/10.1074/jbc.M212160200.

(140) Konietzko, U. AICD Nuclear Signaling and Its Possible Contribution to Alzheimers Disease. *Curr Alzheimer Res* **2012**, *9* (2), 200–216. https://doi.org/10.2174/156720512799361673.

(141) Pardossi-Piquard, R.; Checler, F. The Physiology of the β-Amyloid Precursor Protein Intracellular Domain AICD. *J Neurochem* **2012**, *120* (SUPPL. 1), 109–124. https://doi.org/10.1111/j.1471-4159.2011.07475.x.

(142) Biederer, T.; Cao, X.; Südhof, T.; Liu X. Regulation of APP-Dependent Transcription Complexes by Mint/X11s: Differential Functions of Mint Isoforms. *J Neurosci.* **2002**, *22* (17), 7340-7351. https://doi.org/10.1523/JENUROSCI.22-17-07340.2002.

(143) Belyaev, N.; Kellett, K.; Beckett, C.; Makova, N.; Revett, T.; Nalivaeva, N.; Hopper, N.; Turner, A. The Transcriptionally Active Amyloid Precursor Protein (APP) Intracellular Domain Is Preferentially Produced from the 695 Isoform of APP in a β-Secretase. *J Bio Chem*. **2010**, *285* (53), 41443-41454. https://doi.org/10.1074/jbc.M110.141390.

(144) Kerridge, C.; Belyaev, N. D.; Nalivaeva, N. N.; Turner, A. J. The Aβ-Clearance Protein Transthyretin, like Neprilysin, Is Epigenetically Regulated by the Amyloid Precursor Protein Intracellular Domain. *J Neurochem* **2014**, *130* (3), 419–431. https://doi.org/10.1111/JNC.12680.

(145) Landau, M.; Sawaya, M. R.; Faull, K. F.; Laganowsky, A.; Jiang, L.; Sievers, S. A.; Liu, J.; Barrio, J. R.; Eisenberg, D. Towards a Pharmacophore for Amyloid. *PLoS Biol* **2011**, *9* (6), 25–27. https://doi.org/10.1371/journal.pbio.1001080.

(146) Gazit, E. Mechanisms of Amyloid Fibril Self-assembly and Inhibition: Model Short Peptides as a Key Research Tool. *FEBS J.* **2005**, *272* (23), 5971–5978. https://doi.org/10.1111/j.1742-4658.2005.05022.x.

(147) Tjernberg, L.; Näslund, J.;Lindqvist, F.; Johansson, J.; Karlstrom, A.; Thyberg, H.; Terenius, L.; Nordstedt, C. Arrest Of-Amyloid Fibril Formation by a Pentapeptide Ligand. *J Biol Chem.* **1996**, *271* (15), 8545-8548. https://doi.org/10.1074/jbc.271.15.8545.

(148) Chalifour, R.; McLaughlin, R; Lavoie, L.; Morissette, C.; Tremblay, N.; Boule, m.; Sarazin, P.; Stea, D.; Lacombe, D.; Tremblay, P.; Gervais, F. Stereoselective Interactions of Peptide Inhibitors with the β-Amyloid Peptide. *J Biol Chem.* **2003**, *278* (37), 34874-34881. https://doi.org/10.1074/jbc.M212684200.

(149) Ahmed, M.; Davis, J.; Aucoin, D.; Sato, T.; Ahuja, S.; Aimoto, S.; Elliott J.; Nostrand, W.; Smith, S. Structural Conversion of Neurotoxic Amyloid-B1–42 Oligomers to Fibrils. *Nat Struct Mol Biol.* **2010**, *17* (5), 561-567. the β-Amyloid Peptide. *J Biol Chem.* **2003**, *278* (37), 34874-34881.10.1038/nsmb.1799.

(150) Zheng, J.; Ma, B.; Nussinov, R. Consensus Features in Amyloid Fibrils: Sheet-Sheet Recognition via a (Polar or Nonpolar) Zipper Structure. *Phys Biol* **2006**, *3* (3). https://doi.org/10.1088/1478-3975/3/3/P01.

(151) Nakamura, M.; Shishido, N.; Nunomura, A.; Smith, M. A.; Perry, G.; Hayashi, Y.; Nakayama, K.; Hayashi, T. Three Histidine Residues of Amyloid-β Peptide Control the Redox Activity of Copper and Iron. *ACS Publications* **2007**, *46* (44), 12737–12743. https://doi.org/10.1021/bi701079z.

(152) Roche, J.; Shen, Y.; Lee, J. H.; Ying, J.; Bax, A. Monomeric Aβ1-40 and Aβ1-42 Peptides in Solution Adopt Very Similar Ramachandran Map Distributions That Closely Resemble Random Coil. *Biochemistry* **2016**, *55* (5), 762–775. https://doi.org/10.1021/ACS.BIOCHEM.5B01259/SUPPL_FILE/BI5B01259_SI_001.PDF.

(153) Penke, B.; Szűcs, M.; Bogar, F. Oligomerization and Conformational Change Turn Monomeric β-Amyloid and Tau Proteins Toxic: Their Role in Alzheimer's Pathogenesis. *Molecules* **2020**, *25* (7), 1659. https://doi.org/10.3390/molecules25071659.

(154) Palop, J.; Mucke, L. Amyloid-β–Induced Neuronal Dysfunction in Alzheimer's Disease: From Synapses toward Neural Networks. *Nat Neurosci.* **2010**, *13* (7), 812-818. https://doi.org/10.1038/nn.2583.

(155) Hillen, H. The Beta Amyloid Dysfunction (BAD) Hypothesis for Alzheimer's Disease. *Front Neurosci* **2019**, *13*. https://doi.org/10.3389/FNINS.2019.01154/FULL.

(156) Chen, G. F.; Xu, T. H.; Yan, Y.; Zhou, Y. R.; Jiang, Y.; Melcher, K.; Xu, H. E. Amyloid Beta: Structure, Biology and Structure-Based Therapeutic Development. *Acta Pharmacol Sin* **2017**, *38* (9), 1205–1235. https://doi.org/10.1038/aps.2017.28.

(157) Jesus, C.; Almeida, Z.; Vaz, D.; Faria, T.; Brito, R. A New Folding Kinetic Mechanism for Human Transthyretin and the Influence of the Amyloidogenic V30M Mutation. *Int J Mol Sci.* **2016**, *17* (9), 1428. https://doi.org/10.3390/ijms17091428.

(158) Grant, M. A.; Lazo, N. D.; Lomakin, A.; Condron, M. M.; Arai, H.; Yamin, G.; Rigby, A. C.; Teplow, D. B. Familial Alzheimer's Disease Mutations Alter the Stability of the Amyloid Beta-Protein Monomer Folding Nucleus. *Proc Natl Acad Sci U S A* **2007**, *104* (42), 16522–16527. https://doi.org/10.1073/PNAS.0705197104.

(159) Dobson, C. M. Protein Misfolding, Evolution and Disease. *Trends Biochem Sci* **1999**, *24* (9), 329–332. https://doi.org/10.1016/S0968-0004(99)01445-0.

(160) Dobson, C. M. Protein Folding and Misfolding. *Nature* **2003**, *426* (6968), 884–890. https://doi.org/10.1038/NATURE02261.

(161) Makowski, L. The Structural Basis of Amyloid Strains in Alzheimer's Disease. *ACS Biomater Sci Eng* **2020**, *6* (5), 2498–2505. https://doi.org/10.1021/acsbiomaterials.9b01302.

(162) Colletier, J. P.; Laganowsky, A.; Landau, M.; Zhao, M.; Soriaga, A. B.; Goldschmidt, L.; Flot, D.; Cascio, D.; Sawaya, M. R.; Eisenberg, D. Molecular Basis for Amyloid-β Polymorphism. *Proc Natl Acad Sci U S A* **2011**, *108* (41), 16938–16943. https://doi.org/10.1073/pnas.1112600108.

(163) Kodali, R.; Wetzel, R. Polymorphism in the Intermediates and Products of Amyloid Assembly. *Curr Opin Struct Biol.* **2007**, *17* (1), 48-57. https://doi.org/10.1016/j.sbi.2007.01.007.

(164) Chatani, E.; Yuzu, K.; Ohhashi, Y.; Goto, Y. Current Understanding of the Structure, Stability and Dynamic Properties of Amyloid Fibrils. *Int J Mol Sci* **2021**, *22* (9). https://doi.org/10.3390/ijms22094349.

(165) Klunk, W.; Jacob, R.;Mason, R. Quantifying Amyloid β-Peptide (Aβ) Aggregation Using the Congo Red-Aβ (CR–Aβ) Spectrophotometric Assay. *Anal Biochem.* **1999**, *266* (1), 66-76. https://doi.org/10.1006/ABIO.1998.2933.

(166) Howie, A.; Brewer, D. Optical Properties of Amyloid Stained by Congo Red: History and Mechanisms. *Micron.* **2009**, *40* (3), 285-301. https://doi.org/10.1016/j.micron.2008.10.002.

(167) Lorenzo, A.; Yankner, B. Beta-Amyloid Neurotoxicity Requires Fibril Formation and Is Inhibited by Congo Red. *Proc Natl Acad Sci U S A.* **1994**, *91* (25), 12243–12247. https://doi.org/10.1073/pnas.91.25.12243.

(168) Kim, Y. S.; Randolph, T. W.; Manning, M. C.; Stevens, F. J.; Carpenter, J. F. Congo Red Populates Partially Unfolded States of an Amyloidogenic Protein to Enhance Aggregation and Amyloid Fibril Formation. *J Biol Chem* **2003**, *278* (12), 10842–10850. https://doi.org/10.1074/JBC.M212540200.

(169) Science, H. L. I.-P.; 1993, undefined. Thioflavine T Interaction with Synthetic Alzheimer's Disease B-amyloid Peptides: Detection of Amyloid Aggregation in Solution. *Wiley Online Library* **1993**, *2* (3), 404–410. https://doi.org/10.1002/pro.5560020312.

(170) Kelényi, G. Thioflavin S Fluorescent and Congo Red Anisotropic Stainings in the Histologic Demonstration of Amyloid. *Acta Neuropathol* **1967**, *7* (4), 336–348. https://doi.org/10.1007/BF00688089.

(171) Younan, N. D.; Viles, J. H. A Comparison of Three Fluorophores for the Detection of Amyloid Fibers and Prefibrillar Oligomeric Assemblies. ThT (Thioflavin T); ANS (1-Anilinonaphthalene-8-Sulfonic Acid); and BisANS (4,4′-Dianilino-1,1′-Binaphthyl-5,5′-Disulfonic Acid). *Biochemistry* **2015**, *54* (28), 4297–4306. https://doi.org/10.1021/ACS.BIOCHEM.5B00309.

(172) Arosio, P.; Knowles, T.; Linse, S. On the Lag Phase in Amyloid Fibril Formation. *Phys Chem Chem Phys.* **2015**, *17* (12), 7606-7618. https://doi.org/10.1039/c4cp05563b.

(173) Michaels, T. C. T.; Šarić, A.; Habchi, J.; Chia, S.; Meisl, G.; Vendruscolo, M.; Dobson, C. M.; Knowles, T. P. J. Chemical Kinetics for Bridging Molecular Mechanisms and Macroscopic Measurements of Amyloid Fibril Formation. *Annu Rev Phys Chem* **2018**, *69*, 273–298. https://doi.org/10.1146/ANNUREV-PHYSCHEM-050317-021322.

(174) Feng, Y.; Yang, S. gao; Du, X. ting; Zhang, X.; Sun, X. xia; Zhao, M.; Sun, G. yuan; Liu, R. tian. Ellagic Acid Promotes Aβ42 Fibrillization and Inhibits Aβ42-Induced Neurotoxicity. *Biochem Biophys Res Commun* **2009**, *390* (4), 1250–1254. https://doi.org/10.1016/j.bbrc.2009.10.130.

(175) Bieschke, J.; Herbst, M.; Wiglenda, T.; Friedrich, R. P.; Boeddrich, A.; Schiele, F.; Kleckers, D.; Lopez Del Amo, J. M.; Grüning, B. A.; Wang, Q.; Schmidt, M. R.; Lurz, R.; Anwyl, R.; Schnoegl, S.; Fändrich, M.; Frank, R. F.; Reif, B.; Günther, S.; Walsh, D. M.; Wanker, E. E. Small-Molecule Conversion of Toxic Oligomers to Nontoxic β-Sheetg-Rich Amyloid Fibrils. *Nat Chem Biol* **2012**, *8* (1), 93–101. https://doi.org/10.1038/nchembio.719.

(176) Liu, H.; Qian, C.; Yang, T.; Wang, Y.; Luo, J.; Zhang, C.; Wang, X.; Wang, X.; Guo, Z. Small Molecule-Mediated Co-Assembly of Amyloid-β Oligomers Reduces Neurotoxicity through Promoting Non-Fibrillar Aggregation. *Chem Sci* **2020**, *11* (27), 7158–7169. https://doi.org/10.1039/d0sc00392a.

(177) Almeida, Z. L.; Brito, R. M. M. Structure and Aggregation Mechanisms in Amyloids. *Molecules* **2020**, *25* (5). https://doi.org/10.3390/molecules25051195.

(178) Jahn, T.; Radford, S. Folding versus Aggregation: Polypeptide Conformations on Competing Pathways. *Arch Biochem Biophys.* **2008**, *469* (1), 100-117. https://doi.org/10.1016/j.abb.2007.05.015.

(179) Turoverov, K.; Kuznetsova, I.; Uversky, V. The Protein Kingdom Extended: Ordered and Intrinsically Disordered Proteins, Their Folding, Supramolecular Complex Formation, and Aggregation. *Prog Biophys Mol Biol*. **2010**, *102* (2-3), 73-84. https://doi.org/10.1016/j.pbiomolbio.2010.01.003.

(180) Ono, K.; Watanabe-Nakayama, T. Aggregation and Structure of Amyloid β-Protein. *Neurochem Int* **2021**, *151*, 105208. https://doi.org/10.1016/J.NEUINT.2021.105208.

(181) Magni, F.; Galbusera, C.; Tremolada, L.; Ferrarese, C.; Galli Kienle, M. Characterisation of Adducts of the Lipid Peroxidation Product 4-Hydroxy-2-Nonenal and Amyloid β-Peptides by Liquid Chromatography/Electrospray Ionisation Mass Spectrometry. *Rapid Communications in Mass Spectrometry* **2002**, *16* (15), 1485–1493. https://doi.org/10.1002/RCM.743.

(182) Fowler, C.; Ando, Y.; Tiger, G. Comparison of the Effects of Hydrogen Peroxide, 4-Hydroxy-2-Nonenal and β-Amyloid (25–35) upon Calcium Signalling. *Neurochem Int.* **1998**, *33* (2), 161-172. https://doi.org/10.1016/s0197-0186(98)00013-8.

(183) Sciacca, M. F. M.; Rosa, C. La; Milardi, D.; Buck, M. Amyloid-Mediated Mechanisms of Membrane Disruption. *mdpi.com* **2021**. https://doi.org/10.3390/biophysica1020011.

(184) Webers, A.;Heneka, M.; Glesson, P. The Role of Innate Immune Responses and Neuroinflammation in Amyloid Accumulation and Progression of Alzheimer's Disease. *Immunol Cell Biol.* **2020**, *98* (1), 28–41. https://doi.org/10.1111/imcb.12301.

(185) Reiss, A. B.; Arain, H. A.; Stecker, M. M.; Siegart, N. M.; Kasselman, L. J. Amyloid Toxicity in Alzheimer's Disease. *Rev Neurosci* **2018**, *29* (6), 613–627. https://doi.org/10.1515/REVNEURO-2017-0063/XML.

(186) Demuro, A.; Parker, I.; Stutzmann, G. Calcium Signaling and Amyloid Toxicity in Alzheimer Disease. *J Biol Chem.* **2010**, *285* (17), 12463-12468. https://doi.org/10.1074/jbc.R109.080895.

(187) Atwood, C. S.; Obrenovich, M. E.; Liu, T.; Chan, H.; Perry, G.; Smith, M. A.; Martins, R. N. Amyloid-β: A Chameleon Walking in Two Worlds: A Review of the Trophic and Toxic Properties of Amyloid-β. *Brain Res Rev* **2003**, *43* (1), 1–16. https://doi.org/10.1016/S0165-0173(03)00174-7.

(188) Huang, Z.; Yan, Q.; Wang, Y.; Zou, Q.; Li, J.; Liu, Z.; Cai, Z. Role of Mitochondrial Dysfunction in the Pathology of Amyloid-b. *Journal of Alzheimer's Disease* **2020**, *78* (2), 505–514. https://doi.org/10.3233/JAD-200519.

(189) Barsoum, M. J.; Yuan, H.; Gerencser, A. A.; Liot, G.; Kushnareva, Y.; Gräber, S.; Kovacs, I.; Lee, W. D.; Waggoner, J.; Cui, J.; White, A. D.; Bossy, B.; Martinou, J. C.; Youle, R. J.; Lipton, S. A.; Ellisman, M. H.; Perkins, G. A.; Bossy-Wetzel, E. Nitric Oxide-Induced Mitochondrial Fission Is Regulated by Dynamin-Related GTPases in Neurons. *EMBO Journal* **2006**, *25* (16), 3900–3911. https://doi.org/10.1038/SJ.EMBOJ.7601253.

(190) Cline, E. N.; Bicca, M. A.; Viola, K. L.; Klein, W. L. The Amyloid-β Oligomer Hypothesis: Beginning of the Third Decade. *J Alzheimers Dis* **2018**, *64* (s1), S567–S610. https://doi.org/10.3233/JAD-179941.

(191) Lambert, M. P.; Barlow, A. K.; Chromy, B. A.; Edwards, C.; Freed, R.; Liosatos, M.; Morgan, T. E.; Rozovsky, I.; Trommer, B.; Viola, K. L.; Wals, P.; Zhang, C.; Finch, C. E.; Krafft, G. A.; Klein,

W. L. Diffusible, Nonfibrillar Ligands Derived from Abeta1-42 Are Potent Central Nervous System Neurotoxins. *Proc Natl Acad Sci U S A* **1998**, *95* (11), 6448–6453. https://doi.org/10.1073/PNAS.95.11.6448.

(192) Evangelisti, E.; Wright, D.; Zampagni, M.; Cascella, R.; Fiorillo, C.; Bagnoli, S.; Relini, A.; Nichino, D.; Scartabelli, T.; Nacmias, B.; Sorbi, S.; Cecchi, C. Lipid Rafts Mediate Amyloid-Induced Calcium Dyshomeostasis and Oxidative Stress in Alzheimer's Disease. *Curr Alzheimer Res* **2013**, *10* (2), 143–153. https://doi.org/10.2174/1567205011310020004.

(193) Crestini, A.; Santilli, F.; Martellucci, S.; Carbone, E.; Sorice, M.; Piscopo, P.; Mattei, V. Prions and Neurodegenerative Diseases: A Focus on Alzheimer's Disease. *Journal of Alzheimer's Disease* **2022**, *85* (2), 503–518. https://doi.org/10.3233/JAD-215171.

(194) Nygaard, H. B. Targeting Fyn Kinase in Alzheimer's Disease. *Biol Psychiatry* **2018**, *83* (4), 369–376. https://doi.org/10.1016/j.biopsych.2017.06.004.

(195) Um, J. W.; Nygaard, H. B.; Heiss, J. K.; Kostylev, M. A.; Stagi, M.; Vortmeyer, A.; Wisniewski, T.; Gunther, E. C.; Strittmatter, S. M. Alzheimer Amyloid-Î 2 Oligomer Bound to Postsynaptic Prion Protein Activates Fyn to Impair Neurons. *Nat Neurosci* **2012**, *15* (9), 1227–1235. https://doi.org/10.1038/nn.3178.

(196) Costa, R. O.; Lacor, P. N.; Ferreira, I. L.; Resende, R.; Auberson, Y. P.; Klein, W. L.; Oliveira, C. R.; Rego, A. C.; Udia, C.; Pereira, M. F. Endoplasmic Reticulum Stress Occurs Downstream of GluN2B Subunit of N-methyl-D-aspartate Receptor in Mature Hippocampal Cultures Treated with Amyloid-β. *Wiley Online Library* **2012**, *11* (5), 823–833. https://doi.org/10.1111/j.1474-9726.2012.00848.x.

(197) Snyder, E. M.; Nong, Y.; Almeida, C. G.; Paul, S.; Moran, T.; Choi, E. Y.; Nairn, A. C.; Salter, M. W.; Lombroso, P. J.; Gouras, G. K.; Greengard, P. Regulation of NMDA Receptor Trafficking by Amyloid-β. *nature.com* **2005**, *8* (8). https://doi.org/10.1038/nn1503.

(198) Wang, H.; Li, W.; Benedetti, N.; Lee, D. A7 Nicotinic Acetylcholine Receptors Mediate β-Amyloid Peptide-Induced Tau Protein Phosphorylation. *J Biol Chem.* **2003**, *278* (34), 31547-31553. https://doi.org/10.1074/jbc.M212532200.

(199) Chao, M. The P75 Neurotrophin Receptor. *J Neurobiol.* **1994**, *25* (11), 1373-1385. https://doi.org/10.1002/neu.480251106.

(200) Hashimoto, Y.; Kaneko, Y.; Tsukamoto, E.; Frankowski, H.; Kouyama, K.; Kita, Y.; Niikura, T.; Aiso, S.; Bredesen, D. E.; Matsuoka, M.; Nishimoto, I. Molecular Characterization of Neurohybrid Cell Death Induced by Alzheimer's Amyloid-β Peptides via P75NTR/PLAIDD. *J Neurochem.* **2004**, *90* (3), 549–558. https://doi.org/10.1111/j.1471-4159.2004.02513.x.

(201) Perini, G.; Della-Bianca, V.; Politi, V.; Valle, G.; Dal-Pra, I.; Rossi, F.; Armato, U. Role of P75 Neurotrophin Receptor in the Neurotoxicity by β-Amyloid Peptides and Synergistic Effect of Inflammatory Cytokines. *J Exp Med.* **2002**, *195* (7), 907-918. https://doi.org/10.1084/jem.20011797.

(202) Zhang, F.; Gannon, M.; Chen, Y.; Yan, S.; Zhang, S.; Feng, W.; Tao, J.; Sha, B.; Liu, Z.; Saito, T.; Saido, T.; Dirk Keene, C.; Jiao, K.; Roberson, E. D.; Xu, H.; Wang, Q. β-Amyloid Redirects Norepinephrine Signaling to Activate the Pathogenic GSK3β/Tau Cascade. *Sci Transl Med* **2020**, *12* (526). https://doi.org/10.1126/SCITRANSLMED.AAY6931/SUPPL_FILE/AAY6931_SM.PDF.

(203) Brockwell, D. J.; Radford, S. E. Intermediates: Ubiquitous Species on Folding Energy Landscapes? *Curr Opin Struct Biol* **2007**, *17* (1), 30–37. https://doi.org/10.1016/J.SBI.2007.01.003.

(204) Vendruscolo, M.; Paci, E.; Karplus, M.; Dobson, C. M. Structures and Relative Free Energies of Partially Folded States of Proteins. *Proc Natl Acad Sci U S A* **2003**, *100* (25), 14817–14821. https://doi.org/10.1073/PNAS.2036516100.

(205) Pardridge, W. M. The Blood-Brain Barrier: Bottleneck in Brain Drug Development. *NeuroRx* **2005**, *2* (1), 3–14. https://doi.org/10.1602/NEURORX.2.1.3.

(206) Abbott, N.; Patabendige, A.;Dolman, D.; Yusof, S.; Begley, D. Structure and Function of the Blood–Brain Barrier. *Neurobiol Dis.* **2010**, *37* (1), 13-25. https://doi.org/j.nbd.2009.07.030.

(207) Ballabh, P.; Braun, A.; Nedergaard, M. The Blood–Brain Barrier: An Overview: Structure, Regulation, and Clinical Implications. *Neurobiol Dis.* **2004**, *16* (1), 1-13. https://doi.org/10.1016/j.nbd.2003.12.016.

(208) Begley, D. J. Structure and Function of the Blood-Brain Barrier. *Enhancement in Drug Delivery* **2006**, 575–592. https://doi.org/10.3389/CONF.FPHAR.2010.02.00002/EVENT_ABSTRACT.

(209) Rubin, L. L.; Staddon, J. M. The Cell Biology of the Blood-Brain Barrier. *Annu Rev Neurosci* **1999**, *22*, 11–28. https://doi.org/10.1146/ANNUREV.NEURO.22.1.11.

(210) Deane, R.; Yan, S. Du; Submamaryan, R.; LaRue, B.; Jovanovic, S.; Hogg, E.; Welch, D.; Manness, L.; Lin, C.; Yu, J.; Zhu, H.; Ghiso, J.; Frangione, B.; Stern, A.; Schmidt, A.; Armstrong, D.; Arnold, B.; Liliensik, B.; Nawroth, P.; Hofman, F.; Kindy, M.; Stern, D.; Zlokovic, B. RAGE Mediates Amyloid-β Peptide Transport across the Blood-Brain Barrier and Accumulation in Brain. *Nat Med.* **2003**, *9* (7), 907-913. https://doi.org/10.1038/nm890.

(211) Choi, B.; Cho, W.; Kim, J.; Lee, H.; Chung, C.; Jeon, W.; Han, J. Increased Expression of the Receptor for Advanced Glycation End Products in Neurons and Astrocytes in a Triple Transgenic Mouse Model of Alzheimer's. *Exp Mol Med.* **2014**, *46* (2), e75. https://doi.org/10.1038/emm.2013.147.

(212) Wang, Y. J.; Zhou, H. D.; Zhou, X. F. Clearance of Amyloid-Beta in Alzheimer's Disease: Progress, Problems and Perspectives. *Drug Discov Today*. **2006**, *11* (19-20), 931–938. https://doi.org/10.1016/j.drudis.2006.08.004.

(213) Deane, R.; Zlokovic, B. Role of the Blood-Brain Barrier in the Pathogenesis of Alzheimer's Disease. *Curr Alzheimer Res*. **2007**, *4* (2), 191-197. https://doi.org/10.2174/156720507780362245.

(214) Etique, N.; Verzeaux, L.; Dedieu, S.; Emonard, H. LRP-1: A Checkpoint for the Extracellular Matrix Proteolysis. *Bioimed Red Int.* **2013**, *2013* (152163). https://doi.org/10.1155/2013/152163.

(215) Ruzali, W.; Kehoe, P.;Love, S. Influence of LRP-1 and Apolipoprotein E on Amyloid-β Uptake and Toxicity to Cerebrovascular Smooth Muscle Cells. *J Alzheimers Dis*. **2013**, *33* (1), 95-110. https://doi.org/10.3233/JAD-2012-121336.

(216) Wijnberg, M. J.; Quax, P. H. A.; Nieuwenbroek, N. M. E.; Verheijen, J. H. The Migration of Human Smooth Muscle Cells in Vitro Is Mediated by Plasminogen Activation and Can Be Inhibited by A2-Macroglobulin Receptor Associated Protein. *Thromb Haemost.* **1997**, *78* (2), 880–886. https://doi.org/10.1055/S-0038-1657646.

(217) Marzolo, M.; Bu, G. Lipoprotein Receptors and Cholesterol in APP Trafficking and Proteolytic Processing, Implications for Alzheimer's Disease. *Semin Cell Dev Biol.* **2009**, *20* (2), 191-200. https://doi.org/10.1016/j.semcdb.2008.10.005.

(218) Turner, A. J.; Tanzawa, K. Mammalian Membrane Metallopeptidases: NEP, ECE, KELL, and PEX. *The FASEB Journal* **1997**, *11* (5), 355–364. https://doi.org/10.1096/FASEBJ.11.5.9141502.

(219) Hersh, L.; Rodgers, D. Neprilysin and Amyloid Beta Peptide Degradation. *Curr Alzheimer Res.* **2008**, *5* (2), 225-231. https://doi.org/10.2174/156720508783954703.

(220) Eckman, E.; Reed, D.; Eckman, C. Degradation of the Alzheimer's Amyloid β Peptide by Endothelin-Converting Enzyme. *J Biol Chem.* **2001**, *276* (27), 24540-24548. https://doi.org/10.1074/jbc.M007579200.

(221) Edbauer, D.; Willem, M.; Lammich, S.; Steiner, G.; Haass, C. Insulin-Degrading Enzyme Rapidly Removes the β-Amyloid Precursor Protein Intracellular Domain (AICD). *J Biol Chem.* **2002**, *277* (16), 133889-13393. https://doi.org/10.1074/jbc.M111571200.

(222) Tucker, H. M.; Kihiko, M.; Caldwell, J. N.; Wright, S.; Kawarabayashi, T.; Price, D.; Walker, D.; Scheff, S.; Mcgillis, J. P.; Rydel, R. E.; Estus, S. The Plasmin System Is Induced by and Degrades

Amyloid-β Aggregates. *Soc Neuroscience* **2000**, *16* (10), 1973-1977. https://doi.org/10.4103/1673-5374.308076.

(223) Vassar, R.; Kandalepas, P. C. The -Secretase Enzyme BACE1 as a Therapeutic Target for Alzheimer's Disease. *Alzheimers Res Ther* **2011**, *3* (3). https://doi.org/10.1186/ALZRT82.

(224) Lahiri, D. K.; Farlow, M. R.; Greig, N. H.; Sambamurti, K. Current Drug Targets for Alzheimer's Disease Treatment. *Drug Dev Res* **2002**, *56* (3), 267–281. https://doi.org/10.1002/DDR.10081.

(225) Cao, J.; Hou, J.; Ping, J.; Cai, D. Advances in Developing Novel Therapeutic Strategies for Alzheimer's Disease. *Mol Neurodegener* **2018**, *13* (1). https://doi.org/10.1186/S13024-018-0299-8.

(226) Lahiri, D.; Farlow, M.; Sambamurti, K.; Greig, N.; Giacobini, E.; Schneider, L. A Critical Analysis of New Molecular Targets and Strategies for Drug Developments in Alzheimer's Disease. *Curr Drug Targets.* **2003**, *4* (2), 97-112. https://doi.org/10.2174/1389450033346957.

(227) Braak, H.; Braak, E. Staging of Alzheimer's Disease-Related Neurofibrillary Changes. *Neurobiol Aging* **1995**, *16* (3), 271-278. https://doi.org/10.1016/0197-4580(95)00021-6.

(228) Selkoe, D. J.; Hardy, J. The Amyloid Hypothesis of Alzheimer's Disease at 25 Years. *EMBO Mol Med* **2016**, *8* (6), 595–608. https://doi.org/10.15252/emmm.201606210.

(229) Aisen, P. S.; Cummings, J.; Jack, C. R.; Morris, J. C.; Sperling, R.; Frölich, L.; Jones, R. W.; Dowsett, S. A.; Matthews, B. R.; Raskin, J.; Scheltens, P.; Dubois, B. On the Path to 2025: Understanding the Alzheimer's Disease Continuum. *Alzheimers Res Ther* **2017**, *9* (1), 1–10. https://doi.org/10.1186/s13195-017-0283-5.

(230) Chen, X. Q.; Mobley, W. C. Alzheimer Disease Pathogenesis: Insights From Molecular and Cellular Biology Studies of Oligomeric Aβ and Tau Species. *Front Neurosci* **2019**, *13* (JUN). https://doi.org/10.3389/FNINS.2019.00659.

(231) Ittner, L.; Gotz, J. Amyloid-β and Tau — a Toxic Pas de Deux in Alzheimer's Disease. *Nat Rev Neurosci* **2011**, *12* (2), 65-72. https://doi.org/10.1038/nrn2967.

(232) Arendt, T.; Stieler, J. T.; Holzer, M. Tau and Tauopathies. *Brain Res Bull* **2016**, *126* (Pt 3), 238–292. https://doi.org/10.1016/J.BRAINRESBULL.2016.08.018.

(233) Niranjan, A.; Singh, S.; Dhiman, M.; Tewari, S. K. Biochemical Composition of Curcuma Longa L. Accessions. *Anal Lett* **2013**, *46* (7), 1069–1083. https://doi.org/10.1080/00032719.2012.751541.

(234) Molecules, K. P.. The Chemistry of Curcumin: From Extraction to Therapeutic Agent. *Molecules* **2014**, *19* (12), 20091-20112. https://doi.org/10.3390/molecules191220091.

(235) Begum, A. N.; Kayed, R.; Cole, G. M.; Ubeda, O. J.; Frautschy, S. A.; Glabe, C. G.; Chen, P. P.; Lim, G. P.; Ambegaokar, S. S.; Yang, F.; Simmons, M. R. Curcumin Inhibits Formation of Amyloid β Oligomers and Fibrils, Binds Plaques, and Reduces Amyloid in Vivo . *Journal of Biological Chemistry* **2004**, *280* (7), 5892–5901. https://doi.org/10.1074/jbc.m404751200.

(236) Belkacemi, A.; Doggui, S.; Dao, L.; Ramassamy, C. Challenges Associated with Curcumin Therapy in Alzheimer Disease. *Expert Rev Mol Med* **2011**, *13* (November 2011), 1–15. https://doi.org/10.1017/s1462399411002055.

(237) Endo, H.; Nikaido, Y.; Nakadate, M.; Ise, S.; Konno, H. Structure Activity Relationship Study of Curcumin Analogues toward the Amyloid-Beta Aggregation Inhibitor. *Bioorg Med Chem Lett* **2014**, *24* (24), 5621–5626. https://doi.org/10.1016/j.bmcl.2014.10.076.

(238) Chin, D.; Huebbe, P.; Pallauf, K.; Rimbach, G. Neuroprotective Properties of Curcumin in Alzheimer's Disease – Merits and Limitations. *Curr Med Chem* **2013**, *20* (32), 3955–3985. https://doi.org/10.2174/09298673113209990210.

(239) Begum, A. N.; Kayed, R.; Cole, G. M.; Ubeda, O. J.; Frautschy, S. A.; Glabe, C. G.; Chen, P. P.; Lim, G. P.; Ambegaokar, S. S.; Yang, F.; Simmons, M. R. Curcumin Inhibits Formation of Amyloid

β Oligomers and Fibrils, Binds Plaques, and Reduces Amyloid in Vivo . *Journal of Biological Chemistry* **2004**, *280* (7), 5892–5901. https://doi.org/10.1074/jbc.m404751200.

(240) Kotha, R. R.; Luthria, D. L. Curcumin: Biological, Pharmaceutical, Nutraceutical, and Analytical Aspects. *Molecules* **2019**, *24* (16). https://doi.org/10.3390/molecules24162930.

(241) He, Y.; Yue, Y.; Zheng, X.; Zhang, K.; Chen, S.; Du, Z. Curcumin, Inflammation, and Chronic Diseases: How Are They Linked? *Molecules* **2015**, *20* (5), 9183–9213. https://doi.org/10.3390/molecules20059183.

(242) Moghadamtousi, S. Z.; Kadir, H. A.; Hassandarvish, P.; Tajik, H.; Abubakar, S.; Zandi, K. A Review on Antibacterial, Antiviral, and Antifungal Activity of Curcumin. *Biomed Res Int* **2014**, *2014*, 186864. https://doi.org/10.1155/2014/186864.

(243) Tomeh, M. A.; Hadianamrei, R.; Zhao, X. A Review of Curcumin and Its Derivatives as Anticancer Agents. *Int J Mol Sci* **2019**, *20* (5). https://doi.org/10.3390/ijms20051033.

(244) Chainoglou, E.; Hadjipavlou-Litina, D. Curcumin in Health and Diseases: Alzheimer's Disease and Curcumin Analogues, Derivatives, and Hybrids. *Int J Mol Sci* **2020**, *21* (6). https://doi.org/10.3390/ijms21061975.

(245) Mbese, Z.; Khwaza, V.; Aderibigbe, B. A. Curcumin and Its Derivatives as Potential Therapeutic Agents in Prostate, Colon and Breast Cancers. *Molecules* **2019**, *24* (23). https://doi.org/10.3390/molecules24234386.

(246) Gupta, S. C.; Patchva, S.; Aggarwal, B. B. Therapeutic Roles of Curcumin: Lessons Learned from Clinical Trials. *AAPS Journal* **2013**, *15* (1), 195–218. https://doi.org/10.1208/s12248-012-9432-8.

(247) Nelson, K. M.; Dahlin, J. L.; Bisson, J.; Graham, J.; Pauli, G. F.; Walters, M. A. The Essential Medicinal Chemistry of Curcumin. *J Med Chem* **2017**, *60* (5), 1620–1637. https://doi.org/10.1021/acs.jmedchem.6b00975.

(248) Payton, F.; Sandusky, P.; Alworth, W. L. NMR Study of the Solution Structure of Curcumin. *J Nat Prod* **2007**, *70* (2), 143–146. https://doi.org/10.1021/NP060263S.

(249) Jagannathan, R.; Abraham, P. M.; Poddar, P. Temperature-Dependent Spectroscopic Evidences of Curcumin in Aqueous Medium: A Mechanistic Study of Its Solubility and Stability. *Journal of Physical Chemistry B* **2012**, *116* (50), 14533–14540. https://doi.org/10.1021/JP3050516.

(250) Wang, Y.; Pan, M.; Cheng, A.; Lin, L.;Ho, Y.; Hsieh, C.; Lin, J. Stability of Curcumin in Buffer Solutions and Characterization of Its Degradation Products. *J Pharm Biomed Anal.* **1997**, *15* (12), 1867-1876. https://doi.org/10.1016/s0731-7085(96)02024-9.

(251) Ho, C. T. High Performance Liquid Chromatographic Analysis of Curcuminoids and Their Photo-Oxidative Decomposition Compounds in Curcuma Longal. *J Liq Chromatogr* **1988**, *11* (11), 2295–2304. https://doi.org/10.1080/01483918808067200.

(252) Griesser, M.; Pistis, V.; Suzuki, T.; Tejera, N.; Pratt, D.; Schneider, C. Autoxidative and Cyclooxygenase-2 Catalyzed Transformation of the Dietary Chemopreventive Agent Curcumin. *J Biol Chem.* **2011**, *286* (2), 1114-1124. https://doi.org/10.1074/jbc.M110.178806.

(253) Yang, K.; Lin, L.; Tseng, T.; Wang, S.; Tsai, T. Oral Bioavailability of Curcumin in Rat and the Herbal Analysis from Curcuma Longa by LC–MS/MS. *J Chromatogr B Analyt Technol Biomed Life Sci.* **2007**, *853* (1-2), 183-189. https://doi.org/10.1016/j.jchromb.2007.03.010.

(254) Takagi, T.; Ramachandran, C.; Bermejo, M.; Yamashita, S.; Yu, L. X.; Amidon, G. L. A Provisional Biopharmaceutical Classification of the Top 200 Oral Drug Products in the United States, Great Britain, Spain, and Japan. *Mol Pharm* **2006**, *3* (6), 631–643. https://doi.org/10.1021/MP0600182.

(255) Pauli, G. F.; Chen, S.-N.; Friesen, J. B.; Mcalpine, J. B.; Jaki, B. U. Analysis and Purification of Bioactive Natural Products: The AnaPurNa Study. *ACS Publications* **1998**, *75* (6), 1243–1255. https://doi.org/10.1021/np300066q.

(256) Simmler, C.; Hajirahimkhan, A.; Lankin, D. C.; Bolton, J. L.; Jones, T.; Soejarto, D. D.; Chen, S. N.; Pauli, G. F. Dynamic Residual Complexity of the Isoliquiritigenin-Liquiritigenin Interconversion during Bioassay. *J Agric Food Chem* **2013**, *61* (9), 2146–2157. https://doi.org/10.1021/JF304445P.

(257) Ireson, C.; Orr, S.; Jones, D.; Verschoyle, R.; Lim, C.; Luo, J.; Howells, L.; Plummer, S.; Jukes, R.; Williams, M.; Steward, W.; Gescher, A. Characterization of Metabolites of the Chemopreventive Agent Curcumin in Human and Rat Hepatocytes and in the Rat in Vivo, and Evaluation of Their Ability to Inhibit Phorbol. *Cancer Res.* **2001**, *61* (3), 1058-1064.

(258) Siviero, A.; Gallo, E.; Maggini, V.; Gori, L.; Mugelli, A.; Firenzuoli, F.; Vannacci, A. Curcumin, a Golden Spice with a Low Bioavailability. *Elsevier* **2015**. https://doi.org/10.1016/j.hermed.2015.03.001.

(259) Metzler, M.; Pfeiffer, E.; Schulz, S. I.; Dempe, J. S. Curcumin Uptake and Metabolism. *BioFactors* **2013**, *39* (1), 14–20. https://doi.org/10.1002/BIOF.1042.

(260) Awasthi, S.; Pandya, U.; Singhal, S.; Lin, J.; Thiviyanathan, V.; Seifert, W.; Awasthi, Y.; Ansari, G. Curcumin-Glutathione Interactions and the Role of Human Glutathione S-Transferase P1-1. *Chem Biol Interact.* **2000**, *128* (1), 19-38. https://doi.org/10.1016/s0009-2797(00)00185-x.

(261) Appiah-Opong, R.; Commandeur, J. N. M.; Van Vugt-Lussenburg, B.; Vermeulen, N. P. E. Inhibition of Human Recombinant Cytochrome P450s by Curcumin and Curcumin Decomposition Products. *Elsevier* **2007**, *235*, 83–91. https://doi.org/10.1016/j.tox.2007.03.007.

(262) Oetari, S.; Sudibyo, M.;Commandeur, J.; Samhoedi, R.; Vermeulen, N. Effects of Curcumin on Cytochrome P450 and Glutathione S-Transferase Activities in Rat Liver. *Biochem Pharmacol.* **1996**, *51* (1), 39-45. https://doi.org/10.1016/0006-2952(95)02113-2.

(263) Mancuso, C.; Barone, E. Curcumin in Clinical Practice: Myth or Reality? *Trends Pharmacol Sci.* **2009**, *30* (7), 333-334. https://doi.org/10.1016/j.tips.2009.04.004.

(264) Baell, J.; Walters, M. A. Chemistry: Chemical Con Artists Foil Drug Discovery. *Nature* **2014**, *513* (7519), 481–483. https://doi.org/10.1038/513481A.

(265) Kamran, M.; Dangles, O. A Comprehensive Review on Flavanones, the Major Citrus Polyphenols. *Journal of Food Composition and Analysis* **2014**, *33* (1), 85–104. https://doi.org/10.1016/j.jfca.2013.11.004.

(266) Buer, C. S.; Imin, N.; Djordjevic, M. A.; Buer, C. S. Flavonoids : New Roles for Old Molecules. **2010**, *52* (1), 98–111. https://doi.org/10.1111/j.1744-7909.2010.00905.x.

(267) Rozmer, Z. Naturally Occurring Chalcones and Their Biological Activities. **2016**, 87–120. https://doi.org/10.1007/s11101-014-9387-8.

(268) Thapa, P.; Upadhyay, S. P.; Suo, W. Z.; Singh, V.; Gurung, P.; Lee, E. S.; Sharma, R.; Sharma, M. Chalcone and Its Analogs: Therapeutic and Diagnostic Applications in Alzheimer's Disease. *Bioorg Chem* **2021**, *108* (September 2020), 104681. https://doi.org/10.1016/j.bioorg.2021.104681.

(269) Watanabe, H.; Saji, H.; Ono, M. Novel Fluorescence Probes Based on the Chalcone Scaffold for in Vitro Staining of β-Amyloid Plaques. *Bioorg Med Chem Lett* **2018**, *28* (19), 3242–3246. https://doi.org/10.1016/j.bmcl.2018.08.009.

(270) Bello, M.; Chiaradia, L.; Dias, L.;Pacheco, L.; Stumpf, T.; Mascarello, A.; Steindel, M.; Yunes, R.; Castro, H.; Nunes, R.; Rodrigues, C. Trimethoxy-Chalcone Derivatives Inhibit Growth of Leishmania Braziliensis: Synthesis, Biological Evaluation, Molecular Modeling and Structure–Activity Relationship. *Bioorg Med Chem.* **2011**, *19* (16), 5046-5052. https://doi.org/10.1016/j.bmc.2011.06.023.

(271) Kumar, S. K.; Hager, E.; Pettit, C.; Gurulingappa, H.; Davidson, N. E.; Khan, S. R. Design, Synthesis, and Evaluation of Novel Boronic-Chalcone Derivatives as Antitumor Agents. *J Med Chem* **2003**, *46* (14), 2813–2815. https://doi.org/10.1021/jm030213+.

(272) Modzelewska, A.; Pettit, C.; Achanta, G.; Davidson, N. E.; Huang, P.; Khan, S. R. Anticancer Activities of Novel Chalcone and Bis-Chalcone Derivatives. *Bioorg Med Chem* **2006**, *14* (10), 3491–3495. https://doi.org/10.1016/j.bmc.2006.01.003.

(273) Li, R.; Kenyon, G. L.; Cohen, F. E.; Chen, X.; Gong, B.; Dominguez, J. N.; Davidson, E.; Kurzban, G.; Miller, R. E.; Nuzum, E. O.; Rosenthal, P. J.; McKerrow, J. H. In Vitro Antimalarial Activity of Chalcones and Their Derivatives. *J Med Chem* **1995**, *38* (26), 5031–5037. https://doi.org/10.1021/jm00026a010.

(274) Sivakumar, P. M.; Prabhakar, P. K.; Doble, M. Synthesis, Antioxidant Evaluation, and Quantitative Structure–Activity Relationship Studies of Chalcones. *Medicinal Chemistry Research* **2011**, *20* (4), 482–492. https://doi.org/10.1007/s00044-010-9342-1.

(275) El Sayed Aly, M. R.; Abd El Razek Fodah, H. H.; Saleh, S. Y. Antiobesity, Antioxidant and Cytotoxicity Activities of Newly Synthesized Chalcone Derivatives and Their Metal Complexes. *Eur J Med Chem* **2014**, *76*, 517–530. https://doi.org/10.1016/J.EJMECH.2014.02.021.

(276) Sharma, H.; Patil, S.; Sanchez, T. W.; Neamati, N.; Schinazi, R. F.; Buolamwini, J. K. Synthesis, Biological Evaluation and 3D-QSAR Studies of 3-Keto Salicylic Acid Chalcones and Related Amides as Novel HIV-1 Integrase Inhibitors. *Bioorg Med Chem* **2011**, *19* (6), 2030–2045. https://doi.org/10.1016/J.BMC.2011.01.047.

(277) Liu, Z.; Tang, L.; Zou, P.; Zhang, Y.; Wang, Z.; Fang, Q.; Jiang, L.; Chen, G.; Xu, Z.; Zhang, H.; Liang, G. Synthesis and Biological Evaluation of Allylated and Prenylated Mono-Carbonyl Analogs of Curcumin as Anti-Inflammatory Agents. *Eur J Med Chem* **2014**, *74*, 671–682. https://doi.org/10.1016/J.EJMECH.2013.10.061.

(278) Zhuang, C.; Zhang, W.; Sheng, C.; Zhang, W.; Xing, C.; Miao, Z. Chalcone: A Privileged Structure in Medicinal Chemistry. **2017**. https://doi.org/10.1021/acs.chemrev.7b00020.

(279) Lee, Y.-H.; Yoon, H.-G.; Kwak, J.-E.; Kim, M.-J.; Na, Y.-H. Protective Effects of a Chalcone Derivative against Aβ-Induced Oxidative Stress and Neuronal Damage. *BMB Rep* **2012**, *44* (11), 730–734. https://doi.org/10.5483/bmbrep.2011.44.11.730.

(280) Zhang, X.; Rakesh, K. P.; Bukhari, S. N. A.; Balakrishna, M.; Manukumar, H. M.; Qin, H. L. Multi-Targetable Chalcone Analogs to Treat Deadly Alzheimer's Disease: Current View and Upcoming Advice. *Bioorg Chem* **2018**, *80* (June), 86–93. https://doi.org/10.1016/j.bioorg.2018.06.009.

(281) Wang, L.; Wang, Y.; Tian, Y.; Shang, J.; Sun, X.; Chen, H.; Wang, H.; Tan, W. Design, Synthesis, Biological Evaluation, and Molecular Modeling Studies of Chalcone-Rivastigmine Hybrids as Cholinesterase Inhibitors. *Bioorg Med Chem* **2017**, *25* (1), 360–371. https://doi.org/10.1016/j.bmc.2016.11.002.

(282) Liu, H.; Liu, X.; Fan, H.; Tang, J.; Gao, X.; Liu, W. Bioorganic & Medicinal Chemistry Design , Synthesis and Pharmacological Evaluation of Chalcone Derivatives as Acetylcholinesterase Inhibitors. *Bioorg Med Chem* **2014**, *22* (21), 6124–6133. https://doi.org/10.1016/j.bmc.2014.08.033.

(283) Pan, Y.; Chen, Y.; Li, Q.; Yu, X.; Wang, J.; Zheng, J. The Synthesis and Evaluation of Novel Hydroxyl Substituted Chalcone Analogs with in Vitro Anti-Free Radicals Pharmacological Activity and in Vivo Anti-Oxidation Activity in a Free Radical-Injury Alzheimer's Model. *Molecules* **2013**, *18* (2), 1693–1703. https://doi.org/10.3390/molecules18021693.

(284) Cao, Z.; Yang, J.; Xu, R.; Song, Q.; Zhang, X.; Liu, H.; Qiang, X. Bioorganic & Medicinal Chemistry Design , Synthesis and Evaluation of 4 0 -OH-Flurbiprofen-Chalcone Hybrids as Potential Multifunctional Agents for Alzheimer ' s Disease Treatment. *Bioorg Med Chem* **2018**, *26* (5), 1102–1115. https://doi.org/10.1016/j.bmc.2018.01.030.

(285) Pruccoli, L.; Iriepa, I.; Rampa, A.; Moraleda, I.; Tarozzi, A.; Gobbi, S.; Bartolini, M.; Belluti, F.; Bisi, A.; Naldi, M. Exploiting the Chalcone Scaffold to Develop Multifunctional Agents for Alzheimer's Disease. *Molecules* **2018**, *23* (8), 1902. https://doi.org/10.3390/molecules23081902.

(286) Sashidhara, K. V.; Kumar, M.; Modukuri, R. K.; Sonkar, R.; Bhatia, G.; Khanna, A. K.; Rai, S.; Shukla, R. Synthesis and Anti-Inflammatory Activity of Novel Biscoumarin–Chalcone Hybrids. *Bioorg Med Chem Lett* **2011**, *21* (15), 4480–4484. https://doi.org/10.1016/j.bmcl.2011.06.002.

(287) Sashidhara, K. V.; Modukuri, R. K.; Jadiya, P.; Dodda, R. P.; Kumar, M.; Sridhar, B.; Kumar, V.; Haque, R.; Siddiqi, M. I.; Nazir, A. Benzofuran-Chalcone Hybrids as Potential Multifunctional Agents against Alzheimer's Disease: Synthesis and in Vivo Studies with Transgenic Caenorhabditis Elegans. *ChemMedChem* **2014**, *9* (12), 2671–2684. https://doi.org/10.1002/CMDC.201402291.

(288) Ono, M.; Haratake, M.; Nakayama, M. Novel Chalcones as Probes for in Vivo Imaging of b -Amyloid Plaques in Alzheimer' s Brains. **2007**, *15*, 6802–6809. https://doi.org/10.1016/j.bmc.2007.07.052.

(289) Cui, M.; Ono, M.; Kimura, H.; Li, B.; Saji, H. Bioorganic & Medicinal Chemistry Letters Synthesis and Biological Evaluation of Indole-Chalcone Derivatives as b -Amyloid Imaging Probe. *Bioorg Med Chem Lett* **2011**, *21* (3), 980–982. https://doi.org/10.1016/j.bmcl.2010.12.045.

(290) Fuchigami, T.; Yamashita, Y.; Haratake, M.; Ono, M.; Yoshida, S. Bioorganic & Medicinal Chemistry Synthesis and Evaluation of Ethyleneoxylated and Allyloxylated Chalcone Derivatives for Imaging of Amyloid b Plaques by SPECT. *Bioorg Med Chem* **2014**, *22* (9), 2622–2628. https://doi.org/10.1016/j.bmc.2014.03.032.

(291) Park, S. J. S.; Je, E.; Jeong, L.; Park, H. Development of Fluorescent Probes That Bind and Stain Amyloid Plaques in Alzheimer ' s Disease. *Arch Pharm Res* **2015**, *38* (11), 1992–1998. https://doi.org/10.1007/s12272-015-0617-4.

(292) Ono, M.; Hori, M.; Haratake, M.; Tomiyama, T. Structure – Activity Relationship of Chalcones and Related Derivatives as Ligands for Detecting of b -Amyloid Plaques in the Brain. **2007**, *15*, 6388–6396. https://doi.org/10.1016/j.bmc.2007.06.055.

(293) Baell, J. B. Observations on Screening-Based Research and Some Concerning Trends in the Literature. *Future Med Chem* **2010**, *2* (10), 1529–1546. https://doi.org/10.4155/fmc.10.237.

(294) Baell, J. B. Screening-Based Translation of Public Research Encounters Painful Problems. *ACS Med Chem Lett* **2015**, *6* (3), 229–234. https://doi.org/10.1021/acsmedchemlett.5b00032.

(295) Baell, J. B. Broad Coverage of Commercially Available Lead-like Screening Space with Fewer than 350,000 Compounds. *J Chem Inf Model* **2013**, *53* (1), 39–55. https://doi.org/10.1021/ci300461a.

(296) Baell, J. B. Feeling Nature's PAINS: Natural Products, Natural Product Drugs, and Pan Assay Interference Compounds (PAINS). *J Nat Prod* **2016**, *79* (3), 616–628. https://doi.org/10.1021/acs.jnatprod.5b00947.

(297) Baell, J.; Walters, M. A. Chemistry: Chemical Con Artists Foil Drug Discovery. *Nature* **2014**, *513* (7519), 481–483. https://doi.org/10.1038/513481a.

(298) Baell, J. B.; Nissink, J. W. M. Seven Year Itch: Pan-Assay Interference Compounds (PAINS) in 2017 - Utility and Limitations. *ACS Chem Biol* **2018**, *13* (1), 36–44. https://doi.org/10.1021/acschembio.7b00903.

(299) Nissink, J. W. M.; Blackburn, S. Quantification of Frequent-Hitter Behavior Based on Historical High-Throughput Screening Data. *Future Med Chem* **2014**, *6* (10), 1113–1126. https://doi.org/10.4155/FMC.14.72.

(300) Schneider, P.; Schneider, G. Privileged Structures Revisited. *Angewandte Chemie - International Edition* **2017**, *56* (27), 7971–7974. https://doi.org/10.1002/ANIE.201702816.

(301) Devine, S. M.; Mulcair, M. D.; Debono, C. O.; Leung, E. W. W.; Nissink, J. W. M.; Lim, S. S.; Chandrashekaran, I. R.; Vazirani, M.; Mohanty, B.; Simpson, J. S.; Baell, J. B.; Scammells, P. J.; Norton, R. S.; Scanlon, M. J. Promiscuous 2-Aminothiazoles (PrATs): A Frequent Hitting Scaffold. *J Med Chem* **2015**, *58* (3), 1205–1214. https://doi.org/10.1021/jm501402x.

(302) Baell, J. B.; Holloway, G. A. New Substructure Filters for Removal of Pan Assay Interference Compounds (PAINS) from Screening Libraries and for Their Exclusion in Bioassays. *J Med Chem* **2010**, *53* (7), 2719–2740. https://doi.org/10.1021/jm901137j.

(303) Bruns, R. F.; Watson, I. A. Rules for Identifying Potentially Reactive or Promiscuous Compounds. *J Med Chem* **2012**, *55* (22), 9763–9772. https://doi.org/10.1021/jm301008n.

(304) Pearce, B. C.; Sofia, M. J.; Good, A. C.; Drexler, D. M.; Stock, D. A. An Empirical Process for the Design of High-Throughput Screening Deck Filters. *J Chem Inf Model* **2006**, *46* (3), 1060–1068. https://doi.org/10.1021/CI050504M.

(305) Roche, O.; Schneider, P.; Zuegge, J.; Guba, W.; Kansy, M.; Alanine, A.; Bleicher, K.; Danel, F.; Gutknecht, E. M.; Rogers-Evans, M.; Neidhart, W.; Stalder, H.; Dillon, M.; Sjögren, E.; Fotouhi, N.; Gillespie, P.; Goodnow, R.; Harris, W.; Jones, P.; Taniguchi, M.; Tsujii, S.; Von der Saal, W.; Zimmermann, G.; Schneider, G. Development of a Virtual Screening Method for Identification of "Frequent Hitters" in Compound Libraries. *J Med Chem* **2002**, *45* (1), 137–142. https://doi.org/10.1021/JM010934D.

(306) Huth, J. R.; Mendoza, R.; Olejniczak, E. T.; Johnson, R. W.; Cothron, D. A.; Liu, Y.; Lerner, C. G.; Chen, J.; Hajduk, P. J. ALARM NMR: A Rapid and Robust Experimental Method to Detect Reactive False Positives in Biochemical Screens. *J Am Chem Soc* **2005**, *127* (1), 217–224. https://doi.org/10.1021/JA0455547.

(307) Yang, J. J.; Ursu, O.; Lipinski, C. A.; Sklar, L. A.; Oprea, T. I.; Bologa, C. G. Badapple: Promiscuity Patterns from Noisy Evidence. *J Cheminform* **2016**, *8* (1). https://doi.org/10.1186/S13321-016-0137-3.

(308) Jackson, P. A.; Widen, J. C.; Harki, D. A.; Brummond, K. M. Covalent Modifiers: A Chemical Perspective on the Reactivity of α,β-Unsaturated Carbonyls with Thiols via Hetero-Michael

Addition Reactions. *J Med Chem* **2017**, *60* (3), 839–885. https://doi.org/10.1021/ACS.JMEDCHEM.6B00788.

(309) Baell, J. B. Redox-Active Nuisance Screening Compounds and Their Classification. *Drug Discov Today* **2011**, *16* (17–18), 840–841. https://doi.org/10.1016/j.drudis.2011.06.011.

(310) Priyadarsini, K. Photophysics, Photochemistry and Photobiology of Curcumin: Studies from Organic Solutions, Bio-Mimetics and Living Cells. *J Photochem Photobiol.* **2009**, *10* (2), 81-95. https://doi.org/j.jphotochemrev.2009.05.001.

(311) Burgos-Moron, E.; Calderon-Montano, J. M.; Salvador, J.; Robles, A.; Lopez-Lazaro, M. The Dark Side of Curcumin Estefanı´a. *Int J Cancer* **2010**, *126*, 1771–1775.

(312) Thapliyal, R.; Maru, G. Inhibition of Cytochrome P450 Isozymes by Curcumins in Vitro and in Vivo. *Food Chem Toxicol.* **2001**, *39* (6), 541-547. https://doi.org/10.1016/s0278-6915(00)00165-4.

(313) Schneider, C.; Gordon, O. N.; Edwards, R. L.; Luis, P. B. Degradation of Curcumin: From Mechanism to Biological Implications. *J Agric Food Chem* **2015**, *63* (35), 7606–7614. https://doi.org/10.1021/ACS.JAFC.5B00244.

(314) Chin, D.; Huebbe, P.; Frank, J.; Rimbach, G.; Pallauf, K. Curcumin May Impair Iron Status When Fed to Mice for Six Months. *Redox Biol* **2014**, *28* (2), 563-569. https://doi.org/10.1016/j.redox.2014.01.018.

(315) Fang, J.; Lu, J.; Holmgren, A. Thioredoxin Reductase Is Irreversibly Modified by Curcumin: A Novel Molecular Mechanism for Its Anticancer Activity. *J Biol Chem.* **2005**, *280* (26), 25284-25290. https://doi.org/10.1074/jbc.M414645200.

(316) Jung, Y.; Xu, W.; Kim, H.; Ha, N.;Neckers, L. Curcumin-Induced Degradation of ErbB2: A Role for the E3 Ubiquitin Ligase CHIP and the Michael Reaction Acceptor Activity of Curcumin. *Biochim Biophys Acta* **2007**, *1773* (3), 383-390. https://doi.org/10.1016/j.bbamcr.2006.11.004.

(317) Reinke, A. A.; Gestwicki, J. E. Structure-Activity Relationships of Amyloid Beta-Aggregation Inhibitors Based on Curcumin: Influence of Linker Length and Flexibility. *Chem Biol Drug Des* **2007**, *70* (3), 206–215. https://doi.org/10.1111/J.1747-0285.2007.00557.X.

(318) Meanwell, N. A. The Influence of Bioisosteres in Drug Design: Tactical Applications to Address Developability Problems. *Tactics in Contemporary Drug Design* **2015**, *9*, 283. https://doi.org/10.1007/7355_2013_29.

(319) Kumari, S.; Carmona, A. V.; Tiwari, A. K.; Trippier, P. C. Amide Bond Bioisosteres: Strategies, Synthesis, and Successes. *J Med Chem* **2020**, *63* (21), 12290–12358. https://doi.org/10.1021/ACS.JMEDCHEM.0C00530/ASSET/IMAGES/MEDIUM/JM0C00530_0123.GIF.

(320) Mohamed, T.; Rao, P. P. N. 2,4-Disubstituted Quinazolines as Amyloid-β Aggregation Inhibitors with Dual Cholinesterase Inhibition and Antioxidant Properties: Development and Structure-Activity Relationship (SAR) Studies. *Eur J Med Chem* **2017**, *126*, 823–843. https://doi.org/10.1016/j.ejmech.2016.12.005.

(321) Montalbetti, C. A. G. N.; Falque, V. Amide Bond Formation and Peptide Coupling. *Tetrahedron* **2005**, *61* (46), 10827–10852. https://doi.org/10.1016/j.tet.2005.08.031.

(322) Ruff, F.; Farkas, Ö. Concerted SN2 Mechanism for the Hydrolysis of Acid Chlorides: Comparisons of Reactivities Calculated by the Density Functional Theory with Experimental Data. *J Phys Org Chem* **2011**, *24* (6), 480–491. https://doi.org/10.1002/POC.1790.

(323) Sheehan, J. C.; Boshart, G. L.; Cruickshank, P. A. A Convenient Synthesis of Water-Soluble Carbodiimides. *Journal of Organic Chemistry* **1961**, *26* (7), 2525–2528. https://doi.org/10.1021/JO01351A600.

(324) Rebek, J.; Feitler, D. An Improved Method for the Study of Reaction Intermediates. The Mechanism of Peptide Synthesis Mediated by Carbodiimides. *J Am Chem Soc* **1973**, *95* (12), 4052–4053. https://doi.org/10.1021/JA00793A039.

(325) Windridge, G. C.; Jorgensen, E. C. 1-Hydroxybenzotriazole as a Racemization-Suppressing Reagent for the Incorporation of Im-Benzyl-L-Histidine into Peptides. *J Am Chem Soc* **1971**, *93* (23), 6318–6319. https://doi.org/10.1021/JA00752A081.

(326) Pasieka, A.; Panek, D.; Szałaj, N.; Espargaró, A.; Więckowska, A.; Malawska, B.; Sabaté, R.; Bajda, M. Dual Inhibitors of Amyloid-β and Tau Aggregation with Amyloid-β Disaggregating Properties: Extended in Cellulo, in Silico, and Kinetic Studies of Multifunctional Anti-Alzheimer's Agents. *ACS Chem Neurosci* **2021**, *12* (11), 2057–2068. https://doi.org/10.1021/ACSCHEMNEURO.1C00235/ASSET/IMAGES/MEDIUM/CN1C00235_0010.GIF.

(327) Mohamed, T.; Gujral, S. S.; Rao, P. P. N. Tau Derived Hexapeptide AcPHF6 Promotes Beta-Amyloid (Aβ) Fibrillogenesis. *ACS Chemical Neurosci*. **2018**, *9* (4), 773–782. https://doi.org/10.1021/acschemneuro.7b00433.

(328) Mohamed, T.; Shakeri, A.; Tin, G.; Rao, P. P. N. Structure-Activity Relationship Studies of Isomeric 2,4-Diaminoquinazolines on β-Amyloid Aggregation Kinetics. *ACS Med Chem Lett* **2016**, *7* (5), 502–507. https://doi.org/10.1021/ACSMEDCHEMLETT.6B00039/SUPPL_FILE/ML6B00039_SI_001.PDF.

(329) Tin, G.; Mohamed, T.; Shakeri, A.; Pham, A. T.; Rao, P. P. N. Interactions of Selective Serotonin Reuptake Inhibitors with β-Amyloid. **2018**. https://doi.org/10.1021/acschemneuro.8b00160.

(330) Biancalana, M.; Koide, S. Molecular Mechanism of Thioflavin-T Binding to Amyloid Fibrils. *Biochim Biophys Acta* **2010**, *1804* (7), 1405–1412. https://doi.org/10.1016/J.BBAPAP.2010.04.001.

(331) PS, V.; CF, C. Fluorescent Stains, with Special Reference to Amyloid and Connective Tissues. *Arch Patrol* **1959**, No. 68, 487–498.

(332) Naiki, H.; Higuchi, K.; Hosokawa, M.; Takeda, T. Fluorometric Determination of Amyloid Fibrils in Vitro Using the Fluorescent Dye, Thioflavin T1. *Anal Biochem* **1989**, *177* (2), 244–249. https://doi.org/10.1016/0003-2697(89)90046-8.

(333) Levine, H. Thioflavine T Interaction with Synthetic Alzheimer's Disease Beta-Amyloid Peptides: Detection of Amyloid Aggregation in Solution. *Protein Sci.* **1993**, *2* (3), 404–410. https://doi.org/10.1002/PRO.5560020312.

(334) Jia, Y.; Wang, N.; Liu, X. Resveratrol and Amyloid-Beta: Mechanistic Insights. *Nutrients* **2017**, *9* (10). https://doi.org/10.3390/NU9101122.

(335) Thapa, A.; Jett, S. D.; Chi, E. Y. Curcumin Attenuates Amyloid-β Aggregate Toxicity and Modulates Amyloid-β Aggregation Pathway. *ACS Chem Neurosci* **2016**, *7* (1), 56–68. https://doi.org/10.1021/ACSCHEMNEURO.5B00214.

(336) Churches, Q.; Caine, J.; Cavanagh, K.; Epa, V.; Waddington, L.; Tranberg, C.; Meyer, A.; Varghese, J.; streltsov, V.; Duggan, P. Naturally Occurring Polyphenolic Inhibitors of Amyloid Beta Aggregation. *Bioorg Med Chem Lett.* **2014**, *24* (14), 3108-3112. https://doi.org/10.1016/j.bmcl.2014.05.008.

(337) Su, H.; Yang, F.; Fu, R.; Li, X.; French, R.; Mose, E.; Pu, X.; Trinh, B.; Kumar, A.; Liu, J.; Antonucci, L.; Todoric, J.; Liu, Y.; Hu, Y.; Diaz-Meco, M. T.; Moscat, J.; Metallo, C. M.; Lowy, A. M.; Sun, B.; Karin, M. Cancer Cells Escape Autophagy Inhibition via NRF2-Induced Macropinocytosis. *Cancer Cell* **2021**, *39* (5), 678-693.e11. https://doi.org/10.1016/J.CCELL.2021.02.016.

(338) Lv, X. J.; Tang, Q.; Tu, Y. Q.; Yan, D. D.; Wei, Q. C. Long Noncoding RNA PCAT6 Regulates Cell Growth and Metastasis via Wnt/β-Catenin Pathway and Is a Prognosis Marker in Cervical

Cancer. *Eur Rev Med Pharmacol Sci* **2019**, *23* (5), 1947–1956. https://doi.org/10.26355/EURREV_201903_17233.

(339) Rao, P. P. N.; Du, D. In Silico Strategies to Design Small Molecules to Study Beta-Amyloid Aggregation. *Neuromethods* **2018**, *132*, 249–261. https://doi.org/10.1007/978-1-4939-7404-7_10/COVER.

(340) Colvin, M. T.; Silvers, R.; Ni, Q. Z.; Can, T. V.; Sergeyev, I.; Rosay, M.; Donovan, K. J.; Michael, B.; Wall, J.; Linse, S.; Griffin, R. G. Atomic Resolution Structure of Monomorphic Aβ42 Amyloid Fibrils. *J Am Chem Soc* **2016**, *138* (30), 9663–9674. https://doi.org/10.1021/JACS.6B05129.

(341) El Shatshat, A.; Pham, A. T.; Rao, P. P. N. Interactions of Polyunsaturated Fatty Acids with Amyloid Peptides Aβ40 and Aβ42. *Arch Biochem Biophys* **2019**, *663* (December 2018), 34–43. https://doi.org/10.1016/j.abb.2018.12.027.

(342) Wolff, M.; Zhang-Haagen, B.; Decker, C.; Barz, B.; Schneider, M.; Biehl, R.; Radulescu, A.; Strodel, B.; Willbold, D.; Nagel-Steger, L. Aβ42 Pentamers/Hexamers Are the Smallest Detectable Oligomers in Solution. *Scientific Reports* **2017**, *7* (1), 1–13. https://doi.org/10.1038/s41598-017-02370-3.

(343) Chen, G. F.; Xu, T. H.; Yan, Y.; Zhou, Y. R.; Jiang, Y.; Melcher, K.; Xu, H. E. Amyloid Beta: Structure, Biology and Structure-Based Therapeutic Development. *Acta Pharmacologica Sinica* **2017**, *38* (9), 1205–1235. https://doi.org/10.1038/aps.2017.28.

(344) Cho, S. J.; Roh, J. S.; Sun, W. S.; Kim, S. H.; Park, K. D. N-Benzylbenzamides: A New Class of Potent Tyrosinase Inhibitors. *Bioorg Med Chem Lett* **2006**, *16* (10), 2682–2684. https://doi.org/10.1016/J.BMCL.2006.02.018.

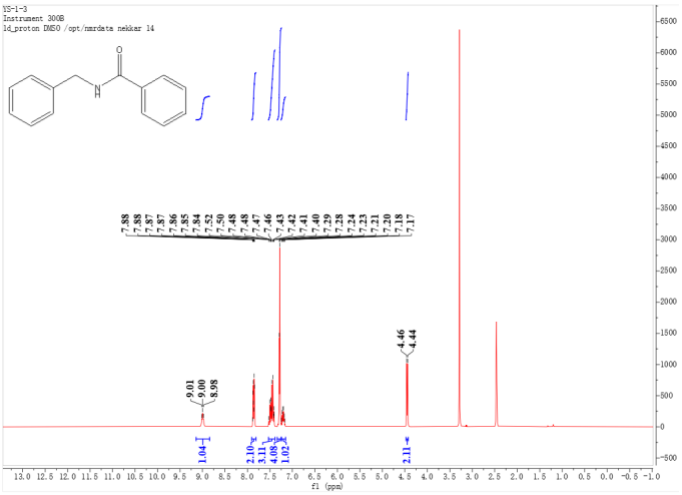
(345) Mohamed, T.; Shakeri, A.; Tin, G.; Rao, P. P. N. Structure-Activity Relationship Studies of Isomeric 2,4-Diaminoquinazolines on β-Amyloid Aggregation Kinetics. *ACS Med Chem Lett* **2016**, *7* (5), 502–507. https://doi.org/10.1021/ACSMEDCHEMLETT.6B00039.

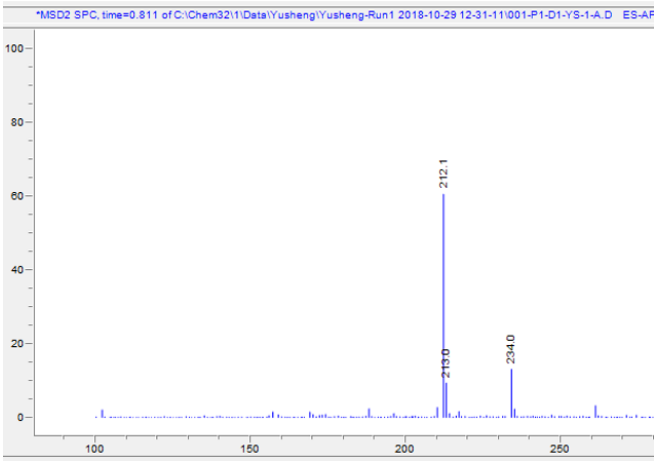
(346) Gujral, S. S.; Shakeri, A.; Hejazi, L.; Rao, P. P. N. Design, Synthesis and Structure-Activity Relationship Studies of 3-Phenylpyrazino[1,2-a]Indol-1(2H)-Ones as Amyloid Aggregation and Cholinesterase Inhibitors with Antioxidant Activity. *European Journal of Medicinal Chemistry Reports* **2022**, *6*, 100075. https://doi.org/10.1016/J.EJMCR.2022.100075.

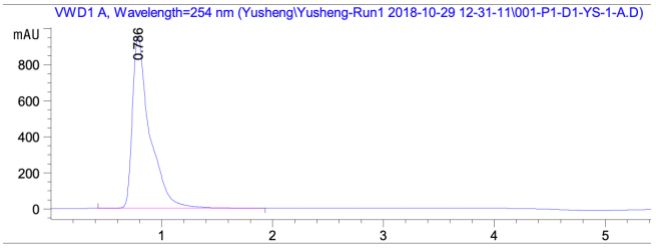
(347) Rao, P. P. N.; Zhao, Y.; Huang, R. Understanding the Mechanisms of Amyloid Beta (Aβ) Aggregation by Computational Modeling. *Neuromethods* **2023**, *203*, 51–71. https://doi.org/10.1007/978-1-0716-3311-3_2/COVER.

Appendix A – Spectra for Chapter 2

N-Benzylbenzamide (3a)



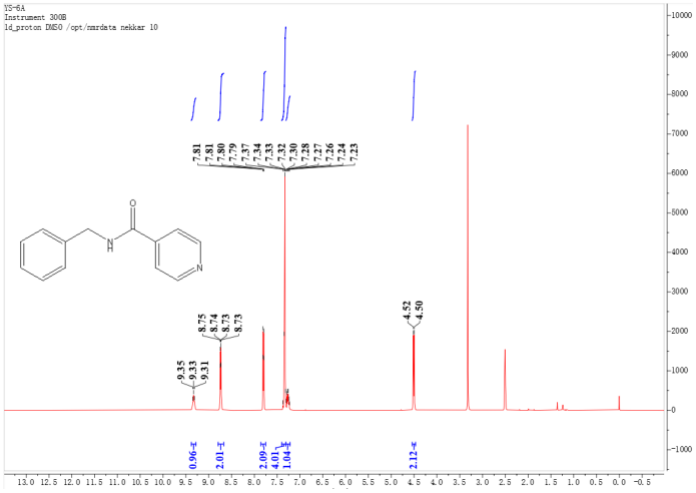


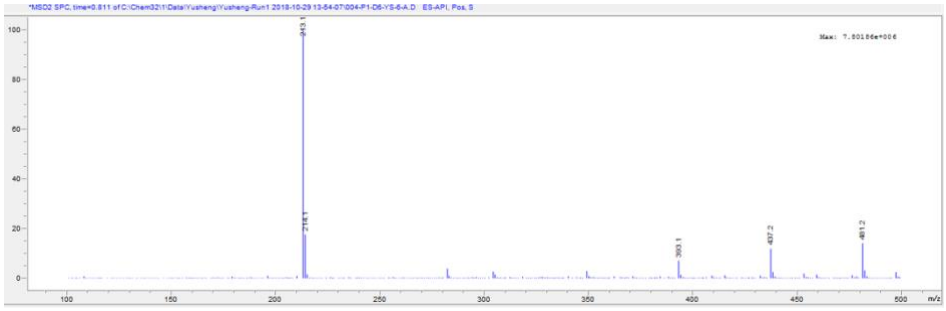


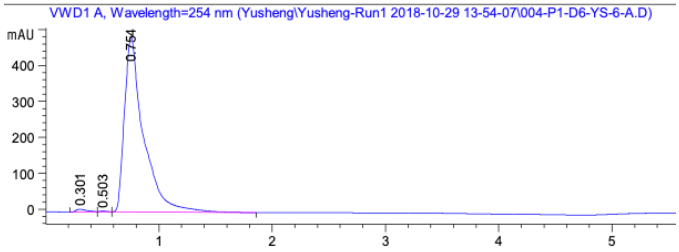
Signal 3: VWD1 A, Wavelength=254 nm

Peak #	RetTime [min]	Type	Width [min]	Area [mAU*s]	Height [mAU]	Area %
1	0.786	BB	0.1555	1.03697e4	956.58026	100.0000
Totals :				1.03697e4	956.58026	

N-Benzylisonicothinamide (3b)



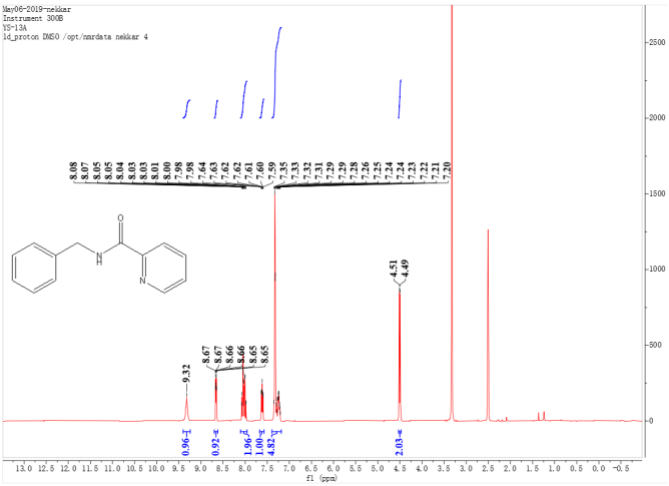


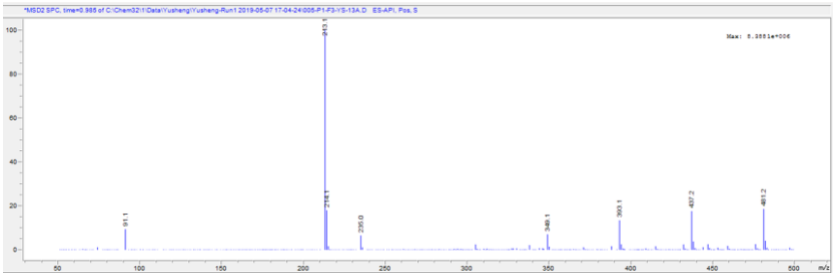


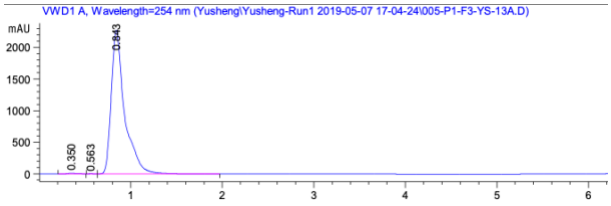
Signal 3: VWD1 A, Wavelength=254 nm

Peak #	RetTime [min]	Type	Width [min]	Area [mAU*s]	Height [mAU]	Area %
1	0.301	BB	0.0883	47.15461	7.71669	0.8166
2	0.503	BB	0.0582	7.25016	1.95767	0.1256
3	0.754	BB	0.1718	5720.12939	487.99649	99.0579
Totals :				5774.53416	497.67085	

N-Benzylpicolinamide (3c)



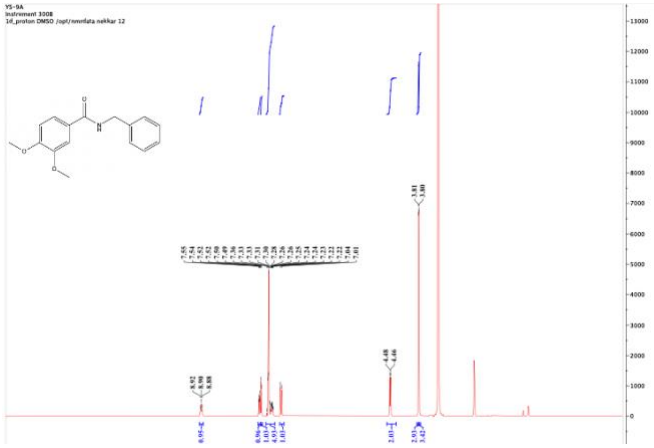




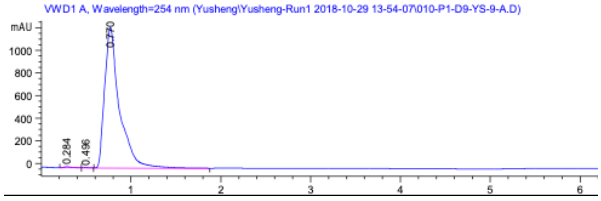
Signal 3: VWD1 A, Wavelength=254 nm

Peak #	RetTime [min]	Type	Width [min]	Area [mAU*s]	Height [mAU]	Area %
1	0.350	BB	0.0974	64.54716	9.72547	0.2779
2	0.563	BB	0.0540	8.92316	2.66946	0.0384
3	0.843	BB	0.1478	2.31550e4	2274.20044	99.6837
Totals :				2.32285e4	2286.59538	

N-Benzyl-3,4-dimethoxybenzamide (3d)

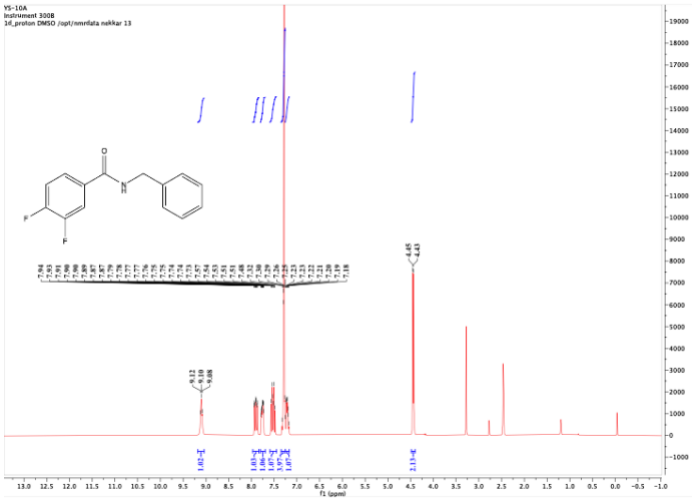


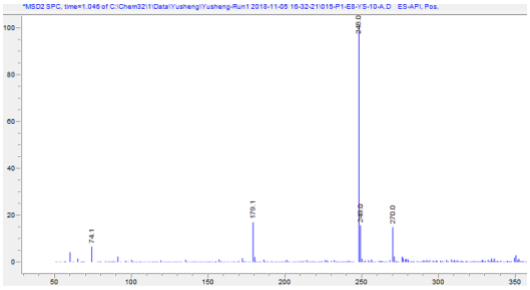


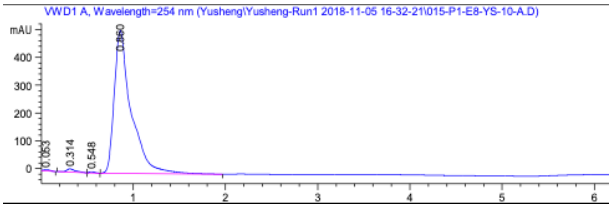


Peak #	RetTime [min]	Type	Width [min]	Area [mAU*s]	Height [mAU]	Area %
1	0.284	BB	0.0872	54.61726	9.07742	0.3822
2	0.496	BB	0.0597	11.23026	3.00115	0.0786
3	0.770	BB	0.1607	1.42237e4	1241.15820	99.5392
Totals :				1.42895e4	1253.23677	

N-Benzyl-3,4-difluorobenzamide (3e)

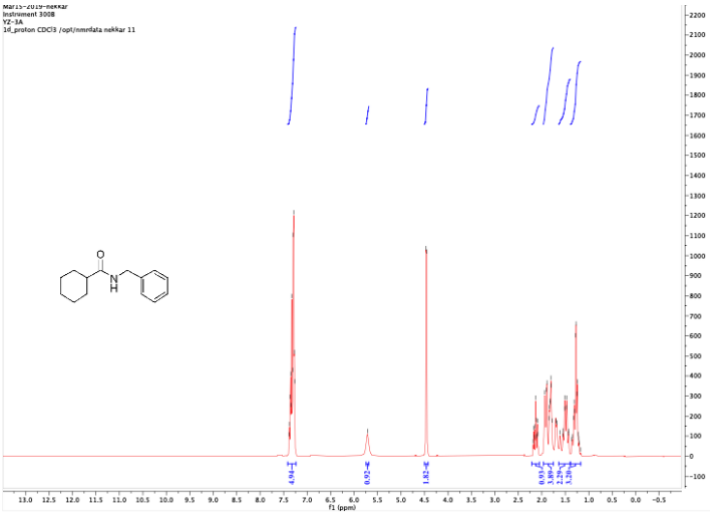




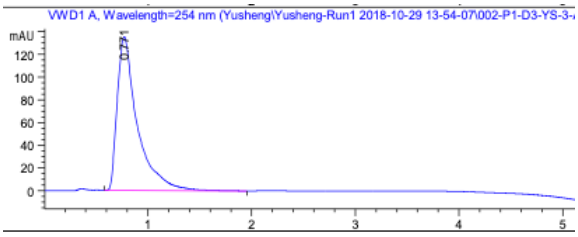


Peak #	RetTime [min]	Type	Width [min]	Area [mAU*s]	Height [mAU]	Area %
1	0.053	BB	0.0815	19.51118	3.95680	0.2911
2	0.314	BB	0.0976	84.73615	12.25835	1.2641
3	0.548	BB	0.0611	17.74451	4.58534	0.2647
4	0.860	BB	0.1815	6581.30664	513.59381	98.1801
Totals :				6703.29848	534.39430	

N-Benzylcyclohexanecarboxamide (3f)



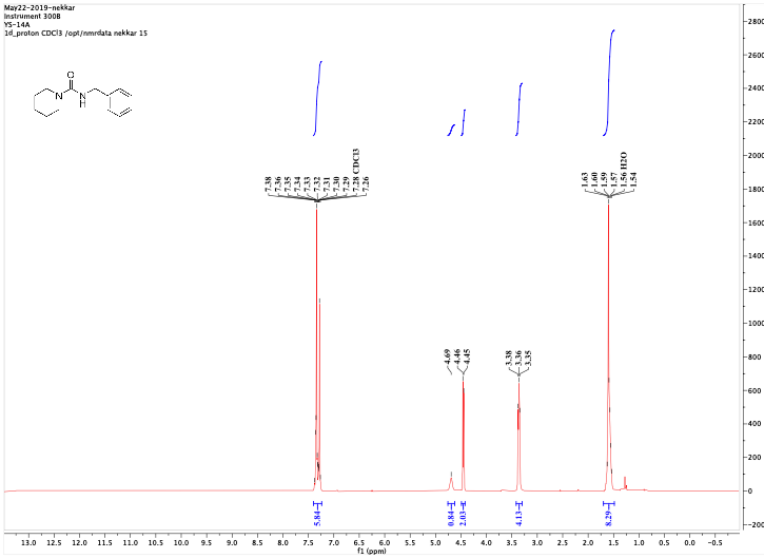


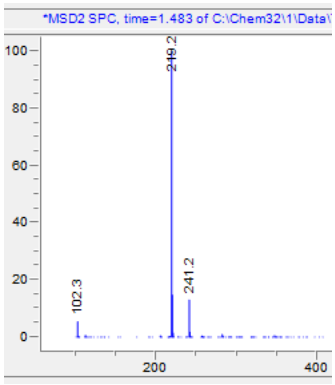


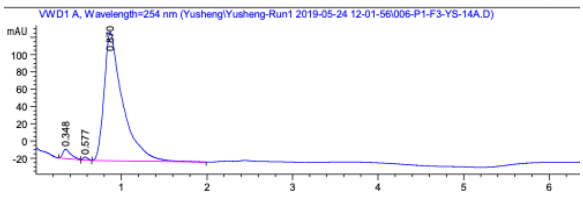
Signal 3: VWD1 A, Wavelength=254 nm

Peak #	RetTime [min]	Type	Width [min]	Area [mAU*s]	Height [mAU]	Area %
1	0.771	BB	0.1994	1823.98401	135.19371	100.0000
Totals :				1823.98401	135.19371	

N-Benzylpiperidine-1-carboxamide (3g)



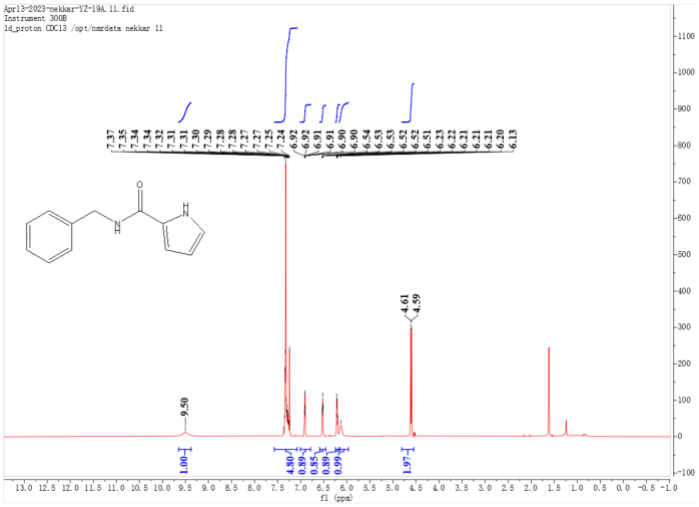


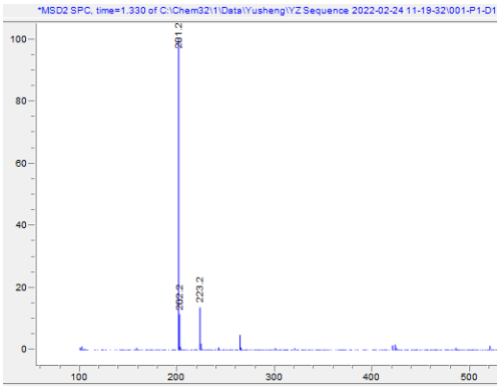


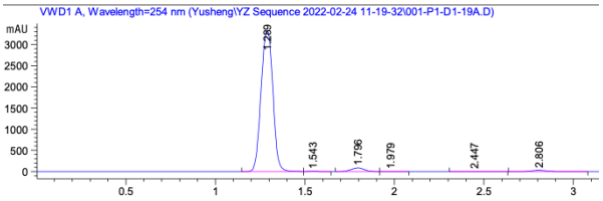
Signal 3: VWD1 A, Wavelength=254 nm

Peak #	RetTime [min]	Type	Width [min]	Area [mAU*s]	Height [mAU]	Area %
1	0.348	BB	0.0946	68.99563	10.64981	2.9675
2	0.577	BB	0.0574	12.41806	3.50244	0.5341
3	0.870	BB	0.2086	2243.65723	149.05824	96.4984
Totals :				2325.07092	163.21048	

N-Benzyl-1*H*-pyrrole-2-carboxamide (3h)





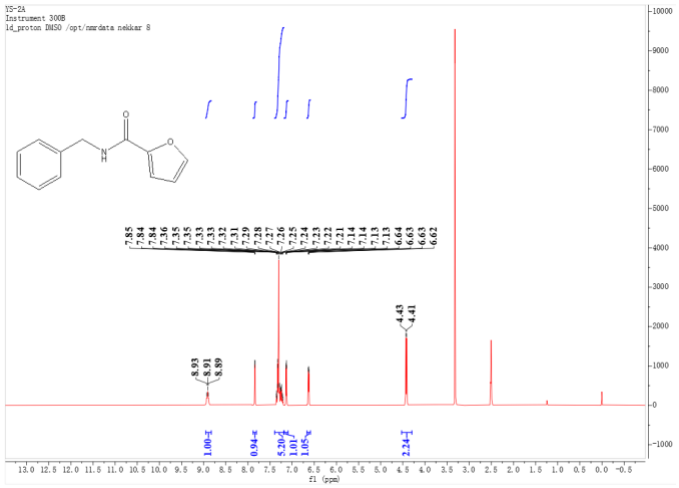


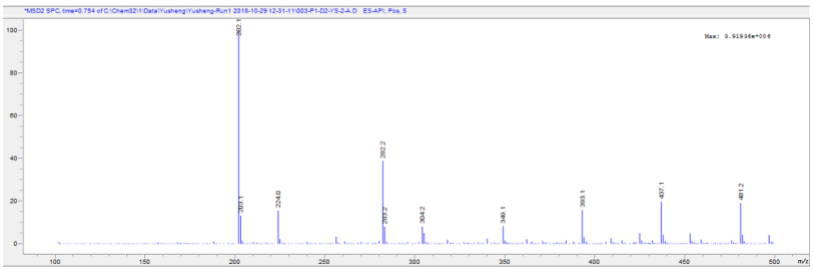
Signal 3: VWD1 A, Wavelength=254 nm

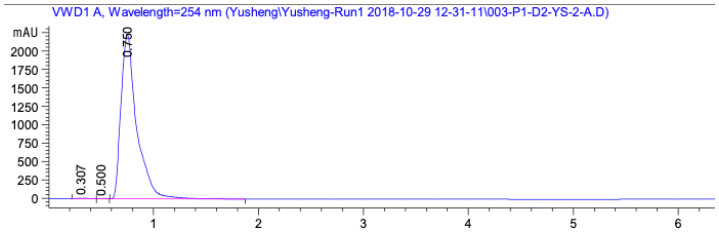
Peak #	RetTime [min]	Type	Width [min]	Area [mAU*s]	Height [mAU]	Area %
1	1.289	BB	0.0734	1.52345e4	3330.34692	96.1782
2	1.543	BB	0.0564	10.81121	2.97664	0.0683
3	1.796	BB	0.0797	411.93530	81.93833	2.6006
4	1.979	BB	0.0632	7.96060	2.01045	0.0503
5	2.447	BB	0.1009	13.56135	2.11119	0.0856
6	2.806	BB	0.0885	161.09576	28.25652	1.0170

Peak #	RetTime [min]	Type	Width [min]	Area [mAU*s]	Height [mAU]	Area %
Totals :				1.58399e4	3447.64005	

N-Benzylfuran-2-carboxamide (3i)



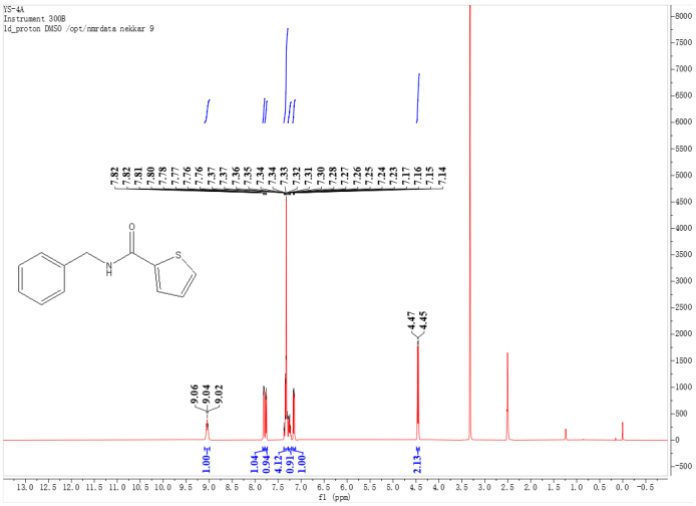


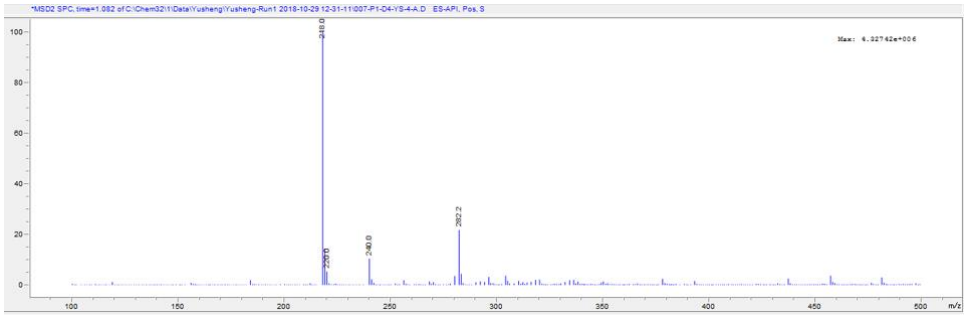


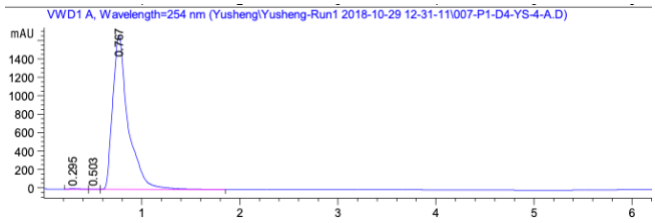
Signal 3: VWD1 A, Wavelength=254 nm

Peak #	RetTime [min]	Type	Width [min]	Area [mAU*s]	Height [mAU]	Area %
1	0.307	BB	0.0893	48.26459	7.78848	0.2068
2	0.500	BB	0.0543	6.06147	1.79736	0.0260
3	0.750	BB	0.1584	2.32831e4	2237.72974	99.7672
Totals :				2.33374e4	2247.31557	

N-Benzylthiophene-2-carboxamide (3j)



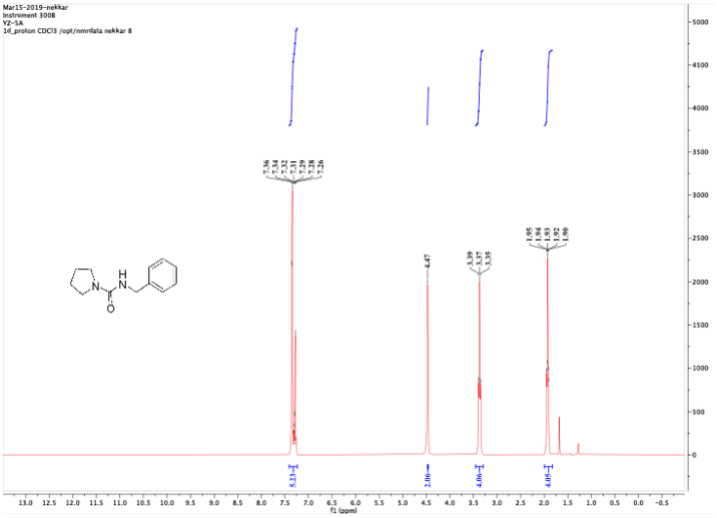


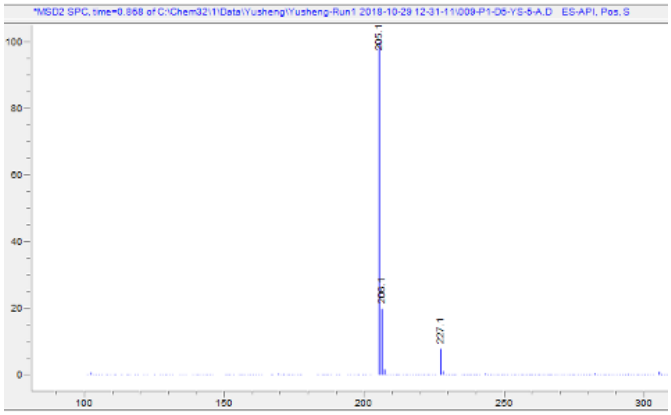


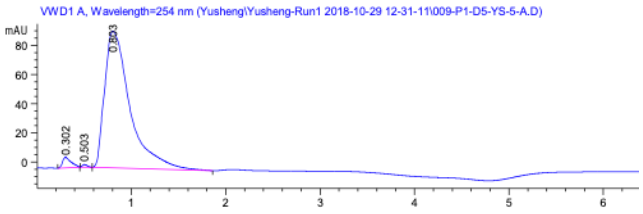
Signal 3: VWD1 A, Wavelength=254 nm

Peak #	RetTime [min]	Type	Width [min]	Area [mAU*s]	Height [mAU]	Area %
1	0.295	BB	0.0874	51.43388	8.51790	0.2804
2	0.503	BB	0.0523	7.19305	2.19278	0.0392
3	0.767	BB	0.1533	1.82872e4	1675.63208	99.6804
Totals :				1.83458e4	1686.34276	

N-Benzylpyrrolidine-1-carboxamide (3k)

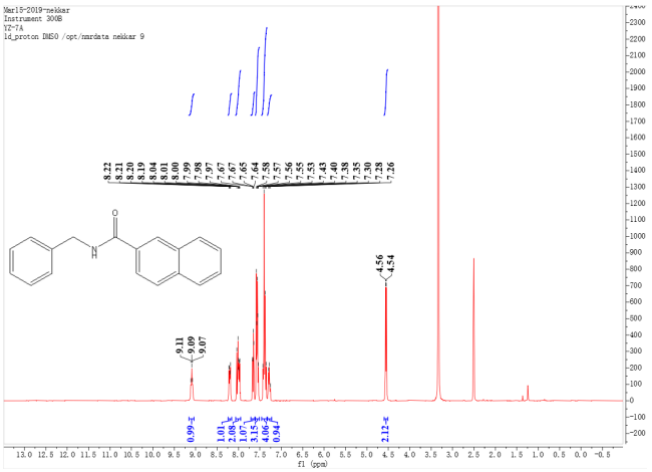


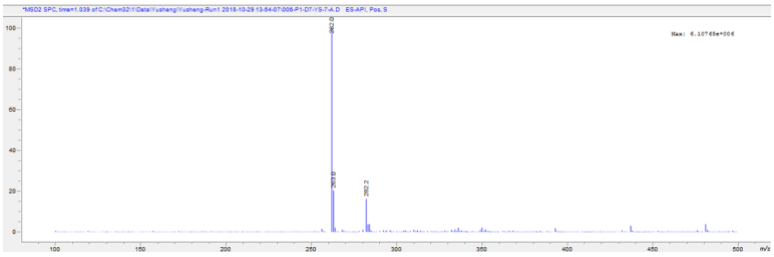


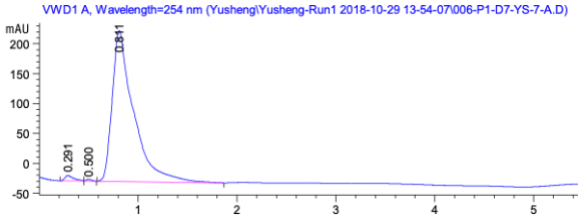


Peak #	RetTime [min]	Type	Width [min]	Area [mAU*s]	Height [mAU]	Area %
1	0.302	BB	0.0884	44.57109	7.18041	2.4821
2	0.503	BB	0.0558	6.13859	1.75713	0.3419
3	0.803	BB	0.2753	1744.98425	93.67278	97.1760
Totals :				1795.69394	102.61033	

N-Benzyl-2-naphthamide (3l)



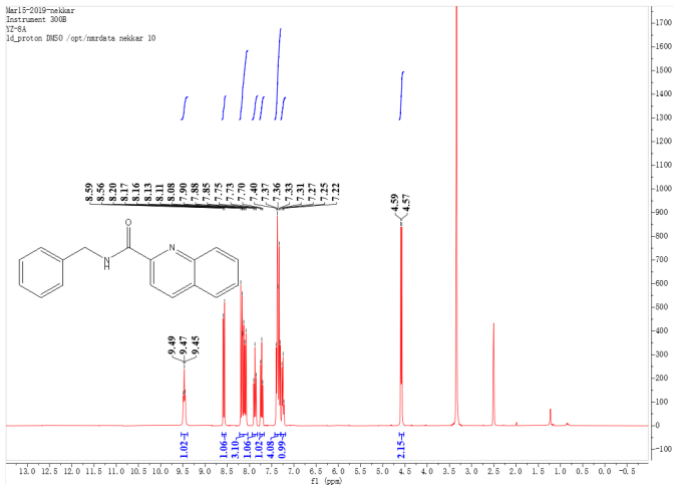


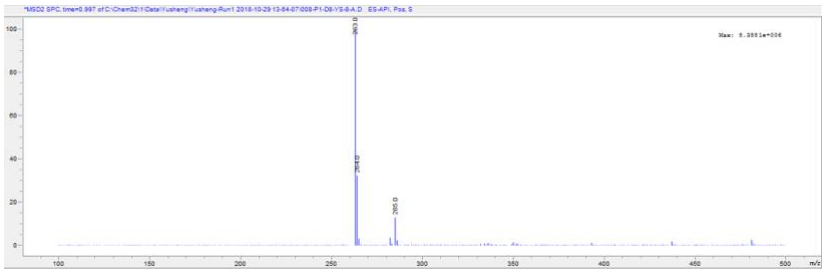


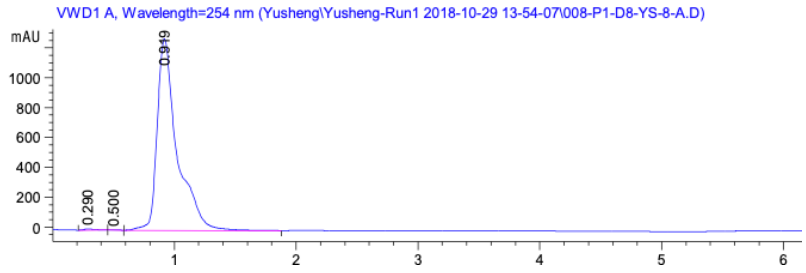
Signal 3: VWD1 A, Wavelength=254 nm

Peak #	RetTime [min]	Type	Width [min]	Area [mAU*s]	Height [mAU]	Area %
1	0.291	BB	0.0859	53.02962	8.84879	1.3760
2	0.500	BB	0.0544	9.44736	2.73155	0.2451
3	0.811	BB	0.2051	3791.50879	252.60011	98.3789
Totals :				3853.98577	264.18046	

N-Benzylquinoline-2-carboxamide (3m)



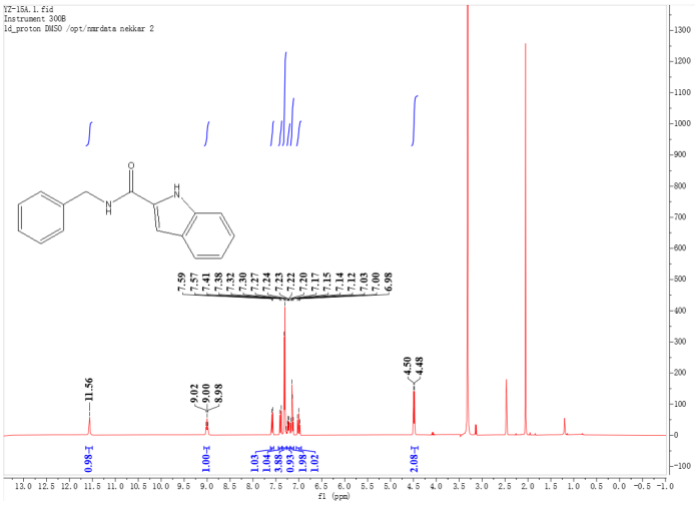


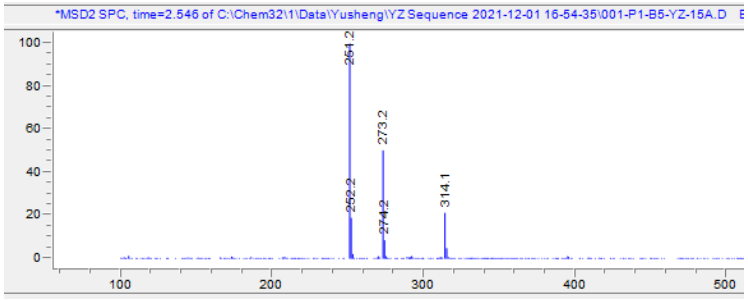


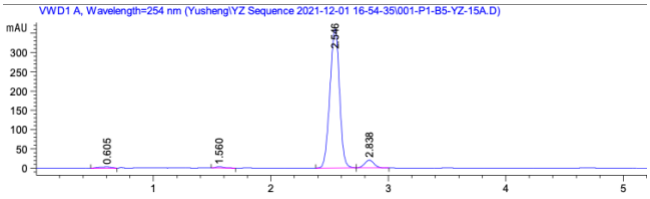
Signal 3: VWD1 A, Wavelength=254 nm

Peak #	RetTime [min]	Type	Width [min]	Area [mAU*s]	Height [mAU]	Area %
1	0.290	BB	0.0876	51.51709	8.51353	0.3511
2	0.500	BB	0.0549	8.94929	2.55373	0.0610
3	0.919	BB	0.1659	1.46133e4	1282.70581	99.5879
Totals :				1.46738e4	1293.77306	

N-Benzyl-1*H*-indole-2-carboxamide (5a)



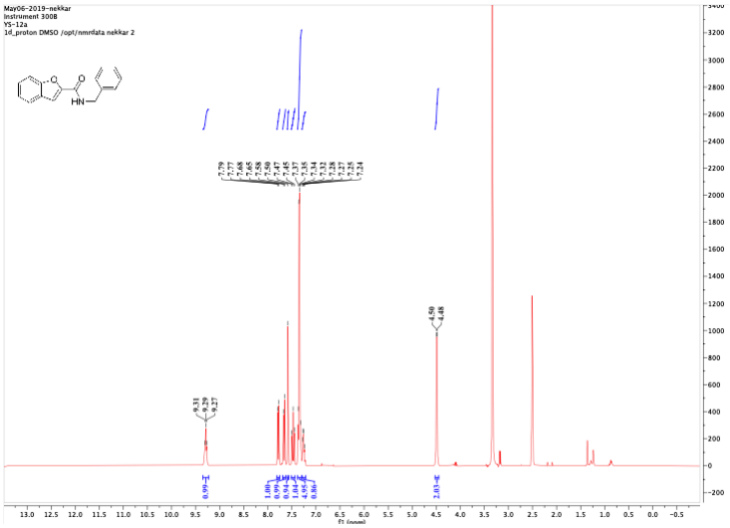




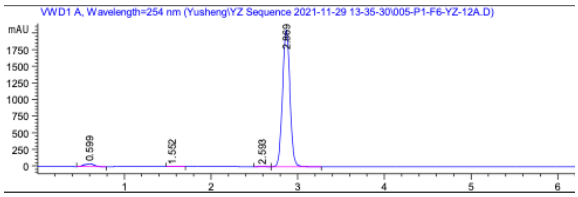
Signal 3: VWD1 A, Wavelength=254 nm

Peak #	RetTime [min]	Type	Width [min]	Area [mAU*s]	Height [mAU]	Area %
1	0.605	BB	0.1055	22.23650	3.03414	1.0145
2	1.560	BB	0.0638	12.78103	3.05618	0.5831
3	2.546	BB	0.0895	2047.27222	359.38120	93.4040
4	2.838	BB	0.0860	109.55555	19.96122	4.9983
Totals :				2191.84530	385.43273	

N-Benzylbenzofuran-2-carboxamide (5b)

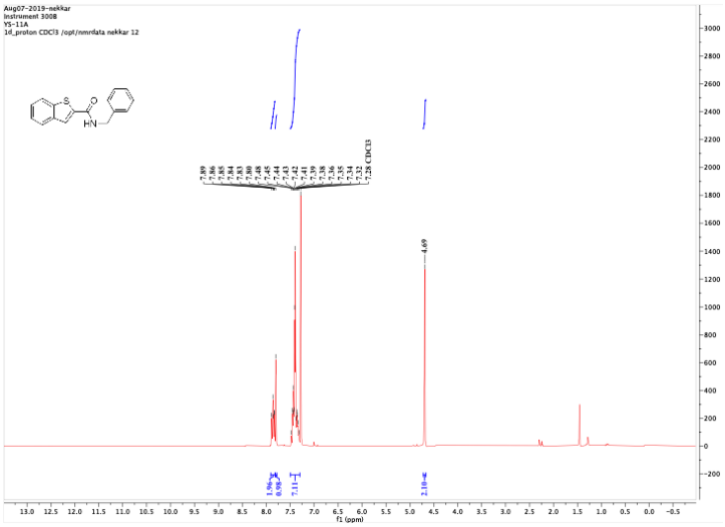


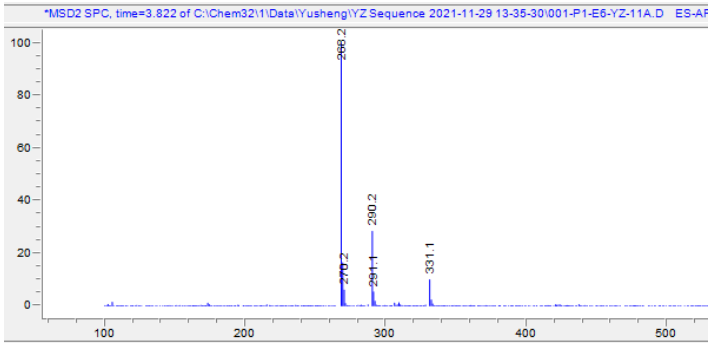


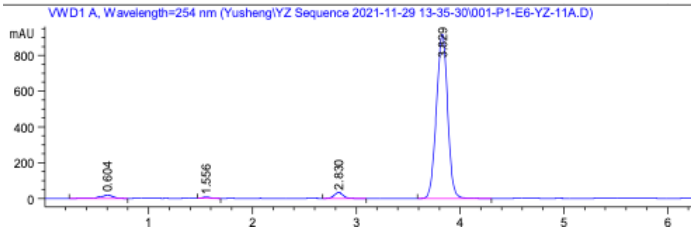


Peak #	RetTime [min]	Type	Width [min]	Area [mAU*s]	Height [mAU]	Area %
1	0.599	BB	0.1179	330.89352	40.66376	2.6396
2	1.552	BB	0.0670	11.08669	2.48534	0.0884
3	2.593	BB	0.0795	11.30231	2.25595	0.0902
4	2.869	BB	0.0931	1.21826e4	2056.80859	97.1818
Totals :				1.25359e4	2102.21364	

N-Benzylbenzo[*b*]thiophene-2-carboxamide (5c)



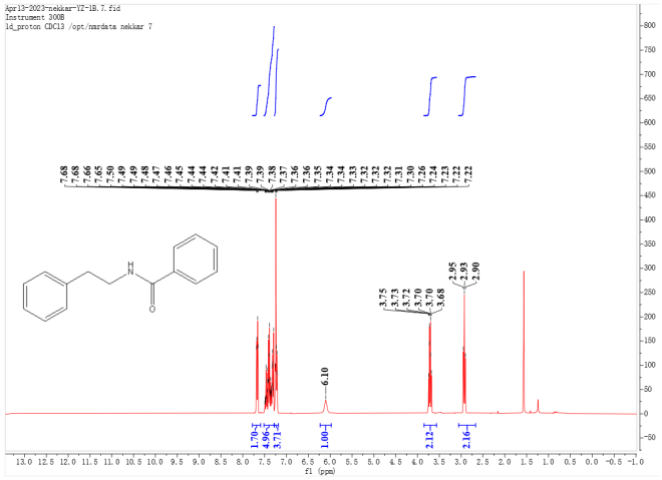


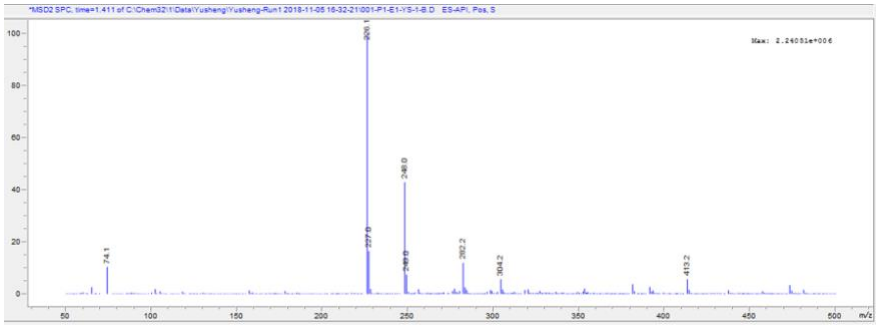


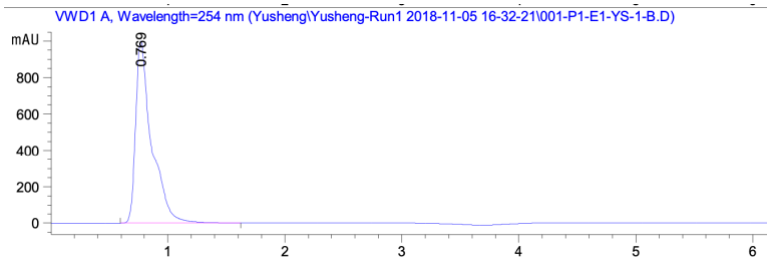
Peak #	RetTime [min]	Type	Width [min]	Area [mAU*s]	Height [mAU]	Area %
1	0.604	BB	0.1233	153.35013	18.77196	2.1099
2	1.556	BB	0.0689	33.08437	7.43977	0.4552
3	2.830	BB	0.0883	190.25639	33.49378	2.6177
4	3.829	BB	0.1167	6891.43311	917.23615	94.8172
Totals :				7268.12400	976.94165	

Appendix B – Spectra for Chapter 3

N-Phenethylbenzamide (7a)



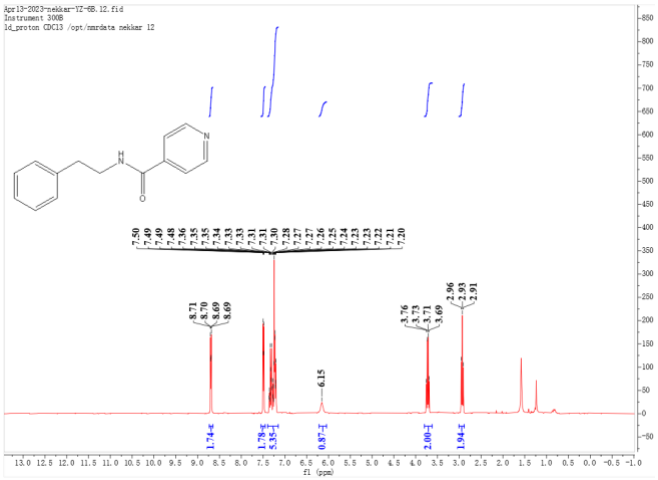


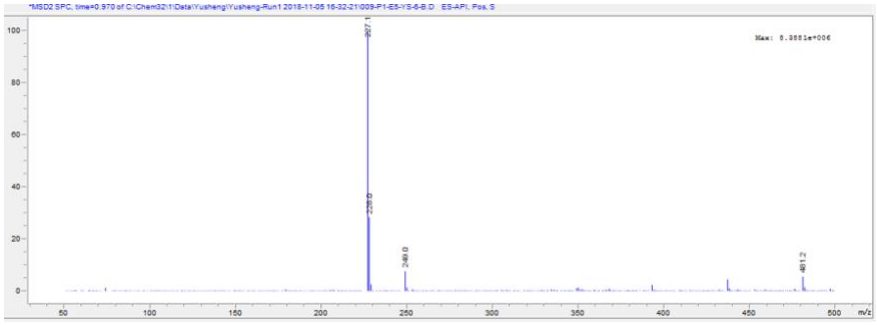


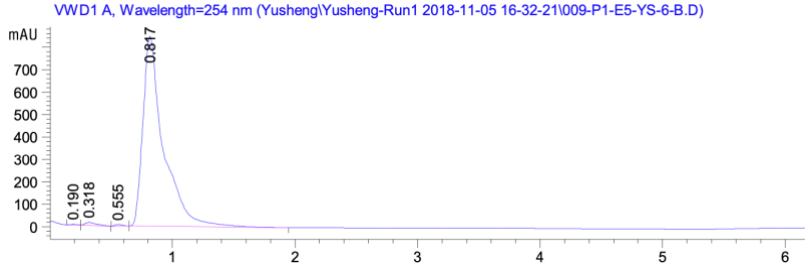
Signal 3: VWD1 A, Wavelength=254 nm

Peak #	RetTime [min]	Type	Width [min]	Area [mAU*s]	Height [mAU]	Area %
1	0.769	BB	0.1375	9555.92480	999.99927	100.0000
Totals :				9555.92480	999.99927	

N-Phenethylisonicotinamide (7b)



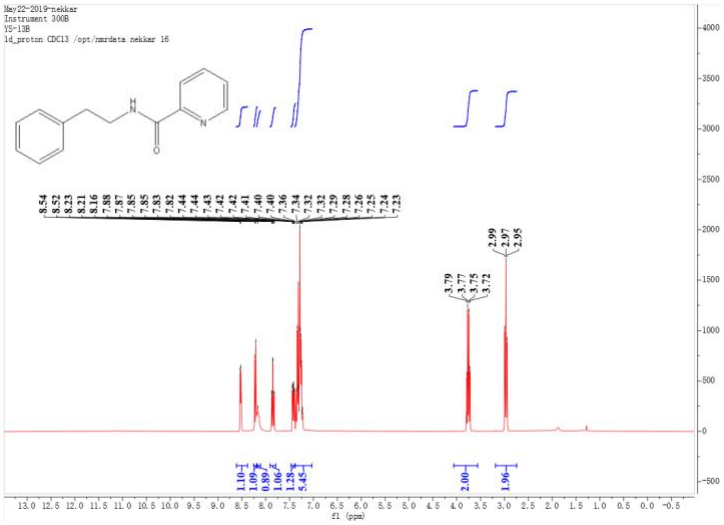


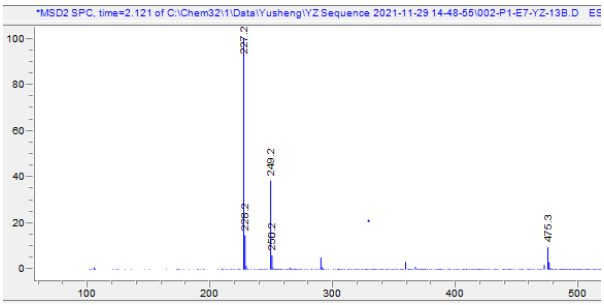


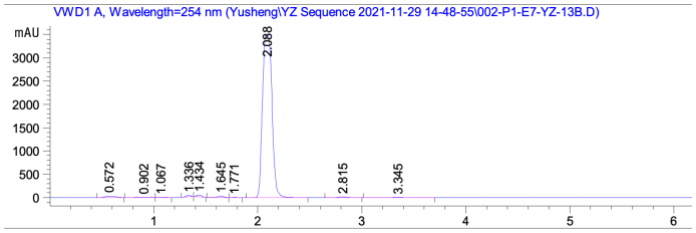
Signal 3: VWD1 A, Wavelength=254 nm

Peak #	RetTime [min]	Type	Width [min]	Area [mAU*s]	Height [mAU]	Area %
1	0.190	BB	0.0610	10.39162	2.88790	0.1042
2	0.318	BB	0.0949	84.33754	12.80234	0.8459
3	0.555	BB	0.0635	30.06406	7.38881	0.3016
4	0.817	BB	0.1628	9844.82324	845.69971	98.7483
Totals :				9969.61646	868.77875	

N-Phenethylpicolinamide (7c)



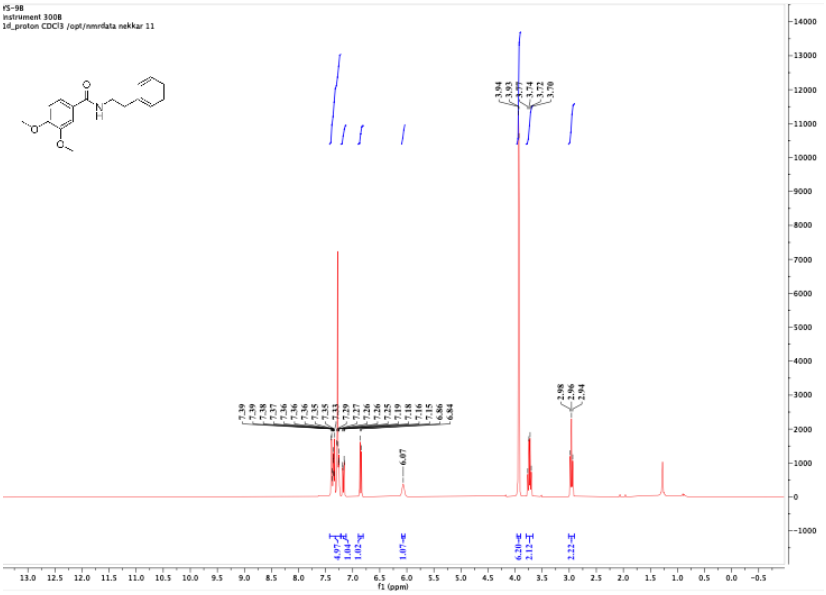


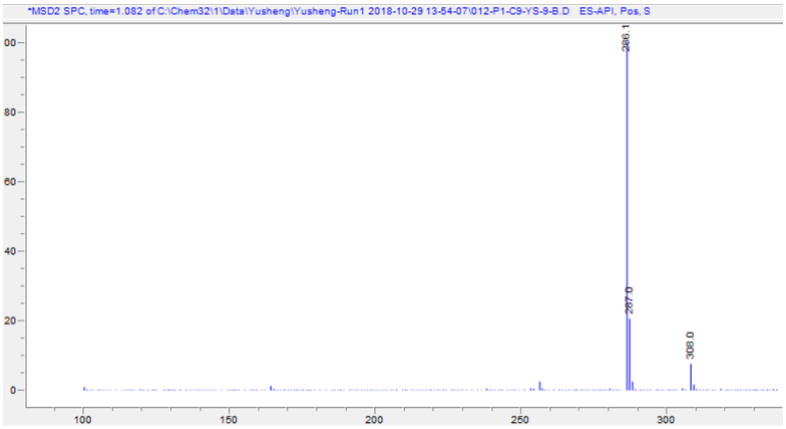


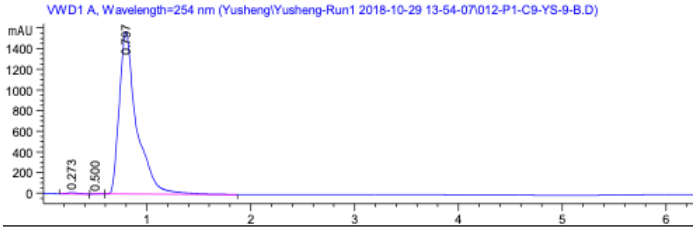
Signal 3: VWD1 A, Wavelength=254 nm

Peak #	RetTime [min]	Type	Width [min]	Area [mAU*s]	Height [mAU]	Area %
1	0.572	BB	0.1019	217.22046	30.56280	0.9448
2	0.902	BB	0.1078	52.00901	6.68062	0.2262
3	1.067	BB	0.0866	21.79871	4.19840	0.0948
4	1.336	BB	0.0518	118.03725	36.40870	0.5134
5	1.434	BB	0.0537	146.22427	44.09386	0.6360
6	1.645	BB	0.0709	129.48734	28.01407	0.5632
7	1.771	BB	0.0546	9.47280	2.78828	0.0412
8	2.088	BB	0.1026	2.21565e4	3513.99927	96.3698
9	2.815	BB	0.0899	89.04155	15.51994	0.3873
10	3.345	BB	0.1378	51.32631	5.50244	0.2232
Totals :				2.29912e4	3687.76839	

N-Phenethyl-3,4-dimethoxybenzamide (7d)

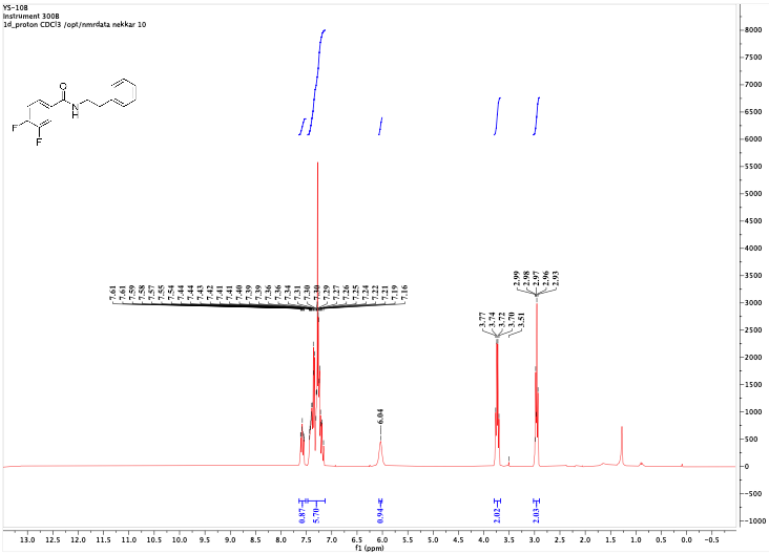




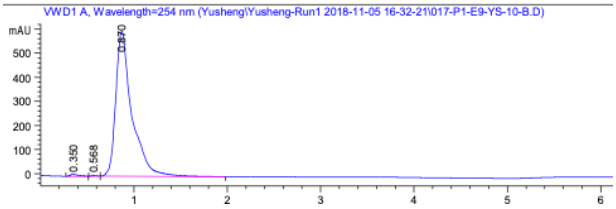


Peak #	RetTime [min]	Type	Width [min]	Area [mAU*s]	Height [mAU]	Area %
1	0.273	BB	0.0949	88.13316	13.20415	0.4778
2	0.500	BB	0.0654	15.19635	3.51829	0.0824
3	0.797	BB	0.1660	1.83416e4	1573.59119	99.4398
Totals :				1.84449e4	1590.31363	

N-Phenethyl-3,4-difluorobenzamide (7e)

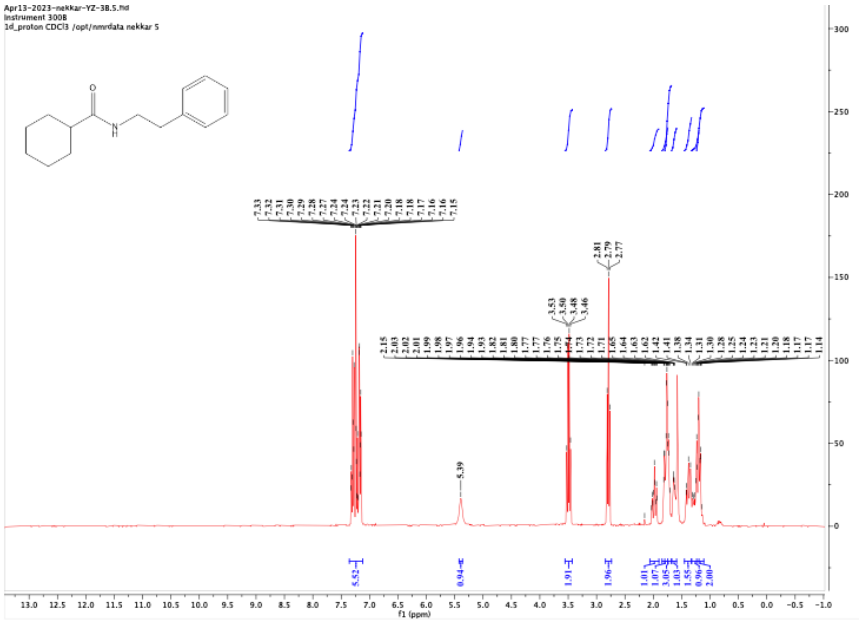




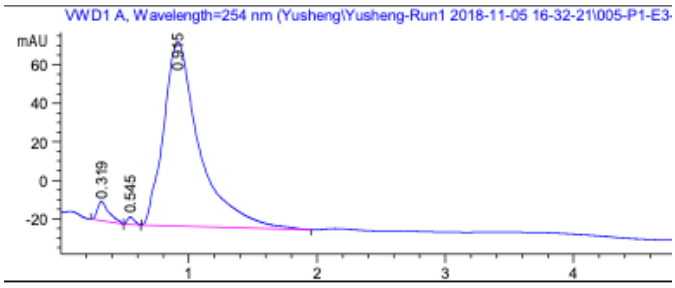


Peak #	RetTime [min]	Type	Width [min]	Area [mAU*s]	Height [mAU]	Area %
1	0.350	BB	0.0895	50.11028	8.05984	0.6855
2	0.568	BB	0.0585	10.28884	2.82637	0.1408
3	0.870	BB	0.1734	7249.35547	602.60059	99.1737
Totals :				7309.75459	613.48679	

N-Phenethylcyclohexanecarboxamide (7f)

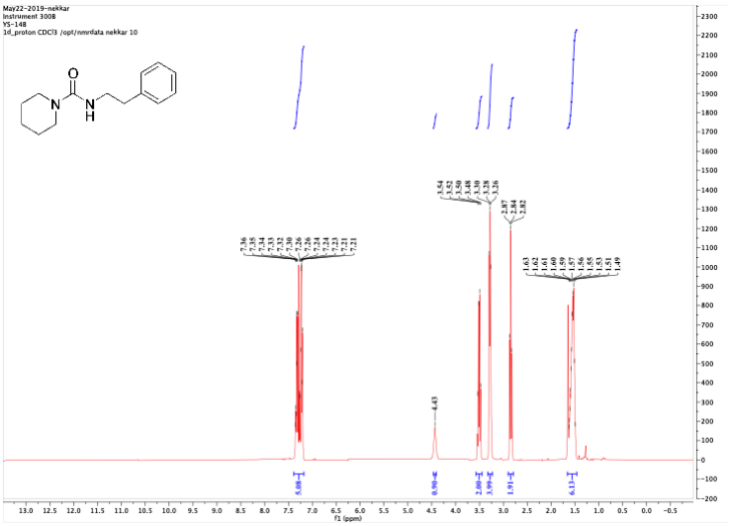


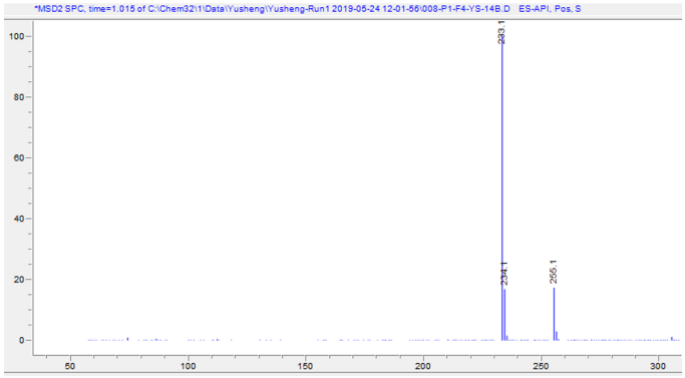


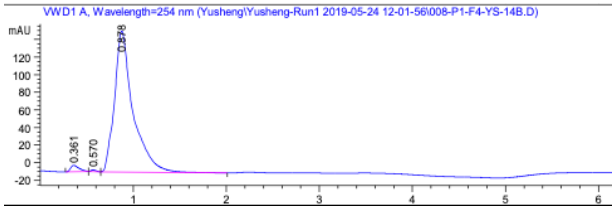


Peak #	RetTime [min]	Type	Width [min]	Area [mAU*s]	Height [mAU]	Area %
1	0.319	BB	0.0910	62.66331	10.01311	3.2289
2	0.545	BB	0.0587	13.86511	3.69770	0.7144
3	0.915	BB	0.2795	1864.17651	95.58437	96.0567
Totals :				1940.70493	109.29517	

N-Phenethylpiperidine-1-carboxamide (7g)

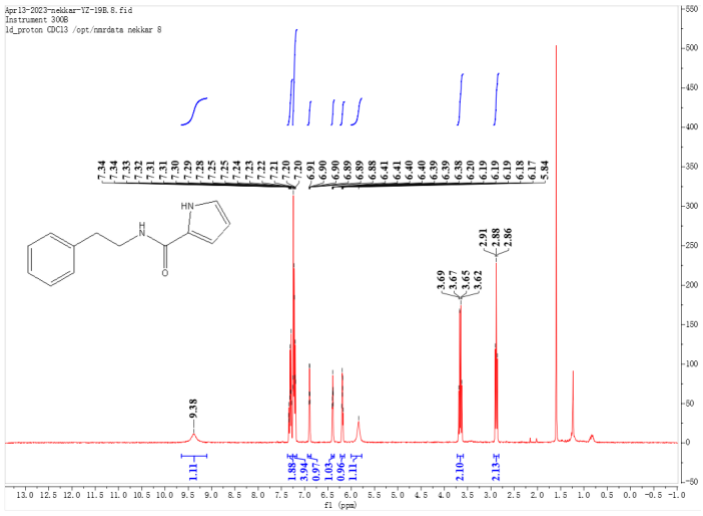


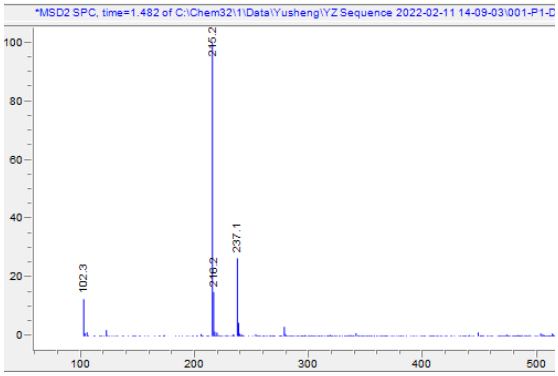


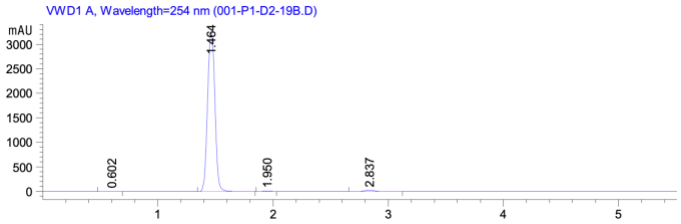


Peak #	RetTime [min]	Type	Width [min]	Area [mAU*s]	Height [mAU]	Area %
1	0.361	BB	0.0939	46.76297	7.38248	2.0562
2	0.570	BB	0.0574	6.80734	1.87450	0.2993
3	0.878	BB	0.1961	2220.63062	159.86613	97.6444
Totals :				2274.20092	169.12312	

N-Phenethyl-1*H*-pyrrole-2-carboxamide (7h)



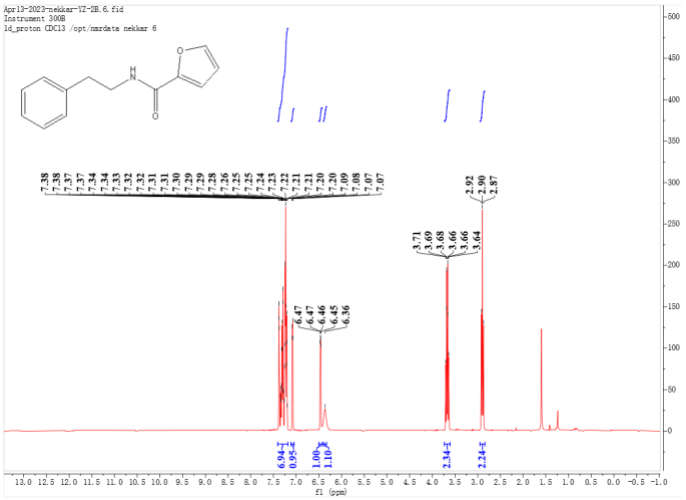


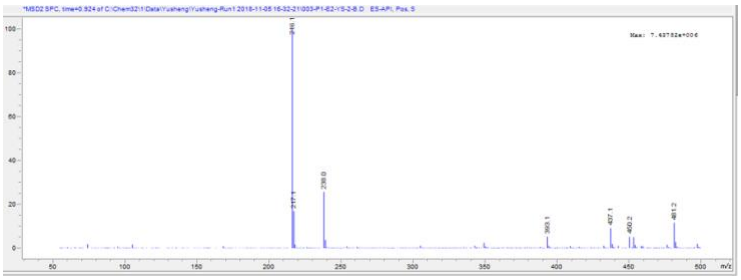


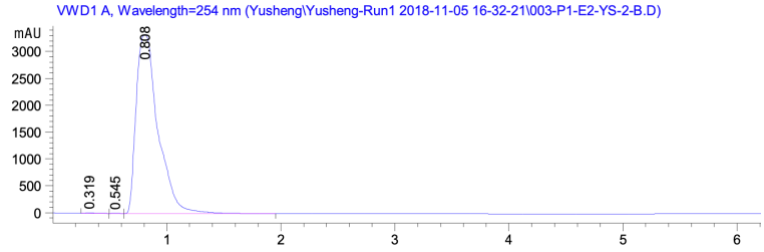
Signal 3: VWD1 A, Wavelength=254 nm

Peak #	RetTime [min]	Type	Width [min]	Area [mAU*s]	Height [mAU]	Area %
1	0.602	BB	0.0943	18.53612	2.65877	0.1278
2	1.464	BB	0.0714	1.43090e4	3245.00415	98.6779
3	1.950	BB	0.0688	35.83778	8.22454	0.2471
4	2.837	BB	0.0902	137.34126	23.84404	0.9471
Totals :				1.45007e4	3279.73150	

N-Phenethylfuran-2-carboxamide (7i)



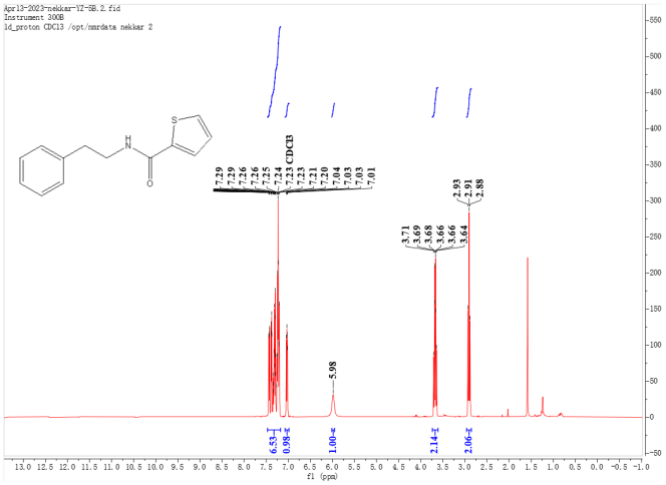




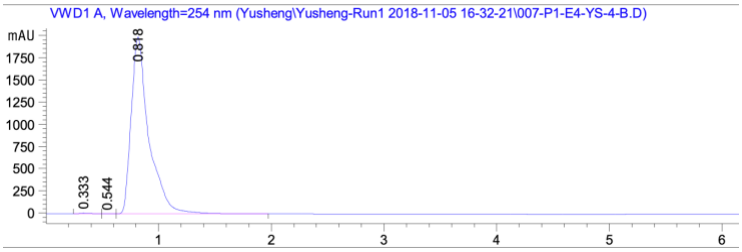
Signal 3: VWD1 A, Wavelength=254 nm

Peak #	RetTime [min]	Type	Width [min]	Area [mAU*s]	Height [mAU]	Area %
1	0.319	BB	0.0901	68.22042	10.88554	0.1534
2	0.545	BB	0.0591	15.08416	4.07991	0.0339
3	0.808	BB	0.2025	4.43926e4	3329.57666	99.8127
Totals :				4.44759e4	3344.54211	

N-Phenethylthiophene-2-carboxamide (7j)



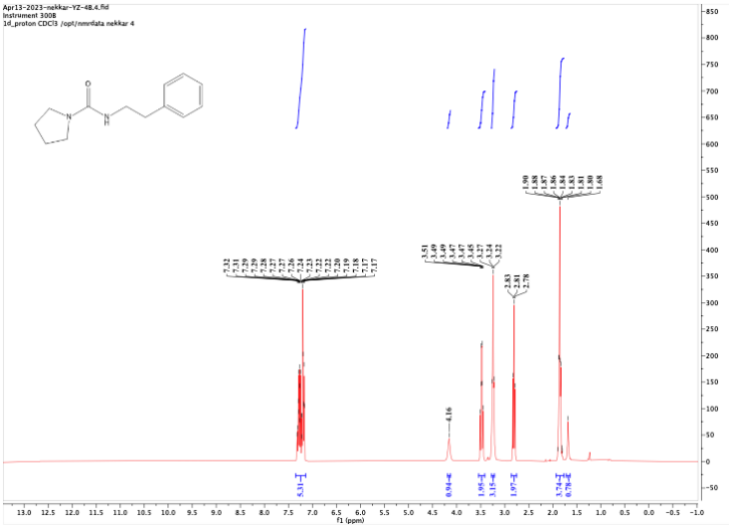


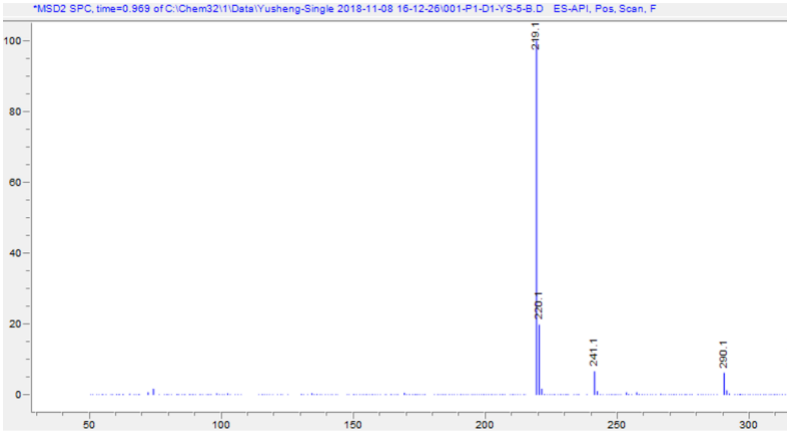


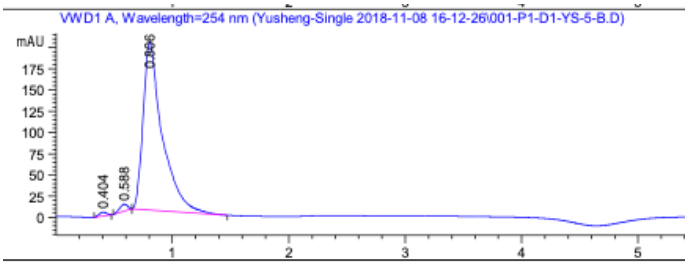
Signal 3: VWD1 A, Wavelength=254 nm

Peak #	RetTime [min]	Type	Width [min]	Area [mAU*s]	Height [mAU]	Area %
1	0.333	BB	0.0892	48.47415	7.83272	0.2224
2	0.544	BB	0.0558	7.82269	2.23492	0.0359
3	0.818	BB	0.1564	2.17374e4	1989.88611	99.7417
Totals :				2.17937e4	1999.95375	

N-Phenethylpyrrolidine-1-carboxamide (7k)

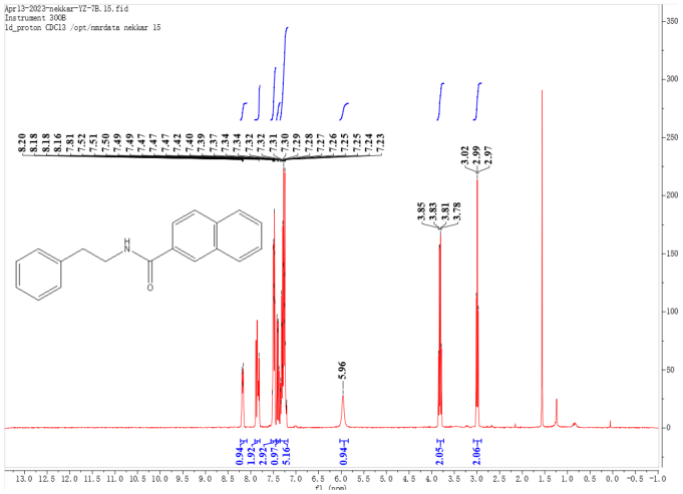


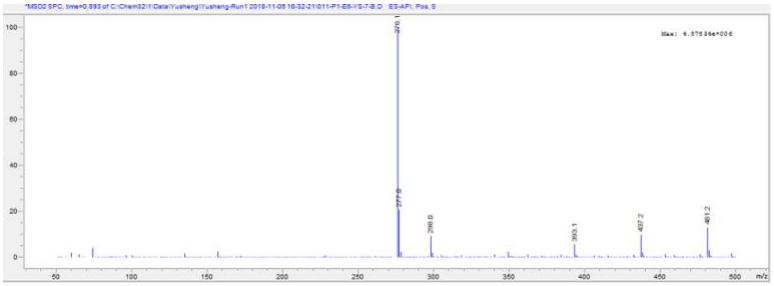


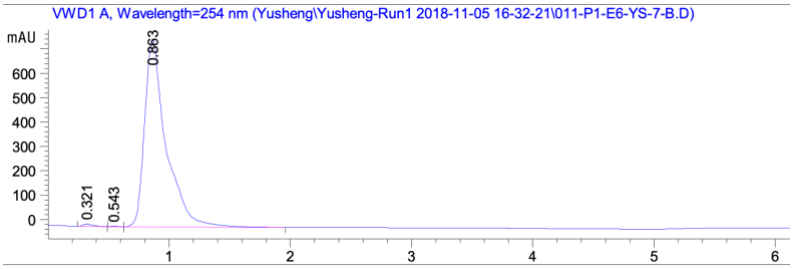


Peak #	RetTime [min]	Type	Width [min]	Area [mAU*s]	Height [mAU]	Area %
1	0.404	BB	0.0754	19.60376	4.28583	0.8461
2	0.588	BB	0.0804	40.14584	8.15518	1.7328
3	0.806	BB	0.1623	2257.13159	197.52422	97.4211
Totals :				2316.88119	209.96523	

N-Phenethyl-1-naphthamide (7l)



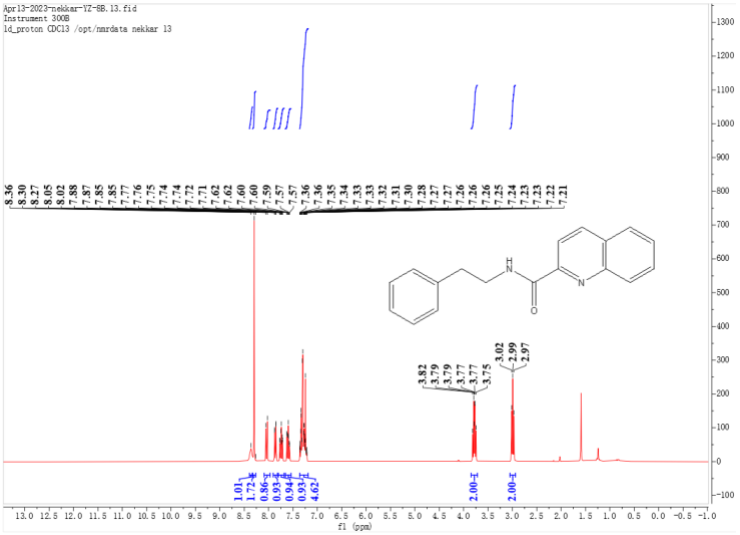


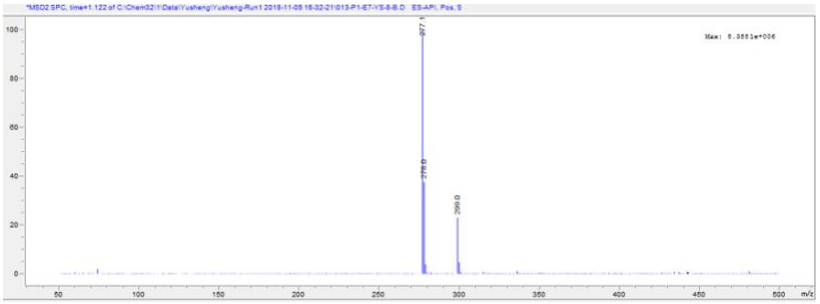


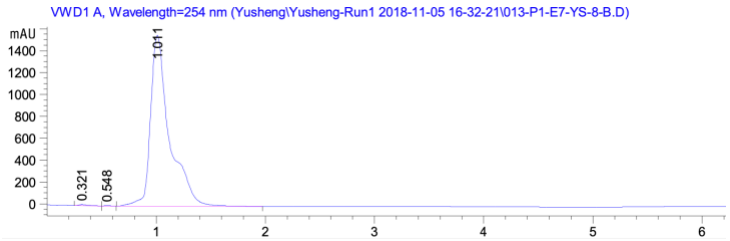
Signal 3: VWD1 A, Wavelength=254 nm

Peak #	RetTime [min]	Type	Width [min]	Area [mAU*s]	Height [mAU]	Area %
1	0.321	BB	0.0873	56.24035	9.33331	0.5863
2	0.543	BB	0.0577	12.75108	3.48541	0.1329
3	0.863	BB	0.1780	9523.69531	771.66309	99.2808
Totals :				9592.68674	784.48181	

N-Phenethylquinoline-2-carboxamide (7m)



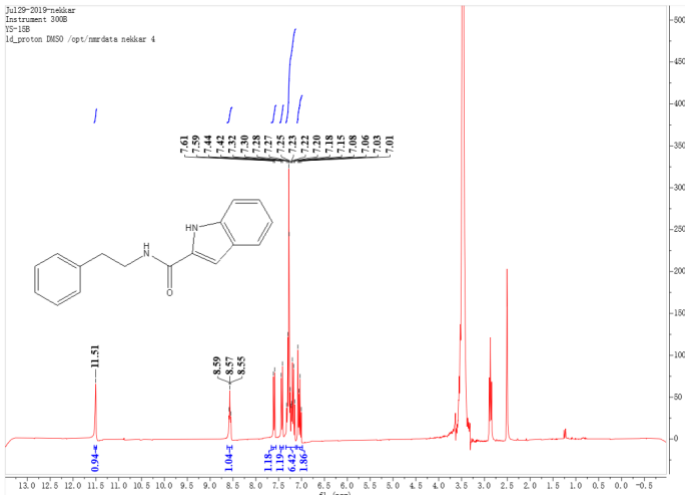


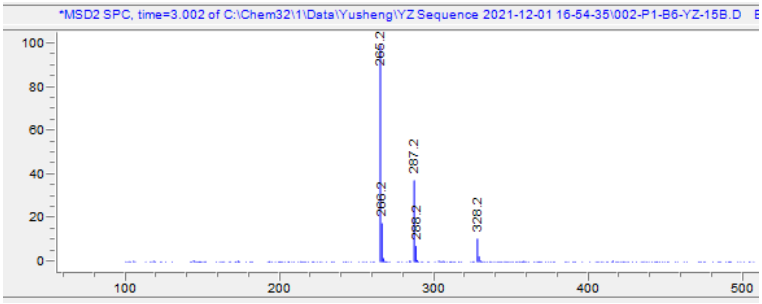


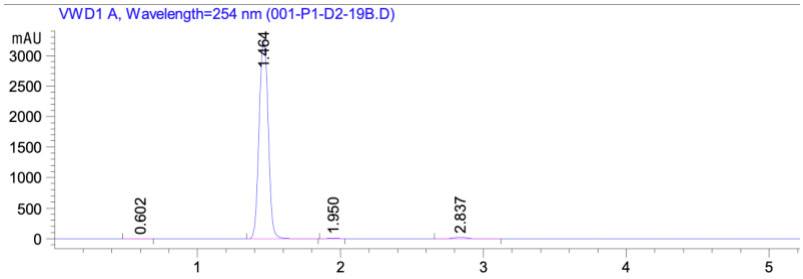
Signal 3: VWD1 A, Wavelength=254 nm

Peak #	RetTime [min]	Type	Width [min]	Area [mAU*s]	Height [mAU]	Area %
1	0.321	BB	0.0913	67.47826	10.74664	0.3558
2	0.548	BB	0.0602	15.61020	4.11750	0.0823
3	1.011	BB	0.1751	1.88836e4	1561.58350	99.5619
Totals :				1.89666e4	1576.44764	

N-Phenethyl-1*H*-indole-2-carboxamide (8a)



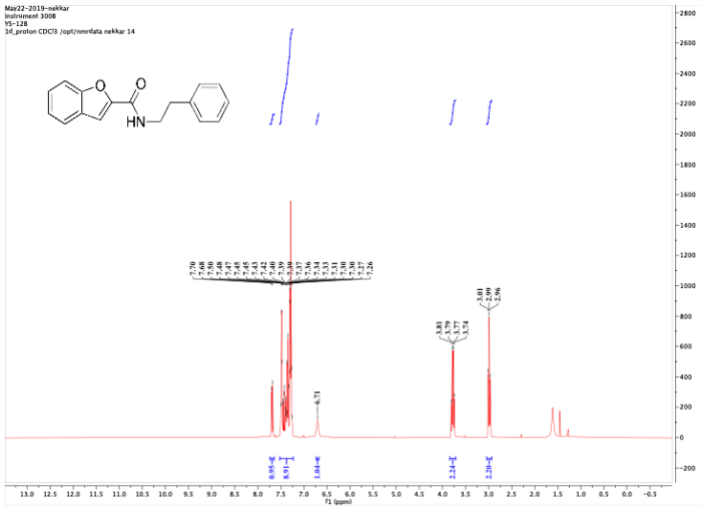




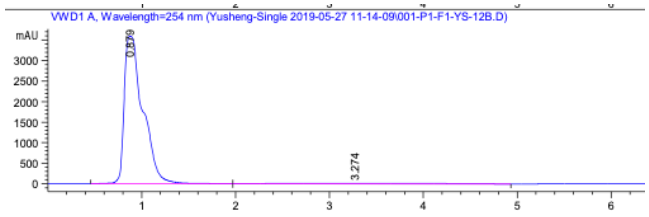
Signal 3: VWD1 A, Wavelength=254 nm

Peak #	RetTime [min]	Type	Width [min]	Area [mAU*s]	Height [mAU]	Area %
1	0.602	BB	0.0943	18.53612	2.65877	0.1278
2	1.464	BB	0.0714	1.43090e4	3245.00415	98.6779
3	1.950	BB	0.0688	35.83778	8.22454	0.2471
4	2.837	BB	0.0902	137.34126	23.84404	0.9471
Totals :				1.45007e4	3279.73150	

N-Phenethylbenzofuran-2-carboxamide (8b)

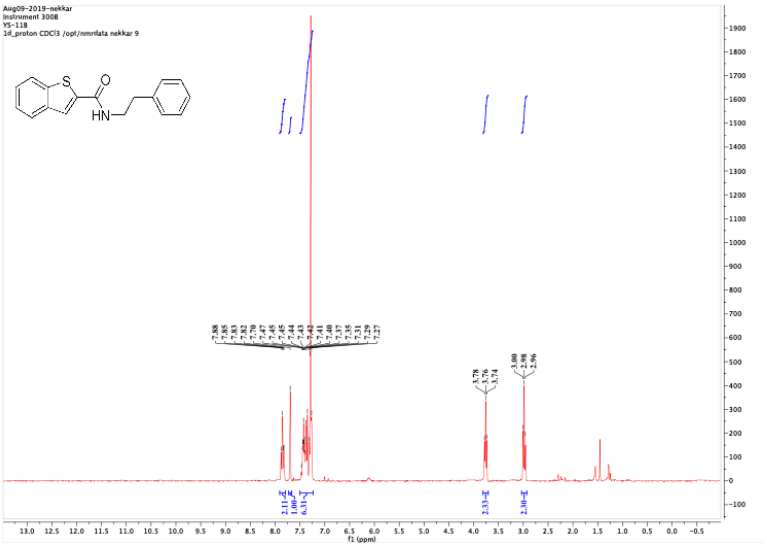


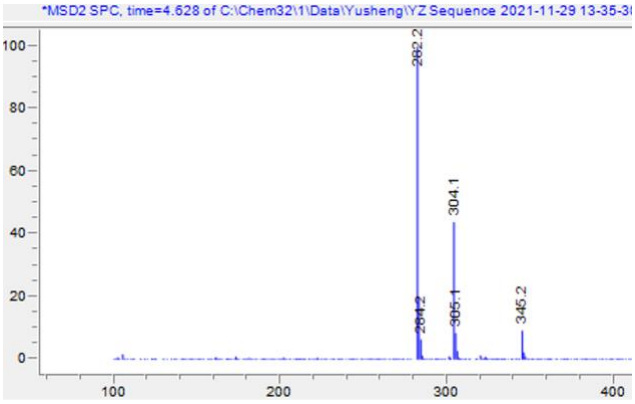


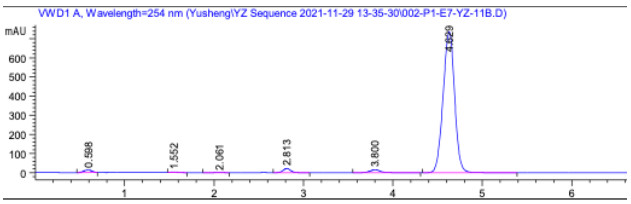


Peak #	RetTime [min]	Type	Width [min]	Area [mAU*s]	Height [mAU]	Area %
1	0.879	BB	0.2004	4.94069e4	3593.61670	97.9308
2	3.274	BB	1.7442	1043.95264	7.02702	2.0692
Totals :				5.04508e4	3600.64372	

N-Phenethylbenzo[*b*]thiophene-2-carboxamide (8c)



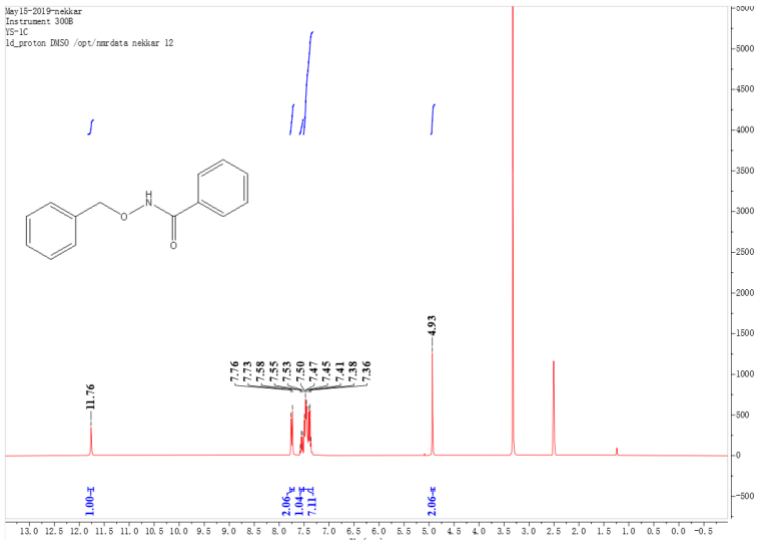


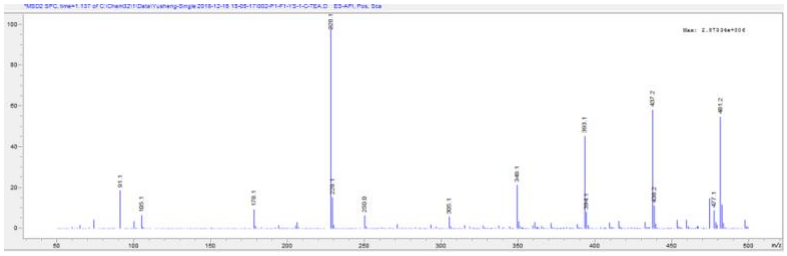


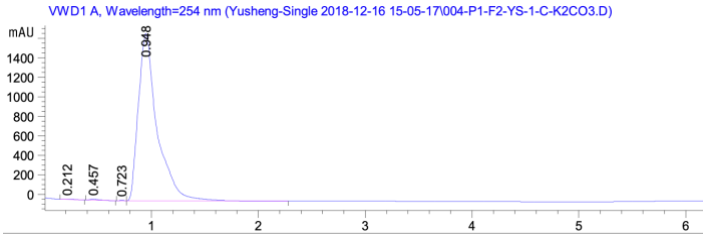
Peak #	RetTime [min]	Type	Width [min]	Area [mAU*s]	Height [mAU]	Area %
1	0.598	BB	0.1019	84.59447	13.00277	1.2240
2	1.552	BB	0.0726	15.68651	3.29214	0.2270
3	2.061	BB	0.0741	9.53135	1.98392	0.1379
4	2.813	BB	0.0890	122.93577	21.39625	1.7788
5	3.800	BB	0.1206	115.53159	14.88500	1.6716
6	4.629	BB	0.1390	6562.97949	735.98138	94.9607
Totals :				6911.25917	790.54147	

Appendix C – Spectra for Chapter 4

N-(Benzyloxy)benzamide (10a)



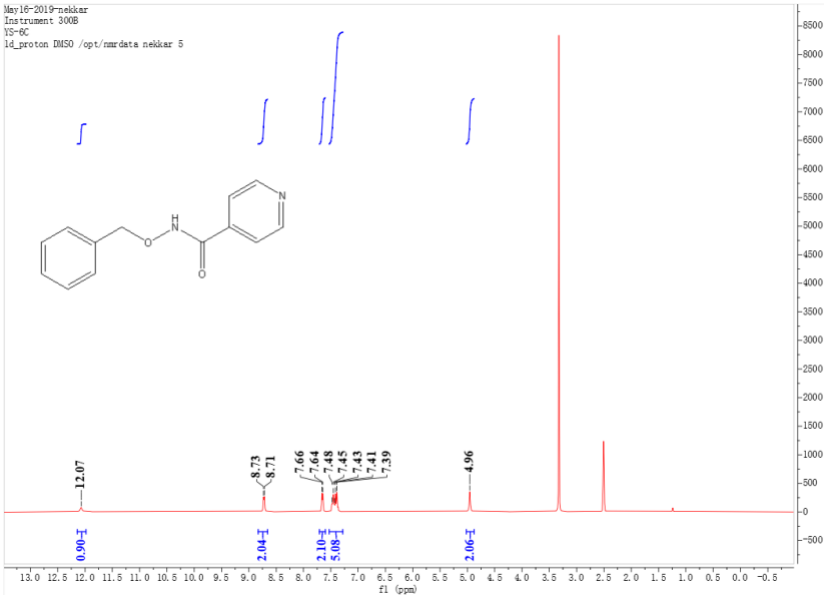


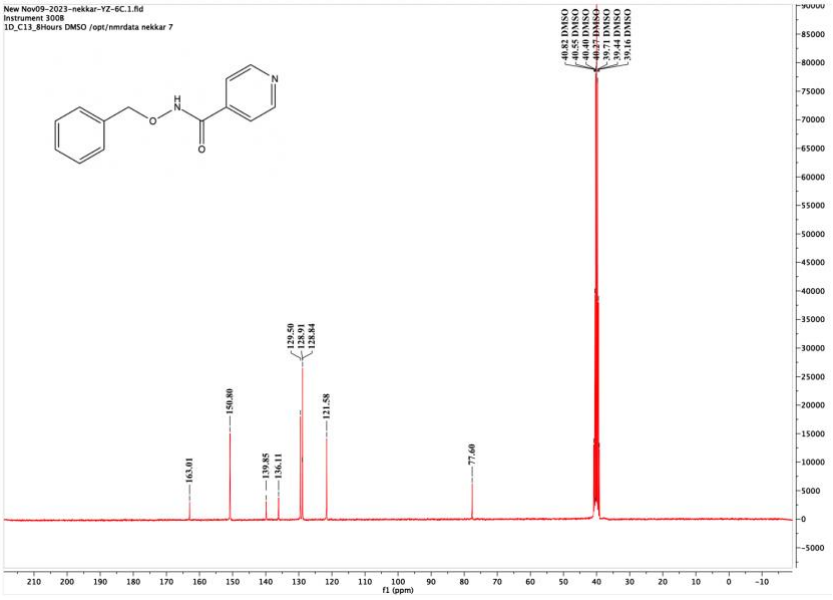


Signal 3: VWD1 A, Wavelength=254 nm

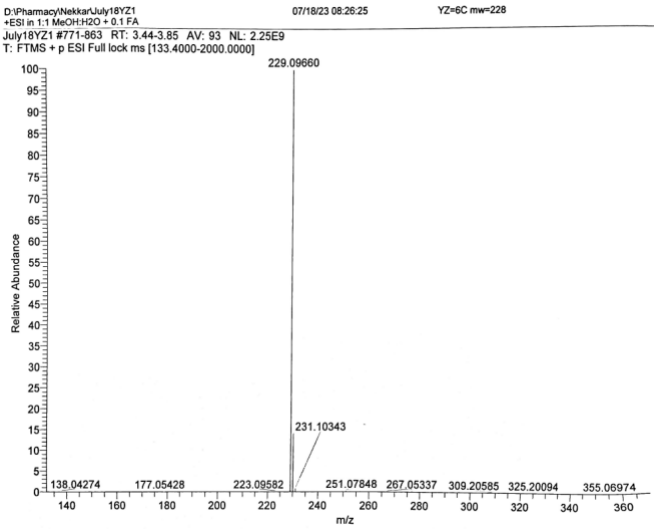
Peak #	RetTime [min]	Type	Width [min]	Area [mAU*s]	Height [mAU]	Area %
1	0.212	BB	0.1086	37.04523	5.49770	0.1754
2	0.457	BB	0.0905	71.47015	11.65478	0.3385
3	0.723	BB	0.0487	11.32616	3.91882	0.0536
4	0.948	BB	0.1869	2.09968e4	1714.01270	99.4325
Totals :				2.11167e4	1735.08400	

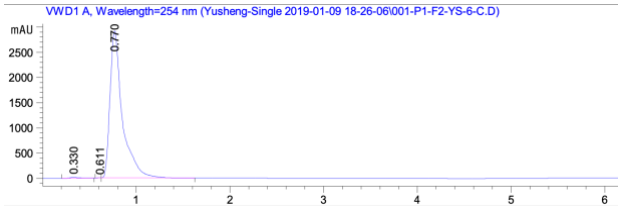
N-(Benzyloxy)isonicotinamide (10b)





N-(Benzyloxy)isonicotinamide (10b) - Continued

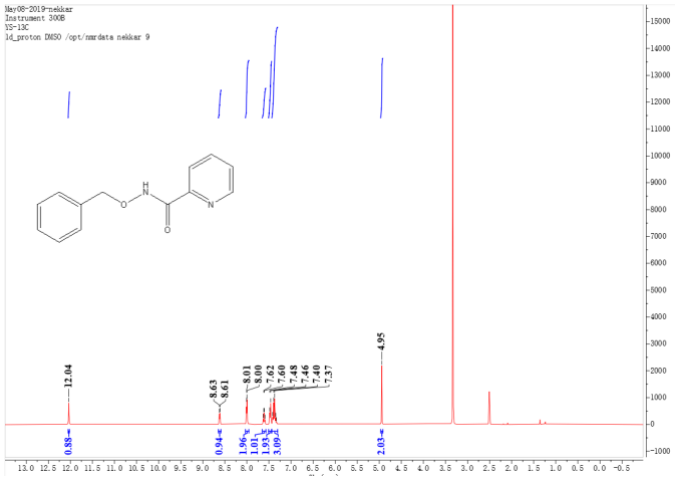


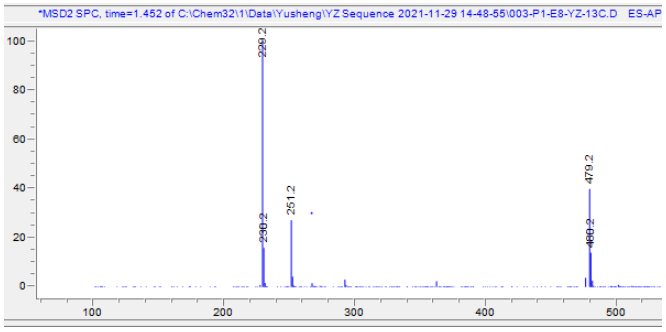


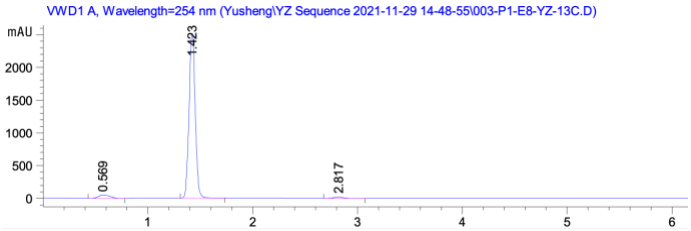
Signal 3: VWD1 A, Wavelength=254 nm

Peak #	RetTime [min]	Type	Width [min]	Area [mAU*s]	Height [mAU]	Area %
1	0.330	BB	0.1004	148.93549	21.09735	0.5556
2	0.611	BB	0.0429	8.00722	3.02226	0.0299
3	0.770	BB	0.1338	2.66498e4	2910.06787	99.4145
Totals :				2.68067e4	2934.18749	

N-(Benzyloxy)picolinamide (10c)



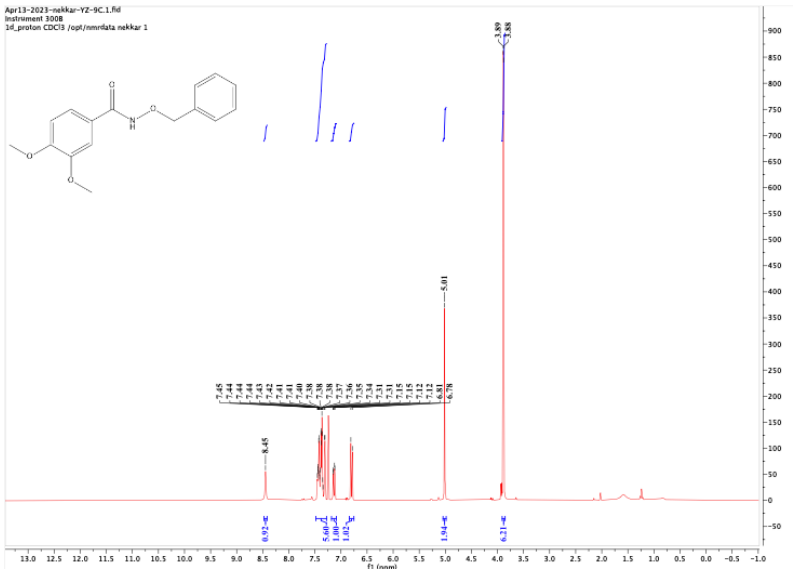


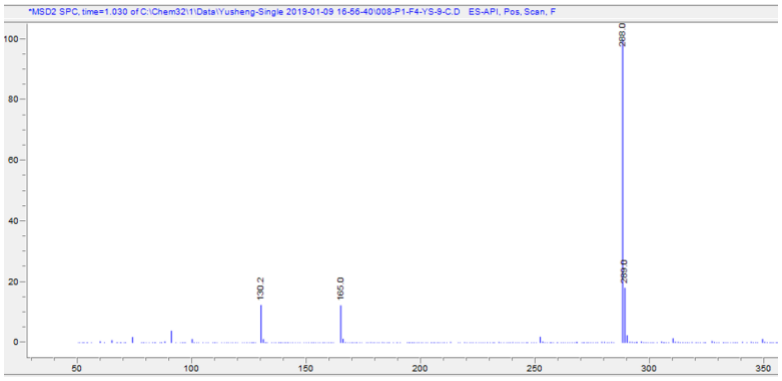


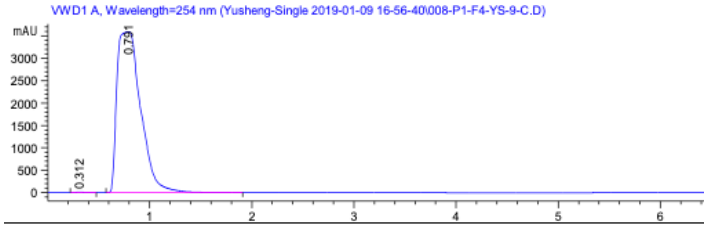
Signal 3: VWD1 A, Wavelength=254 nm

Peak #	RetTime [min]	Type	Width [min]	Area [mAU*s]	Height [mAU]	Area %
1	0.569	BB	0.1267	389.15341	49.50260	3.6008
2	1.423	BB	0.0636	1.02964e4	2523.08838	95.2728
3	2.817	BB	0.0873	121.73360	21.75009	1.1264
Totals :				1.08073e4	2594.34107	

N-Benzyloxy-3,4-dimethoxybenzamide (10d)

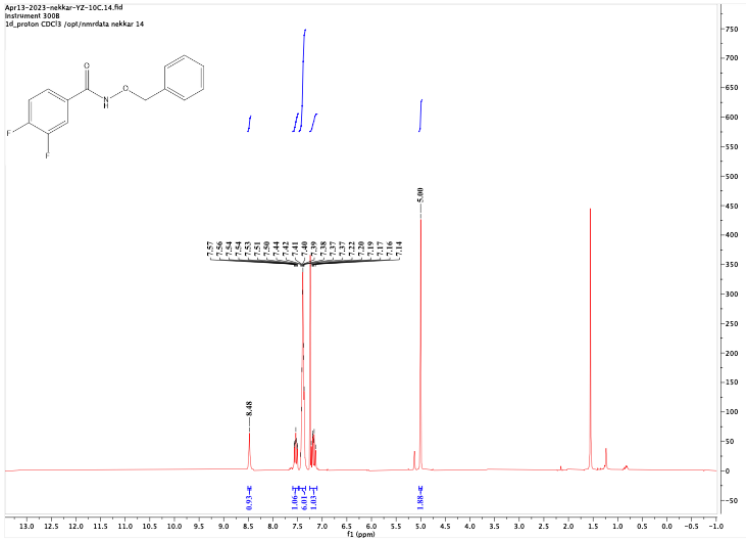


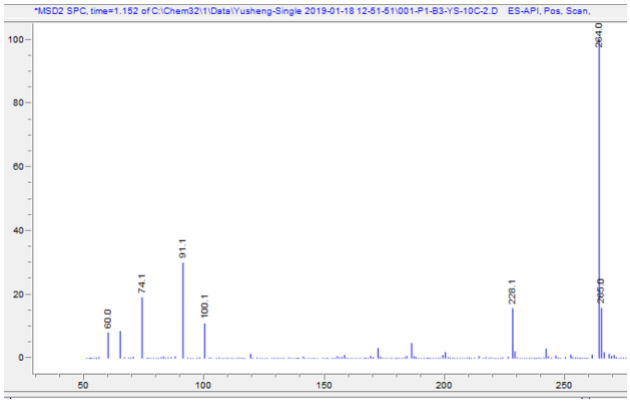


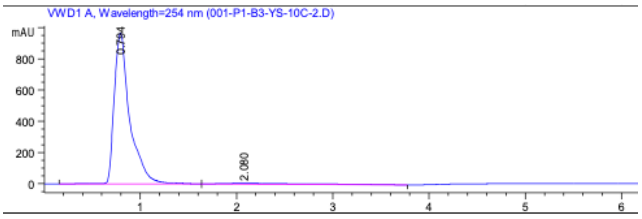


Peak #	RetTime [min]	Type	Width [min]	Area [mAU*s]	Height [mAU]	Area %
1	0.312	BB	0.0916	52.16743	8.37982	0.0900
2	0.791	BB	0.2460	5.78890e4	3592.93750	99.9100
Totals :				5.79411e4	3601.31732	

N-Benzyloxy-3,4-difluorobenzamide (10e)

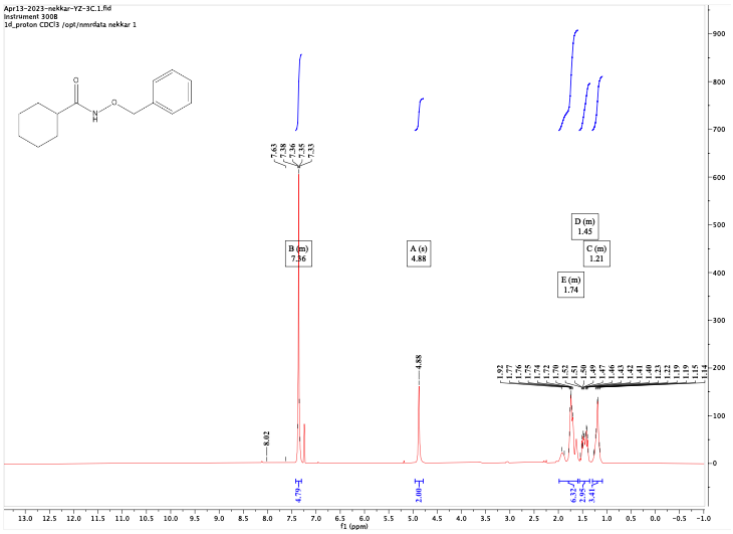


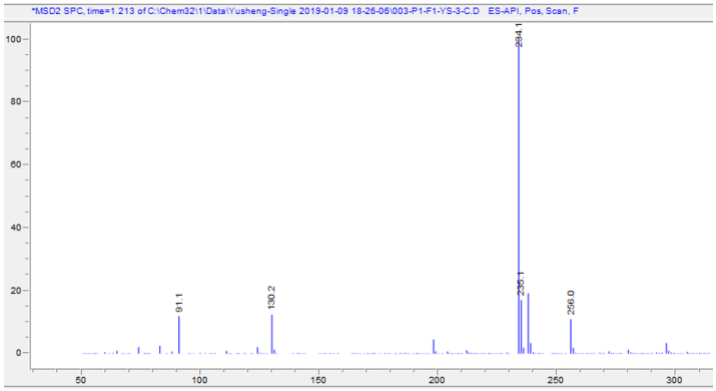


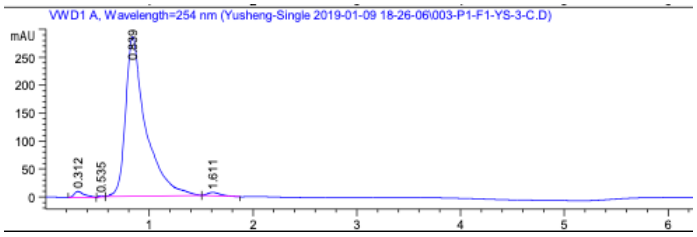


Peak #	RetTime [min]	Type	Width [min]	Area [mAU*s]	Height [mAU]	Area %
1	0.794	BB	0.1689	1.08224e4	964.57153	96.4476
2	2.080	BB	0.8055	398.61465	6.19620	3.5524
Totals :				1.12210e4	970.76774	

N-(Benzyloxy)cyclohexanecarboxamide (10f)

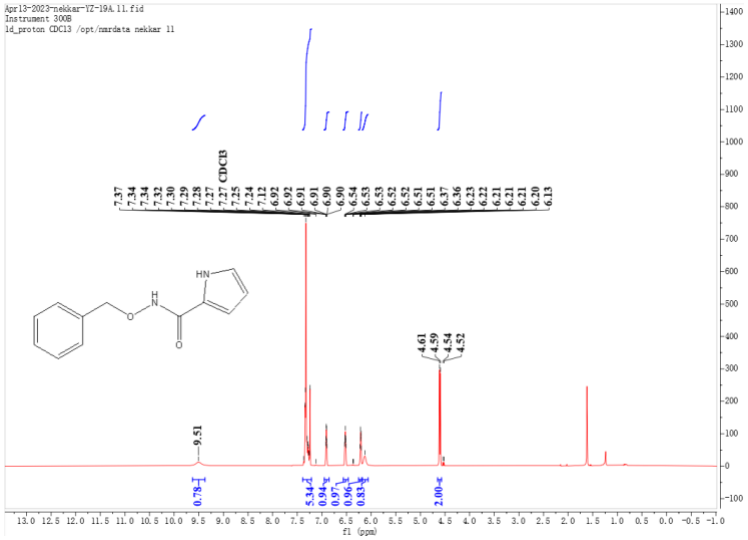


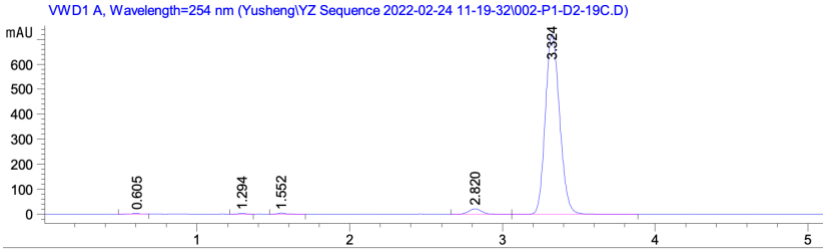




Peak #	RetTime [min]	Type	Width [min]	Area [mAU*s]	Height [mAU]	Area %
1	0.312	BB	0.0937	66.92039	10.45254	1.6813
2	0.535	BB	0.0443	5.09549	1.89863	0.1280
3	0.839	BB	0.1918	3857.92505	285.24017	96.9272
4	1.611	BB	0.1330	50.28979	5.86854	1.2635
Totals :				3980.23071	303.45988	

N-Benzyloxy-1*H*-pyrrole-2-carboxamide (10h)

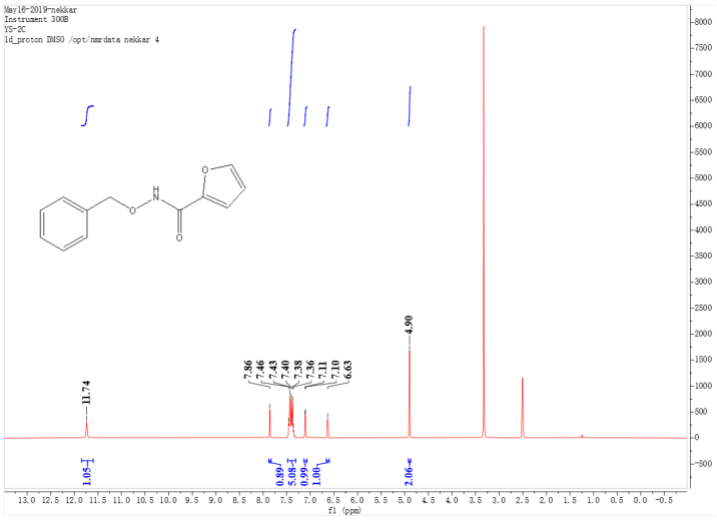


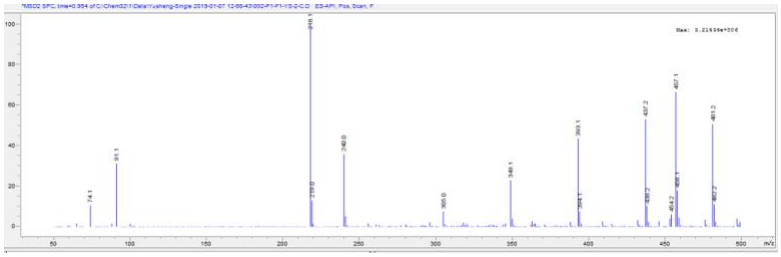


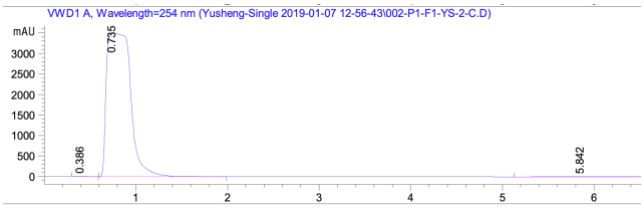
Signal 3: VWD1 A, Wavelength=254 nm

Peak #	RetTime [min]	Type	Width [min]	Area [mAU*s]	Height [mAU]	Area %
1	0.605	BB	0.1094	14.49872	2.21357	0.2997
2	1.294	BB	0.0567	10.54117	2.87800	0.2179
3	1.552	BB	0.0651	16.10789	3.74940	0.3330
4	2.820	BB	0.0882	124.56176	21.95784	2.5748
5	3.324	BB	0.1007	4672.03857	719.99878	96.5747
Totals :				4837.74811	750.79759	

N-(Benzyloxy)furan-2-carboxamide (10i)



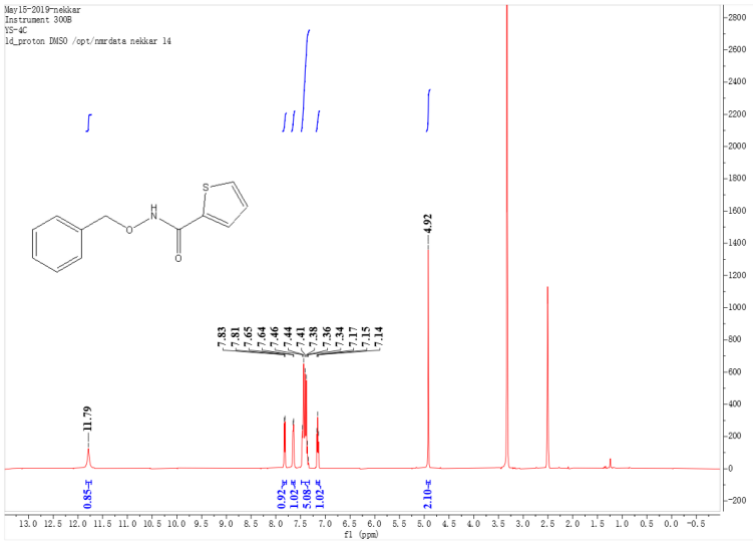


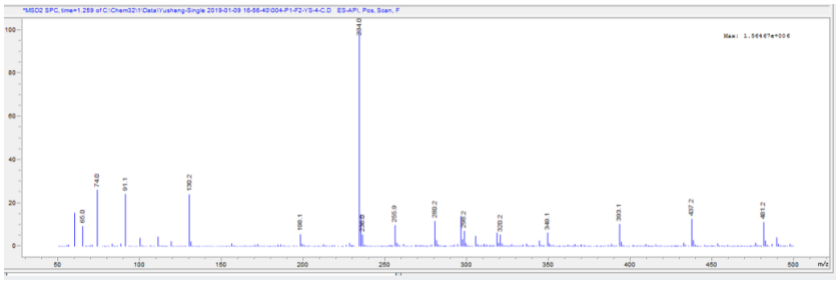


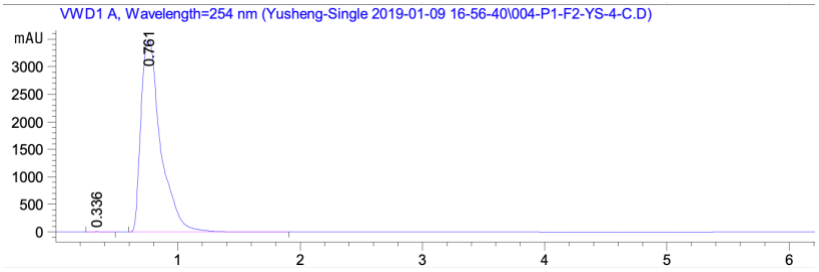
Signal 3: VWD1 A, Wavelength=254 nm

Peak #	RetTime [min]	Type	Width [min]	Area [mAU*s]	Height [mAU]	Area %
1	0.386	BB	0.0942	17.40071	2.77368	0.0270
2	0.735	BB	0.2497	6.37063e4	3510.62646	98.7889
3	5.842	BB	1.1752	763.63055	8.82755	1.1842
Totals :				6.44874e4	3522.22770	

N-(Benzyloxy)thiophene-2-carboxamide (10j)



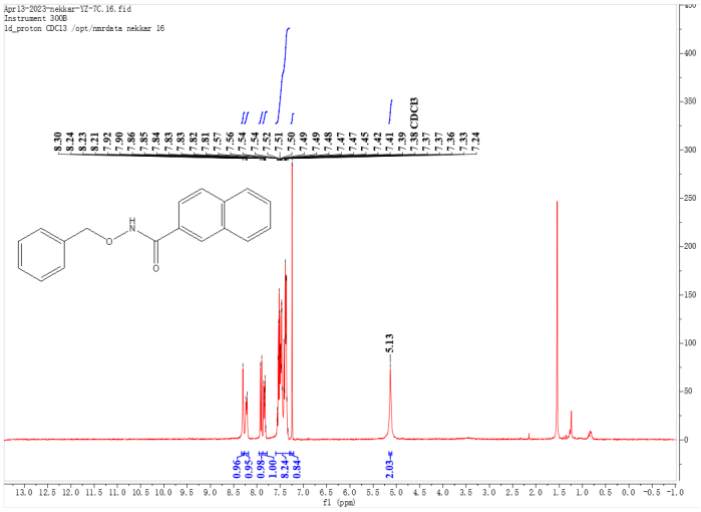


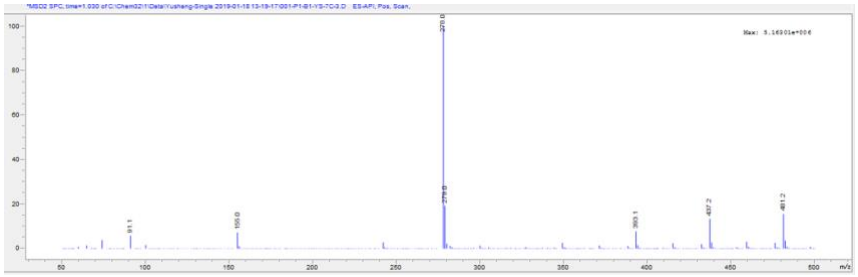


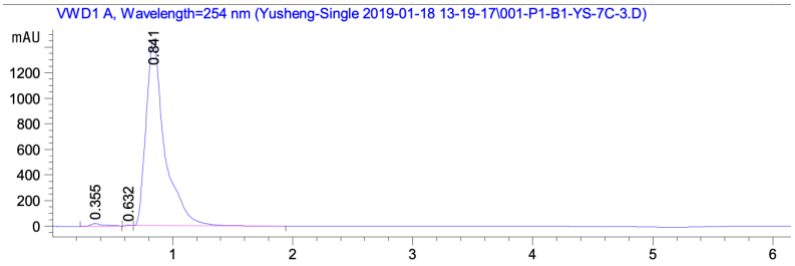
Signal 3: VWD1 A, Wavelength=254 nm

Peak #	RetTime [min]	Type	Width [min]	Area [mAU*s]	Height [mAU]	Area %
1	0.336	BB	0.0900	36.68628	6.11134	0.0937
2	0.761	BB	0.1697	3.91043e4	3490.12622	99.9063
Totals :				3.91410e4	3496.23757	

N-Benzyloxy-1-naphthamide (10l)



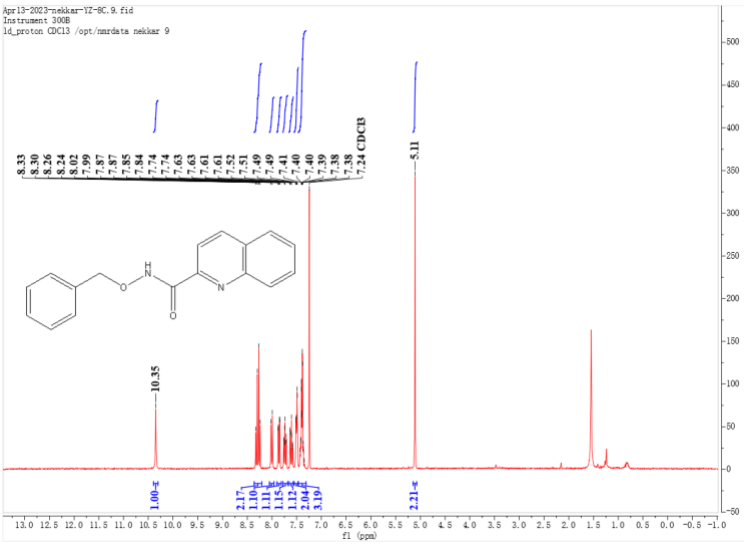


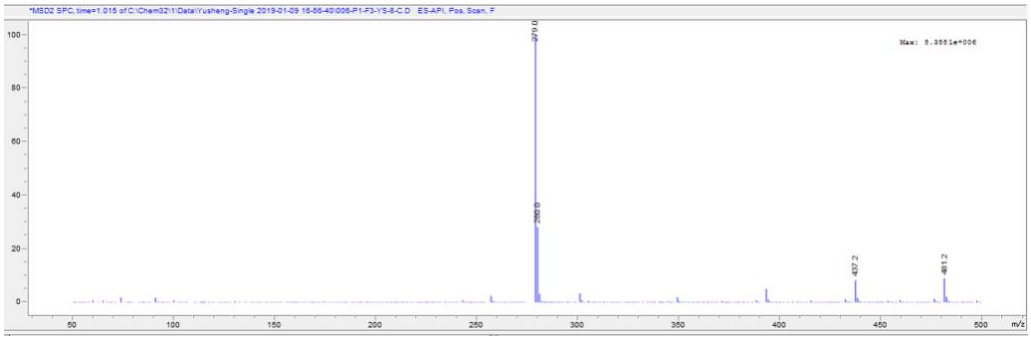


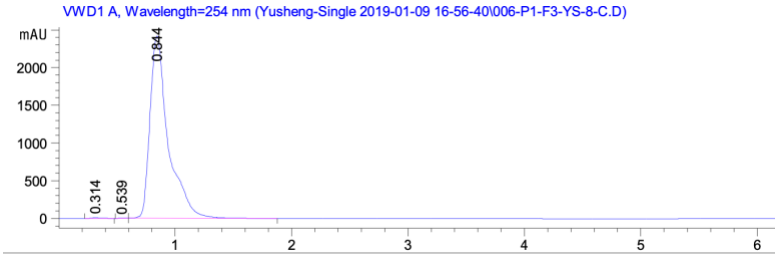
Signal 3: VWD1 A, Wavelength=254 nm

Peak #	RetTime [min]	Type	Width [min]	Area [mAU*s]	Height [mAU]	Area %
1	0.355	BB	0.1022	147.00700	20.37167	0.9256
2	0.632	BB	0.0471	17.99472	6.35175	0.1133
3	0.841	BB	0.1545	1.57171e4	1461.24426	98.9611
Totals :				1.58821e4	1487.96767	

N-(Benzyloxy)quinoline-2-carboxamide (10m)



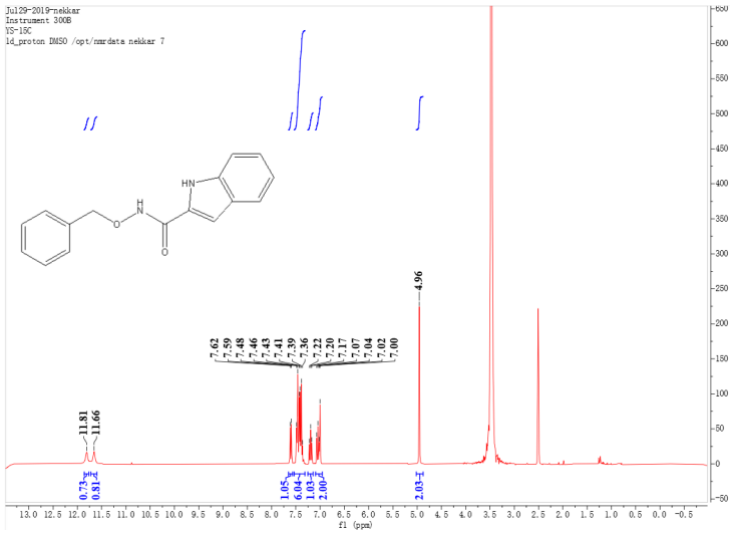


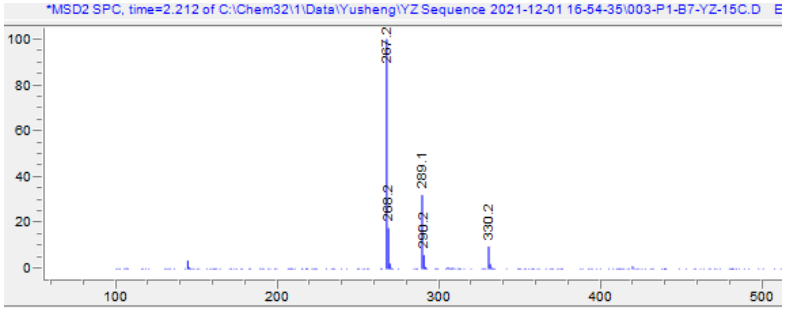


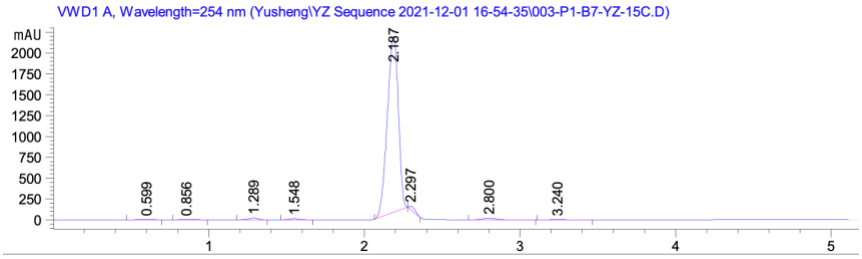
Signal 3: VWD1 A, Wavelength=254 nm

Peak #	RetTime [min]	Type	Width [min]	Area [mAU*s]	Height [mAU]	Area %
1	0.314	BB	0.0910	55.62336	9.01060	0.2099
2	0.539	BB	0.0588	8.25692	2.30271	0.0312
3	0.844	BB	0.1606	2.64339e4	2417.45996	99.7589
Totals :				2.64978e4	2428.77327	

N-Benzyloxy-1*H*-indole-2-carboxamide (11a)



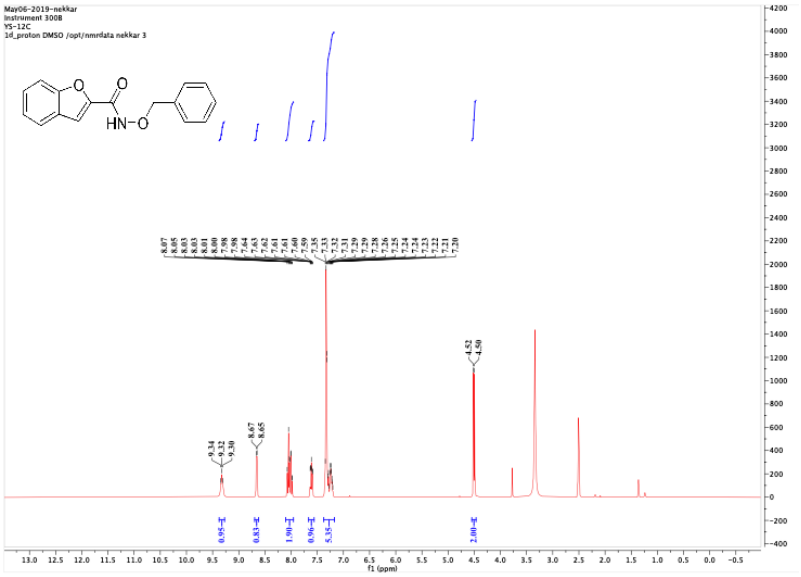


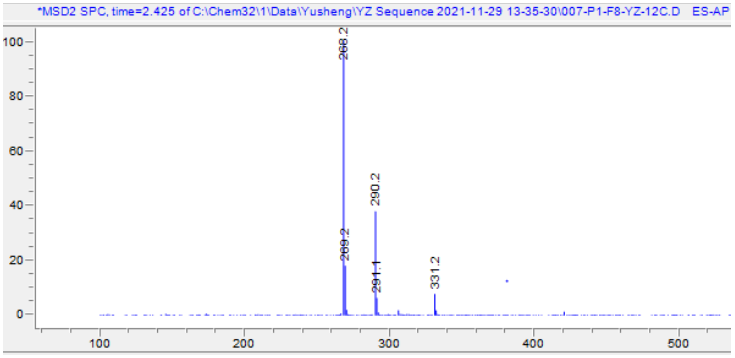


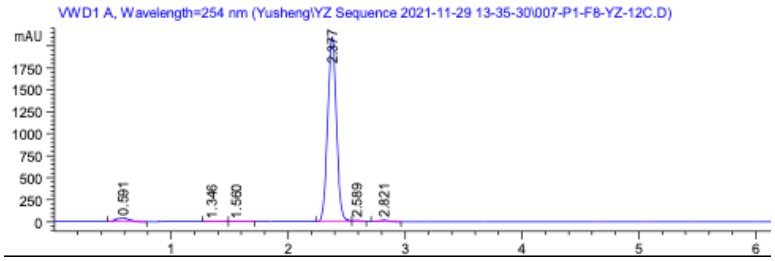
Signal 3: VWD1 A, Wavelength=254 nm

Peak #	RetTime [min]	Type	Width [min]	Area [mAU*s]	Height [mAU]	Area %
1	0.599	BB	0.1078	44.84306	6.31980	0.4144
2	0.856	BB	0.0969	26.90494	4.62288	0.2486
3	1.289	BB	0.0604	89.73374	22.57887	0.8292
4	1.548	BB	0.0662	52.77443	12.50796	0.4877
5	2.187	BB	0.0783	1.03461e4	2105.16382	95.6037
6	2.297	BB	0.0498	124.98322	39.62838	1.1549
7	2.800	BB	0.0886	120.21738	21.06138	1.1109
8	3.240	BB	0.0969	16.30640	2.61071	0.1507
Totals :				1.08219e4	2214.49379	

N-(Benzyloxy)benzofuran-2-carboxamide (11b)

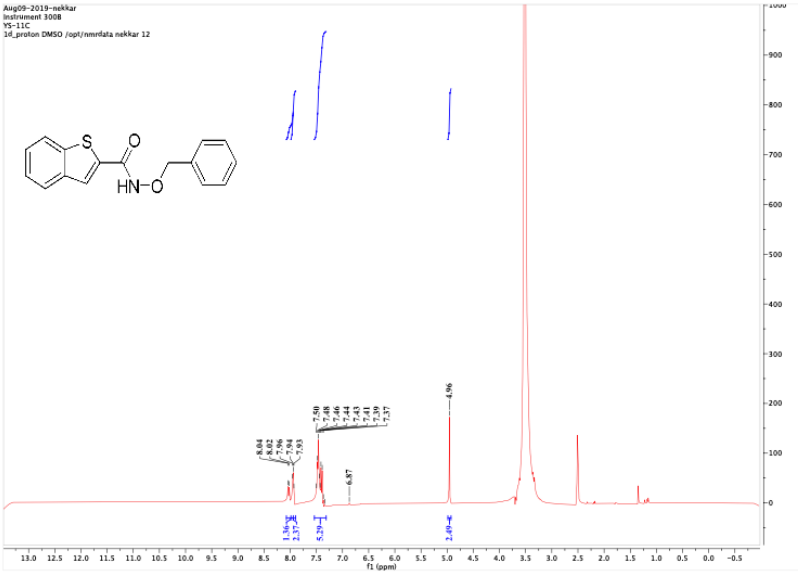


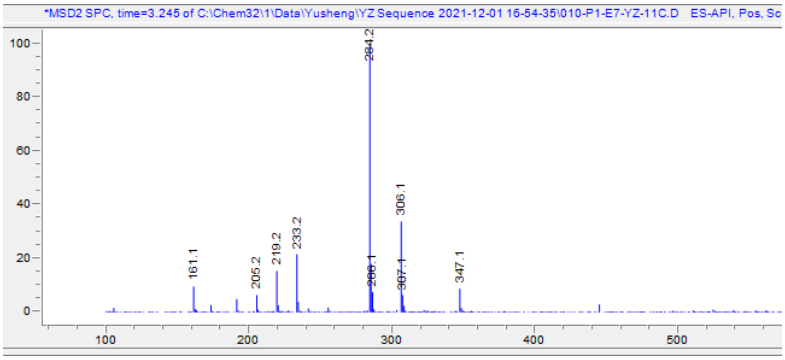


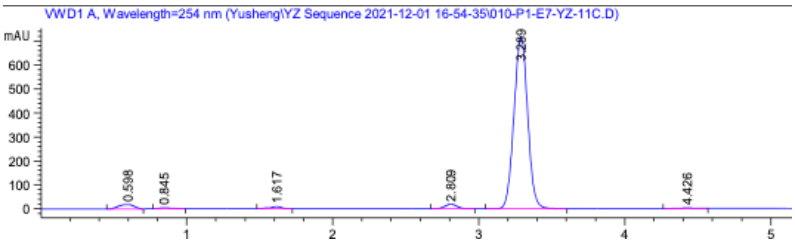


Peak #	RetTime [min]	Type	Width [min]	Area [mAU*s]	Height [mAU]	Area %
1	0.591	BB	0.1184	309.54269	35.95613	2.7287
2	1.346	BB	0.0581	12.15666	3.21799	0.1072
3	1.560	BB	0.0679	9.49812	2.13379	0.0837
4	2.377	BB	0.0818	1.09079e4	2093.78247	96.1549
5	2.589	BB	0.0637	21.50268	5.49487	0.1895
6	2.821	BB	0.0877	83.49500	15.05152	0.7360
Totals :				1.13441e4	2155.63677	

N-(Benzyloxy)benzo[*b*]thiophene-2-carboxamide (11c)



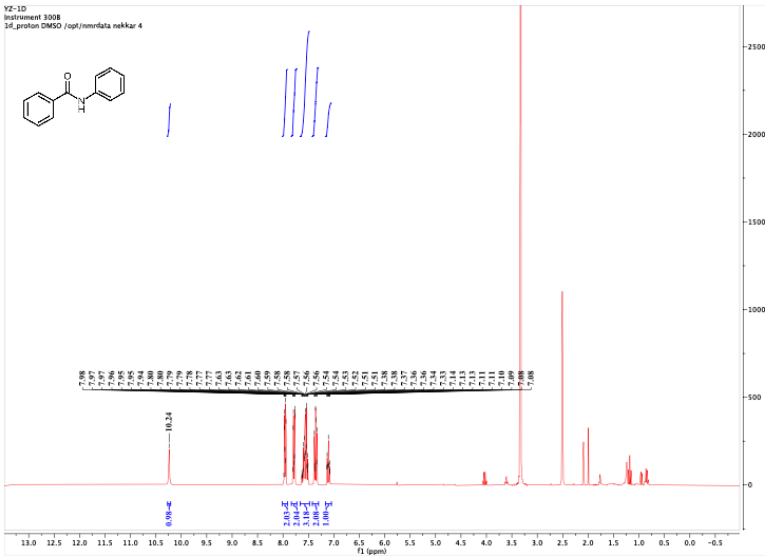


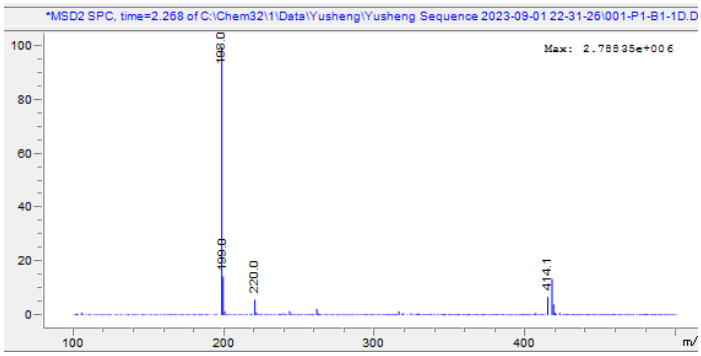


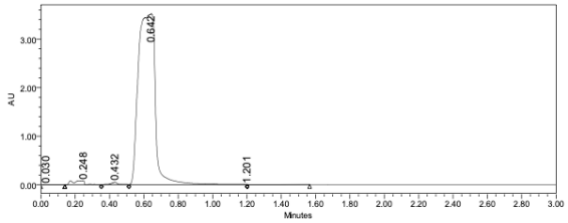
Peak #	RetTime [min]	Type	Width [min]	Area [mAU*s]	Height [mAU]	Area %
1	0.598	BB	0.1271	140.26582	18.56676	2.8015
2	0.845	BB	0.0878	25.29255	4.16819	0.5052
3	1.617	BB	0.0747	47.04551	9.20057	0.9396
4	2.809	BB	0.0892	108.03835	19.05080	2.1578
5	3.289	BB	0.1019	4670.54443	717.67700	93.2843
6	4.426	BB	0.1182	15.59673	2.08708	0.3115
Totals :				5006.78340	770.75040	

Appendix D – Spectra for Chapter 5

N-Benzylbenzamide (13a)

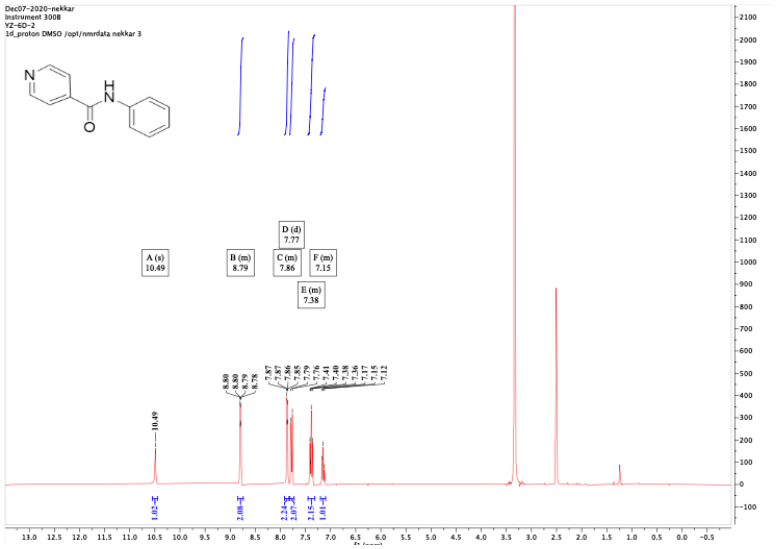


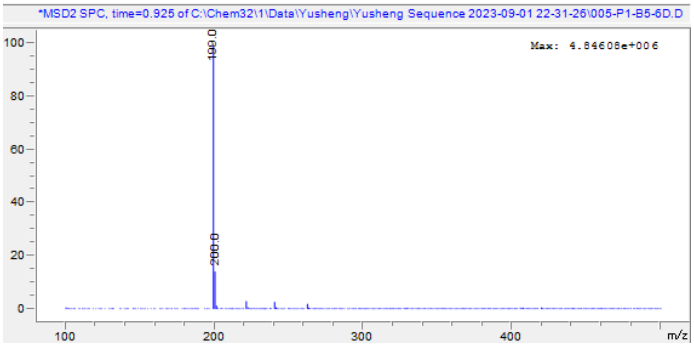


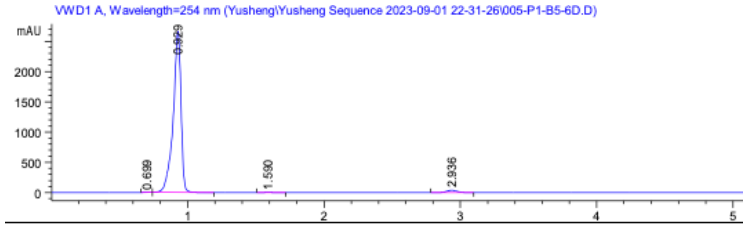


	RT	Area	% Area	Height
1	0.030	1549	0.01	571
2	0.248	395932	1.60	84003
3	0.432	152167	0.61	50330
4	0.642	24183587	97.70	3527383
5	1.201	20585	0.08	5353

N-Benzylisonicotinamide (13b)

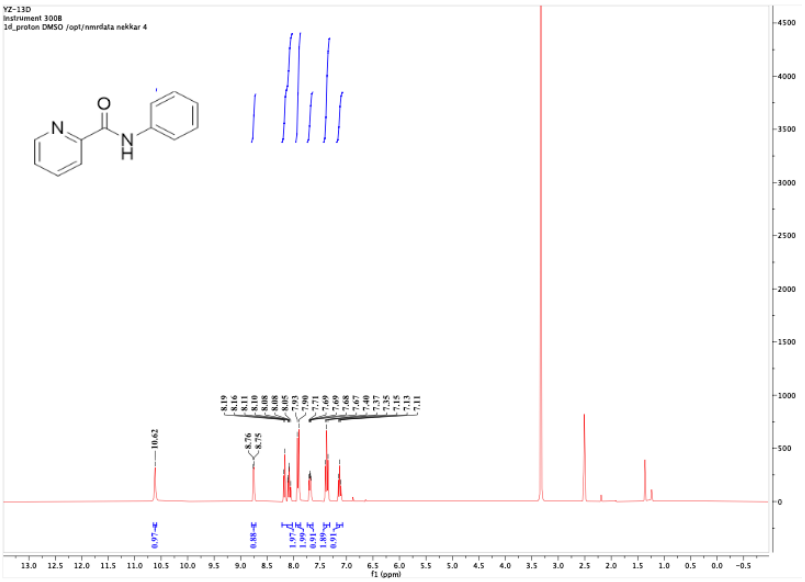


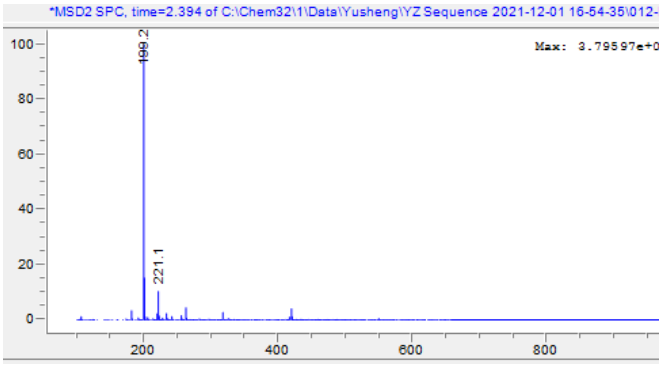


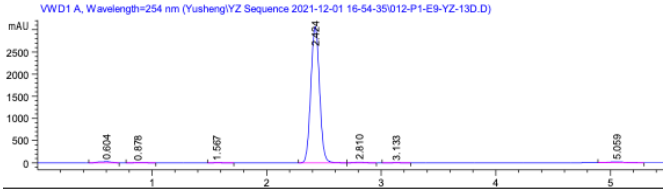


Peak #	RetTime [min]	Type	Width [min]	Area [mAU*s]	Height [mAU]	Area %
1	0.699	BB	0.0403	12.38318	4.93667	0.1146
2	0.929	BB	0.0585	1.05887e4	2654.77295	97.9929
3	1.590	BB	0.0553	15.73548	4.34273	0.1456
4	2.936	BB	0.0801	188.76466	36.65938	1.7469
Totals :				1.08056e4	2700.71172	

N-Benzylpicolinamide (13c)

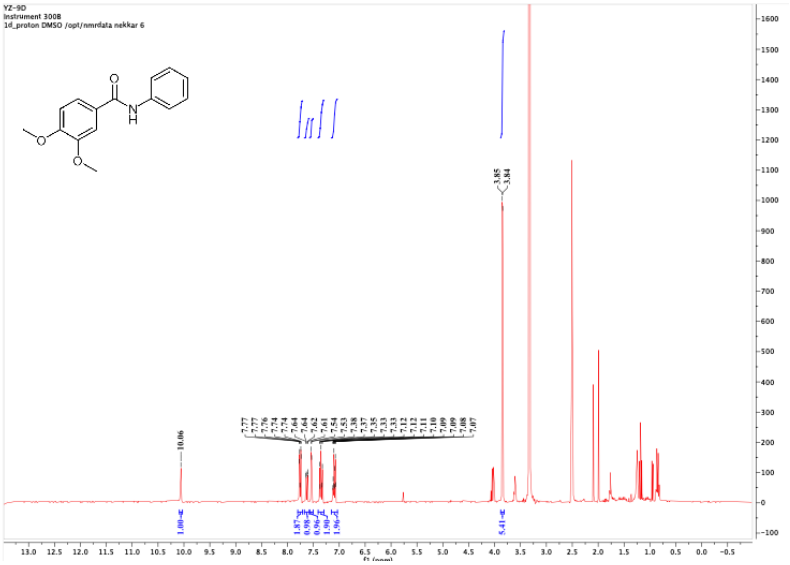


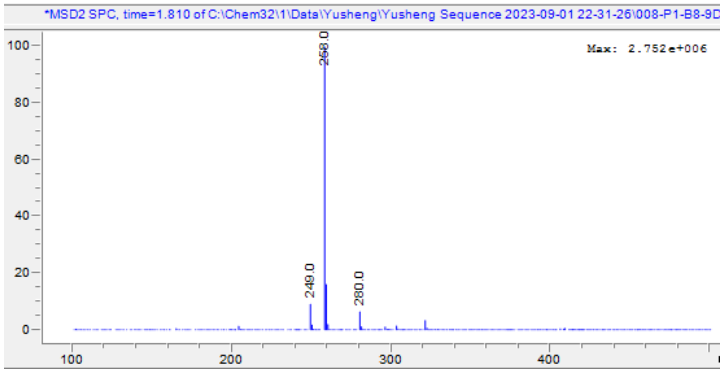


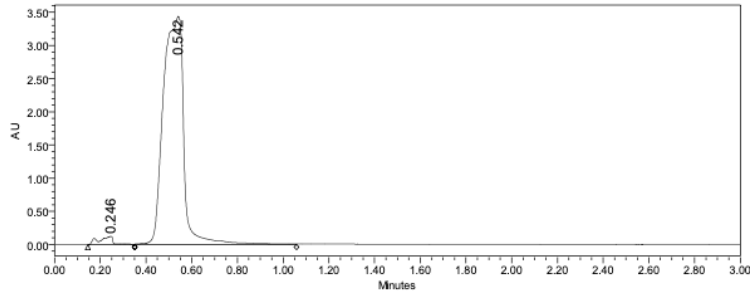


Peak #	RetTime [min]	Type	Width [min]	Area [mAU*s]	Height [mAU]	Area %
1	0.604	BB	0.1085	202.36359	25.25326	1.2093
2	0.878	BB	0.1184	34.27405	4.06504	0.2048
3	1.567	BB	0.0787	13.08797	2.59969	0.0782
4	2.424	BB	0.0837	1.62126e4	3067.21265	96.8846
5	2.810	BB	0.0853	73.19774	13.49270	0.4374
6	3.133	BB	0.0914	16.67705	2.88695	0.0997
7	5.059	BB	0.1411	181.72316	20.37486	1.0860
Totals :				1.67339e4	3135.88516	

N-Benzyl-3,4-dimethoxybenzamide (13d)

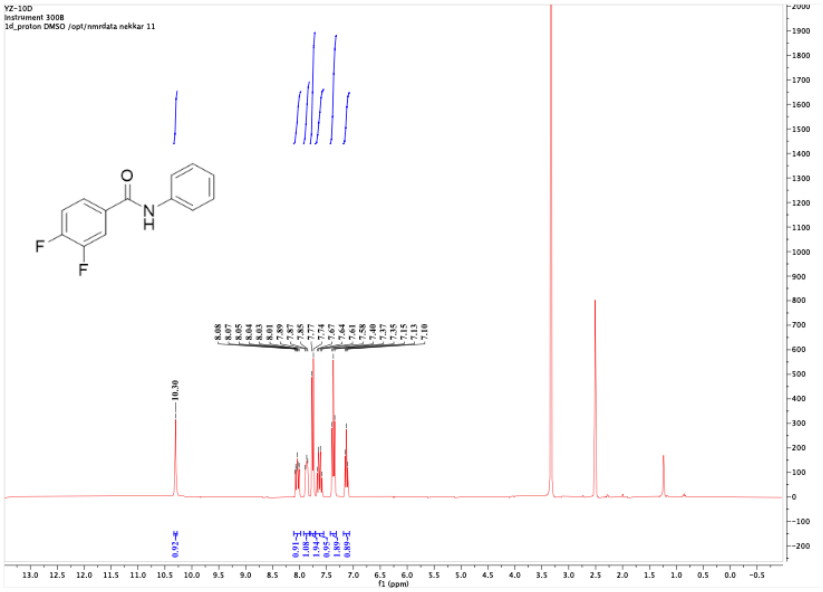


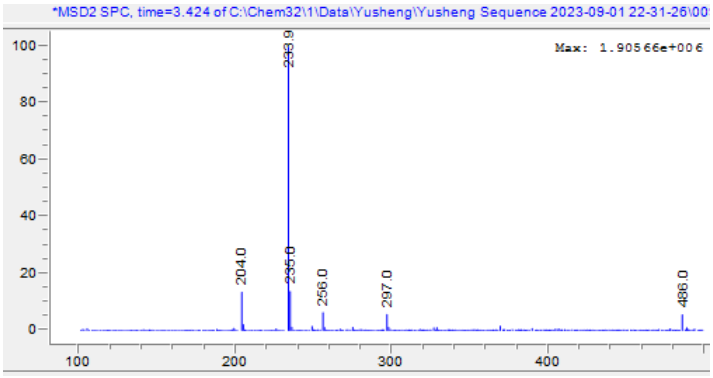


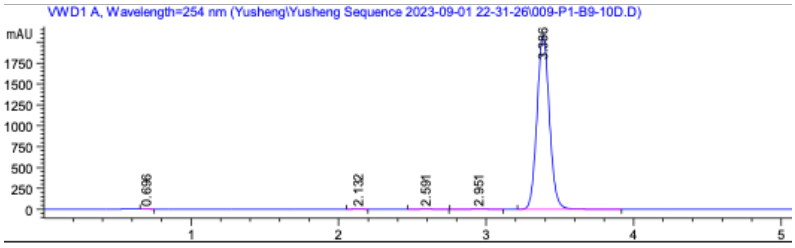


	RT	Area	% Area	Height
1	0.246	511858	2.35	122952
2	0.542	21309063	97.65	3436754

N-Benzyl-3,4-difluorobenzamide (13e)

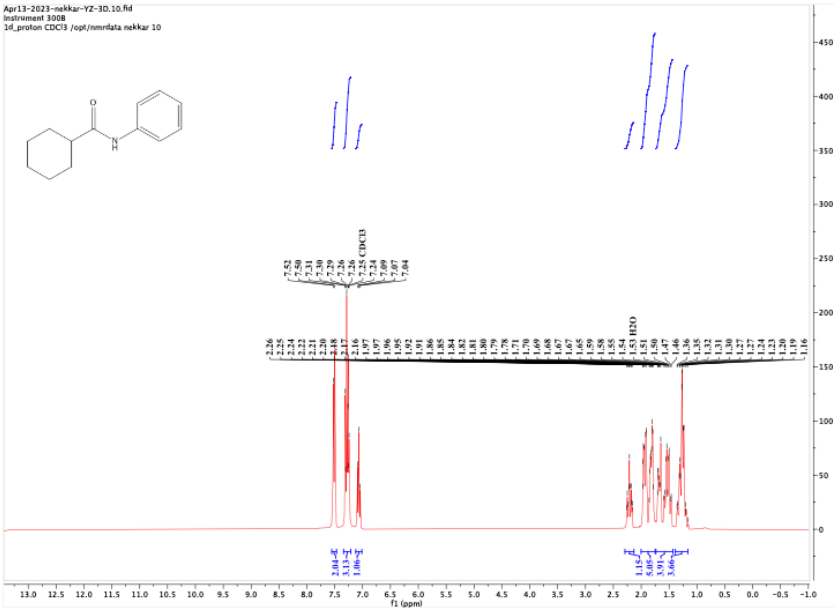


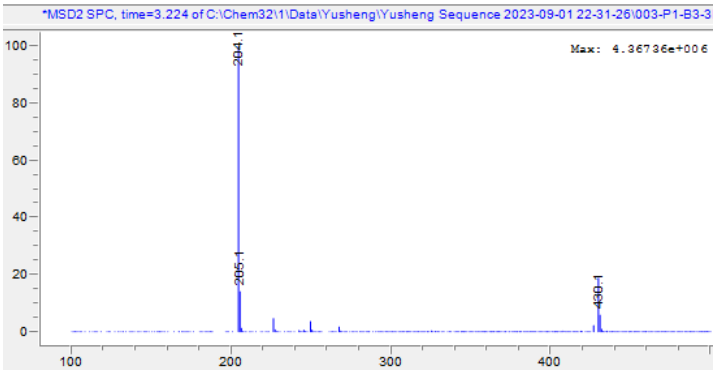


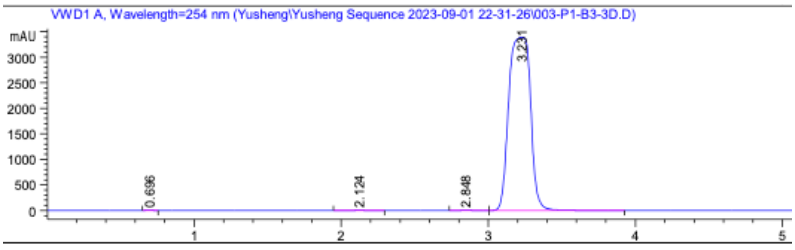


Peak #	RetTime [min]	Type	Width [min]	Area [mAU*s]	Height [mAU]	Area %
1	0.696	BB	0.0427	14.08895	5.35675	0.1148
2	2.132	BB	0.0588	14.56165	3.96823	0.1186
3	2.591	BB	0.0745	15.97093	3.29509	0.1301
4	2.951	BB	0.0848	25.81439	4.64921	0.2103
5	3.386	BB	0.0912	1.22027e4	2086.90674	99.4261
Totals :				1.22731e4	2104.17602	

N-Benzylcyclohexanecarboxamide (13f)

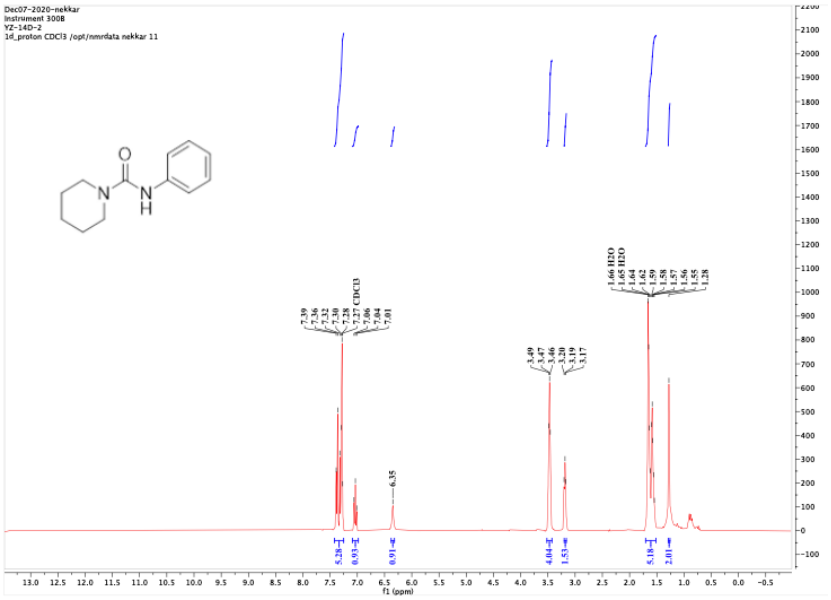


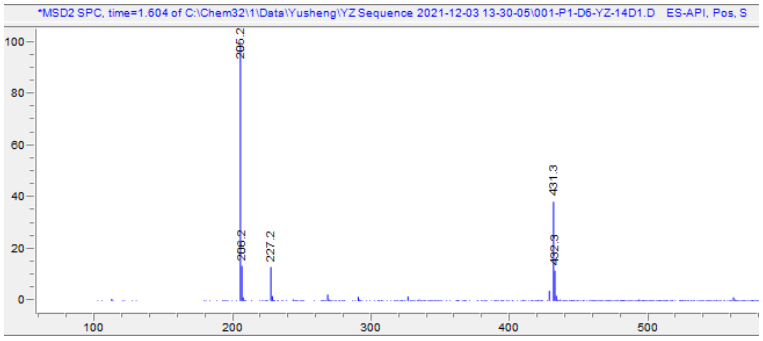


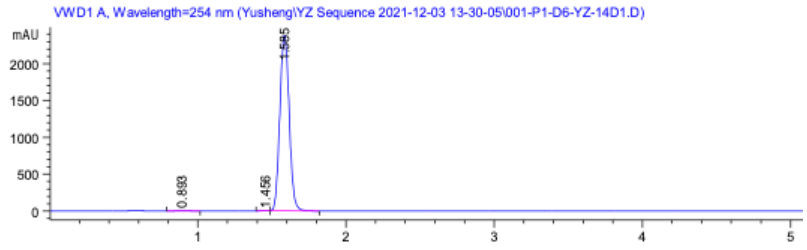


Peak #	RetTime [min]	Type	Width [min]	Area [mAU*s]	Height [mAU]	Area %
1	0.696	BB	0.0460	19.21062	6.79292	0.0552
2	2.124	BB	0.0701	20.73974	4.38878	0.0596
3	2.848	BB	0.0894	25.59720	4.24031	0.0736
4	3.231	BB	0.1665	3.47112e4	3390.11084	99.8115
Totals :				3.47768e4	3405.53285	

N-Benzylpiperidine-1-carboxamide (13g)

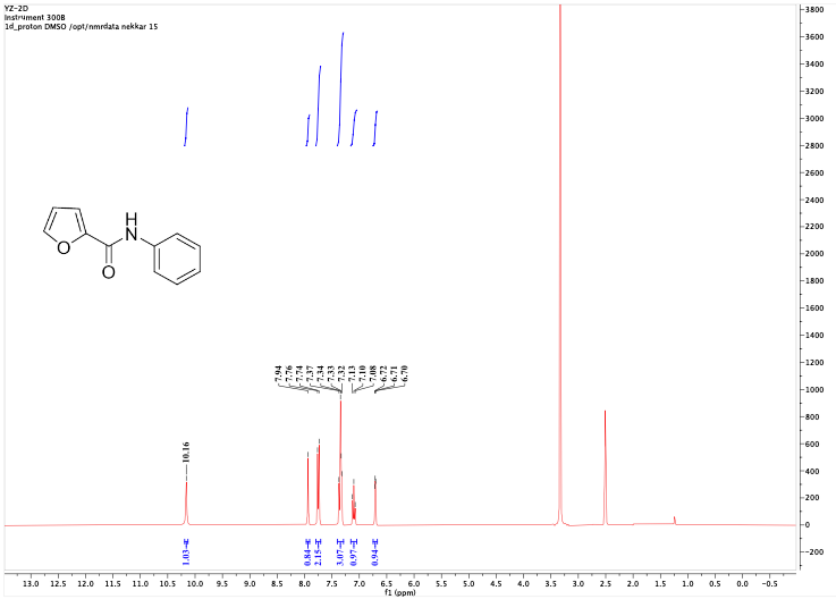


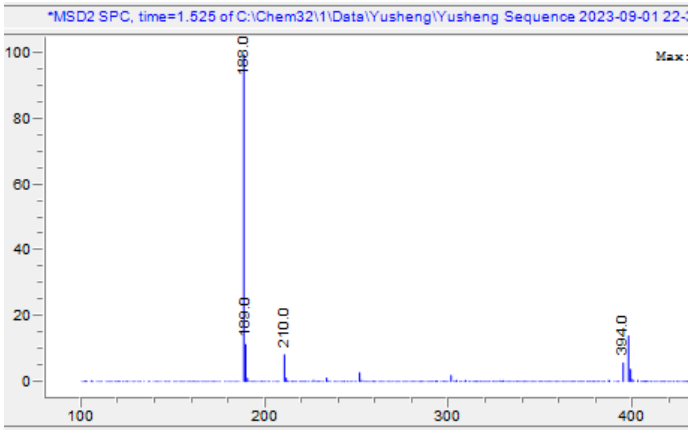


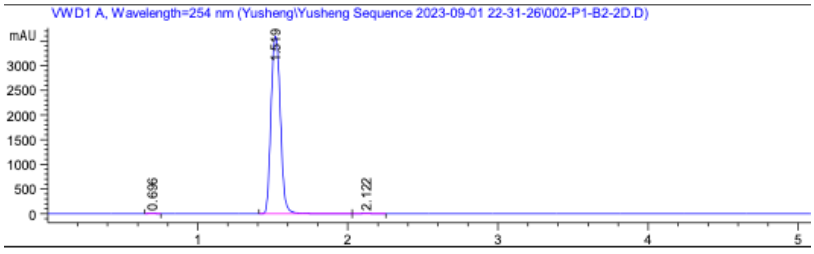


Peak #	RetTime [min]	Type	Width [min]	Area [mAU*s]	Height [mAU]	Area %
1	0.893	BB	0.1303	25.14053	3.28302	0.2400
2	1.456	BB	0.0469	10.10011	3.57985	0.0964
3	1.585	BB	0.0692	1.04380e4	2379.97852	99.6635
Totals :				1.04733e4	2386.84138	

N-Benzylfuran-2-carboxamide (13i)

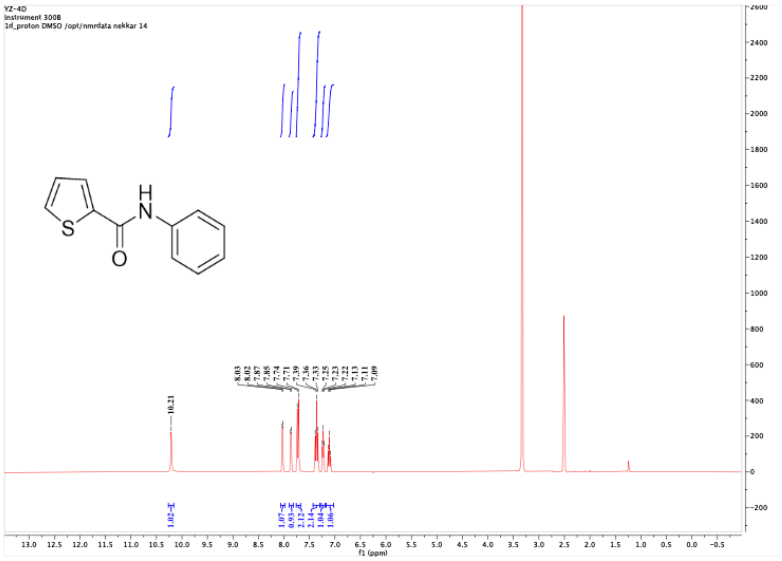


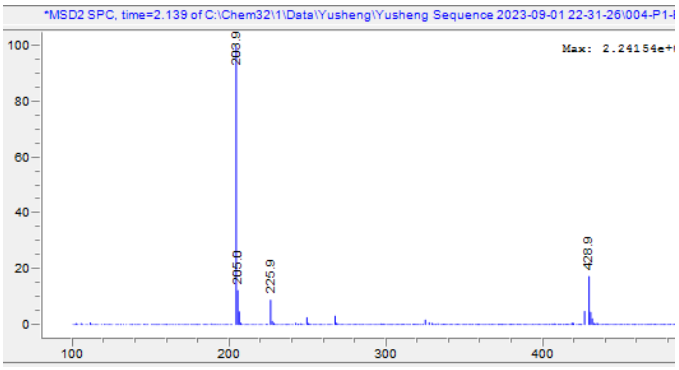


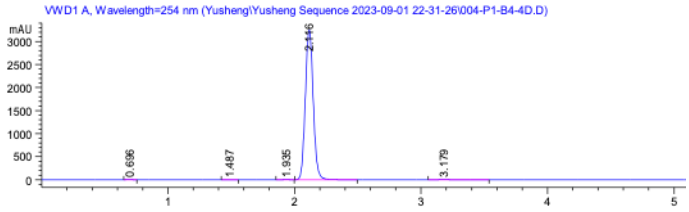


Peak #	RetTime [min]	Type	Width [min]	Area [mAU*s]	Height [mAU]	Area %
1	0.696	BB	0.0465	20.63075	7.18999	0.1329
2	1.519	BB	0.0693	1.54880e4	3595.25171	99.7396
3	2.122	BB	0.0640	19.81284	4.81067	0.1276
Totals :				1.55284e4	3607.25237	

N-Benzylthiophene-2-carboxamide (13j)

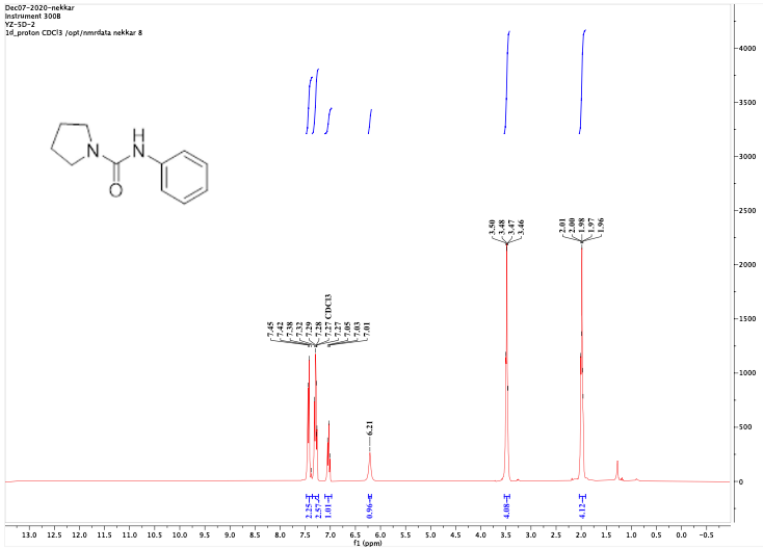


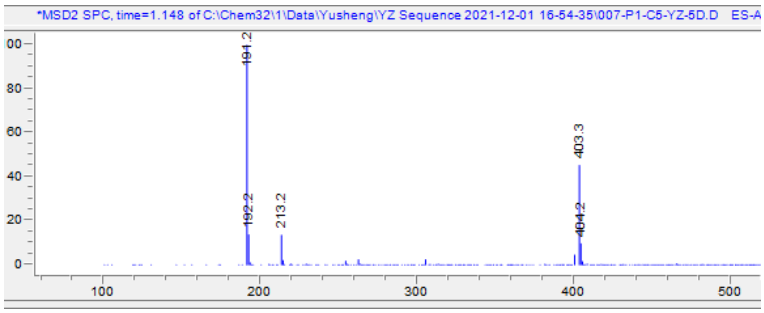


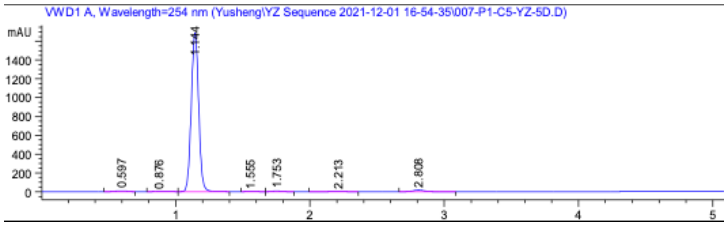


Peak #	RetTime [min]	Type	Width [min]	Area [mAU*s]	Height [mAU]	Area %
1	0.696	BB	0.0444	17.78570	6.39768	0.1259
2	1.487	BB	0.0547	6.45059	1.84837	0.0457
3	1.935	BB	0.0572	12.37934	3.42170	0.0876
4	2.116	BB	0.0685	1.40677e4	3248.12354	99.5640
5	3.179	BB	0.0952	24.98960	4.03996	0.1769
Totals :				1.41293e4	3263.83124	

N-Benzylpyrrolidine-1-carboxamide (13k)

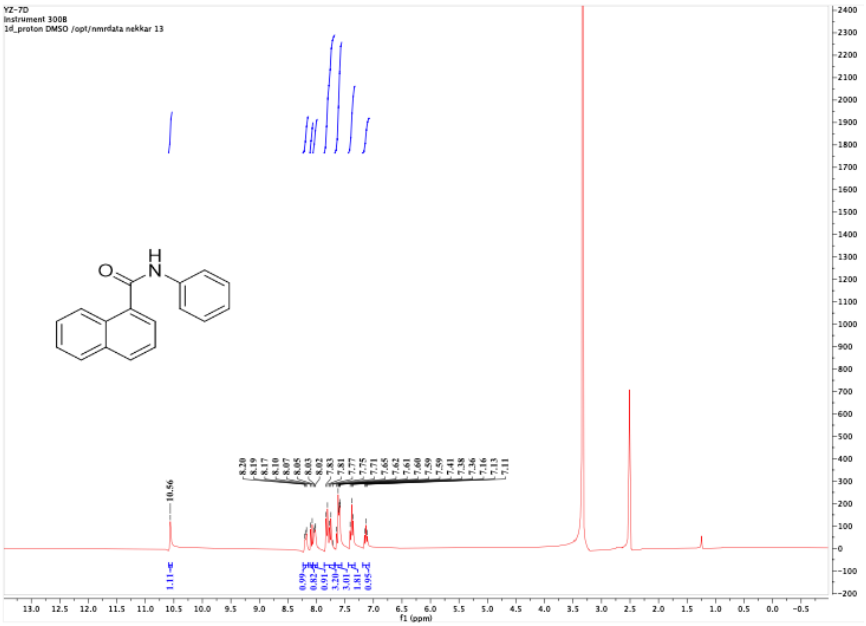


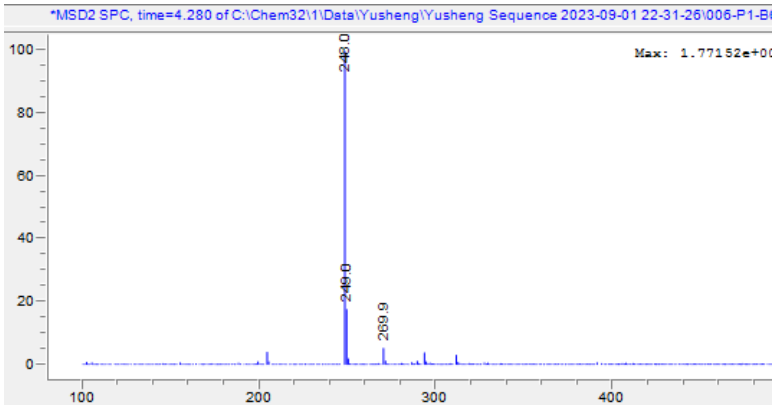


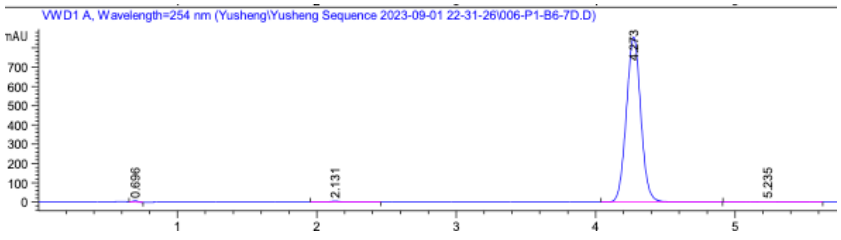


Peak #	RetTime [min]	Type	Width [min]	Area [mAU*s]	Height [mAU]	Area %
1	0.597	BB	0.1020	54.85469	8.20562	0.8219
2	0.876	BB	0.1100	22.10728	2.89957	0.3313
3	1.144	BB	0.0595	6447.17529	1688.85767	96.6043
4	1.555	BB	0.0636	9.75270	2.34013	0.1461
5	1.753	BB	0.0649	23.70467	5.76953	0.3552
6	2.213	BB	0.0838	22.35616	4.15237	0.3350
7	2.808	BB	0.0884	93.84410	16.49474	1.4062
Totals :				6673.79490	1728.71961	

N-Benzyl-1-naphthamide (13l)

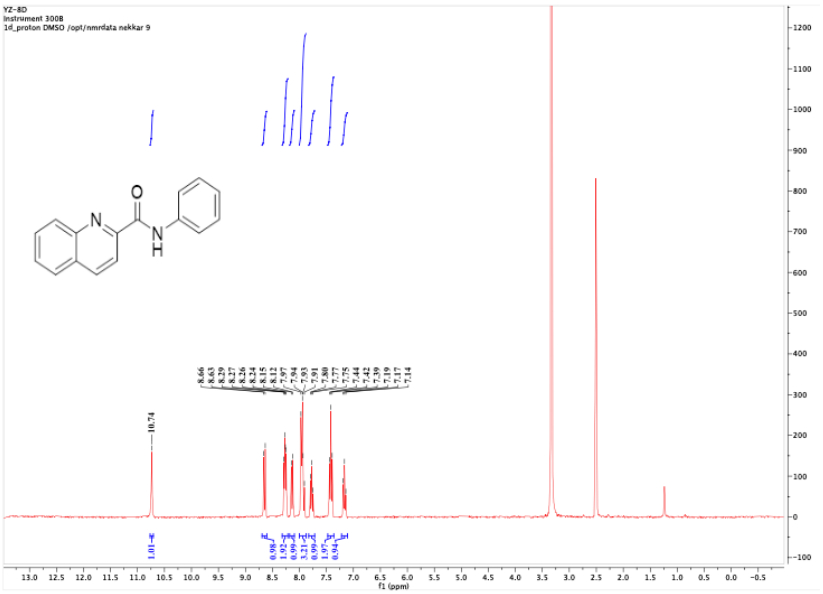


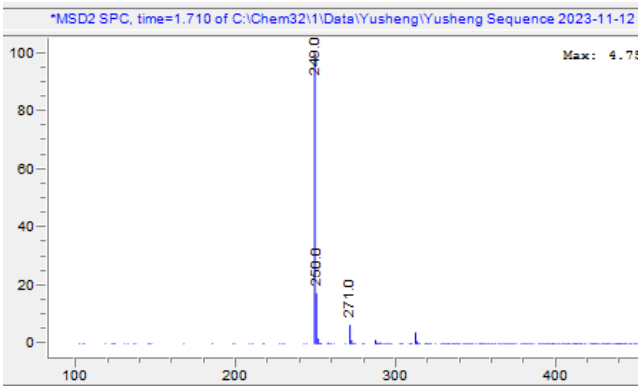


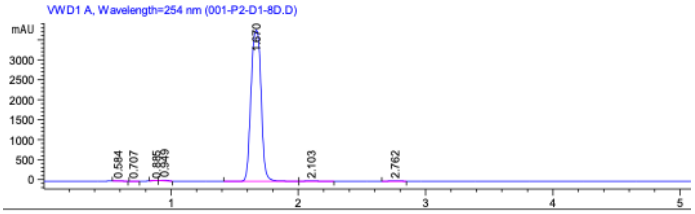


Peak #	RetTime [min]	Type	Width [min]	Area [mAU*s]	Height [mAU]	Area %
1	0.696	BB	0.0441	16.18757	5.89242	0.2595
2	2.131	BB	0.0672	21.67088	4.93385	0.3474
3	4.273	BB	0.1121	6167.10010	855.37445	98.8672
4	5.235	BB	0.1414	32.80510	3.52970	0.5259
Totals :				6237.76364	869.73042	

N-Benzylquinoline-2-carboxamide (13m)

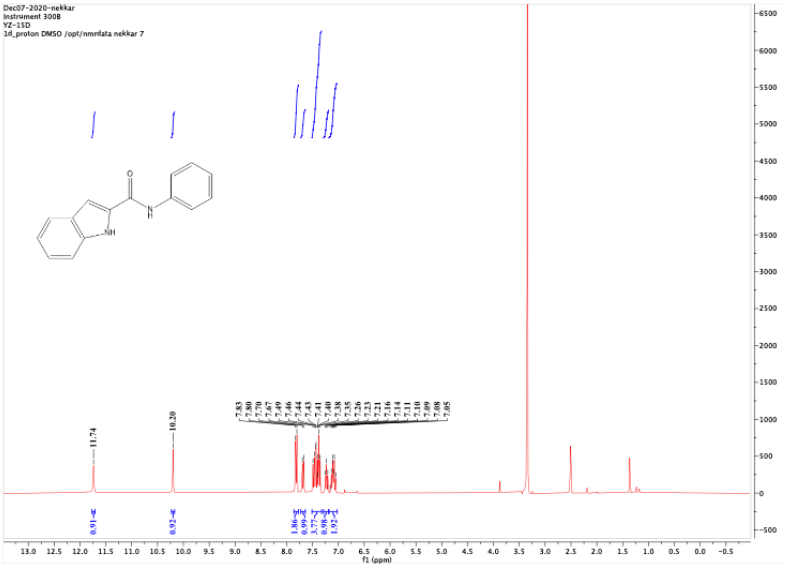


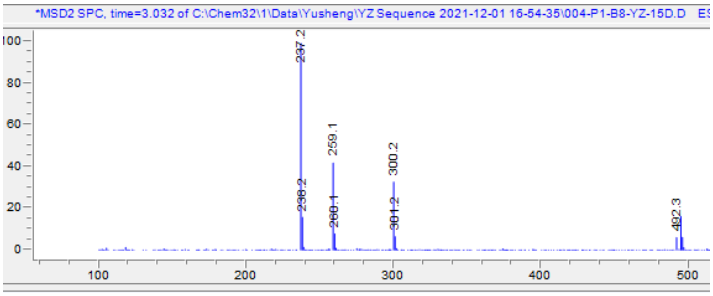


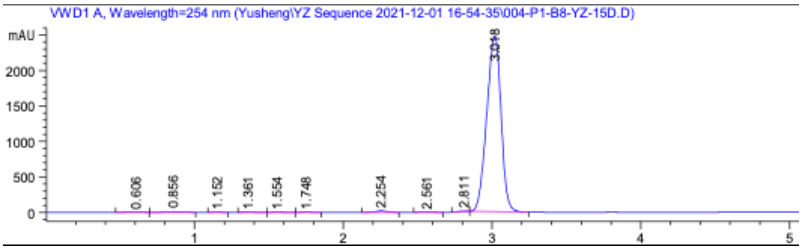


Peak #	RetTime [min]	Type	Width [min]	Area [mAU*s]	Height [mAU]	Area %
1	0.584	BB	0.0696	8.18844	1.88951	0.0391
2	0.707	BB	0.0368	4.91355	2.13510	0.0235
3	0.885	BB	0.0509	10.29360	3.08374	0.0491
4	0.949	BB	0.0557	44.41766	12.74547	0.2121
5	1.670	BB	0.0891	2.07778e4	3779.19482	99.2100
6	2.103	BB	0.0746	53.29751	11.17657	0.2545
7	2.762	BB	0.0811	44.34081	8.74818	0.2117
Totals :				2.09433e4	3818.97339	

N-Benzyl-1*H*-indole-2-carboxamide (14a)

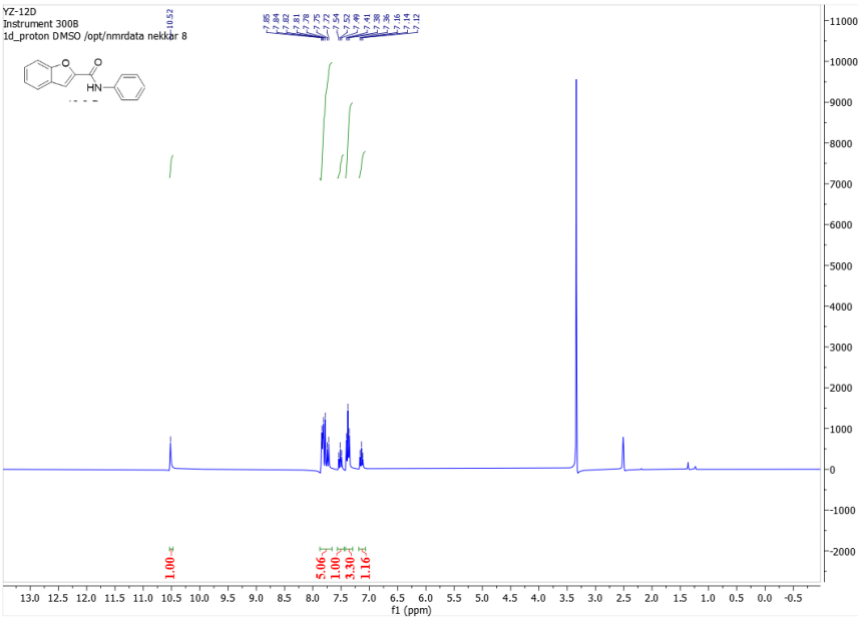


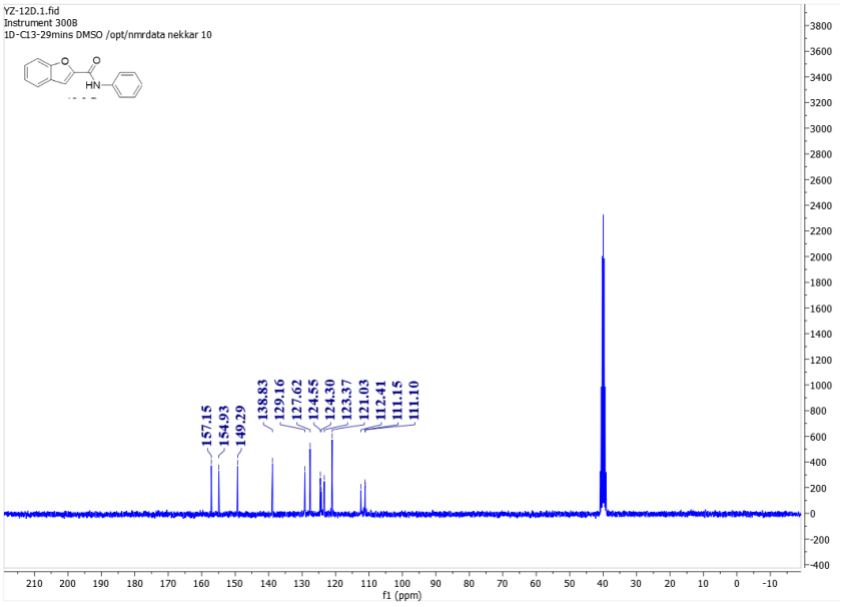




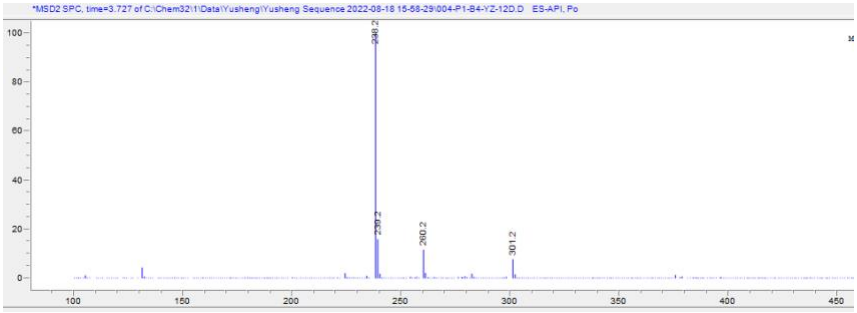
Peak #	RetTime [min]	Type	Width [min]	Area [mAU*s]	Height [mAU]	Area %
1	0.606	BB	0.1078	50.30656	7.26584	0.2993
2	0.856	BB	0.1139	59.75117	7.34534	0.3555
3	1.152	BB	0.0524	8.20217	2.43150	0.0488
4	1.361	BB	0.0571	21.52703	5.83139	0.1281
5	1.554	BB	0.0639	10.71939	2.55540	0.0638
6	1.748	BB	0.0571	10.41903	2.82355	0.0620
7	2.254	BB	0.0754	90.36063	18.69574	0.5376
8	2.561	BB	0.0758	23.03028	4.81206	0.1370
9	2.811	BB	0.0619	33.33471	8.85481	0.1983
10	3.018	BB	0.1048	1.64992e4	2474.35449	98.1695
Totals :				1.68069e4	2534.97011	

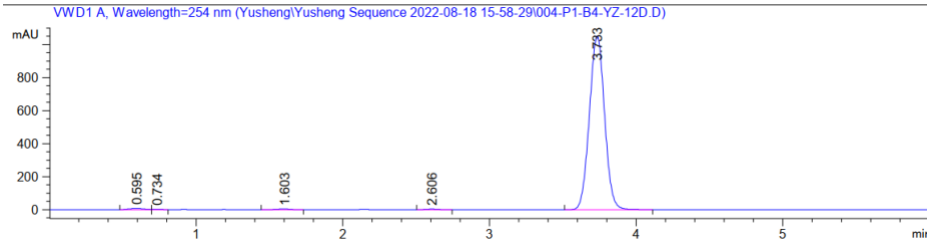
N-Benzylbenzofuran-2-carboxamide (14b)





N-Benzylbenzofuran-2-carboxamide (14b) – Continued

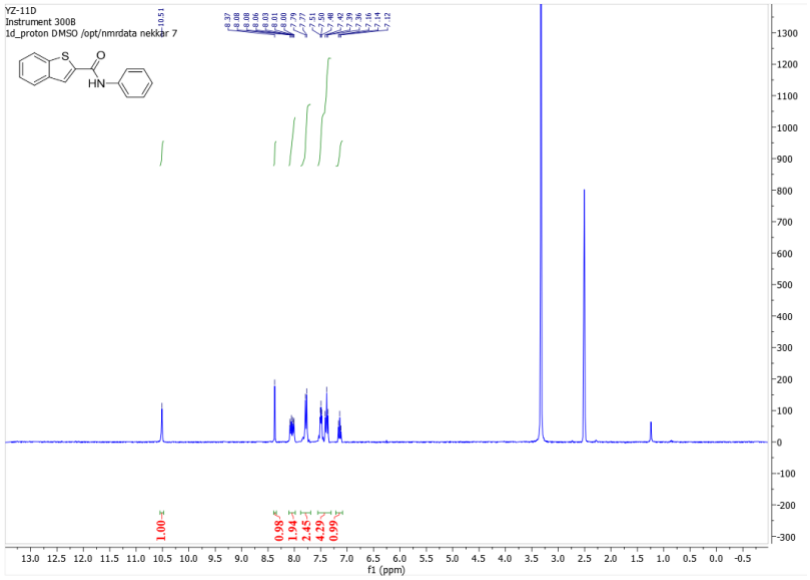


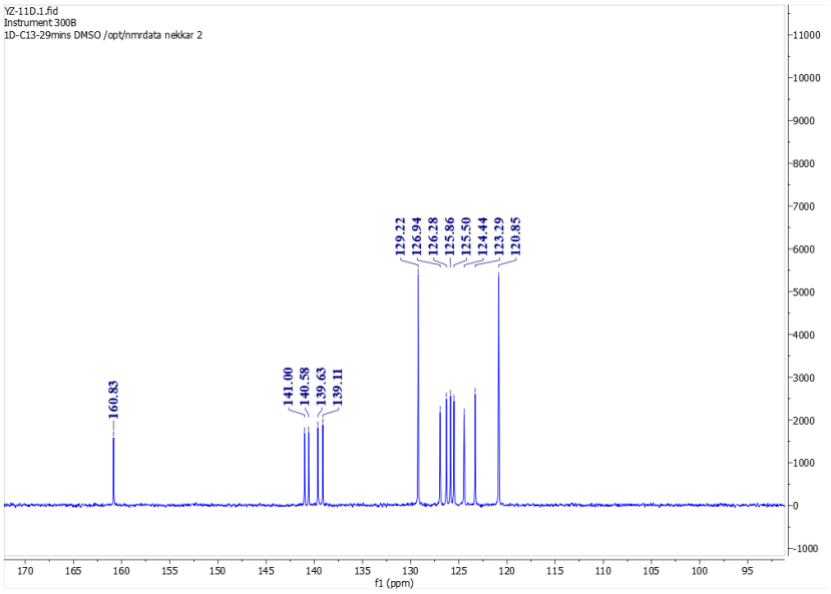


Signal 3: VWD1 A, Wavelength=254 nm

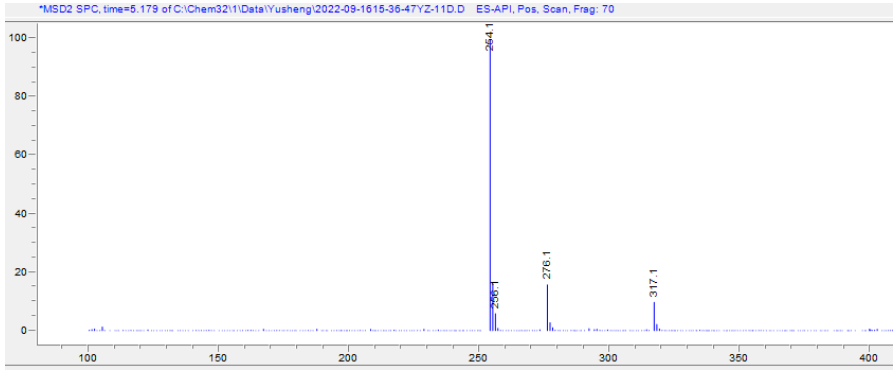
Peak #	RetTime [min]	Type	Width [min]	Area [mAU*s]	Height [mAU]	Area %
1	0.595	BB	0.1165	45.76490	6.63619	0.5981
2	0.734	BB	0.0507	8.38166	2.66648	0.1095
3	1.603	BB	0.1071	25.79080	3.95645	0.3371
4	2.606	BB	0.0785	18.61697	3.71313	0.2433
5	3.733	BB	0.1128	7552.89600	1051.16724	98.7120
Totals :				7651.45033	1068.13948	

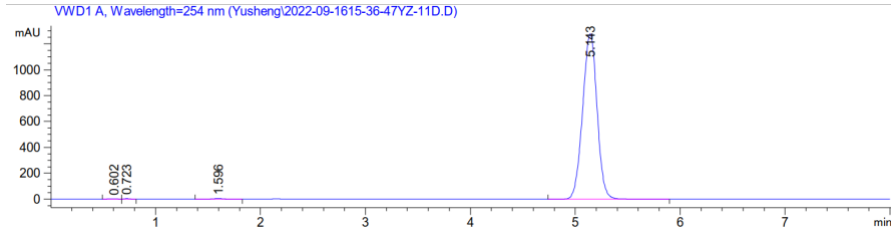
N-Benzylbenzo[*b*]thiophene-2-carboxamide (14c)





N-Benzylbenzo[*b*]thiophene-2-carboxamide (14c) – Continued

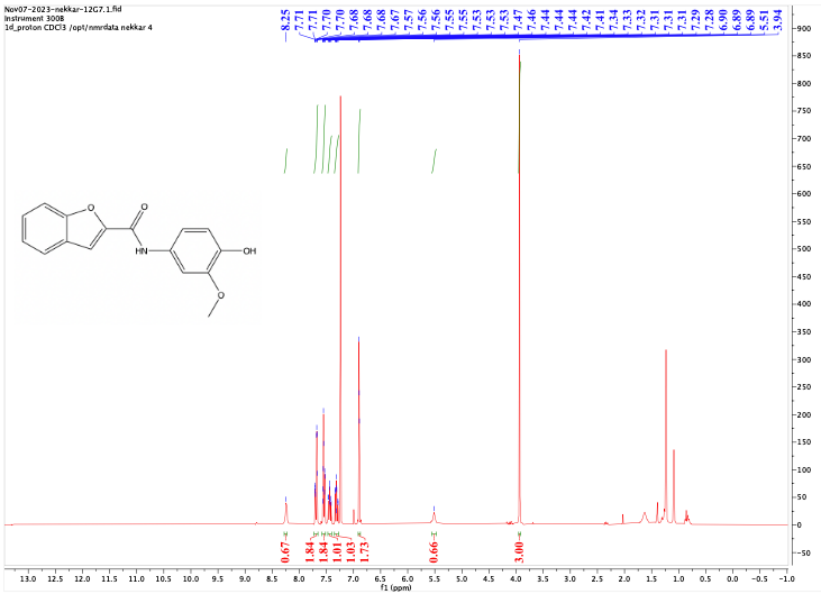


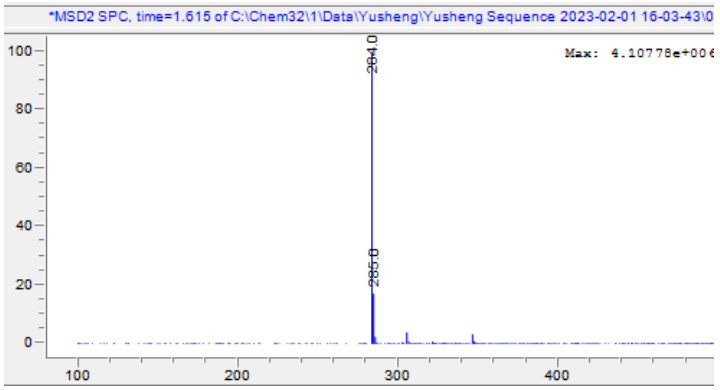


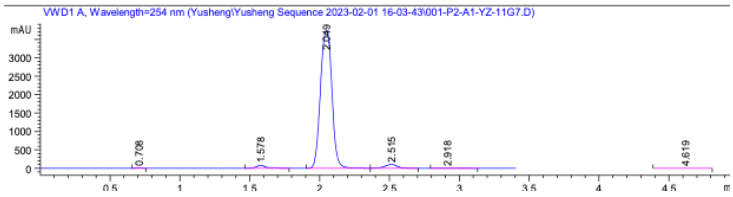
Signal 3: VWD1 A, Wavelength=254 nm

Peak #	RetTime [min]	Type	Width [min]	Area [mAU*s]	Height [mAU]	Area %
1	0.602	BB	0.0858	10.52153	1.71025	0.0859
2	0.723	BB	0.0470	12.84582	4.27947	0.1049
3	1.596	BB	0.1085	30.01047	4.51563	0.2451
4	5.143	BB	0.1483	1.21892e4	1277.24744	99.5640
Totals :				1.22426e4	1287.75279	

N-(4-hydroxy-3-methoxyphenyl)benzofuran-2-carboxamide (16a)

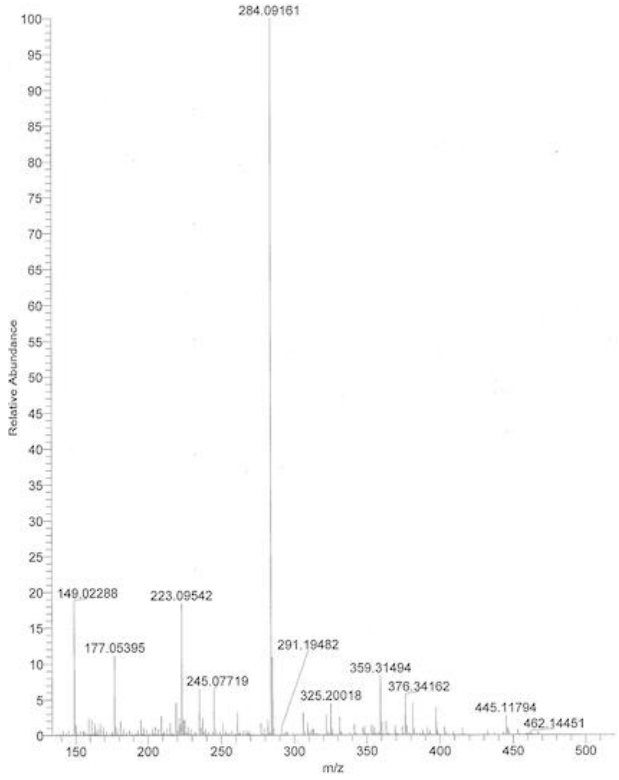


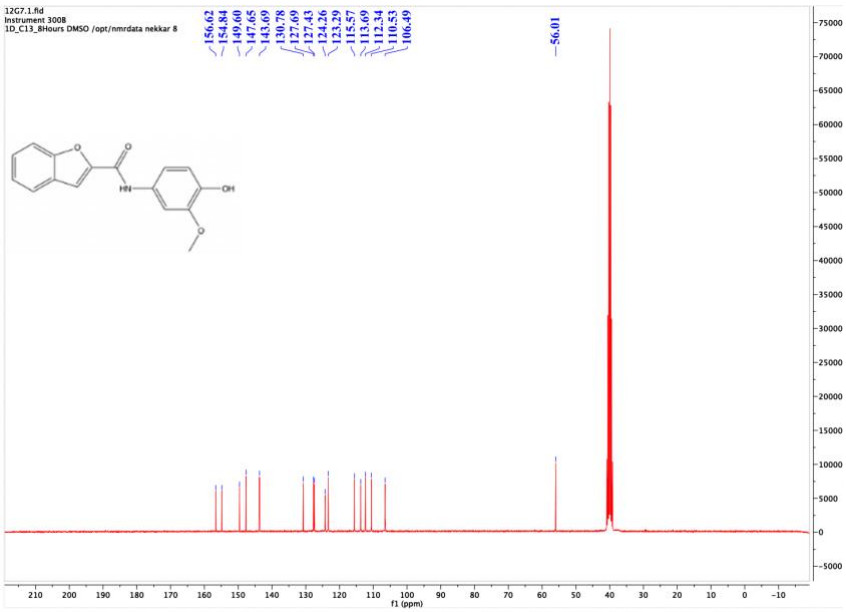




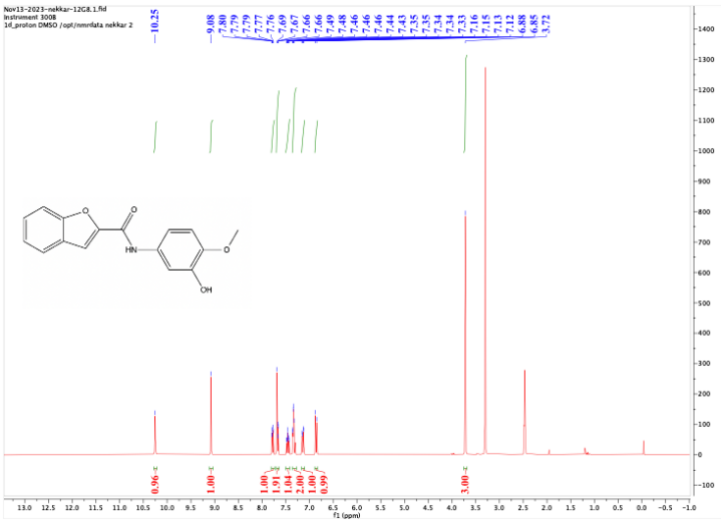
Peak #	RetTime [min]	Type	Width [min]	Area [mAU*s]	Height [mAU]	Area %
1	0.708	BB	0.0430	15.61483	5.87745	0.0702
2	1.578	BB	0.0734	379.87283	77.19826	1.7069
3	2.049	BB	0.0912	2.12289e4	3738.49683	95.3879
4	2.515	BB	0.0900	599.76508	102.93907	2.6949
5	2.918	BB	0.1040	11.98579	1.72714	0.0539
6	4.619	BB	0.1648	19.18929	1.83861	0.0862
Totals :				2.22553e4	3928.07736	

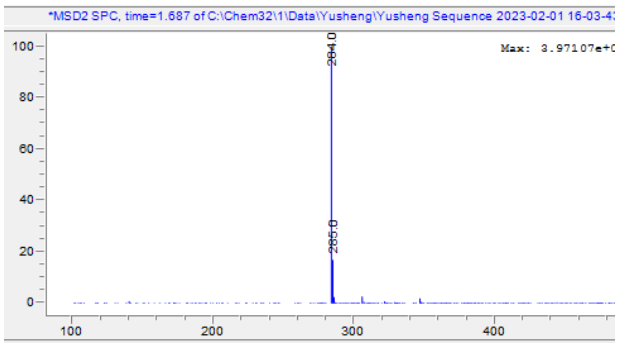
N-(4-hydroxy-3-methoxyphenyl)benzofuran-2-carboxamide (16a) – Continued

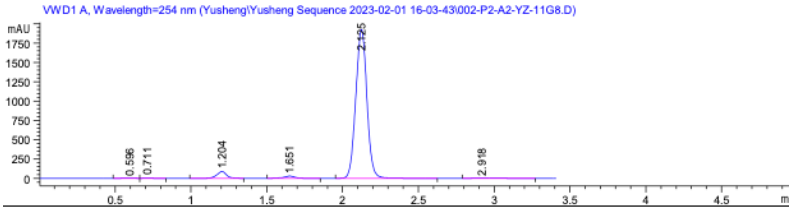




N-(3-hydroxy-4-methoxyphenyl)benzofuran-2-carboxamide (16b)





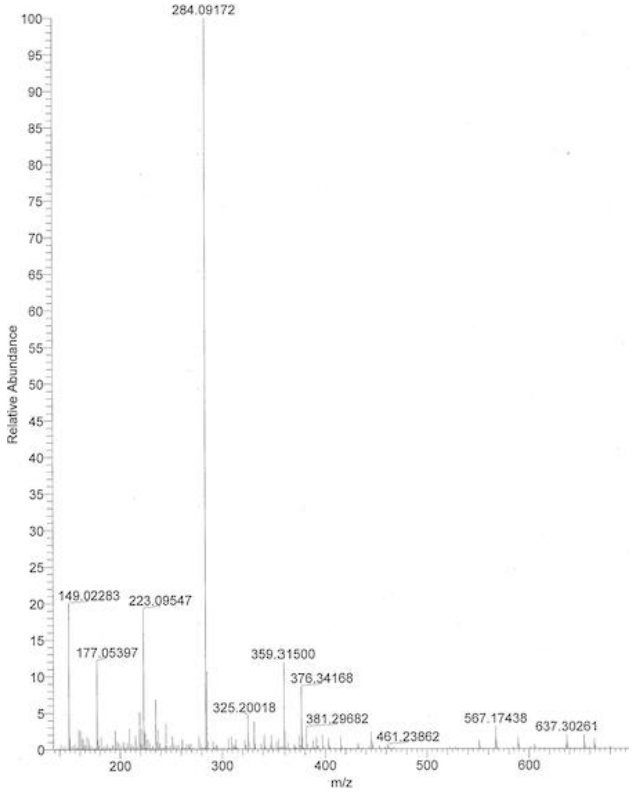


Peak #	RetTime [min]	Type	Width [min]	Area [mAU*s]	Height [mAU]	Area %
1	0.596	BB	0.0930	13.75507	2.19850	0.1323
2	0.711	BB	0.0468	15.31911	5.13313	0.1474
3	1.204	BB	0.0647	381.74744	87.88802	3.6720
4	1.651	BB	0.0729	137.77516	28.25671	1.3253
5	2.125	BB	0.0794	9802.79883	1925.58923	94.2935

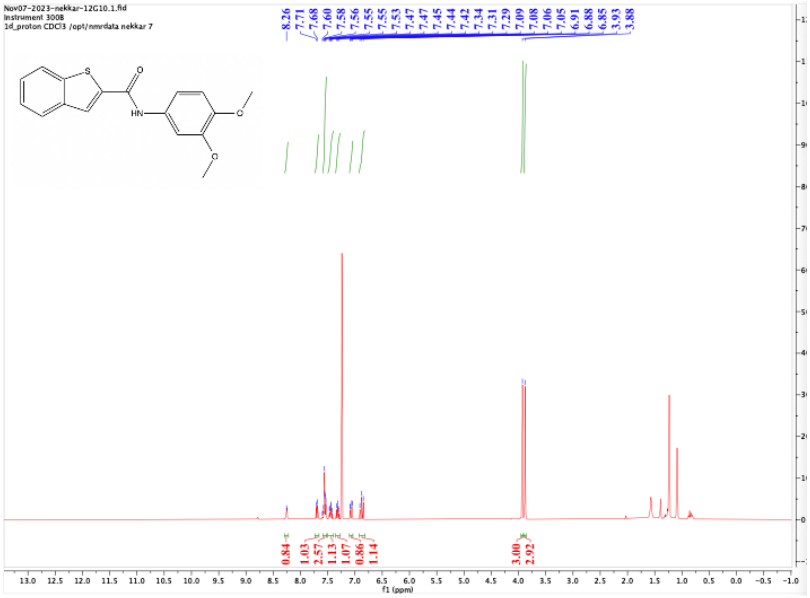
Peak #	RetTime [min]	Type	Width [min]	Area [mAU*s]	Height [mAU]	Area %
6	2.918	BB	0.1184	44.65556	5.40580	0.4295

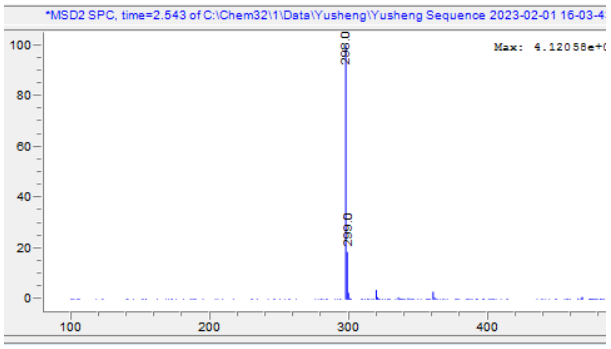
Totals : 1.03961e4 2054.47139

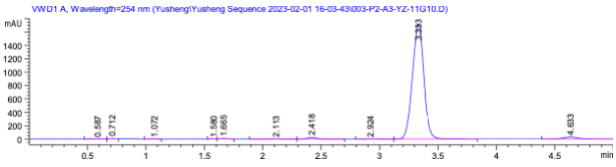
***N*-(3-hydroxy-4-methoxyphenyl)benzofuran-2-carboxamide (16b) – Continued**



N-(3,4-dimethoxyphenyl)benzofuran-2-carboxamide (16c)



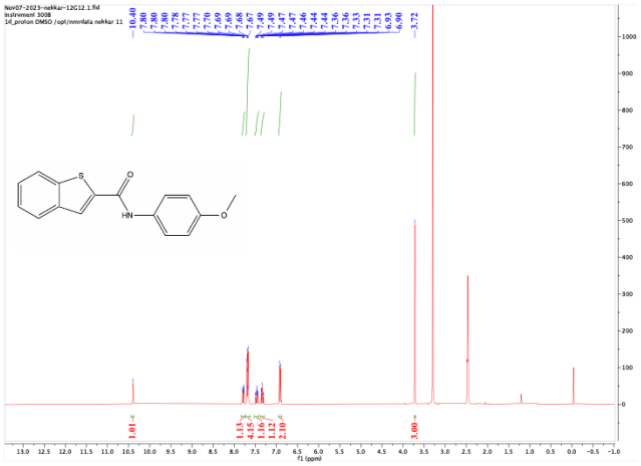


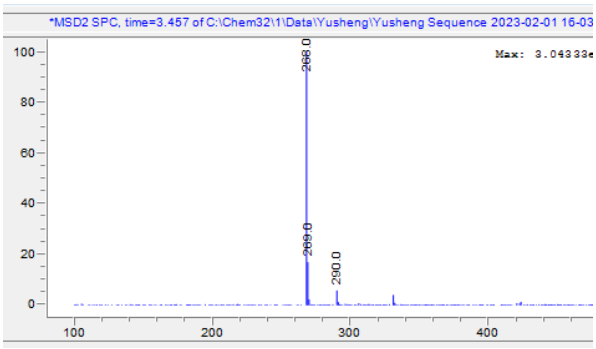


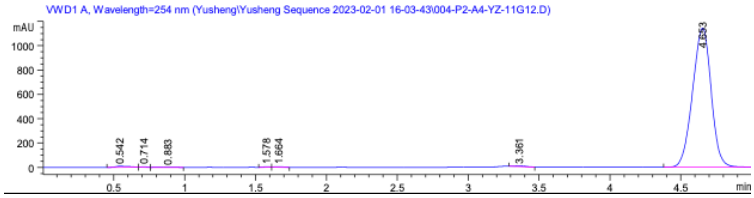
Peak #	RetTime [min]	Type	Width [min]	Area [mAU*s]	Height [mAU]	Area %
1	0.587	BB	0.1088	25.55523	3.98546	0.2094
2	0.712	BB	0.0445	12.27538	4.55153	0.1006
3	1.072	BB	0.0589	7.05302	1.87513	0.0578
4	1.580	BB	0.0416	4.48856	1.76673	0.0368
5	1.665	BB	0.0612	30.60577	8.08403	0.2508
6	2.113	BB	0.1003	18.67484	2.78120	0.1531
7	2.418	BB	0.0846	132.72072	24.34251	1.0877
8	2.924	BB	0.1104	14.17255	1.87020	0.1162
9	3.333	BB	0.1054	1.17001e4	1719.84351	95.8882
10	4.633	BBA	0.1357	256.16074	29.09146	2.0994

Peak #	RetTime [min]	Type	Width [min]	Area [mAU*s]	Height [mAU]	Area %
Totals :				1.22018e4	1798.19176	

N-(4-methoxyphenyl)benzofuran-2-carboxamide (16d)

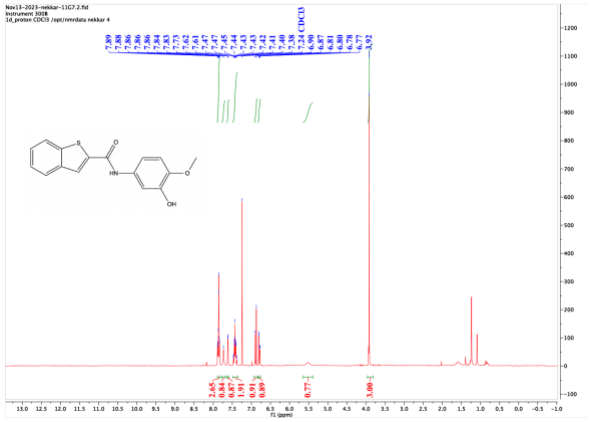


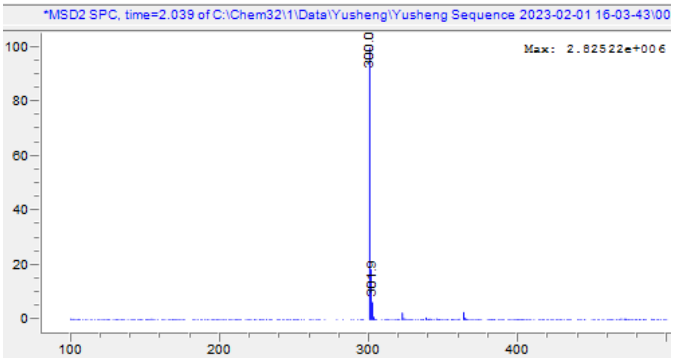


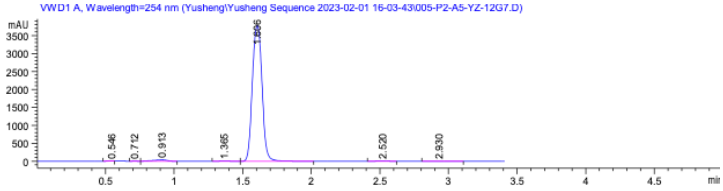


Peak #	RetTime [min]	Type	Width [min]	Area [mAU*s]	Height [mAU]	Area %
1	0.542	BB	0.0863	59.07301	9.15759	0.5616
2	0.714	BB	0.0387	9.52620	4.00770	0.0906
3	0.883	BB	0.0954	15.68039	2.22070	0.1491
4	1.578	BB	0.0453	5.91851	2.13864	0.0563
5	1.664	BB	0.0581	12.74531	3.52930	0.1212
6	3.361	BB	0.0868	30.76379	5.71166	0.2925
7	4.653	BBA	0.1420	1.03850e4	1142.70837	98.7289
Totals :				1.05187e4	1169.47398	

N-(4-hydroxy-3-methoxyphenyl)benzo[*b*]thiophene-2-carboxamide (17a)

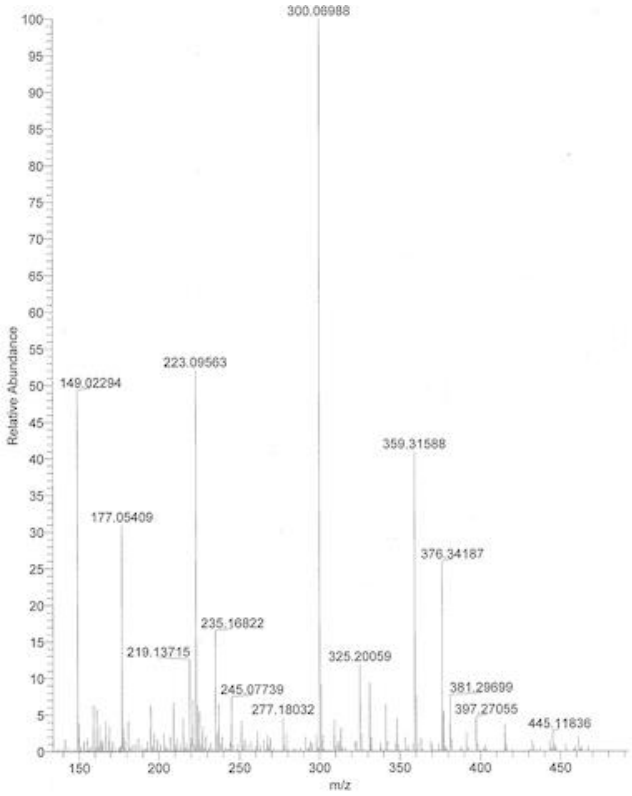


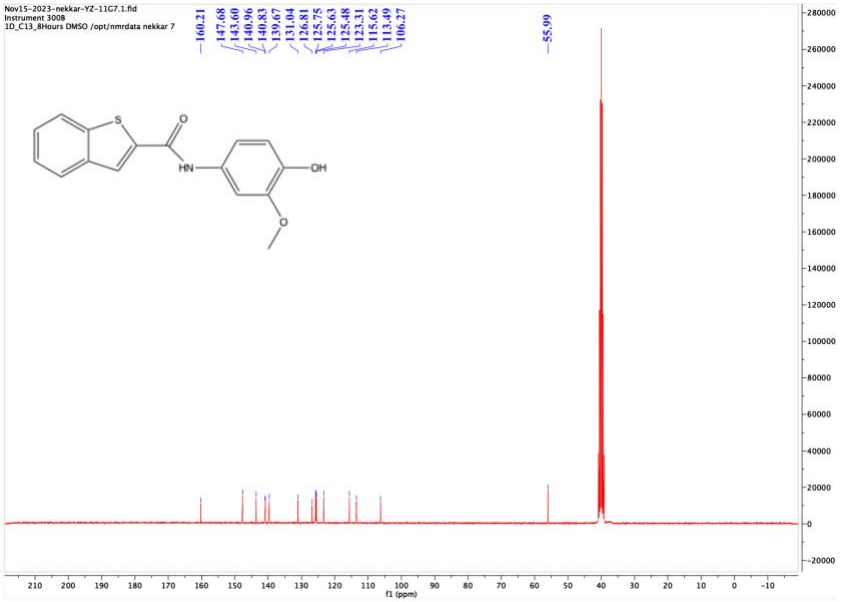




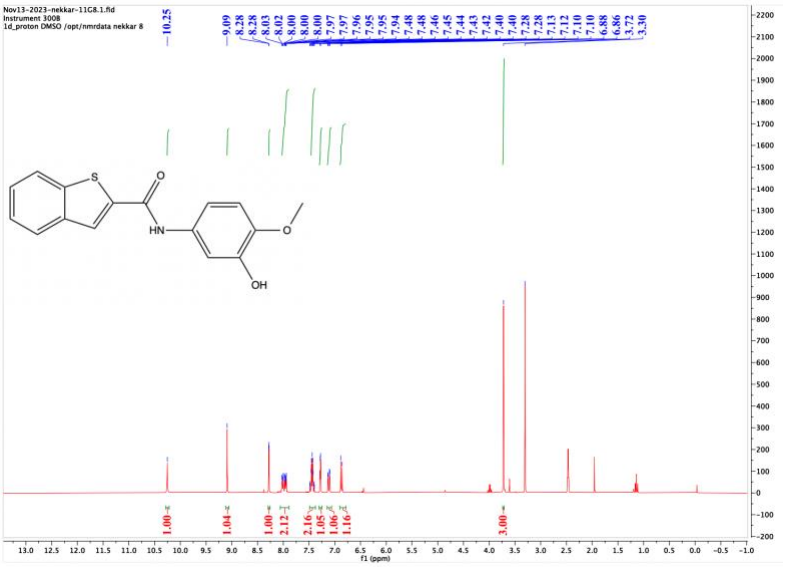
Peak #	RetTime [min]	Type	Width [min]	Area [mAU*s]	Height [mAU]	Area %
1	0.546	BB	0.0595	8.16533	2.09548	0.0432
2	0.712	BB	0.0388	7.64854	3.20799	0.0405
3	0.913	BB	0.1042	268.51862	38.13187	1.4211
4	1.365	BB	0.0621	47.01423	11.65625	0.2488
5	1.606	BB	0.0792	1.85021e4	3776.62402	97.9228
6	2.520	BB	0.0807	48.40391	9.45237	0.2562
7	2.930	BB	0.1038	12.72194	1.83742	0.0673
Totals :				1.88946e4	3843.00540	

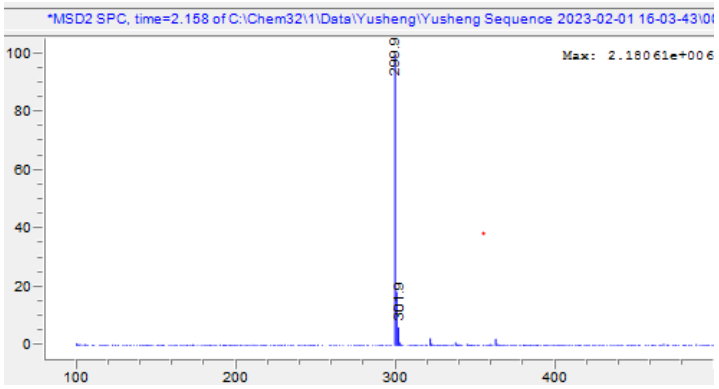
N-(4-hydroxy-3-methoxyphenyl)benzo[*b*]thiophene-2-carboxamide (17a) - Continued

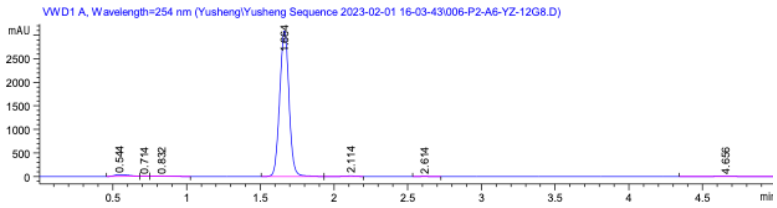




N-(3-hydroxy-4-methoxyphenyl)benzo[*b*]thiophene-2-carboxamide (17b)

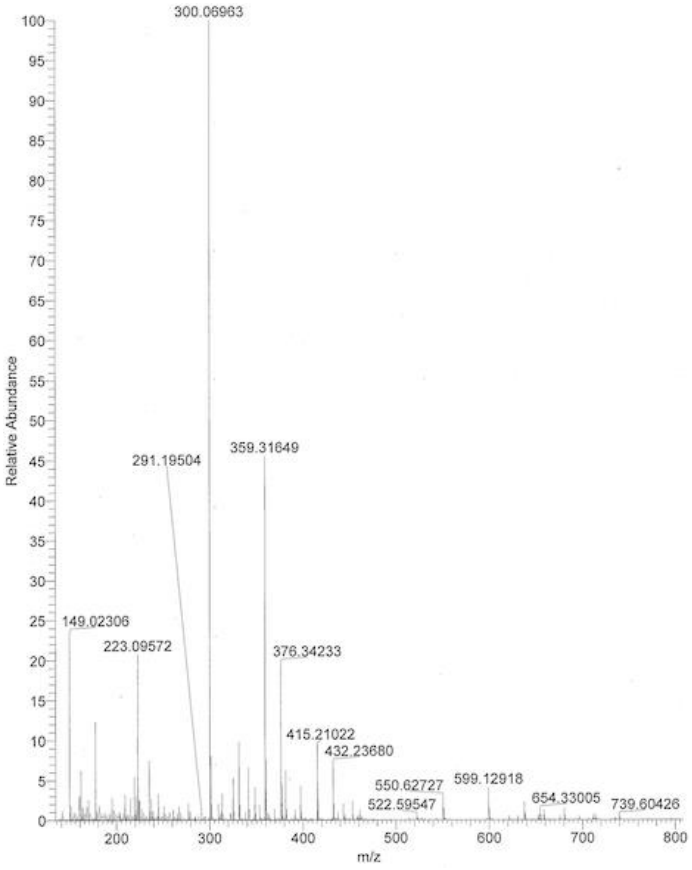


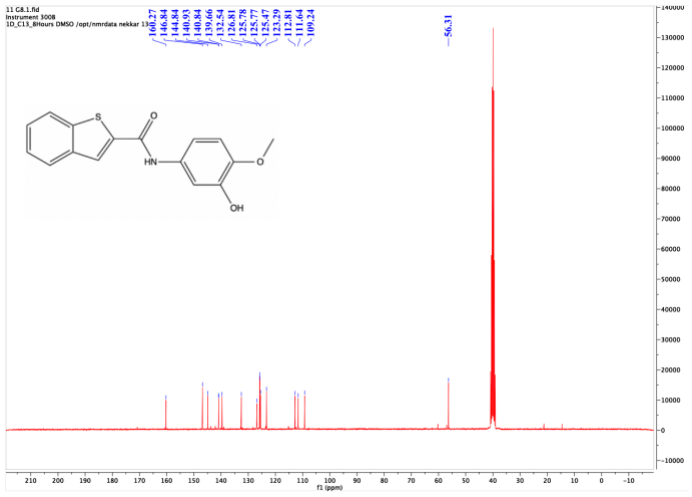




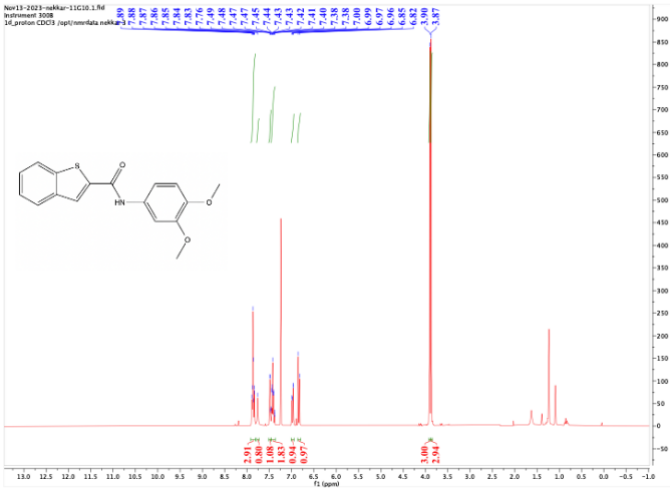
Peak #	RetTime [min]	Type	Width [min]	Area [mAU*s]	Height [mAU]	Area %
1	0.544	BB	0.0924	244.85555	36.88563	1.7449
2	0.714	BB	0.0345	4.53921	2.16488	0.0323
3	0.832	BB	0.1312	54.95166	6.46300	0.3916
4	1.664	BB	0.0684	1.36022e4	3089.33960	96.9346
5	2.114	BB	0.0751	45.44403	9.45236	0.3239
6	2.614	BB	0.0778	15.67872	3.22137	0.1117
7	4.656	BBA	0.1379	64.68129	7.26115	0.4609

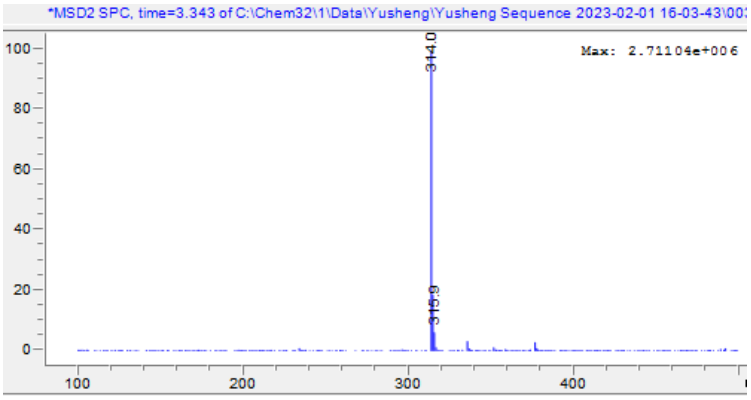
N-(3-hydroxy-4-methoxyphenyl)benzo[*b*]thiophene-2-carboxamide (17b) – Continued

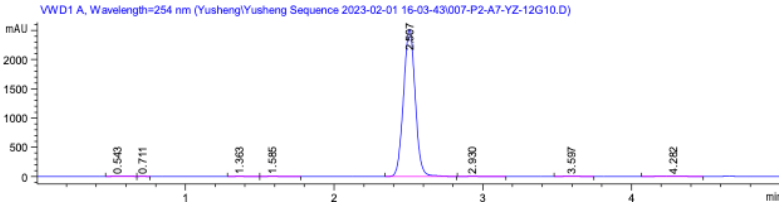




N-(3,4-dimethoxyphenyl)benzo[*b*]thiophene-2-carboxamide (17c)

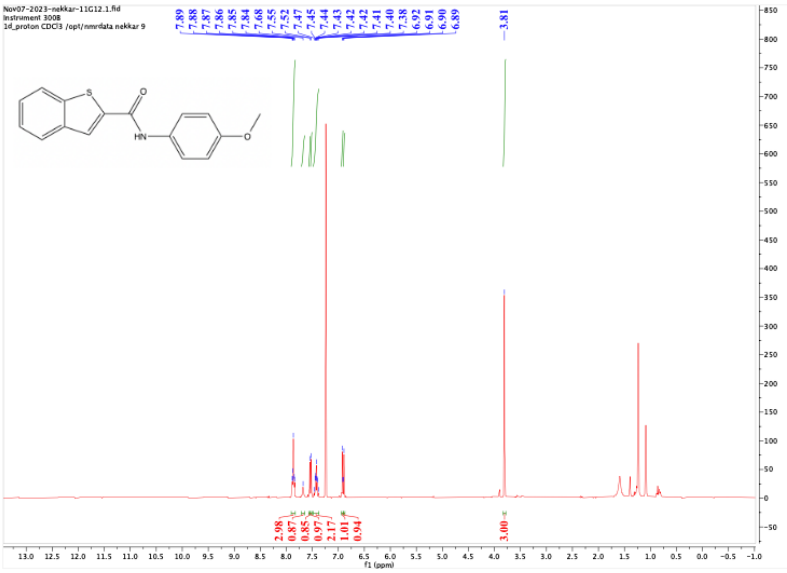


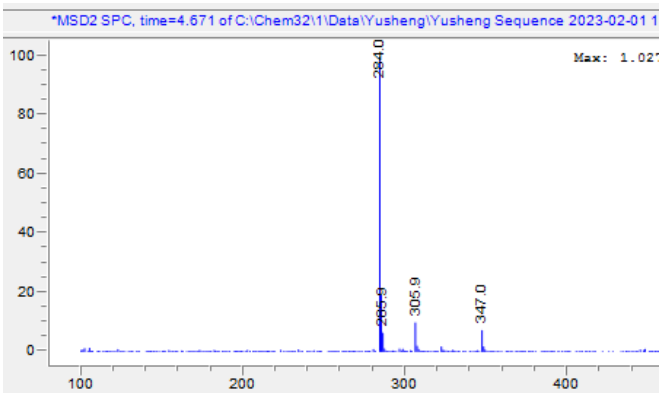


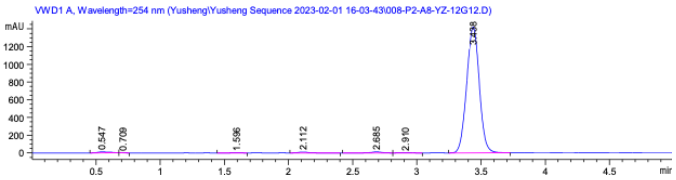


Peak #	RetTime [min]	Type	Width [min]	Area [mAU*s]	Height [mAU]	Area %
1	0.543	BB	0.0916	49.06858	7.28762	0.3526
2	0.711	BB	0.0412	7.97535	3.08173	0.0573
3	1.363	BB	0.0604	17.66060	4.44508	0.1269
4	1.585	BB	0.0661	23.18388	5.29710	0.1666
5	2.507	BB	0.0847	1.37490e4	2516.75195	98.8108
6	2.930	BB	0.1007	13.40386	2.01255	0.0963
7	3.597	BB	0.0999	14.15774	2.26428	0.1017
8	4.282	BB	0.1401	40.02562	4.32154	0.2877
Totals :				1.39145e4	2545.46186	

N-(4-methoxyphenyl)benzo[*b*]thiophene-2-carboxamide (17d)







Peak #	RetTime [min]	Type	Width [min]	Area [mAU*s]	Height [mAU]	Area %
1	0.547	BB	0.0972	72.36466	10.52991	0.7274
2	0.709	BB	0.0397	6.78568	2.75368	0.0682
3	1.596	BB	0.0690	9.26006	2.11881	0.0931
4	2.112	BB	0.0763	50.42281	10.26890	0.5068
5	2.685	BB	0.0827	62.03573	11.54520	0.6235
6	2.910	BB	0.0863	13.47597	2.48512	0.1354
7	3.438	BB	0.1069	9734.72559	1421.36951	97.8456